



Bournemouth University

Design and dynamic simulation of  
mobile manipulators incorporating  
tribological analysis of  
16MnCr5 and EN19 steels

Vivek Chacko

A thesis submitted in partial fulfilment of the requirements of  
Bournemouth University for the degree of Doctor of Philosophy

August 2018

Faculty of Science and Technology  
Bournemouth University

BLANK

## **Copyright statement**

This copy of the thesis has been supplied on condition that anyone who consults it is understood to recognise that its copyright rests with its author and due acknowledgement must always be made of the use of any material contained in, or derived from, this thesis.

BLANK

Vivek Chacko

## **Design and dynamic simulation of mobile manipulators incorporating tribological analysis of 16MnCr5 and EN19 steels**

### **Abstract**

Search and Rescue (SAR) robotics is a growing research area in spite of which reports show that heavy equipment like excavators are still used in SAR operations despite their unsuitability. Literature reveals the need for new designs for application-specific manipulators in time-critical SAR operations. To this end, the Computer Aided Design (CAD)-Multibody dynamics (MBD) simulation technique was applied instead of traditional numerical modelling and roofs-of-concept for two types for manipulators, i.e. anthropoid and complex closed-loop manipulators are presented. The combined friction model (CFM) was incorporated into this simulation considering the importance of friction as a tribological component affecting the dynamic performance of such mobile manipulators. To surmount the limitations of friction models, scaled-down tribological experiments were conducted to determine the coefficient of friction (COF) for two contact geometries - sliding cylinder and sliding pin, selected as approximations of manipulator joint contact. Oil lubricant was used to generate reference COF characteristics against which COF of grease-lubricated contacts were compared, and oil-lubrication showed better COF than grease-lubrication. However, oil is a fluid and it cannot be used in the application environment. Subsequently, the effect of nickel alumina nanocomposite coating on COF deposited on 16MnCr5 specimens using pulse electrodeposition (PED) was analysed. The results showed that this coating only reduced the COF by 3.1% compared to uncoated specimens in sliding cylindrical contacts, while in the case of sliding pin contacts the coating proved to be detrimental with a 22.1% increase in COF. The values of COF were used in a linear model for computing joint torque. Results of surface characterisation carried out using white light interferometry, digital microscopy and scanning electron microscopy substantiate the COF measurements. Microhardness of the surface was also analysed and showed that coatings improved the surface hardness by 19.7% to 55.9%. Therefore, this work contributes to the SAR robotics through design and simulation, and tribology.

BLANK

## Table of contents

<b>Copyright statement</b> .....	<b>2</b>
<b>Abstract</b> .....	<b>5</b>
<b>List of figures</b> .....	<b>12</b>
<b>List of tables</b> .....	<b>20</b>
<b>Preface</b> .....	<b>22</b>
<b>Acknowledgments</b> .....	<b>25</b>
<b>Author's declaration</b> .....	<b>28</b>
<b>List of publications</b> .....	<b>30</b>
<b>Chapter 1 Introduction</b> .....	<b>33</b>
<b>1.1 Research background</b> .....	<b>33</b>
1.1.1 Importance of SAR operations .....	35
1.1.2 Design of mechanical manipulators in SAR.....	36
1.1.3 Friction in manipulator joints .....	38
<b>1.2 Statement of research problem</b> .....	<b>39</b>
<b>1.3 Research questions and research aims</b> .....	<b>40</b>
<b>1.4 Structure of thesis</b> .....	<b>41</b>
<b>1.5 Summary</b> .....	<b>43</b>
<b>Chapter 2 Literature review – 1: Design, modelling and dynamic simulation of mobile manipulators</b> .....	<b>44</b>
<b>2.1 Introduction</b> .....	<b>44</b>
2.1.1 Methodology for literature review.....	45
2.1.2 Search and rescue (SAR).....	46
2.1.3 The case for utilisation of CAD and MBD .....	50
2.1.4 Design and simulation process.....	52
<b>2.2 Design analysis of mobile manipulators</b> .....	<b>54</b>
2.2.1 Design and modelling of manipulator mechanics .....	54
2.2.2 Dynamics .....	59

2.2.3 Friction in manipulator joints.....	62
2.2.4 Commonly used actuators.....	67
2.2.5 Simulation .....	68
<b>2.3 Knowledge gaps and research objectives .....</b>	<b>69</b>
<b>2.4 Summary.....</b>	<b>70</b>
<b>Chapter 3 Literature review – 2: Tribological analysis .....</b>	<b>71</b>
<b>3.1 Introduction: From design modelling and simulation to tribological analysis.....</b>	<b>71</b>
3.1.1 Selection of steel alloy pair.....	73
<b>3.2 Tribological analysis.....</b>	<b>74</b>
3.2.1 Selection of tribometer .....	74
3.2.2 Selection of test parameters for tribo-testing .....	75
3.2.3 Tribometer adapter designs .....	78
<b>3.3 Surface modifications for improved tribo- characteristics.....</b>	<b>79</b>
3.3.1 Use of nickel alumina nanocomposite coatings.....	79
3.3.2 Pulse Electrodeposition (PED) .....	81
3.3.3 Influence of nanocomposite coatings on COF.....	91
3.3.4 Surface characterisation.....	94
<b>3.4 Knowledge gaps and research objectives .....</b>	<b>95</b>
<b>3.5 Combined scope of research and study restrictions .....</b>	<b>96</b>
<b>3.6 Summary.....</b>	<b>97</b>
<b>Chapter 4 Design, modelling and dynamic simulation of mobile manipulators .....</b>	<b>98</b>
<b>4.1 Introduction .....</b>	<b>98</b>
4.1.1 Relevance and context of research .....	99
<b>4.2 Design of mobile manipulators.....</b>	<b>101</b>
4.2.1 Selection of design input parameters .....	101
4.2.2 Design case studies .....	104
4.2.3 Exporting CAD model to MBD environment .....	111
4.2.4 Modelling sensitivity and validation .....	112



<b>4.3 Multibody dynamic (MBD) simulation analysis.....</b>	<b>113</b>
4.3.1 Block diagram representation of physical systems.....	113
4.3.2 Validation of simulation.....	134
4.3.3 Simulation parameters.....	137
4.3.4 Input signal modification .....	139
<b>4.4 Simulation case studies with friction .....</b>	<b>141</b>
4.4.1 Input signal for actuating the validation simulation .....	141
4.4.2 Case 1: Anthropoid manipulator .....	143
4.4.3 Case 2: Serial open-chain manipulator.....	150
4.4.4 Case 3: Closed-loop complex manipulator .....	153
<b>4.5 Summary .....</b>	<b>159</b>
<b>Chapter 5 Tribological analysis of 16MnCr5 and EN19 steels</b>	<b>160</b>
<b>5.1 Introduction .....</b>	<b>160</b>
<b>5.2 Measurement of coefficient of friction (COF) using the reciprocating tribometer .....</b>	<b>161</b>
5.2.1 Tribometer test rig to simulate sliding contact.....	162
5.2.2 Kinematics of the reciprocating tribometer.....	164
5.2.3 Parameters and procedure for conducting experiments .....	165
5.2.4 Design of modified adapters for tribo-testing .....	168
5.2.5 Design and preparation of test specimens .....	173
<b>5.3 Pulse Electro Deposition (PED) of nickel alumina nanocomposite on 16MnCr5.....</b>	<b>176</b>
<b>5.4 Analysis of surface characteristics of the test specimens .....</b>	<b>180</b>
5.4.1 White light interferometry.....	181
5.4.2 Digital microscopy .....	182
5.4.3 Surface hardness testing.....	185
5.4.4 Scanning Electron Microscopy .....	187
<b>5.5 Summary .....</b>	<b>189</b>
<b>Chapter 6 Results and discussion – 1: Mechanics simulation</b>	<b>190</b>
.....	
<b>6.1 Introduction .....</b>	<b>190</b>

<b>6.2 Simulation results: case studies .....</b>	<b>190</b>
6.2.1 Case 1 – Anthropoid manipulator .....	190
6.2.2 Case 2 – serial open-chain manipulator .....	195
6.2.3 Case 3 – closed loop complex manipulator .....	200
<b>6.3 Discussion .....</b>	<b>227</b>
6.3.1 Evaluation of CAD-MBD simulation analysis .....	227
<b>6.4 Summary .....</b>	<b>229</b>
<b>Chapter 7 Results and discussion – 2: Tribological analysis of 16MnCr5 and EN19 steels .....</b>	<b>230</b>
7.1 Introduction .....	230
7.2 Simulation of tribometer kinematics .....	231
<b>Part – 1: Experimental determination of COF for uncoated 16MnCr5 and EN19 steels .....</b>	<b>233</b>
7.3 Sliding cylindrical contacts .....	234
7.3.1 COF from tribo-analysis .....	234
7.4 Sliding pin contacts .....	237
7.4.1 COF from tribo-analysis .....	237
<b>Part – 2: Experimental determination of COF for coated specimens....</b>	<b>240</b>
7.5 Sliding cylindrical contact with nanocomposite coating .....	240
7.6 Sliding pin contact with nanocomposite coating .....	242
7.7 Discussion .....	243
<b>Part – 3: Analysis of surface characteristics .....</b>	<b>249</b>
7.8 Measurement of surface hardness .....	249
7.9 Measurement of surface characteristics .....	250
7.10 Discussion .....	263
7.11 Summary .....	264
<b>Chapter 8 Conclusions and Future Research.....</b>	<b>266</b>
8.1 Background .....	266

8.2 Research outcomes .....	266
8.3 Contributions to knowledge .....	268
8.4 Practical applications and benefits.....	269
8.5 Limitations and difficulties of this work .....	270
8.6 Future directions .....	271
8.7 Final considerations and summary .....	272
References.....	274
Appendix A: Excavator manipulator parameters.....	1
Appendix B: Design of anthropoid and complex manipulator ...	2
Appendix C: MATLAB code for revolute friction joint.....	23
Appendix D: Kinematics of manipulator.....	24
Appendix E: Simulink diagram for tribometer kinematics.....	27
Appendix F: Lubricant properties .....	28
Appendix G: Models governing pulse electro deposition (PED) .....	30
Appendix H: Hertzian contact parameters .....	32
Appendix I: Calculation of pulse current parameters and coating thickness.....	34
Appendix J: Additional images .....	35
Appendix K: Buehler Vickers hardness micro-indentation manual.....	37
Appendix L: Nickel graphene nanocomposite coatings.....	41
Appendix M: Uncertainty measurements .....	43
Appendix N: Publications.....	44
Glossary .....	56

## List of figures

Figure 1 a) excavators in SAR environment (Z. Ahmed 2014) and b) miniature robot with sensor-mounted arm (Carlson and Murphy 2005) .....	33
Figure 2 Victim survival rate (Walker 1991).....	35
Figure 3 A robot with mobile manipulator (Murphy et al. 2009) .....	37
Figure 4 Structure of thesis .....	41
Figure 5 Workflow of research .....	44
Figure 6 Schematic representation of the literature review .....	46
Figure 7 Schematic representation of the interdisciplinary nature of the research area (Khan et al. 2017) .....	47
Figure 8 a) Different SAR domains (Statheropoulos et al. 2014) and b) three zones in SAR site (Murphy 2004b) .....	49
Figure 9 Procedure for CAD-MBD simulation adapted from (Barone et al. 2002) .....	53
Figure 10 a) Serial open chain manipulator and b) closed-loop manipulator (Chacko 2014) .....	55
Figure 11 Block diagram model of the wiper system presented in (Dooner et al. 2015) .....	58
Figure 12 Forces and moments acting on a moving link connected to a fixed link through a sDOF revolute joint (Chacko and Khan 2017).....	60
Figure 13 Combined friction model (CFM) with zero velocity crossing (Khan et al. 2017).....	64
Figure 14 Simple model with a point load for friction torque computation .....	66
Figure 15 Contact forces and pressure profile in pin and bushing (Colbert et al. 2010) .....	66
Figure 16 Range of COF against lubrication condition (Armstrong-Hélouvry et al. 1994).....	77
Figure 17 V-notch design in the tribometer adapter (Sebastian and Bhaskar 1995) .....	78
Figure 18 Different types of waveforms a) sine b) rectangular and c) triangular waveforms .....	83
Figure 19 Current intensity and particle incorporation for 50nm $\gamma$ -alumina ( $Al_2O_3$ ) particles for different loading rates: (■) 10g/l, (□) 30g/l, (●) 60g/l, (○) 90g/l, (▲) 120 g/l (Thiemig et al. 2009).....	84

Figure 20 Effect of duty cycle on volume of alumina nanoparticles incorporated into the matrix (Jung et al. 2009).....	86
Figure 21 Table showing COF from various tests (Mahidashti et al. 2017) .....	92
Figure 22 Layout of Chapter 4 design, modelling and dynamic simulation of mobile manipulators .....	98
Figure 23 Procedure for the development and validation of manipulator models .....	100
Figure 24 Design and case studies .....	101
Figure 25 Pin and bushing joint assembled in CAD .....	103
Figure 26 Process of design of a link in CAD beginning with two-dimensional sketch and ending with three-dimensional part .....	105
Figure 27 CAD Design for the anthropoid manipulator with sDOF joints (Khurshid et al. 2016).....	107
Figure 28 Links of the manipulator mechanism .....	108
Figure 29 Four-link serial open-chain linkage assembled using links from above figure .....	109
Figure 30 CAD design assembly of closed-loop manipulator prototype .....	110
Figure 31 a) Exporting from CAD environment to MBD package b) tolerance and geometry settings during export .....	112
Figure 32 Importing CAD data into the MBD simulation environment in MATLAB .....	113
Figure 33 Block diagram representation of closed-loop complex manipulator mechanism and parts labelled (Chacko and Khan 2017) .....	115
Figure 34 Core blocks of the model – a) world, system configuration and solver blocks b) world frame, c) configuration, d) solver, and e) rigid transform	118
Figure 35 Core blocks of the model – a) rigid body blocks, b) settings for the solid block, c) reference frame for the rigid body block d) transformation frames and e) physical modelling connection port connecting the body to a joint block .....	121
Figure 36 a) Block element and b) property settings for the sDOF revolute joint block c) Block diagram and d) properties and settings for the two degrees of freedom cylindrical joint block constrained in the rotational direction ..	124
Figure 37 a) 'Goto' block b) configuration c) 'From' block and d) its configuration .....	125
Figure 38 a) 'To workspace' block and b) configuration settings .....	126

Figure 39 Mux bar converts multiple signals into a composite signal .....	127
Figure 40 a) External force and torque block and b) parametric settings for the block .....	128
Figure 41 a) Signal builder block used for generating simulation input signals and b) parametric settings for the block .....	128
Figure 42 a) Simulink to Physical Systems block b-c) and parameter settings .....	129
Figure 43 a) Physical Signal to Simulink conversion block and b) parameter settings .....	130
Figure 44 a) Mechanical translational reference b) specifications of the block c) ideal translational reference block d) specifications of the block e) Ideal force sensor block f) specifications g) translational friction block and h) block parameters .....	132
Figure 45 Block diagram representation of the translational friction model ....	133
Figure 46 The model based graphical visualization form of the first loop of the manipulator linkage a) for first generation simulation and b) for second generation simulation (Chacko and Khan 2017) .....	136
Figure 47 a) Sine Wave block and b) parameters settings for the sine wave generator block .....	138
Figure 48 a) Signal builder block used for generating simulation input signals and b) parametric settings for the block .....	138
Figure 49 Generation of input signal incorporating a transfer function based differentiation method where the parameter <i>tau</i> can be adjusted (Chacko and Khan 2017) .....	139
Figure 50 a) Input signal and time derivatives and b) parameters for differential function .....	140
Figure 51 a) Modified differential functions and b) coefficient <i>s</i> and denominators for the transfer functions .....	140
Figure 52 Actuator input signal: amplitude = 0.025, bias = 0.02, frequency = 1 rad/sec, the velocity and acceleration are derivatives of the main input signal .....	142
Figure 53 Manipulator design showing input parameters adapted from (Khurshid et al. 2016).....	143
Figure 54 SimMechanics 2 <sup>nd</sup> generation block diagram representation of the anthropoid manipulator (Khurshid et al. 2016) .....	144

Figure 55 Input signals generated with four different solvers for the anthropoid manipulator corresponding to simulations 1-4 .....	149
Figure 56 SimMechanics 2 <sup>nd</sup> generation model for serial open-chain manipulator .....	150
Figure 57 a) Angular displacement, b) angular velocity (rad/s) and c) angular acceleration of the revolute joint (rad/s <sup>2</sup> ) .....	152
Figure 58 Block-model layout of the closed-loop mechanism in SimScape showing three kinematic loops .....	153
Figure 59 Visualisation of the simulation output .....	154
Figure 60 Input signals for simulation 1 .....	156
Figure 61 Input signals for simulation 2 .....	157
Figure 62 Input signals for simulation 3 .....	158
Figure 63 Layout for experimental procedures followed in this chapter .....	160
Figure 64 Reciprocating tribometer .....	163
Figure 65 a) sliding cylindrical contact pair and b) sliding pin contact pair .....	163
Figure 66 Normal load and friction force generated in a sliding contact .....	164
Figure 67 Scotch-yoke mechanism (Sawyer et al. 2003) .....	164
Figure 68 Use of lubricants in the tribo-tests .....	166
Figure 69 Placement of cylindrical specimen in a conventional adapter showing contact between specimen and adapter .....	168
Figure 70 a) Engineering drawing of modified adapter design for holding cylindrical specimens, b-d) detailed views of modified adapter fabricated using EDM .....	170
Figure 71 a) Engineering drawing of the modified adapter design for holding pin specimens, b-c) detailed views of modified adapter manufactured using EDM .....	172
Figure 72 Calculation of specimen thicknesses using internal clearance between upper and lower shafts of the reciprocating tribometer .....	173
Figure 73 Original rectangular design of the reciprocating test specimen a) physical specimen and b) CAD design .....	174
Figure 74 a) Circular reciprocating specimen, b) fixed cylindrical specimen and c) fixed pin specimen .....	175
Figure 75 Rotary table polisher .....	175
Figure 76 Workflow for PED of nanocomposite coating on 16MnCr5 specimen .....	177

Figure 77 Schematic representation of the modified Watts bath for PED.....	178
Figure 78 Experimental setup for PED.....	179
Figure 79 White light interferometer.....	181
Figure 80 Digital microscope.....	183
Figure 81 Objective lens attachments a) x30-x150, b) x250-x2500.....	184
Figure 82 Vickers micro-hardness tester.....	186
Figure 83 Hardness measurement of micro-indentation.....	186
Figure 84 Scanning Electron Microscope with EDS attachment.....	187
Figure 85 a-c) End-effector motion in two-dimensional task space and d) for three-dimensional task space for different simulations of the anthropoid manipulator.....	193
Figure 86 Comparison of friction torque computed at the first two joints using different solvers.....	194
Figure 87 Comparison of execution times for 4 solvers used in simulations ..	195
Figure 88 Serial open-chain manipulator showing the joints 1,2 and 3.....	196
Figure 89 Computed torque from SimMechanics 1 <sup>st</sup> generation simulation ...	197
Figure 90 Reaction torque from SimMechanics 1 <sup>st</sup> generation simulation.....	197
Figure 91 Computed torque generated in SimMechanics 2 <sup>nd</sup> generation.....	198
Figure 92 Reaction torques for the 3 joints computed in SimMechanics 2 <sup>nd</sup> generation.....	199
Figure 93 Difference between a) computed torque and b) reaction torque from the two simulation results.....	200
Figure 94 First kinematic loop of the closed-loop manipulator mechanism ....	201
Figure 95 Comparison of friction torque computed at the revolute joint using SimMechanics 1 <sup>st</sup> and 2 <sup>nd</sup> generation simulations.....	201
Figure 96 a) Friction force and b) torque computed using the combined friction for sDOF prismatic and revolute joints.....	202
Figure 97 Output joint kinematic parameters including a) joint angle b) angular velocity and c) angular acceleration.....	204
Figure 98 End-effector motion in planar task space.....	205
Figure 99 a-c) Friction force at actuator.....	206
Figure 100 a-c) Actuation force.....	207
Figure 101 a-c) Total force.....	208
Figure 102 a-c) Friction torque at revolute joint.....	209
Figure 103 a-c) Torque.....	210



Figure 104 Output - angular parameters .....	211
Figure 105 Motion of the end-effector in planar task space .....	212
Figure 106 a-c) Friction force at actuator .....	213
Figure 107 a-c) Actuation force .....	214
Figure 108 a-c) Total force .....	215
Figure 109 a-c) Friction torque at revolute joint .....	216
Figure 110 a-c) Torque.....	217
Figure 111 a-c) Output - angular parameters .....	218
Figure 112 Motion of the end-effector in planar task space .....	219
Figure 113 a-c) Friction force at actuator .....	220
Figure 114 a-c) Actuation force .....	221
Figure 115 a-c) Total force .....	222
Figure 116 a-c) Friction torque at revolute joint .....	223
Figure 117 a-c) Torque.....	224
Figure 118 a) Mechanics explorer window showing the dynamic simulation views and b) components of the simulation model .....	227
Figure 119 Classification of test results based on lubrication .....	230
Figure 120 Kinematics of the reciprocating mechanism for $r = 5\text{mm}$ and frequency $F = 10\text{Hz}$ a) displacement (mm) b) velocity (mm/s) and c) acceleration ( $\text{mm/s}^2$ ) .....	233
Figure 121 COF for oil-lubricated sliding cylindrical contact .....	235
Figure 122 COF for grease-lubricated sliding cylindrical contacts .....	236
Figure 123 COF for oil-lubricated sliding pin contacts .....	238
Figure 124 COF for grease-lubricated sliding pin contacts .....	239
Figure 125 COF for grease-lubricated nickel alumina nanocomposite coated sliding cylindrical contacts .....	241
Figure 126 COF for grease-lubricated nickel alumina nanocomposite coated sliding pin contacts .....	243
Figure 127 Average COF for coated and uncoated sliding cylindrical contacts .....	246
Figure 128 Average COF for coated and uncoated sliding pin contacts .....	246
Figure 129 Average COF for coated and uncoated sliding pin and cylindrical contacts.....	247
Figure 130 Friction computed using the equation presented in (Colbert et al. 2010).....	248

Figure 131 a-e) Profiles for rough surfaces, f-j) profiles for the polished surface and k-m) coated surface profiles .....	252
Figure 132 Test specimen surface for nickel alumina nanocomposite coating deposited at 5A/dm <sup>2</sup> at a) x100 b) x500 and c) x1000 magnification factor .....	254
Figure 133 Test specimen surface for nickel alumina nanocomposite coating deposited at 10A/dm <sup>2</sup> at a) x100 b) x500 and c) x1000 magnification.....	255
Figure 134 Oil-lubricated specimens a-b) CO1 c) CO2 d) CO3 .....	255
Figure 135 Grease-lubricated uncoated specimen, CG1 .....	256
Figure 136 Grease-lubricated coated specimen, CA1 .....	256
Figure 137 Grease-lubricated coated specimen, CA2.....	257
Figure 138 a-b) Grease-lubricated coated specimen, CA3 .....	257
Figure 139 a-b) Grease-lubricated coated specimen, CA4 .....	258
Figure 140 a-b) Grease-lubricated coated specimen, CA5 .....	258
Figure 141 a-b) Oil-lubricated uncoated specimen, FO1 .....	258
Figure 142 a-b) Oil-lubricated uncoated specimen, FO2.....	259
Figure 143 Oil-lubricated uncoated specimen, FO3 .....	259
Figure 144 Grease-lubricated uncoated specimen, FG1 .....	260
Figure 145 Grease-lubricated uncoated specimen, FG2.....	260
Figure 146 Grease-lubricated uncoated specimen, FG3.....	261
Figure 147 Grease-lubricated uncoated specimen, FG4.....	261
Figure 148 Grease-lubricated uncoated specimen, FG5.....	261
Figure 149 Grease-lubricated uncoated specimen, FG6.....	261
Figure 150 Grease-lubricated uncoated specimen, FG7.....	261
Figure 151 Grease-lubricated coated specimen, FA01 .....	262
Figure 152 Grease-lubricated coated specimen, FA02, FA03.....	262
Figure 153 Grease-lubricated coated specimen, FA04 .....	262
Figure 154 Grease-lubricated coated specimen, FA05, FA06.....	263
Figure 155 Application of modelling outcomes for practical applications.....	270
Figure 156 Physical parameters of the excavator manipulator (Vähä et al. 1991) .....	1
Figure 157 Two-dimensional sketch of the anthropoid manipulator created in CAD .....	2
Figure 158 Upper arm of the anthropoid manipulator.....	3
Figure 159 Lower arm of the anthropoid manipulator.....	5

Figure 160 Forearm of the anthropoid manipulator .....	7
Figure 161 Hand of the anthropoid manipulator .....	9
Figure 162 Base of the complex closed-loop manipulator .....	11
Figure 163 Boom of the complex closed-loop manipulator .....	13
Figure 164 Stick of the complex closed-loop manipulator .....	15
Figure 165 Bucket of the complex closed-loop manipulator .....	17
Figure 166 Boom actuator of the complex closed-loop manipulator .....	19
Figure 167 Stick actuator of the complex closed-loop manipulator.....	21
Figure 168 MATLAB code for torque generated in sDOF revolute joint using CFM .....	23
Figure 169 Generic robot manipulator as a serial open-chain linkage with the link coordinate and base coordinate system (Chacko et al. 2014, Chacko and Khan 2017).....	25
Figure 170 a) revolute joint b) prismatic joint (Uicker et al. 2003).....	25
Figure 171 Block diagram representation of tribometer kinematics in Simulink environment .....	27
Figure 172 Specifications of the 10W40 oil lubricant .....	28
Figure 173 Specifications of the molybdenum grease lubricant .....	29
Figure 174 The process of nanocomposite surface coating development based on (Jung et al. 2009) .....	31
Figure 175 a) Hertzian contact pressure b) shear stress depth and c) maximum pressure and shear stress.....	33
Figure 176 Calculation of pulse current parameters and coating thickness.....	34
Figure 177 a-d) Specimens coated with 2A exhibit inferior deposition characteristics for lower current intensities.....	35
Figure 178 a-b) Specimens coated with 2.0A current b) 0.05A current exhibit inferior characteristics .....	35
Figure 179 Grease-lubricated uncoated specimens CG4-7.....	36
Figure 180 Manual for Vickers micro-hardness indenter .....	40
Figure 181 a-c) COF for grease-lubricated sliding pin contacts with nickel graphene coating .....	41
Figure 182 Peak and average COF for nickel graphene coated sliding pin contact .....	42
Figure 183 SEM images for nickel graphene nanocomposite coating .....	42

## List of tables

Table 1 Research questions and aims .....	40
Table 2 Outline of chapters and focus areas .....	43
Table 3 Research aims and corresponding objectives for literature review-1...	70
Table 4 Composition of 16MnCr5 steel alloy (West Yorkshire Steel 2017) .....	73
Table 5 Composition of EN19 steel (Steel 2017) .....	73
Table 6 Comparison of electrolyte compositions for PED of nickel alumina nanocomposite coating .....	90
Table 7 Research aims and corresponding objectives for literature review-2...	96
Table 8 Design input parameters for anthropoid manipulator .....	105
Table 9 Link specifications and parameters for the serial open-chain manipulator .....	108
Table 10 Link specifications and parameters for actuators .....	110
Table 11 Input parameters for simulation using sine wave block .....	155
Table 12 Composition of electrolyte used for PED .....	177
Table 13 Pulse parameters for PED .....	179
Table 14 Average and maximum COF for sliding oil-lubricated cylindrical contacts .....	235
Table 15 Average and maximum COF for sliding grease-lubricated cylindrical contacts .....	237
Table 16 Average and maximum COF for sliding oil-lubricated pin contacts..	238
Table 17 Average and maximum COF for sliding grease-lubricated pin contacts .....	240
Table 18 Average and maximum COF for grease-lubricated sliding cylindrical contacts with nickel alumina nanocomposite coating .....	242
Table 19 Average and maximum COF for grease-lubricated sliding pin contacts with nickel alumina nanocomposite coating .....	243
Table 20 Results of Vickers micro-indentation tests for uncoated 16MnCr5 specimens.....	249
Table 21 Results of Vickers micro-indentation tests for coated 16MnCr5 specimens.....	249
Table 22 Surface profiles parameters corresponding to images from interferometry measurements .....	253
Table 23 Measurement uncertainties for $R_a$ from interferometry data .....	253
Table 24 Parameters for computing Hertzian contact characteristics.....	32

Table 25 Average and maximum COF for grease-lubricated pin contact with  
nickel graphene coating ..... 42

BLANK

## Preface

The genesis of this thesis has not been a straightforward process to say the least. The working titles have undergone substantial change from the time of starting work in 2014 as have the research direction and the team. Originally titled “Analysis of wheel-leg hybrid rescue robots”, the initial scope of the thesis included the design, simulation and control of small robots for deployment in Search and Rescue (SAR) environments. While the challenge of working in robotics/control systems at postgraduate level as a mechanical engineer specialising in machine design was very interesting, there had been more than one factor (including a period of supervisory change) contributing to the change in research direction in mid-2015 to “Dynamic modelling of complex interacting systems deployed in harsh operating conditions.” It was initially envisaged that the research would focus on an in-depth analysis of wear of coated samples, which was also the research theme of the new team. However, this was re-assessed and changed to “Design and dynamic simulation of mobile manipulators incorporating tribological analysis of 16MnCr5 and EN19 steels” following the initial submission of the thesis in 2017 in order to be able to cohesively connect the work undertaken in the first phase of the research to the tribological study undertaken in the second phase. The thesis in its final form looks at proposing a first level design of mobile manipulators in a time-critical and application-specific manner as necessitated by SAR conditions using the Computer Aided Design (CAD)-Multibody Dynamics (MBD) approach and thereafter is aimed at factoring in friction, which is a very important factor affecting dynamic performance of manipulator joints. This part of the research begins with friction modelling in the MBD environment and moves onto scaled-down tribo-testing, thereby segueing the two major streams of research undertaken during the course of this thesis. This work was an initial investigation which sets the stage for further research, and this is outlined in the final chapter of this thesis. Some of the work undertaken (such as kinematics) had to be relegated to the appendix to remain within the scope of the final thesis title as well as to ensure the coherence of the research problem. It goes without saying that this work would not have been possible but for the support (both financial and otherwise) and love from a lot of people and I have taken the liberty of acknowledging them at least in spirit if not in name (since it would be a task too tedious) in the Acknowledgements page succeeding this brief preface.

BLANK



## **Acknowledgments**

I wish to thank my supervisors Professor Zulfiqar Khan and Dr Mehran Koohgilani, especially for their support and encouragement during the challenging period after initial supervisory change. I also wish to thank my examiners, Professor Rakesh Mishra and Professor Kamran Tabeshfar, and the examination chair, Professor Peter Hogarth, for their valuable comments and suggestions which have helped reshape this thesis. I wish to acknowledge with gratitude the research funding received from the EACEA as well as from Bournemouth University.

I wish to express my sincerest gratitude to Dr Simon Watts (UEA), Dr Antti Lyyra (LSE), Dr T J Moorhouse and Mrs R Moorhouse for their valuable feedback on the thesis chapters. Many thanks for the support and advice received from Professor Siamak Noroozi, Dr Nigel Garland, Dave Fletcher Jones of M/s FJ engineering, Dr Dean Burnard, Robert Gardiner, Will Lambert and Shaun Bendall. I wish to thank Anne Mackay and Hannah Coles of SUBU Advice, Sharon Hartwell (Associate Chaplain), Dr Andrew Main, Professor Matt Bentley and Professor Christine Maggs for their professionalism and support during the supervisory change and the administrative challenges thereafter.

I would like to sincerely thank Rev Dr I Terry, Rev Dr D G MacEwan, Rev A Humphreys, Rev R Higgins, Rev B Oxburgh and the Very Rev J Auld, all of whom have not only lent me an ear at the time of need, but also made me feel welcome and loved without any prejudice. I also wish to thank Mr D L Ross for his kindness, support and the visits to all those quaint cafés, which bolstered my fledgling faith in humanity.

Family is important, especially when sojourning through paths less trodden. For this, I wish to thank my father, P C Chacko, for having instilled the spirit of patience, enquiry and the most cat-like curiosity, as well as my mother, Alice, who has been a great support. Gratitude goes out to my parents-in-law, Desmond and Nalini Netto, especially for their wonderful daughter, my wife Anisha, who has been by my side with unwavering devotion and love through the trials and tumults of this wee journey.

BLANK

This thesis is dedicated to the memory of my late grandfather, Professor P C Chacko, whose sheer brilliance has inspired me to strive and not yield in the face of adversity.

*Tho' much is taken, much abides; and tho'  
We are not now that strength which in old days  
Moved earth and heaven, that which we are, we are;  
One equal temper of heroic hearts,  
Made weak by time and fate, but strong in will  
To strive, to seek, to find, and not to yield.*

Alfred, Lord Tennyson, *Ulysses*

BLANK

## **Author's declaration**

I, Vivek Chacko, hereby certify that this thesis has been written by me, and that it is the record of work carried out by me, or principally by myself in collaboration with others as acknowledged, and that it has not been submitted in any previous application for a higher degree.

BLANK

## List of publications

### Peer-reviewed journal publications

- 1) **Chacko, V.** and Khan, Z. A., 2017. Dynamic Simulation of a Mobile Manipulator with Joint Friction. *Tribology in Industry* [online], 39 (2), 152–167. Available from: <http://eprints.bournemouth.ac.uk/29280/>.
- 2) Khan, Z. A., **Chacko, V.**, & Nazir, H. (2017). A review of friction models in interacting joints for durability design. *Friction*, 5(1), 1–22. Available from: <https://doi.org/10.1007/s40544-017-0143-0>
- 3) Bajwa, R., Khan, Z., Nazir, H., **Chacko, V.**, & Saeed, A. (2016). Wear and Friction Properties of Electrodeposited Ni-Based Coatings Subject to Nano-enhanced Lubricant and Composite Coating. *Acta Metallurgica Sinica (English Letters)*, 29(10), 902–910. Available from: <https://doi.org/10.1007/s40195-016-0470-6>
- 4) Khurshid, A., Khan, Z. A., **Chacko, V.**, Ghafoor, A., Malik, M. A., and Ayaz, Y., 2016. Modelling and Simulation of a Manipulator with Stable Viscoelastic Grasping Incorporating Friction. *Tribology in Industry* [online], 38 (4), 559–574. Available from: <http://www.tribology.fink.rs/journals/2016/2016-4/13.pdf>.

### Conference presentations

- 1) **Chacko, V.** and Khan, Z. A., 2017. Tribological characteristics of EN-19 and 16MnCr5 steel under varying roughness and lubrication. In: 2017 STLE Annual Meeting and Exhibition.
- 2) **Chacko, V.**, Yu, H., Cang, S., and Vladareanu, L., 2014. State of the art in excavators. In: Proceedings of the 2014 International Conference on Advanced Mechatronic Systems [online]. IEEE, 481–488. Available from: <https://doi.org/10.1109/ICAMechS.2014.6911593>

### Online articles

- 1) **Chacko, V.** and Yu, H., 2015. Multi-body simulation methods for rigid manipulators. Eurathlon/SHERPA [online]. Available from: <http://www.eurathlon.eu/wp-content/uploads/2015/09/Multi-body-simulation-methods-for-rigid-manipulators.pdf>

## **Poster presentations**

- 1) **Chacko, V.**,2018. Design, Manufacture and Commissioning of a New Adapter Design for the Reciprocating Tribometer. In: 10<sup>th</sup> Annual Postgraduate Research Conference, Bournemouth University [7 March 2018]
- 2) **Chacko, V.**,2016. Complex interacting systems working in harsh operating conditions. In: 8<sup>th</sup> Annual Postgraduate 2 Day Conference, Bournemouth University [9-10 March 2016]
- 3) **Chacko, V.**,2015. Simulations in the design of a 3-link manipulator prototype. In: SciTech Postgraduate Research Conference, Bournemouth University [20 May 2015]
- 4) **Chacko, V.**,2015. Modelling, Control and Simulation of Excavator Manipulator. In: 7th Annual Postgraduate Conference 2015, Bournemouth University [20-21 January 2015]
- 5) **Chacko, V.**,2014. Modelling and Adaptive control of an excavator. In: 7th Annual Post Graduate Research Student Poster Competition, Bournemouth University [21 May 2014]

## **Summer school**

- 1) euRathlon/SHERPA Summer School 2015 on Field Robotics, 1-5th June 2015, Oulu, Finland (Fully funded).



# Chapter 1 Introduction

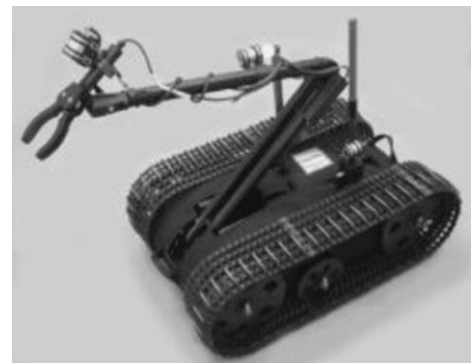
## 1.1 Research background

Search and rescue (SAR) operations are conducted in the aftermath of natural or man-made disasters. These operations have gained widespread importance considering the increasing number of urban disasters. In this context, the use of expendable robots which mitigate risk to humans and canine rescue agents is an area of increasing research.

SAR operations are extremely time-critical and there exists only a narrow window of opportunity to find and rescue victims (Adams et al. 2007). While (Lioy et al. 2002) have noted that harsh environments adversely affect the health and well-being of rescue workers, it has been shown that risk to rescue agents (both human and canine) can be mitigated through the use of robots (Marconi et al. 2012). However, it has been reported that in several cases, especially in developing countries, excavators having heavy manipulators have been deployed after urban disasters in the absence of specialised robots. The use of these equipment occurs in two phases: i) during the ingress and egress of rescuers by clearing debris, and ii) during the process of site restoration after SAR operation is complete. Rubble removal using excavators generally occurs at the beginning of the rescue operation for providing site access to rescue agents. The operation continues after the rescue of victims is complete and involves removal of debris and site restoration – this is called the economic recovery phase (Murphy 2014).



a)



b)

Figure 1 a) excavators in SAR environment (Z. Ahmed 2014) and b) miniature robot with sensor-mounted arm (Carlson and Murphy 2005)

From literature, it has been understood that robots have been deployed successfully in disaster sites with the primary objective of searching for victims trapped under debris (Egawa et al. 2013) as seen in Figure 1. Mobile robotic platforms capable of carrying load have been developed over the past decade and are becoming increasingly versatile (Raibert et al. 2008, Anon. 2012). However, these mobile robots do not appear to have manipulators or robotic arms capable of lifting heavy loads such as rubble found in SAR sites. Also, very few durable and resilient robotic equipment for SAR operations have been reported in literature (Hirayama and Ito 2008, Chacko et al. 2014) and machinery used in the construction industry continues to be deployed in first response to disasters (Egawa et al. 2013). This is either due to the fact that the development of task-specific robotic equipment for SAR is either still in its early stages or because the design and fabrication of such equipment is a resource and expertise intensive process. Therefore, the solution envisaged in the first part of this research was to improve the excavator manipulator for use in SAR operations.

However, a review of literature on SAR revealed that this idea would be unfeasible because these machines have not been designed or tested for use in SAR environments. Moreover, vibration from heavy equipment can destabilise debris leading to secondary incidents which would adversely affect site, victims and rescuers in addition to causing setbacks to the rescue operation. Also, failure of equipment can further hinder SAR operations with very serious repercussions for victims (Carlson and Murphy 2003, Murphy 2004a, Kramer and Murphy 2006). Therefore, deploying equipment which have not been designed specifically for use in SAR environments could jeopardise rescue missions and may result in the loss of life.

In order to prevent this eventuality, SAR missions require specialised equipment that has been designed specifically and purpose-built for such operations, ideally without the burden of high cost. The importance of mobile manipulators in SAR operations can be fully be appreciated only once the importance of SAR operations is analysed and for this reason, the context for the development of mobile manipulators in SAR is presented in the next section.

### 1.1.1 Importance of SAR operations

Natural and urban disasters have received increasing news coverage in recent years. Recent hurricanes Harvey and Irma [2017], Isaac [2012], Fukushima [2011] which led to the nuclear disaster, Katarina [2005], and Andrew [1992]; earthquakes in Mexico [2017], Nepal [2015], Haiti [2010], Kobe [1995] and San Francisco [1989] (Anthes 2010) are only a few examples of natural disasters which have had affected people seriously. News reports (Z. Ahmed 2014, BBC 2015, Aleem Maqbool 2017) and literature (Benson and Clay 2004, Wisnivesky et al. 2011, Murphy 2014) also reveal the long and short-term impact of natural disasters on economic and human development, which directly implies that the lives and welfare of people are seriously affected. These reports have highlighted the necessity for incorporation of disaster management systems into the long-term policies governing risk-prone areas (Benson and Clay 2004), given that some disasters have had a significantly higher impact e.g. the mortality rate(s) (for the Haiti earthquake) exceeded '10 standard deviations to comparable earthquakes' (Noy 2012). The quantifiable economic impact of disasters runs into hundreds of billions of dollars, even without considering the 'human cost' - over a million people are affected by disasters annually (Kliesen and Mill 1994).

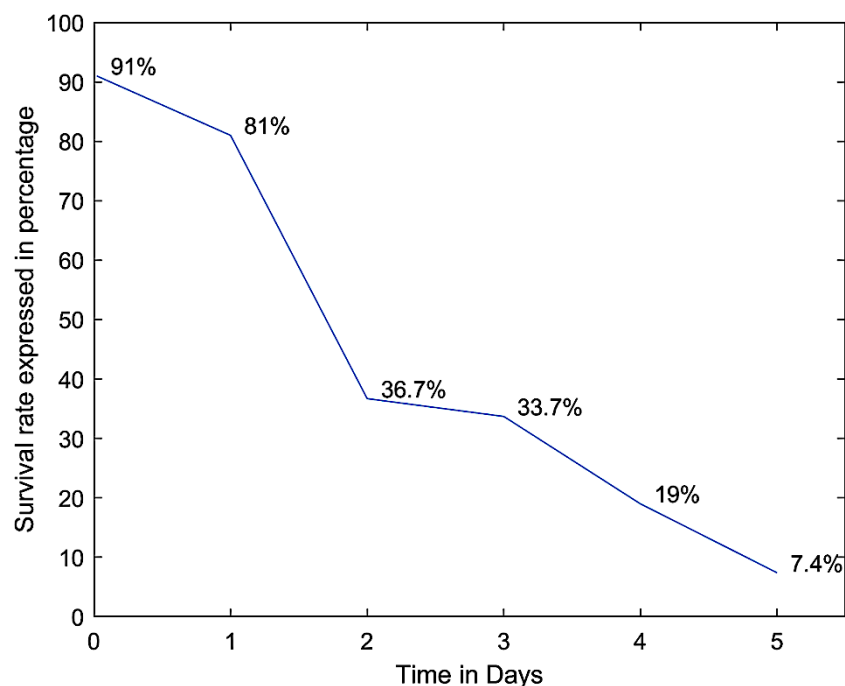


Figure 2 Victim survival rate (Walker 1991)

From the operational perspective, the probability of victim survival drops sharply after 72 hours of the incident as shown in Figure 2 (Walker 1991). Therefore, a rapid and efficient initial response to disasters is crucial for improving chances of survival for trapped victims. According to (Murphy 2014), one method of effectively addressing this issue has been to improve the first response time. Leading researchers in the SAR domain, such as Professor Robin Murphy (Texas A&M University 2008), have advocated the use of mechanical robots to accelerate the SAR process, not only to reduce the impact of the disaster, but also to expedite the complete recovery of an affected region. As mentioned before, having a strategy in place can accelerate recovery from a disaster by several years (Casper and Murphy 2003, Burke et al. 2004). According to (Casper and Murphy 2003, Burke et al. 2004, Stepanova et al. 2017), the use of robotic equipment has expedited rescue operation by assisting human operators working in hazardous environments. Therefore, the future of efficient SAR operations involves the utilisation of specialised robotic actors. In this context, the use of mechanical manipulators for SAR operations has been presented.

### **1.1.2 Design of mechanical manipulators in SAR**

Since the 2001 WTC incident (AAAI 2002), robotic technology has made rapid advancements (Stepanova et al. 2017). Despite these advancements in robotics, excavators and backhoes continue to be used for disaster rescue operations (Egawa et al. 2013, Anon. 2015), although they are not designed for such operations. As mentioned in the previous section, this practice of deploying heavy construction equipment has been deemed to be potentially unsafe due to significant vibration signatures generated by them (Yoo et al. 2010), which may lead to the collapse of volatile debris in disaster sites and trigger cascading incidents. Besides this, the rising number of accidents within the construction industry itself demonstrates the inherent risks associated with heavy construction equipment (Lingard et al. 2013). According to (Statheropoulos et al. 2014), the right tools for the right job are required, which in this case would mean that mobile manipulators which are capable of assisting rescuers can potentially increase the chances of survival of trapped victims by accelerating the first response. Figure 3 shows an example of a robot

platform fitted with a mobile manipulator designed for operation in mine rescue operations (Murphy et al. 2009).



Figure 3 A robot with mobile manipulator (Murphy et al. 2009)

Whilst robotic platforms such as ‘the baby elephant robot’ (Raibert et al. 2008, Anon. 2012, Rashid et al. 2012) and manipulators for operation in especially constricted environments have been reported (Tadokoro et al. 1999, Hirayama and Ito 2008), the requirement for specialised scaled-down mobile manipulators that can assist rescue agents working in SAR operations is emphasised. Also, compared to human and canine agents, mechanical aids such as mobile manipulators are expendable at worst or repairable in the least, and their use leads to mitigation of operational risks, acceleration of rescue operations and reduction of risk of injury to human beings (Lima 2012). This both necessitates and justifies the deployment of specialised mobile manipulators in SAR operations. Therefore, this research firstly investigates mobile manipulator designs.

From literature, it has been seen that previous studies (Vähä et al. 1991, Vähä and Skibniewski 1993, Koivo 1994, Beater and Otter 2003, Towarek 2003, Hoan et al. 2011, Le et al. 2013, Patel and Prajapati 2013, 2014) have reported the numerical modelling and simulation of the mechanics of manipulator linkages including their kinematics and dynamics. However, the use of the conventional method for design, modelling, simulation and manufacturing of manipulators is both time consuming and resource intensive (Lu et al. 2018) and therefore cannot meet the quick turnaround requirements for SAR operations which are time-critical. Also, there appears to be a dearth of new

designs which can be attributed to the complexity of modelling of manipulator mechanics.

### **1.1.3 Friction in manipulator joints**

To develop mobile manipulators for assisting rescue personnel during SAR operations, the use of alternative modelling and simulation techniques have been investigated and an attempt has been made to incorporate friction into the simulation as well. Friction in machine joints is a resistive, non-linear and dissipative dynamic component and is one of three key tribological elements, besides lubrication and wear. (Bhushan 2013a) defines tribology as ‘the art of applying operational analysis to problems of great economic significance, namely, reliability, maintenance, and wear of technical equipment, ranging from spacecraft to household appliances,’ and states that the purpose of research in tribology is to minimise and eliminate ‘losses resulting from friction and wear at all levels of technology where the rubbing of surfaces is involved,’ leading to ‘greater plant efficiency, better performance, fewer breakdowns, and significant savings’. (Bhushan 2013a) also further reiterates that ‘[...] approximately one-third of the world’s energy resources in present use appear as friction in one form or another. Thus, the importance of friction reduction and wear control cannot be overemphasized for economic reasons and long-term reliability’.

In the case of manipulator linkages and mechanisms, friction affects their dynamic performance. According to (Lischinsky et al. 1999, Bai and Zhao 2012), high friction in the manipulator joint leads to actuator fatigue and power loss, which then prevents the manipulator from achieving its designated objective. Therefore, improved friction characteristics in the manipulator joints would improve dynamic performance, thereby resulting in the optimal design of the manipulator. This highlights the need for design and simulation of new mobile manipulators driven by the themes of design and tribology, i.e., design and simulation of manipulators for application-specific tasks in time-critical environments (such as SAR) in whose joints, friction reduction becomes a key parameter for improvement of dynamic performance.

## 1.2 Statement of research problem

It has been seen that large excavators and heavy manipulators that are not designed specifically for use in SAR environments are usually deployed, introducing additional risk of damage in such environments, putting even more lives at risk. This highlights the necessity for specialised equipment for deployment in SAR environments. Even though the use of robots has been increasingly reported in literature in the context of SAR especially in the aftermath of the WTC-9/11 incident the need for application-specific mobile manipulators continues to exist. Although mechanics of heavy mobile manipulators has been investigated in the past couple of decades, the use of conventional numerical modelling methods does not ensure a quick turnaround time from design to fabrication, thereby making this approach unviable for application-specific SAR mobile manipulators. Therefore, there arises the need to explore alternate methods to pure numerical modelling for investigating design, simulation and subsequent fabrication of mobile manipulators with quick turnaround time from design to fabrication – an element which is of paramount importance in time-critical SAR operations.

Friction is a key tribological parameter influencing the dynamic performance of manipulator joints and therefore it is necessary to incorporate joint friction into the design and simulation of the mobile manipulator. Thereafter, as the first step towards improving the dynamic performance of the manipulator, coefficient of friction (COF) in the contact needs to be investigated with the aim of friction reduction. This necessitates the experimental investigation of COF for selected materials and determining whether any surface engineering method would improve the COF and consequently the dynamic performance.

Thus, the problem that is addressed in this work is divide into two parts – firstly design, modelling and simulation of mobile manipulator of dynamics and secondly experimental characterisation of COF which influences manipulator dynamics.

### 1.3 Research questions and research aims

From the above statement of research problem, the following four research questions were formulated, and corresponding aims identified. In the context of this work, the research questions and the corresponding research aims are presented in Table 1. These questions formed the basis of aims which are addressed in the literature review chapters from which the research objectives and parameters are defined.

Design and dynamic simulation	RQ1: How can a mobile manipulator be designed and simulated for SAR application?	RA1: To explore alternative method for design and simulation of mechanical linkages
	RQ2: How can friction be incorporated into the simulation?	RA2: To consider the role of friction in manipulator dynamics
Tribology	RQ3: How can friction in manipulator joints be experimentally measured?	RA3: To analyse feasibility and identify appropriate methods for experimental measurement of COF
	RQ4: How can tribo-characteristics (mainly COF) of contact surface be optimised in manipulator joints?	RA4: To investigate the use of surface engineering techniques for improving contact tribo-characteristics

Table 1 Research questions and aims

As seen from Table 1, the scope of the present work is interdisciplinary, linking design and tribology.



## 1.4 Structure of thesis

Considering the interdisciplinary nature of the work, the thesis has two primary aspects of investigation i.e. design and tribology, which is reflected in the structure of the thesis as well, as can be seen from Figure 4. The thesis is structured as follows:

Chapter 1	• Introduction
Chapter 2	• Literature review-1: Design, modelling and dynamic simulation of mobile manipulators
Chapter 3	• Literature review-2: Tribological analysis
Chapter 4	• Design, modelling and dynamic simulation of mobile manipulators
Chapter 5	• Tribological analysis of 16MnCr5 and EN19 steels
Chapter 6	• Results and discussion – 1: Mechanics simulation
Chapter 7	• Results and discussion - 2: Tribological analysis of 16MnCr5 and EN19 steels
Chapter 8	• Conclusions and future research direction

Figure 4 Structure of thesis

Chapter 1 introduced the research background and context against the backdrop of SAR with focus on mobile manipulators. From the research problem presented, research questions and corresponding aims were identified. Chapters 2 and 3 comprise the detailed literature review and are built on the research aims identified in Chapter 1. The detailed literature review in these two chapters encompass the research themes which include manipulator design, modelling, simulation, experimental determination of coefficient of friction (COF), and finally pulse electro deposition (PED) of nanocomposite coatings. The methodology for the process of literature review is presented in the introduction to Chapter 2 and the combined scope of research and study

restrictions are presented at the end of Chapter 3. It may be noted that the research objectives and knowledge gaps were presented separately in both Chapter 2 and 3. The objectives and scope of research are presented at the end of Chapter 3, drawing on the knowledge gaps identified through literature review. Chapters 4 and 5 comprise the main methods chapters for this thesis. Chapter 4 looks at the detailed modelling procedure for the design of manipulator mechanism, development of virtual prototype, and data exchange between design and simulation packages, thereby implementing CAD-MBD method for design and simulation of mobile manipulators. Chapter 5 provides details of experimental investigations which include analysis of the COF which is a key tribological parameter as well as investigation of PED of nickel alumina nanocomposite coatings. Results are presented in Chapters 6 and 7: Chapter 6 presents the results of modelling and simulation analysis while Chapter 7 presents results of the experimental determination of COF under various contact conditions and a brief analysis of the surface characteristics of the specimens. Chapter 8 brings together the conclusion drawn from the previous two results chapters and also outlines possible future research avenues.

The main focus areas of each chapter are presented in Table 2.

<b>Chapter number</b>	<b>Chapter name</b>	<b>Focus areas</b>
1	Introduction	Research outline, problem definition, statement of research problem, research questions and aims, research objectives
2	Literature review-1	
3	Literature review-2	
4	Design, modelling and dynamic simulation of mobile manipulators	Research focus 1: Utilization of new techniques for designing and simulating the mechanics of SAR manipulators, inclusion of friction model
5	Tribological analysis of 16MnCr5 and EN19 steels	Research focus 2: Experimental methodology for determining COF in joint contact, development of modified adapters, development of nickel alumina nanocomposite coating
6	Results and discussions - 1	Interpretation of data from simulation of manipulator linkages

Chapter number	Chapter name	Focus areas
7	Results and discussions - 2	Results of experimental measurement of COF for coated and uncoated samples
8	Conclusions and future research directions	Contribution to knowledge, practical applications, limitations of research and future research directions

Table 2 Outline of chapters and focus areas

## 1.5 Summary

The introduction chapter to this thesis sets the research context and background from SAR to the need for mobile manipulators. From this, the research problem was stated, and research questions were formulated. The corresponding research aims for this thesis were identified and these form the basis of the detailed literature review presented in Chapters 2 and 3. Thereafter, an overview of the structure of this thesis was presented.

## Chapter 2 Literature review – 1: Design, modelling and dynamic simulation of mobile manipulators

### 2.1 Introduction

The literature reviewed for this thesis is divided into two chapters (Chapter 2 and Chapter 3) and therefore, the methodology followed for literature review in both these chapters is first presented here. As this chapter represents the first part of the literature for this research pertaining to design, modelling and simulation of mobile manipulators, literature on Search and Rescue (SAR) operations is reviewed, elaborating the ideas presented in Chapter 1. Chapter 2 also presents a review of literature on friction and friction models, since the incorporation of friction in the simulation of manipulators, taking into consideration the effect of tribo-characteristics is envisaged. The workflow of this part of the research is diagrammatically presented in Figure 5.

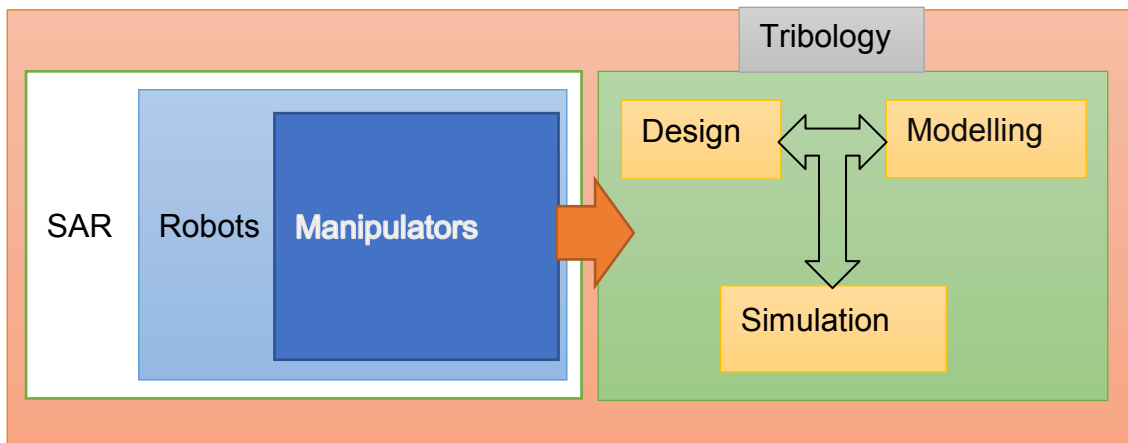


Figure 5 Workflow of research

Chapter 3 deals with friction in greater detail and looks into experimental determination of coefficient of friction (COF) and also surveys literature on techniques to improve COF such as use of nanocomposite coatings. In summary, literature review conducted for this thesis covers the following themes within the scope of this research:

- i. Manipulator dynamic modelling methods and simulation techniques,
- ii. Friction models,
- iii. Measurement of COF ( $\mu$ ), and
- iv. Surface engineering techniques, especially nanocomposite coatings.

The methodology used for conducting the literature review is presented briefly in the following section.

### **2.1.1 Methodology for literature review**

First, literature on SAR environments, methods and considerations were reviewed, followed by literature on SAR robotics. Since this is a comparatively new field of application, key contributors and research centres were identified and literature from these sources were given priority. Thereafter, modelling and simulation literature in the domain of manipulators were reviewed. Techniques and types of analysis of mechanism dynamics were analysed, and special attention was given to the methodology for modelling of manipulator dynamics.

Friction is a resistive and dissipative component in these joints and can adversely affect the dynamic performance. Therefore, literature on friction models was surveyed. Types of joints were summarised, and it was identified that only limited scientific literature was available on the COF characteristics of a widely used steel alloy pair namely 16MnCr5 and EN19 steels used in pin and bushing joints. Following this, techniques for conducting tribo-analysis were also reviewed in order to investigate the tribo-contact characteristics of this steel alloy pair. Surface engineering techniques to improve surface characteristics of contacts were identified along with nanocomposite coatings. Review of coating processes was conducted to identify the optimal coating parameters to include nanocomposite coated surfaces in the tribological analysis to assess COF.

In summary, the literature reviewed covers SAR, design and modelling, simulation, dynamics, and friction model, tribo-analysis and surface engineering techniques. Key focus areas of the literature review are presented in Figure 6.

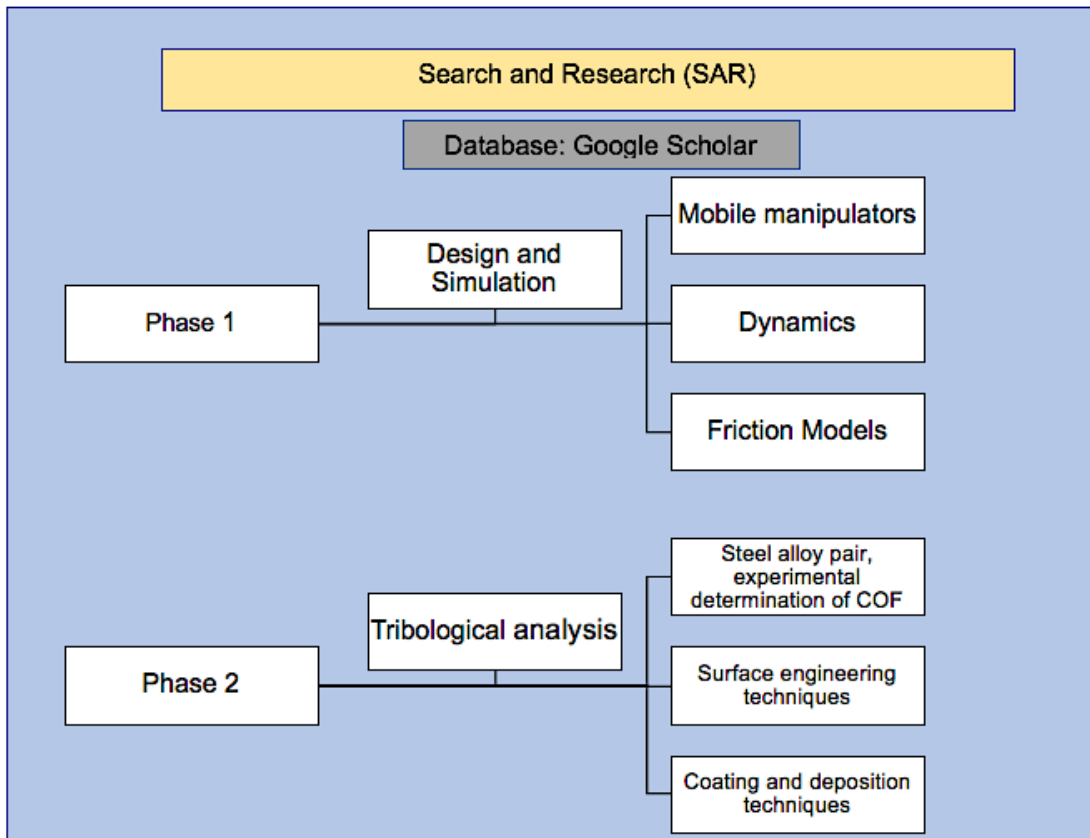


Figure 6 Schematic representation of the literature review

The main questions addressed in this review are: placing mobile manipulators within the context of SAR, substantiating use of Computer Aided Design – Multibody Dynamic simulation approach (CAD-MBD) for SAR, selecting appropriate manipulator joints, and finally selecting appropriate friction model for conducting simulation.

### 2.1.2 Search and rescue (SAR)

SAR robotics is a multi-domain, multi-disciplinary research area combining mechanical design, theory of machines, tribology, materials science and human-machine interaction as presented in Figure 7. Much of the important literature in this area can be attributed to the work of Professor Robin Murphy (Texas A&M University 2008), one of the first-responders to the WTC-9/11 disaster and leading academic in the domain of SAR. Professor Murphy's research group is counted among the world's leading experts on SAR.

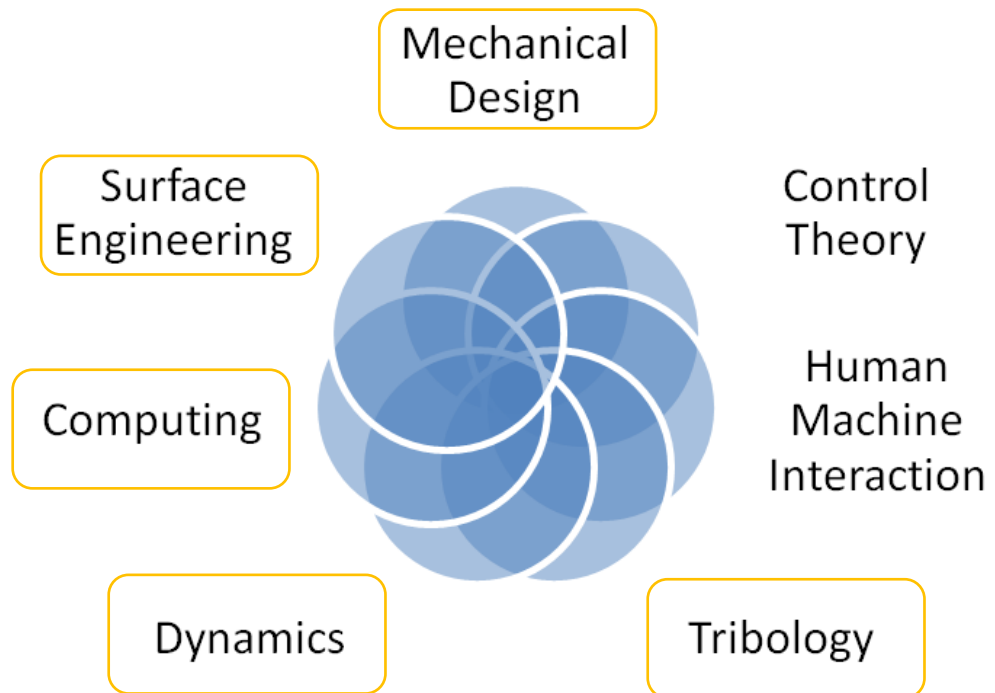


Figure 7 Schematic representation of the interdisciplinary nature of the research area (Khan et al. 2017)

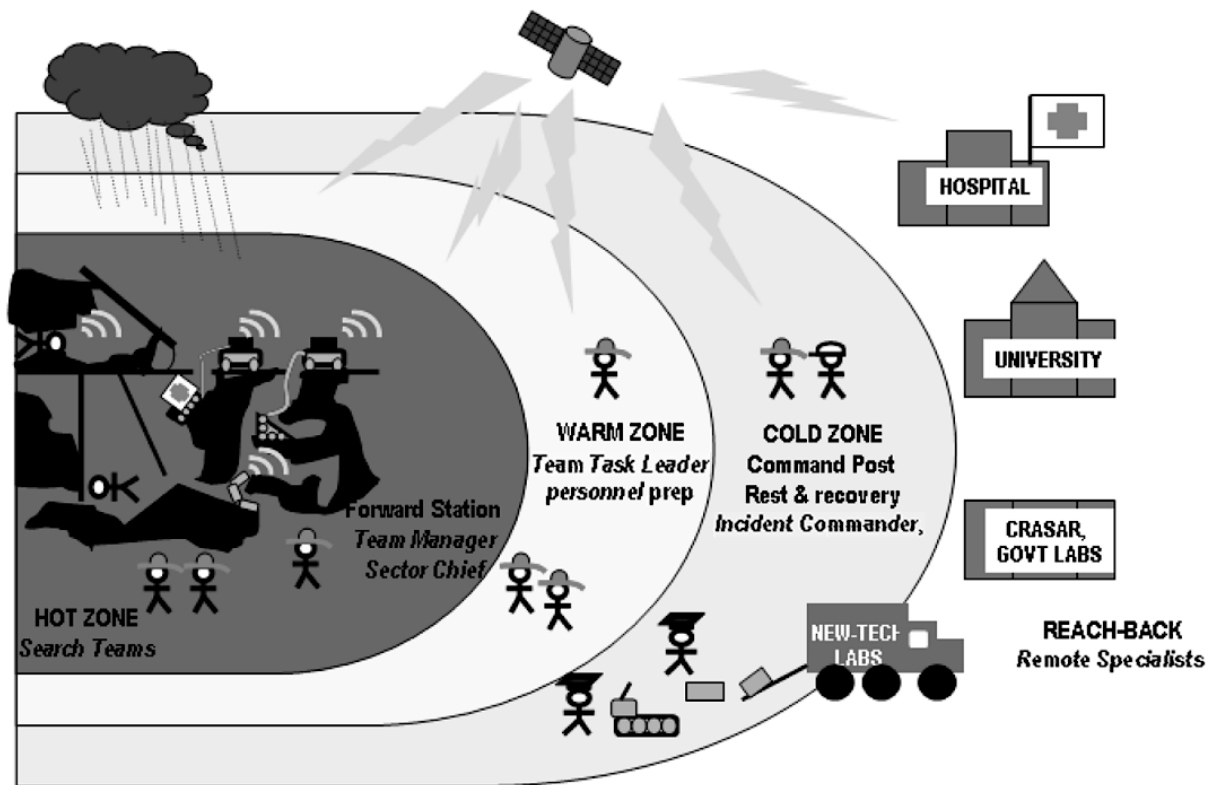
It would be important to define what a disaster means within the context of SAR before delving into the specifics. According to the dictionary (Merriam-Webster n.d.), a disaster is defined as ‘something (such as a flood, tornado, fire, plane crash, etc.) that happens suddenly and causes much suffering or loss to many people’. Within the theme of SAR, disasters may be natural, man-made or a combination of the two (Murphy et al. 2008). SAR can be described as the human response to a disaster. According to (Government Queen’s Printer and Controller and Government Maritime Coastguard Agency 2008), the formal definition of SAR in the United Kingdom has been given as the ‘activity of locating and recovering persons either in distress, potential distress or missing and delivering them to a place of safety’. According to (Murphy 2004b), the affected geographical area is called a disaster site and is divided into cold, warm and hot zones (Figure 8 b). Rescue agents and machines deployed within the hot zone are exposed to dangerous substances under extreme conditions (Stone and Edmonds 1992, Liyo et al. 2002, Wisnivesky et al. 2011, Panas et al. 2014, Statheropoulos et al. 2014), as would be the case with rescue agents under other conditions as well. In terms of time-frame, there are four phases associated with disasters namely, prevention, preparation, response and recovery. These phases may occur sequentially or independently (Murphy et al. 2008, Murphy 2014), emphasising the fact that SAR is a time-critical operation

aimed at saving human lives, which are at risk in a disaster site mainly in the form of i) victims trapped under the rubble, and ii) rescuers (human and dog teams) attempting to save victims. This can be seen from Figure 2 in section 1.1.1 of Chapter 1, where the graph shows that victim survival ranges from 72 hours in urban search and rescue (Voyles and Choset 2008) to about 15 minutes in the avalanche environment (Falk et al. 2002). Although the growing incidence of disasters highlights the requirement for specialized SAR, currently only a few countries have dedicated SAR teams as part of disaster management programmes.



a)





b)

Figure 8 a) Different SAR domains (Statheropoulos et al. 2014) and b) three zones in SAR site (Murphy 2004b)

The use of robots in SAR operations can be traced back to the World Trade Centre (WTC) incident in 2001 (Murphy 2004c, Murphy et al. 2008), which implies that the research area of robotic SAR is relatively new (Murphy 2014). The use of robots in high-risk operations serves to mitigate risk of life to both human and dog rescue agents. These search robots are broadly categorized into man-packable, man-portable (Casper and Murphy 2003) and maxi-sized (Murphy et al. 2008). However, it has been reported that excavators are used for accessing SAR sites in the initial phase of disaster response and accessing/clearing rubble in the long term especially in developing countries (Murphy et al. 2008, Z. Ahmed 2014, BBC 2015). The site affected by disaster eventually needs to be restored through the removal of debris i.e., the rubble removal phase (Murphy et al. 2008). This is the second phase, also called the economic recovery phase, and it is in this phase that heavy machinery such as excavators have been used widely. Rubble removal is indeed a key task in SAR, but rubble removal in a disaster site is different from a construction site because victim safety takes priority (Murphy et al. 2008).

Excavators are heavy machines with significant vibration signatures (Alphin et al. 2010). However, high precision operation and reliability are required for robots used in SAR (Murphy 2014). Excavators are not designed for performing precision operations because these machines are primarily built for operation in controlled construction environments and may contribute to increased risk when deployed for SAR tasks. Even in construction sites, an increasing number of accidents have been attributed to excavators (Lingard et al. 2013). Besides, catastrophic failure of a robot disrupts rescue operation (Carlson and Murphy 2003, 2005) and design failures contribute to equipment breakdown in the challenging rescue environments (Carlson and Murphy 2003). The underlying principle of SAR that 'no one type of robot fits all missions' (Murphy 2014) only strengthens this argument in favour of specialised equipment. Most existing technologies are also untested in SAR-specific tasks leading to a greater risk of further damage (Statheropoulos et al. 2014). While several researches consider robotics aspects, only very few have reported analysis of the existing robotic actors such as excavators in the context of SAR. Therefore, the design and modelling of manipulators are reviewed below, with a view to address this dearth of manipulators.

Although mechanics i.e., kinematics and dynamics of heavy manipulators has been investigated within the framework of numerical modelling and control theory aspect since the 1990s (Koivo 1994, Koivo et al. 1996), these investigations only serve to highlight the complexity of the modelling and simulation process for multi-link manipulators owing to the number of influencing parameters. It may therefore be concluded that the need of the hour in SAR operations is a method to design, simulate and fabricate application specific equipment with minimal turnaround time.

### **2.1.3 The case for utilisation of CAD and MBD**

In light of the above, it has been reported that the utilisation of CAD in the design phase reduces design cycle time for complex geometries (Tan and Vonderembse 2006). It also leads to the rapid development of mechanism components incorporating complex designs (Hardell 1996, Groover Jr. and Zimmers Jr. 1997, Barone et al. 2002, Vergnano et al. 2017). Geometric parameter data include the distances, angles, surface areas and volumes of the

machine members or links. Physical parameters such as mass, moment of inertia and centre of gravity are also computed automatically (Barone et al. 2002), which in turn results in acceleration of the design phase (Vergnano et al. 2017).

However, while CAD is a suitable tool for design, CAD models by themselves provide only limited insight into the mechanics of linkages since the simulation capabilities of CAD are restricted to forward kinematics which refers to calculation of end-effector position for a given set of input kinematic parameters. Since the research problem also includes factoring in of the tribo-characteristic friction in manipulator joints, the use of CAD alone proves inadequate, since the platform is not capable of running advanced simulations, and it is in this context that multibody dynamic simulation (MDB) was selected. CAD-MBD approach has been successfully used across several advanced domains such as space applications (Volle 2014), two-wheeled vehicles (Barone et al. 2002, Wu 2013), robots (Dede and Tosunoglu 2006) and automotive applications (Dooner et al. 2015). Therefore, CAD-MBD approach has found increased application for analysis of the mechanical performance characteristics of linkages.

Designers and control engineers who are not experts in the complex kinematics and dynamics of mechanisms would require inputs to develop the pertinent systems. This is another important motivation for using this approach as the outputs from simulation which comprise kinematic and dynamic characteristics can be used by these specialists (Schiehlen 1997). Part development and concurrent modification of dynamic simulation is also expedited using this technique (Choi and Chan 2004). The use of this approach also provides a stable platform for control systems designers to design, test and verify control systems for complex mechanisms without creating physical prototypes (Song et al. 2013), which can then be extended to include hardware-in-loop testing in the future (Karkee et al. 2011, Dooner et al. 2015). This also enables collaborative large-scale modelling which enhances design and reduces modelling error probabilities (Ruff et al. 2012).

Application of continual, rapid, design improvements, i.e. iterative design, leads to the continuous revision of system models which can improve controller

performance. Therefore, the model should reflect and transmit design changes effectively, and near instantaneously. This investigation would also therefore be an example of the application of concurrent engineering, making it possible for mechanical and control systems designers to work simultaneously on the model, leading to a substantial reduction in design cycle time, which is of importance in time-critical SAR environments. Also, development of a manipulator physical prototype is both expensive and time-consuming. The use of virtual prototypes overcomes the cost and materials constraints leading to a reduction of design cost. The several investigations reviewed previously analyse planar operation and therefore only consider two-dimensional or planar modelling and simulation, which highlights the necessity for having a manipulator virtual prototype capable of three-dimensional operation incorporating three-dimensional mechanics analysis.

In the case of SAR robots, the end-effector design and its environmental interaction are areas of particular interest; applying this technique translates to designing and testing new end-effectors suitable for each scenario (Bicchi and Member 2000, Alqasemi et al. 2007). The new designs can be used directly for in-situ disaster simulations, which would enable engineers as well as operators to prepare and train for effective handling of disaster sites through the meticulous planning out of different scenarios (Mathis et al. 2009).

In conclusion, the CAD-MBD approach was selected to design and simulate mobile manipulators in this work. The process of design and simulation is briefly reviewed in the next section.

#### **2.1.4 Design and simulation process**

The six-stage process of design and simulation is illustrated in the workflow diagram for design and MBD simulation (Figure 9). The process begins with the creation of a 3-dimensional design in CAD leading to the simulation of linkage in the MBD environment (Barone et al. 2002). Individual links are designed based on a requirement analysis, following which they are assembled by assigning the kinematic joint relations between the links. After this step, assembled CAD virtual prototype is exported to the MBD package and simulation is conducted after setting inputs, boundary conditions and measurands.

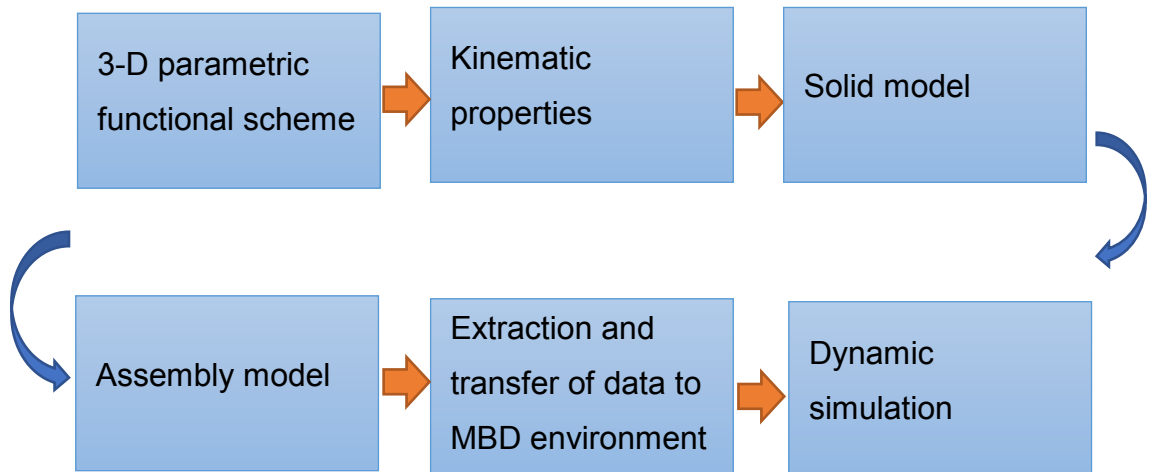


Figure 9 Procedure for CAD-MBD simulation adapted from (Barone et al. 2002)

Combining the process of CAD virtual prototyping and MBD expedites the design refinement process and reduces design costs by utilizing a virtual prototype instead of a physical prototype for conducting the simulation of manipulator mechanics in two or three-dimensional task space, thereby also working within budgetary constraints. This technique draws on design process improvement and also aids the selection of appropriate actuator technology (Wang 2002, Choi and Chan 2004). More efficient and elegant design solutions are expected to evolve from application of this technique.

Animation of virtual prototypes helps the end-users evaluate a design more effectively. An overload of 'graphical information' (two-dimensional graphs) often becomes indecipherable for the end user, echoing the well-known adage that a picture is worth a thousand words and it has also been argued that future engineers would process information more visually (Mahapatra 2013).

Therefore, virtual prototyping (VP) and virtual environments (VE) help the design engineer to visualize and communicate design concepts. More importantly they help identify design issues such as manipulator interference during task space manipulation (Wang 2002, Choi and Chan 2004). Key advantages of such prototypes include reduction in product development costs, rapid product development cycles, intelligible spatial performance and accessible performance measurement (Groover Jr. and Zimmers Jr. 1997).

In the fabrication of mobile manipulators, the economic aspect also plays a major role, for instance (Murphy et al. 2009) reports that a customised SAR

robot for mine rescue cost US\$280,000. Also, informal enquiries which were conducted by this researcher in 2015 with local manufacturers in the UK revealed that the cost of fabricating a working prototype was estimated to be at least £5000 which provided economic justification for using virtual prototypes in the design phase. Therefore, the CAD-MBD approach accelerates design-simulation process, which results in expedited preliminary design for the SAR manipulator. The block diagrammatic approach accelerates testing phase for the linkage mechanics besides providing insight into several kinematic and dynamic parameters.

One noticeable drawback of such systems is the occurrence of algebraic loops which require user intervention to reorganise the systemic equations by simplifying kinematic loops (Sinha et al. 2001). This issue had continued unresolved in the past, but has been addressed recently by breaking up the loop using a transfer function (Rouleau 2015). This issue is expected to be relevant for incorporating closed-loop friction feedback model. Besides these issues, mastery of CAD and MBD packages is also a prerequisite for the usage of this approach.

These notwithstanding, the CAD-MBD approach can be seen as a very effective solution and this having been substantiated, the next section of the literature review deals with the design analysis of mobile manipulators.

## **2.2 Design analysis of mobile manipulators**

This section reviews literature on mobile manipulators with a focus on the structure, geometry and configuration and is divided into three sections namely, design and modelling of mobile manipulators, dynamics and friction.

### **2.2.1 Design and modelling of manipulator mechanics**

This section reviewing the literature on manipulator modelling within the context of SAR, consists of literature on the selection of manipulator mechanisms, design synthesis and prototyping and finally on the types of modelling used in physical systems.

### 2.2.1.1 Serial open chain and closed-loop mechanisms

According to (Merlet and Gosselin 2008), robotic manipulators can be classified into two types:

- i. (serial) open kinematic chains and
- ii. closed-loop kinematic chains.



Figure 10 a) Serial open chain manipulator and b) closed-loop manipulator (Chacko 2014)

In open-chain manipulators, individual links are connected to two other links through kinematic joints (Figure 10 a), whereas in (complex) closed-loop kinematic chains, one of the links other than the base has a degree of connectivity equal to or greater than three ( $\geq 3$ ) (Merlet and Gosselin 2008). Open-chain mechanisms have greater dexterity and also the ability to extend fully i.e., to the extent of the sum of the individual link lengths, besides weighing lesser than closed-loop kinematic chains of similar dimensions. On the other hand, closed-loop manipulators provide additional load-carrying capacity, increased structural stiffness e.g., backhoes or excavator manipulators, and precision positioning e.g., space manipulators (Merlet and Gosselin 2008). However, the additional weight of actuators links, manufacturing tolerances, joint friction, extension of actuators, and mechanical interference between links affect the dynamic performance characteristics of these manipulators.

Therefore, while the manipulator linkage design selection is a trade-off between dexterity and load-carrying capacity (Merlet and Gosselin 2008), the selection of design is based on application. In the case of manipulators for SAR, payload capacity as well as positioning are important criteria. For sensitive environments or applications involving fragile objects, a more dextrous serial open-chain robotic manipulator is required (Peiper 1968). Therefore, both serial open-chain and closed-loop mechanisms are considered for evaluation in Chapter 4.

### 2.2.1.2 Design synthesis and prototyping

Design synthesis is the process of selection of structure and design parameters to provide the best solution to a design problem. According to (Merlet and Gosselin 2008), the design synthesis of robots have been classified into the following categories namely:

- i. structural synthesis - in which the structure of the robot is designed, and
- ii. geometric synthesis - in which the geometric parameters of the linkages are designed.

In this work, the basic structure of the robotic manipulators has been derived from two references namely, the human arm (Peiper 1968) and the heavy manipulator arm found in excavators reported in literature (Vähä et al. 1991, Koivo 1994) which translate into the serial-open chain (anthropoid) manipulator and closed-loop manipulator respectively. Also, two methods for design optimisation of linkages have been presented in literature (Merlet and Gosselin 2008) namely:

- i. cost function optimisation, and
- ii. appropriate design method.

The first method does not necessarily yield realistic design solutions because of the numerous parameters which influence manipulator performance such as payload, actuator performance etc., whereas the second method provides a more practical approach to design based on the performance requirements of the manipulator within parameter space. Since this investigation is a first step towards the design of manipulators for SAR, the appropriate design method, i.e. CAD, was selected for use in this research.

Design of a new multi-link manipulator mechanism with complex closed-loop kinematic chains remains a challenging multi-stage, interdisciplinary process. Also, conventional physical prototyping technique has been reported to be expensive and time-consuming, especially in the case of complicated multi-link mechanisms (Chang 2015). Besides this, design engineers may be unable to address all engineering requirements because of the overall engineering knowledge required for addressing the different aspects of design. One method of addressing these issues is through the utilisation of the concept of concurrent engineering in which specialist engineers collaborate to optimise the virtual



prototype in real-time (Barone et al. 2002, Vergnano et al. 2017), as mentioned earlier in section 2.1.3.

Techniques for manipulator mechanics simulation, along with numerical modelling methods, have also progressed greatly over the past three decades years as reported in literature (Uicker et al. 2003, Siciliano and Khatib 2008). Based on this, it was envisaged that a virtual prototype combined with two-dimensional graphical representation of output parameters would provide better insight into the physical performance of a mechanism rather than just the two-dimensional graphical representation alone (Mahapatra 2011). Therefore, the utilisation of computer aided design (CAD) along with multibody dynamic (MBD) simulation techniques for fulfilling this task stands justified.

### **2.2.1.3 Types of modelling used in physical systems**

It would be important to analyse the different types of modelling utilised in simulation presented in literature. (Szewczyk et al. 2015) have classified the modelling of multibody physical systems into:

- i. equation-based or declarative modelling, and
- ii. object-oriented modelling leading to component-based modelling.

In addition to the above classification, the modelling of physical systems can be classified into three graphical paradigms:

- i. bond graphs (Granda and Montgomery 2003, Borutzky 2010),
- ii. linear graphs (Papadopoulos et al. 2003), and
- iii. block diagrams (Schlotter 2003, Daumas et al. 2005, Hroncova and Pastor 2013).

Linear and bond graph methods are both energy modelling methods. The block diagram method has been applied as early as 1996 (Hardell 1996). In the block diagram modelling technique, the systems and sub-systems are hierarchically modelled, and the sub-systems populate the lower hierarchies of the block model (Figure 11). Therefore, vast amounts of data are classified into visually manipulatable form which makes it coherent and systematic. For these reasons, this method was selected for simulating the linkage mechanics in this work and the principles are explained briefly below.

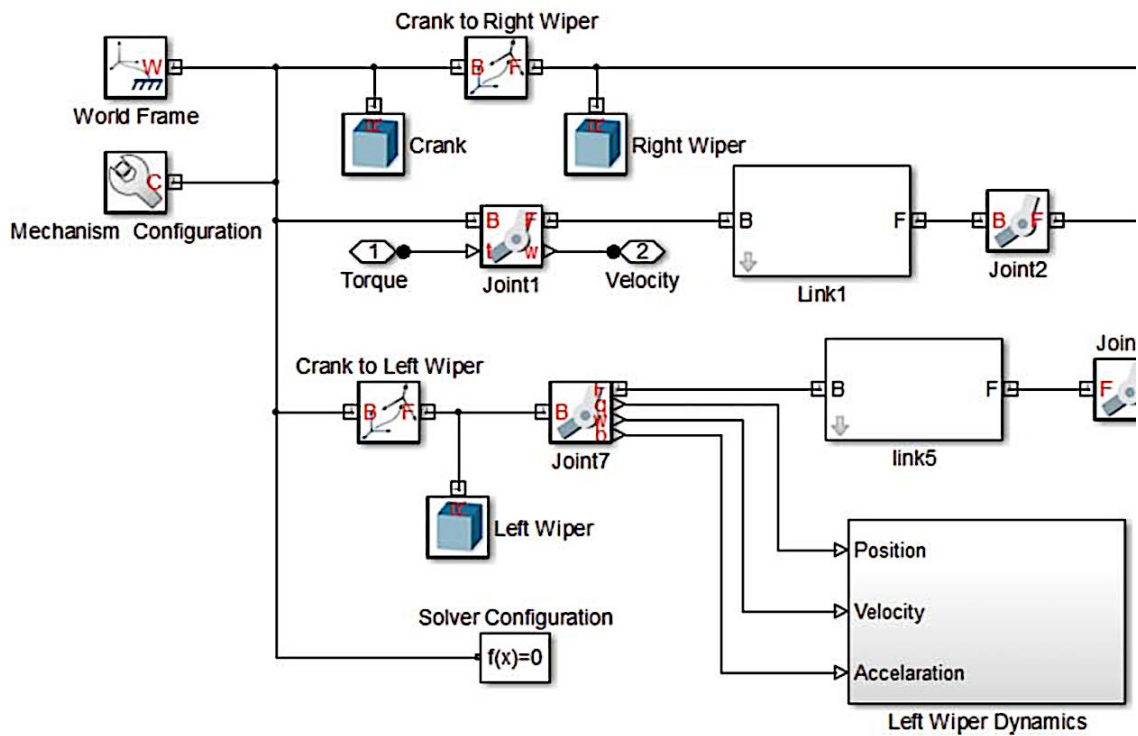


Figure 11 Block diagram model of the wiper system presented in (Dooner et al. 2015)

Block diagrams are generated based on the kinematics and dynamic relationships. The differential algebraic equations (DAEs) for the physical system which have been analysed in these investigations were generated based on the kinematic relations assigned in CAD during the assembly stage, along with the values of physical parameters computed for individual links based on the materials assigned to them. CAD software is utilised for designing complex engineering parts.

MATLAB/SimMechanics approach is the most commonly used platform for conducting block diagrammatic simulation of physical system; use of SimMechanics 1<sup>st</sup> generation platform has been widely reported (Wang, Jin, et al. 2013). MBD packages (SimMechanics/SimScape ®) were used to conduct rigid body simulation of the CAD models and SimScape or SimMechanics 2<sup>nd</sup> generation has been used previously in several works (Udai et al. 2011, Dooner et al. 2015, Mahapatra 2015). Also, simulation of the mechanics of complex mechanical rigid linkages using MBD simulation platforms such as SimScape (Figure 11 which is the example of a wiper system) and MSC Adams have been reported widely in literature (Barone et al. 2002, Ding et al. 2015, Dooner et al. 2015).

The use of MBD analysis contributes to improved process efficiency for developing the manipulator mechanics thereby resulting in cost-reduction through the obsolescence of the physical prototype (Wood and Kennedy 2003, Grossman and Gmitterko 2008, Udai et al. 2011, Le et al. 2013, Dooner et al. 2015, Mahapatra 2015).

In order to understand the modelling process, the general dynamics model of a linkage from literature is presented below.

### **2.2.2 Dynamics**

Dynamics of mechanical systems defines the set of relationships between actuation forces or torques and kinematic parameters such as motion, velocity and acceleration (Featherstone and Orin 2008). Computation of dynamics is classified into forward and inverse dynamics, similar to the classification used for kinematics (Appendix D). Forward dynamics is used to compute the joint kinematic parameters based on the actuation forces or torques whereas inverse dynamics refers to the calculation of forces and/or torques at joints given the joint positions and its derivatives. Therefore, inverse dynamics can be used to compute forces and torques for actuator selection, and control system design for a given end-effector motion. The end-effector motion in the case of excavators is the dig-path of the bucket, which is a kinematic parameter (Tiwari et al. 2013). Three main methods for developing dynamic models of mechanisms have been reported in literature, namely:

- i. Force balance approach i.e. Newton-Euler method (NE) (Vähä et al. 1991),
- ii. Energy approach i.e. Euler- Lagrange method (EL) (Sarata et al. 1995, Virgala et al. 2012), and
- iii. Gibbs Appel method (Korayem and Shafei 2013) or Kane's equation method (Piedboeuf 1993, Šalinić et al. 2014).

According to (Balafoutis 1994), NE method is computationally more efficient compared to the EL method but contains pseudo-forces or constraint forces in the joints i.e., reaction forces between links at the joints. These are required for design investigations but increase the complexity of equations and errors in formulation. The EL method, on the other hand, eliminates pseudo-forces in the

joints due to the energy approach utilised, and therefore does not provide insight into the interactive dynamics between links (Balafoutis 1994). Therefore, the selection of modelling technique for the manipulator is based on the type and objective of the dynamics analysis.

In this section, the dynamic model of the manipulator based on the NE method from literature is presented.

### 2.2.2.1 Dynamic model of the mobile manipulator

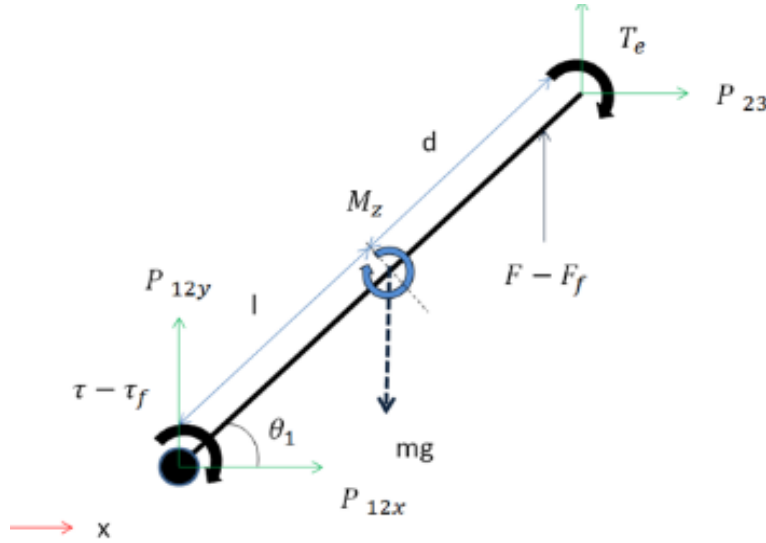


Figure 12 Forces and moments acting on a moving link connected to a fixed link through a SDOF revolute joint (Chacko and Khan 2017)

The dynamic components acting on an individual generalised link is illustrated in Figure 12. The general form of Newton's equation can be expressed as follows (Stoneking 2007):

$$\sum F = m\dot{v} = ma \quad (1)$$

where  $F$  represents the resultant external force,  $m$  is the mass of the link,  $\dot{v}$  is the velocity of the centre of mass and  $a$  is the acceleration.

For a rigid planar manipulator, the recursive relation can be expressed as (Koivo et al. 1996):

$${}^iF_0^i = m_i {}^i a_{0G_i} \quad (2)$$

where  ${}^iF_0^i$  represents the force on the  $i^{th}$  link in the  $i^{th}$  frame,  $m_i$  represents the mass of the link,  ${}^i a_{0G_i}$  represents the acceleration at the centre of gravity.

The general form of the Euler equation for a rigid body undergoing rotation is expressed as (Stoneking 2007):

$$\sum M = I\dot{\omega} = I\alpha \quad (3)$$

where  $M$  is the momentum and  $I$  is the central moment of inertia and  $\alpha$  is the angular acceleration.

For a planar manipulator, the recursive relation angular momentum relationship is expressed as (Koivo et al. 1996):

$${}^i\vec{M}_0^i = {}^iI_{0i}{}^i\vec{\omega}_0^i + {}^i\vec{\omega}_{0i} \times {}^iI_{0i}({}^i\vec{\omega}_{0i}) \quad (4)$$

where  ${}^i\vec{M}_0^i$  is the momentum,  ${}^iI_{0i}$  is the central moment of inertia and  ${}^i\vec{\omega}_{0i}$  is the angular momentum.

Literature on dynamic modelling and analysis of the planar operation of the multi-link excavator manipulator mechanism has been presented as early as 1991 (Vähä et al. 1991). Despite progress in technology, research on dynamic modelling of multi-link heavy manipulators continues to pose several challenges, amongst which are mechanism modelling for complex linkages such as closed-loop manipulators, and friction in manipulator joints (Bernold 1993, Andrade-Cetto and Koivo 1995, Singh 1995a, 1995b, Koivo et al. 1996, Qing-hua et al. 2006, Kim et al. 2013, Shen et al. 2015, Erdemir et al. 2016). The general manipulator dynamics model of a multi-link mobile manipulator has been presented in the form of the following equation (Vähä et al. 1991):

$$D(\theta)\ddot{\theta} + C(\theta, \dot{\theta})\dot{\theta} + G(\theta) + B(\dot{\theta}) = \tau - \tau_L \quad (5)$$

$$\text{where } D(\theta) = \begin{bmatrix} D_{11} & D_{12} & D_{13} & D_{14} \\ D_{21} & D_{22} & D_{23} & D_{24} \\ D_{31} & D_{32} & D_{33} & D_{34} \\ D_{41} & D_{42} & D_{43} & D_{44} \end{bmatrix}, C(\theta, \dot{\theta}) = \begin{bmatrix} C_{11} & C_{12} & C_{13} & C_{14} \\ C_{21} & C_{22} & C_{23} & C_{24} \\ C_{31} & C_{32} & C_{33} & C_{34} \\ C_{41} & C_{42} & C_{43} & C_{44} \end{bmatrix},$$

$G(\theta) = [G_1 \ G_2 \ G_3 \ G_4]$ ,  $\theta$  represents joint angles,  $\dot{\theta}$  represents the angular velocity,  $\ddot{\theta}$  represents the angular accelerations,  $D(\theta)$  represents pseudo-inertia matrix,  $C(\theta, \dot{\theta})$  represents Coriolis' and centripetal forces,  $G(\theta)$  represents gravity forces,  $B(\dot{\theta})$  represents joint frictional forces,  $\tau$  represents the joint

torques,  $\tau_L$  represents interaction forces at the end-effector between machine and environment e.g. soil,  $D(\theta), C(\theta, \dot{\theta}) \in \mathfrak{R}^{n \times n}$ ,  $\theta, \dot{\theta}, \ddot{\theta}, G(\theta), \tau, \tau_L, B(\dot{\theta}) \in \mathfrak{R}^{n \times 1}$  and  $n$  is the number of links. The magnitudes of Coriolis's force/centripetal force can be ignored at low link velocities but influences dynamics at higher velocities (Khan et al. 2017).

The model presented in literature includes the joint friction forces and torques. However, in most analyses this effect has been ignored due to modelling complexities. Only very few researches have considered the effect of joint friction, even though it forms an important component of dynamics (Tafazoli et al. 1996, Bilandi 1997, Lischinsky et al. 1999). Friction in manipulator joints measured under ideal and controlled conditions using torque sensors has been incorporated into the dynamic model for the large excavator manipulator (Bilandi 1997, Tafazoli et al. 1999, 2002). However, there is a limited understanding of data and models regarding friction in such linkages because of which the effect has been ignored in modelling.

In this context, friction in manipulator joints requires further analysis and is reviewed below.

### **2.2.3 Friction in manipulator joints**

Friction is a complex, non-linear, resistive phenomenon that affects the positioning and control of linkages as explained in section 2.1.1. High magnitudes of coefficient of friction (COF) generates noise, vibration and harshness, depletion of actuator power and performance loss leading to seizure and failure of components etc., (Ibrahim 1994), and it is not without reason that friction has been called 'the nemesis of precision control' (Haessig and Friedland 1991). According to (Lischinsky et al. 1999), 'as much as 30% of manipulator actuator effort may be used to overcome frictional resistance' and (Bittencourt et al. 2010) add that 'the need to model friction for control purposes, where a precise friction model can considerably improve the overall performance of a manipulator with respect to accuracy and control stability. In a robot joint, the complex interaction of components such as gears, bearings and shafts which are rotating/sliding at different velocities, makes physical modelling difficult.' This justifies the importance of friction as the main tribo-characteristic

in manipulator joints and for this reason, incorporation of friction model is attempted. More specifically, a pin and bushing joint is used to connect different links of an excavator arm. These revolute joints are single (one) degree of freedom (sDOF) joints initially i.e., they have very close fit (Waldron et al. 2008). Multi-DOF (mDOF) revolute joints have been investigated as a separate class of mechanisms due to increased complexity and more information on these systems can be found elsewhere in literature (Khan et al. 2017).<sup>1</sup>

Friction force which is generated in the interface of two surfaces in contact depends on several factors such as load, lubrication, contact geometry, topology, displacement and relative surface velocity (Machado et al. 2012), which are tribological elements. Due to the influence of multiple parameters in addition to those mentioned above (such as temperature and time), formulation of a unified friction model has not been reported. Friction models have been selected on the basis of application requirements, dominant component of friction, complexity and compatibility with existing simulation package and numerical solution scheme (Mare 2012). Additionally, the identification of dominant parameters that affect contact friction is often tedious, expensive, time-consuming and intrusive. Therefore, the best method of determining the friction characteristics for a particular material pair and operating conditions would be through experimental analyses (Blau 1997). As mentioned above, only one-degree of freedom (sDOF) joints were considered in this work and friction models applicable to these joints are presented below.

### **2.2.3.1 Friction models**

At the outset, only sDOF revolute joints were considered to limit the scope of this investigation as this research deals with a first level design of mobile manipulators.

---

<sup>1</sup> This researcher contributed to this publication as second author.

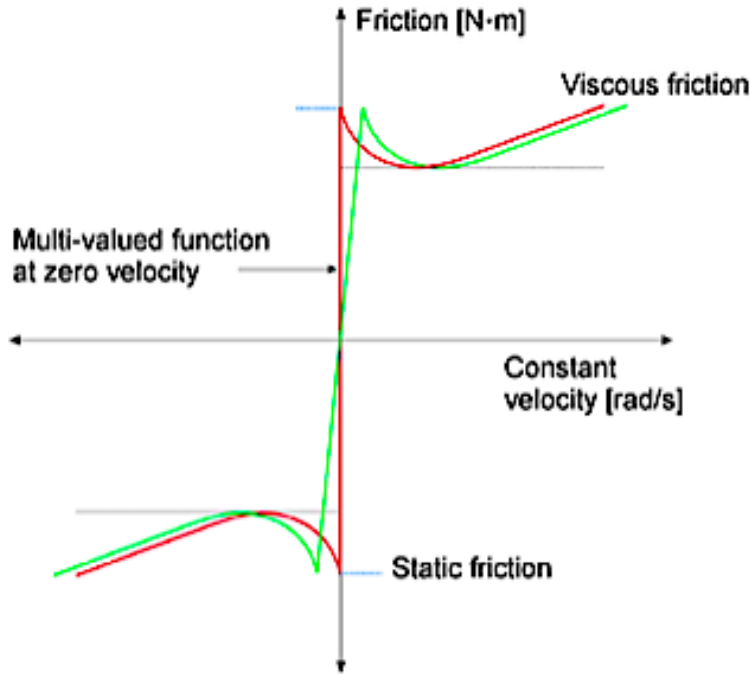


Figure 13 Combined friction model (CFM) with zero velocity crossing (Khan et al. 2017)

A friction model must be able to capture real physical effects including distinguishing between static and kinetic contact and direction reversals. Also, model discontinuity at near zero velocity causes friction values to oscillate leading to the failure of computation model (Figure 13). This problem is addressed by utilising two-state friction models and these are presented below in equations 7 to 10. Friction modelling for sDOF revolute joints present in the relatively simple slider-crank mechanism has been reported to be complex. It has also been reported that even the modelling of such closed-loop kinematic systems requires considerable formulation and computational effort (Marques et al. 2015, 2016). The generalised friction model (GFM) is presented below as:

$$\mathcal{F}(\kappa, \theta) = \sum_{i=1}^N f_i(\kappa, \theta) \quad (6)$$

where  $\kappa = [z, q, \dot{q}]$  gives the set of GFM structures,  $z$  is an internal state related to the dynamic behaviour of friction,  $q$  is a generalized coordinate and  $\dot{q}$  is the first time derivative of the state variable  $q$  (Bittencourt et al. 2010). In order to compute the friction force or torque generated in the joints, the combined friction model (CFM) available in literature was considered first. This model incorporates Coulomb, viscous and Stribeck friction.



### Translational friction model equations:

This model has been used to compute the friction in sDOF translational joints e.g. prismatic joint found in the actuator of the mechanism and is expressed through the following equations (van Geffen 2009, The Mathworks Inc. UK 2015a):

$$F_f = F_c + (F_{brk} - F_c) \cdot e^{(-c_v|v|)sign(v)} + fv \quad (7)$$

$$F_f = \frac{v}{v_{thr}} (F_c + (F_{brk} - F_c) \cdot e^{-c_v|v_{thr}|} + fv_{thr}) \quad (8)$$

The following default parameters have been reported: Coulomb friction force  $F_c = 25N$ , breakaway friction force  $F_{brk} = 24.995N$ , velocity coefficient  $c_v = 100N/(\frac{m}{s})$  and velocity threshold  $v_{thr} = 1e - 4 m/s$  using which the total friction force  $F_f$  is computed.

### Revolute friction model equations:

Similarly, the combined revolute friction model has been used to simulate joint friction in sDOF revolute joints and is presented below (The Mathworks Inc. UK 2015b):

$$T_f = \tau_c + (\tau_{brk} - \tau_c) \cdot e^{-c_\omega|\omega_{thr}|} + f\omega_{thr} \quad (9)$$

$$T_f = \frac{\omega}{\omega_{thr}} (\tau_c + (\tau_{brk} - \tau_c) \cdot e^{-c_\omega|\omega_{thr}|} + f\omega_{thr}) \quad (10)$$

The following default parameters have been reported: Coulomb friction torque  $\tau_c = 25Nm$ , breakaway friction torque  $\tau_{brk} = 24.995Nm$ , angular velocity coefficient  $c_\omega = 100Nm/(\frac{rad}{s})$ , and velocity threshold  $\omega_{thr} = 1e - 4 rad/s$  from which the total friction torque,  $T_f$  is computed.

However, the estimation of equation parameters in the CFM is not a straightforward process, and its effectiveness is difficult to validate for a pin and bush joint commonly found in manipulators. Although literature reports measurement of joint friction parameters using torque sensors (Bilandi 1997) and the incorporation of these parametric values into the dynamic model, this approach was found to be infeasible for this research due to limited availability of resources and time constraints. Theoretical friction torque models which have been reported in literature for the pin and bushing joint, are presented (Colbert

et al. 2010). As mentioned previously, the combined friction model does not accurately capture friction characteristics of pin and bushing joints used in manipulator mechanisms. Therefore, a specific friction model is required for computing the friction torque generated in the pin and bushing joint. The elementary frictional torque model for the pin and bushing joints has been given by (Colbert et al. 2010):

$$T_f = \mu F_n R_s \quad (11)$$

where  $T_f$  represents the frictional torque generated,  $\mu$  represents the COF for the material pair under investigation,  $F_n$  represents the normal force and  $R_s$  represents the radius of contact (Figure 14).

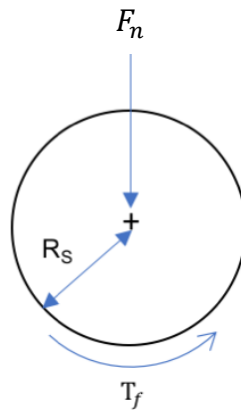


Figure 14 Simple model with a point load for friction torque computation

However, the above equation represents an underestimation of frictional torque since point loading has been considered. In reality, a pressure profile is developed in contacts as shown in Figure 15. This creates a traction force tangential to the load direction.

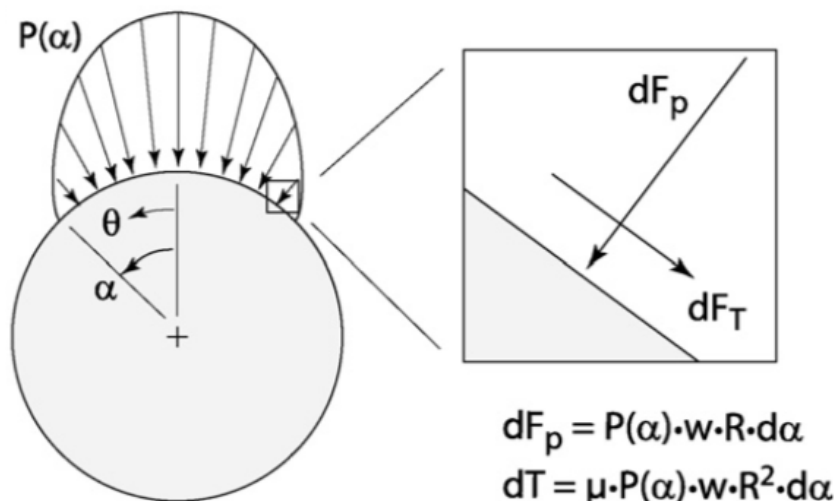


Figure 15 Contact forces and pressure profile in pin and bushing (Colbert et al. 2010)

After some manipulation, the friction torque equation for the pin and bushing type joint can be presented in the reduced form presented in equations 12 and 13 based on (Colbert et al. 2010):

$$T_f = 2 \mu P_{\max} w R^2 \int_0^\alpha \cos \frac{\pi\theta}{2\alpha} d\theta \quad (12)$$

$$T_f = \frac{4 \mu \alpha}{\pi} P_{\max} w R^2 \sin \pi \alpha \quad (13)$$

where  $\mu$  is the COF,  $P_{\max}$  is the maximum pressure developed in the joint,  $w$  is the width of the contact,  $R$  is the radius of the joint,  $\alpha$  is half the  $\theta$  is the contact wrap angle and  $T_f$  is the friction torque. However, the inclusion of debris can lead to an increase in internal pressure, the effects of which have not been included in this model (Mosleh et al. 2002). Due to these reasons, tribological analysis is preferred to evaluate the frictional effects to assess the mechanical performance characteristics rather than parametric tuning of friction models (Blau 1997), and literature on this will be discussed in detail in Chapter 3.

#### 2.2.4 Commonly used actuators

Excavator systems use hydraulic actuators to achieve the desired end-effector positioning i.e., to execute operations such as digging soil, dislodging rocks and transferring heavy objects. These manipulators have robust construction and move comparatively slowly due to the slow response of hydraulics systems. Hydraulic actuators provide robust operation, high-power transmission capacity and availability besides having low compressibility of the working fluid. Due to inherent damping, hydraulic actuators have lesser mechanical stiffness compared to electric motors. Therefore, these actuators are used in applications involving unsteady loads such as load-lifting. However, they are not very energy efficient (Liljeström and Isomaa 2013). This is partly because conventional hydraulic control valves require as much as a third of the total power for operation (Quan et al. 2014). Usage of electrohydraulic proportional valves to retrofit excavator shows potential-energy saving compared to fluid controlled valves (Qing-hua et al. 2006).

With the increasing focus on efficient operation, regeneration of energy from actuators is finding increasing application across the industry. Progress in the

domain of robotic actuators technologies and different actuator arrangements have been presented in literature (Hollerbach et al. 1991, Vanderborght et al. 2013), as have new actuators including hybrid electro-hydraulic and the McKibben/PAM actuators have been presented in literature (Ching-Ping Chou and Hannaford 1996, Tondu 2012, Chen and Ushijima 2014). When the excavator manipulator is lowered, energy is dissipated in the form of heat from the throttling which happens in the control valves. Recovering this energy would improve energy efficiency of such machines. Adding an ultra-high capacitor (UHC) adversely affected power consumption in the test excavator due to engine shuttling phenomenon (Wang, Wang, et al. 2013). Therefore, hydraulic actuation remains the superior choice for excavators. However, hydraulic actuators are untenable for smaller robotic platforms, especially in the case of mobile robots, because pneumatic actuators carry the inherent risk of sudden depressurisation (bursting), which can have catastrophic effects on the SAR sites.

Therefore, despite the undesirable stiffness issue, electric or servo-controlled actuators continue to be the safest option for SAR sites. These actuators also offer precision control and can be integrated into the electrical systems that operate in most mobile robotic platforms (Anon. 2012). Two actuators were selected for design and simulation namely, i) a linear electric actuator (Gimson Robotics 2015), and ii) a high-torque servo motor (Sparkfun 2015) for the serial open-chain model based on the specifications made available on the product websites which provides input for CAD designs.

### **2.2.5 Simulation**

Aviation and automotive industries rely on simulations for both equipment performance measurements, as well as to improve operator training (Barone et al. 2002, Dede and Tosunoglu 2006, Choi and Cheung 2008, Karkee et al. 2011, Le et al. 2012, Ni et al. 2013, Dooner et al. 2015) The use of simulations highlights their importance in improving performance in the medical domain (Seymour et al. 2002, Giannotti et al. 2013, Vaughan et al. 2013). It may be noted that use of virtual prototypes of large excavators for training simulators for commercial training have also been reported (Oh et al. 2011, Ni et al. 2013). Dynamic simulation of complex and precision mechanical systems which have

complex numerical models can be conducted through the use of the CAD-MBD approach as demonstrated in literature above.

Therefore, design of application-specific mobile manipulators for use in time-critical SAR operations can be achieved through the CAD-MBD method and these can be adopted to facilitate simulations of virtual prototypes to be used as training tools for training rescue agents and operators in the future. This implies that the CAD-MBD approach is very beneficial in terms of both immediate and extended outcomes. In order to make the dynamic models the best approximation of physical models, friction in the joints must be considered especially in cases where it plays an important role.

### **2.3 Knowledge gaps and research objectives**

Literature reveals that there exists a dearth of specialized manipulators for SAR and also justifies this need because the use of heavy machinery tools such as excavators has been identified to be detrimental. From the design perspective, application-specific SAR mobile manipulators with quick turnaround time have not been reported, giving rise to the eventuality of a cascading effect of accidents, because they do not address the time-criticality of SAR operations. Application of CAD-MBD approach holds the prospect of not only reducing turnaround time but also affords the opportunity for virtual prototyping thereby becoming a powerful training tool for SAR rescue agents and operators in their preparation for disaster management. Friction has been acknowledged as an important component in the dynamic performance but modelling of friction and its incorporation into dynamic simulation has not been reported. This opens the scope of study to the analysis of friction using numerical models.

As mentioned in the introduction to this chapter, this literature review was conducted on the first two aims (RA1 and RA2) to identify corresponding research objectives and parameters (ROs) presented in Table 3.

	Research Aim	Research Objective
Design and dynamic simulation	RA1: To explore more efficient methods for design, modelling and simulation of mobile manipulators used in SAR	RO1: Design virtual prototypes of mobile manipulators RO2: Simulate virtual prototypes in MBD simulation environment
	RA2: To consider the role of friction in manipulator dynamics	RO1: To apply and assess friction models for sDOF joint RO2: Simulate these friction models

Table 3 Research aims and corresponding objectives for literature review-1

Since limitations on friction models were envisaged, tribo-testing with a focus on COF is discussed in Chapter 3.

## 2.4 Summary

The methodology for literature review followed in Chapters 2 and 3 are presented following which the main themes within Search and Rescue (SAR) robotics and the need for mobile manipulators, manipulator mechanics, use of CAD-MBD approach and joint friction models were surveyed. Knowledge gaps were identified and based on these and the research aims, corresponding research objectives were formulated.

## **Chapter 3 Literature review – 2: Tribological analysis**

### **3.1 Introduction: From design modelling and simulation to tribological analysis**

The second part of the literature review is built on the last two research aims referred to in the introduction i.e., to analyse the feasibility and identify appropriate methods for experimental evaluation of tribological characteristics of the contact mainly COF. The methodology followed is outlined in the introduction to Chapter 2. In the previous chapter, literature on the utilisation of computer aided design (CAD) and multibody dynamics simulation (MBD) approach for designing, modelling and simulating application-specific mobile manipulators were reviewed, besides literature on friction models.

The dynamic performance of pin and bushing joint connecting the different links in load-lifting and heavy manipulators which are sliding contact joints, are affected by three tribological components namely friction, lubrication and wear (Bilandi 1997, Tafazoli et al. 1999). Simulation and testing are required to characterise the performance of contact materials, lubricants, surface conditions and surface modifications, especially for applications like Search and Rescue (SAR). Where data for conducting computer simulations are not available, experimental investigation of the coefficient of friction (COF) for the material pair is necessary to fully understand the operating characteristics (Blau 1997). To find out the parameters of the combined friction model (CFM) presented in section 2.2.3 of the previous chapter extensive experimental testing is required. Considering the scope of this present work, the use of scaled-down experimental testing as a cost and time-effective solution in literature is investigated in this chapter.

Methodology for investigation involves defining nature and scope, scale of simulation, field compatible metrics, apparatus selection, baseline tests for repeatability, test result analysis using established metrics, and refinement of results to achieve requisite confidence levels (standard deviation and standard error calculations were selected). This implies that several iterations of each test are required to establish the test results for each material pair (Blau 2001). Experimental conditions have been identified by following the guidelines for

tribo-system analyses presented in literature (Blau 2001) and are presented in section 5.2.3 of Chapter 5. While a single test may not be sufficient to encompass the operating conditions for equipment during deployment, it is expected to provide a reasonable basis for conducting future simulations. The selection of appropriate test parameters enables the replication of actual operating conditions and this has been highlighted in (Blau 2001), where he presents the argument that test results are useful only when they pertain to field performance. In the same book chapter, (Blau 2001) classifies tribo-simulations into four categories:

- i. Level 1: Use of full-scale machines e.g. field studies
- ii. Level 2: Sub-assemblies subject to approximate operating conditions e.g. (Tafazoli et al. 1996, 1999)
- iii. Level 3: Test rigs designed to test specific components such as bearings e.g. (Cann 2006)
- iv. Level 4: Tribo-simulations based on shapes (Thomas et al. 2009, Anand et al. 2016, 2017).

Following the discussion regarding the incorporation of CFM to the manipulator model, the need for extensive physical testing like a level 1 tribo-simulation becomes evident in order to establish the parameters of the combined friction model. However, as shown in literature, the solution to the problem of cost and time constraints would be to adopt an approach combining level iii and level iv tribo-simulation. This involves the selection of experimental apparatus for conducting tests primarily to assess COF and wear characteristics using white light interferometry, digital microscopy, SEM etc. (Blau 2001). However, since the scope of the research is restricted to sDOF revolute joints found in manipulators (as mentioned in section 2.2.3.1), COF and surface characterisation become the main focus, which can then form the basis for understanding wear. Sufficient wear has to take place for the joint fit to alter from sDOF to mDOF joints, and this has been studied in detail in (Flores 2009, Mukras et al. 2010) which has been analysed separately. Therefore, the main questions dealt with in this chapter are the identification of appropriate material pair, equipment, surface engineering techniques to assess effect on COF, method and type of coating. Therefore, selection of materials to form the



scaled-down version of the manipulator joint in order to conduct experimental analysis of tribo-characteristics is discussed in the following section.

### 3.1.1 Selection of steel alloy pair

16MnCr5 is an important steel alloy used for bushings, shafts, gears, pinions, collets, pins, camshafts and other automotive components. It is also a case-hardening steel, which can be welded, forged and hardened and can be carburised and carbo-nitrided, possessing 80% machinability of mild steel (Johansson et al. 2002, Kiapei 2014, SantAna et al. 2017). As a result, it has been used as material for manufacturing bushings used in manipulator joints, especially in retrofits, i.e., in the joints of excavator arms used as lifting equipment in the construction industry. EN19 alloy (709M40 (BS), also 708M40 and WN1.7225) is ductile, shock and wear resistant and is commonly used for shafts and gears, with a high tensile strength close to 1000 N/mm<sup>2</sup>. The pin-bushing combination found in aftermarket retrofits comprises 16MnCr5-EN19 steel alloy pair and was selected for investigation in this work, which makes the results relevant both academically and techno-commercially. Despite the wide use of the steel alloy pair, detailed tribological analysis, especially focussing on its coefficient of friction (COF) has not been presented in detail in literature. In order to address this knowledge gap, the tribo-characteristics for the steel alloy pair was investigated in this work and their compositions are given below in Table 4 and Table 5 respectively.

16MnCr5						
Component	C	Si	S	Cr	Mn	P
Composition	0.14-0.19%	0.40% max	0.035% max	0.80-1.10%	1.00-1.30%	0.035% max

Table 4 Composition of 16MnCr5 steel alloy (West Yorkshire Steel 2017)

EN19							
Component	C	Mn	S	Cr	Mo	P	Si
Composition	0.35-0.45%	0.50-0.80%	0.050% max	0.90-1.50%	0.20-0.40%	0.035% max	0.10-0.35%

Table 5 Composition of EN19 steel (Steel 2017)

## **3.2 Tribological analysis**

Friction, wear and lubrication are the three components of tribology and they affect the dynamic performance of the manipulator. In order to estimate the parameters of the CFM incorporated in the design and modelling of the manipulator joint, scaled-down experimental testing was selected as discussed in section 3.1. To understand the COF characteristics of the selected 16MnCr5-EN19 steel alloy pair with reference to the manipulator dynamics, as the investigation of friction and wear behaviour of lubricated surfaces is crucial to the development of sliding contact surfaces. Suitability of the specimens can be determined through tribo-tests and the measurand in this work is the COF for the material pair. Following the selection of steel alloy pair, literature regarding the appropriate equipment to be used to analyse the COF is reviewed below.

### **3.2.1 Selection of tribometer**

The tribometer is generally used to conduct tribological analysis and estimation of COF, wear and lubrication performance in moving contacts. Depending on the application, several different types of tribometers have been reported in literature such as block on ring tribometer, bouncing ball tribometer, four ball tribometer, twin disc tribometer and reciprocating tribometer (University of Twente 2016).

In this work, the contact surfaces undergo reversible sliding motion. In the context of this research, (Mohan et al. 2009) has investigated the suitability of reciprocating tribometers to conduct simulations of low-speed reciprocating sliding behaviour encountered in industrial applications such as machine tool slide ways and for measuring COF under controlled environments and simulated test-conditions (Thomas et al. 2009, Anand et al. 2016, 2017, Bajwa, Khan, Nazir, et al. 2016). These tribometers have been used to measure average COF ( $\mu_{\text{average}}$ ) under both dry and lubricated test conditions using different contact geometries which include pin on plane, ball on plane, and cylinder on plane (Thomas et al. 2009, Anand et al. 2016, 2017, Bajwa, Khan, Nazir, et al. 2016). Controllable test parameters in reciprocating tribometers include load, frequency, stroke length and temperature (Bhushan 2013b).

### 3.2.2 Selection of test parameters for tribo-testing

Classification of testing methodology has been reported by (Bhushan 2013b) as follows:

- i. Selection of test geometry:
  - a. point contact – eliminates alignment issues, wear analysis in initial test stages,
  - b. line contact – provides accurate contact simulation but faces alignment issues,
  - c. conforming contact (pin or flat on flat) – provides uniform wear and stable contact, wear-in phenomena cannot be observed since there is no method for regular monitoring of wear behaviour.
- ii. Accelerated testing – achieved by increasing load, speed and temperature, or by decreasing the amount of lubricant in the contact interface and also by continuous operation.
- iii. Specimen preparation – include parameters such as surface roughness, specimen geometry, microstructure, homogeneity, hardness etc., and
- iv. Friction and wear measurements – measured using piezo-electric transducers or load cells, and surface analysis techniques.

Regarding i) the contact geometries selected in this work are approximations of the contact geometries present in the manipulator joint i.e., the sliding cylinder and sliding pin (corresponding to types b and c). According to (Bhushan 2013b) the shape of the pin-end can a flat ended cylinder. Bhushan also elaborates that using ii) as tribo-analysis and testing is economical and time-saving, and therefore accelerated tribo-testing forms part of screening tests which are conducted for design validation of machine parts. Measurements taken with longer strokes and direction reversals simulate pin and bushing joints of a manipulator by the principle of accelerated testing (Blau 2001).

Therefore, tribo-analysis which simulates actual test conditions can be considered to be an approximation, and this necessitates a wide range of testing to encompass actual operating conditions. 'Function of lubricant is to control friction and wear in a given system' (Stachowiak and Batchelor 2013), a view which is supported by (Bhushan 2013a) who says that 'lubricants are commonly used for reducing friction at, and wear of, interfaces'. Lubrication is

an important parameter influencing joint friction since its reduction saves 5% of the total cost (Kato 2014). One of the most effective methods of reducing friction in mechanical joints is through the application of an appropriate lubricant (De Laurentis et al. 2016). To this end, oil or grease lubricants have been commonly used in machine joints.

‘Greases are used where circulating liquid lubricant cannot be contained because of space and cost and where cooling by the oil is not required or the application of a liquid lubricant is not feasible’ (Bhushan 2013a). This has been reiterated by (Stachowiak and Batchelor 2013), according to whom ‘most widespread application of greases is as low-maintenance, semi-permanent lubricants in rolling contact bearings and some gears’. According to (Lugt 2016), grease is a major bearing component, even though it only accounts for about 3% of the total volume of the lubricant industry and provides better performance compared to oil lubricants under selected operating conditions by providing longer bearing life, sealing from environment, and reducing bearing friction and noise. Grease is classified according to the NLGI system and multipurpose grease has been classified as NLGI No.2 greases (Stachowiak and Batchelor 2013). Factors such as grease film thickness and regimes (i.e., hydrodynamic, elastohydrodynamic, boundary and full film) influence the effectiveness of grease lubrication. (Lugt 2016) reports that the delicate balance between feed and loss in grease-lubricated contacts affects bearing surface interaction and sustainability of the grease film. Grease forms a thicker film than corresponding oils and the difference in film build-up mechanism is determined by the type of thickener used. At low speeds, grease friction is governed by the complex nature of the protective films rather than the lambda ( $\lambda$ ) ratio and base-oil properties (De Laurentis et al. 2016).

Oil lubricant, on the other hand, is free-flowing and low viscosity oils have higher fluidity which promotes the supply of oil into the contact (Lugt 2016). This would ensure that the contact is lubricated under all operating conditions. However, the disadvantage would be that oil requires recirculation which in turn requires additional equipment which leads to extra weight and power consumption. Therefore oil lubrication is not feasible for equipment such as manipulator arms. Viscous frictional properties of the base-oil affect COF in

sliding friction, and full-film lubrication leads to longer life of both machine component and grease besides the obvious in reduction in the COF. Figure 16 shows the range of COF for lubrication conditions reported in literature (Armstrong-Hélouvy et al. 1994).

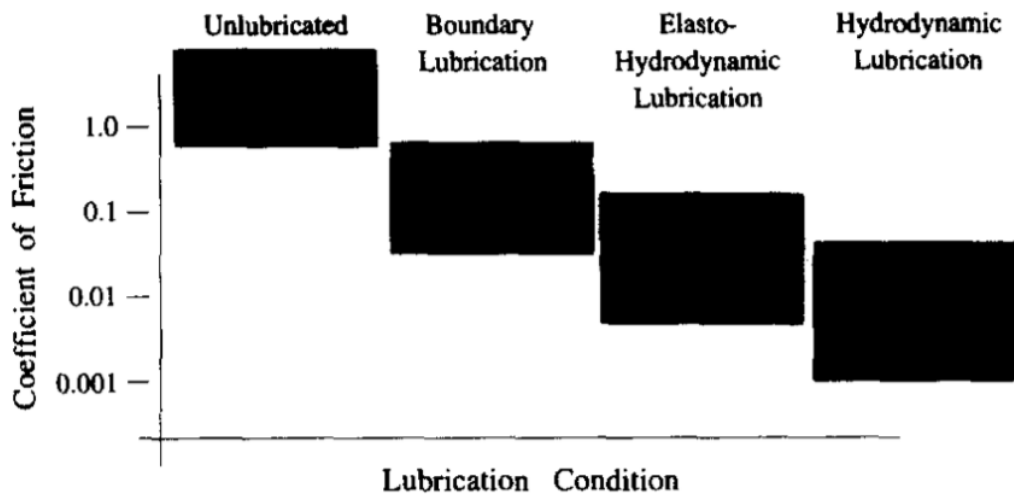


Figure 16 Range of COF against lubrication condition (Armstrong-Hélouvy et al. 1994)

Surfactants improve the durability of surfaces by altering the surface contact characteristics (Sahoo and Das 2011, Zhang et al. 2015). Molybdenum grease has high pressure and anti-wear characteristics and protects surfaces against shock loading (and corrosion) and these have been widely used in industrial equipment and construction plants. Solid additives such as molybdenum disulphide ( $\text{MoS}_2$ ) known as dichalcogenides (Stachowiak and Batchelor 2013), helps lower the COF (especially in the partial slip regime) 'because these do not require high flash temperatures to build up protective layers' and the use of molybdenum with non-molybdenum additives significantly lowers the COF (Lugt 2016). Additionally, molybdenum disulphide provides extreme-pressure characteristics as well as oxidation resistance at high-temperatures (Stachowiak and Batchelor 2013). Also, there exists limited understanding of the mechanisms that operate within grease lubrication. Therefore, experimental determination of COF and other tribo-characteristics for grease-lubricated contacts is required (Lugt 2016) and in this work, oil lubrication is used to generate reference COF values against which COF values using molybdenum grease are contrasted.

### 3.2.3 Tribometer adapter designs

Machine modifications may be required to accommodate minor differences in test parameters and other requirements (Blau 2001). In this work, the reciprocating tribometer was selected for measuring COF and the test specimens were machined locally<sup>2</sup>, giving rise to the possibility of variation from design dimensions. While design improvements to linear reciprocating tribometers through the design improvement of linear reciprocating slideways (Mohan et al. 2009) and modifications to pin and disk tribometer (Kelly and Finlayson 1998) have been reported, adapter designs for reciprocating tribometers have not been revealed through the literature review. It has also been noted that asymmetric holding of the specimen has not been investigated in literature and the adapters presented therein do not possess the capacity to accommodate variation in specimen dimensions arising from low machining tolerances. In the case of tribometer adapters, adapter design for holding specimen based on the V-block has been reported in literature (Sebastian and Bhaskar 1995, Tadić et al. 2002, Minami et al. 2007) as shown in Figure 17.

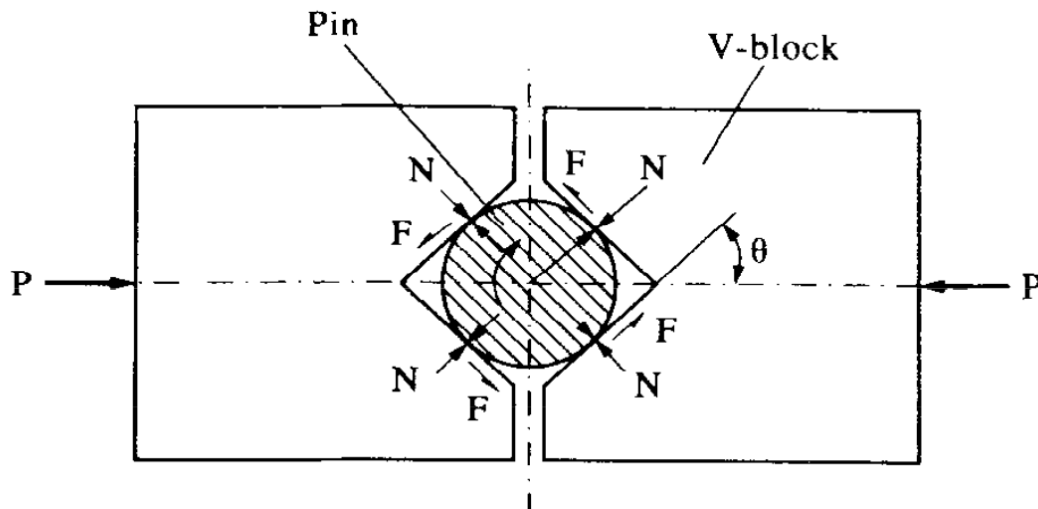


Figure 17 V-notch design in the tribometer adapter (Sebastian and Bhaskar 1995)

Based on this concept, adapter designs based on the v-notch, capable of accommodating specimens with dimensional variation as well as with self-aligning properties were developed.

---

<sup>2</sup> A local manufacturer, M/s FJ engineering, New Milton, Hampshire supplied the test specimens because of the high cost of specimens from the original equipment supplier and budgetary constraints for the project.

### **3.3 Surface modifications for improved tribo- characteristics**

Three surface engineering techniques which could improve COF, wear resistance and surface durability of interacting surfaces are surface treatment, surface modification and surface coating (Ludema 1996, Leyland and Matthews 2000, Schneider and Chatterjee 2013). In addition to the three techniques mentioned above, flame, induction and high energy beam hardening, laser melting, shot peening, chemical hardening (such as phosphate coatings, chromate coatings, anodizing, oxidation), heat treatment (such as carburising, nitriding, carbonitriding and ferritic carburising), ion implantation and laser alloying have been reported (Davis 2001). Surface coatings such as diamond like carbon (DLC) coatings improve the COF characteristics and surface wear resistance (Andersson et al. 2008). As regards coating of 16MnCr5, DLC coating of 16MnCr5 using Plasma Immersion Ion Implantation and Deposition (PIIID) has been presented in (SantAna et al. 2017). Analysis of interaction characteristics of PEEK and Al 7075 alloy for robot cam joints shows improved performance (Koike et al. 2013). Surface texturing also improves the retention of lubrication and wear resistance in the contact (Erdemir 2005).

Even though the application of nanocomposite coatings to sliding surfaces have been reported (Musil 2000, Gomes et al. 2011, Mahidashti et al. 2017), the adaptation of this technique to improve COF characteristics in sliding contact of manipulator joints has to be investigated. The following section looks at the use of nanocomposite coatings in such contacts.

#### **3.3.1 Use of nickel alumina nanocomposite coatings**

Nanocomposites are metal matrix composites (MMC) in which one of the components have a dimension less than 100nm (Roy et al. 1986).

Nanocomposite coatings have been selected for this research since it has been shown that they have superior properties compared to microcomposites. This difference occurs due to the ratio of particle surface property to volume that determines the growth of coating crystals and nature of occlusions that occur within the matrix (Shafiei and Alpas 2008). These coatings have been used widely in industry as evidenced by a large number of scientific studies in recent years (Musil 2000, Gomes et al. 2011, Mahidashti et al. 2017). Coated surfaces

exhibit improved hardness in the range of 250-2000 HV (Thiemig et al. 2007), higher ultimate tensile strength, low ductility and improved wear resistance (Gurrappa and Binder 2008, Jung et al. 2009, Saha and Khan 2010).

Nanocomposite coatings have also been used to improve surface properties including mechanical properties, and improved contact characteristics including COF (Leyland and Matthews 2000), which is a key focus area in this research.

The improved mechanical and chemical properties of these coatings make them both suitable and economical for specialised applications such as the contact interfaces of machine tools and also in the automotive and aircraft industries (Bahrololoom and Sani 2005, Gurrappa and Binder 2008, Thiemig et al. 2009, Gomes et al. 2011), which require enhanced surface characteristics.

Nickel alumina nanocomposite coatings have alumina nanoparticles embedded in the nickel matrix (Camargo et al. 2009) and possess better mechanical characteristics over pure nickel coatings (Thiemig et al. 2009) including improved wear resistance (Shafiei and Alpas 2008), lower friction resistance, higher hardness, and wear and corrosion resistance (Feng et al. 2008, Gurrappa and Binder 2008, Jung et al. 2009, Saha and Khan 2010). Addition of nanoparticles restricts particle agglomeration, which improves hardness and wear resistance (Gomes et al. 2011). The quantity of nanoparticles incorporated into the matrix influences COF and coating properties such as wear resistance (Feng et al. 2008, Mahidashti et al. 2017), corrosion protection (Ciubotariu et al. 2008), oxidation resistance (Musil 2012) and self-lubrication (Julthongpiput et al. 2002, Donnet and Erdemir 2004, Findik 2014).

Nickel alumina nanocomposite coatings are preferred over plain nickel coatings because mechanical characteristics of nanocrystalline coatings improve due to the resistance of the atomic jumps at the thermal barrier at the grain boundaries (Shafiei and Alpas 2008) and microstructural changes (Thiemig and Bund 2009). The presence of alumina (disperoid)<sup>3</sup> nanoparticles perturbs the nickel crystal growth patterns leading to surface morphology and structural changes

---

<sup>3</sup> The suspended particles in a dispersion



(Ciubotariu et al. 2008, Feng et al. 2008). The un-oriented texture of nickel alumina nanocomposites results in improved mechanical characteristics over nickel composites which have a field oriented texture (Thiemig et al. 2007). Wear resistance of nickel alumina nanocomposites has also been shown to be one order higher than nickel coatings due to the change in morphology (Mahidashti et al. 2017).

Therefore, it has been shown that the use of nickel alumina nanocomposites reduces COF and provides better surface properties (Gurrappa and Binder 2008, Jung et al. 2009, Saha and Khan 2010).

### **3.3.2 Pulse Electrodeposition (PED)**

Nanocomposite coatings have been deposited on specimen surfaces using a number of techniques such as chemical vapour deposition (CVD) (Bose et al. 2005), physical vapour deposition (PVD) (Grzesik et al. 2006), magnetron sputtering (Farhat et al. 1996, Singh et al. 2016), brush plating (Wu et al. 2007), electroless coating (Li et al. 2013), electrodeposition (ED) (Raghavendra et al. 2016) and hot isostatic pressing (Mahidashti et al. 2017).

Of these, ED has been classified into direct current, pulse plating (PP) and pulse reverse plating or coating (PRP/PRC) in literature (Thiemig et al. 2009). Pulse electro deposition (PED) has been chosen for this research since its use for coating of nickel nanocomposite coatings has not only proven to be economical but can also be used to produce high quality coatings for complex shapes. Additionally, this method has been considered in this work because it offers better COF characteristics and wear resistance especially in the case of nickel alumina nanocomposites (Raghavendra et al. 2016). It has been shown that composition, structure, nature and concentration of the dispersed phase and the grain size of metal matrix influence the properties of nanocomposite coatings (Thiemig et al. 2007, 2009, Thiemig and Bund 2009, Gomes et al. 2011, Mahidashti et al. 2017).

The use of pulse (or interrupted direct) currents for producing nanocomposite coatings has been reported as early as mid-1980s (Osero 1986). However, the process has undergone refinement over the years and now presents

advantages which include process rapidity, low cost, high purity, industrial applicability, control over parameters such as deposition rates and coating thickness (to atomic width), ability to develop functionally graded coatings or multi-layer porosity-free coatings having different phases, ability to coat complex shapes on different substrates, precise control over crystal size, microstructure, chemistry, deposition rate, redundancy of post-deposition treatment and reduction of additive requirement by 50-60% (Chandrasekar and Pushpavanam 2008, Rashidi and Amadeh 2009, Saha and Khan 2010).

Perturbation at the surface of the specimen promotes the adsorption-desorption process (Kollia et al. 1990). Also, coatings developed using PED have lesser internal stress compared to those developed using direct current (Bahrololoom and Sani 2005) and PED reduces particle agglomeration in the coating (Thiemig et al. 2007), which as referred to earlier, improves hardness and wear resistance (Gomes et al. 2011). This makes PED a favoured method for deposition of a nanocomposite coating.

### **3.3.2.1 Pulse Electrodeposition (PED) parameters influencing coating properties**

There are three main theoretical models governing PED of MMCs (Appendix G) and these models have been validated for specific coating conditions and materials only. Therefore, experimental determination of optimal coating parameters for 16MnCr5 specimens is required (Thiemig et al. 2007, Gomes et al. 2011). Coating parameters which influence nickel alumina nanocomposite coatings have been identified through trial and error (Thiemig et al. 2007).

Key parameters which control the properties of nanocomposite coating deposited using PED are current density, duty cycle, pulse frequency, substrate type, composition and pH value of the electrolyte, ionic concentration, nanoparticle size, temperature of electrolyte, hydrodynamic agitation or stirring (hydrodynamics) and ultrasonic agitation (Gomes et al. 2011). Mass transport, electrical double layer, pulse parameters, surface toughness and morphology also affect coatings (Chandrasekar and Pushpavanam 2008). It has also been seen from (Gomes et al. 2011) that the most important coating current parameters which influence coating quality and coating properties are pulse shape, pulse current intensity, duty cycle, particle loading and additives (composition of electrolyte). Pulse parameters such as cathodic pulse length

( $T_{on}$ ), pulse pause ( $T_{off}$ ), cathodic peak current density ( $I_p$ ), anodic pulse length ( $T_{rev}$ ), anodic peak current density ( $I_{an}$ ) and average current density ( $I_{av}$ ) characterise the nature of electrical pulses used in PED (Thiemig et al. 2007).

The influence of pulse current parameters (pulse shape, pulse current, duty cycle, and composition of electrolyte) on coating properties is discussed below.

### Pulse shape

Pulse shapes have been classified into unipolar and bipolar, cathodic and anodic, intermittent, direct current with superimposed modulations, duplex, pulse-on-pulse, sequential cathodic pulse followed by anodic pulse, high frequency pulse with superimposed periodic reverse pulse, modified sine-wave, square wave (Xuetao et al. 2008), rectangular wave (Thiemig et al. 2009), saw-tooth wave and ramp or triangular wave (Chandrasekar and Pushpavanam 2008).

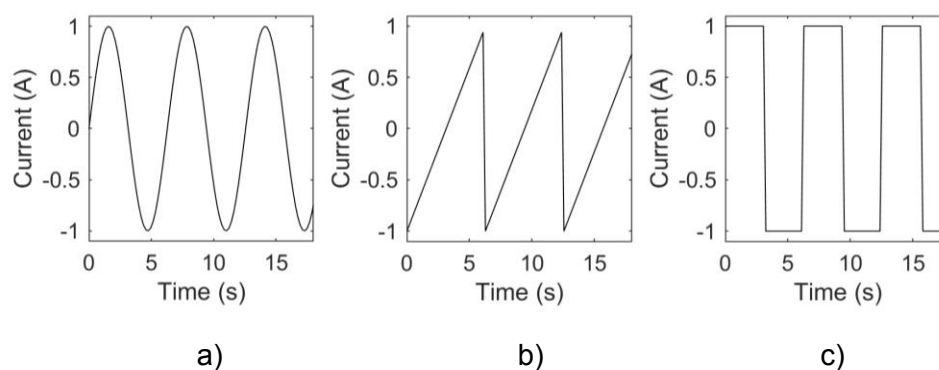


Figure 18 Different types of waveforms a) sine b) rectangular and c) triangular waveforms

Examples of sine, triangular and rectangular waveforms have been shown in Figure 18. Amongst these, the use of rectangular wave improves the mechanical properties for nickel alumina nanocomposite coatings (Thiemig et al. 2009) and therefore this waveform was used in this research.

### Pulse current

Pulse current influences coating properties such as microstructure of nanocomposite coatings, rates of nucleation and crystal growth (Thiemig et al. 2007, Chandrasekar and Pushpavanam 2008, Gomes et al. 2011). Density of the deposition current determines the growth rate of coating film (Gomes et al. 2011). Lower particle incorporation at higher current densities has been reported (El-Sherik et al. 1997) and this is due to the insufficient time for the particles to be absorbed and the release of hydrogen bubbles on the surface

causing surface pitting (El-Sherik et al. 1997). The corollary that higher particle incorporation occurs at lower values of average current density has also been reported (Thiemig et al. 2007). Areas under the influence of high current density experience ion depletion (Chandrasekar and Pushpavanam 2008) which is replenished during the pulse off-time as well as by stirring the electrolyte.

Pulse currents of different intensities for nickel alumina nanocomposite coatings have been reported as follows: 20mA/cm<sup>2</sup> (Jung et al. 2009), 3A/dm<sup>2</sup> (Chen et al. 2006, Feng et al. 2008), 20mA/cm<sup>2</sup> (Jung et al. 2009), 30mA/cm<sup>2</sup> (Badarulzaman et al. 2009), 5A/dm<sup>2</sup> (Bahrololoom and Sani 2005, García-Lecina et al. 2012, Majidi et al. 2016), 2.3mA/cm<sup>2</sup> (Peipmann et al. 2007), 5A/dm<sup>2</sup> (Mirzamohammadi et al. 2017), 1-2A/dm<sup>2</sup> (Raghavendra et al. 2016), 2A/dm<sup>2</sup> (Ciubotariu et al. 2008). (Thiemig et al. 2009) have investigated the relationship between current intensity and particle incorporation for different loading rates for 50nm  $\gamma$ -alumina (Al<sub>2</sub>O<sub>3</sub>) as shown in Figure 19. Although a strong correlation has not been observed between the parameters, the particle incorporation appears to be substantially more around a current intensity of 10A/dm<sup>2</sup> for different loading rates. Therefore, current intensity (*i*) in this range is expected to promote coating and therefore this was selected for conducting coatings. Since the size of the alumina nanoparticles used in this research lies in the similar range of 40-50nm (Bajwa, Khan, Nazir, et al. 2016), current intensity in the range of 5-10A/m<sup>2</sup> was used for coating.

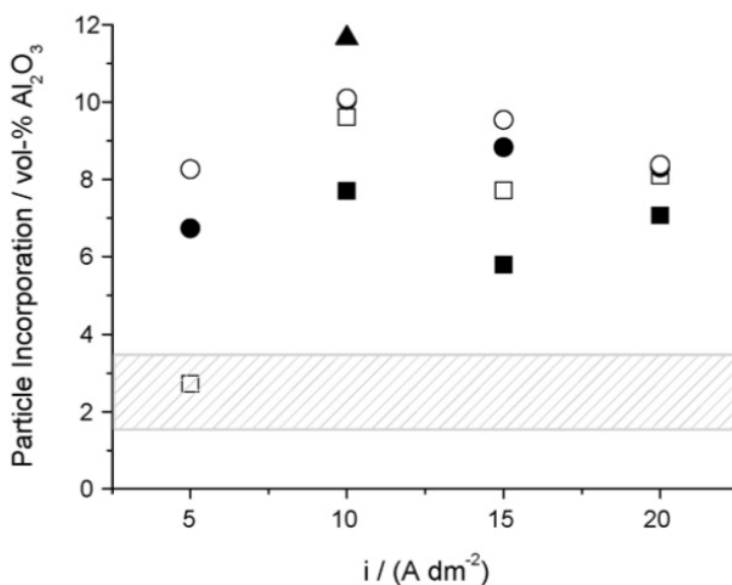


Figure 19 Current intensity and particle incorporation for 50nm  $\gamma$ -alumina (Al<sub>2</sub>O<sub>3</sub>) particles for different loading rates: (■) 10g/l, (□) 30g/l, (●) 60g/l, (○) 90g/l, (▲) 120 g/l (Thiemig et al. 2009)

## Duty Cycle

The relationship between three independent variables in PED namely cathodic pulse length ( $T_{on}$ ), pulse pause ( $T_{off}$ ) and cathodic peak current density ( $I_p$ ) has been reported as follows (Chandrasekar and Pushpavanam 2008):

$$\gamma = \frac{T_{on}}{T_{on}+T_{off}} = T_{on} f \quad (14)$$

where  $\gamma$  is the duty cycle,  $f$  is the frequency of the pulse current defined as inverse of cycle time  $T = T_{on} + T_{off}$ .

Also, the relationship between average coating, peak coating current and duty cycle has been reported as follows (Chandrasekar and Pushpavanam 2008):

$$I_{av} = I_p \cdot \gamma \quad (15)$$

where  $I_{av}$  is the average current density and  $I_p$  is the cathodic peak current density.

Duty cycle influences coating properties, and has a greater effect on coating hardness compared to pulse frequency (Kim and Weil 1989). Lower duty cycle improves particle deposition and mechanical/structural properties such as hardness (Bahrololoom and Sani 2005). However, contrary to the above observation, it has been found that particle incorporation decreases with decreasing duty cycle in the case of both 13nm  $\gamma$ -alumina nanoparticles (Thiemig et al. 2009) and 45nm  $\alpha$ -alumina nanoparticles (Jung et al. 2009). It has also been observed that decreasing duty cycle and frequency results in increased wear resistance for nickel alumina micro-composites (Bahrololoom and Sani 2005).

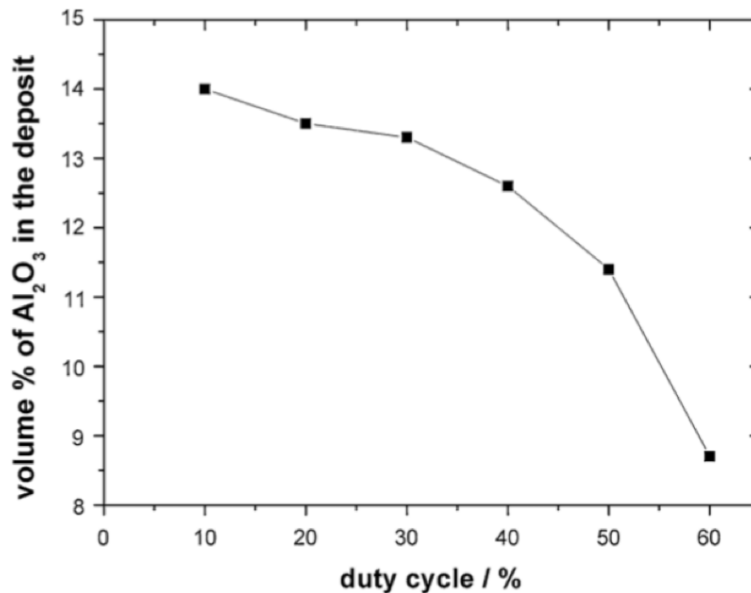


Figure 20 Effect of duty cycle on volume of alumina nanoparticles incorporated into the matrix (Jung et al. 2009)

From Figure 20, it can be inferred that particle incorporation decreases with an increase in duty cycle and drops off sharply at 40% duty cycle for 45nm  $\gamma$  - alumina nanoparticles due to the development of a negative charge layer around the cathode, whose thickness increases under the action of a direct current and prevents further deposition of ions on the substrate surface (Jung et al. 2009). Turning off or pausing the current causes this layer to dissipate and ion concentration to increase, which then allows deposition to resume in the subsequent cycle and also increases the limiting current density ( $I_L$ ) (Jung et al. 2009).

However, increasing the pulse frequency reduces coating efficiency because metal ions are unable to discharge at the substrate surface in the short off-time (Bahrololoom and Sani 2005). Pulses having duration of the order of milliseconds i.e. short on-times, improve coating deposition rate and distribution of alumina nanoparticles (Gomes et al. 2011). Also, at low duty cycle and high current intensity, deposition rates for PED approach that of direct current coatings for nickel (Chandrasekar and Pushpavanam 2008). It has also been observed that increase of duty cycle and frequency results in increased wear resistance for multilayer nickel alumina nanocomposite coatings (Majidi et al. 2016).

The following duty cycles for PED have been reported in literature: 5% or higher (Chandrasekar and Pushpavanam 2008), 10-20% (Bajwa, Khan, Nazir, et al. 2016), 10% to 60% (Jung et al. 2009), 67% (Thiemig et al. 2009), 20,50,80% (Majidi et al. 2016), 50% (Mirzamohammadi et al. 2017), 20-80% (Bahrololoom and Sani 2005), 20-67% (Thiemig et al. 2009) and 85% (Feng et al. 2008).

Thus, a range of duty cycles appears to have been used in literature. This makes it imperative to select of duty cycle through a process of trial and error rather than use a rule-based approach for determining appropriate duty cycle to coat 16MnCr5 specimens with nickel alumina nanocomposite.

### **3.3.2.2 Composition of electrolyte**

Experimental parameters used for PED of nickel alumina nanocomposite coatings from literature is consolidated in Table 6. According to (Cooke 2016), properties of nanocomposite coatings are affected by the electrolyte composition which is influenced by particle loading (PL), which is the concentration of nanocomposite particles (here alumina nanoparticles) in the electrolyte and has been reported to be the most influential parameter in addition to the pH of the electrolyte.

#### **Particle loading**

Nanocomposite coatings typically exhibit incorporation rates in the range of 1-2% compared to microcomposites which exhibit a higher incorporation rate of 25% to 30% by weight (Mahidashti et al. 2017). Particle loading (PL) range of 2g/l (Badarulzaman et al. 2009) to 120g/l (Jung et al. 2009, Thiemig et al. 2009) has been reported. 120g/l has been identified as the upper threshold for PL after which sedimentation occurs (Thiemig et al. 2009) and the presence of 120g/l alumina particles has led to the reduction of crystallite size of nickel matrix from 115nm to 30nm (Gomes et al. 2011). Increase in PL from 2g/l to 200g/l increases particle incorporation from 1% to 10% by volume (Gomes et al. 2011). For 10g/l PL, particle incorporation range of 1.6 to 7.7% by volume has been reported. Particle incorporation of 12% by volume for 50nm alumina deposition has been observed (Thiemig et al. 2009). Particle incorporation rate ranges from 2.1 to 6.2% by volume for PED (Thiemig and Bund 2009). Incorporation rate of 3.14% by volume of alumina has been reported for 13nm alumina at 10g/l loading, with higher incorporation rates for pulse reverse plating (Thiemig and Bund 2009). Maximum dispersed phase incorporation

occurs when deposition thickness per cycle approaches particle diameter (Thiemig et al. 2007). Particle content of 15% by volume improves coating characteristics such as hardness, wear resistance and flow stress. Particle incorporation range of 3.5-12% by volume has been achieved by impinging jet technique under similar conditions (Thiemig et al. 2009). 20g/l PL used in previous studies (Bajwa, Khan, Nazir, et al. 2016) has been selected for use in this investigation.

### **Additives**

Several investigations have reported the use of additives such as sodium saccharine, hexadecylpyridinium bromide, sodium dodecyl (or lauryl) sulfate and naphthalene-1,3,6 trisulfonic acid trisodium salt to promote particle incorporation and improve coating characteristics (Table 6). However, the use of these additives has been reported to show both advantages and disadvantages. For instance, naphthalene-1,3,6 trisulfonic acid trisodium salt has been shown to improve wear resistance but also increases the fracture susceptibility of coatings in quasi-static compression (Jung et al. 2009).

Similarly, the presence of ethanol in the electrolyte under low current densities is beneficial for particle entrapment for 13nm alumina through the formation of a thin hydration layer around the nanoparticles. However, lowering ethanol content promotes coating microhardness, along with morphological properties (Thiemig et al. 2009). Interestingly, it has been shown that the use of organic additives such as triethanolamine, glycerol, formaldehyde, ethanol, methanol and carbamide improves particle incorporation rates from 3.1 to 5.6% by weight, although to the contrary, sodium saccharine at a concentration of 5% does not improve coating characteristics in the case of pure nickel coatings (Jung et al. 2009). In this work, electrolyte composition previously utilised by (Bajwa, Khan, Nazir, et al. 2016) was used (Table 6), and this is supported by evidence presented in (Mirzamohammadi et al. 2017), in which additive free baths yield 2.1% alumina incorporation for 35nm alumina nanoparticles.



	Composition	(Feng et al. 2008)	(Ciubotariu et al. 2008)	(Jung et al. 2009)	(Badarulzaman et al. 2009)	(Thiemig et al. 2009)	(Saha and Khan 2010)	(García-Lecina et al. 2012)	(Majidi et al. 2016)	(Bajwa, Khan, Bakolas, et al. 2016a)	(Mirzamohammadi et al. 2017)
Basic composition	NiSO <sub>4</sub> .6H <sub>2</sub> O	240	1M	281	300	1.08M (Nickel Sulfamate)	1.0 mol/dm <sup>3</sup>	250	250	265	250
	NiCl <sub>2</sub> .6H <sub>2</sub> O	40	1M	60	50	0.04M	0.2 mol/dm <sup>3</sup>	45	40	48	40
	H <sub>3</sub> BO <sub>3</sub>	35	0.2M	30	40	0.65M	0.5 mol/dm <sup>3</sup>	40	35	31	-
	Al <sub>2</sub> O <sub>3</sub>	0-10	20	120	2	0-120	0.5 mol/dm <sup>3</sup>	25,50,100	50	20	10
	H <sub>2</sub> SO <sub>4</sub>	yes	-	-	10%	-	-	-	-	-	-
Other parameters	pH	4		-	3.6-4	4.3	4	4	-	4.5-5.10	3.6±0.2
	Temperature °C	50	40	50	27	40	20	55	25±2	-	53±2

	Composition	(Feng et al. 2008)	(Ciubotariu et al. 2008)	(Jung et al. 2009)	(Badarulzaman et al. 2009)	(Thiemig et al. 2009)	(Saha and Khan 2010)	(García-Lecina et al. 2012)	(Majidi et al. 2016)	(Bajwa, Khan, Bakolas, et al. 2016a)	(Mirzamohammadi et al. 2017)
Organic Additives	Sodium Saccharine, $C_7H_4NO_3S.Na$	-	-	3.54		-	-	5	-	-	-
	Hexadecylpyridinium bromide (brightener)/Organic Solvents	-	-	-	0.3	-	-	-	-	-	10
	Sodium dodecyl (or lauryl) Sulfate $NaC_{12}H_{25}SO_4$ , <i>naphthalene-1,3,6 trisulfonic acid trisodium salt</i> $C_{10}H_5(SO_3Na)_3 \cdot xH_2O$	-	1.2e-3M	0.2/7.5	0.1	-	-	-	-	-	-

Table 6 Comparison of electrolyte compositions for PED of nickel alumina nanocomposite coating

### **3.3.2.3 Other parameters influencing PED of nickel alumina nanocomposite coatings**

The use of several other parameters such as ultrasonic agitation, stirring and heating for improving coating properties have been reported in literature. At low duty cycles, driven by hydrodynamic effect, particles replenish the supply at cathode surface. Electromagnetic stirring at 200 - 300rpm induces hydrodynamic flow which improves particle distribution and ion replenishment at the surface of the specimen being coated (Aruna et al. 2009) and rate for maximum particle incorporation has been recorded to be in the range of 2 to 3lmin<sup>-1</sup> (Thiemig et al. 2009). Electromagnetic stirring of up to 120rpm causes an increase in incorporated SiC particles and beyond this upper threshold, a decline has been observed in the incorporation rate, which is attributed to the hydrodynamic removal of particles before absorption at the surface (Gomes et al. 2011). The increased availability of particles leads to ready absorption during the subsequent pulse-on cycle (Bahrololoom and Sani 2005). It has also been reported that ultrasonic agitation during coating process alleviates agglomeration of nanoparticles (García-Lecina et al. 2012, Bajwa, Khan, Nazir, et al. 2016). In light of these reports, electromagnetic stirring and ultrasonic agitation were included in the experimentation conducted as part of this research to improve coating deposited by PED. Use of bath temperatures in the range of 20-55°C (Table 6) without any significant improvements in coating properties has been reported. In this work, PED was conducted at 40°C to standardize the coating process.

### **3.3.3 Influence of nanocomposite coatings on COF**

In this context, existing literature broadly covering the effect of nanocomposite coating is presented below. COF for nickel alumina nanocomposite coating deposited using PED has been reported in ranges of 0.3 to 0.7 and 0.55 to 0.7 when using sediment co-deposition technique over a range of 0 to 10g/l PL of alumina in the electrolyte (Feng et al. 2008). According to (Mahidashti et al. 2017), COF from 0.2 to 0.7 has been reported for 3.5-12% particle incorporation by volume in the case of 80nm alumina, 0.04-0.5 for 4-13% by volume for 80nm alumina, 0.1-0.12 for 30nm alumina and high COF values in the range of 0.819 for 40nm alumina as presented in Figure 21. Therefore, it is evident that higher particle incorporation leads to higher COF.

Coating composition	Particles percentage inside coating	Thickness (μm)	Particle size (nm)	Hardness (HV)	Wear rate	Counter body	COF	Roughness (R <sub>a</sub> ) (μm)
Ni-Al <sub>2</sub> O <sub>3</sub>	3.5–12 vol%	50–200	80	460–625	Reciprocating 8–12 × 10 <sup>-4</sup> mm <sup>3</sup> /Nm	M50 Steel ball	0.2–0.7	N.R.
Ni-Al <sub>2</sub> O <sub>3</sub> + HPB	8–15 vol%	90	800	470–550	Reciprocating 3.5–11.5 × 10 <sup>-4</sup> mm <sup>3</sup> /Nm	AISI-52100 stainless steel ball	N.R.	N.R.
Ni-Al <sub>2</sub> O <sub>3</sub>	0–45 vol%	100	100	300–680	Erosion tester Weight loss 1–24 mg*	angular alumina	N.R.	N.R.
Ni-Al <sub>2</sub> O <sub>3</sub> -SiC	Al <sub>2</sub> O <sub>3</sub> : 9.2 SiC: 7.7 vol%	36	50	767	Grinding Weight loss 0–5 mg/cm <sup>2</sup> *	2000-grit SiC waterproof paper	N.R.	N.R.
Ni-Al <sub>2</sub> O <sub>3</sub>	4–13 vol%	N.R.	80	PC: 360–690 HVDC: 440–680	Reciprocating 1–9 × 10 <sup>-4</sup> mm <sup>3</sup> /Nm	M50 steel ball	0.04–0.5	N.R.
Ni-Al <sub>2</sub> O <sub>3</sub>	7–11 vol%	100–120	600	450–540	Reciprocating 3–9 × 10 <sup>-4</sup> mm <sup>3</sup> /Nm	AISI-52100 stainless steel ball	N.R.	N.R.
Ni-nanoAl <sub>2</sub> O <sub>3</sub>	N.R.	50	30	Vertical: 6.96 ± 0.025 Horizontal: 6.94 ± 0.05	N.R.	45 steel	0.1–0.12	N.R.
Ni-nanoAl <sub>2</sub> O <sub>3</sub>	N.R.	100	30	350–600	Fretting wear test Wear depth 8–24 μm**	Steel ball	N.R.	N.R.
Ni-Al <sub>2</sub> O <sub>3</sub>	Conventional bath: 17.4 Supercritical bath: 16.8–18.6 vol%	30	300	Conventional bath: 480 Supercritical bath: 800	Pin on disk Conventional bath: 78.8 μm Supercritical bath: 50.8–52.1 μm**	Diamond	N.R.	N.R.
Ni-Al <sub>2</sub> O <sub>3</sub>	N.R.	11	α: 40 γ: 5 Commercial: 40	α: 483 ± 19 γ: 390 ± 9 Commercial: α + γ+δ: 350 ± 12	Pin on disk Wear coefficient: α: 1.9 × 10 <sup>-7</sup> γ: 7.37 × 10 <sup>-7</sup> α + γ+δ: 1.8 × 10 <sup>-6</sup> mm <sup>3</sup> /Nm	Brass	α: 0.819 γ: 0.760 α + γ+δ: 0.764	N.R.

Figure 21 Table showing COF from various tests (Mahidashti et al. 2017)

However, it is important to note that these COF values have been measured for various materials in elliptical sliding contact configuration i.e., ball on disc or on pin on disc contacts and for materials ranging from M50 steel, AISI-52100 stainless steel, SiC abrasive paper, 45 steel, diamond and brass (Mahidashti et al. 2017). Measurement of COF for cylindrical and pin sliding contacts for nanocomposite coated steels are yet to be reported in literature and this work

explores the COF of the coated 16MnCr5 specimen with EN19 counter-face in sliding reciprocating contacts which simulate the reversible operation of the manipulator joint designated for use in SAR environment.

Reduction of COF for applications in SAR environments would result in optimal design, reduction in vibration signatures of equipment and improved dynamic performance of the manipulator. Comparing the measured COF values to those presented in literature would also provide insight into the contact COF characteristics and performance of nanocomposite coating.

### **3.3.3.1 Nanocomposite coating characteristics affecting COF**

Characteristics of nanocomposite coatings i.e., hardness and particle incorporation which influences hardness from literature are reviewed in this section. Presence of ceramic particles alters the microstructure of coating, resulting in increased coating hardness (Bahrololoom and Sani 2005, Shafiei and Alpas 2008, Thiemig and Bund 2009). Particle reinforced nanocomposite coatings have isotropic properties (Chawla and Shen 2001). Among nanocomposites, higher nanoparticle content increases coating hardness (Jung et al. 2009) and among the ceramic particles, nano-crystalline alumina exhibits greater strength and hardness compared to microcrystalline alumina (Saha and Khan 2010) substantiating the choice of nanocomposites over microcomposites in this research. Also, nanocomposite coatings possess superior properties compared to pure-nickel coatings (Bajwa, Khan, Nazir, et al. 2016) and it has been observed from literature that nanocomposites with smaller grain sizes have greater hardness due to i) grain refinement, ii) dispersion hardening and iii) particle strengthening (El-Sherik et al. 1997, Feng et al. 2008, Mahidashti et al. 2017).

Coatings having 726HV (Vickers hardness value) has been reported in the case of direct current (DC) plating conducted using 5nm alumina and a coating current of 0.01A/cm<sup>2</sup>, although it decreases to 593HV for current intensities of 0.02A/cm<sup>2</sup> and 0.03A/cm<sup>2</sup>. Coating hardness has not been reported for 0.005A/cm<sup>2</sup> because of limitations imposed by coating thickness (Saha and Khan 2010). For 13nm alumina, DC plating produces hardness value of 522HV (Thiemig et al. 2009). For 30nm alumina under 0.03A/cm<sup>2</sup> (3A/dm<sup>2</sup>), hardness of 330 HV has been recorded (Saha and Khan 2010) and hardness of 295HV

has been reported for coatings developed using organic additive-free bath and 35nm alumina (Bajwa, Khan, Nazir, et al. 2016). Hardness of 465HV has been reported for 100g/l particle loading for 40-47nm alumina (García-Lecina et al. 2012). For 100nm alumina, hardness of the order of 550HV has been recorded for 5g/l PL and 700HV for 10g/l PL using conventional electrodeposition. Also, increase of PL from 0 to 10g/l has the effect of wear rate reduction from approximately  $21 \times 10^{-4} \text{ mm}^3/\text{Nm}$  to  $4 \times 10^{-4} \text{ mm}^3/\text{Nm}$  (Feng et al. 2008).

Hardness of 406HV for 45nm alumina nanocomposite coatings, 285HV with sodium saccharine and 429HV for sodium naphthalene-1,3,6 trisulfonic acid trisodium salt have been reported (Jung et al. 2009). Hardness value of 395HV has been recorded in the presence of triethanolamine and 510HV in the presence of carbamide (Mirzamohammadi et al. 2017), which indicates that some additives may improve coating hardness in specific cases. The order of hardness decreases from 700HV to 550HV for increase in duty cycle from 20 to 80 (Majidi et al. 2016). The use of ultrasonic stirring increased coating hardness by more than 10% over the use of mechanical stirring alone (García-Lecina et al. 2012).

### **3.3.4 Surface characterisation**

Surface analyses comprise the study of surface characteristics, wear and hardness. In this section, the various techniques that can be used are reviewed and appropriate techniques in the context of this work have been identified from literature. Blau (2001) lists precision microbalances, profiling instruments, hardness testers, and microscopes of various types as common equipment for analysing surface characteristics and wear. White light interferometry which is a non-contact optical method for measuring the surface profile of specimens whose height lies in the range of nanometres to centimetres, has been used in (Bajwa, Khan, Bakolas, et al. 2016b) for characterising the wear track on the surface of the test specimens. White-light interferometry was used to measure surface characteristics of the specimens. An alternative technique for characterising specimen surfaces is digital microscopy (Beake et al. 2006), which provides magnifications from x30 to x2500, and this technique has been applied to large wear scars which exceeded the measurement capabilities of the white light interferometer. Scanning electron microscopy (SEM) on the other

hand provides magnifications from x30 to x40000 or above, and has been used in literature for closer examination of wear scars and microstructural analysis of nanocomposite coated surfaces (Chen et al. 2006, Feng et al. 2008, Aruna et al. 2009, Saha and Khan 2010, Borkar and Harimkar 2011, Majidi et al. 2016, Góral et al. 2017). However, it has also been noted that 'SEM does not provide best microstructural analysis' for nanocomposites (Thiemig et al. 2007).

Surface hardness of specimens have been measured by using Vickers microhardness indentation tests in literature and these tests have been conducted for varying loads for thick coatings (Leyland and Matthews 2000, Bahrololoom and Sani 2005, Chen et al. 2006, Feng et al. 2008, Jung et al. 2009, Saha and Khan 2010). In this work, the surface hardness of specimens both plain and coated were measured using the Vickers microhardness indenter.

### **3.4 Knowledge gaps and research objectives**

Literature reveals that friction in manipulator joints affects manipulator dynamics and positioning (Lischinsky et al. 1999) and the incorporation of friction modelling into dynamic simulation is not expected to provide a comprehensive understanding of the tribo-characteristics. This necessitates scaled-down tribo-testing using a reciprocating tribometer as reported in literature.

However, investigations into the tribo-characteristics of the 16MnCr5-EN19 steel alloy pair have not been reported in the context of manipulator joints in the extensive literature review conducted, despite this steel alloy pair being widely used for retrofitting in the excavator industry and associated equipment. While surface modifications to 16MnCr5 have been reported in literature, the use of PED for nickel alumina nanocomposite coating deposition on this alloy has hitherto not been reported and this opens up a venue for investigation and prospective improvement of tribo-characteristics.

As mentioned in the introduction, this literature review was conducted on the last two aims (RA3 and RA4) with the intention of identifying corresponding research objectives and setting test parameters (ROs). These are presented below in Table 7.

	Research Aim	Research Objective
Tribology	RA3: To analyse feasibility and identify appropriate methods for experimental measurement of COF	RO1: Investigate the influence of parameters affecting COF of plain specimens RO2: Generate reference values of COF for comparison with COF values under selected operating conditions RO3: Analyse surface characteristics of plain specimens
	RA4: To investigate the use of surface engineering techniques for improving contact tribo-characteristics	RO1: Apply nanocomposite coating RO2: Investigate the effect of coating on tribo-characteristics and compare with plain contacts RO3: Analyse surface characteristics of coated specimens

Table 7 Research aims and corresponding objectives for literature review-2

### 3.5 Combined scope of research and study restrictions

Taking into consideration the design aspect of the thesis (reviewed in Chapter 2), the combined scope of the work encompasses the following:

- i. Developing proof of concept for the application of CAD design technique to SAR mobile manipulator using virtual prototyping approach,
- ii. Developing block diagrammatic modelling and simulation of manipulator mechanics incorporating combined joint friction model using multibody simulation,
- iii. Experimentally determining COF for the 16MnCr5-EN19 steel, and
- iv. Developing nickel alumina nanocomposite coating for 16MnCr5 using PED for assessing the influence of newly developed nanocomposite coatings on tribo-characteristics including COF.

Due to budgetary constraints of the project, physical prototypes could not be fabricated and therefore, virtual prototyping was selected. This acts as proof of concept that the CAD-MBD approach allows for cost-effective quick turnaround from design to deployment. Given that the scope of this research is interdisciplinary and straddles two major domains- design and simulation and tribological analysis, there several limitations that were put in place in order to ensure coherence. In the first place, owing to complexity, simulation of friction



modelling was attempted but it has also had to be limited. However, this was addressed through tribo-tests as suggested in literature. In the area of tribo-tests, only reciprocating tribometer was selected and test specimens were fabricated locally because of budgetary constraints. Design of 16MnCr5 specimens had to be altered because of machining issues reported by the manufacturer. As part of the tribological analysis, the scope of study was restricted mainly to COF because this parameter affects the dynamics of the sDOF joint directly. Wear analysis can be pursued in the future and will help determine the transition of joint between sDOF and mDOF (Flores et al. 2006). Although several parameters influence the COF generated in the contact, this study was restricted to contact geometry, load, lubricant and surface properties such as roughness. Detailed parameter testing is envisaged in future works and this is presented in section 8.5.

### **3.6 Summary**

Firstly, the literature review of this chapter was built on the basis of research questions and research aims pertaining to tribological analysis presented in Chapter 1 and these are delineated into specific research objectives. From reviewing literature, appropriate material and equipment identified and the parameters for experimental design were set. The combined scope of research and study restrictions covering Chapter 2 and the present chapter has also been presented.

# Chapter 4 Design, modelling and dynamic simulation of mobile manipulators

## 4.1 Introduction

Even though robotic platforms and manipulators have been presented in literature, there is little evidence supporting robotic manipulators capable of lifting heavy loads for assisting rescue personnel, although some specialised manipulators exist for other applications. However, numerical modelling and computation of dynamics for new manipulator designs is a time and resource intensive process requiring considerable expertise in mathematical formulation (Barone et al. 2002). Therefore, this chapter investigates the use of Computer Aided Design (CAD) -Multi Body Dynamics (MBD) simulation approach for the design and simulation of mobile manipulators for time-critical deployment in SAR operations.

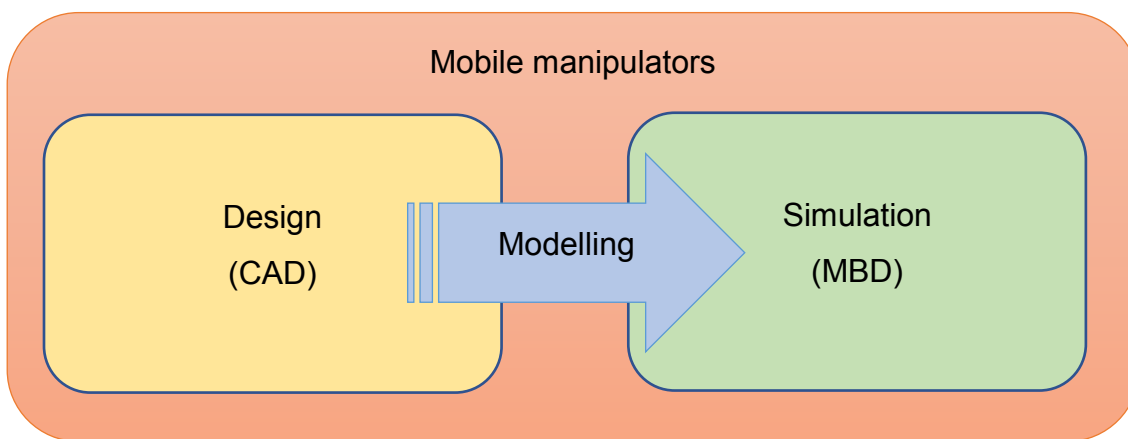


Figure 22 Layout of Chapter 4 design, modelling and dynamic simulation of mobile manipulators

Therefore, modelling and simulation of a serial open-chain anthropomorphic arm and a scaled-down closed-loop mobile manipulator design inspired by excavator manipulator are presented. The latter is presented in two stages resulting in three case-studies built on two designs. Given that friction has been reported as the most significant tribological aspect in the manipulator joint, friction models are also incorporated into the simulations.

#### **4.1.1 Relevance and context of research**

In the context of the brief introduction above, this research project can be considered to be the first step in the direction of developing application-specific mobile manipulators for SAR operations, which can be mounted on robotic platforms. To this end, CAD is used to produce new virtualised designs based on the approximation approach (Merlet and Gosselin 2008). This investigation presents proof-of-concept for the application of CAD for modelling and Multi Body Dynamics (MBD) for simulating the new design. The use of this method in literature is aimed at accelerating the design process of application specific mobile manipulators thereby reducing both development costs in the early stage of design and failure rate in critical deployments (Vergnano et al. 2017).

CAD-MBD approach has been used successfully in several applications including manipulators in space, development of two-wheeled vehicles and robots as explained in section 2.1.3 of the literature review. In addition to design and simulation, this approach is also envisaged to help and aid the effective preparation for SAR operations as mentioned in the same section of the literature review. Therefore, selected application-specific manipulator designs were developed based on the anthropoid limb dimensions and scaled-down excavator manipulator using the combination of CAD and MBD.

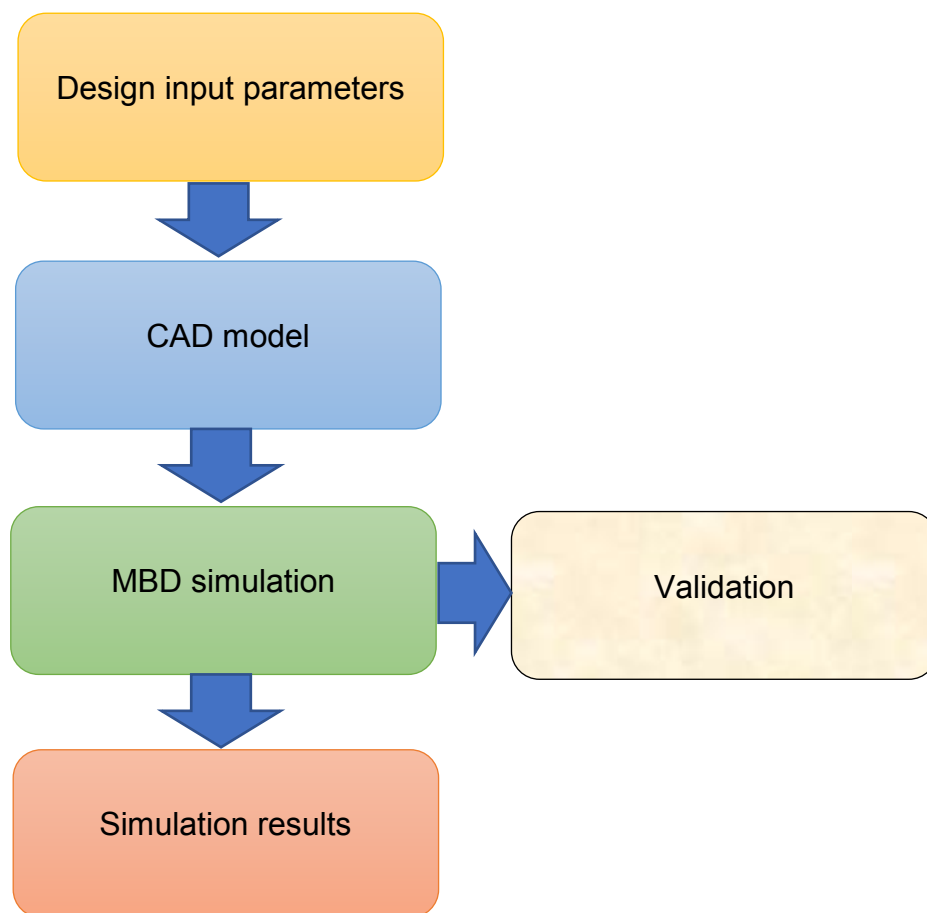


Figure 23 Procedure for the development and validation of manipulator models

The workflow used for design and simulation is presented in Figure 23. In the first stage, the design input parameters are identified from literature and real models based on which the CAD model is generated in the second stage. The CAD model is then exported to the MBD simulation environment in the third stage. The block diagram representation in the MBD environment provides greater clarity into the design besides simplifying simulation data into visualisations, which are easier to comprehend as opposed to two-dimensional graphical representations. For validation, simulation output from a simple model is compared with the output from previously established technique presented in literature (SimMechanics 1<sup>st</sup> generation) neither of which have been previously applied to SAR. The simulation output of the complex manipulator linkages is recorded and presented in the fourth stage. Robotic manipulators almost always operate in three-dimensional space as opposed to two-dimensional space and existing literature on the mechanics of heavy manipulators is also restricted to two-dimensional modelling and simulation (section 2.1.3).

In summary, the relevance of this work can be summed up as follows: this work analyses the development of mobile manipulator designs for deployment in SAR environments and investigates the use of CAD for design, MBD for simulation and also attempts to include friction model in the simulation as friction is a very important component influencing the dynamic performance of the manipulator.

## 4.2 Design of mobile manipulators

As substantiated in section 2.2.1 of the literature review, application specific designs for SAR would be more suited to the operating conditions as it has been shown that large excavators could cause more collateral damage. As a first step towards developing such a manipulator mechanism, two types of manipulator designs were considered in this thesis as presented in Figure 24, as proofs-of-concept for use while mounted on a robotic platform. These are discussed in detail in section 4.2.2.

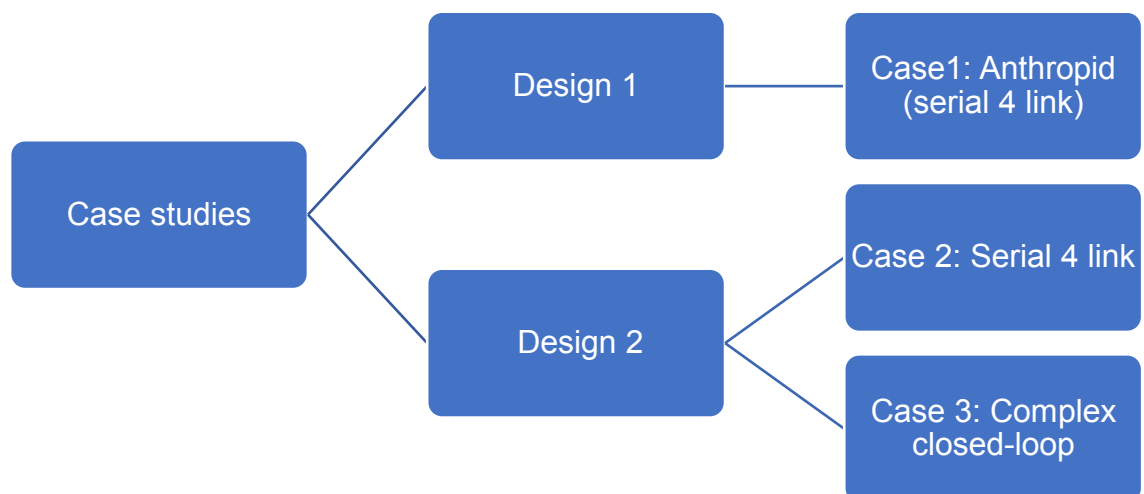


Figure 24 Design and case studies

### 4.2.1 Selection of design input parameters

As shown in Figure 23, the CAD modelling process begins with the selection of design input parameters. As explained above, two manipulator designs are presented in three case studies. The parameters for cases 2 and 3 are the

same since they are both part of the second design. The details are presented in Appendix B.

### **Design input parameters for anthropoid manipulator**

Nominal limb lengths were used as the design input parameters since the manipulator mimics the action of the human arm. Specific details are presented in section 4.2.2.1.

### **Design input parameters for closed-loop complex manipulator**

The following parameters were used as design inputs:

- i. The links of the manipulator were designed using scaled-down dimensions of the large manipulator available in literature (Koivo 1994).
- ii. Shape of the end-effector was also designed based on industrial equipment used for earthmoving (Koivo 1994).
- iii. Actuator dimensions such as length of actuation travel were obtained from dimensions of commercially available actuators (Gimson Robotics 2015). This approach was used since commercial actuators are easily available, are designed based on industry standards, and are therefore easily replaceable in damaged robots compared to specialised actuators which are expensive and difficult to replace.
- iv. Material for links was also selected from literature (Billing and Fleischner 2011, Popić and Miloradović 2015).

The specifics are considered in the individual case studies as in the case of the anthropoid manipulator.

#### **4.2.1.1 Selection of revolute joint**

Selection of an appropriate joint is essential for smooth operation and longevity of the manipulator mechanism as motion occurs at the joints of the linkage or mechanism. In this type of manipulator linkage, the motion between two main links of the manipulator is revolute and the motion between links of the actuator is prismatic. The revolute joint is the focus of design considerations in this work as mentioned in the previous section.

In smaller robotic mechanisms, anti-friction bearings have been used in the revolute joints connecting two links of the manipulator. However, from design considerations, failure of anti-friction bearings is likely to occur rapidly for heavy as well as unsteady loads, which are present in manipulator mechanisms interacting with soil or rock (Chacko et al. 2014). The design of anti-friction

bearings to prevent such type of failure is infeasible because of the resulting large size of the bearing.

Therefore, sliding bearings are commonly used for connecting links in large robotic manipulators such as excavator manipulators. More specifically, a pin and bushing joint is used to connect different links of an excavator/backhoe arm. These revolute joints are single (one) degree of freedom (sDOF) joints initially i.e., they are a very close fit.

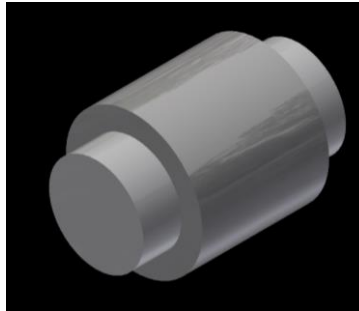


Figure 25 Pin and bushing joint assembled in CAD

In this design, a pin-bushing joint (Figure 25) was considered because of the load lifting requirement for the manipulator, which is able to withstand high impact and other irregular loads. These sliding joints are lubricated by grease, which in addition to increasing load carrying capacity, also acts as a natural sealant to the joint and prevents the entry of particles.

#### 4.2.1.2 Mobility of the linkages

Mobility of linkages is considered here because it determines the number of inputs required to control the mechanism. Equation for the mobility of a linkage is given as (Uicker et al. 2003):

$$M = 6(n - 1 - j) + \sum_{i=1}^n f_i \quad (16)$$

where  $M$  is the mobility,  $n$  is the number of links,  $j$  is the number of joints and  $f_i$  is the degrees of freedom.

In case 1, for the anthropoid manipulator,  $n = 4$ ,  $j = 3$  and  $\sum_{i=1}^n f_i = 3$ .

Therefore,  $M = 3$  which means that three inputs are required to actuate the linkage, and these correspond to the torques at three sDOF revolute joints of the arm.

In case 2, the mobility of a planar linkage is given as (Uicker et al. 2003):

$$M = 3(n - 1 - j) + \sum_{i=1}^n f_i \quad (17)$$

In the case of the serial open-chain manipulator,  $n = 4$ ,  $j = 3$  and  $\sum_{i=1}^n f_i = 3$  and this is similar to the case presented above.  $M = 3$  implies that three inputs are required to actuate the linkage, and these correspond to the applied torques at three sDOF revolute joints of the manipulator.

For the closed-loop manipulator i.e., the third case, mobility for each kinematic closed-loop is determined individually using equation 17. For each loop,  $n = 4$ ,  $j = 4$  and  $\sum_{i=1}^n f_i = 4$  and therefore,  $M = 1$ . Instead of three sDOF revolute joints which exist in case 2, this linkage comprises three revolute joints, and one prismatic joint of the actuator. Therefore, one input for every link is required for actuation, i.e., linear extension of the actuator.

## 4.2.2 Design case studies

As mentioned in the previous section, two manipulator designs – anthropoid manipulator and closed-loop manipulator are considered, and these are presented as three case studies. The closed-loop manipulator is complex in design and is divided into case 2 and 3. Detailed CAD drawings are presented in Appendix B.

### 4.2.2.1 Case 1: Anthropoid manipulator

The design of the anthropoid manipulator mechanism having a serial open-chain configuration is presented in this section. The bottom-up design procedure, in which the links are designed incorporating increasing complexity and assembled into the linkage, is used for creating the CAD prototypes of complex linkages and mechanisms (Groover Jr. and Zimmers Jr. 1997). Dimensions of the links and derived mass parameters derived from nominal limb measurement<sup>4</sup> corresponding to each link are presented in Table 8.

---

<sup>4</sup> The measurements were approximated from dimensions of the author's arm.




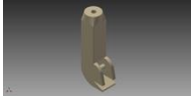

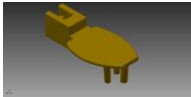
Part	Component	Design	Length (mm)	Mass (kg)	Material
1	Upper Arm		118	0.140	Al6061
2	Lower Arm		249	0.947	
3	Forearm		423	0.257	
4	Hand		170	0.395	

Table 8 Design input parameters for anthropoid manipulator

Based on this method, the procedure or work-flow followed for the part design of the first link of the anthropoid manipulator beginning with two-dimensional sketch and finishing with the final three-dimensional link is presented in Figure 26.

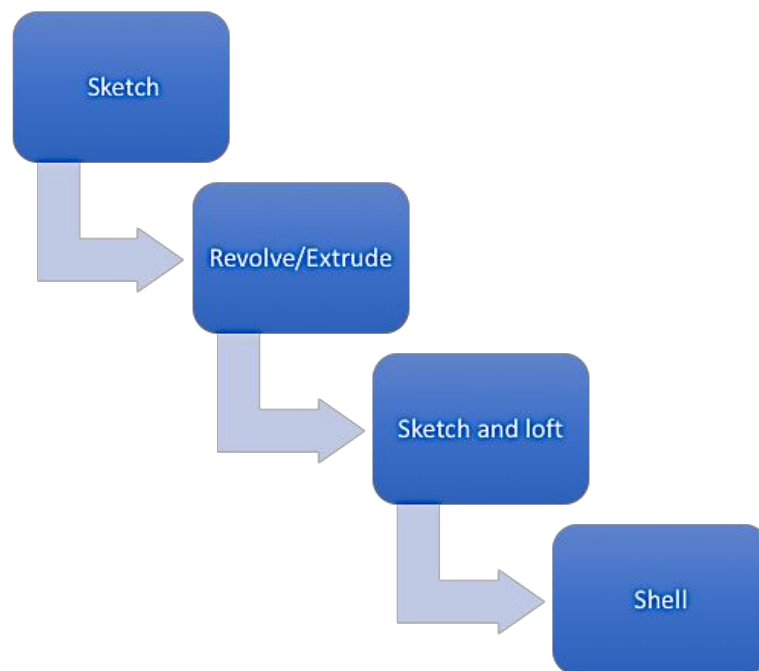


Figure 26 Process of design of a link in CAD beginning with two-dimensional sketch and ending with three-dimensional part

The steps in part modelling are summarized below with respect to the development of the anthropoid manipulator:

- i. Open a new drawing template in CAD incorporating,

- ii. Create a two-dimensional sketch on design inputs from requirement analysis,
- iii. Transform the two-dimensional sketch into three-dimensional part by using commands such as revolve, loft etc.,
- iv. Append additional features to the three-dimensional object by repeating steps i & ii,
- v. Use 'shell' command to convert the solid object into a shell with desired thicknesses,
- vi. Apply material to the part from the material library (in this case Al6061) as shown in Table 8,
- vii. Save the link design a part file ('.sldprt').

After modelling the individual links, they were assembled in the CAD assembly environment following the procedure given below:

- i. Create new assembly file,
- ii. Import and place individual links in the assembly,
- iii. Assign relation between individual links e.g. revolute joint,
- iv. Ensure limbs do not interfere using interference checking,
- v. Apply limit on range of motion if necessary (It may be noted that this constraint cannot be exported to MBD environment).

Calculation of link properties such as mass, centre of gravity and moments of inertia were automated in the process of CAD design. The assembled view of the anthropoid manipulator is shown in Figure 27, where sDOF revolute joints which connect consecutive links are annotated by circular arrows and the end-effector in this case is in the shape of a hand and the upper arm is stationary (Khurshid et al. 2016).

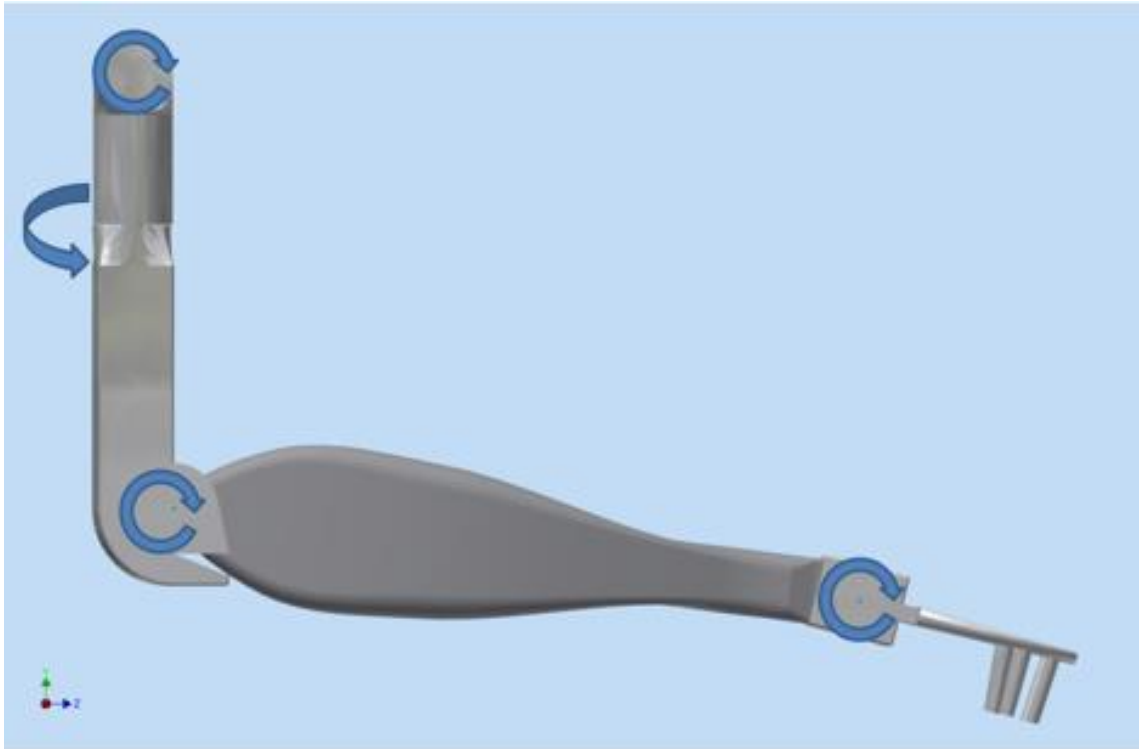


Figure 27 CAD Design for the anthropoid manipulator with sDOF joints (Khurshid et al. 2016)<sup>5</sup>

#### 4.2.2.2 Case 2: Serial open-chain manipulator

The manipulator links were designed using 1:10 scale of dimensions (Appendix A) presented in literature (Vähä et al. 1991) and connected by three revolute joints. Generic material in CAD environment was applied at first for calculating link parameters after which the link geometries were redesigned to extension range of linear actuators available in the market (Gimson Robotics 2015) in order to optimise the range of motion of links considering the limit of actuator extensions. In the third iteration, Al7075-O alloy, which is widely used for robotic manipulator fabrication, was applied to the links.

Different end-effectors exist such as high-pressure water jets, flame cutters and grippers. The bucket end-effector was selected for the manipulator as it is primarily used for soil removal and nudging/dislodging small rocks or debris determined by the operator. This end-effector can be replaced with other attachments according to requirement, directly into the SimMechanics package. In this case the material applied was A2 tool steel.

---

<sup>5</sup> The CAD prototype was part of the work contributed by this author to the co-authored publication referenced.





No.	Component	Design	Length (mm)	Mass (kg)	Material
1	Base		90.0	1.29	Al7075-O
2	Boom		457.4	3.92	
3	Stick		255.6	0.94	
4	Bucket		131.1	1.19	A2 tool steel

Table 9 Link specifications and parameters for the serial open-chain manipulator

The physical parameters corresponding to each component are presented in Table 9. Based on excavator manipulator terminology, the nomenclature of the links is as follows: base, boom, stick and bucket (Figure 28). The assembled serial open-chain linkage is presented in Figure 29.

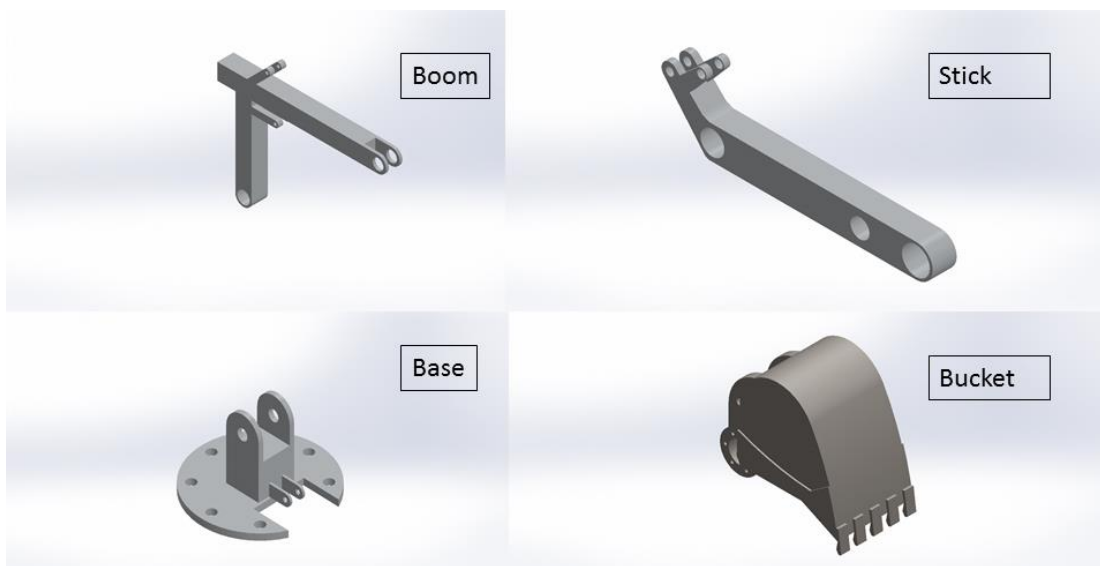


Figure 28 Links of the manipulator mechanism

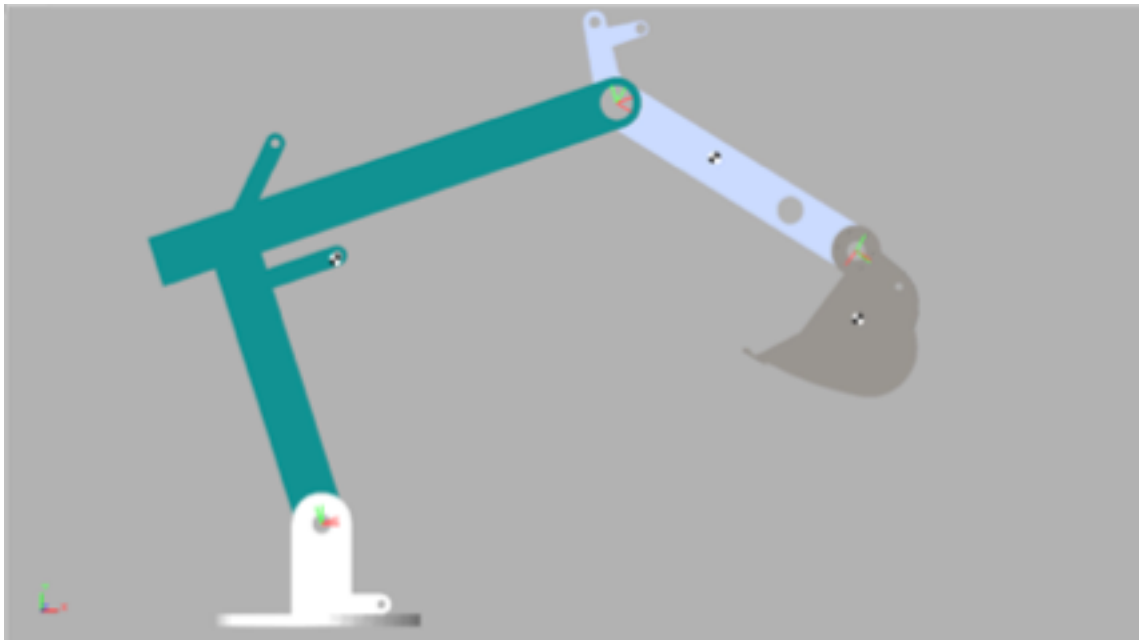


Figure 29 Four-link serial open-chain linkage assembled using links from above figure

#### **4.2.2.3 Case 3: Closed-loop complex manipulator**

This case is the development of case 2 by incorporating linear actuators. The manipulator comprises links shown in the previous section and also includes the actuators whose specifications are presented in Table 10 and stainless steel is assigned to these links.

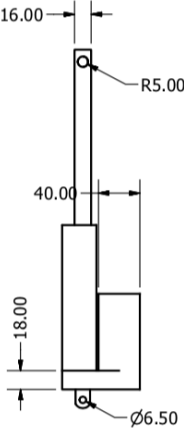
No.	Component	Design	Length (mm)	Mass (kg)	Material
1a	Boom Actuator Base		380	0.60	Stainless steel
1b	Boom Actuator Follower		0.10		
2a	Stick Actuator Base		0.64		
2b	Stick Actuator Follower		0.10		
3a	Bucket Actuator Base		0.60		
3b	Bucket Actuator Follower		0.03		

Table 10 Link specifications and parameters for actuators

The manipulator kinematic configuration for planar operation includes 3 prismatic joints for the actuators and 9 revolute joints, and therefore the final configuration is 3P9R as shown in Figure 30.



Figure 30 CAD design assembly of closed-loop manipulator prototype

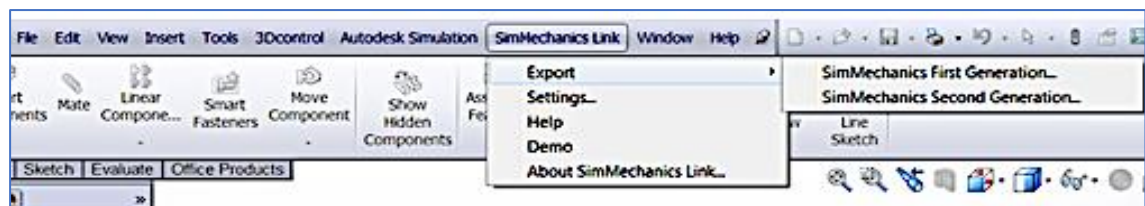
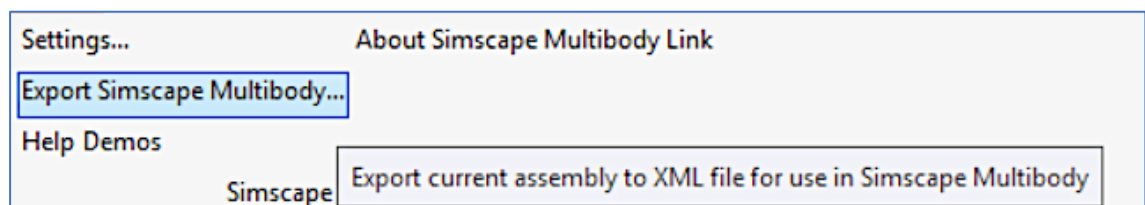
### 4.2.3 Exporting CAD model to MBD environment

After assembly, the CAD model was exported to the MBD environment using the export command from the graphical user interface (GUI) as presented in Figure 31. Here, Figure 31 a and b show the GUI procedure for exporting CAD assembly to MBD simulation platform in Autodesk Inventor and Solidworks, and b presents the dimensional tolerance settings in Inventor. The linear and angular tolerance presented in Figure 31 b represents the least count of the data exported and, in this case, was set to 1e-05mm and 1e-05radians.

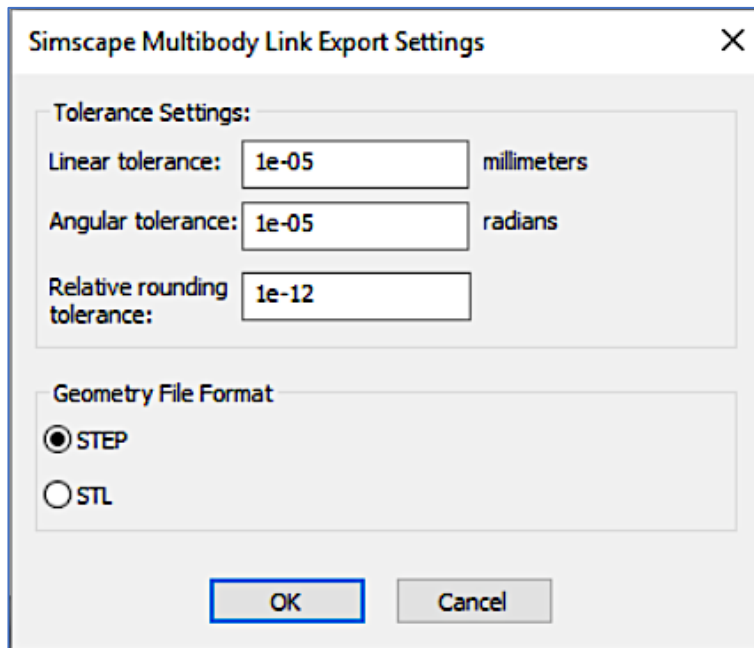
The exported data falls into two categories:

- i. Link physical parameter data which is exported as a '.xml' file and contains link parameters such as computed mass, moments of inertia, link orientation and joint constraints,
- ii. The visualization contents which are exported as '.stl' (or stereolithography) files as shown in Figure 31 b.

Before looking into the simulation in the MBD environment, modelling sensitivity and validation are briefly explored below.



a)



b)

Figure 31 a) Exporting from CAD environment to MBD package b) tolerance and geometry settings during export

#### 4.2.4 Modelling sensitivity and validation

The sensitivity of the model was determined by the precision of measurements used. In the CAD environment, the precision is normally set to  $1\mu\text{m}$ , which can be further improved to  $1\text{e-}3\mu\text{m}$  (Figure 31). In the MBD environment, the precision was set to from 17-19 significant digits e.g. for mass in kg, a precision of  $1\text{e-}17$  was recorded. This accuracy is dependent on the computing hardware used to conduct the simulation. A default solver consistency tolerance of  $1\text{e-}09$  was set with a filtering time constant of 0.001. Linearization delta of 0.001 was used in SimMechanics 1<sup>st</sup> generation solvers. The geometric precision in CAD was natively set by default to  $1\mu\text{m}$  but this can be improved to  $1\text{e-}2\mu\text{m}$ .

Validation of any model is an important step in confirming the validity of the simulation outputs. Considering the time and cost requirements to determine the validity of a model over the domain of its intended application, it would be necessary to conduct tests and evaluations until sufficient confidence is obtained that a model can be considered valid for its intended application (Sargent 2005). To stay within budgetary and time limits, alternate methods of validation described below were used:

- i. The results of simulation from SimMechanics 1<sup>st</sup> generation (used in literature) and SimMechanics 2<sup>nd</sup> generation were compared,



- ii. The same technique was applied to the elementary model i.e. one-link model, in this research, and the difference between output parameters was recorded,
- iii. The simulation results of successive iterations for different sets of simulation input parameters were compared and the precision of generated results provided insight into the validity of the model.

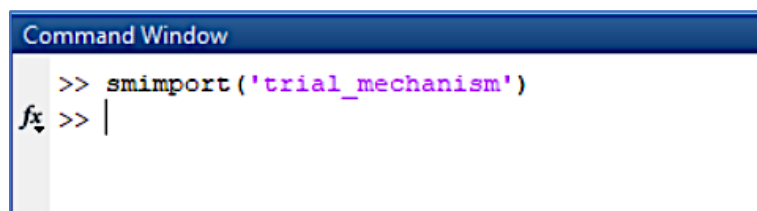
### 4.3 Multibody dynamic (MBD) simulation analysis

In this section, block diagram representation of the physical system, validation of simulation, importing CAD assembly data into MBD simulation environment, elements of validation of the simulation, followed by simulation parameters and input signal modification are presented. The simulation of the three manipulators and corresponding input signal generation (as cases 1 to 3) is presented in section 4.4.

#### 4.3.1 Block diagram representation of physical systems

In this section, the elements constituting block diagram are identified and explained in context. In most cases, the definitions and explanations provided originally in SimScope are retained as it is concise, and this is presented in the form of screenshots of the graphical user interface (GUI) where applicable. Where possible, brief explanations are also provided in the text.

##### 4.3.1.1 Importing CAD model into MBD simulation environment



```
Command Window
>> smimport('trial_mechanism')
fx >> |
```

Figure 32 Importing CAD data into the MBD simulation environment in MATLAB

The process of importing CAD assembly data into MBD simulation environment is carried out using the 'smimport' command in MATLAB terminal as presented in Figure 32. In the command, the name 'trial\_mechanism' denotes the exported data file from the CAD environment. The imported data was converted into the block diagram representation. The joint constraints i.e., the relationship between the links were verified after importing the data into the MBD simulation

environment through inspection of the blocks in the diagram as well as through visual inspection of the simulation output.

### 4.3.1.2 Elements of diagram representation

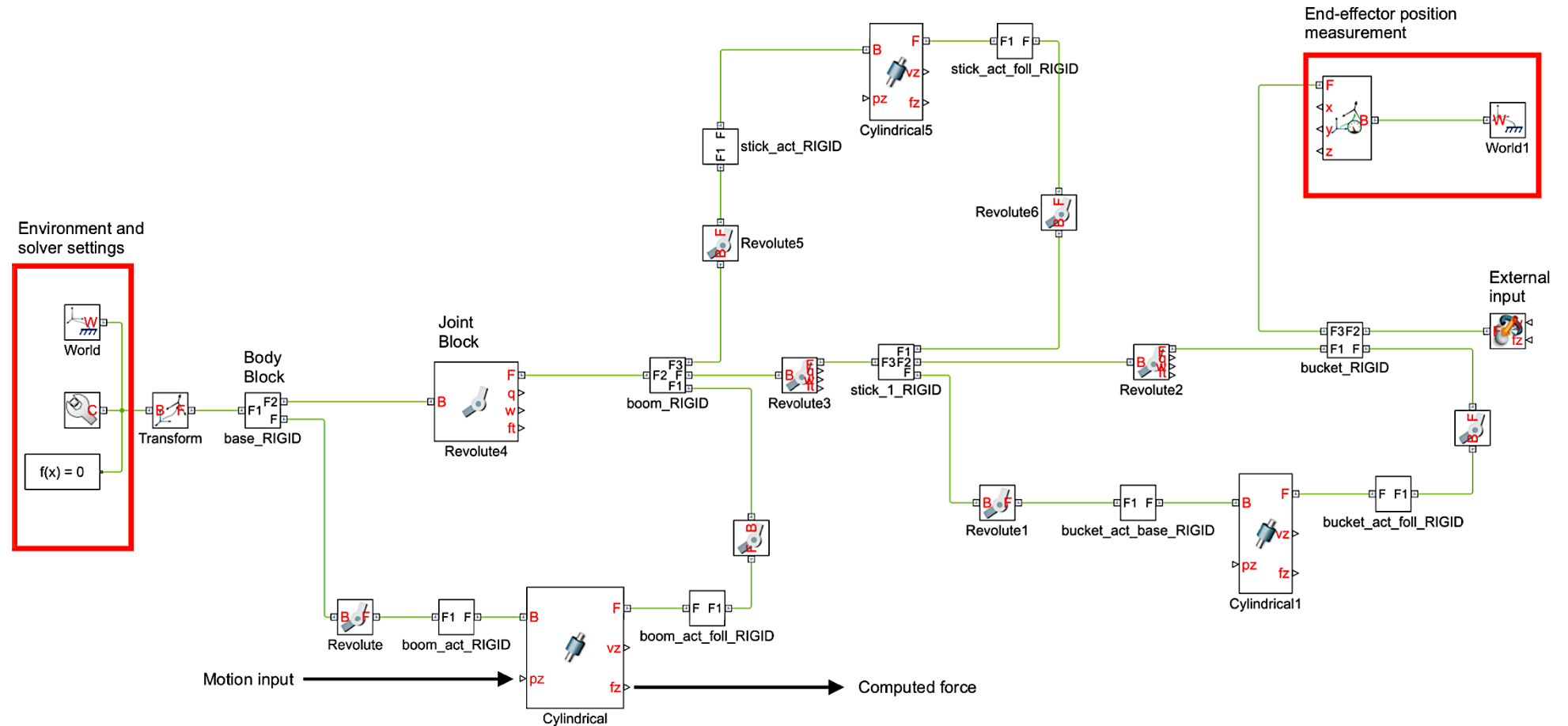
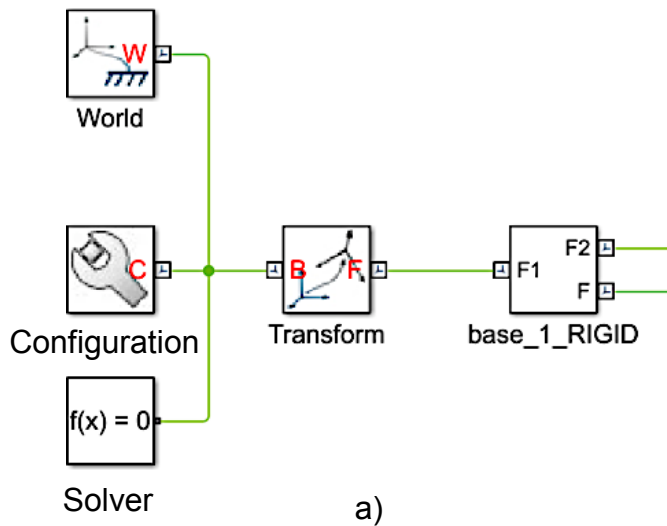
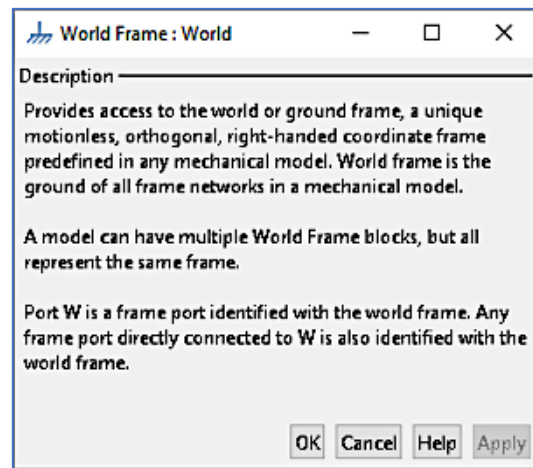


Figure 33 Block diagram representation of closed-loop complex manipulator mechanism and parts labelled (Chacko and Khan 2017)

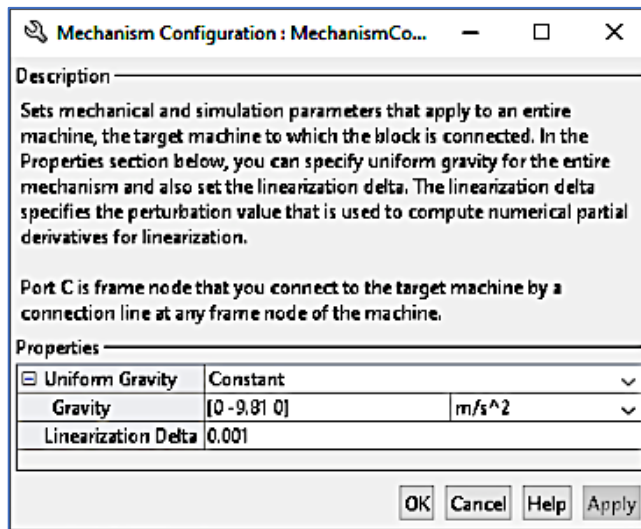
Block diagram representation of the physical system (case 3: closed-loop complex manipulator taken as example) is illustrated in Figure 33 and its elements are explained below in detail. Each element describes one aspect of the physical system. In the first part of the diagram, the 'world' block presents the definition of the global coordinate system.



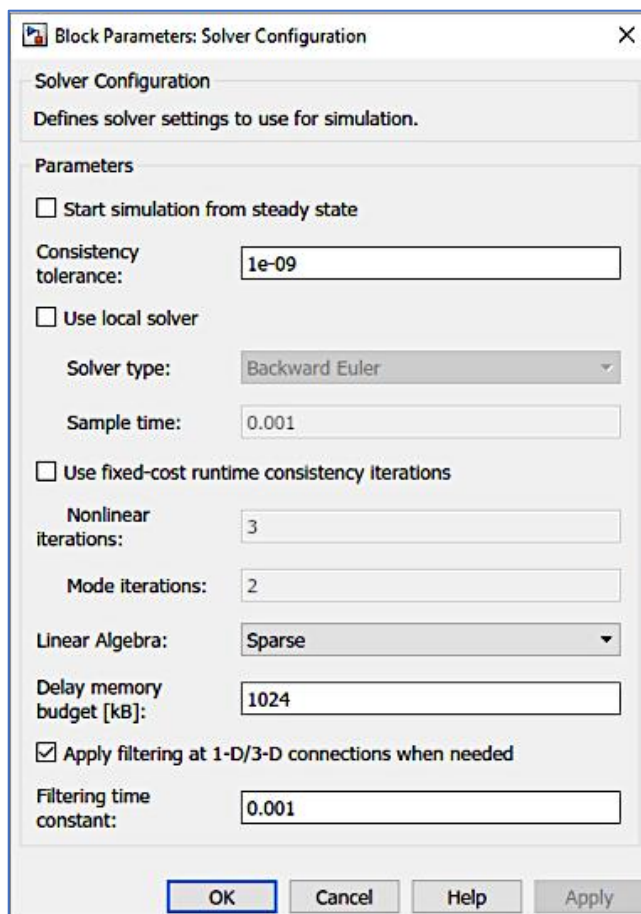
a)



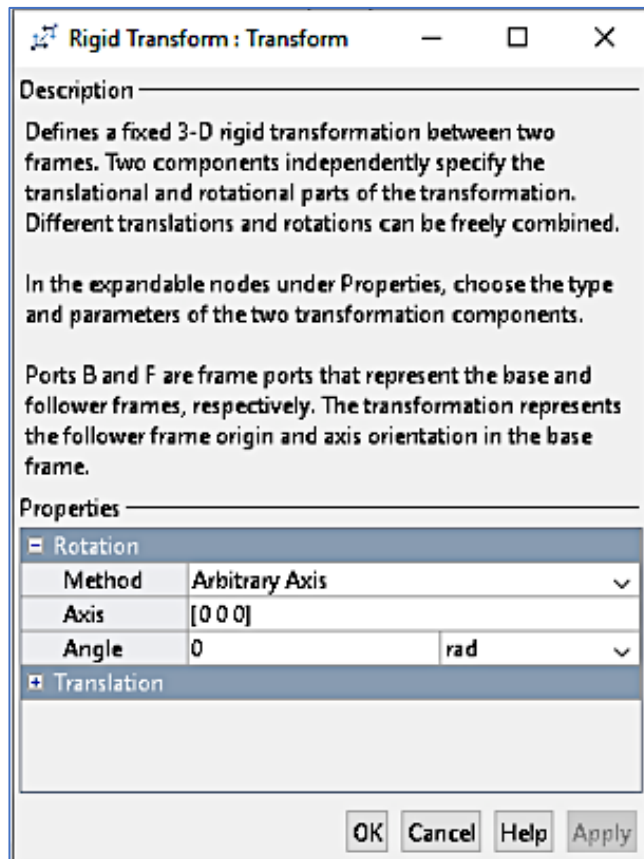
b)



c)



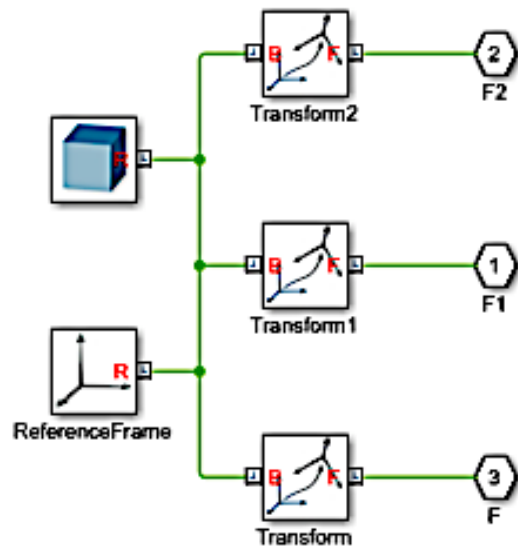
d)



e)

Figure 34 Core blocks of the model – a) world, system configuration and solver blocks b) world frame, c) configuration, d) solver, and e) rigid transform

Along with this block, the system ‘configuration’ and ‘solver’ blocks are presented as shown in Figure 34 a. The descriptions of these blocks and their property settings are represented in Figure 34 b, c and d respectively and together these blocks define the fundamental simulation parameter settings. Figure 34 e represents the components of the rigid transform block shown in Figure 34 a.



a)

**Solid : Solid**

**Description**

Represents a solid combining a geometry, an inertia and mass, a graphics component, and rigidly attached frames into a single unit. A solid is the common building block of rigid bodies. The Solid block obtains the inertia from the geometry and density, from the geometry and mass, or from an inertia tensor that you specify.

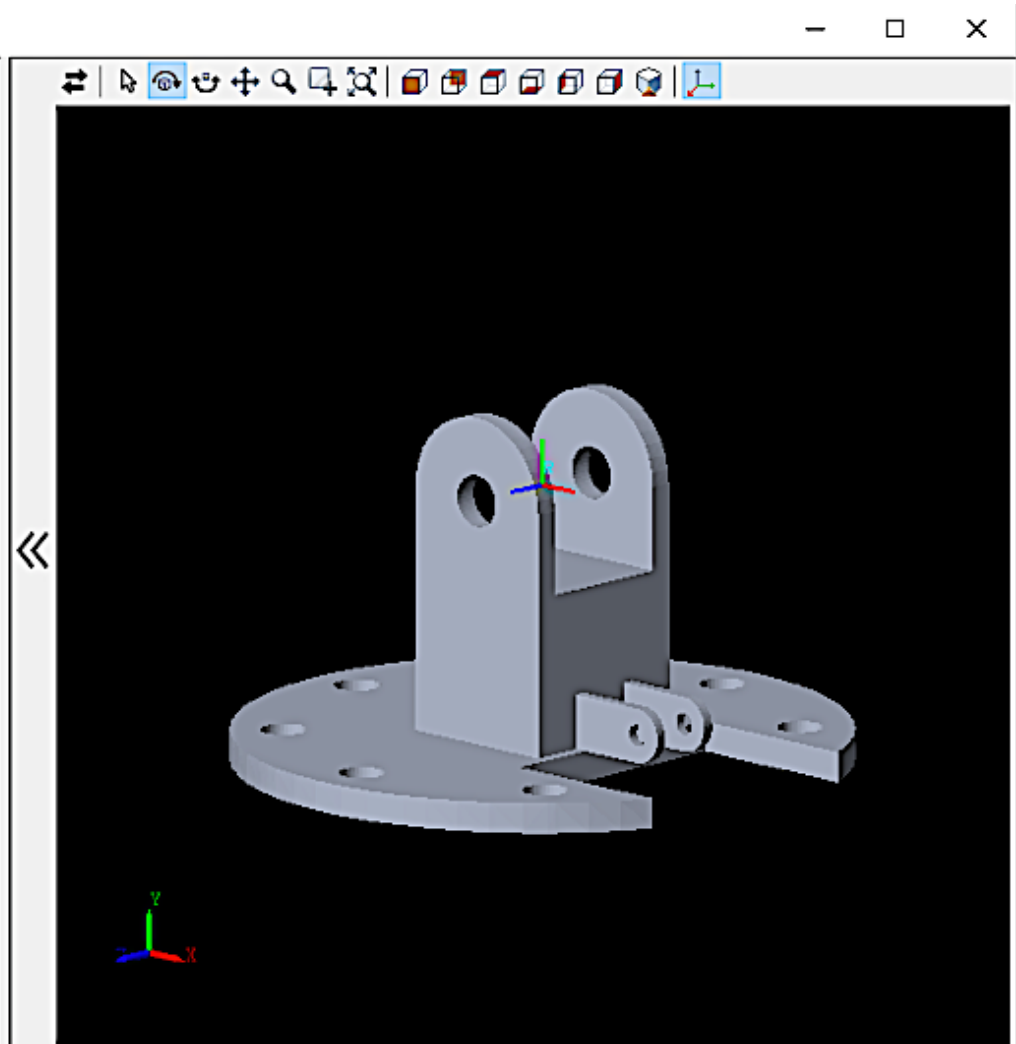
In the expandable nodes under Properties, select the types of geometry, inertia, graphic features, and frames that you want and their parameterizations.

Port R is a frame port that represents a reference frame associated with the geometry. Each additional created frame generates another frame port.

**Properties**

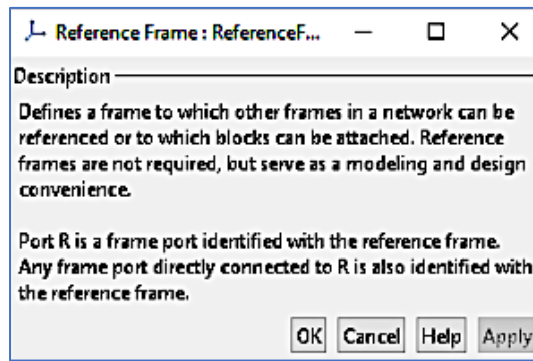
Geometry	
Shape	From File
File Type	STL
File Name	base_Default_sldprt.STL
Units	m
Inertia	
Type	Custom
Mass	1.2933879526022116 kg
Center of...	[-0.0070770409254097711 -0.066489472931562377 ...] m
Moments...	[0.0030815189961325832 0.0037098291705608211 ...] kg*m <sup>2</sup>
Products ...	[0 0 -0.00017638654352739985] kg*m <sup>2</sup>
Graphic	
Type	From Geometry
Visual Pr...	Simple
Color	[0.8666666666666667 0.90980392156E ...]
Opacity	1
Frames	

OK Cancel Help Apply

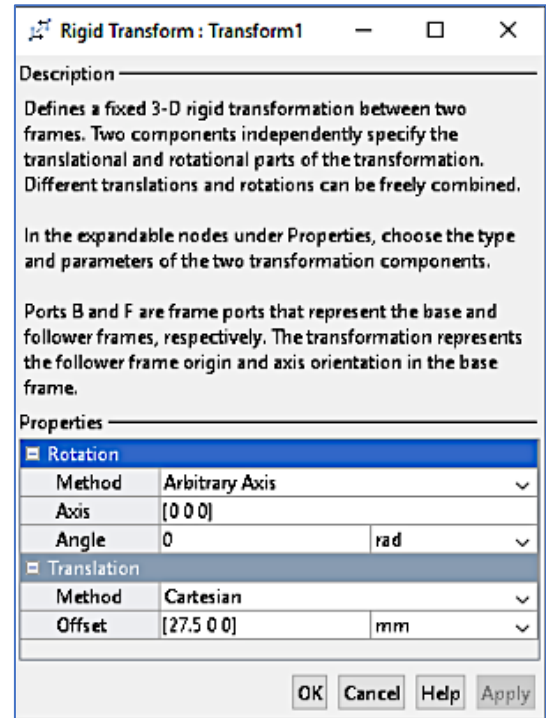
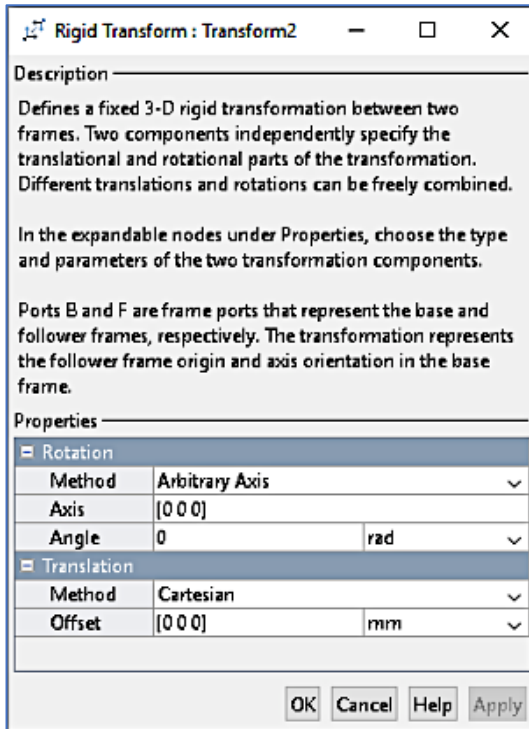


b)

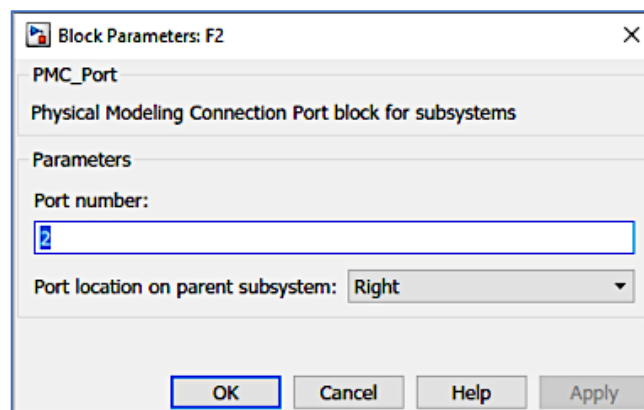




c)



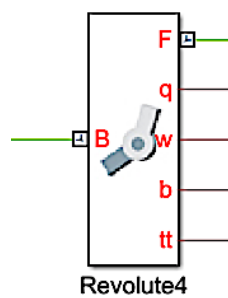
d)



e)

Figure 35 Core blocks of the model – a) rigid body blocks, b) settings for the solid block, c) reference frame for the rigid body block d) transformation frames and e) physical modelling connection port connecting the body to a joint block

Figure 35 a represents the components of the rigid body block shown in Figure 34 a, named 'base\_1\_RIGID'. Figure 35 b represents the rigid body block settings and configurations in which the physical properties of the solid link such as mass, moments of inertia, geometry, transformation and visualisation settings, which were imported from CAD. Description of the reference frame is presented in Figure 35 c. Together, these blocks (Figure 35 a-c) contain the definition of geometric and physical properties of the links which constitute the simulation model. Similarly, rigid transformation coordinate block parameters from Transform 1 and Transform 2 associated with the body block showing translation and rotation components, are presented in Figure 35 d and the difference in parametric settings from Figure 34 e can be seen. Physical modelling connection port which accepts physical signals (PS) from outside the block, i.e. connecting the body block to joint blocks, is presented in Figure 35 e.



a)

**Revolute Joint : Revolute4**

**Description**

Represents a revolute joint acting between two frames. This joint has one rotational degree of freedom represented by one revolute primitive. The joint constrains the origins of the two frames to be coincident and the z-axes of the base and follower frames to be coincident, while the follower x-axis and y-axis can rotate around the z-axis.

In the expandable nodes under Properties, specify the state, actuation method, sensing capabilities, and internal mechanics of the primitives of this joint. After you apply these settings, the block displays the corresponding physical signal ports.

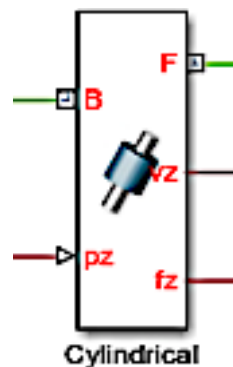
Ports B and F are frame ports that represent the base and follower frames, respectively. The joint direction is defined by motion of the follower frame relative to the base frame.

**Properties**

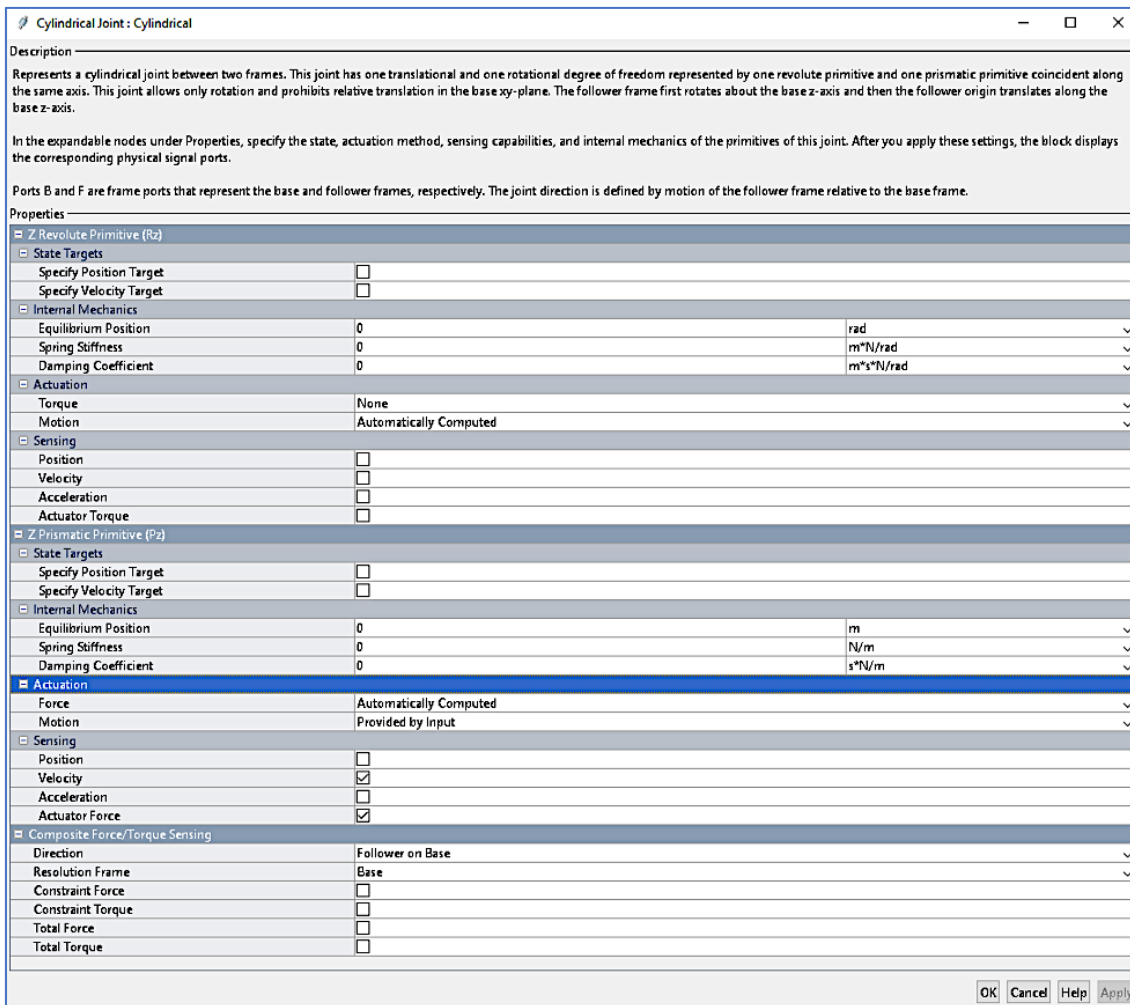
Z Revolute Primitive (Rz)		
State Targets		
Specify Position Target	<input checked="" type="checkbox"/>	
Priority	Low (approximate)	▼
Value	0.26584463009276965	deg ▼
Specify Velocity Target	<input type="checkbox"/>	
Internal Mechanics		
Equilibrium Position	0	rad ▼
Spring Stiffness	0	m*N/rad ▼
Damping Coefficient	0	m*s*N/rad ▼
Actuation		
Torque	None	▼
Motion	Automatically Computed	▼
Sensing		
Position	<input checked="" type="checkbox"/>	
Velocity	<input checked="" type="checkbox"/>	
Acceleration	<input checked="" type="checkbox"/>	
Actuator Torque	<input type="checkbox"/>	
Composite Force/Torque Sensing		
Direction	Follower on Base	▼
Resolution Frame	Base	▼
Constraint Force	<input type="checkbox"/>	
Constraint Torque	<input type="checkbox"/>	
Total Force	<input type="checkbox"/>	
Total Torque	<input checked="" type="checkbox"/>	

OK Cancel Help Apply

b)



c)

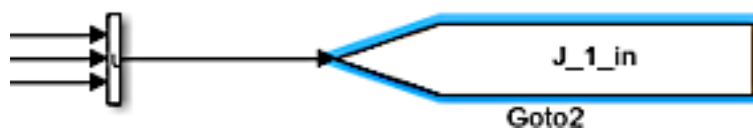


d)

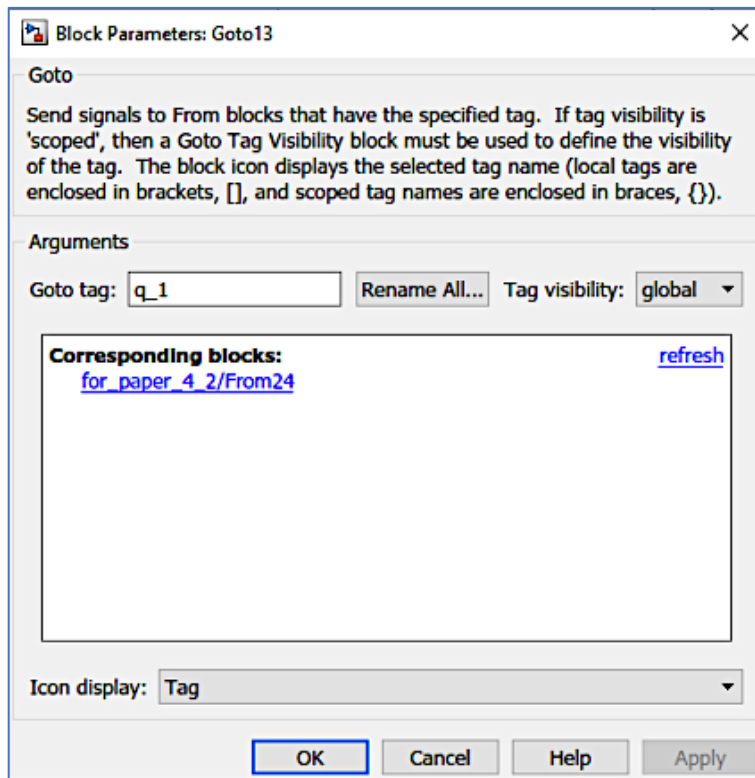
Figure 36 a) Block element and b) property settings for the sDOF revolute joint block c) Block diagram and d) properties and settings for the two degrees of freedom cylindrical joint block constrained in the rotational direction

The revolute joint block is presented in Figure 36 a; b and d represent the parametric settings, and Figure 36 c represents the cylindrical joint - these represent the kinematic relations between the various rigid links in the simulation environment. In this simulation, the cylindrical block is constrained in the direction of rotation which transforms it into an sDOF prismatic joint.

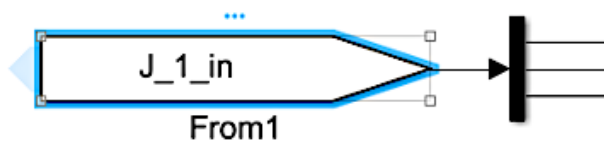
#### 4.3.1.3 Other blocks



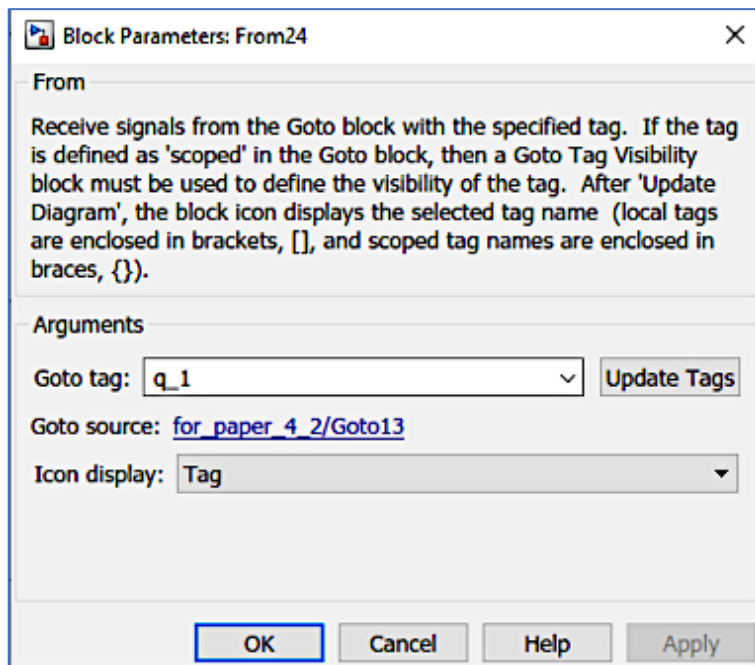
a)



b)



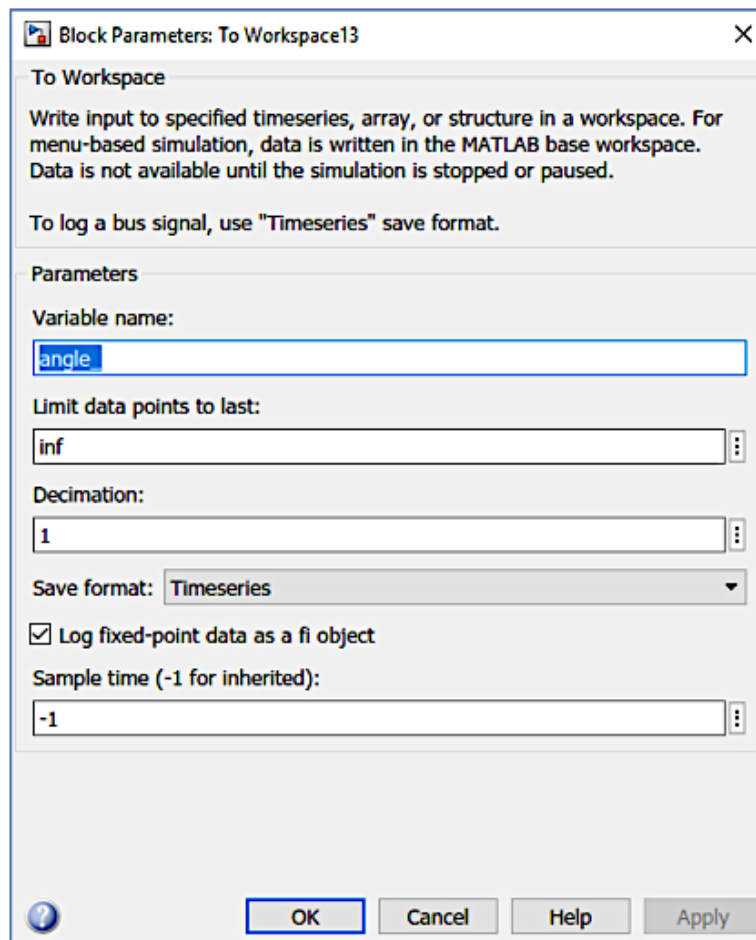
c)



d)

Figure 37 a) 'Goto' block b) configuration c) 'From' block and d) its configuration

Other blocks such as 'goto', 'from' and 'to workspace', which are used for manipulating signals in the simulation block diagram, are presented below. 'Goto' and 'from' blocks presented in Figure 37 a and c respectively are the diagrammatic equivalent of the 'goto' and 'from' routines used in object-oriented programming and the parametric settings for these blocks are presented in Figure 37 b and d. These blocks transport signals remotely without 'wired' connections, enabling the reduction of block diagram complexity for large and complicated systems and also making it possible to transport the same signal to multiple locations without the complexity of multiple signal lines e.g. when a signal is used to drive a simulation and, at the same time, is required to transmit the data for recording or plotting.



b)

Figure 38 a) 'To workspace' block and b) configuration settings

Similarly, Figure 38 a shows the ‘to workspace’ block which records data from the simulation environment i.e., SimMechanics within Simulink, to the MATLAB workspace as data stored in MATLAB workspace can be manipulated with greater ease and stored in the ‘.mat’ file format.

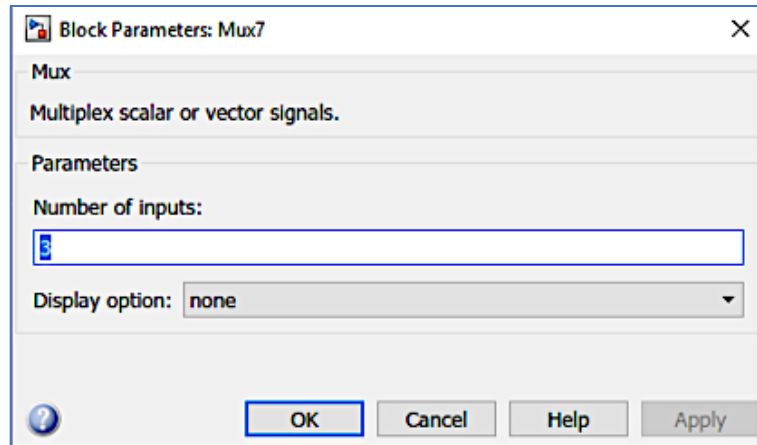
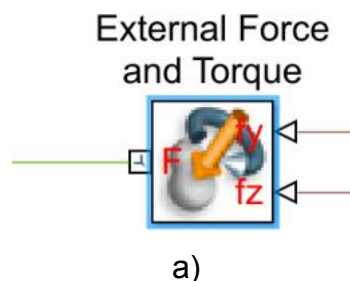
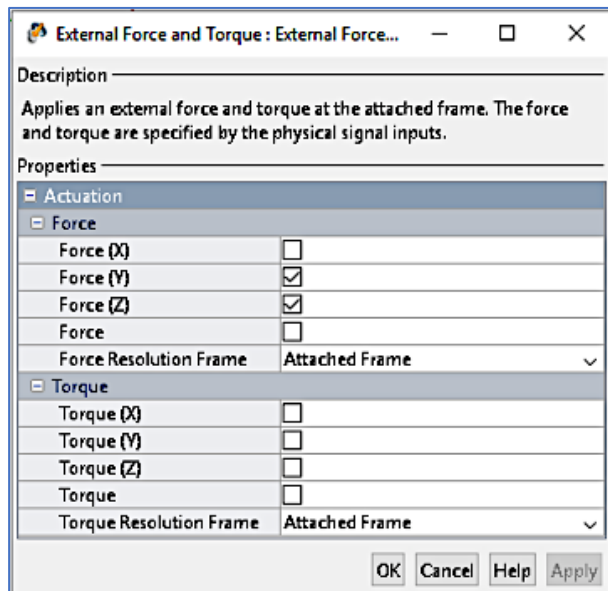


Figure 39 Mux bar converts multiple signals into a composite signal

Figure 39 represents the ‘mux’ or multiplexer bar which combines or ‘multiplexes’ multiple signals into a composite signal, which serve similar function to that of the ‘goto’ and ‘from’ blocks in reducing the diagram complexity (Popinchalk 2008). This is required for efficient transport of several different signals, e.g. position, velocity and acceleration, which can then be transported to a different location in the diagram and demultiplexed using a ‘demux bar’. This can be used in conjunction with the ‘goto’ and ‘from’ block. The number of input signals which are multiplexed is set through the parametric properties of the block.

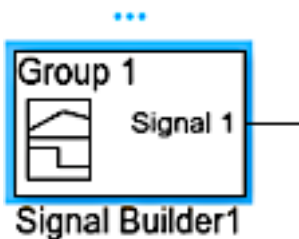




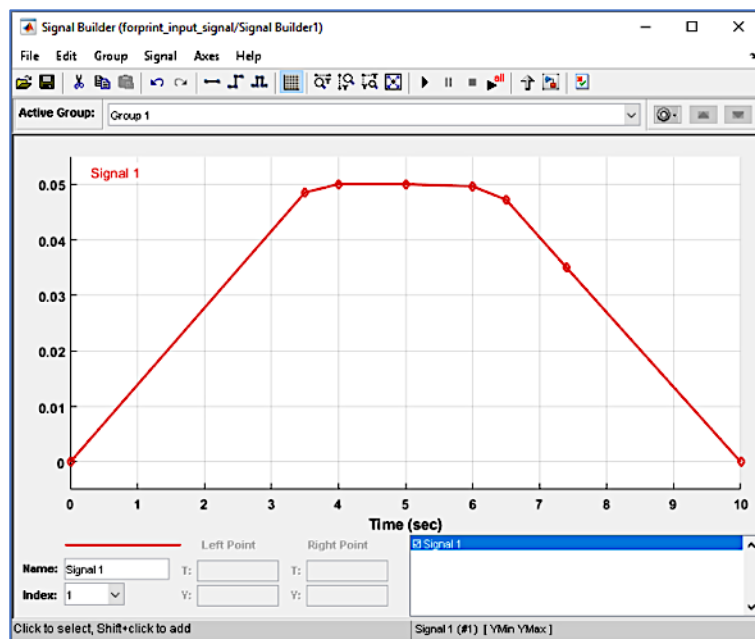
b)

Figure 40 a) External force and torque block and b) parametric settings for the block

Figure 40 a shows the input force parameters and b shows the parametric settings including application axes directions.



a)



b)

Figure 41 a) Signal builder block used for generating simulation input signals and b) parametric settings for the block

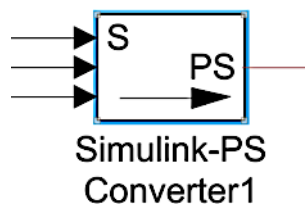
#### 4.3.1.4 Signal types and interconversion of signals

In MATLAB, workspaces are divided into native workspace and Simulink workspace. The Simulink workspace contains time-dependent signals in the form  $[x, t]$  known as Simulink signals. The blocks presented above in

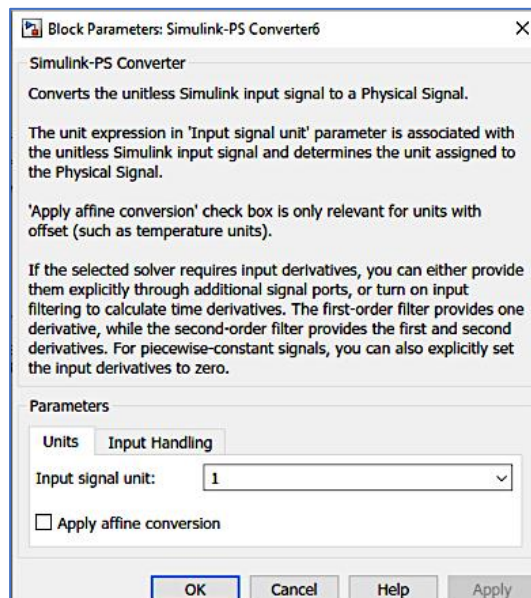


section 4.3.1.1 to 4.3.1.4 belong to the SimScape or SimMechanics environment within Simulink, which is nested in MATLAB. Examples of blocks which belong to the Simulink environment are signal generation and differentiation blocks and the output signals from these blocks belong to the category of Simulink signals.

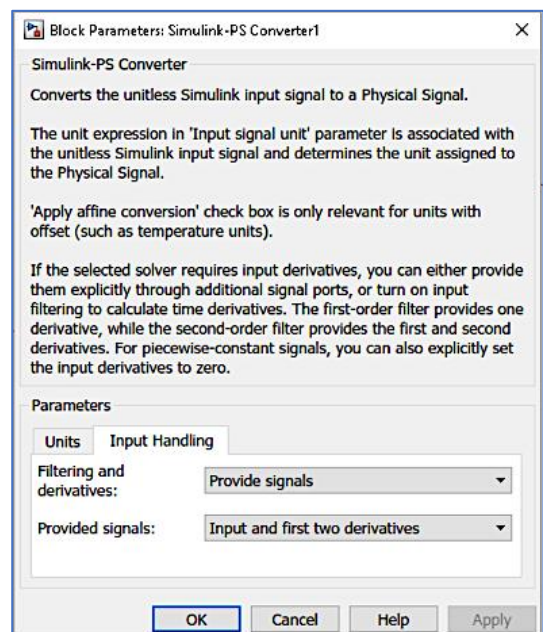
As mentioned above, SimMechanics or SimScape is a specialised package for simulation of physical systems such as rigid body mechanics within Simulink. The signals in SimMechanics are called physical signals and these are different from Simulink signals and connecting these two simulation packages requires signal interconversion. Therefore, when using a combined application of Simulink and SimMechanics, (which is applicable in the case of physical simulations) signal converters are required.



a)



b)



c)

Figure 42 a) Simulink to Physical Systems block b-c) and parameter settings

In order to use the input signal generated in Simulink as actuation input signal for the physical system modelled in SimMechanics or SimScape, the Simulink to Physical Signals block, which is labelled 'S→PS' as shown in Figure 42 a, is used. The parametric options for the block are presented in Figure 42 b and c. In this work, the time derivatives of the input displacement actuation are provided as input to the physical system using the signal generated in Simulink, which are converted using the 'S→PS' block.

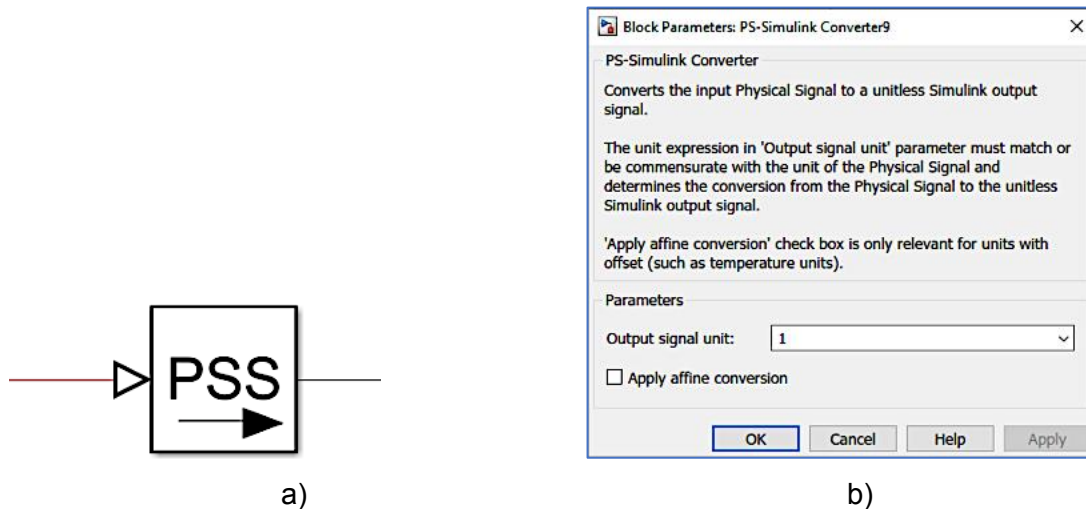


Figure 43 a) Physical Signal to Simulink conversion block and b) parameter settings

Similarly, the output from the physical system which include torque, spatial displacement etc., fall under the category of physical signals. These signals are converted to Simulink signals using the Physical system to Simulink convertor 'PS→S' presented in Figure 43 a. Parametric settings for the block are presented in Figure 43 b. The signal converted to Simulink domain was either stored or graphically presented for future manipulation. The input signals for the simulations are presented in the following section. The diagrammatic representations of the physical constituted by these blocks are presented in the next section.

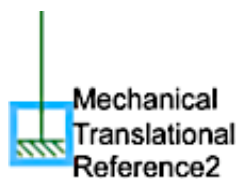
#### 4.3.1.5 Incorporation of friction models

Friction is an important factor that affects the dynamic performance of manipulators (Lischinsky et al. 1999). The selection of the friction model for simulation depends on the type of joint, area of application and the operating conditions (Bilandi 1997, Olsson et al. 1998, Khan et al. 2017). In this work, the

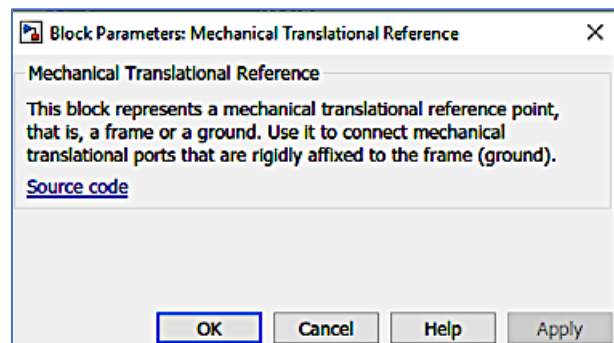
combined friction model comprising Coulomb, Viscous and Stribeck friction, presented in section 2.2.3.1 of the literature review was used to simulate effects of friction in the manipulator joints within the CAD-MBD approach for both translational and revolute sDOF joints and these are presented below.

### Components of the translational friction model

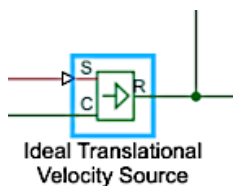
Components of the friction model diagram are explained below. The mechanical translational reference block is presented in Figure 44 a, and the description for the block is presented in Figure 44 b. This block presents a reference point or frame for mechanical translational ports connected to it. The ideal velocity block and its description are presented in Figure 44 c and d respectively and it provides velocity differential at the output. Similarly, the ideal force sensor block is presented in Figure 44 e and its description is presented in Figure 44 f. The output of this block provides an ideal force proportional to the input. The translational friction block and its parametric components are presented in g and h respectively and the output of this block is the proportional friction force generated using the combined friction model.



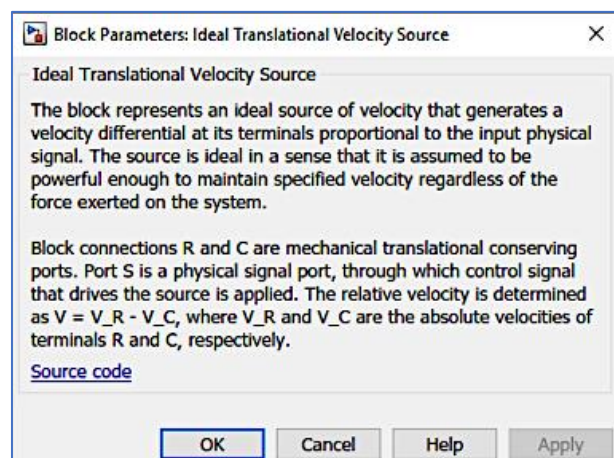
a)



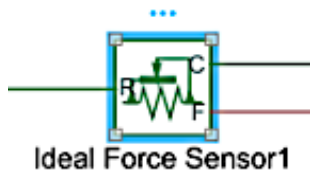
b)



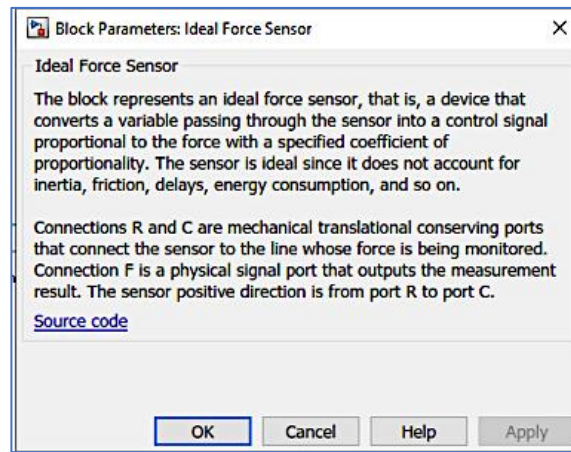
c)



d)



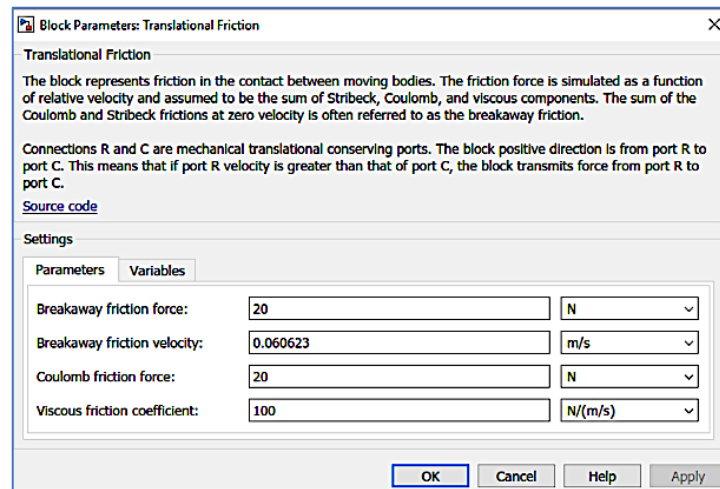
e)



f)



g)



h)

Figure 44 a) Mechanical translational reference b) specifications of the block c) ideal translational reference block d) specifications of the block e) Ideal force sensor block f) specifications g) translational friction block and h) block parameters

### Translational friction model

The multibody representation of the physical system for generating friction is presented in Figure 45. The Physical Modelling Connection (PMC) port on the left carries the input signal, which in this case is the velocity. This is connected to the ideal translational velocity block which is connected to two other blocks namely ideal force sensor block and mechanical translational reference block. The ideal force sensor block is connected on the left to the ideal translational velocity block and on the right to the friction force block, which is again connected to the mechanical translational reference and a separate ideal translational velocity block. The output from the ideal translational velocity block is connected to the 'PS→S' convertor and the signal represents the magnitude of the friction torque.

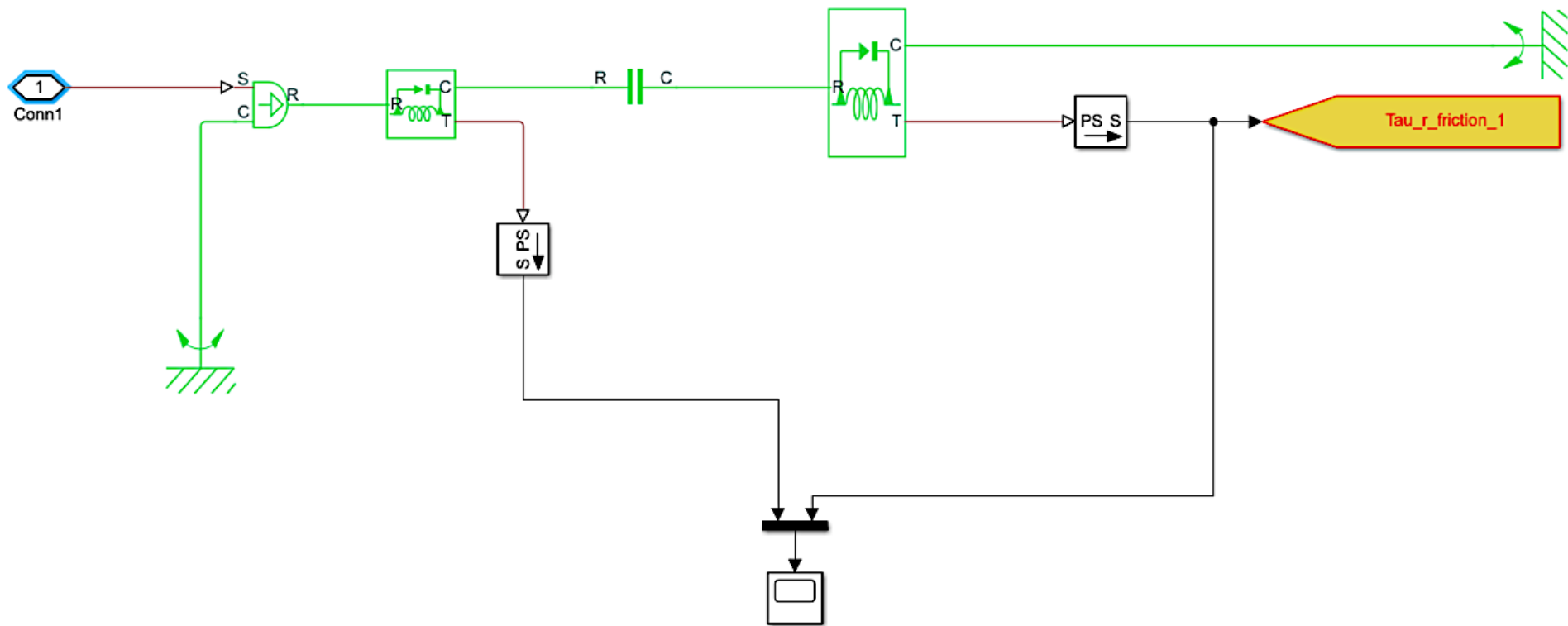


Figure 45 Block diagram representation of the translational friction model

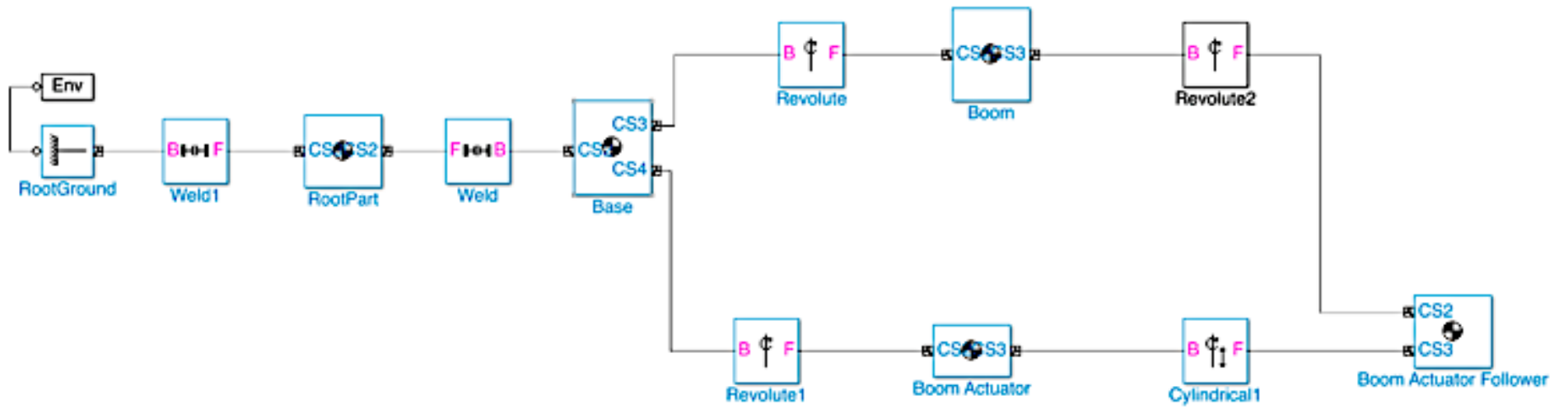
### **Revolute friction model**

MATLAB m-code was used for simulating the above friction model which is presented in the Appendix C for the sake of brevity.

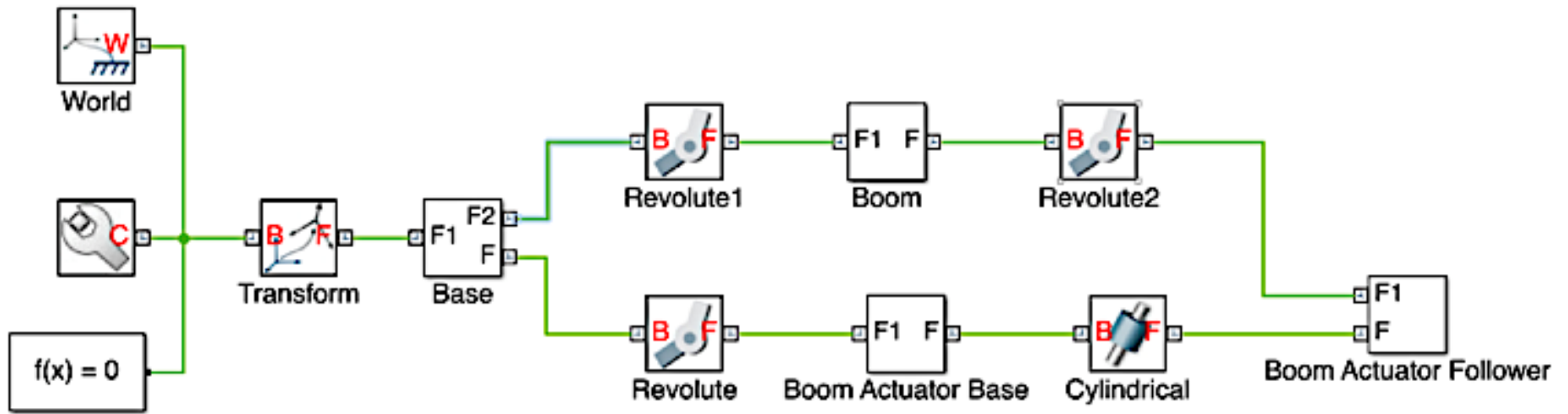
#### **4.3.2 Validation of simulation**

For validating the simulation, the dynamics of the first closed-loop of the complex manipulator mechanism with linear actuation, having three revolute and one prismatic joint configuration (3R1P) was simulated. This was compared across two simulation platforms namely SimMechanics 1<sup>st</sup> generation, used widely in literature e.g. (Wu 2013), and SimMechanics 2<sup>nd</sup> generation used in this work and reported in (Dooner et al. 2015). The graphical representation of the kinematic loop in SimMechanics 1st generation is illustrated in Figure 46 a, and the representation in the SimMechanics 2nd generation package is illustrated in Figure 46 b. From the figure, it can be observed that the representation of the general structure of the physical system in block diagram form are similar with differences only in components and their organisation.

In order to simulate the mechanism in inverse dynamics mode, an input kinematic signal comprising displacement, velocity and acceleration is required and the simulation inputs are presented in the following section. The key mechanics parameter considered for comparing the simulation outputs generated in the different simulation environments is the computed joint torque generated at the revolute joint. After validation, this method was applied to three cases and the results were reported in the Chapter 6.



a)



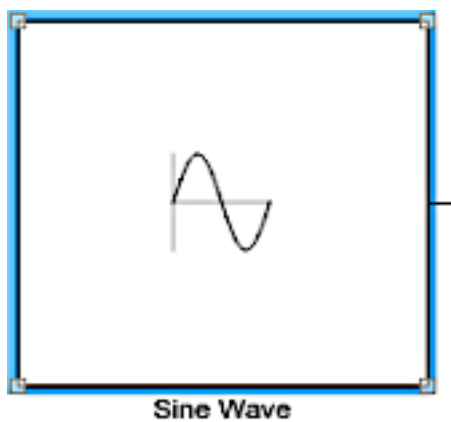
b)

Figure 46 The model based graphical visualization form of the first loop of the manipulator linkage a) for first generation simulation and b) for second generation simulation (Chacko and Khan 2017)

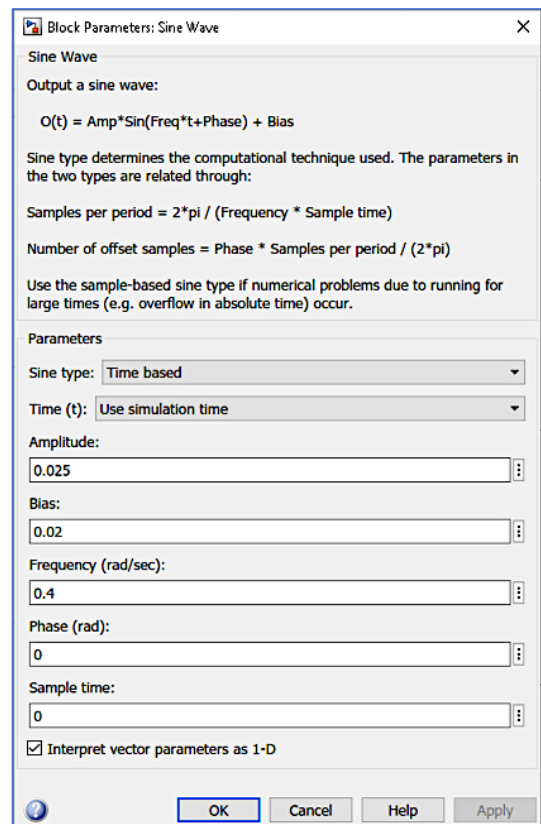


### 4.3.3 Simulation parameters

Inputs for actuating inverse dynamics simulation of the three cases include actuation using joint angle and its first and second time derivatives namely velocity and acceleration. Corresponding to each set of input signals, output parameters were recorded from the simulations. For case 1, the outputs recorded included the end-effector path traced by the hand and computed friction torque for joints 1 and 2 which were actuated. The outputs for case 2 included the computed and reaction torques for SimMechanics 1<sup>st</sup> generation as well as SimMechanics 2<sup>nd</sup> generation simulation environments for computing inverse dynamics. For case 3, the input signals comprised linear extension of the actuators and its time derivatives, and also time-invariant loading at the end-effector, and the simulation outputs comprised both kinematic parameters such as computed angular parameters for the revolute joints and end-effector motion (approximate digging motion), and dynamic parameters such as actuator force, friction force, computed torque and friction torque.



a)



Block Parameters: Sine Wave

Sine Wave

Output a sine wave:

$$O(t) = \text{Amp} * \text{Sin}(\text{Freq} * t + \text{Phase}) + \text{Bias}$$

Sine type determines the computational technique used. The parameters in the two types are related through:

Samples per period =  $2 * \pi / (\text{Frequency} * \text{Sample time})$

Number of offset samples =  $\text{Phase} * \text{Samples per period} / (2 * \pi)$

Use the sample-based sine type if numerical problems due to running for large times (e.g. overflow in absolute time) occur.

Parameters

Sine type: Time based

Time (t): Use simulation time

Amplitude: 0.025

Bias: 0.02

Frequency (rad/sec): 0.4

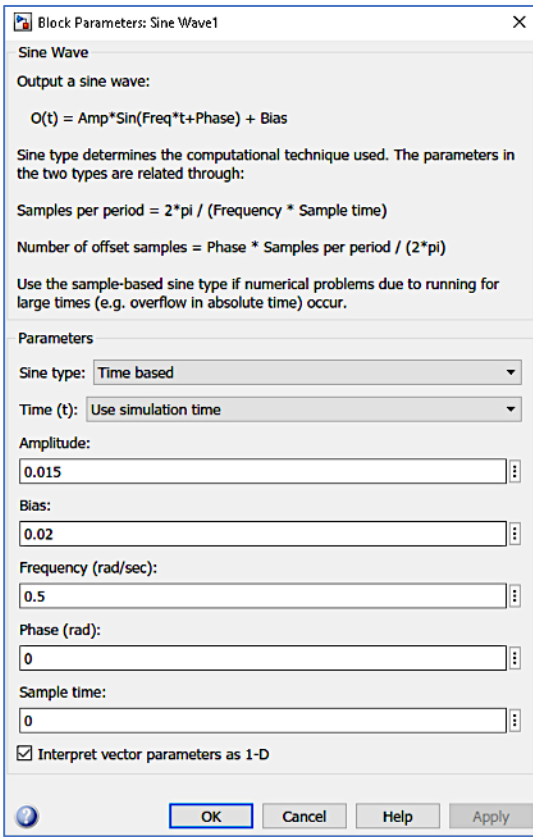
Phase (rad): 0

Sample time: 0

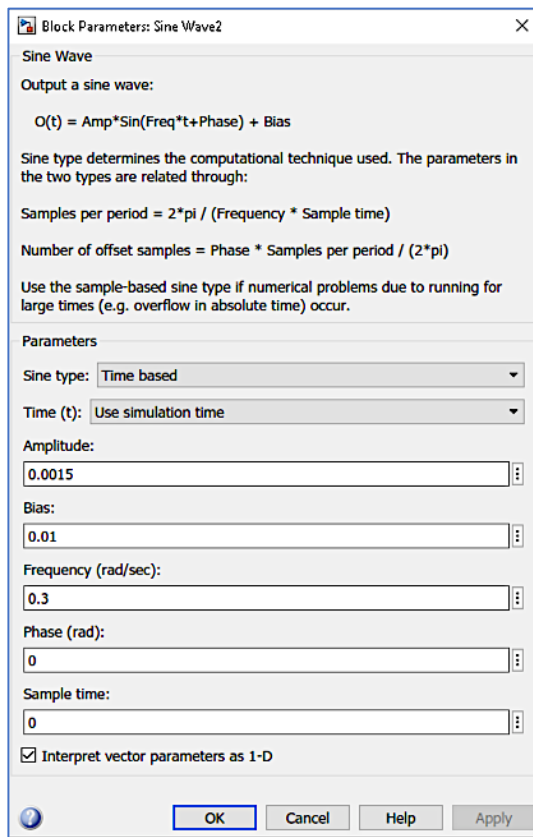
Interpret vector parameters as 1-D

OK Cancel Help Apply

b)

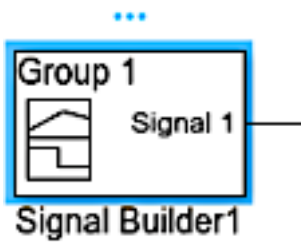


c)

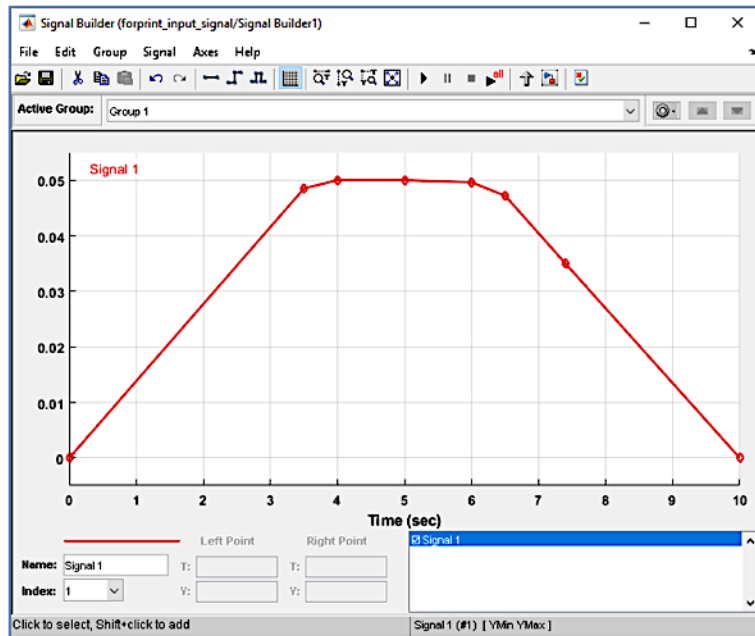


d)

Figure 47 a) Sine Wave block and b) parameters settings for the sine wave generator block



a)



b)

Figure 48 a) Signal builder block used for generating simulation input signals and b) parametric settings for the block

Sine wave block and parameters are presented in Figure 47 and similarly, signal builder block is presented in Figure 48. These blocks were used to

generate input kinematic signals for the inverse dynamics simulations of the linkages.

#### 4.3.4 Input signal modification

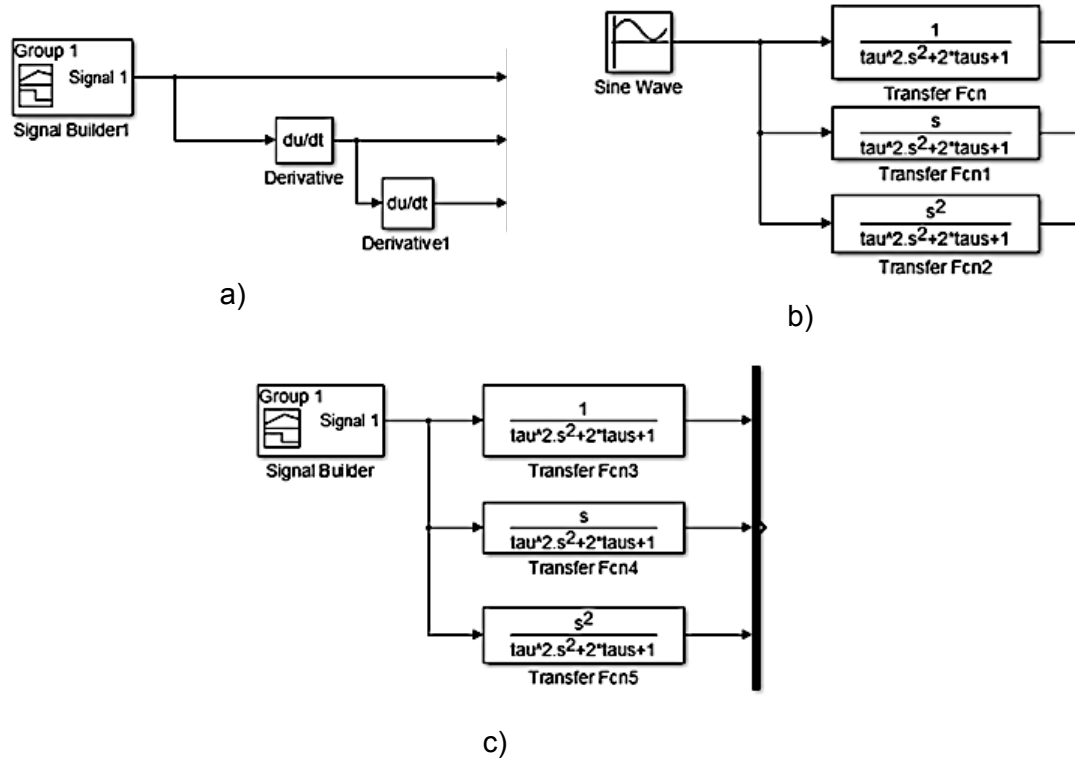
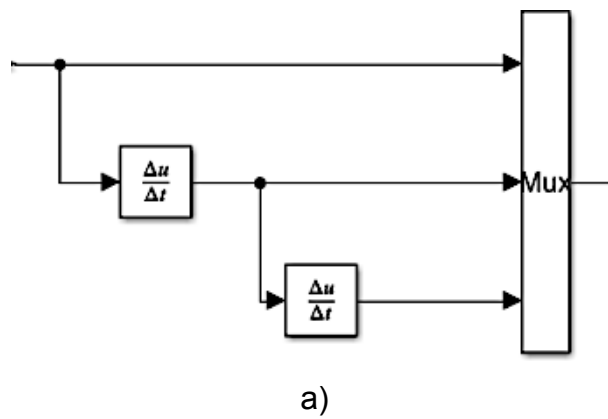
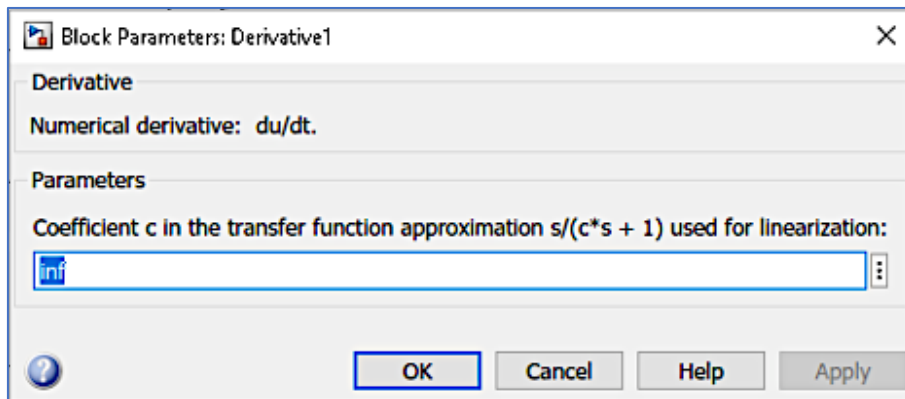


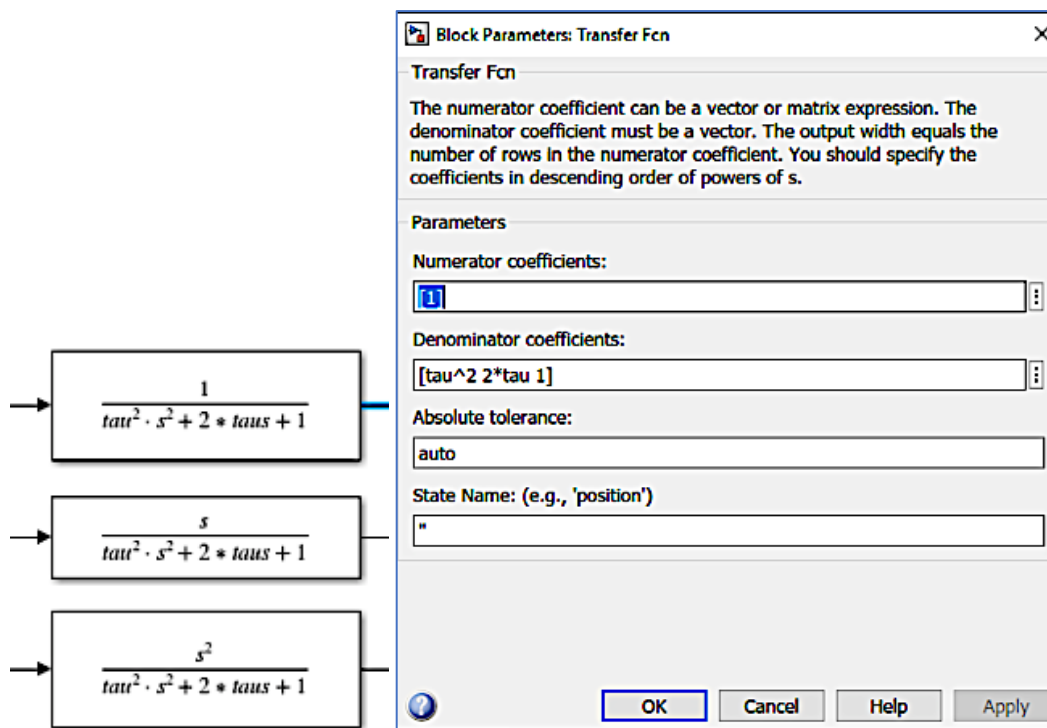
Figure 49 Generation of input signal incorporating a transfer function based differentiation method where the parameter  $\tau$  can be adjusted (Chacko and Khan 2017)





b)

Figure 50 a) Input signal and time derivatives and b) parameters for differential function



a)

b)

Figure 51 a) Modified differential functions and b) coefficient s and denominators for the transfer functions

Differentiation of input signals such as displacement using conventional techniques usually affects the simulation results in terms of stability and accuracy because of the high magnitudes. Signal smoothing to produce better simulations constitutes a little-known prerequisite, especially in the case of dynamic simulations and this is explained below.

The conventional differentiation block representing the first-order time differential  $\left(\frac{du}{dt}\right)$  is presented in Figure 49 a and in Figure 50 where  $u$  is the time-dependent input signal. The first time differential of the input signal  $u$ ,

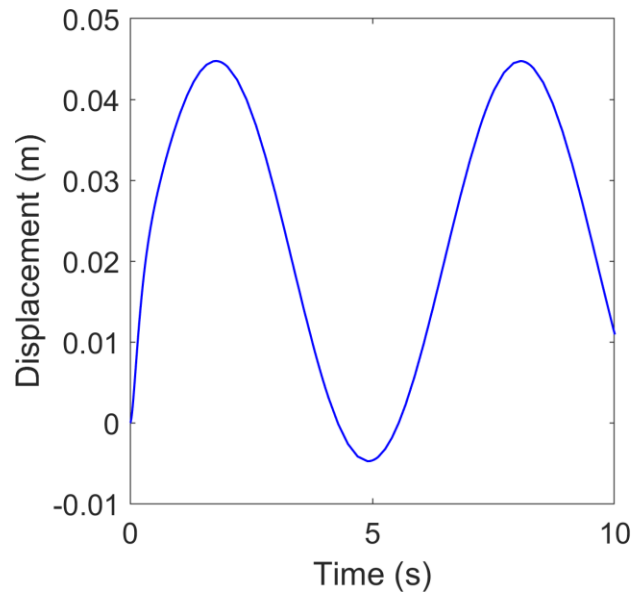
which here represents either linear or angular displacement, provides the velocity signal and the second time differential of the input signal provides the acceleration signal. However, the use of the ordinary differential block presented in Figure 50 leads to abrupt variations in the magnitudes of velocity and acceleration corresponding to the change of input signal magnitude. In order to rectify this defect, the differential function is replaced by a transfer functions and these modified differentials i.e.,  $\frac{1}{\tau^2*s+2*\tau*s+1}$ ,  $\frac{s}{\tau^2*s+2*\tau*s+1}$  and  $\frac{s^2}{\tau^2*s+2*\tau*s+1}$ , as presented in Figure 49 b & c and Figure 51, are applied to the input signal for generating corresponding displacement, velocity and acceleration signals (Rouleau 2012). Figure 51 b shows the definition of the parameters of the modified differential function.

#### 4.4 Simulation case studies with friction

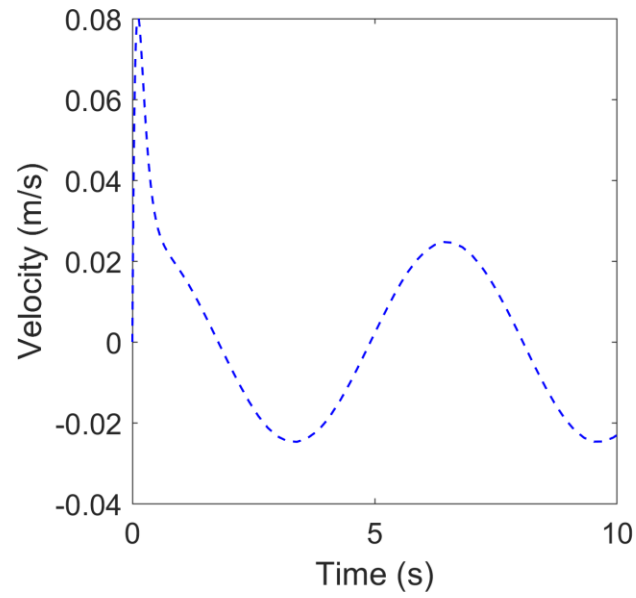
In this section, simulation of design case studies presented in section 4.2.2 are presented. The combined friction model is incorporated in case studies 1 and 3; the friction model is not incorporated in case 2, since it is a preliminary design.

##### 4.4.1 Input signal for actuating the validation simulation

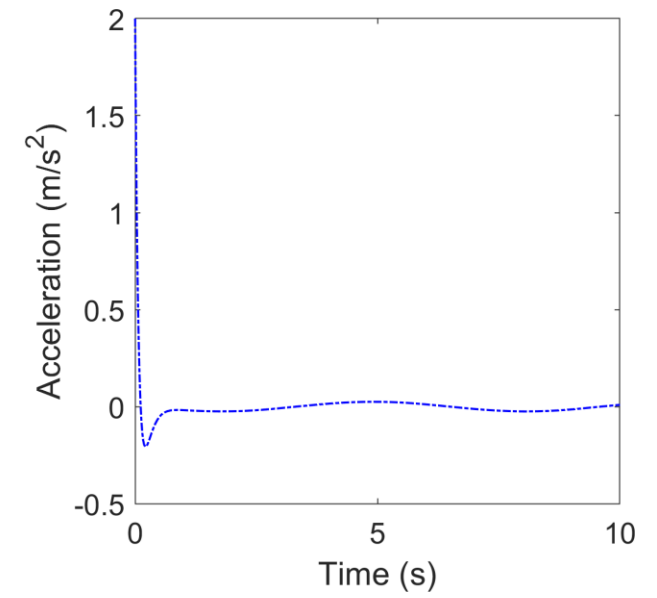
The input signal for actuation consists of a sine wave having duration of one and half periods, beginning at zero displacement. This was selected to produce cyclic oscillation of the manipulator link in which the end-effector retraces its motion, thereby ensuring the reproducibility of the computed outputs. The sine wave block presented in Figure 47 is used to generate this input signal with the following parameters to fulfil the design requirements: amplitude = 0.025, bias = 0.02 and frequency = 1 rad/sec. The generated input signal is shown in Figure 52. The first and second time derivatives of the displacement, i.e., velocity and acceleration components of this input signal are presented in Figure 52 b and c. The maximum displacement of the actuator was computed to be 44.75E-3m in the positive direction and 47.56E-3m in the negative direction, both of which fall within the operational range for the selected actuators from literature (Gimson Robotics 2015). The maximum velocity and acceleration were recorded to be 0.08 ms<sup>-1</sup> and 0.80 ms<sup>-2</sup> respectively.



a)



b)



c)

Figure 52 Actuator input signal: amplitude = 0.025, bias = 0.02, frequency = 1 rad/sec, the velocity and acceleration are derivatives of the main input signal

#### 4.4.2 Case 1: Anthropoid manipulator

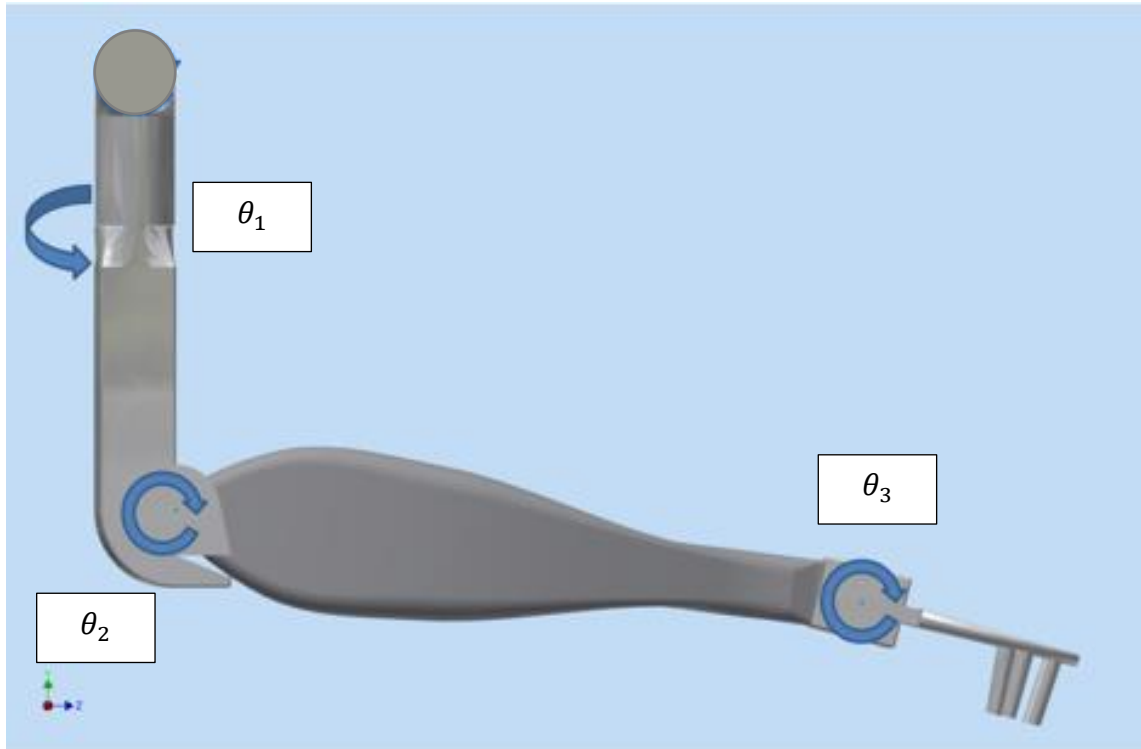


Figure 53 Manipulator design showing input parameters adapted from (Khurshid et al. 2016)

The input signals for simulating the dynamics of the serial manipulator are presented below. Based on the computed mobility of the linkage according to section 4.2.1.2, the input signals for this simulation, which is inverse dynamics, comprised the kinematic angular parameters given below:

$$\theta = \begin{bmatrix} \theta_1 \\ \theta_2 \\ \theta_3 \end{bmatrix}, \dot{\theta} = \begin{bmatrix} \dot{\theta}_1 \\ \dot{\theta}_2 \\ \dot{\theta}_3 \end{bmatrix}, \ddot{\theta} = \begin{bmatrix} \ddot{\theta}_1 \\ \ddot{\theta}_2 \\ \ddot{\theta}_3 \end{bmatrix} \quad (18)$$

where  $i$  represents the number assigned to the sDOF revolute joint as shown in Figure 53,  $\theta_i$  represents the actuation angle for the  $i^{th}$  revolute joint and similarly  $\dot{\theta}_i$  and  $\ddot{\theta}_i$  represents the corresponding angular velocity and acceleration.

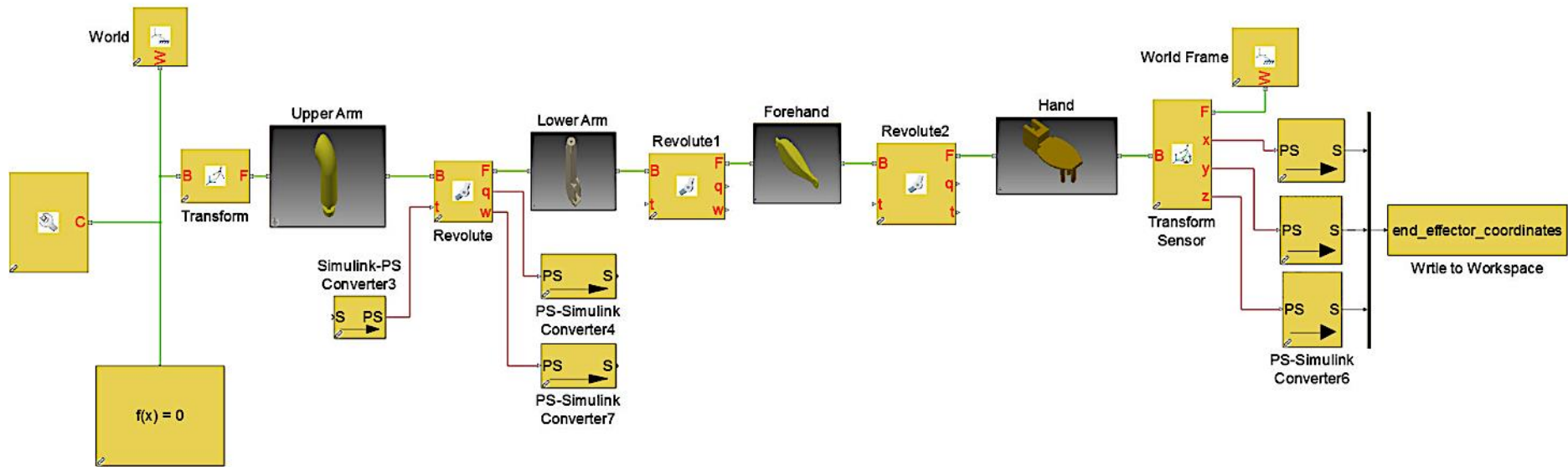


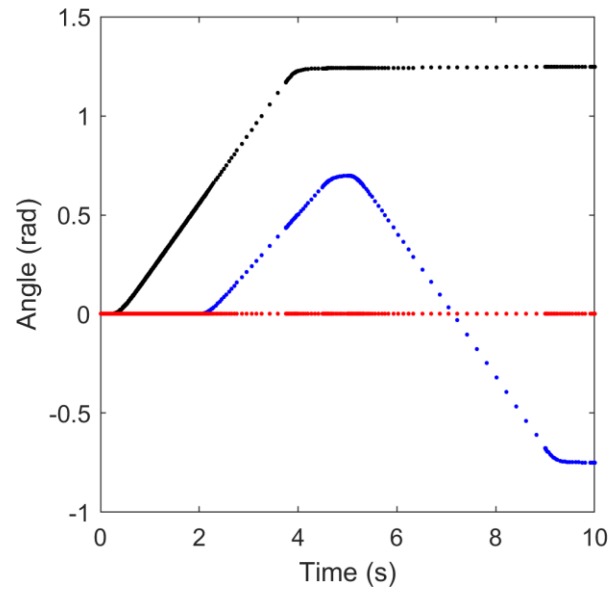
Figure 54 SimMechanics 2<sup>nd</sup> generation block diagram representation of the anthropoid manipulator (Khurshid et al. 2016)<sup>6</sup>

<sup>6</sup> The MBD visualisation was part of the work contributed by this author to the co-authored publication referenced.

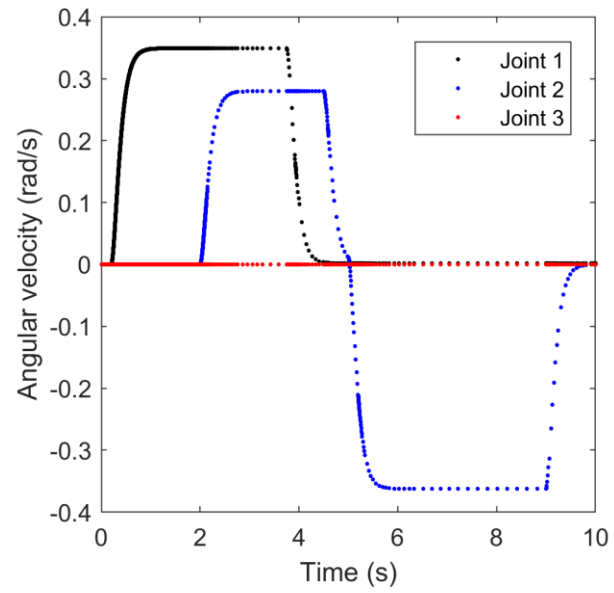


Figure 54 depicts the block diagram for the anthropoid manipulator presented in Figure 53. The input signals for the anthropoid manipulator corresponding to simulations 1-4 are presented in Figure 55. For each simulation, the signals consisted of position, velocity and acceleration. From these figures it can be observed that the time-steps for the signals differed because of the four different solvers used and this is demonstrated by the spacing between successive scatter points in the plot presented in Figure 55. Use of modified input signals by applying input signal modification presented in section 4.3.4 resulted in smooth transition characteristics of the velocity and acceleration profiles.

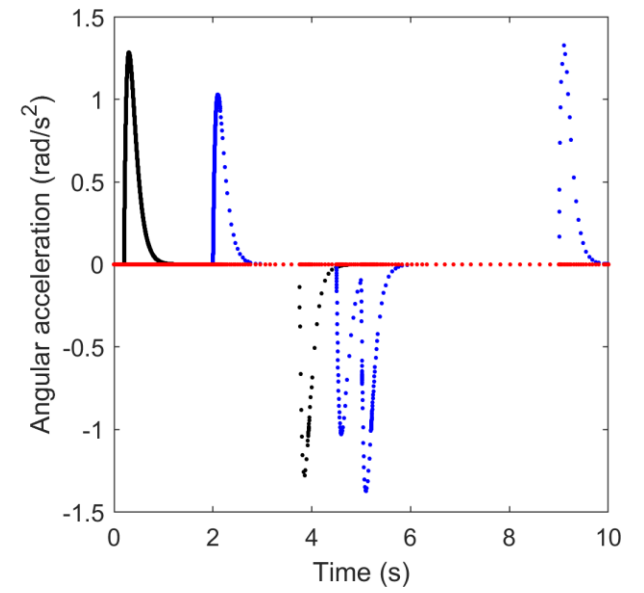
### Simulation 1



a)

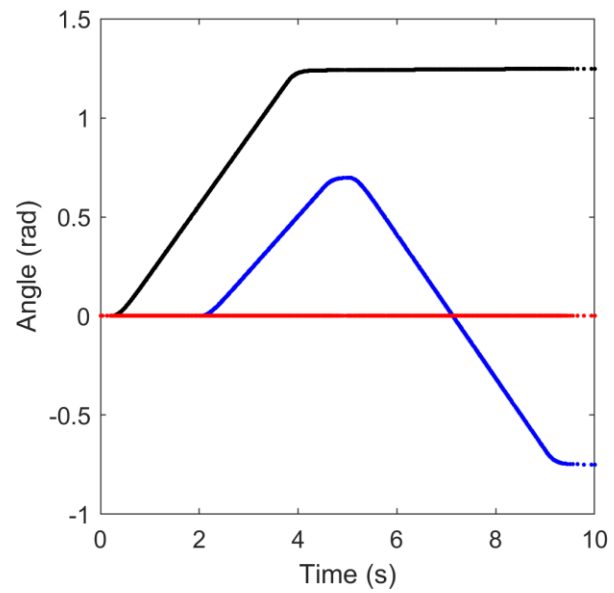


b)

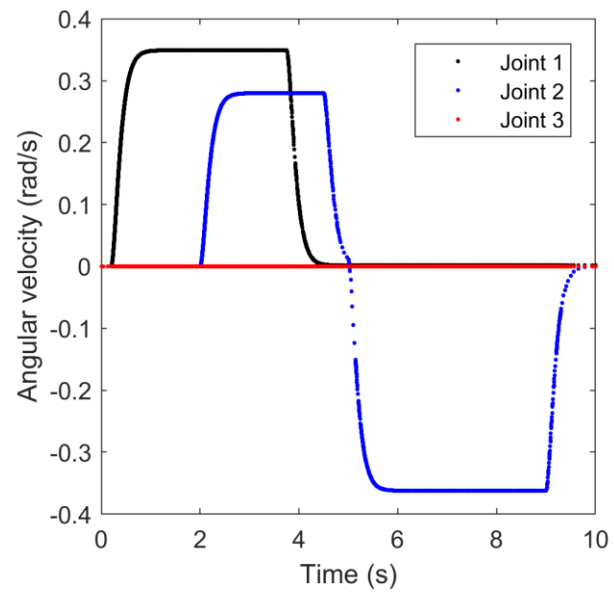


c)

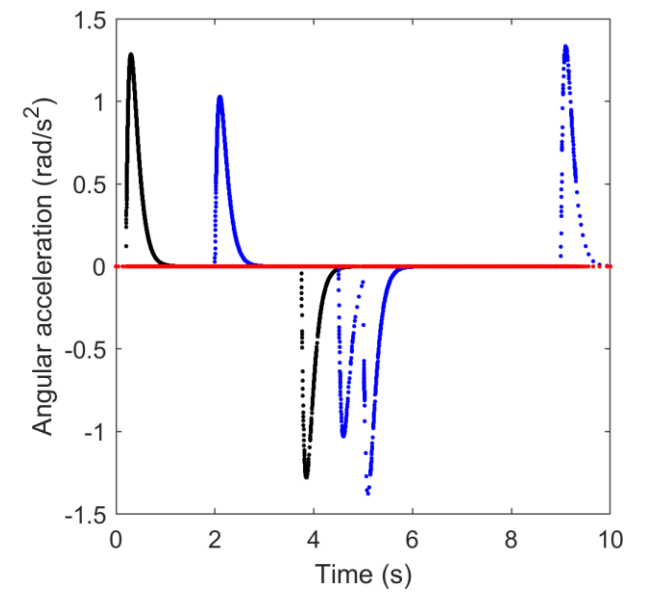
## Simulation 2



a)

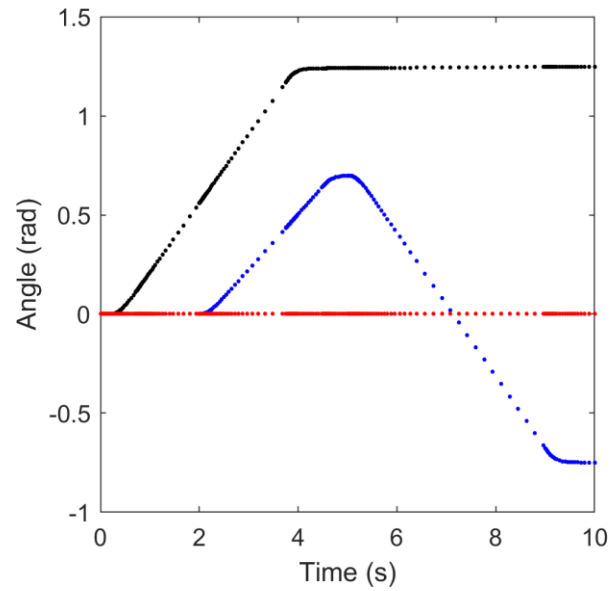


b)

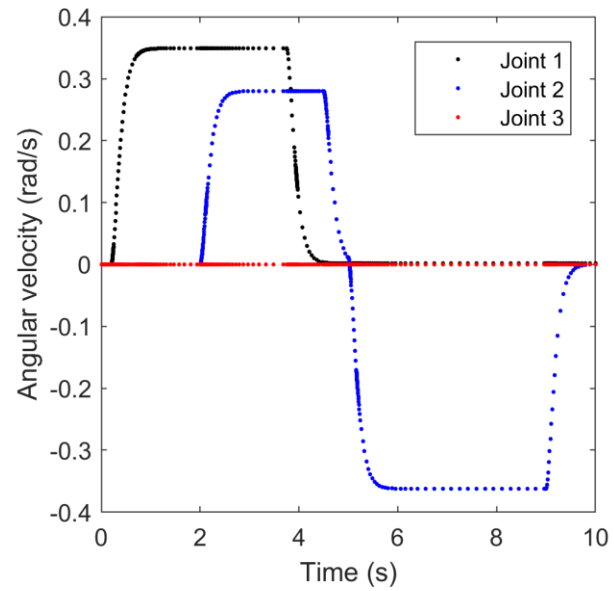


c)

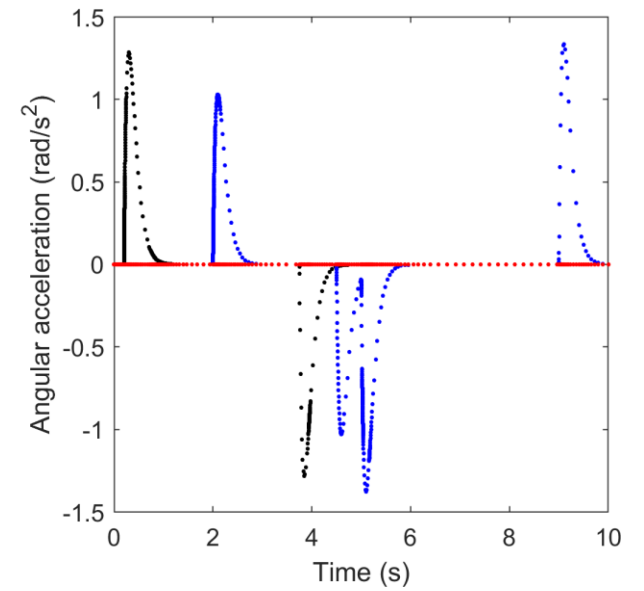
### Simulation 3



a)



b)



c)

### Simulation 4

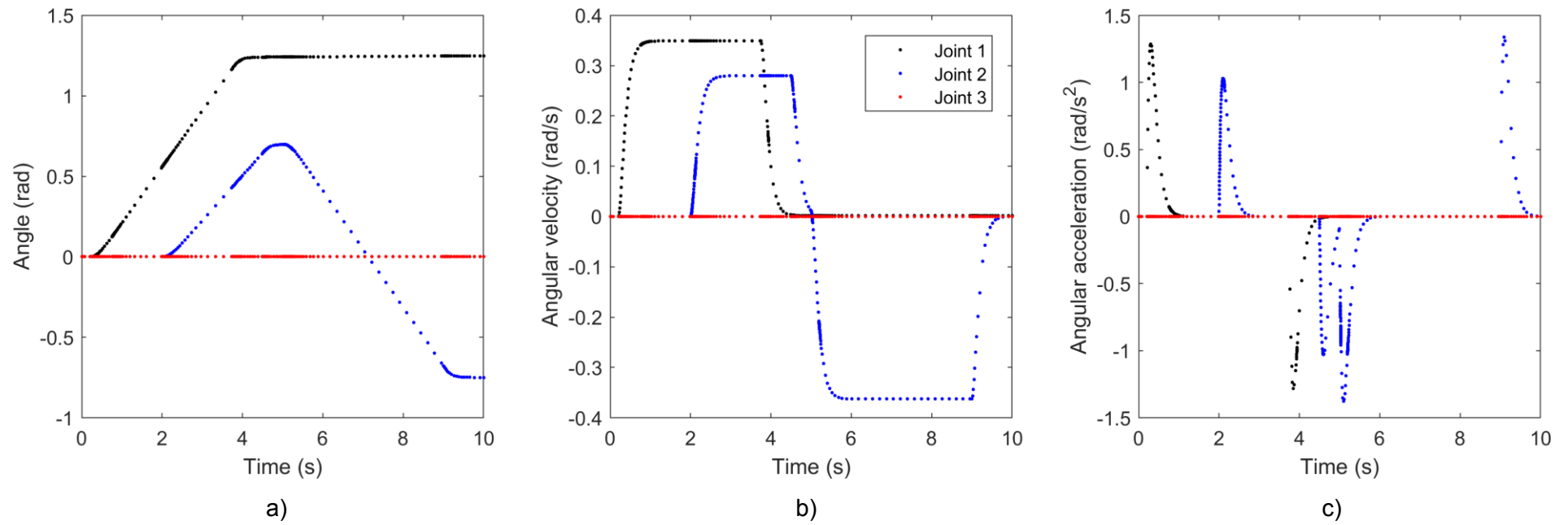


Figure 55 Input signals generated with four different solvers for the anthropoid manipulator corresponding to simulations 1-4

#### 4.4.3 Case 2: Serial open-chain manipulator

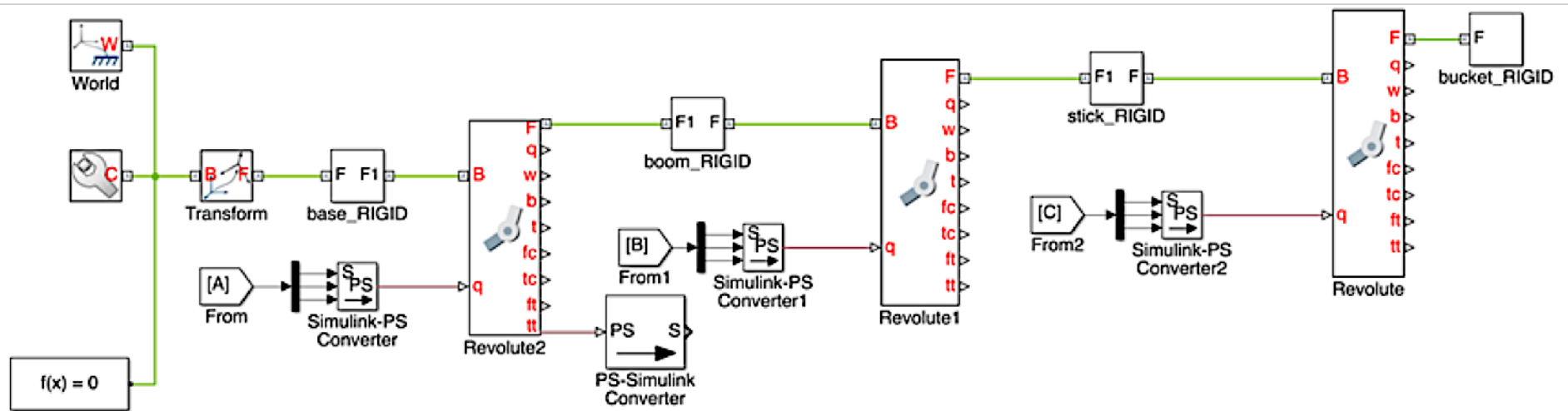
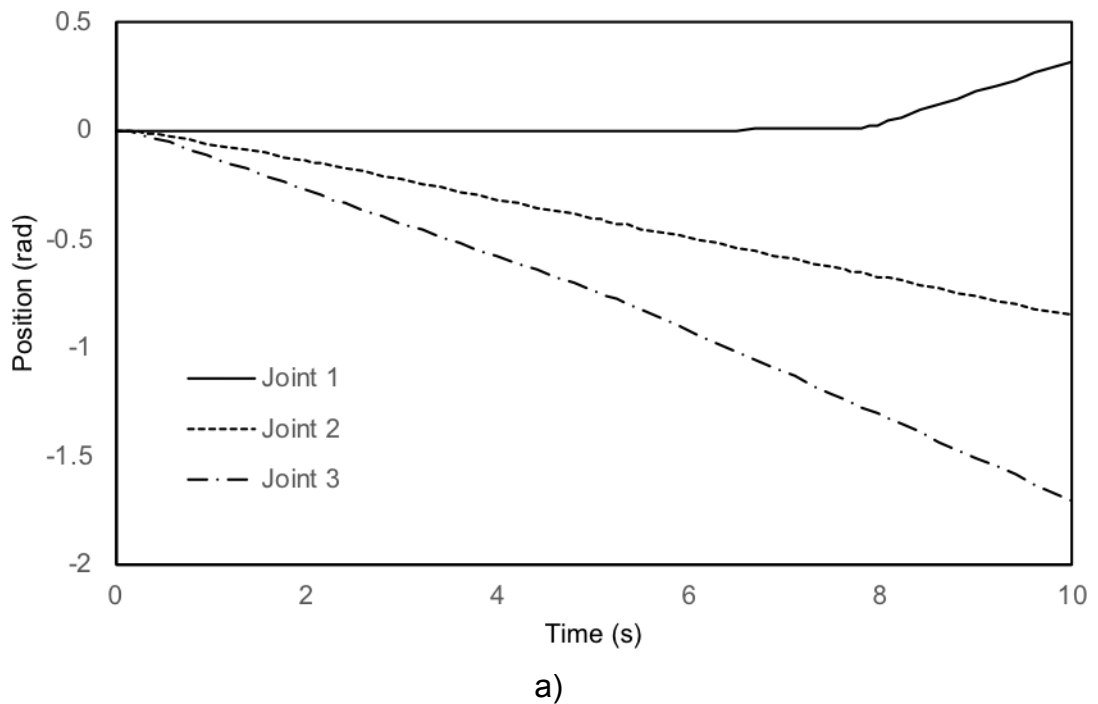
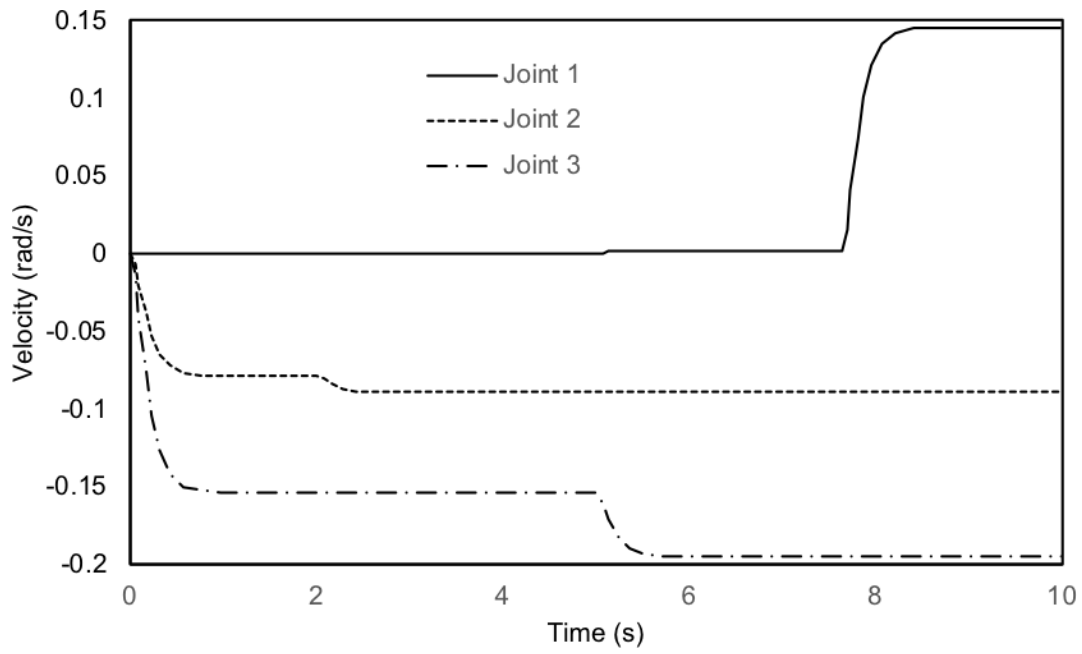


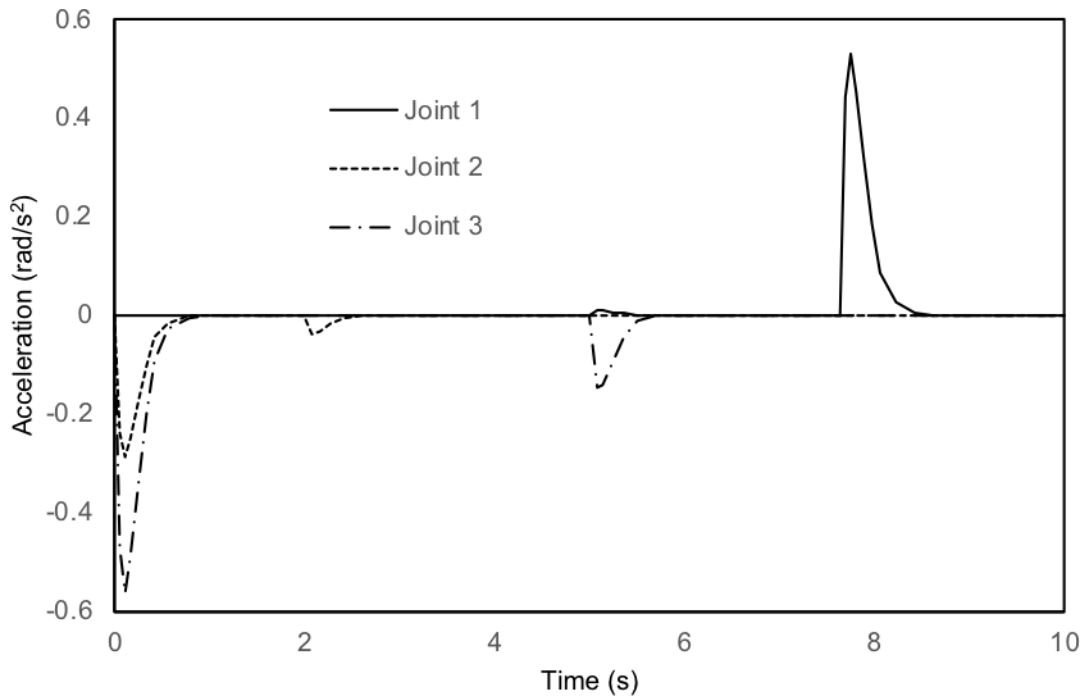
Figure 56 SimMechanics 2<sup>nd</sup> generation model for serial open-chain manipulator

In this section, the input signals for the actuation of the three sDOF revolute joints of the serial manipulator with bucket end-effector are presented. The block diagram representation of the serial open-chain manipulator is presented in Figure 56. The common joint actuation signals for SimMechanics 1st and 2nd generation simulations were generated using the 'signal builder block' presented in Figure 48 and the generated signals are presented in Figure 57. The magnitudes of angular acceleration of 0.5648 rad/s<sup>2</sup> at 0.1023s, and 0.5262 rad/s<sup>2</sup> at 7.427s of the simulation time, resulted in commensurate increase in outputs due to their high magnitudes, and these are presented in the results of simulation in (section 6.2.2) of Chapter 6.





b)



c)

Figure 57 a) Angular displacement, b) angular velocity (rad/s) and c) angular acceleration of the revolute joint (rad/s<sup>2</sup>)



#### 4.4.4 Case 3: Closed-loop complex manipulator

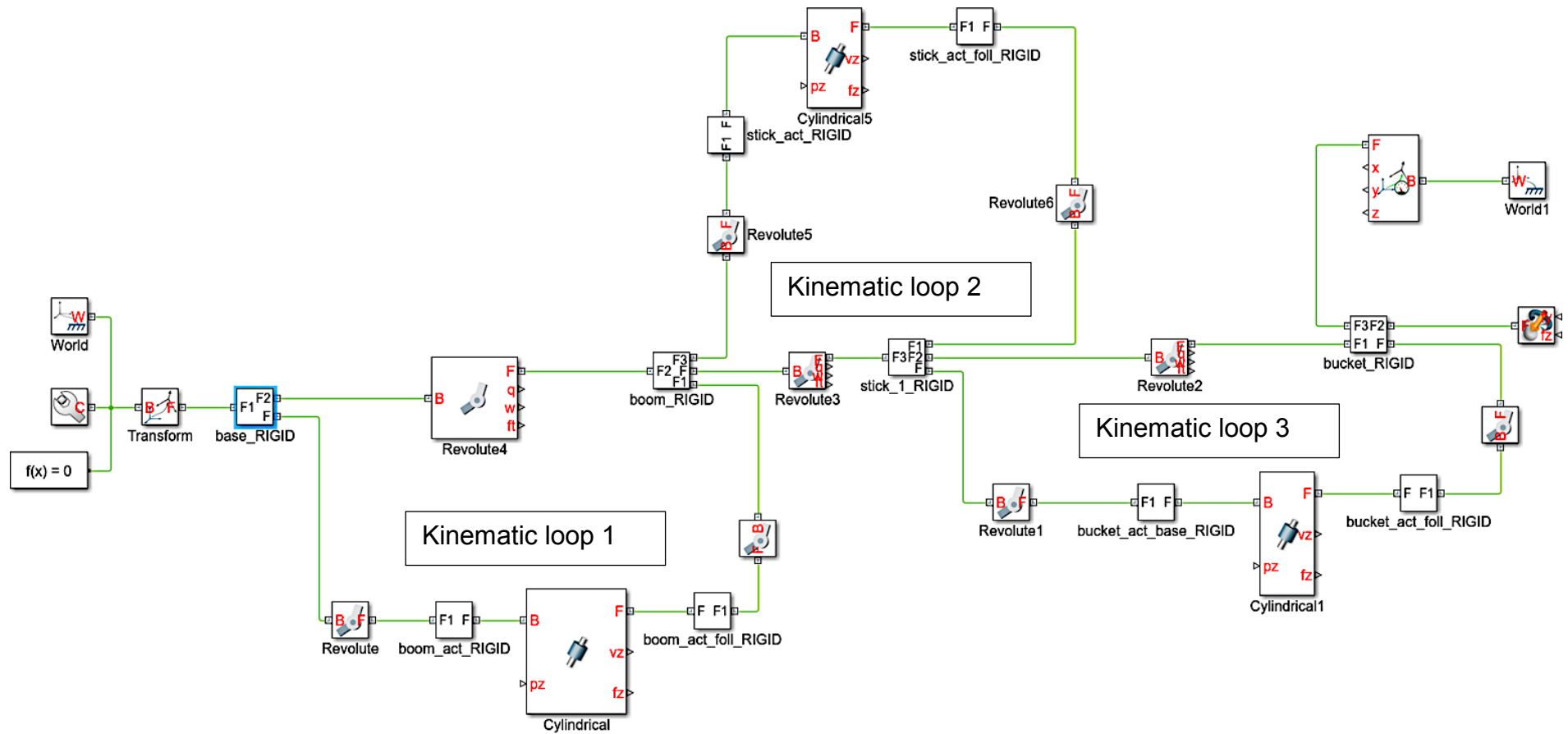


Figure 58 Block-model layout of the closed-loop mechanism in SimScape showing three kinematic loops

Simulation of the full manipulator mechanism was conducted for three different sets of input parameters (simulations 1-3) using SimMechanics 2<sup>nd</sup> generation MBD simulation platform. The manipulator motion was controlled using kinematic inputs, i.e., extension and retraction of the actuators to control the positioning of the end-effector of the manipulator to achieve different dig patterns.

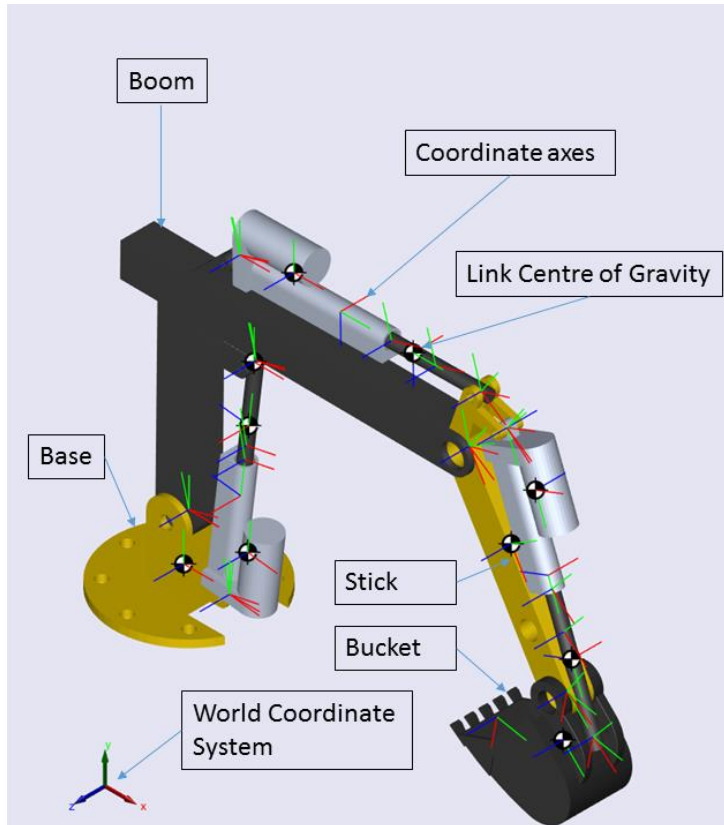


Figure 59 Visualisation of the simulation output

SimMechanics 2<sup>nd</sup> generation block diagram layout of the closed-loop manipulator mechanism is presented in Figure 58 and the three kinematic loops are marked in the figure. Visualisation of the simulation output is presented in Figure 59 and the names of the respective links i.e. base, boom, stick and bucket, centres of gravity of the various links, coordinator transformation axes corresponding to each link and the world coordinate system are marked in the figure.

The signals used for conducting inverse dynamics simulation were kinematic - namely linear displacement, velocity and acceleration. The linear extension of actuators was used to control the end-effector location for which the kinematic input consisted of extension of actuators and its time derivatives given below:

$$x = \begin{bmatrix} x_1 \\ x_2 \\ x_3 \end{bmatrix}, \dot{x} = \begin{bmatrix} \dot{x}_1 \\ \dot{x}_2 \\ \dot{x}_3 \end{bmatrix}, \ddot{x} = \begin{bmatrix} \ddot{x}_1 \\ \ddot{x}_2 \\ \ddot{x}_3 \end{bmatrix} \quad (19)$$

where  $x_i$  represents the actuation displacement for the  $i^{th}$  sDOF prismatic joint and  $\dot{x}_i$  and  $\ddot{x}_i$  represents the corresponding linear velocity and acceleration respectively.

### Input parameters for simulation

Parameters for controlling the sine wave in simulation 1 i.e., amplitude, bias, frequency and phase, are presented in Table 11. A constant load was applied on the end-effector (~200N).

	Amplitude	Bias	Frequency	Phase
Joint 1	0.025	0.02	0.4	0
Joint 2	0.015	0.02	0.5	0
Joint 3	0.0015	0.01	0.3	0

Table 11 Input parameters for simulation using sine wave block

The second method of generating input signals for the linear actuation of prismatic joints for the closed-loop mechanism is applied to simulations 2 and 3 presented below by using the signal builder block presented in Figure 41 and these signals comprise position, velocity and acceleration of the linear actuator as presented in Figure 60, Figure 61 and Figure 62. The inputs were used to create several different dig patterns and to compare the force/torque characteristics of the mechanism corresponding to these patterns i.e., simulation outputs presented in detail in Chapter 6.

### Simulation 1

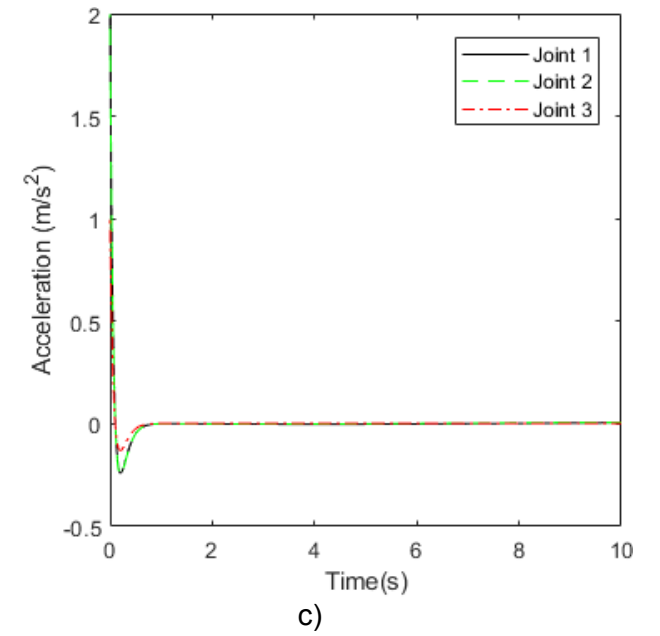
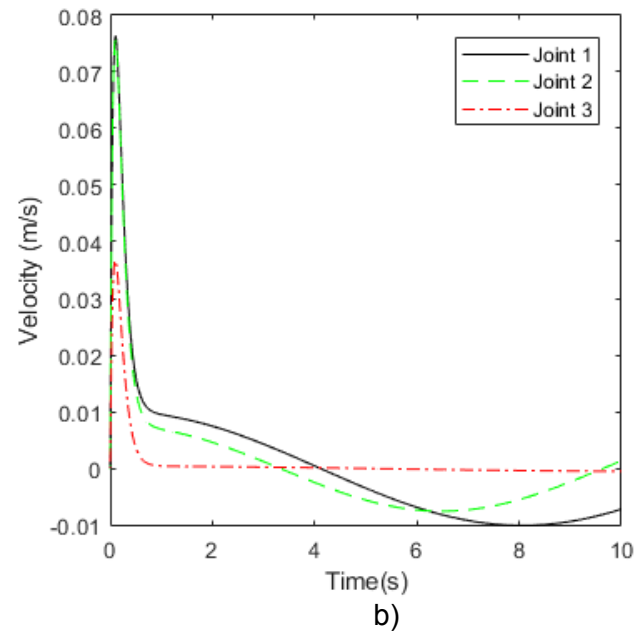
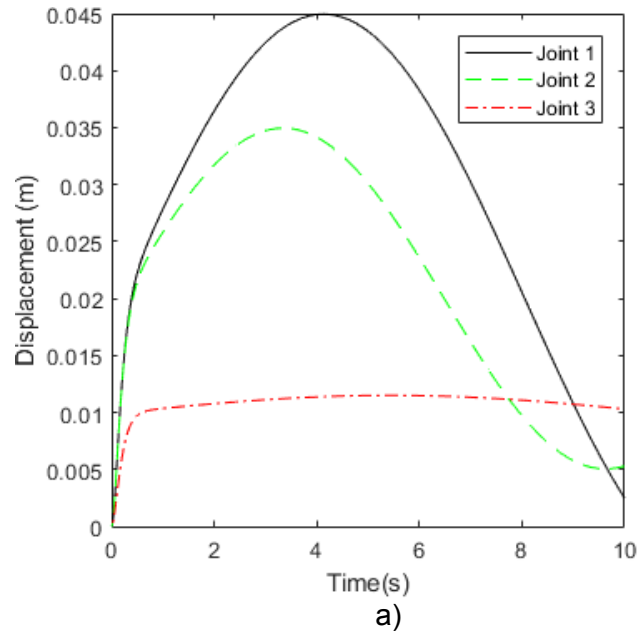


Figure 60 Input signals for simulation 1

## Simulation 2

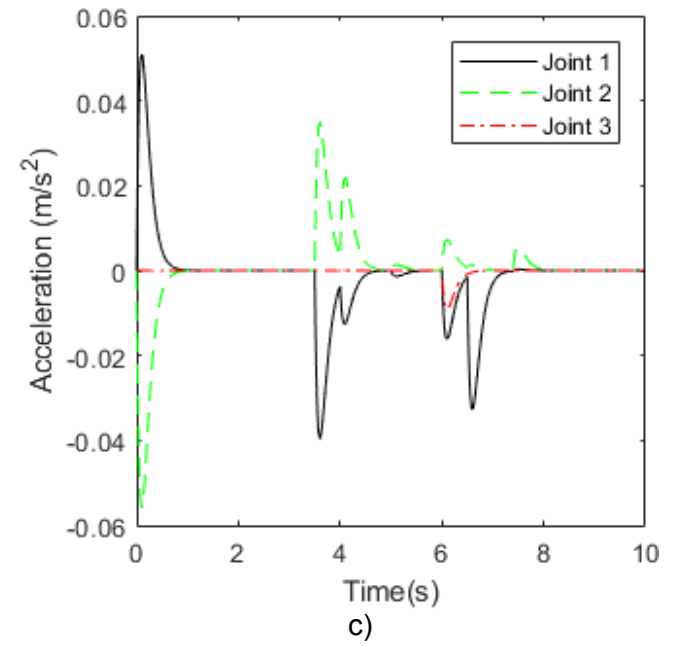
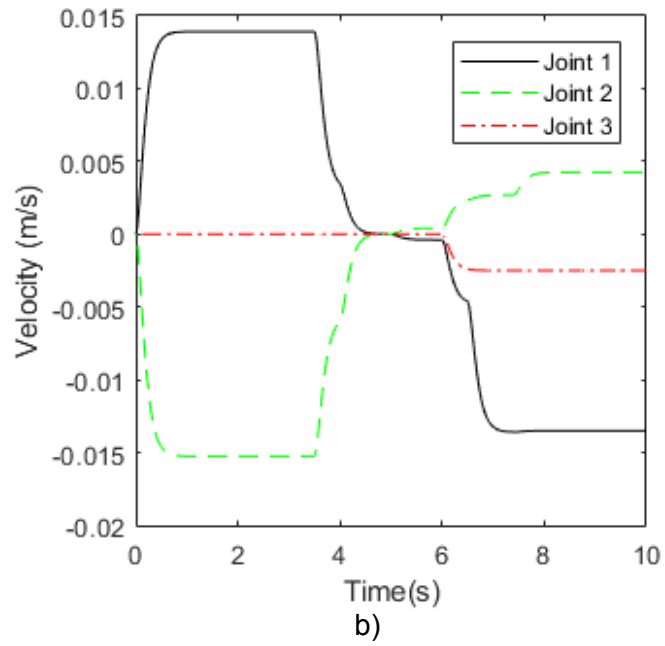
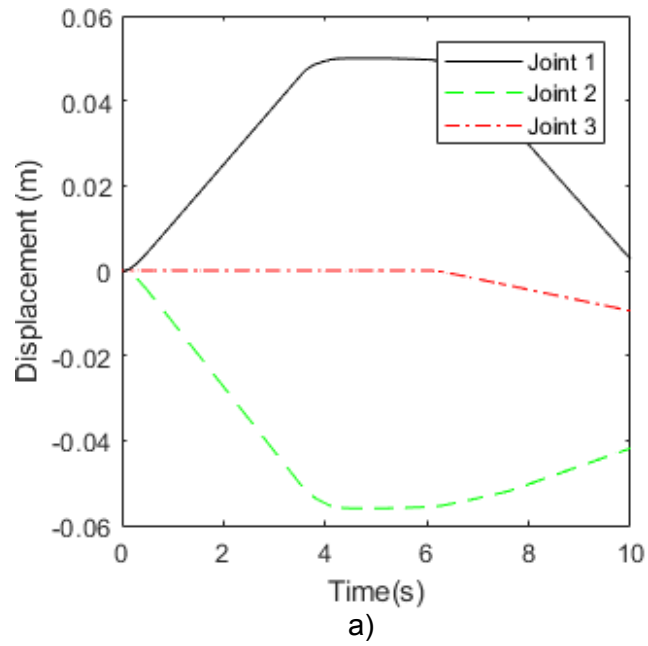
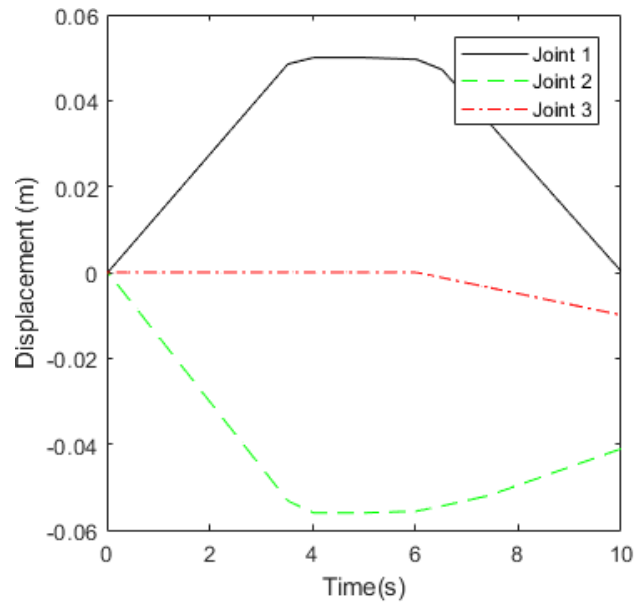
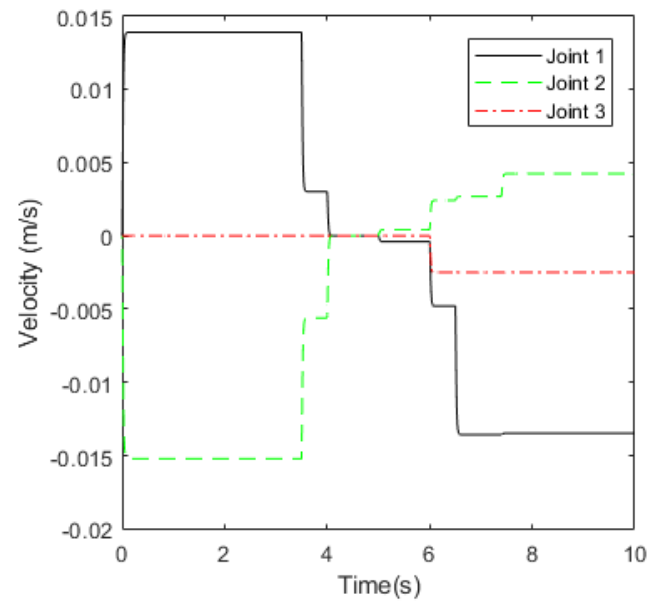


Figure 61 Input signals for simulation 2

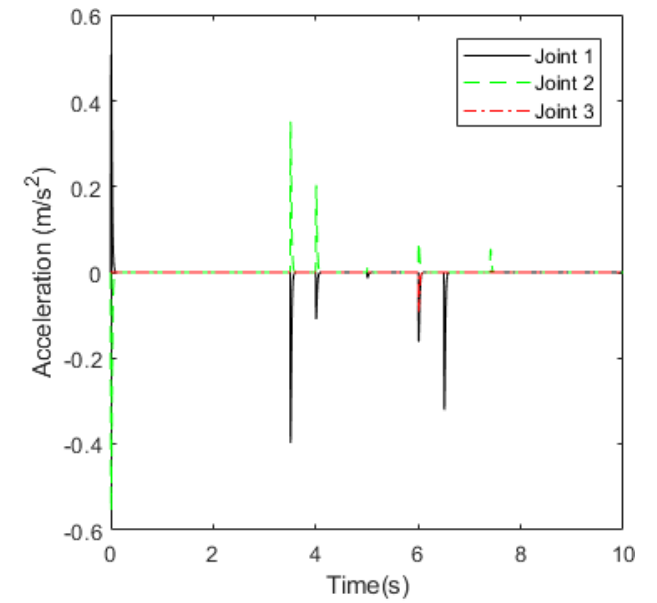
### Simulation 3



a)



b)



c)

Figure 62 Input signals for simulation 3

## 4.5 Summary

In this chapter, the feasibility of developing manipulator design using CAD and simulation using MBD in a time-bound, cost-effective, application-specific manner was investigated. CAD designs were built using the bottom-up approach and the assembled linkages were exported to the MBD simulation environment and inverse dynamics simulations were conducted. To validate the technique, results of simulation for a single link closed-loop linkage was compared with the established technique presented in literature for dynamic parameter namely joint torque. Friction force and torque for the sDOF translational and revolute joint were also computed using the combined friction model with generalized coefficients. The simulation results are presented in Chapter 6.

From literature review, it was understood that incorporation of a friction model into simulation in SAR has hitherto not been reported. However, understanding full friction parameters for the model is not possible within the scope of this work and in order to analyse the effect of COF with a view to minimising it, experimental study involving tribological analysis of mainly COF between a manipulator joint, selected based on literature review, is presented in the next chapter.

# Chapter 5 Tribological analysis of 16MnCr5 and EN19 steels

## 5.1 Introduction

As substantiated in the literature review 3.1.1, 16MnCr5 is an important steel alloy used for bushings, shafts, gears, pinions, collets, pins, camshafts and other automotive components (Johansson et al. 2002, Kiapei 2014, SantAna et al. 2017). Therefore, it has been used as material for manufacturing bushings used in manipulator joints, especially in retrofits, i.e., in the joints of excavator arms used as lifting equipment in construction industry. The pin-bushing combination found in aftermarket retrofits comprises 16MnCr5-EN19 steel alloy pair and this was selected for investigation in this work, which makes the results relevant both academically and techno-commercially. Despite the wide use of the steel alloy pair, detailed tribological analysis, especially focussing on its coefficient of friction (COF) has not been presented in literature. The layout of work presented in this chapter to address this knowledge gaps is illustrated in Figure 63.

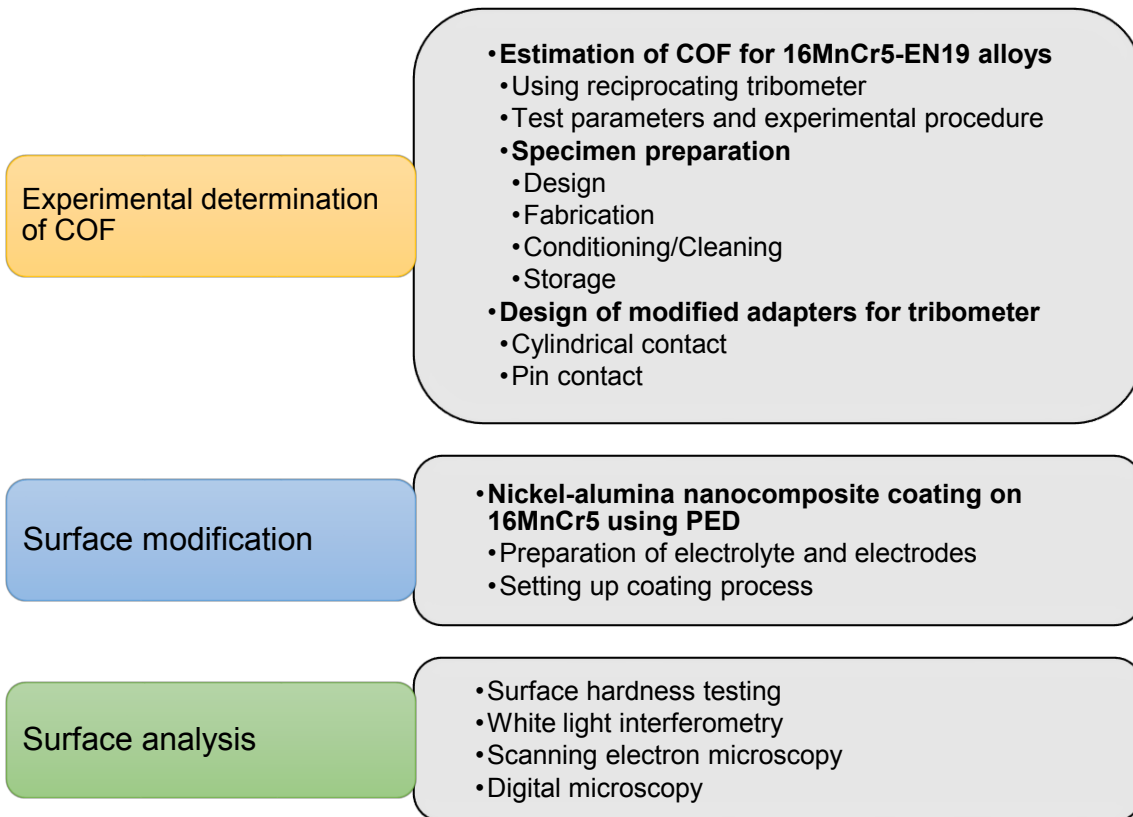


Figure 63 Layout for experimental procedures followed in this chapter



In this chapter the measurement of COF for the 16MnCr5-EN19 steel alloy pair, conducted using the reciprocating tribometer<sup>7</sup> which simulates the operating conditions prevailing in the manipulator pin-bushing joint namely frequent start-stop and direction reversals, is presented. Process of deposition of nickel alumina nanocomposite coating on 16MnCr5 specimens by using pulse electrodeposition (PED) is also presented. The influence of the coating on COF generated in the contact against the EN19 counter-face was measured using the reciprocating tribometer. Tribo-tests for measuring COF were conducted under different conditions including contact geometry, normal load, lubricant and surface characteristics, all of which influence the COF generated in the contact interface.

Test specimens for conducting experiments on this alloy were redesigned using Computer Aided Design (CAD) due to limitations encountered in machining 16MnCr5 to conventional specimen dimensions. The specimen adapters for the tribometer were also redesigned for the two different contact geometries considered in the tribo-tests because of the dimensional variations observed in the fabricated specimens supplied by the local manufacturer.<sup>8</sup> These adapters were fabricated using Electro Discharge Machining (EDM) and were successfully used in the experiments conducted with the reciprocating tribometer. Further to determination of COF, the surface hardness of test specimens was analysed using the Vickers micro-indentation hardness testing device and surface parameters were measured using white light interferometry, scanning electron microscopy and digital microscopy.

## **5.2 Measurement of coefficient of friction (COF) using the reciprocating tribometer**

In the previous chapter, the utilisation of CAD-MBD approach for designing, modelling and simulating mechanical manipulators for application-specific and time-efficient use in the SAR environment was investigated into which combined

---

<sup>7</sup> Hereafter referred to as tribometer.

<sup>8</sup> A local manufacturer, M/s FJ engineering, New Milton, Hampshire supplied the test specimens because of the high cost of specimens from the original equipment supplier and limited budget available for the project, also mentioned in section 3.2.3 of the literature review.

friction model (CFM) was incorporated. To find out the parameters of the CFM, extensive experimental testing is required. However, as a cost and time-effective solution to this problem, scaled-down experimental testing was followed as presented in section 3.1 of the literature review. In the context of this experimental analysis, the study of tribology is commonly understood to comprise friction, wear and lubrication and as these tribological parameters affect the dynamic performance of the manipulator, analysis of COF between the selected steel alloy pair to simulate the dynamic performance of the manipulator joint is presented as the first step towards conducting tribological analysis.

The measurement of the COF of lubricated, sliding reciprocating contact using the TE57 reciprocating tribometer is explained in this section and tribometer rig setup and specifications as well as the experimental parameters (load, lubrication etc.) are discussed in section 5.2.1. Kinematics of tribometer is explained in section 5.2.2. Test parameters and experimental procedure are discussed in section 5.2.3. Self-aligning adapter designs for holding the fixed specimen in the test chamber and specimen preparation are presented in sections 5.2.4 and 5.2.5 respectively.

### **5.2.1 Tribometer test rig to simulate sliding contact**

Plint TE57 reciprocating tribometer shown in Figure 64 was used to conduct the tribo-analyses for simulating the sliding contact present in manipulator pin-bushing joint with frequent start-stops and direction reversals. The tribometer consists of a removable, temperature-controlled test chamber inside which the test specimens are mounted. Normal load was applied to the fixed specimen through the lever-arm arrangement connected to a spring loading system. The range of loads applied was between 10N and 40N which lay within the upper limit of 50N for the machine. Peak load was limited due to the dead-zone of the spring balance (equivalent to traverse for 5N load) and the load measurements were adjusted accordingly.

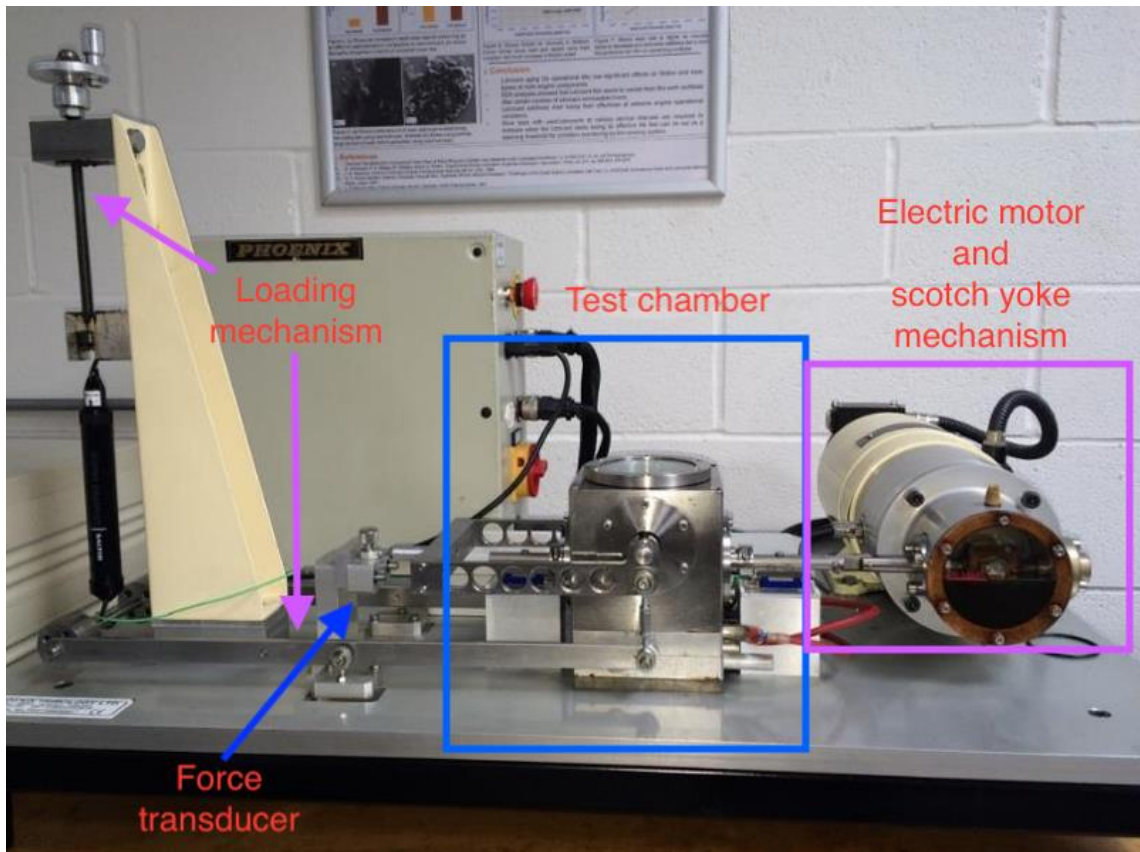


Figure 64 Reciprocating tribometer

Two sets of specimens were developed corresponding to two contact geometries namely, the sliding cylindrical contact pair and the sliding pin contact pair, as shown in Figure 65. The flat 16MnCr5 specimen was placed inside a cup holder which was then mounted on the reciprocating link. This cup was filled with the required lubricant to ensure a fully-flooded lubrication condition. The fixed test specimen i.e. the counter-face, was fitted inside its adapter and this was mounted on the upper shaft of the tribometer.



Figure 65 a) sliding cylindrical contact pair and b) sliding pin contact pair

The magnitude of friction force generated in the contact was measured using the inbuilt Kistler Type 9203 piezo-electric force transducer which generates charge proportional to frictional force with a sensitivity of 45.7pC/N. The Kistler Type 5011 charge amplifier connected to force transducer converts the charge generated into a proportional electrical voltage signal which was amplified using

scaling factor (N/V). The amplified signal represents the tangential friction force generated in the contact. COF was calculated by dividing the magnitude of friction force by the magnitude of normal load applied at the contact according to the relation presented in equation 20 below:

$$\mu = F/R \quad (20)$$

where  $\mu$  represents the COF,  $F$  represents the friction force, and  $R$  represents the normal load acting on the contact, shown in Figure 66 below.

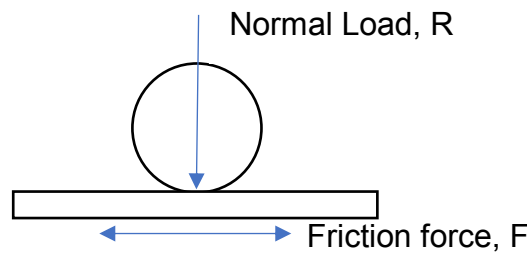


Figure 66 Normal load and friction force generated in a sliding contact

Test conditions such as speed and temperature were controlled through COMPEND-2000, which is the programmable graphical user interface (GUI) running on the workstation on which the measured data was recorded through a data acquisition card.

### 5.2.2 Kinematics of the reciprocating tribometer

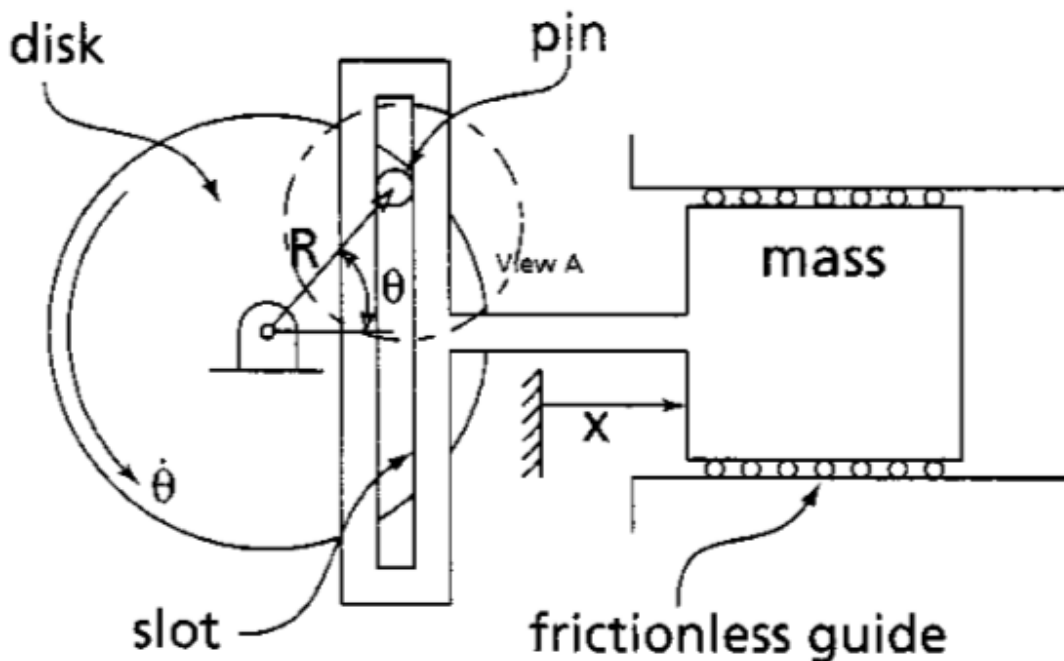


Figure 67 Scotch-yoke mechanism (Sawyer et al. 2003)

The scotch-yoke mechanism, graphically shown in Figure 67, converts the rotational motion of the electric motor into linear reciprocating motion of the reciprocating link. The stroke length for the mechanism ranges from 1mm to 5mm, which represents the specimen displacement. The kinematic equations governing the scotch-yoke mechanism can be expressed through the following equations:

$$x = R \sin (\omega t) \quad (21)$$

$$\dot{x} = R\omega \cos (\omega t) \quad (22)$$

$$\ddot{x} = -R\omega^2 \sin (\omega t) \quad (23)$$

where  $x$  represents the stroke length,  $\dot{x}$  represents the linear velocity of the moving specimen,  $\ddot{x}$  represents the linear acceleration,  $r$  represents the distance of the centre of the pin from the centre of the rotating shaft of the electric motor,  $\omega$  represents the angular frequency of the electric motor shaft and  $\omega.t = \theta$  where  $\theta$  is the angle of inclination of the pin shown in Figure 67. Here  $R = 2.5mm$  which corresponds to the desired displacement of 5mm, and  $\omega = 0.5 \text{ rad/s}$  which corresponds to the reciprocating frequency of 10Hz. The simulation was conducted using Simulink and the block diagrammatic representation of the above equations is presented in Appendix E.

### 5.2.3 Parameters and procedure for conducting experiments

Parameters which affect friction generated in contacts include contact geometry, loading, temperature, lubricant type, lubrication mode and surface condition among others. In line with (Blau 2001), the parameters referred to in section 3.2.2 of the literature review chapter are explained here.

Typical bushing surfaces are characteristically rough with the orientation of roughness lines aligned along the direction of motion. Two types of contact geometries were used to simulate the i) sliding cylinder on plane and ii) sliding pin on plane. Load range of 10N to 40N, was applied in order to measure its effect on the COF generated in the contact. Temperature within the test chamber was recorded using the inbuilt thermometer but not considered in this analysis. The ambient temperature varied from 16°C to 23°C. Even though use of elevated temperatures has been reported in literature for accelerated testing,

the variation of temperature was not considered in this research as the test chamber was hermetically sealed during operation. This was measured in terms of COF, which is the focus of this investigation and is presented in detail.

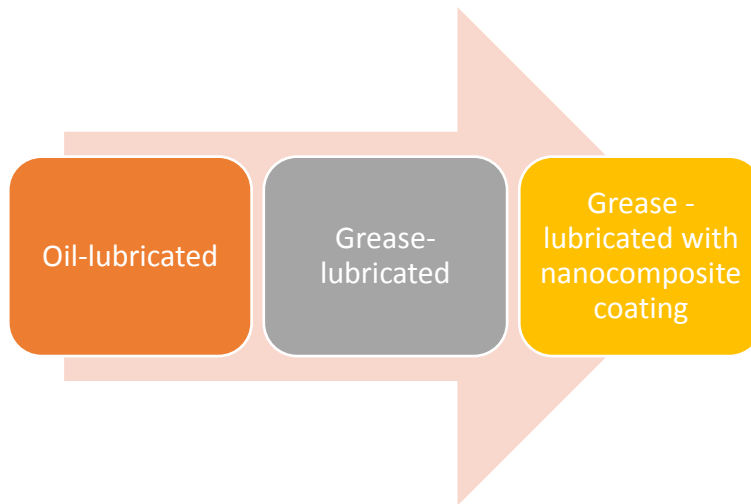


Figure 68 Use of lubricants in the tribo-tests

The grease-lubricated pin and bushing joints are considered to be a closed tribo-system due to joint seals and sealing provided by grease. Oil lubricant (10W40) was used for generating reference values for COF in the contact and the results generated using grease lubricant (commercial molybdenum) were compared, considering fully-flooded condition (Appendix F). A schematic representation of the use of lubricants in this work is presented in Figure 68. The properties of both these lubricants are presented in. The COF for grease-lubricated contacts for the 16MnCr5 specimens coated with nickel alumina nanocomposites was also measured.

Test duration ranged between 5 minutes for oil-lubricated contacts up to 4 hours for grease-lubricated contacts and the corresponding sliding distances were 300m to 1440m and extended duration was used to achieve steady state or till failure occurred. The pin and bushing joint operates bi-directionally because of the motion of the manipulator arm and the speed of motion depends on the design and operating parameters for specific manipulators. 10Hz test speed which has been used in (Bajwa, Khan, Nazir, et al. 2016) was maintained for comparison of test results. Contact pressure was calculated using Hertzian contact equation for cylinder sliding contact and linear relation for pressure was used for conformal contact corresponding to pin sliding contact. The computed

pressure ranged from 73.9MPa to 153.8MPa for cylindrical sliding contact and from 127.3MPa to 572.9MPa for the pin sliding contact (Appendix H).

The experimental procedure followed for the reciprocating tribometer is enumerated below:

- i. Test specimens, adapters and screw fasteners were cleaned ultrasonically to remove any surface contamination,
- ii. White light interferometry was used to measure the surface roughness of specimens at three different points,
- iii. The flat specimen was mounted on the cup adapter which was then filled with lubricant,
- iv. The cup was mounted on the lower shaft i.e., reciprocating link of the tribometer,
- v. The fixed specimen was mounted on the block adapter and together these were mounted on the upper shaft,
- vi. Test parameters were programmed using the GUI of the COMPEND-2000,
- vii. The average COF was measured during the test and data recorded in a data file which was used for analysis of the COF, and
- viii. After completing a test, the specimens were removed from their respective adapters without touching wear tracks and were cleaned ultrasonically.

All specimens were labelled and stored in a hermetically sealed container to prevent corrosion.

The precautions followed while conducting experiments were:

- i. avoiding contact with reciprocating parts,
- ii. ensuring electrical insulation of sensors,
- iii. avoiding twisting of loading arm while mounting and dismounting specimen,
- iv. ensuring the presence of sufficient lubricant in scotch yoke mechanism to prevent breakdown, and
- v. ensuring lubrication in the contact between test specimen surfaces before starting the experiment.

## 5.2.4 Design of modified adapters for tribo-testing

Differences in dimensions of specimens fabricated by the supplier required modified adapter designs to be developed and the design process and outcome for these modified adapters are presented in this section.

### 5.2.4.1 Modified adapter design for cylindrical specimen

The fixed cylindrical specimen in the conventional adapter design is supported against a concave surface with diameter equal to that of the specimen as shown in Figure 69 by the coinciding arcs of contact. Also, the specimen is held in position using a single, threaded set screw. This design works well for test specimens manufactured with very close tolerances.

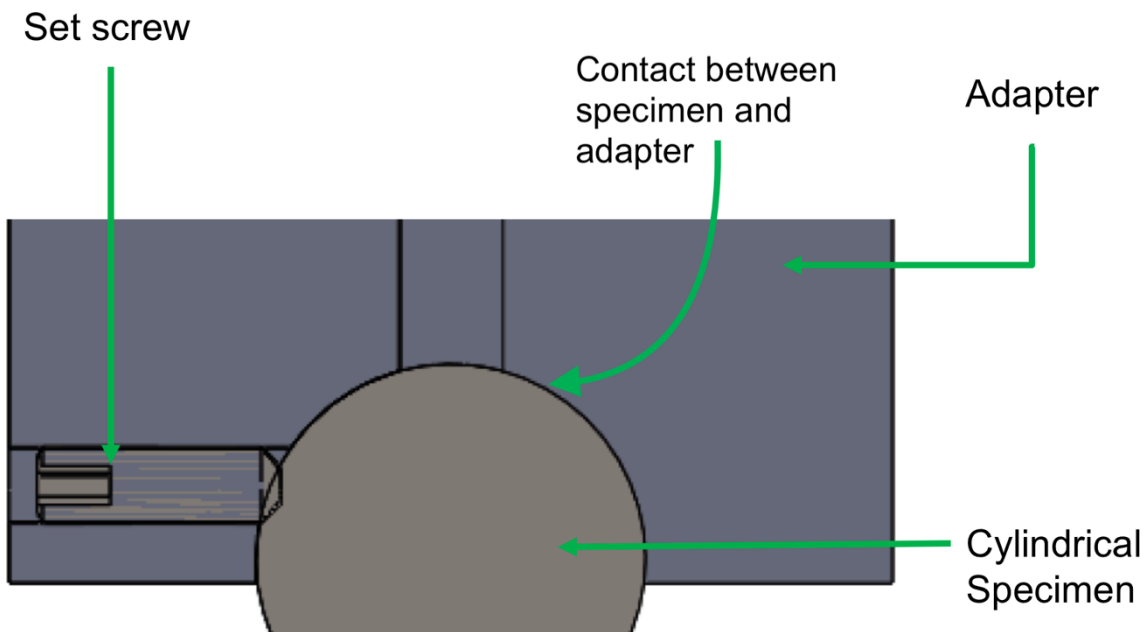


Figure 69 Placement of cylindrical specimen in a conventional adapter showing contact between specimen and adapter

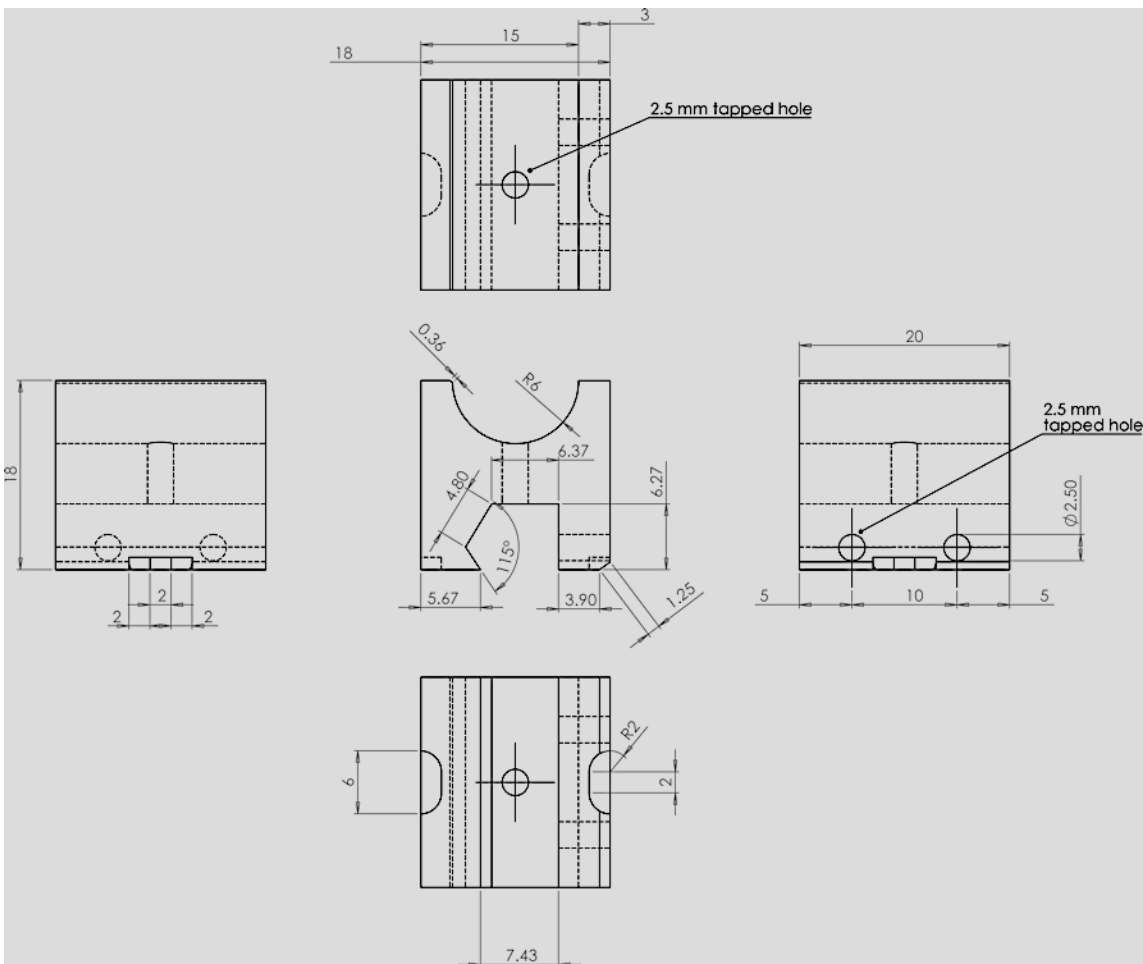
However, the cylindrical test specimens manufactured for the experiments had a diameter of 8mm whereas the diameter of the existing specimen holder was  $9.90 \pm 0.05$ mm, which led to a loose fit for the specimen in the adapter. It was also possible that the cylindrical specimen held in this manner would exhibit a pivoting action about the screw fastener and would move or wobble within the adapter during the reciprocating motion. This would affect the measurement of COF, in addition to creating a vertical gap which could reduce the effective applied normal load on the contact.



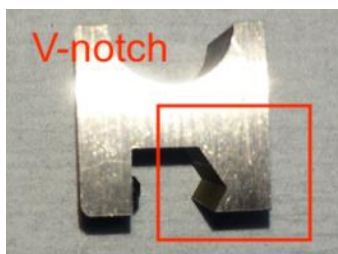
In order to address this issue, a modified design was introduced by extending the concept presented in a previous design, in which the test specimen would be centred automatically through the use of a v-notch for holding and backing the test specimen (Sebastian and Bhaskar 1995) as presented in section 3.2.3 of the literature review. However, in the modified adapter design presented in Figure 70, the issue of additional space between the specimen and the holder was addressed by using two screw fasteners which would constrain the cylindrical specimen in its position without possibility for motion or wobble. The upper shaft of the tribometer, by virtue of its self-aligning design, also accommodated machining tolerances or errors affecting the specimen diameter.

In the original adapter design, an off-size specimen (i.e., not of the specified or standard size) is held in position by two contacts i.e., a line contact at the coinciding arcs of specimen and adapter, and a point contact at the screw fastener. Compared to this, in the modified adapter design presented in Figure 70, the specimen is supported against four contacts in the holder comprising two line-contacts and two point-contacts, which ensures uniform load transfer from the upper shaft onto the contact and also ensures that the specimen is held rigidly in the adapter.

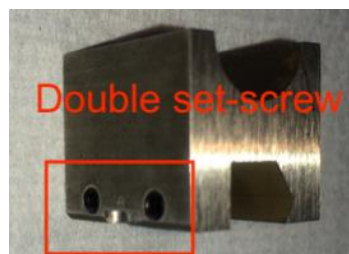
In addition to these modifications, recesses were introduced on the bottom faces of the redesigned adapter to prevent accidental contact with the screw fasteners holding the flat specimen in position on the reciprocating slider when the slider reaches extreme positions at the end of each stroke. The engineering drawing is presented in Figure 70 a using first angle projection. Figure 70 b-d, detailed images of the fabricated adapter are presented showing the v-notch, two threaded holes for the double set-screw and recesses on the bottom face.



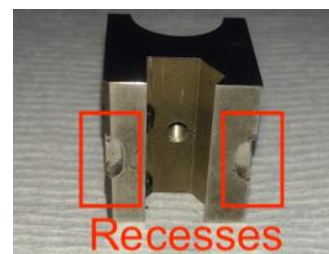
a)



b)



c)



d)

Figure 70 a) Engineering drawing of modified adapter design for holding cylindrical specimens<sup>9</sup>, b-d) detailed views of modified adapter fabricated using EDM

The modified adapters were designed using CAD and fabricated using EDM. EDM was conducted using an Accutex micro-EDM in which the material block was immersed in deionised water and a wire diameter of 0.25 mm was used for cutting the features.<sup>10</sup> '01 Gauge plate in the fully annealed condition' having composition (C-0.95 %, Mn-1.25%, Cr-0.5%, W-0.5%, V-0.2 %) in accordance with DIN17350, BS EN, ISO 4957 and ASTM A681 specifications was used for

<sup>9</sup> The backgrounds of the engineering drawings are set to light grey to improve clarity.

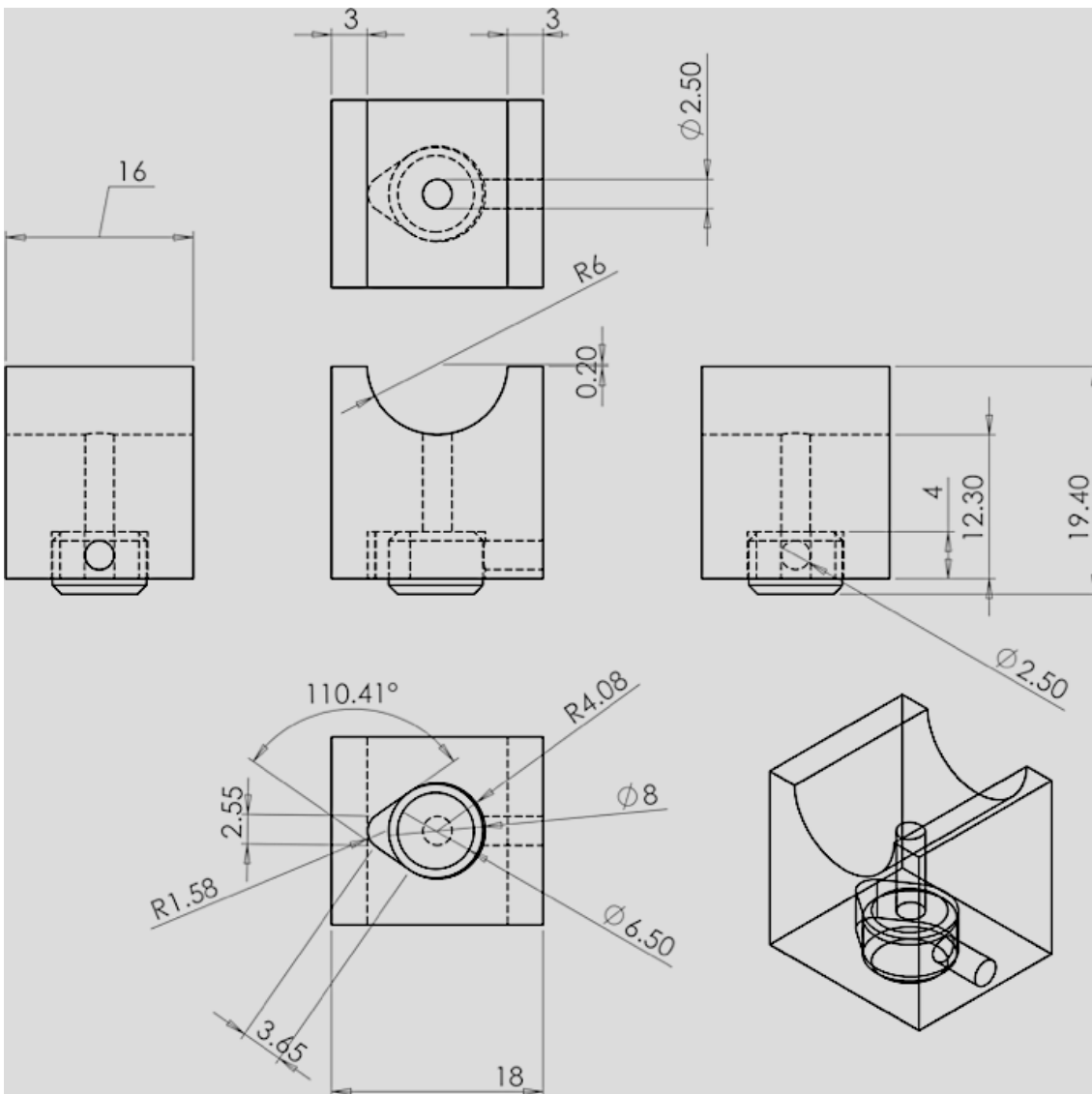
<sup>10</sup> The modified adapter was fabricated by M/s FJ Engineering, New Milton, Hampshire.

fabricating the modified adapter. Theoretical analysis of this modified adapter was not carried out because the range of friction force acting in the contact was limited between 4.0N and 12N corresponding to the COF range of 0.1 to 0.3 for a load range of 10.0N to 40.0N. In the modified adapter, load was transferred over four contacts compared with two contacts in the original design which even further reduces the magnitude acting at any single point. Prototype of the modified adapter design (Figure 70 b-d) was successfully tested on the tribometer.

#### **5.2.4.2 Modified adapter design for pin specimen**

Similarly, a modified adapter design was fabricated for the pin specimen which had a smaller diameter (8.00mm) compared to the bore of the adapters originally supplied with the tribometer (8.15mm and 9.95mm). The original adapter design contained only one set screw to hold the specimen in place. In the modified design, a test specimen having diameter lesser than that of the holder bore would have only one line-contact and one point-contact and this configuration could lead to movement of the test specimen within the adapter during the reciprocating action and introduce a pivoting action of the specimen at the point contact about the vertical axis.

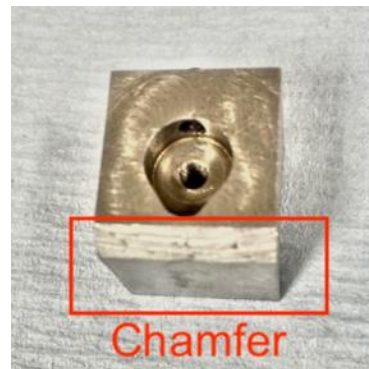
In order to address these issues, the adapter redesign was based on the modification of the existing adapter design to hold the pin specimen with its cylindrical form supported against a vertical notch, locked in place by a set screw shown in Figure 71.



a)



b)



c)

Figure 71 a) Engineering drawing of the modified adapter design for holding pin specimens, b-c) detailed views of modified adapter manufactured using EDM

The engineering drawing is presented in Figure 71 a using first angle projection. In Figure 71 b and c, detailed images of the fabricated adapter are presented showing the vertical notch, threaded hole for the set-screw (visible in the engineering drawing presented in Figure 71 a and chamfer on the bottom face.

The design is self-aligning and can be used for testing specimens of different diameters. This is particularly useful in cases where the manufacturer could not provide specimens of high dimensional accuracy. Moreover, the number of contacts between the adapter and the specimen is increased to two line-contacts and one point-contact which is a more stable configuration compared to the original system in the case of specimens having smaller diameters. This adapter was fabricated using the same high-precision EDM followed in the case of the adapter for the cylindrical specimen presented in section 5.2.4.1. Prototype of this modified adapter design was also tested successfully on the tribometer.

### 5.2.5 Design and preparation of test specimens

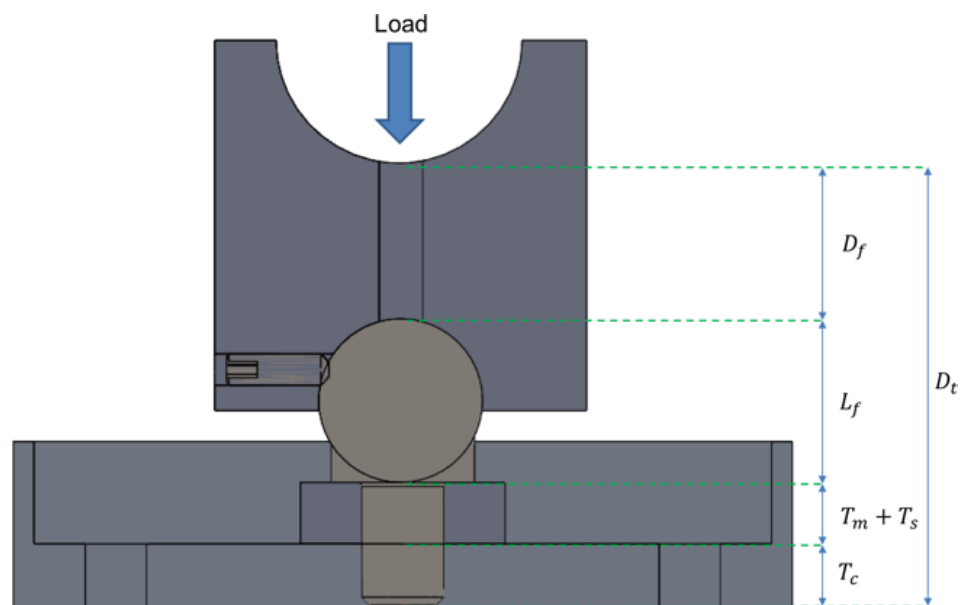


Figure 72 Calculation of specimen thicknesses using internal clearance between upper and lower shafts of the reciprocating tribometer

Test specimens were designed based on measurements taken inside the test chamber between the upper and lower shafts, dimensions of the adapter for holding the fixed specimen on the upper shaft and the cup for holding the flat specimen on the lower shaft as shown in Figure 72. The thickness of the test specimen was calculated from the following equation<sup>11</sup>:

$$D_t = D_f + L_f + T_m + T_s + T_c \quad (24)$$

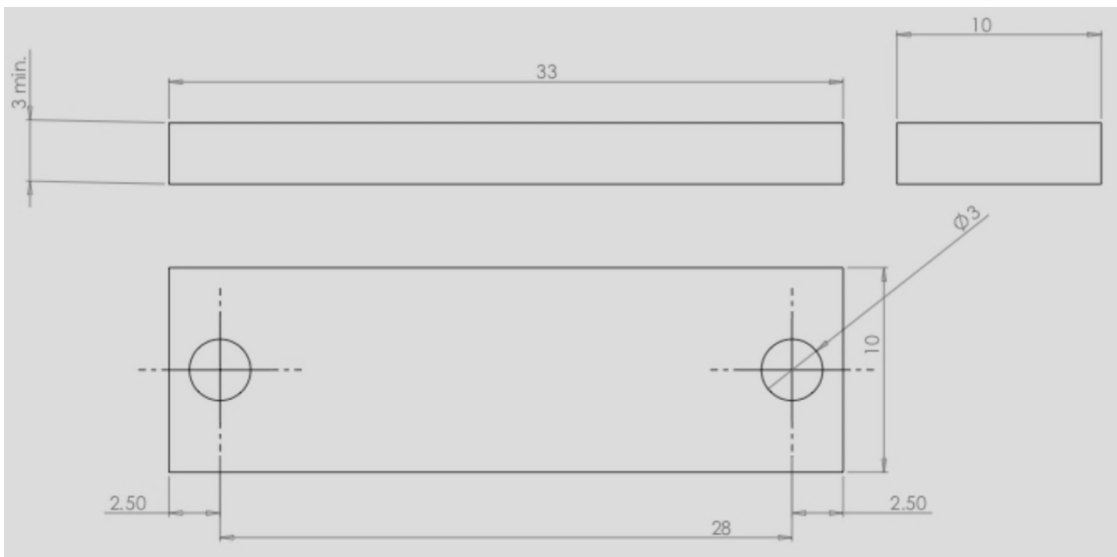
<sup>11</sup> Similar equation for calculating specimen dimensions has been presented in (Garland 2004)

where  $D_t$  is the total inner distance between the upper shaft and the lower shaft,  $D_f$  is the distance from the lowest point of the upper shaft to the top of the fixed specimen,  $L_f$  is the length/radius of the fixed specimen,  $T_m$  is the thickness of the moving flat test specimen,  $T_s$  is the shim thickness and  $T_c$  is the thickness of the cup. In practice, a clearance of approximately 200 $\mu\text{m}$  is maintained between the fixed and reciprocating specimens for specimen mounting and removal.

### 5.2.5.1 Modified specimen design



a)

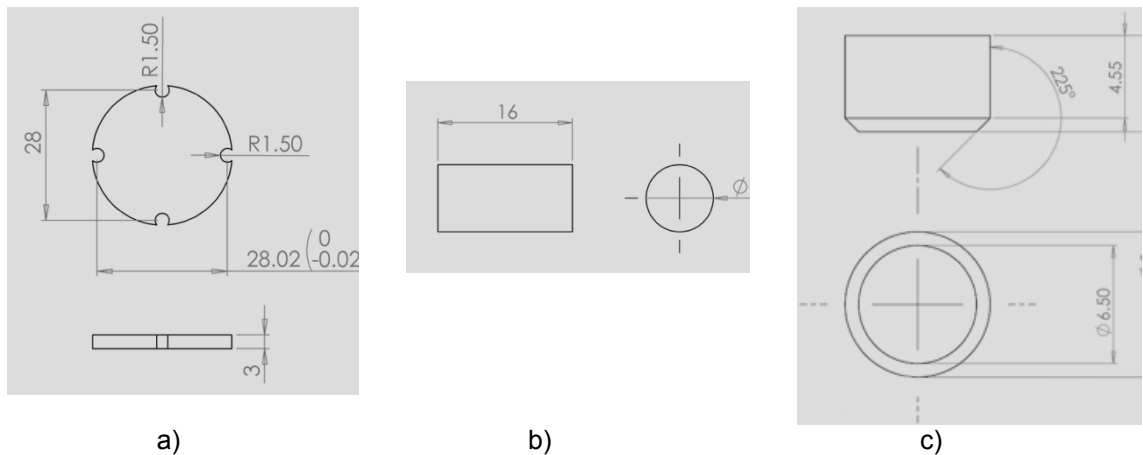


b)

Figure 73 Original rectangular design of the reciprocating test specimen a) physical specimen and b) CAD design

Figure 73 shows the dimensions of the conventional reciprocating specimen used in the tribometer. The shape of the reciprocating test specimen was modified from the original rectangular format presented in Figure 73 to the new circular form presented in Figure 74 a because of difficulty in machining the specimens to the rectangular shape. The circular flat-plate reciprocating specimen had two sets of axisymmetric holes drilled into it for mounting it first

on the cup and then the cup on the lower reciprocating link of the tribometer. This allows for the specimen to be rotated on the adapter. The counter-face specimen was made of EN19 steel having the following dimensions: 8mm diameter and 16mm length for the cylindrical contact (Figure 74 b), and 8mm diameter and 5.30mm length for the pin contact (Figure 74 c) based on equation 24. Due to the negligible weight difference between the specimens, no effect on frictional dynamics of the tribometer was envisaged.



a) Circular reciprocating specimen, b) fixed cylindrical specimen and c) fixed pin specimen

### 5.2.5.2 Polishing of test specimen

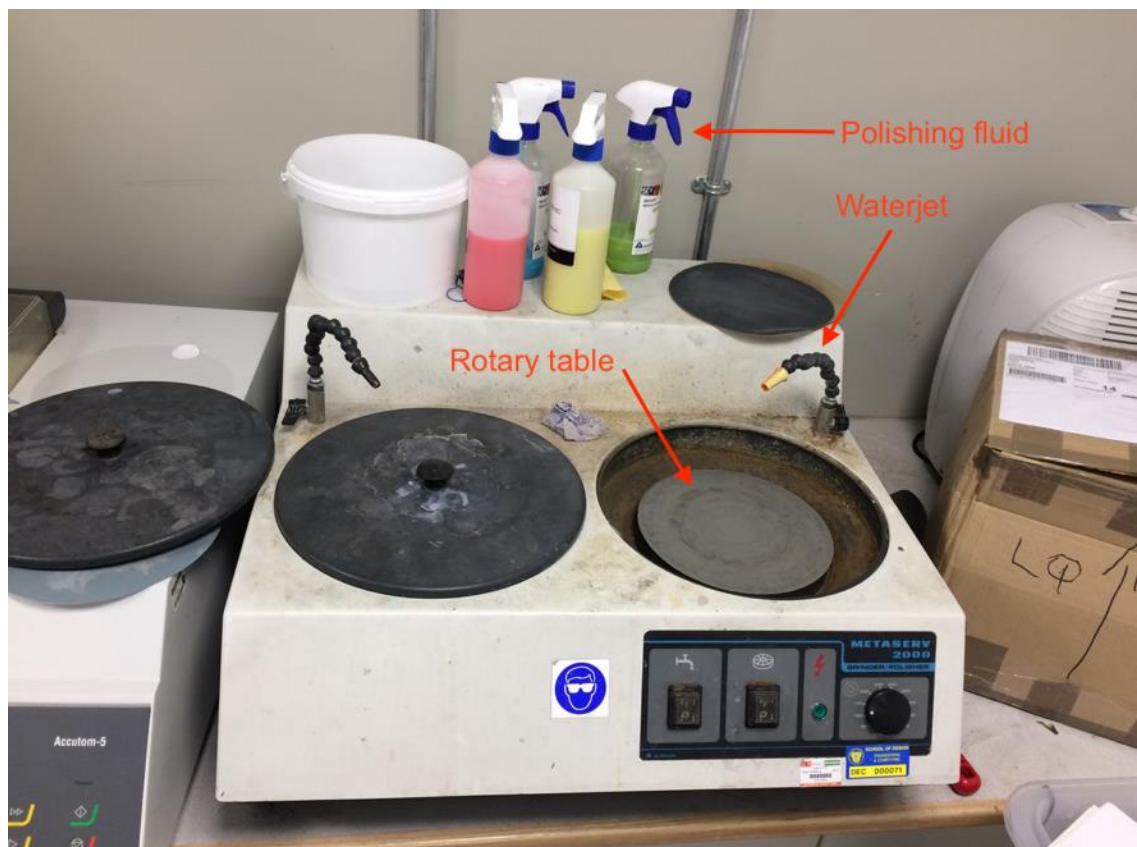


Figure 75 Rotary table polisher

Specimens were polished on the rotary table polisher, shown in Figure 75 capable of holding 6 specimens simultaneously using a jib attachment and the speed of rotation of the table was operator controlled through a dial. Diamond polishing suspension solutions (Buehler MetaDi®), with decreasing particle sizes of 45 $\mu\text{m}$ , 9 $\mu\text{m}$ , 6 $\mu\text{m}$ , 3 $\mu\text{m}$ , and 1 $\mu\text{m}$ , were used to increase polishing rate and improve surface finish to 0.05 $\mu\text{m}$ , for PED and this was achieved by using polishing cloth along with alumina powder (0.05  $\mu\text{m}$ ) in the final polishing stage. A water jet was used to provide lubrication while also removing debris and heat generated between the polishing surface and specimen. After polishing, the specimens were washed in acetone solution and immersed in dilute acetone solution (<10 ml) in a shatter resistant straight-sided glass beaker which was used with the ultrasonic bath for approximately 5 minutes. The cleaned specimens were dried using thermal drier and stored in a hermetically sealed container with silica gel desiccant in order to prevent surface corrosion. The surface was cleaned using acetone solution in the ultrasonic bath before use. The process of PED is described in the next section.

### **5.3 Pulse Electro Deposition (PED) of nickel alumina nanocomposite on 16MnCr5**

In order to improve the dynamic performance of manipulators, the COF characteristics in the joints referred to in section 5.2 have to be improved. Similar work was presented in literature for cam joints in robots (Koike et al. 2013). In this context, coatings have been shown to improve the COF, wear resistance and durability of surfaces in contact (Leyland and Matthews 2000). From literature review, it has also been shown that the use of nickel alumina nanocomposite coating reduces COF in the contact and improves the mechanical properties of the surface (Gurrappa and Binder 2008, Jung et al. 2009, Saha and Khan 2010) such as hardness (Thiemig et al. 2007), higher ultimate tensile strength, low ductility and improved wear resistance (Gurrappa and Binder 2008, Jung et al. 2009, Saha and Khan 2010). Several coating techniques are presented in section 3.3. The use of PED for depositing nickel alumina nanocomposite coatings offer better COF and wear resistance (Raghavendra et al. 2016). 16MnCr5 was selected as the coating specimen since the bushing was fabricated using this alloy. Also, deposition of nickel alumina nanocomposite coating on mild steel has been reported in previous



work (Bajwa, Khan, Bakolas, et al. 2016a, 2016b, Bajwa, Khan, Nazir, et al. 2016). The process of conducting PED on 16MnCr5 is presented in Figure 76 and consists of the preparation of electrolyte, preparation of electrodes and setting up the pulse parameters on the workstation.

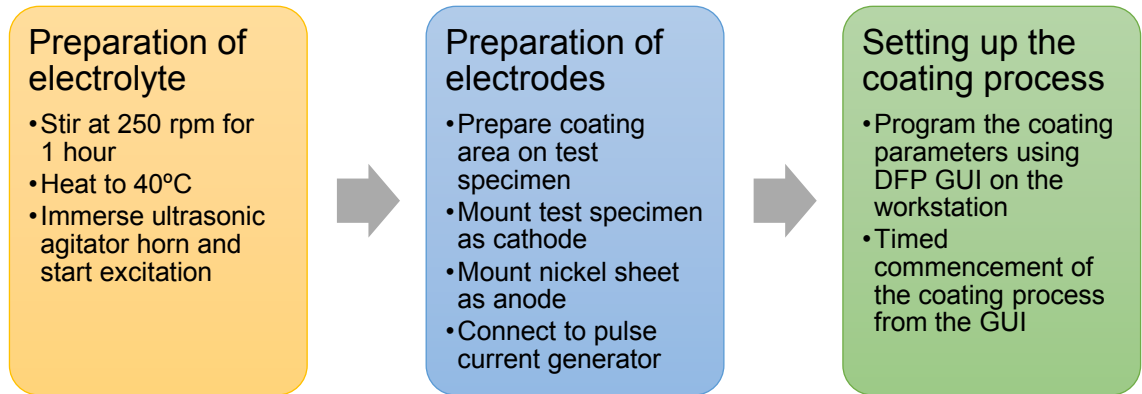


Figure 76 Workflow for PED of nanocomposite coating on 16MnCr5 specimen

In the first step, the electrolyte for conducting PED was prepared with the composition presented in Table 12. The components used for preparing the electrolyte solution were selected from literature review presented in section 3.3.2 and consist of nickel sulphate hexahydrate, nickel chloride hexahydrate, boric acid and alumina nanoparticles whose composition has also been listed in Table 12.

Chemical component	Composition
NiSO <sub>4</sub> .6H <sub>2</sub> O	265 g/L
NiCl <sub>2</sub> .6H <sub>2</sub> O	48 g/L
H <sub>3</sub> BO <sub>3</sub>	31g/L
Alumina nanoparticles (50 nm)	20 g/L

Table 12 Composition of electrolyte used for PED

The solution was prepared in one litre of deionised and distilled water contained in a Pyrex beaker, which was heated, continuously stirred and ultrasonically agitated to obtain uniform particle distribution of the suspension. The schematic diagram of the Modified Watts bath is presented in Figure 77.

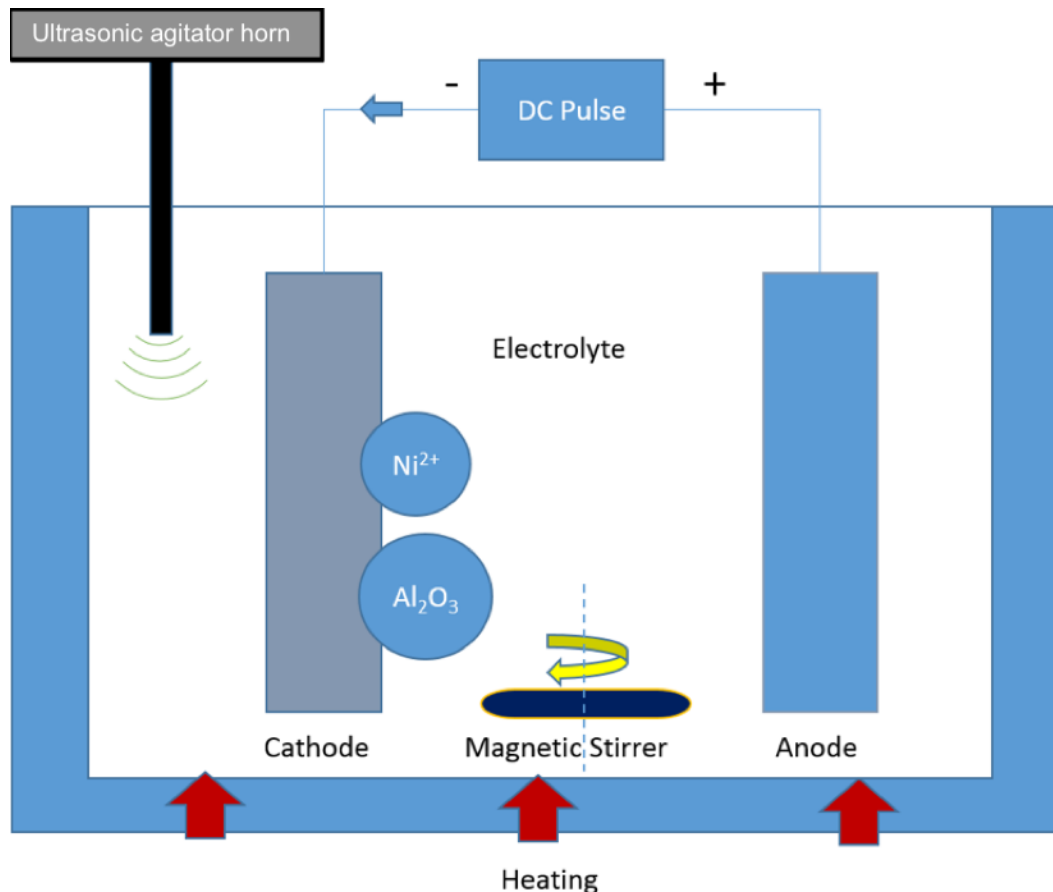


Figure 77 Schematic representation of the modified Watts bath for PED

The pH and temperature of the electrolyte were monitored using the Tecpel pH meter and was maintained between 4.0 and 5.2 by adding base or acid (NaOH or diluted H<sub>2</sub>SO<sub>4</sub>) to promote transportation of nickel ions within the solution.

The ultrasonic agitator horn (exciter) was immersed into the electrolyte prior to commencing the coating process. The electrodes were cleaned using the ultrasonic bath and mounted on the attachments provided. Parallel electrode arrangement was used to carry out the coating process (Figure 77).

Rectangular nickel plate (100mm x 50mm) of 99.99% purity was used as the anode. 16MnCr5 test specimen was cleaned and mounted as the cathode for coating. Polyvinyl chloride (PVC) insulator was used to cover the surface outside the rectangular area to be coated.

Pulse current for the coating was generated using a Dynatronix MicroStar DPR: 20-15-30 unit [product catalogue] shown in Figure 78. Pulse parameters included coating current intensity, plating time, frequency and pulse on/off time which were controlled using the MicroStar Pulse/Dynatronix Front Panel (DFP)

GUI on the workstation. The pulse current parameters were calculated and presented in Table 13 (Appendix I).

Current Density (Adm <sup>-2</sup> )	Duty Cycle	Frequency (Hz)	Peak Current (A)
0.35	20	10	~5A
0.75	20	10	~10A

Table 13 Pulse parameters for PED

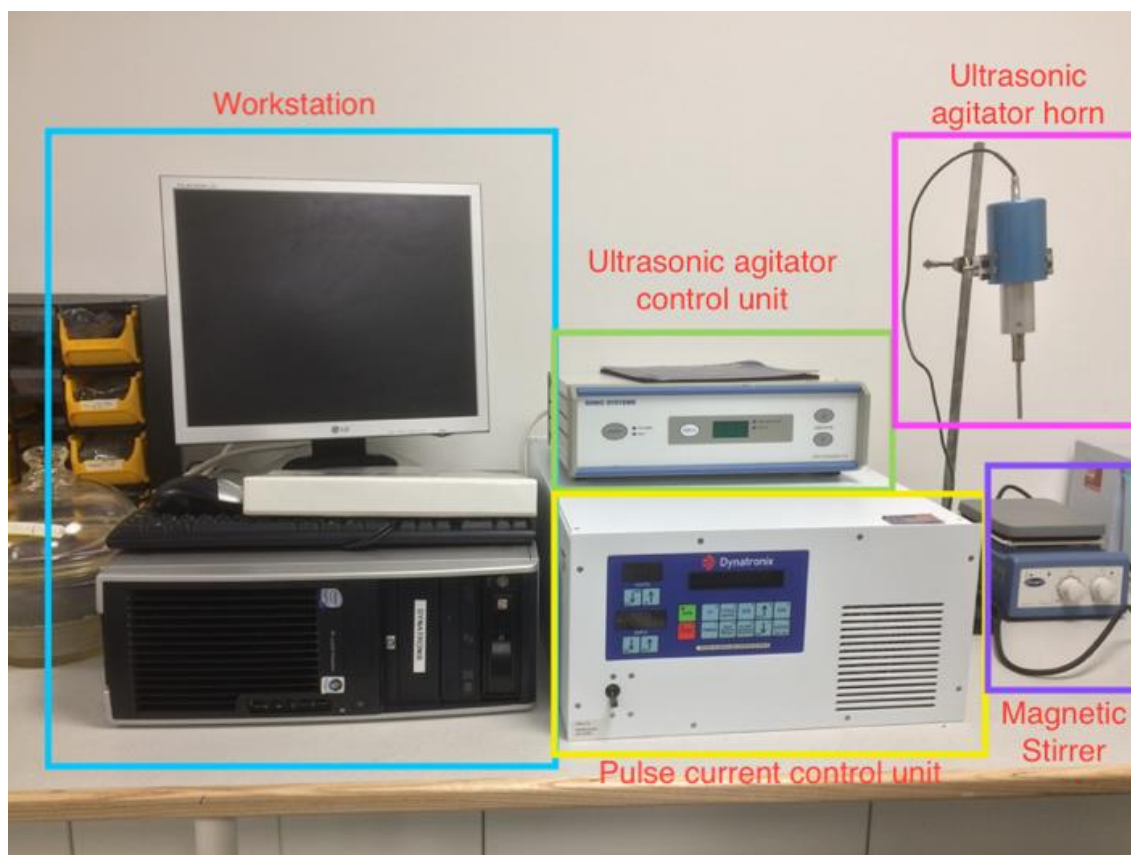


Figure 78 Experimental setup for PED

Coating thickness was calculated according to the equation presented below (Electrolytics inc. 2016):

$$T = \frac{(I \cdot t \cdot A \cdot 1e4)}{(n \cdot F \cdot \rho \cdot S)} \quad (25)$$

where  $I$  is the current in coulombs per second,  $t$  is the time in seconds,  $A$  is the atomic weight of the metal in grams per mole,  $n$  is the valence of the dissolved metal in equivalents per mole,  $F$  is the Faraday's constant in coulombs per equivalent charge,  $T$  is the thickness of coating in microns,  $\rho$  is the density in

grams per cm<sup>3</sup>,  $S$  is the area of coating and  $1E4$  is the cm to  $\mu\text{m}$  conversion factor.

Magnetic stirring was used to generate laminar flow of the electrolyte over the coating surface and to replenish supply of both ions and nanocomposite particles at the surface of the specimen to be coated to promote coating characteristics. This was achieved using a magnetic pellet (or flea), which was driven by the magnetic stirrer. The speed of rotation of the pellet was set to 250rpm as reported in literature (Bahrololoom and Sani 2005). The electrolyte temperature was maintained at 40°C (313K) using the hotplate arrangement built into the magnetic stirrer apparatus to promote ionic transport. After coating, the specimens were dismantled, cleaned in deionized water and further cleaned in the ultrasonic bath using dilute acetone solution. The specimens with thick film coating were stored in the bell jar until required for surface analysis or tribo- testing.

The precautions observed while carrying out the coating process were:

- i. using Personal Protective Equipment (PPE) including dust mask, laboratory coats, protective eye wear and chemical resistant hand gloves while handling test specimens and electrolyte.
- ii. conducting experiment in a well-ventilated area to prevent a build-up of chemical vapours which evolve from the heated electrolyte.
- iii. ensuring that no contact occurred between electrodes and the ultrasonic horn through the use of non-metallic separators.

#### **5.4 Analysis of surface characteristics of the test specimens**

As mentioned in section 3.1, the major tribological parameter affecting the dynamic performance of the manipulator is friction, which is closely related to wear (Bhushan 2013a). The surface characteristics investigated in this work include roughness, hardness and wear track analysis since these parameters influence the COF generated between the contact surfaces. From literature review (section 3.3.4), the following techniques namely white light interferometry, digital microscopy, scanning electron microscopy (SEM) and hardness testing have been used to analyse surface characteristics of specimens (Blau 2001, Beake et al. 2006, Camargo et al. 2009, Bajwa, Khan,

Nazir, et al. 2016). Therefore, in this work, the surface characteristics of the test specimen were analysed using these techniques. The principles and techniques of operation of the instruments which were used to conduct these analyses in this investigation are discussed below.

#### 5.4.1 White light interferometry

White light interferometry utilises depth information of the surface measured using the interference patterns arising from the source and reflected light to measure surface characteristics such as surface roughness, peak values of surface roughness, peak count, wear scar profile and wear volume. In this study Zygo NewView 5000 white light interferometer was used to measure the surface roughness of the test specimens (Figure 79). Least count of the instrument was 1nm and the maximum vertical distance which could be measured was 5mm. A standard area of 0.72mm by 0.54mm was captured by using an objective lens that provided a magnification factor of 10x. Other objective lenses of 2.5x magnification and 50x magnification were also available.

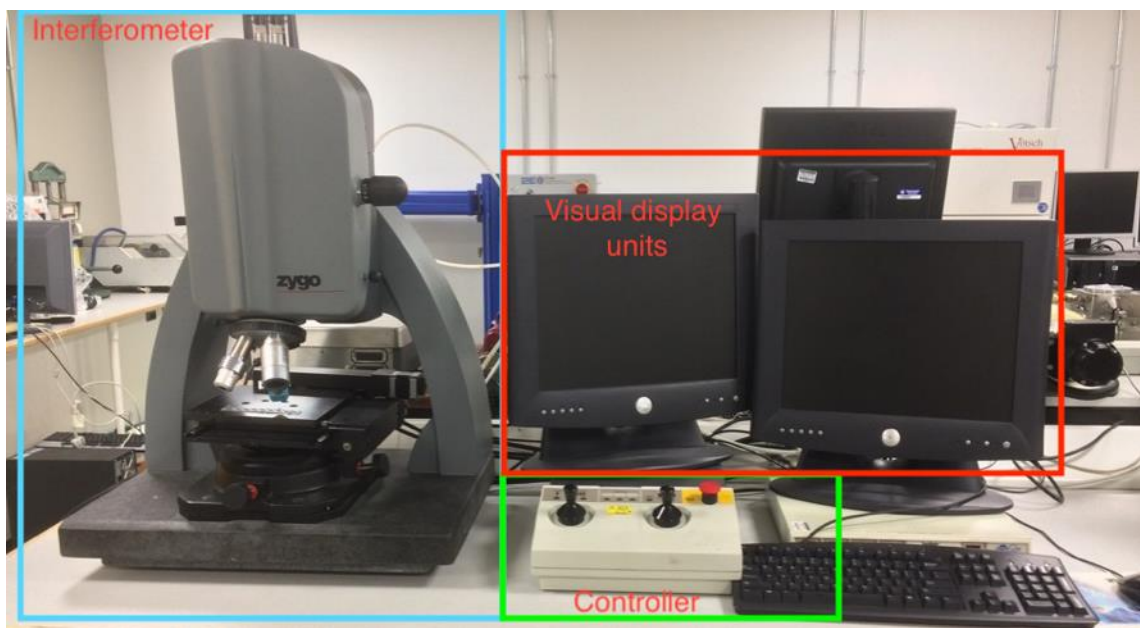


Figure 79 White light interferometer

The process of measurement is given as follows:

- i. The specimen was placed on the table of the interferometer. For adjusting the inclination of the table about the x- and y-axes, two knobs were used,

- ii. The surface profiles of the test specimens were captured using the Zygo software application with a GUI,
- iii. Live video feed from the interferometer was displayed directed on the first of the two visual display units (VDUs),
- iv. The table position was controlled by using the left-hand side joystick on the controller,
- v. Vertical movement of the interferometer head was controlled by using the right-hand side joystick of the control panel,
- vi. Three step-sizes were available for vertical movement (coarse to fine) and these were set from the control panel,
- vii. The interference pattern was detected and fine-tuned through the vertical adjustment of the interferometer head which holds the objective,
- viii. Once the interference pattern was successfully obtained, measurement process was initiated from the GUI,
- ix. The measured data was displayed on the second VDU, and
- x. Further analyses were conducted using available tools such as surface profile measurement at a section of the specimen and depth measurement,
- xi. The data was stored in files with '.dat' extension, which made the data available for future analysis.

Larger areas were measured using image stitching. However, the size of the image was restricted by the random-access memory (RAM) available on the workstation. Using the interferometer, test specimens with different surface textures were analysed and the various surface roughness parameters were recorded for the different specimens.

#### **5.4.2 Digital microscopy**

Digital microscopy provides high-fidelity reconstruction of the specimen surface in two and three dimensions. In the KEYENCE VHX5000 digital microscope shown in Figure 80, a digital imaging sensor replaces the eye-piece of the conventional optical compound microscope. Images data captured by the sensor were displayed and stored on the accompanying workstation. The control panel connected to the workstation allows the user to move the

specimen in biaxially (x- and y-axes) in order to bring the area of interest on the specimen into the field of view. It is also used to focus the lens to obtain a clear and sharp image and to control the brightness of the image. Other functions such as high dynamic range (HDR) and lighting source (two options were available – a main light and a secondary light) were accessible from the control panel. Two objective lenses were available for this microscope as shown in Figure 81, which provided magnification factor ranging from x30 to x150 (Figure 81 a) and the second provided magnification factor ranging from x150 to x2500 (Figure 81 b). The digital microscope was used to capture images of large surface areas that could not be captured using the white-light interferometer using the image stitching mode in which multiple images were combined to represent a large surface area.

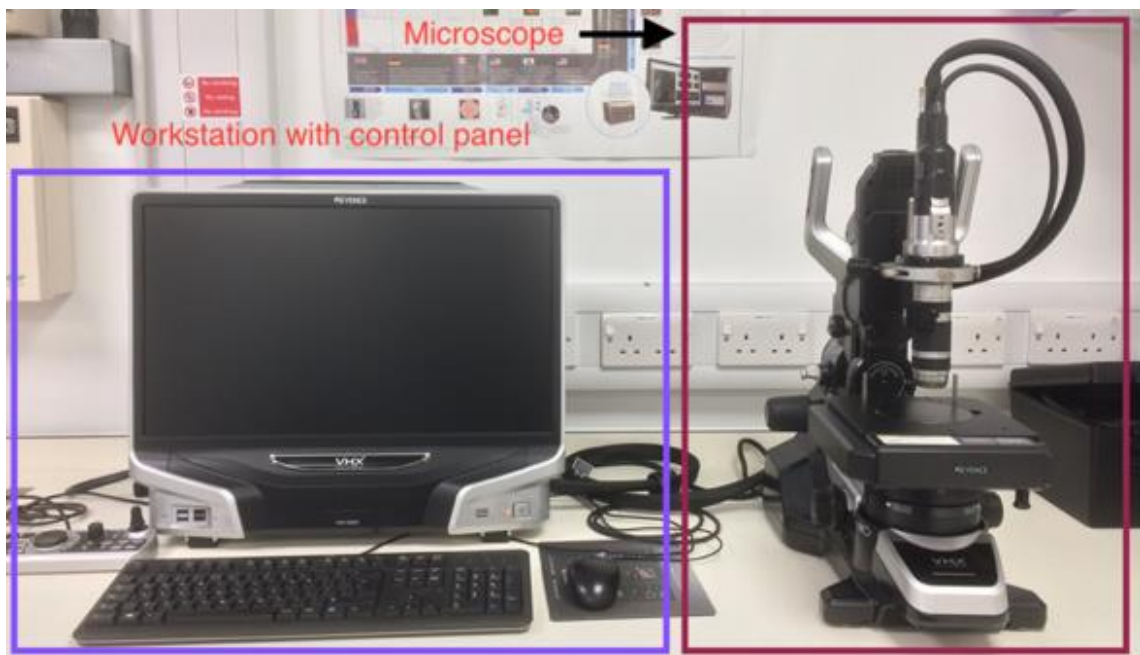


Figure 80 Digital microscope



a)



b)

Figure 81 Objective lens attachments a) x30-x150, b) x250-x2500

In addition to two-dimensional images, the digital microscope was also capable of generated three-dimensional surface data for surface profiling, which provided an alternate technique to the conventional profilometer and white-light interferometer. The three-dimensional surface data was captured by photographing the surface at different focal planes and adding depth data in the vertical dimension (z-axis) to the photographs with an accuracy of  $0.01\mu\text{m}$ . Images of three-dimensional surfaces were also stitched and used to reconstruct the surface profile of the 16MnCr5 specimens and coated specimen surfaces both before and after testing.

The procedure followed for capturing the two-dimensional image data of the specimen surface is described below:

- i. The workstation and microscope were powered on,
- ii. The table of the microscope was raised to its top position (+z axis) and the table was centred (x- and y-axes),
- iii. From the GUI, the calibration process was initiated,
- iv. The specimen was mounted after calibration,
- v. The specimen was brought into the field of view by controlling the x and y motion of the table using the joysticks on the control panel,
- vi. The image was brought into focus by using the jog dial, first using large steps and then by using fine steps (up to  $0.01\mu\text{m}$  step size),
- vii. Brightness was controlled, and glare reduction applied,



- viii. HDR imaging was used for some specimens in order to capture detailed crests and troughs of the surface,
- ix. The image displayed on the screen was captured, and
- x. The image was annotated with dimensions using the GUI.

For capturing three-dimensional surface data, the procedure described above was modified slightly. Once the specimen was focussed, the subroutine for capturing three-dimensional surface data was invoked from the GUI. The depth of measurement, which represented the length traversed by the objective lens while capturing images i.e. the highest and lowest points on the surface of the specimen along the z-axis. Three-dimensional images were constructed using the colour and intensity maps of the captured images. The captured image was measured, annotated and saved. Measurands included dimensioned surface images with scale-factor and surface profile parameters such as surface roughness. The images were saved as image files '.tif' and data as data '.csv' files. In this work, magnification factors ranging from x30 to x2500 were used to capture surface data.

### **5.4.3 Surface hardness testing**

Surface hardness of the specimen is an important property which influences the wear resistance of the material i.e., higher hardness improves wear resistance (Leyland and Matthews 2000). The decrease in COF with increasing surface hardness has been attributed to decrease in adhesion and deformation (Mikhin and Lyapin 1970). Therefore, the hardness of EN19 steel, 16MnCr5 steel and nanocomposite coated 16MnCr5 steel were tested using the Buehler Vickers micro-indenter (Figure 82) over a load range of 1 to 5kgf.

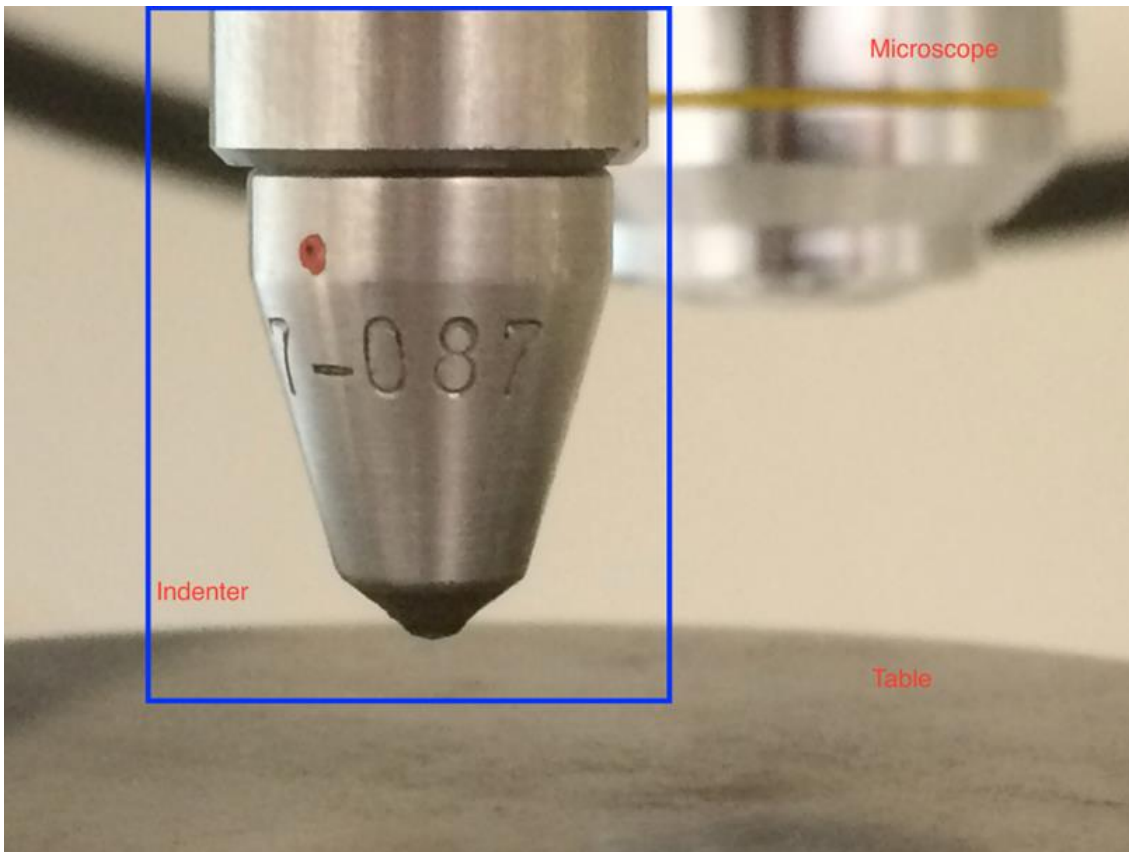


Figure 82 Vickers micro-hardness tester

Indentation tests were conducted for 6 selected specimens at different sites on the specimen surface as shown in Figure 83.

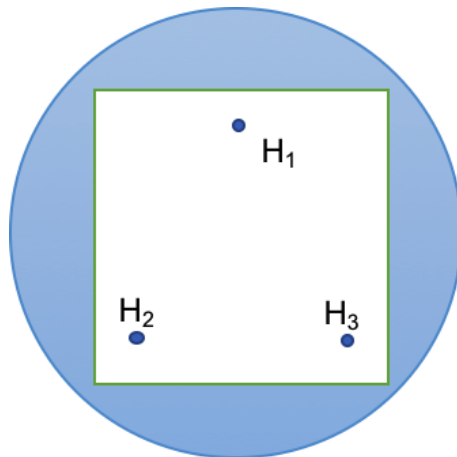


Figure 83 Hardness measurement of micro-indentation

The procedure for conducting the tests is given as follows:

- i. Specimen was mounted on the table and the indenter was aligned with the test region,
- ii. The start button on the equipment was activated and an indentation was made on the specimen surface,

- iii. The microscope was placed over the test area and the diagonal measurements of the indentation were recorded through the eyepiece
- iv. From these measurements and the calibration table supplied (Appendix K), the hardness values corresponding to the specimens were recorded.

#### 5.4.4 Scanning Electron Microscopy

The surface morphology of the test specimens including the newly developed nanocomposite coatings for 16MnCr5 were analysed using the JEOL 6010LA scanning electron microscope (SEM) shown in Figure 84.

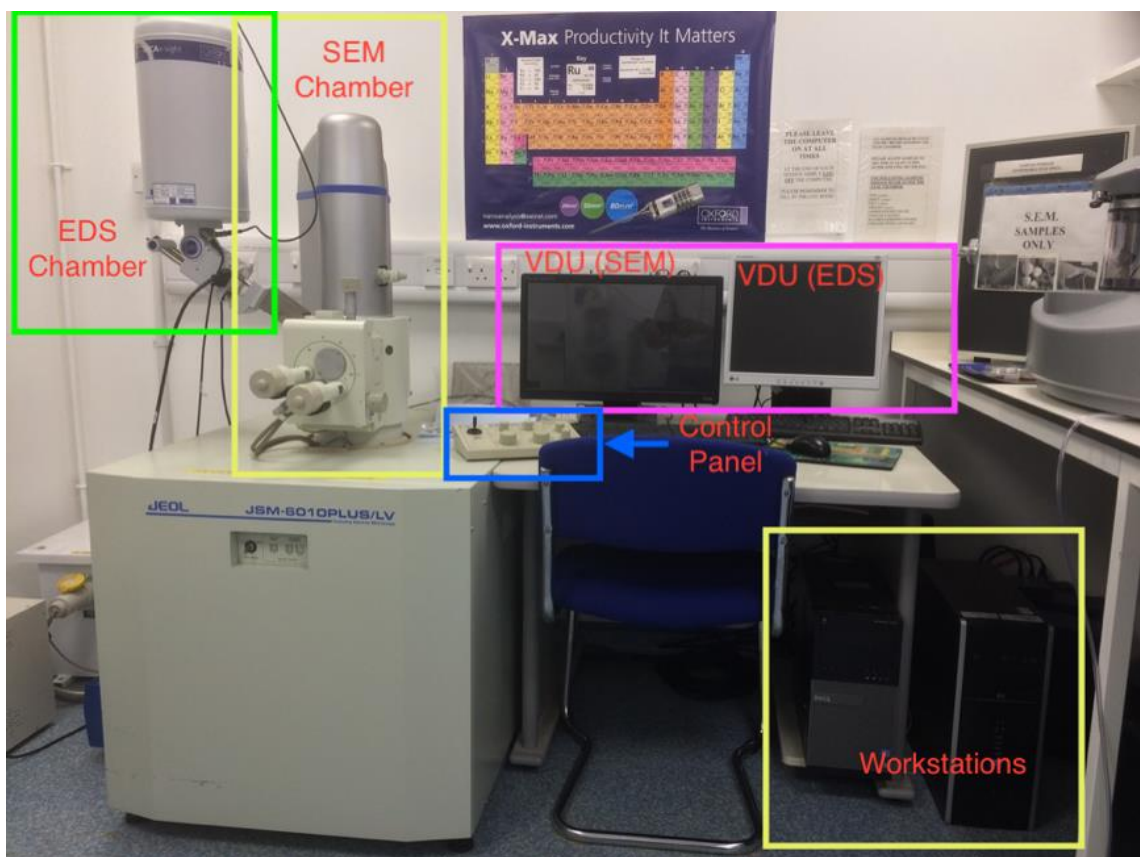


Figure 84 Scanning Electron Microscope with EDS attachment

The SEM consists of a vacuum chamber which contains the electron gun, condenser lens, objective lens, backscatter detector, secondary detector, X-ray detector and specimen tray. The SEM operates in the range of 5-20kV and provides magnification of up to x30,000. Energy Dispersive X-ray spectroscopy (EDS) attachment was available to determine the elemental composition of the test specimens.

The procedure followed for capturing the two-dimensional image data of the specimen surface using SEM is described below:

- i. Specimens which are held in place by double-sided conductive tapes and screw fasteners inside the adapter,
- ii. The SEM test chamber was vented to bring it up to atmospheric pressure,
- iii. The vertical position of the stage was adjusted to provide optimum distance from the sensor and prevent specimen collision with the sensor,
- iv. The specimen adapter was centred using the command from the GUI on the workstation,
- v. The chamber was then closed and evacuated such that the air inside it was evacuated and the pressure inside the chamber was 0.1mbar,
- vi. The electron beam was switched on automatically at the end of the evacuation stage,
- vii. Initial magnification of x30 and voltage range of 5-15kV was used for the metallic alloy surface and the nanocomposite surface,
- viii. Spot size or beam diameter was automatically determined by the program except at high magnification,
- ix. The specimen surface to be examined was brought into the field of view using the joystick on the control panel,
- x. A jog dial was used to focus the image and was also used to control brightness and contrast of the electron beam as well as the beam oscillation at high magnification factors (for normal magnification range, automatic control was sufficient to focus the image, control image properties and regulate beam oscillation).

It was also possible to set the scan/refresh rate of the image from either the GUI or the control panel. The image was captured once it was tuned optimally. From the GUI, it was possible to annotate two-dimensional measurements on the captured images of the area of interest. These images were stored as '.jpeg' files on the workstation.

The following precautions were observed while using the SEM:

- i. Degreasing and removing debris from specimens using ultrasonic cleaning in dilute acetone to prevent damage to the SEM sensor,

- ii. Wearing latex gloves during specimen handling in order to prevent the transfer of oils from skin to the specimen surface.

## 5.5 Summary

In this chapter, the experimental procedures for three aspects of tribo-testing are presented:

- i. **Coefficient of friction (COF) in sliding contacts:**  
This is the main focus areas of this research since it influences the dynamic performance of the manipulator mechanism. COF for oil- and grease-lubricated contacts for plain and coated specimens are measured for experiments conducted under different contact conditions. Nickel aluminium nanocomposite coating was deposited on the 16MnCr5 specimens using PED for this purpose. Because of the low material machinability, the design of the test specimens for the 16MnCr5 alloy was modified. Modified tribometer adapter design was also presented for use with specimens with varying diameter caused by low machining precision.
- ii. **Lubrication:** Grease and oil lubricants were used for conducting the tribo-tests. Oil-lubricated contacts were used to generate reference COF values for comparison of test results.
- iii. **Surface analysis:** Surface characteristics and properties were analysed both before and after tribo-testing. The parameters analysed included surface characteristics such as micro-hardness, which was measured using a Vickers micro-indenter, and morphological characteristics such as roughness average ( $R_a$ ) and wear track dimensions which were measured using white light interferometry and digital microscopy.

Results of experimental analyses described in this chapter are presented in Chapter 6.

## **Chapter 6 Results and discussion – 1: Mechanics simulation**

### **6.1 Introduction**

In this thesis, with the objective of developing time-bound and application-specific mobile manipulators, was approached through design and simulation by method, which has hitherto not been reported in the domain of search and rescue (SAR). For the design and modelling of the mobile manipulator, the virtual prototype was created using computer aided design (CAD). Following this, the virtual prototype was imported into the multibody dynamics (MBD) simulation environment in which the manipulator mechanics simulation was conducted. Serial open-chain manipulator design was investigated along with closed-loop mechanism. As explained in section 4.4, these are presented as three case studies and the rigid-body mechanics simulation outputs were analysed. Simulations conducted in SimMechanics 2<sup>nd</sup> generation simulation platform were validated by comparing with results generated using SimMechanics 1<sup>st</sup> generation simulation package, which has been used widely in literature. Taking into consideration the importance of friction in manipulator joints, combined friction model (CFM) was incorporated into sDOF revolute and translational joints in serial anthropoid manipulator and complex closed-loop manipulator (cases 1 and 3).

Results and analysis of the simulations are presented below.

### **6.2 Simulation results: case studies**

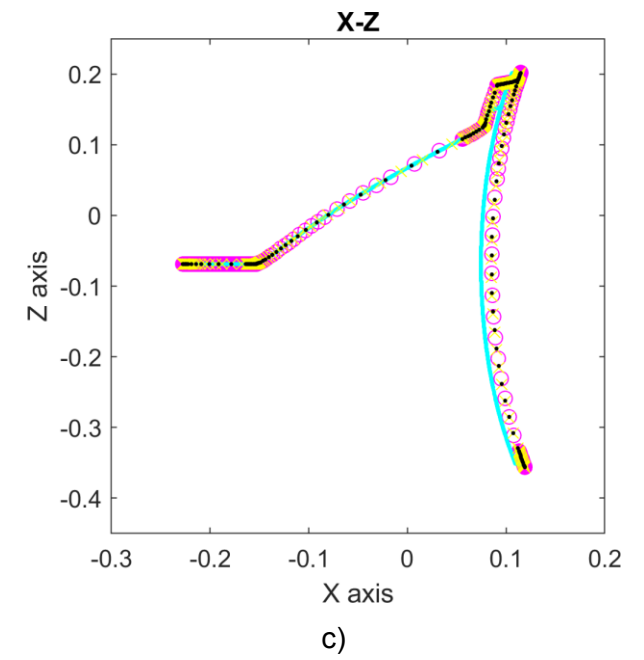
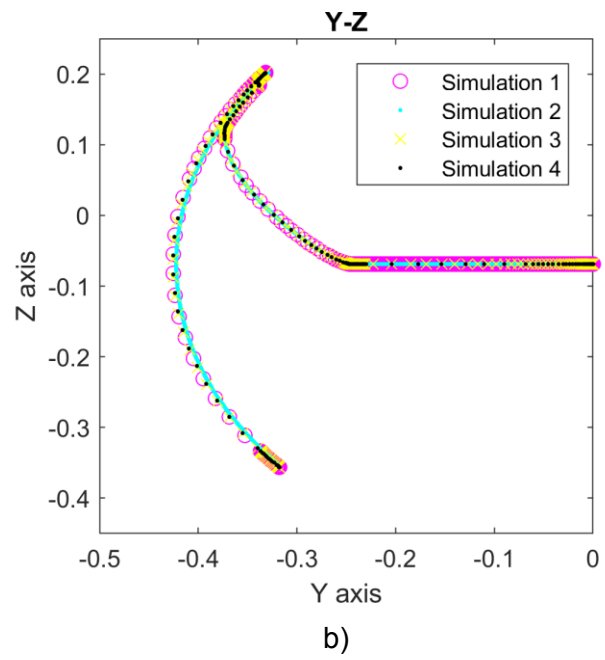
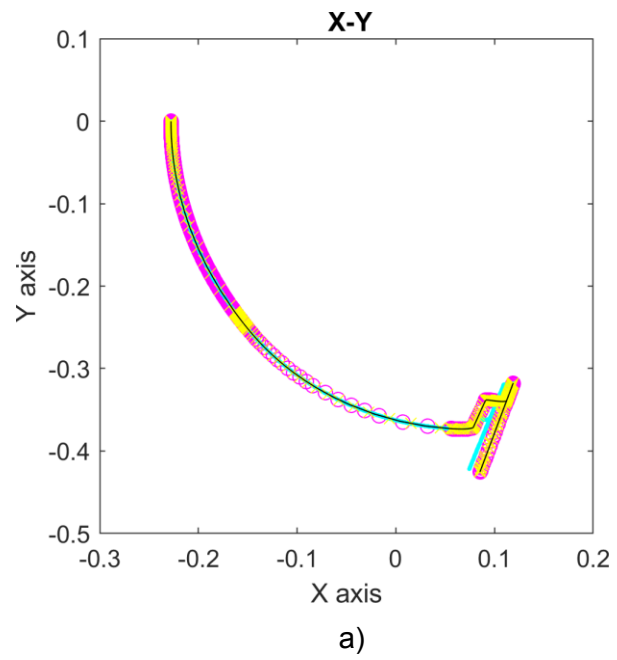
In this section, the results for mechanics simulations i.e. MBD simulations are presented. The simulations are presented as case 1: anthropoid manipulator, case 2: serial open-chain manipulator and case 3: complex closed-loop manipulator.

#### **6.2.1 Case 1 – Anthropoid manipulator**

Results of inverse dynamics simulation of the anthropoid manipulator in three-dimensional space comprise kinematics and dynamic outputs including joint

friction torque computed using CFM model for the sDOF revolute joint (Khurshid et al. 2016). The use of MBD to simulate makes it possible to evaluate the simulation of the mechanism in three-dimensional operation. In this case, the influence of solver selection on simulation results is highlighted. Results of simulation include the end-effector motion presented in Figure 85 where a-c show the planar projection of the end-effector motion in three-dimensional space shown in d. There is a close match in the kinematic output from simulation and therefore, the solver selection does not affect the simulation kinematics output.

However, difference in step-sizes are observable from the figure, which highlights the importance of solver selection for numerical solutions to computational mechanics problems. Simulations 1, 2, 3 and 4 corresponds to solvers ODE15s, ODE23s, ODE23tb and ODE23t.





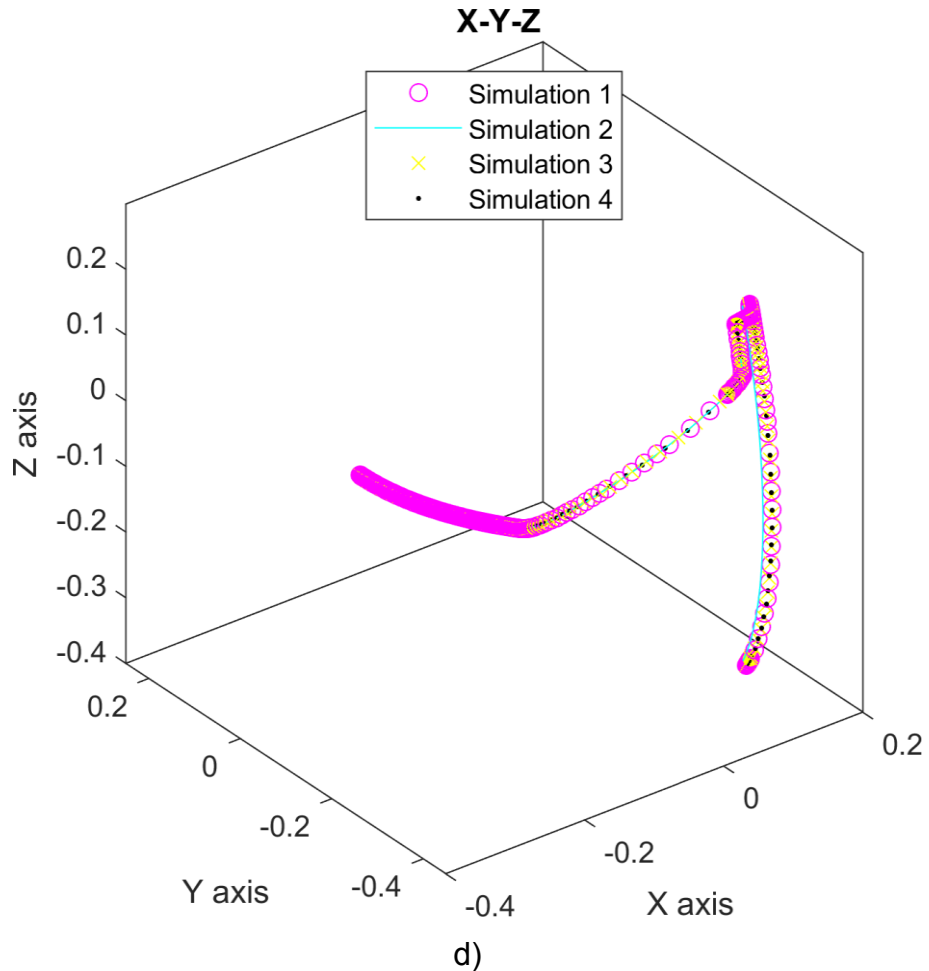
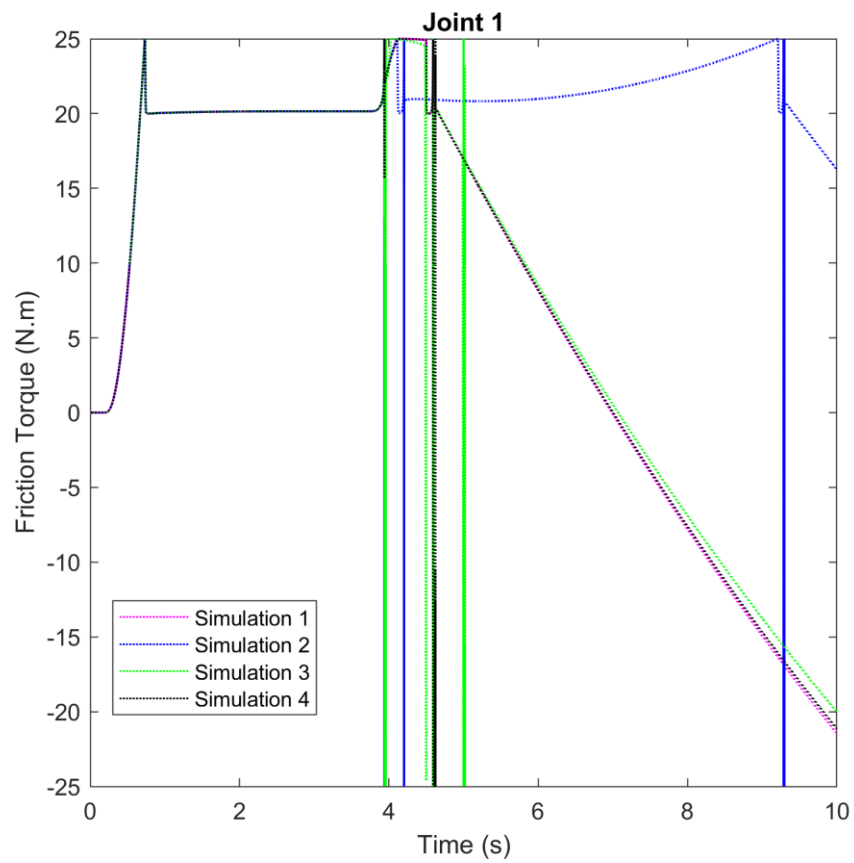
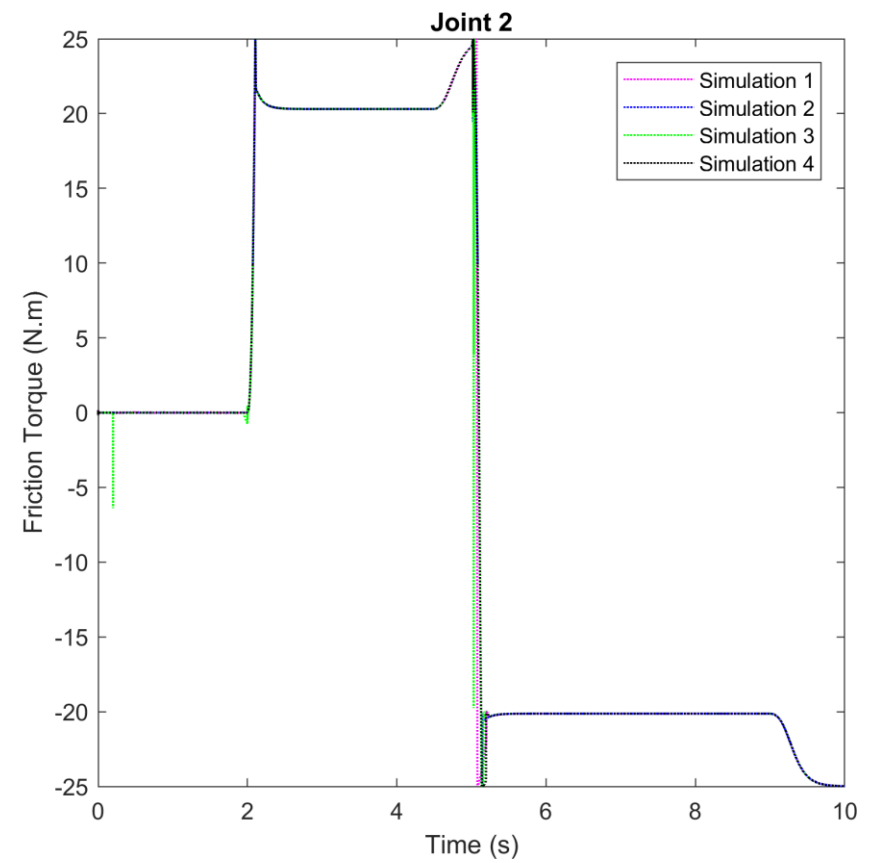


Figure 85 a-c) End-effector motion in two-dimensional task space and d) for three-dimensional task space for different simulations of the anthropoid manipulator

The dynamics parameters namely joint torque and friction torque generated using the CFM presented in section 2.2.3.1 of the literature review are presented in Figure 86. The selection of numerical solvers affects the computed friction torque as seen in Figure 86 a. Simulations 1, 3 and 4 correspond to ODE15s, ODE23tb and ODE23t and the computed joint torques generated for joint 1 using these three solvers match closely as seen in Figure 86 a whereas the friction torque computed in simulation 2 is different, which can be attributed to the solver step-size and stiffness. The computed joint friction torques for simulations conducted for joint 2 using all the four solvers match very closely as seen in Figure 86 b. Therefore, selection of solvers affects the simulation conducted using the CFM for joint 1.



a)



b)

Figure 86 Comparison of friction torque computed at the first two joints using different solvers

Duration of simulation corresponding to each solver was recorded and presented in Figure 87. Longest execution time of 1683.2s was recorded for ODE15s, followed by 63.5s for ODE23s, 4.5s for ODE23tb and 15.8s for ODE23t, which showed the least execution time. Therefore, solver selection influences the simulation execution durations as well as accuracy and this is directly related to solver stiffness. In this respect, it was observed in literature that stiff solvers are used for simulating complex robotic mechanisms since they use smaller step-sizes leading to increased accuracy at a higher computational cost (Ivaldi et al. 2014).

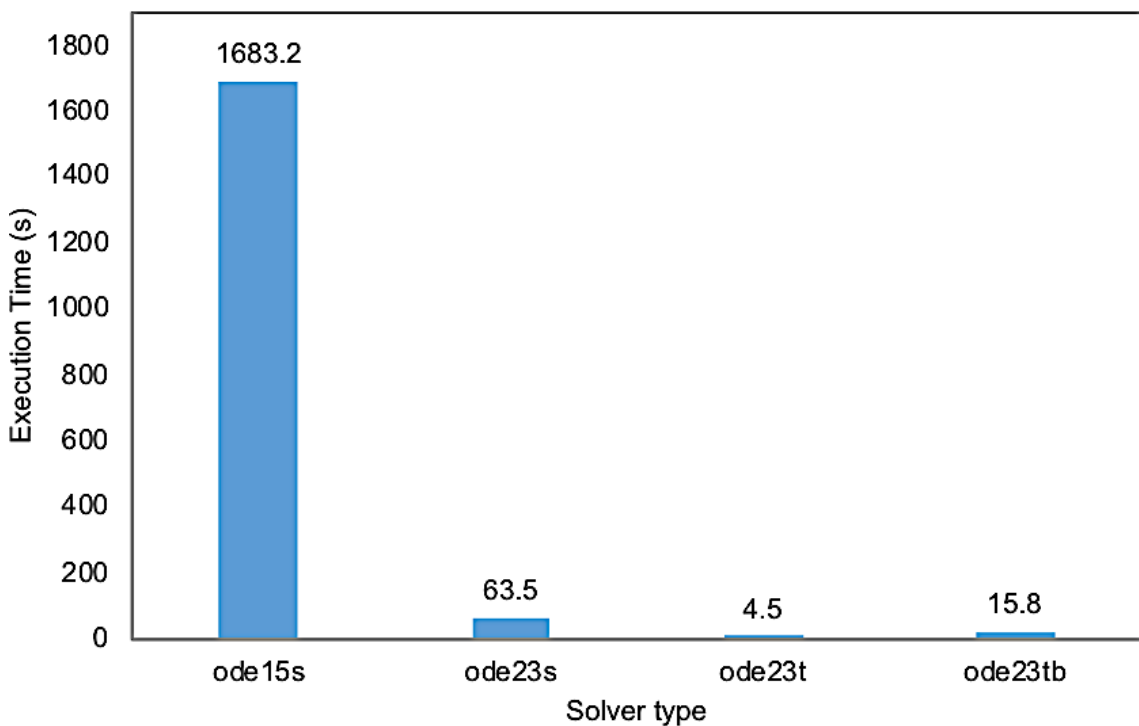


Figure 87 Comparison of execution times for 4 solvers used in simulations

Therefore, this case study demonstrates the importance of selecting appropriate solver for conducting mechanics simulations. The technique applied was extended to the serial open-chain manipulator as a precursor to the complex manipulator presented later on case in 3.

### 6.2.2 Case 2 – serial open-chain manipulator

In this section, the simulation outputs for serial open-chain manipulator are presented. Outputs from SimMechanics 1<sup>st</sup> generation, namely computed torque and reaction torque are presented in Figure 89 and Figure 90 and are compared with the computed torque and reaction torque generated in

SimMechanics 2<sup>nd</sup> generation/SimScape which is presented in Figure 91 and Figure 92 as a validation of the results.

Simulation results from each platform are explained below.

### 6.2.2.1 SimMechanics 1<sup>st</sup> generation

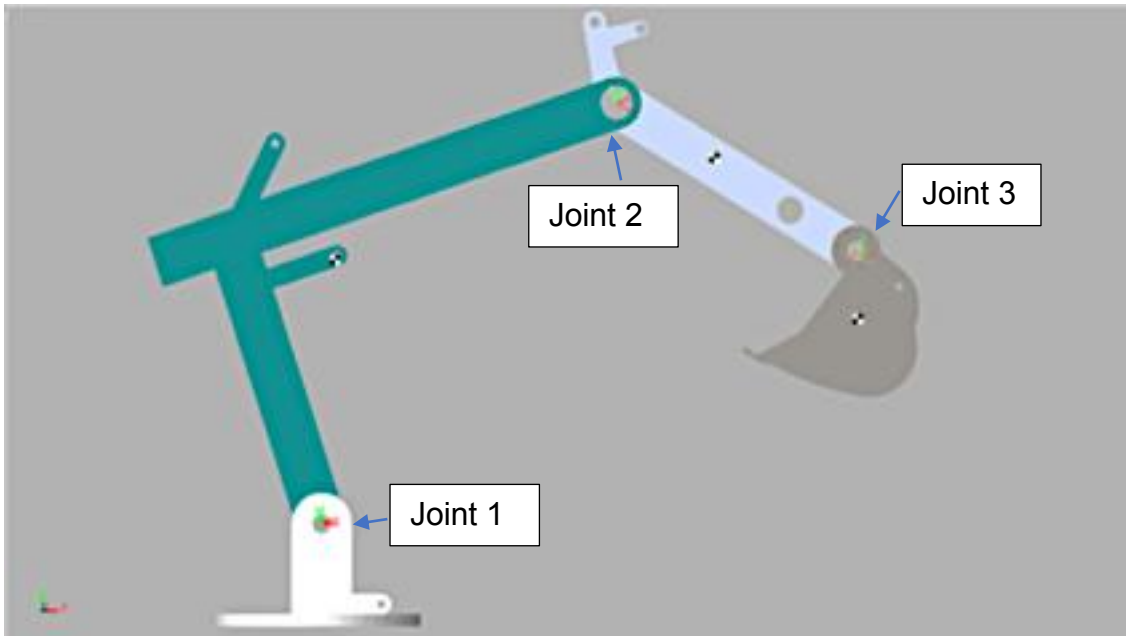


Figure 88 Serial open-chain manipulator showing the joints 1,2 and 3

The computed torque and reaction torque for three joints of the serial open-chain manipulator presented in Figure 88 are evaluated in this section. Maximum and minimum values of computed torque for joint 1 from the simulation are 15.3651Nm and 8.4099Nm respectively, for joint 2 the values were computed as 3.5716Nm and 1.1604Nm, and for joint 3 as 0.6931Nm and 0.0133Nm (Figure 89). Average reaction forces in +y direction were computed as -59.3833N, -20.8934N, and -11.6805N for joints 1, 2 and 3 respectively. The negative sign for the force shows its action in the downward direction, i.e., acting in the direction of gravity. Maximum magnitude of reaction forces was recorded for joint 1 in +y direction i.e., upwards with reference to the plane of the ground. The maximum magnitudes of reaction forces for joints 2 and 3 were also recorded in +y direction; these were in decreasing order of magnitudes since joint 1 supports loads from the successive links. In the x direction, the reaction force was minimal as the direction of action was normal to direction of gravity.

The range of loads for conducting experimental analysis in the tribometer were determined from the computed load. This was used in the tribological analysis, mainly the measurement of coefficient of friction (COF) between the joints outlined in Chapter 5 and whose results are presented in Chapter 7. Mean constraint forces were computed as -59.896N, -20.832N and -10.660N respectively for joints 1, 2 and 3 respectively in the +y direction (Figure 90). Selection of actuators can also be determined using the computed kinematic and dynamic parameters from the simulation e.g. the maximum depth of dig was computed as -0.0569m.

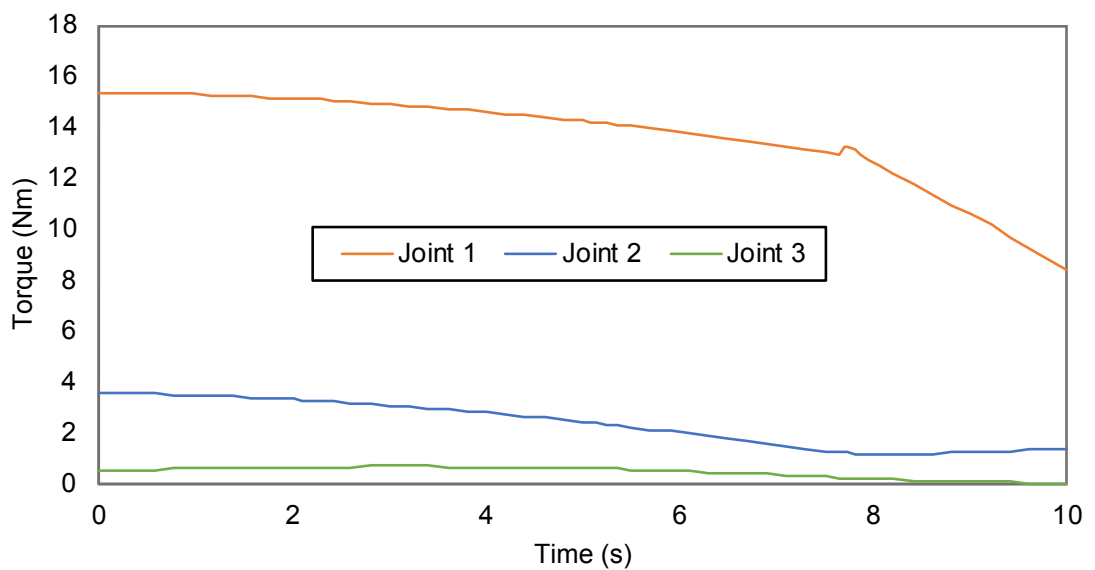


Figure 89 Computed torque from SimMechanics 1<sup>st</sup> generation simulation

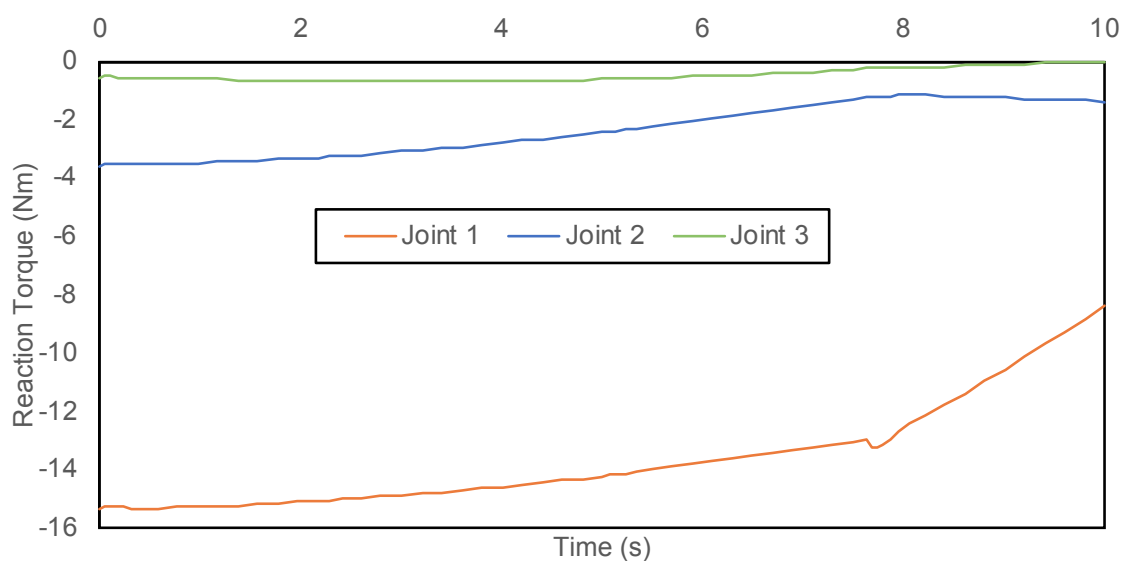


Figure 90 Reaction torque from SimMechanics 1<sup>st</sup> generation simulation

Computed results from the SimScape/ SimMechanics 2<sup>nd</sup> generation platform are presented below.

### 6.2.2.2 SimMechanics 2<sup>nd</sup> generation

Similar to the case presented above, the kinematic and dynamic parameters were computed during the simulation here as well. The dynamic parameters of computed torque and reaction torque for three joints of the serial open-chain manipulator are presented in Figure 91 and Figure 92 respectively. Maximum and minimum values of computed torque for joint 1 were 15.5706Nm and 9.5114Nm, for joint 2 the values were as 4.541Nm and 3.3638Nm, and for joint 3 as 0.6931Nm and 0.0193Nm (Figure 91). Average reaction forces data was not available for this simulation because of platform limitations. Reaction torque curves for this simulation are presented in Figure 92; the maximum and minimum reaction torques were computed as -9.5114Nm and -15.5706Nm for joint 1, -3.3638Nm and -4.5417Nm for joint 2 and -0.01936Nm and -0.6931Nm for joint 3 respectively.

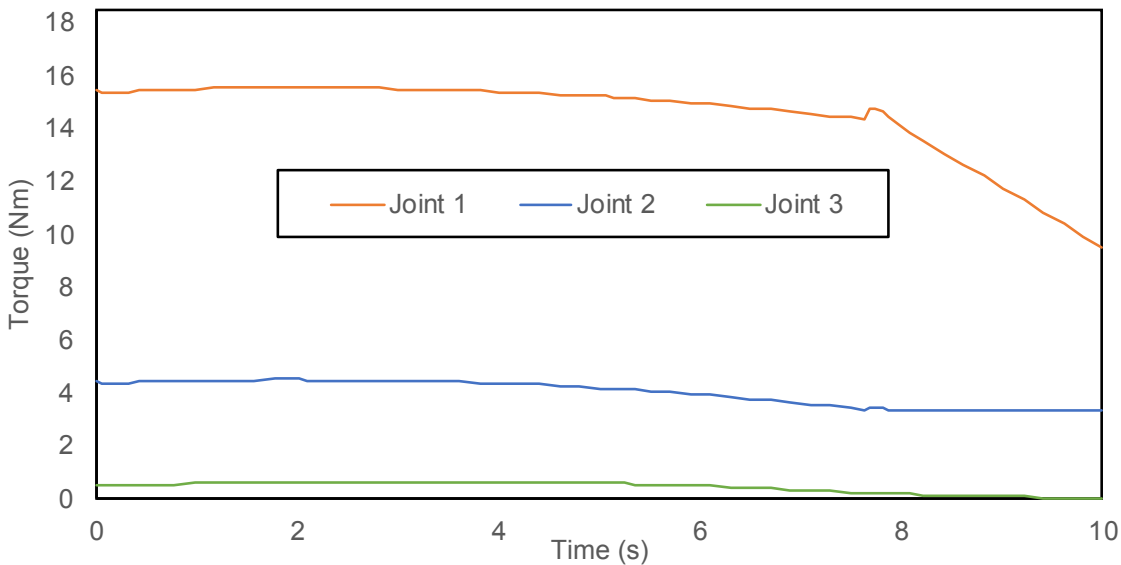


Figure 91 Computed torque generated in SimMechanics 2<sup>nd</sup> generation

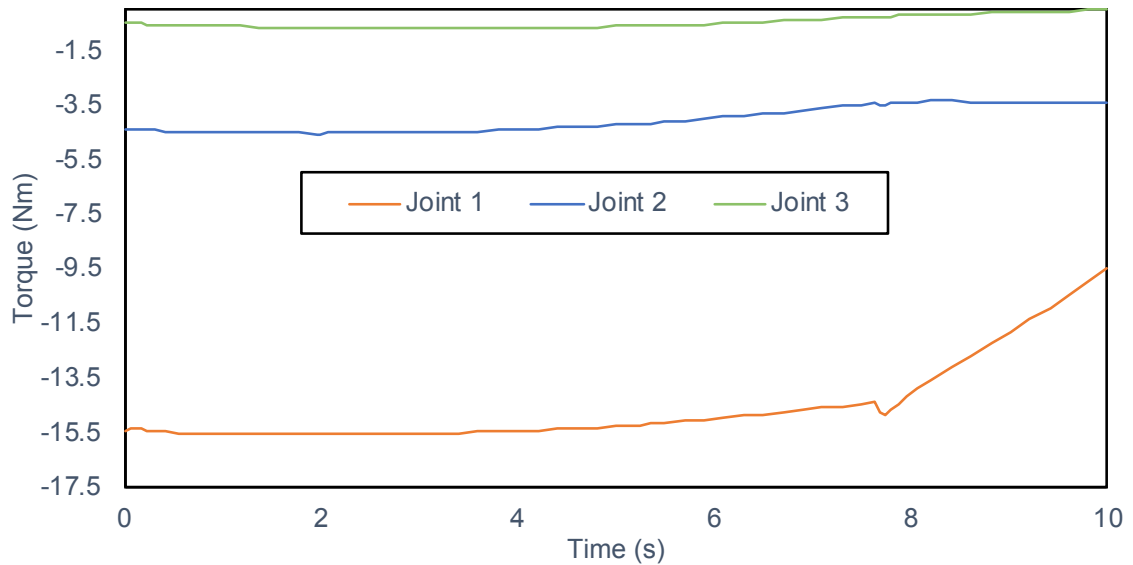
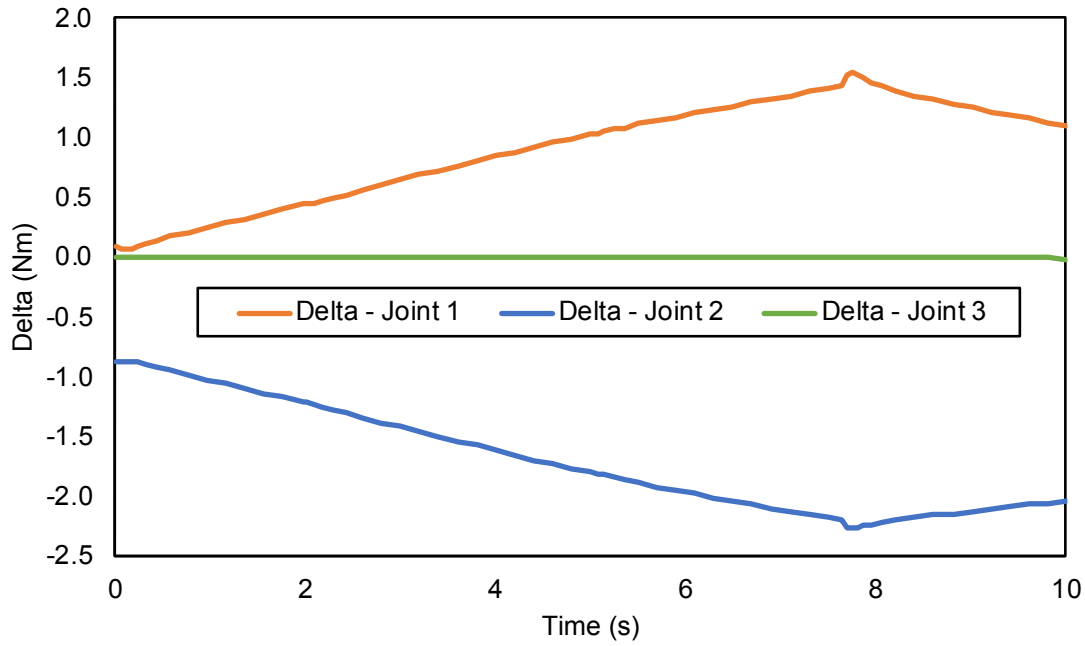


Figure 92 Reaction torques for the 3 joints computed in SimMechanics 2<sup>nd</sup> generation

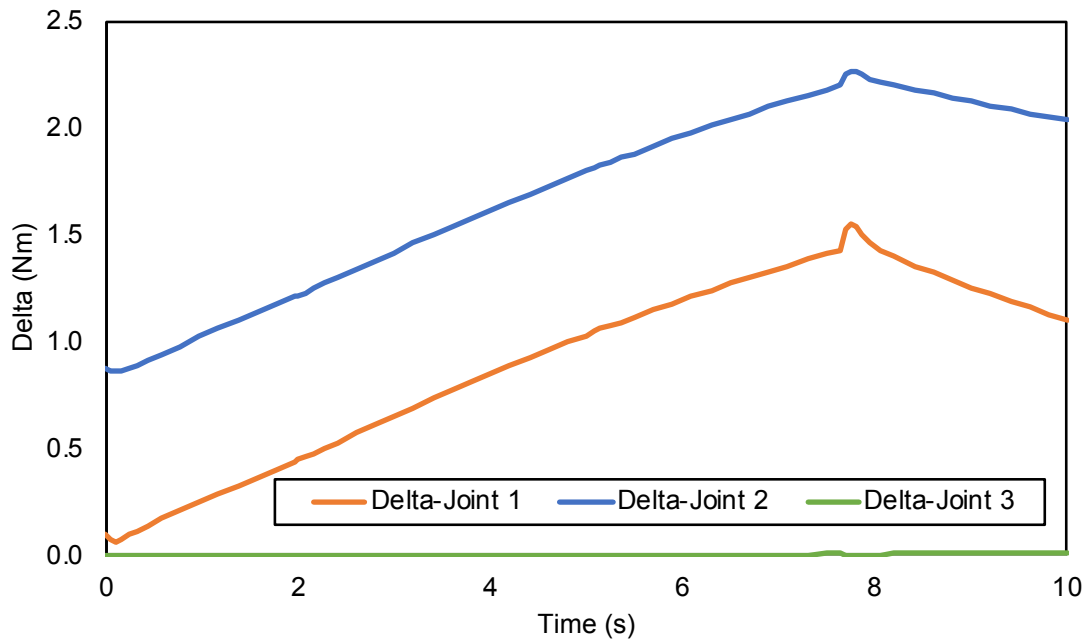
### 6.2.2.3 Comparison of torque computation results

The comparison of computed torques between SimMechanics 1<sup>st</sup> generation and 2<sup>nd</sup> generation is presented. This is because this work is the first of its kind to model and simulate the dynamics of manipulators with friction for SAR applications and therefore, it was not possible for the simulation results to be compared with literature.

The difference in torque values generated in the two simulation platforms was computed and is presented in Figure 93. In Figure 93 a, it is observed that maximum difference occurs around peak value of computed torque, which occurs near 8s of simulation time (on the x-axis). Similarly, difference in computed reaction torques from the two simulations are presented in Figure 93 b and the same observation applies here as well. Joint 2 had the largest magnitude difference followed by joints 1 and 3, and these are labelled with prefix 'Delta'. This can be attributed to cascading computational error for multi-link mechanisms caused by differences in solvers used in each simulation platform. However, the computed torques are found to be in the same region of magnitude, which makes it useful for selection of actuators and further design analysis of links. Also, SimMechanics 2<sup>nd</sup> generation platform is being used increasingly for simulation of dynamics (and kinematics) in literature (Kavitha et al. 2018, Maier et al. 2018).



a)



b)

Figure 93 Difference between a) computed torque and b) reaction torque from the two simulation results

### 6.2.3 Case 3 – closed loop complex manipulator

In this section, the results of validation of the first kinematic loop, followed by the results of three simulations based on three different input signals are presented.



### 6.2.3.1 Simulation of the first kinematic loop of the manipulator mechanism: validation

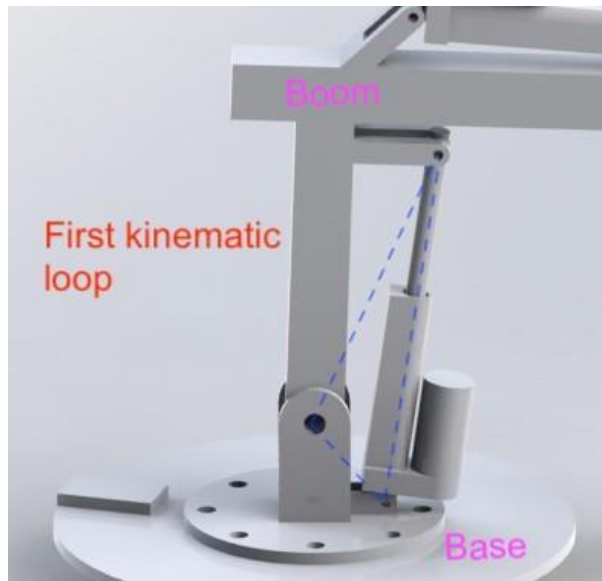


Figure 94 First kinematic loop of the closed-loop manipulator mechanism

Simulation results for the first kinematic loop of the closed loop manipulator shown in Figure 94, is presented in this section. From the comparison of computed joint torque for the main revolute joint connecting the boom to the base presented in Figure 95, it is observed that the computed values from the two simulations match closely. Therefore, equivalence of the dynamics of the first closed-loop linkage for both simulation platforms is established.

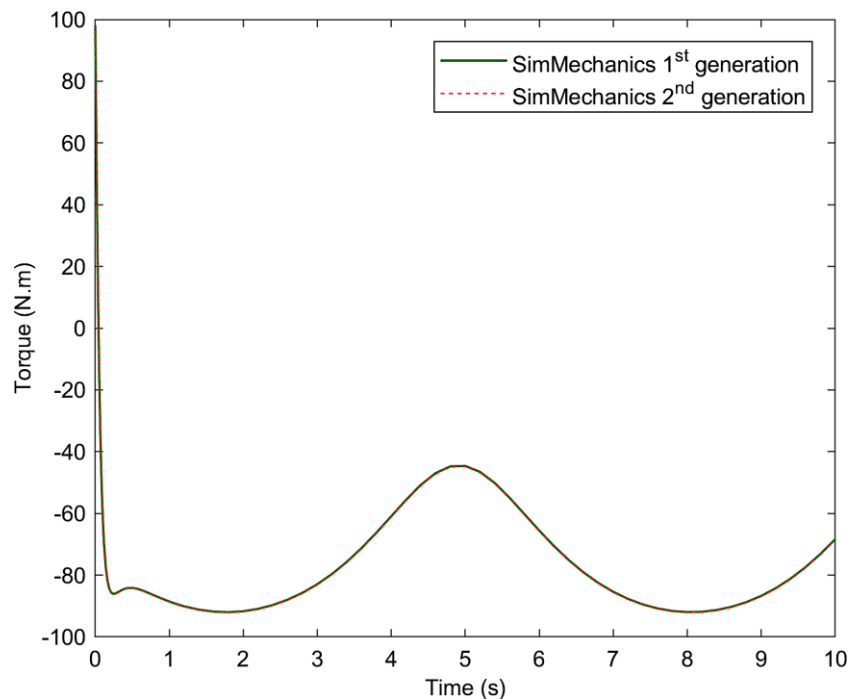


Figure 95 Comparison of friction torque computed at the revolute joint using SimMechanics 1<sup>st</sup> and 2<sup>nd</sup> generation simulations

Using the CFM, the friction force and friction torque were computed at the prismatic and revolute joints and the results are presented in Figure 96 a and b respectively.

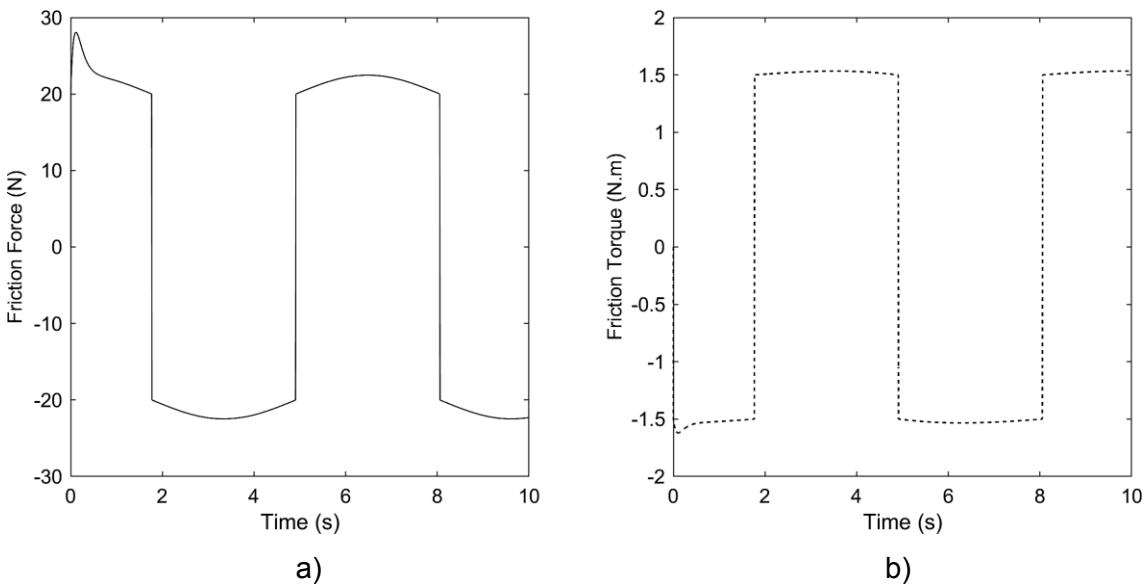


Figure 96 a) Friction force and b) torque computed using the combined friction for sDOF prismatic and revolute joints

### 6.2.3.2 Simulation of the full closed-loop complex manipulator mechanism

In this section, three simulation results for the closed-loop complex manipulator mechanism are presented. The simulation output consists of kinematic parameters such as angular displacement, angular velocity, angular acceleration; displacement, velocity and acceleration of links; end-effector path in planar space, and dynamic parameters such as joint torque, joint friction torque, actuation force and friction force, and the friction force at the linear sliding actuator.

The simulation inputs were controlled in order to analyse their effect on simulation output parameters which include dynamics as well as the end-effector motion. The angular displacement corresponding to the extension of the actuator, which is the input signal, is presented in Figure 97, Figure 104 and Figure 111 for each simulation. Similarly, the corresponding end-effector motion in planar space for the simulations are presented in Figure 98, Figure 105 and Figure 112. This is variable, and operator based, but forms one of the key objectives of manipulation. Using the CFM, friction forces computed for three prismatic sDOF joints of the manipulator are presented in Figure 99, Figure 106

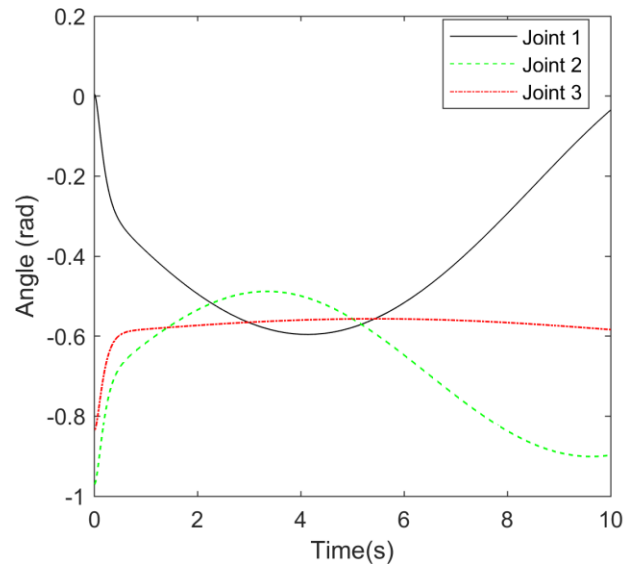
and Figure 113. Figure 100, Figure 107 and Figure 114 present the actuation force computed during the simulation. Figure 101, Figure 108 and Figure 115 present the total force computed during the simulation i.e. sum of friction force and actuation force. Friction torque computed was presented in Figure 102, Figure 109 and Figure 116, and torque computed at the joints was presented in Figure 103, Figure 110 and Figure 117.

It is observed that simulation 1 has a smoother signal profile which was generated using the modified sine wave. Simulations 2 and 3 relied on identical signals generated using the signal builder block from Simulink presented in section 4.3.1.3. The effect of input smoothing parameter 'Tau' is observable in simulation 3 for which the variable value was set to 0.001 and this causes artefacts in the computed dynamic parameters which are visible in Figure 114, Figure 115 and Figure 117 .

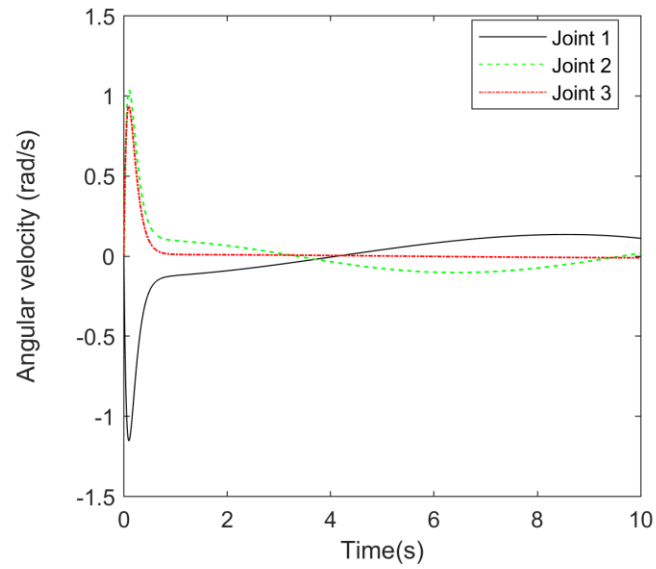
The computed values of peak revolute joint torque were  $-0.2884\text{Nm}$  and  $-0.05511\text{Nm}$  at  $0.1995\text{s}$  and  $0.1810\text{s}$  respectively for joints 1 and 3. The computed torque for joint 3 remained time-invariant due to constant value of applied external load. Values of the revolute joint torque computed using the combined friction model were  $27.63\text{Nm}$  for joint 3,  $27.56\text{Nm}$  for joint 2 and  $23.69\text{Nm}$  for joint 3 at  $0.103\text{s}$ ,  $0.103\text{s}$  and  $0.968\text{s}$  respectively. The inflexion values at the crest and trough for the translational actuator force were recorded as  $-1.094\text{N}$ ,  $-0.8348\text{N}$  and  $0.7819\text{N}$  at  $3.635\text{s}$ ,  $3.404\text{s}$  and  $3.700\text{s}$  respectively.

The computed kinematic and dynamic parameters provide information on the design requirements and actuator selection requirements for optimising manipulator design and performance. The numerical modelling and computation of such parameters through conventional analysis is not only tedious but is also time consuming and error prone and the use of CAD-MBD method to design and simulate the mechanics is a feasible technique for this application which provides a range of output parameters from the inverse dynamic simulations (Schlotter 2003, Daumas et al. 2005, Hroncova and Pastor 2013).

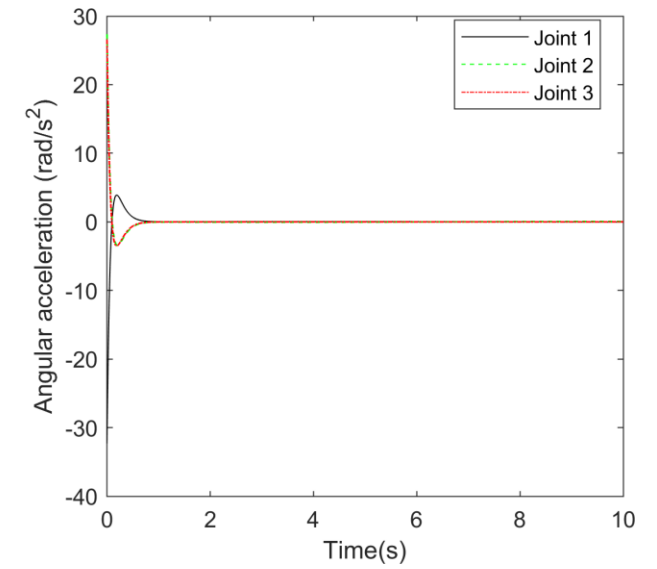
## Simulation 1



a)



b)



c)

Figure 97 Output joint kinematic parameters including a) joint angle b) angular velocity and c) angular acceleration

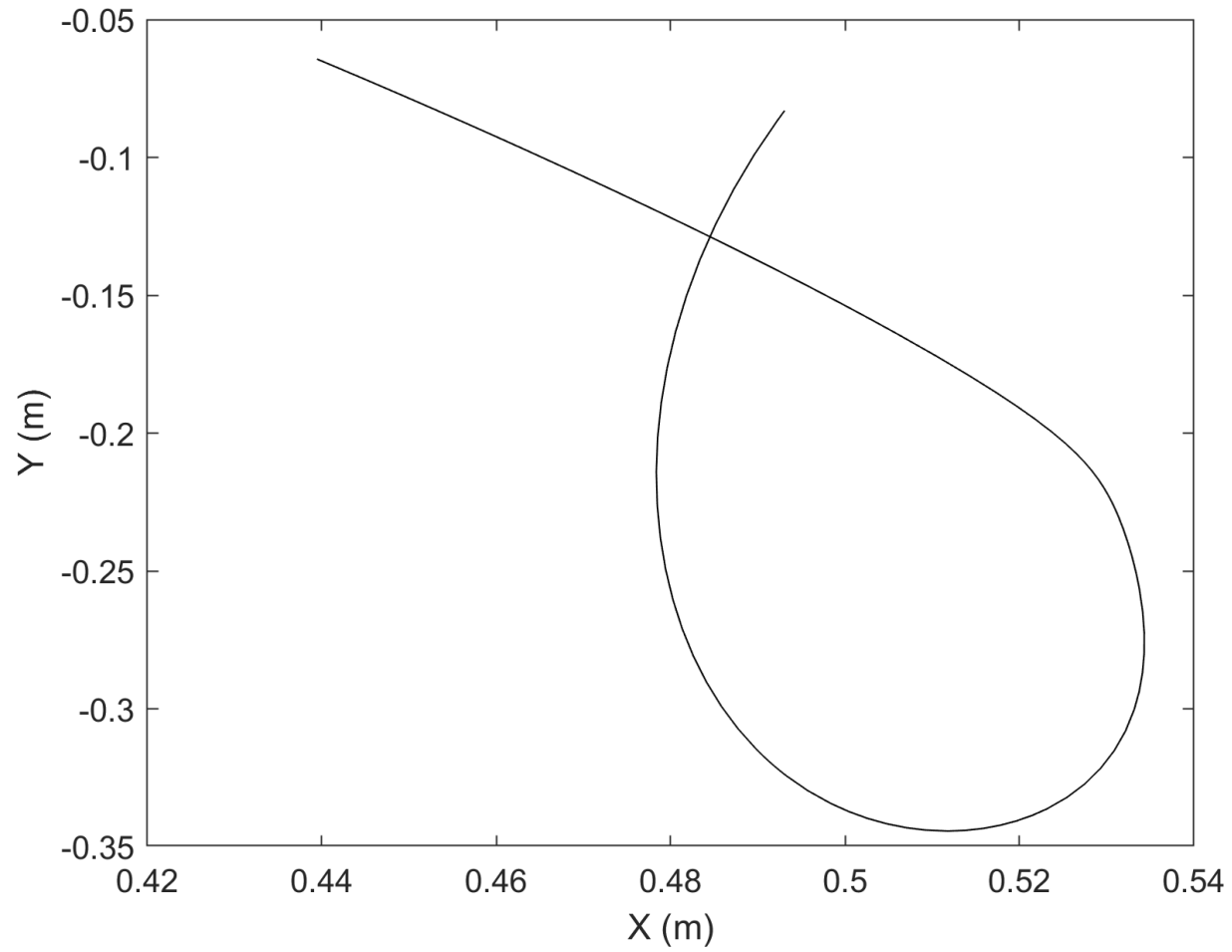
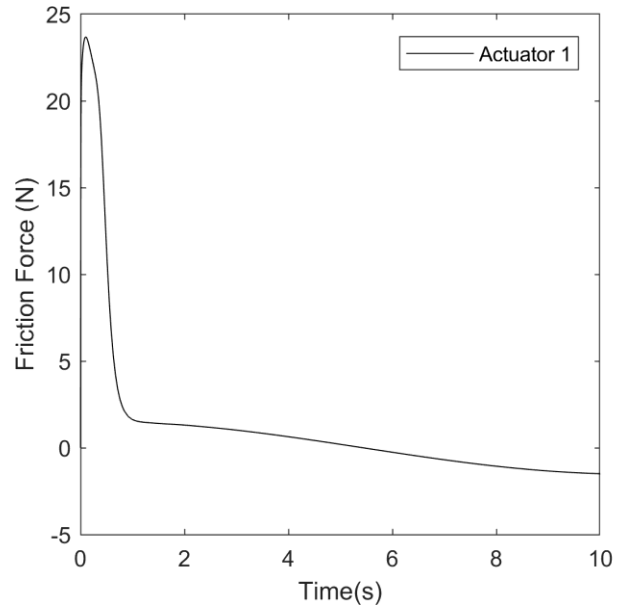
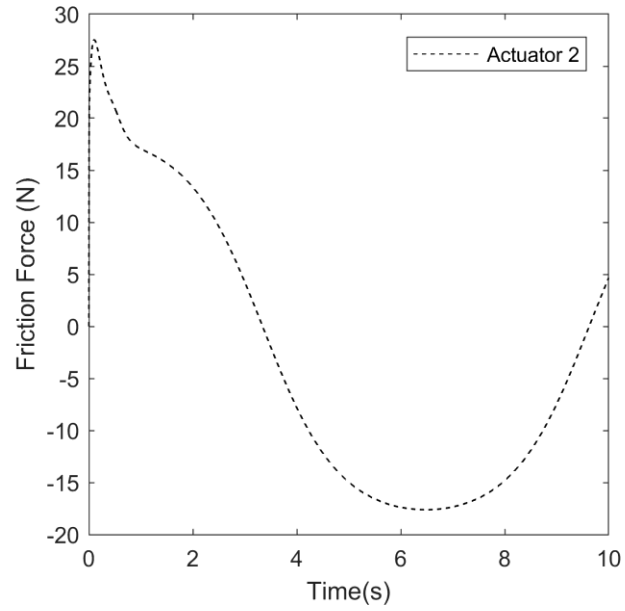


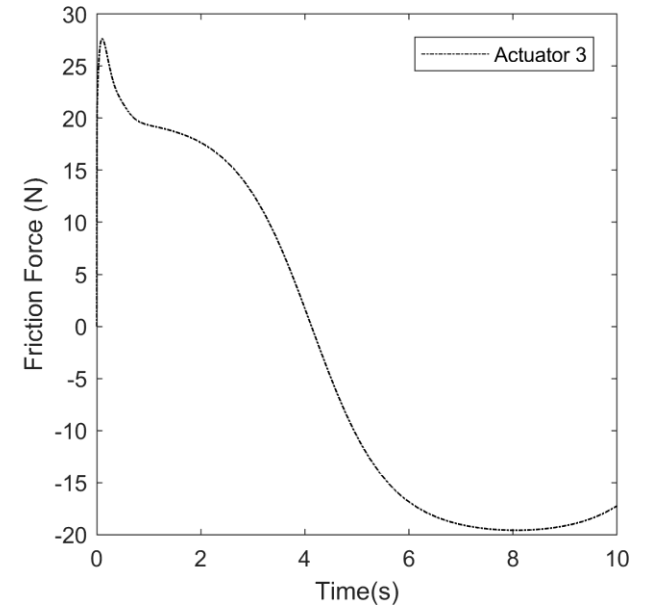
Figure 98 End-effector motion in planar task space



a)

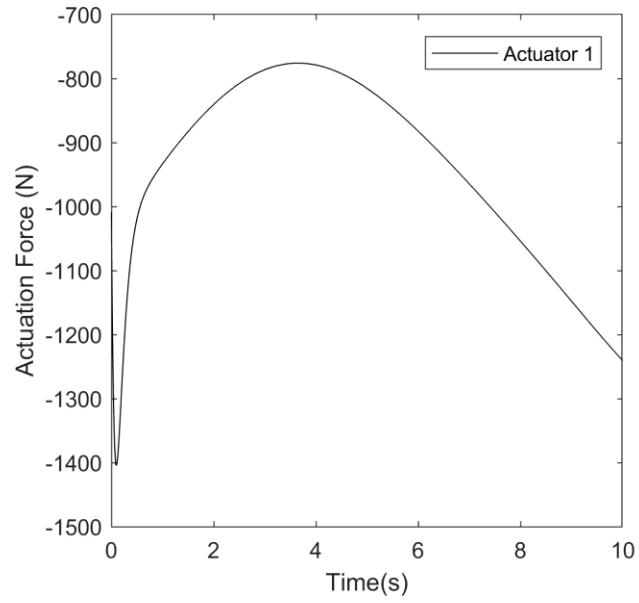


b)

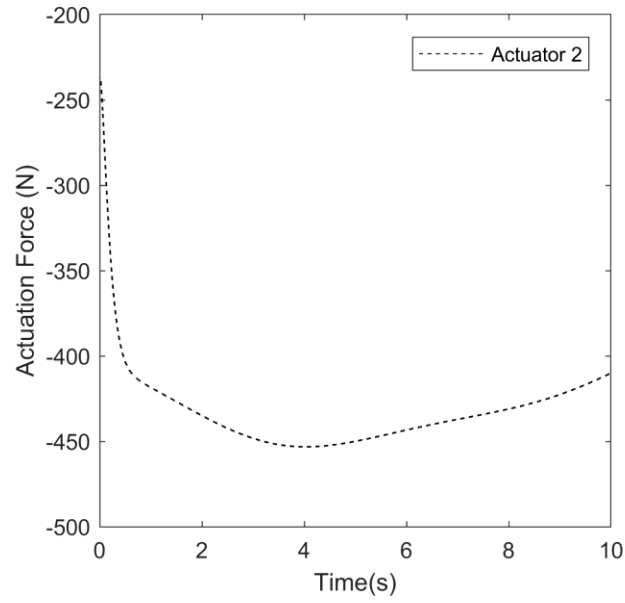


c)

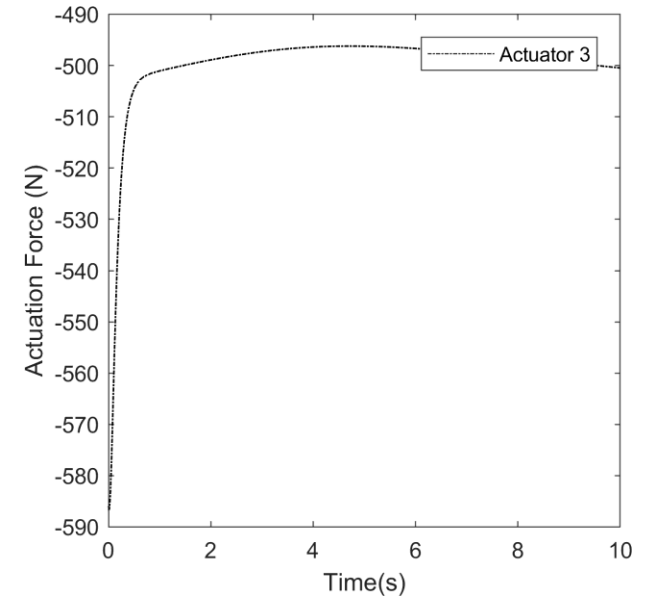
Figure 99 a-c) Friction force at actuator



a)

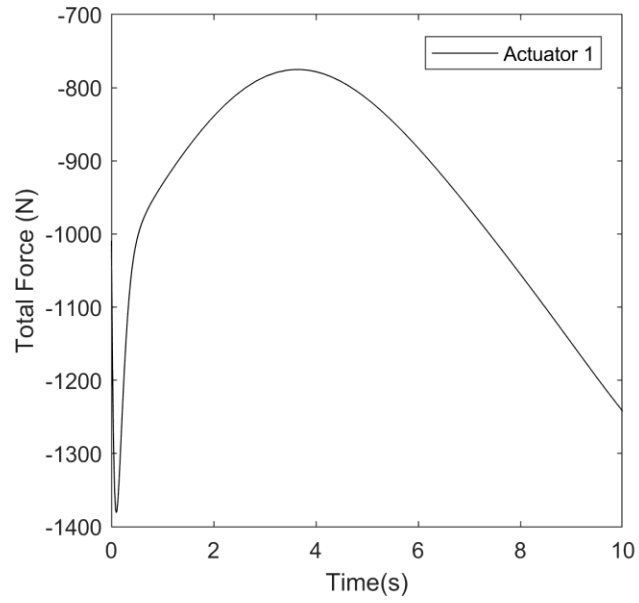


b)

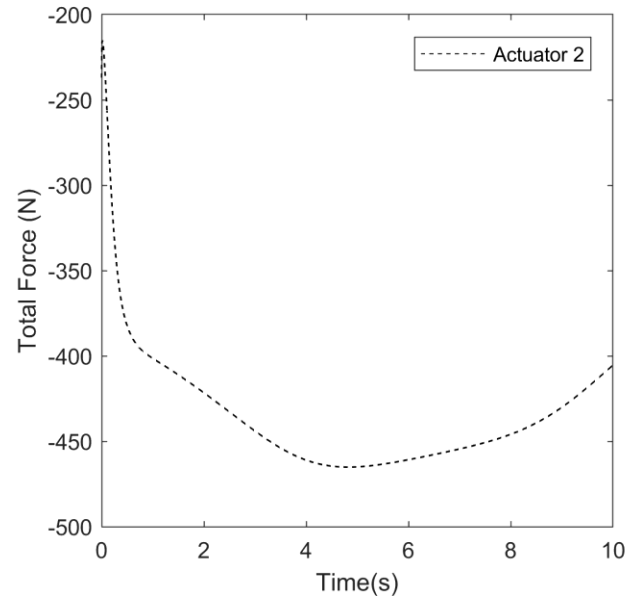


c)

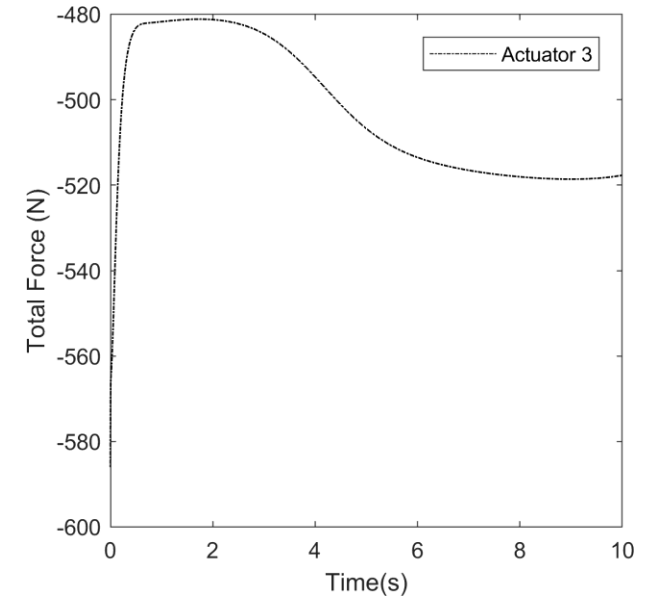
Figure 100 a-c) Actuation force



a)



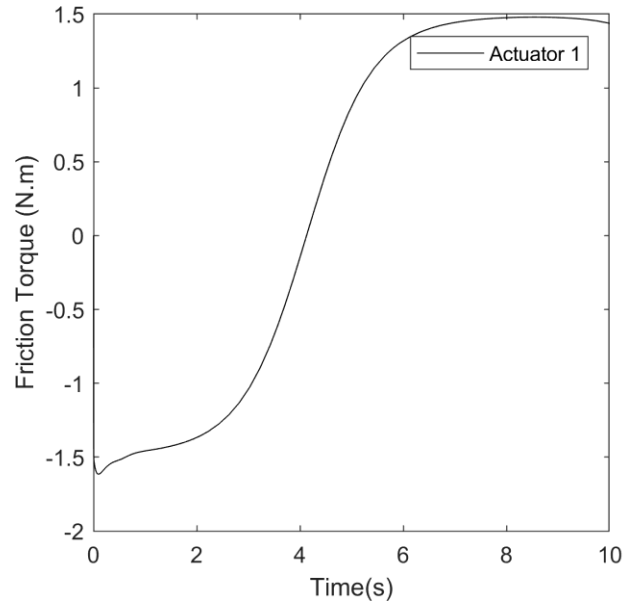
b)



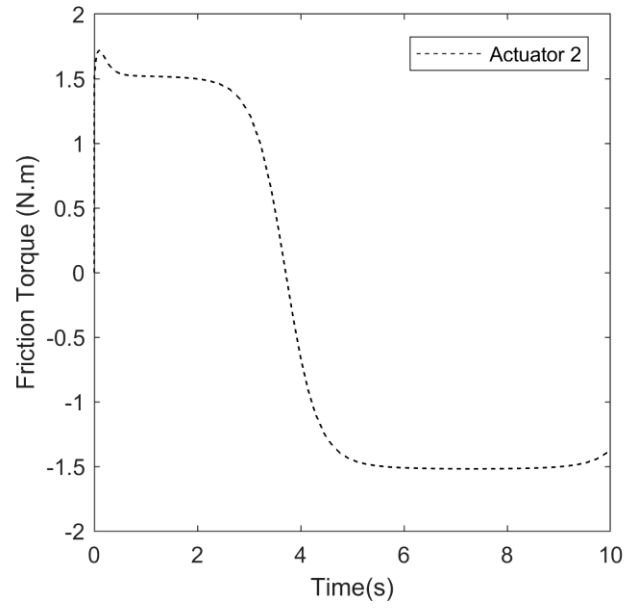
c)

Figure 101 a-c) Total force

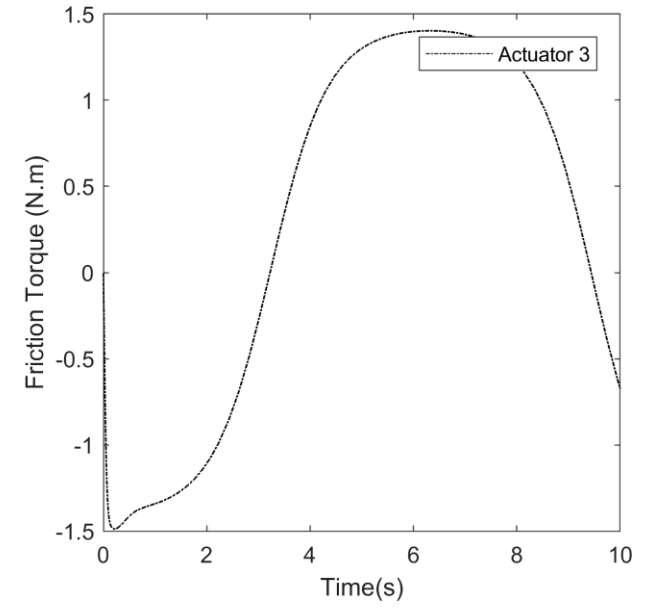




a)

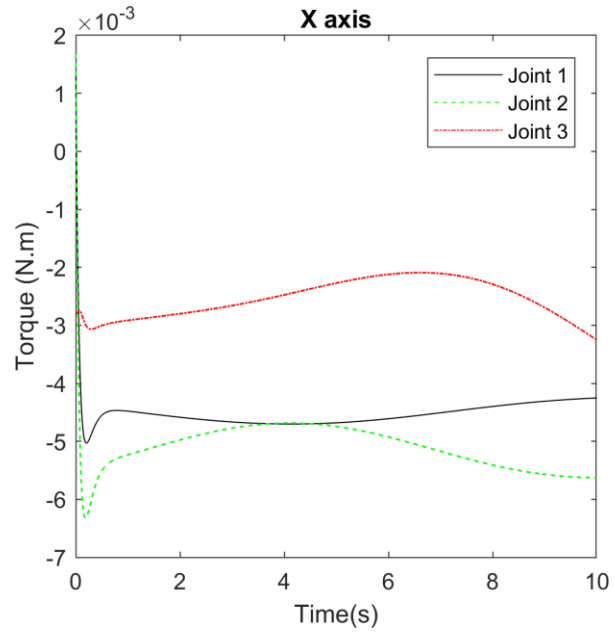


b)

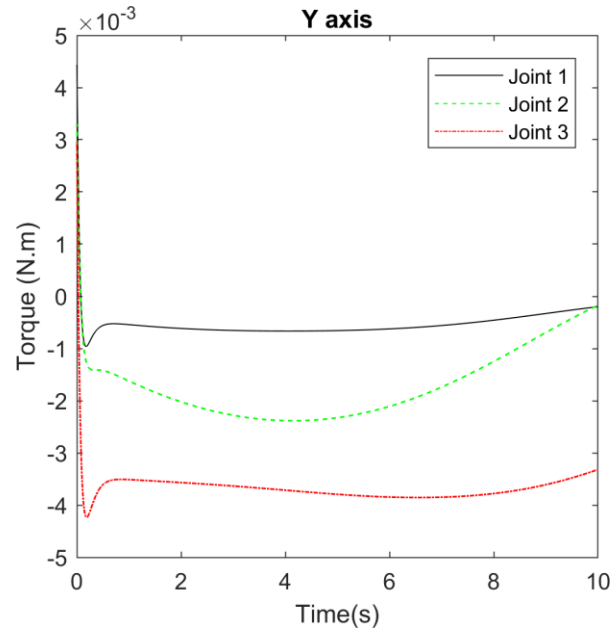


c)

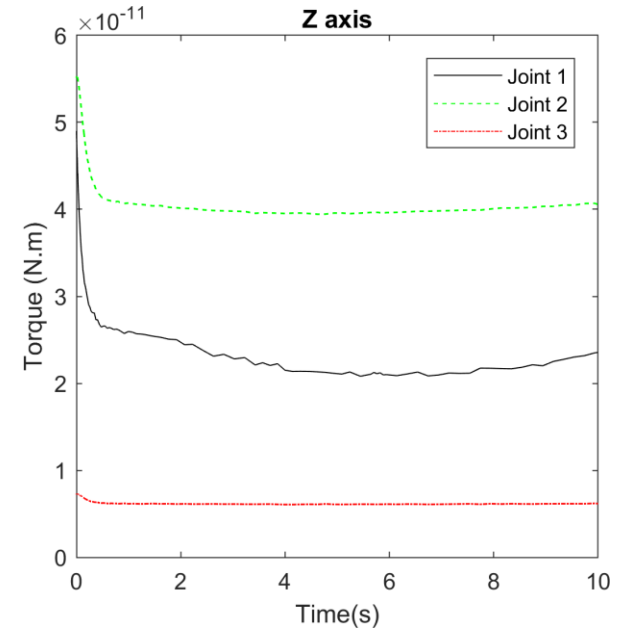
Figure 102 a-c) Friction torque at revolute joint



a)



b)



c)

Figure 103 a-c) Torque

## Simulation 2

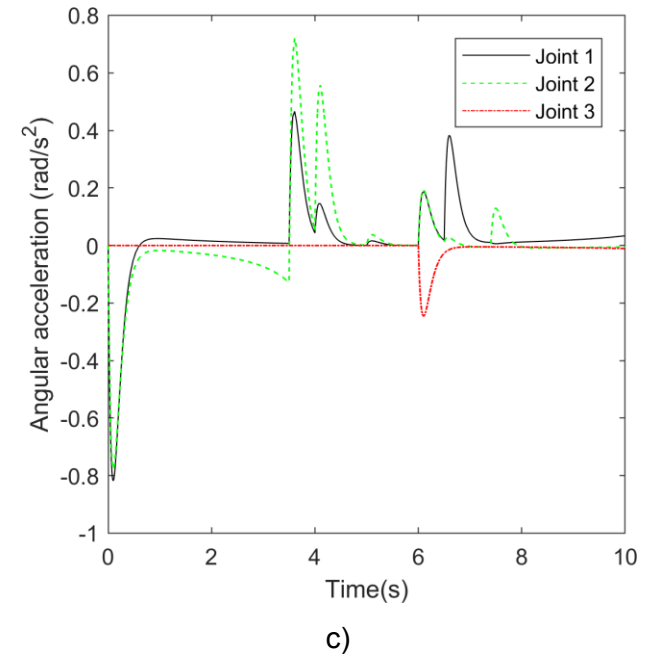
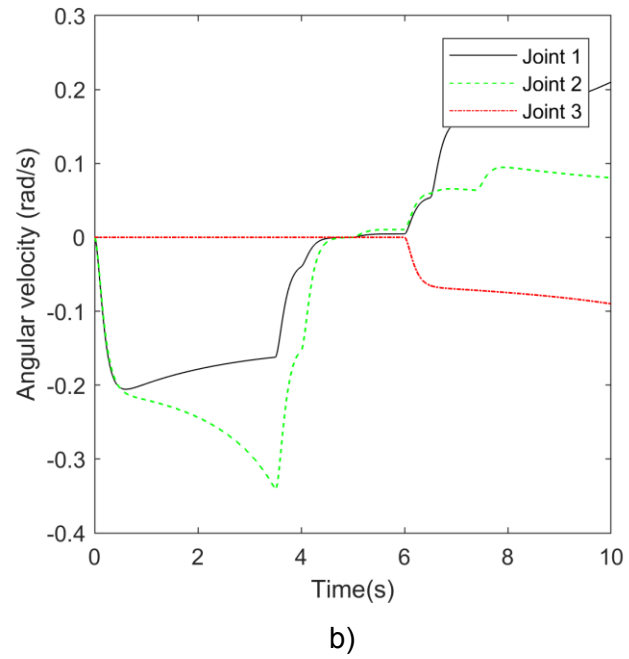
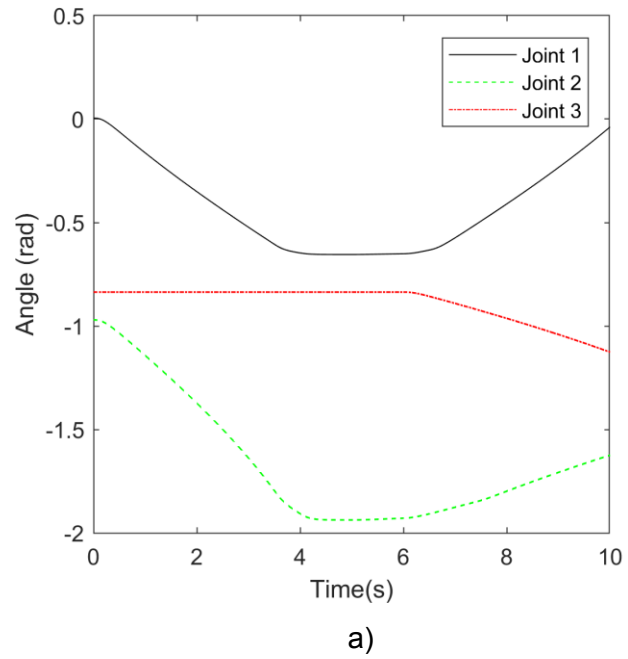


Figure 104 Output - angular parameters

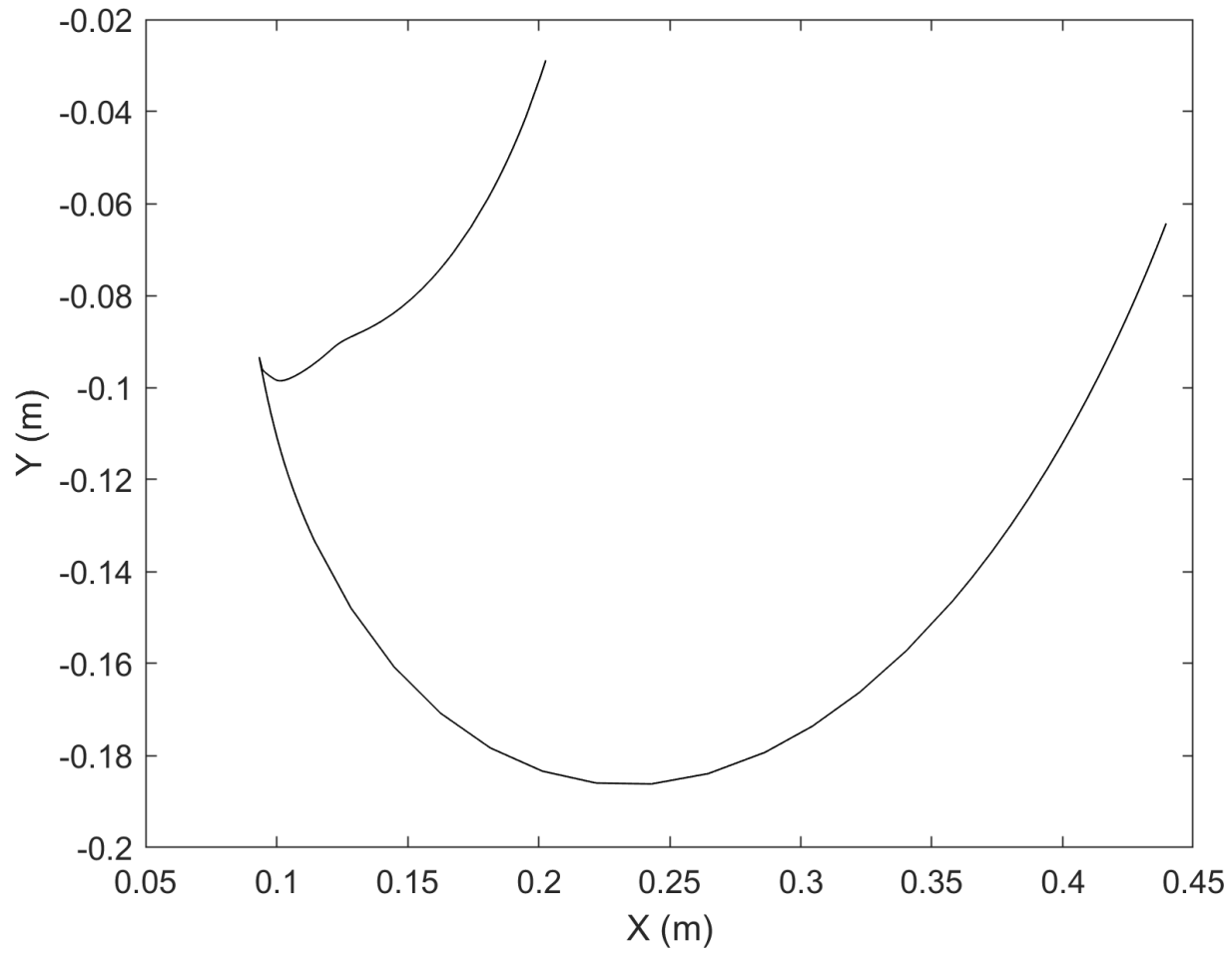
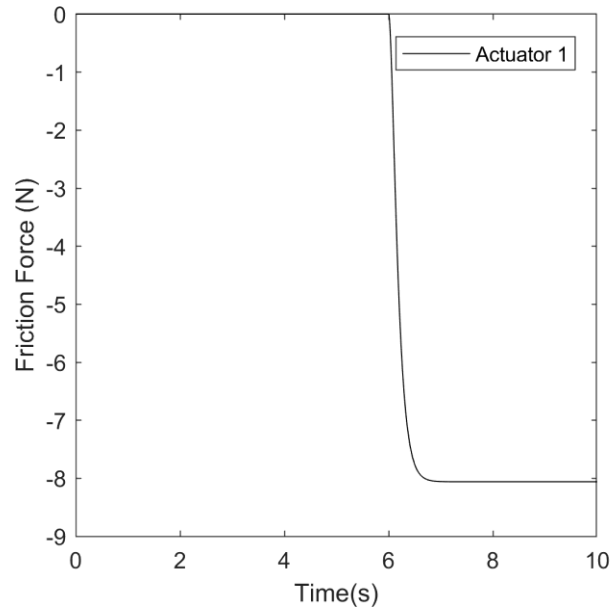
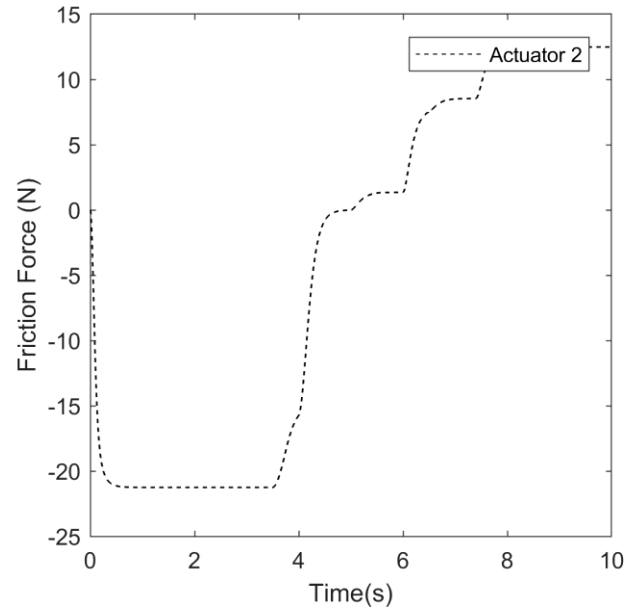


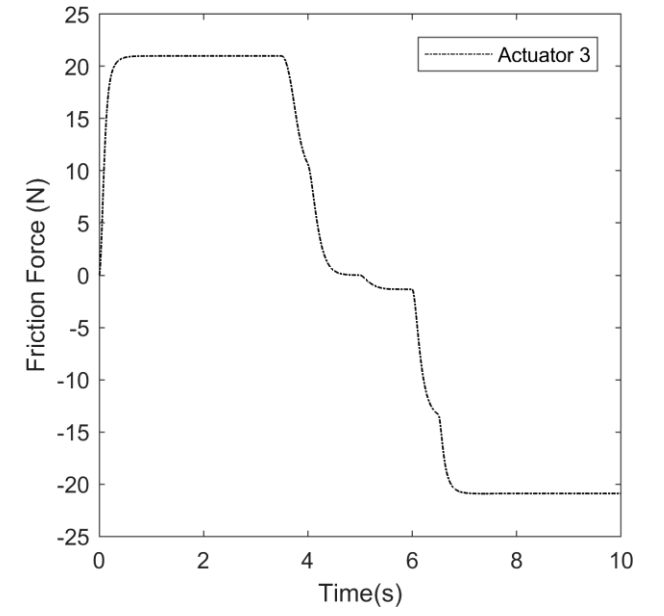
Figure 105 Motion of the end-effector in planar task space



a)

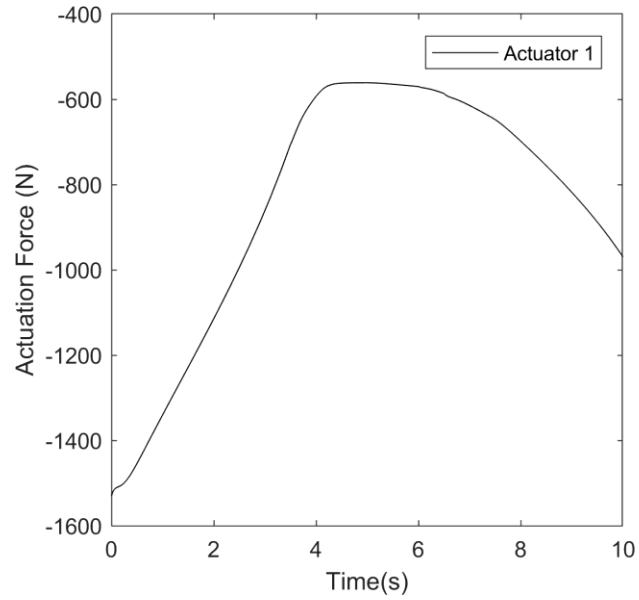


b)

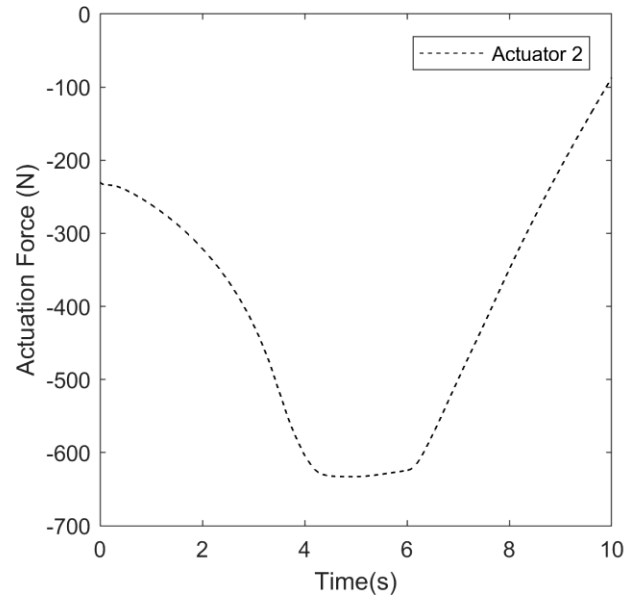


c)

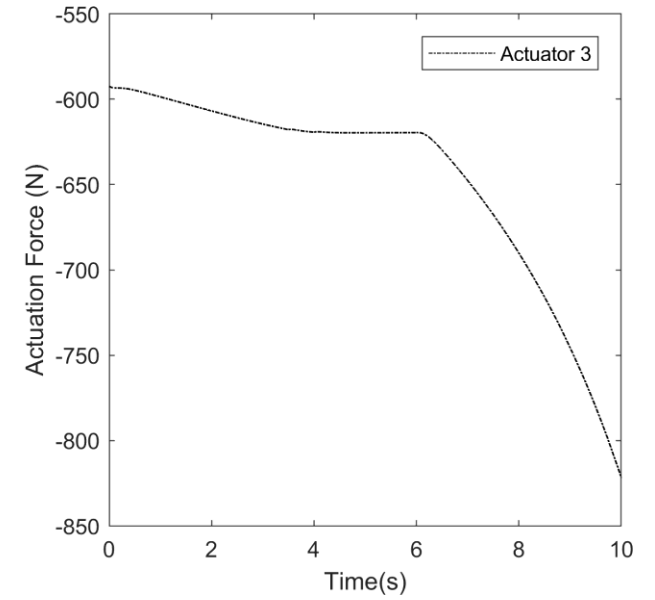
Figure 106 a-c) Friction force at actuator



a)

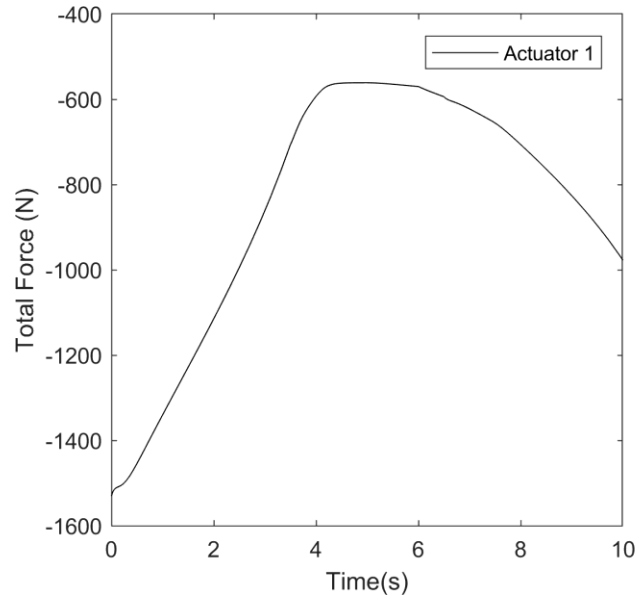


b)

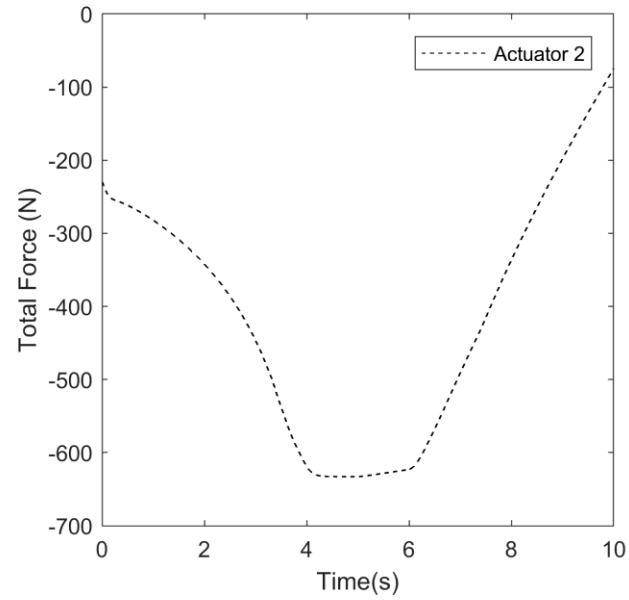


c)

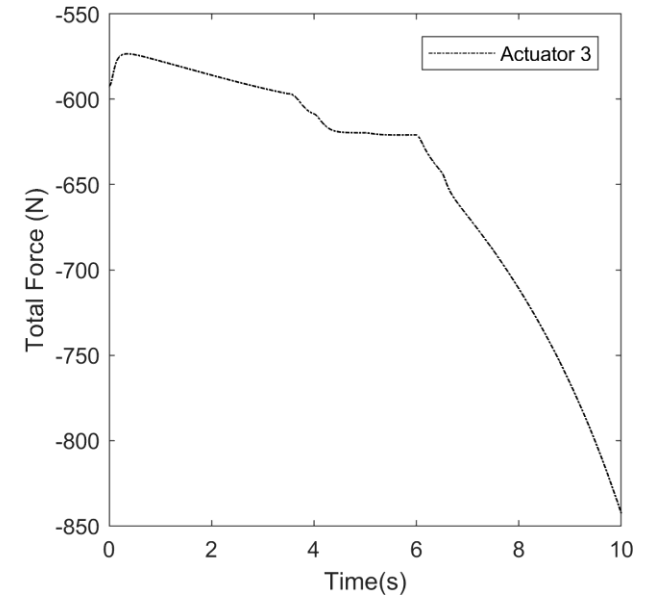
Figure 107 a-c) Actuation force



a)

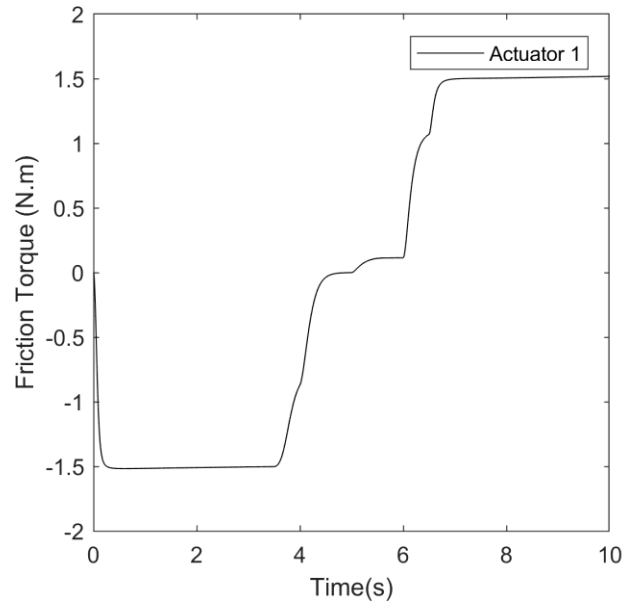


b)

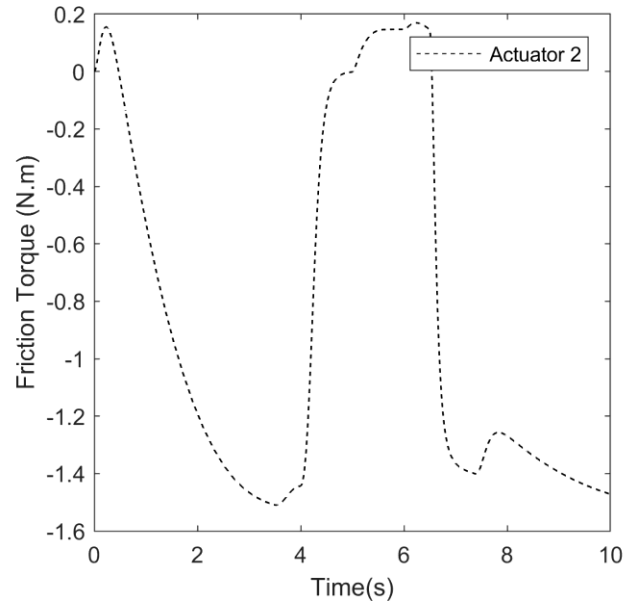


c)

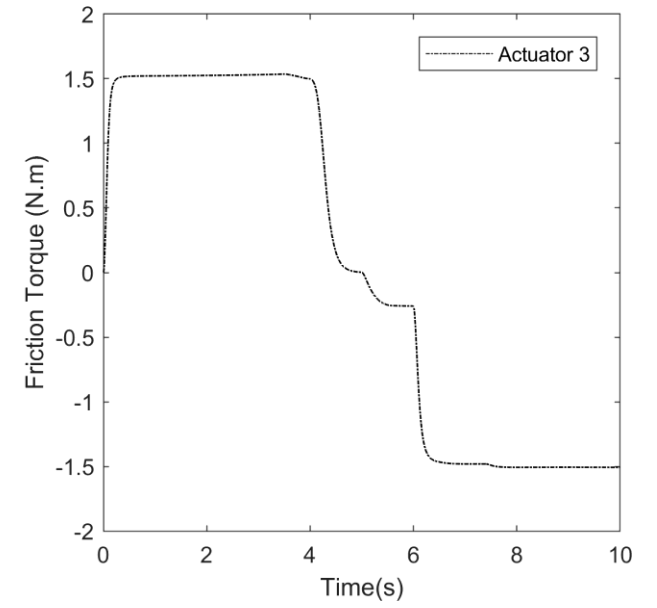
Figure 108 a-c) Total force



a)



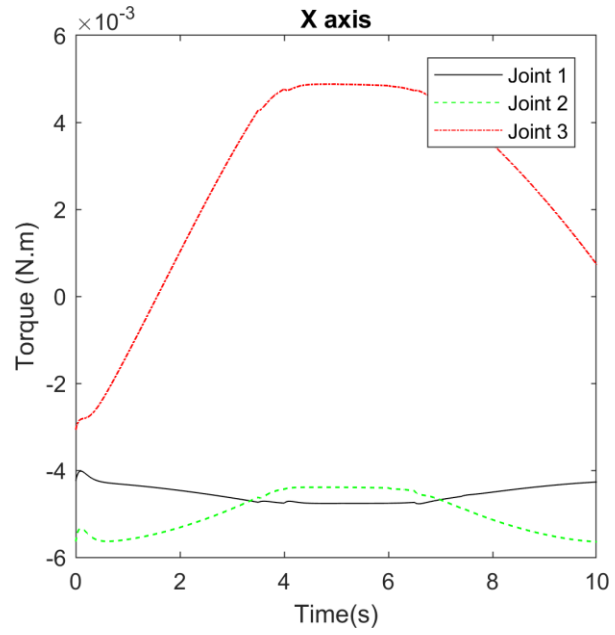
b)



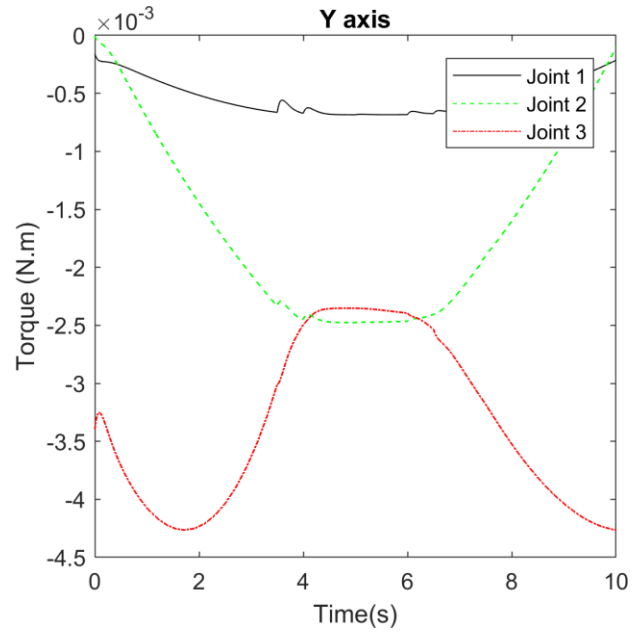
c)

Figure 109 a-c) Friction torque at revolute joint

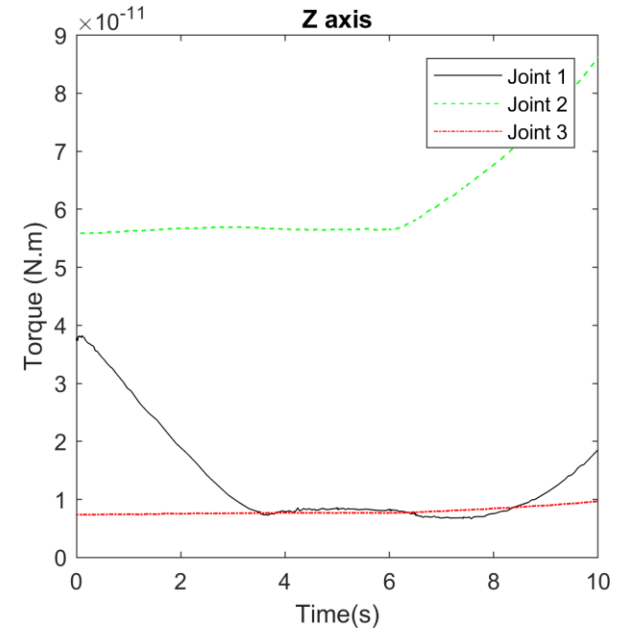




a)



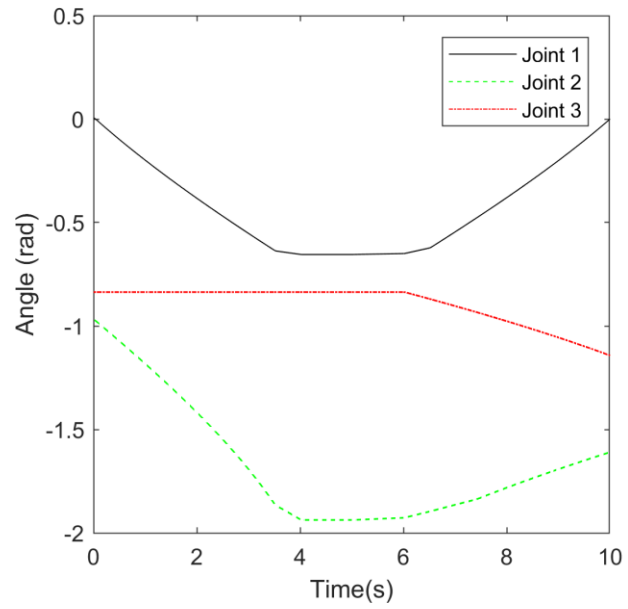
b)



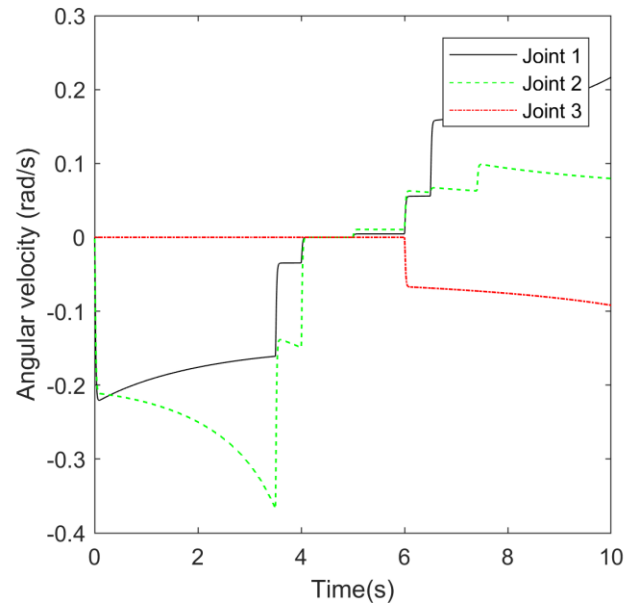
c)

Figure 110 a-c) Torque

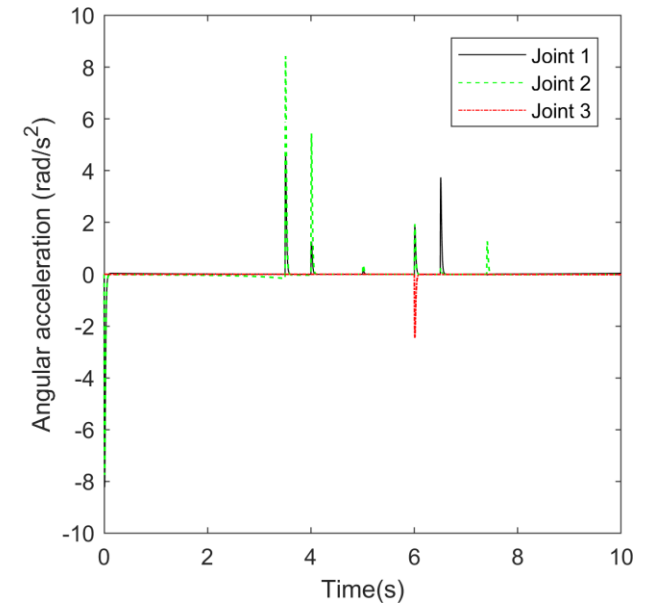
### Simulation 3



a)



b)



c)

Figure 111 a-c) Output - angular parameters

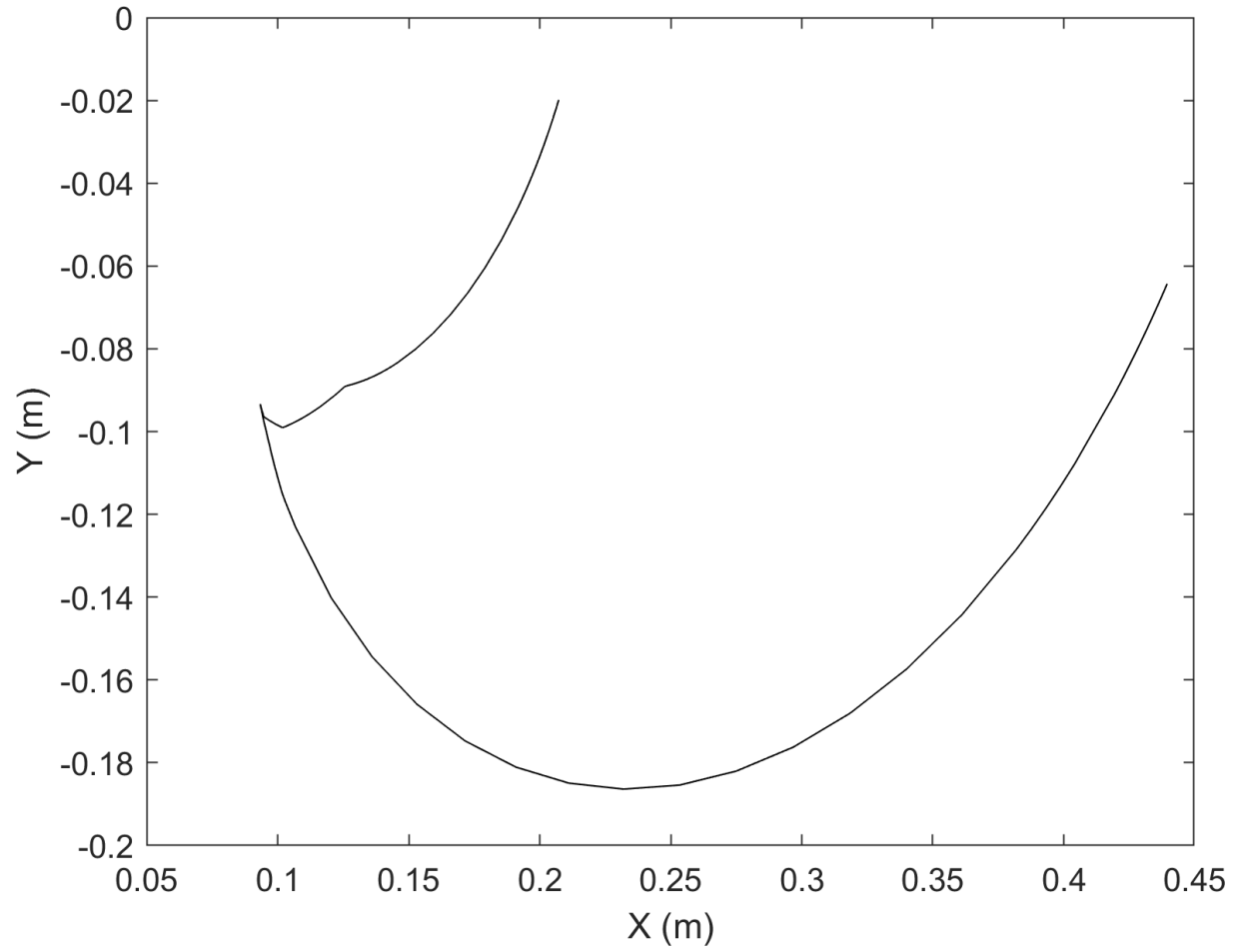
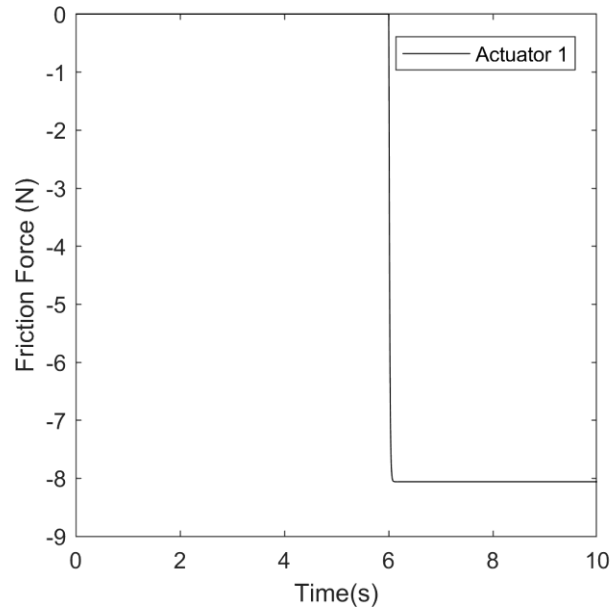
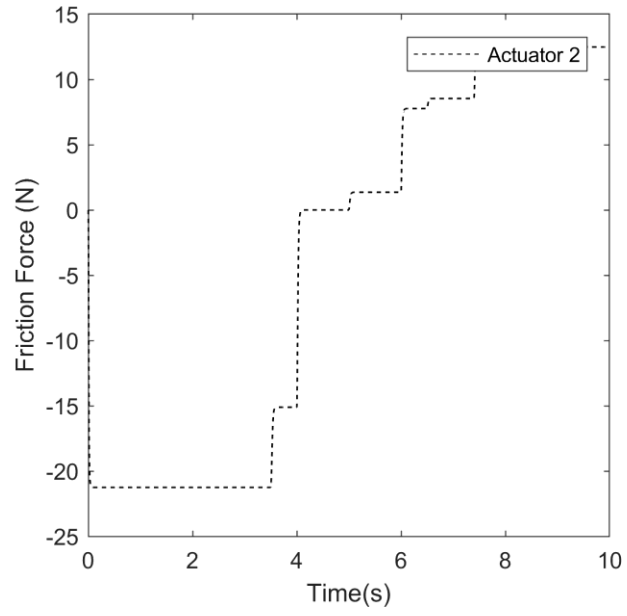


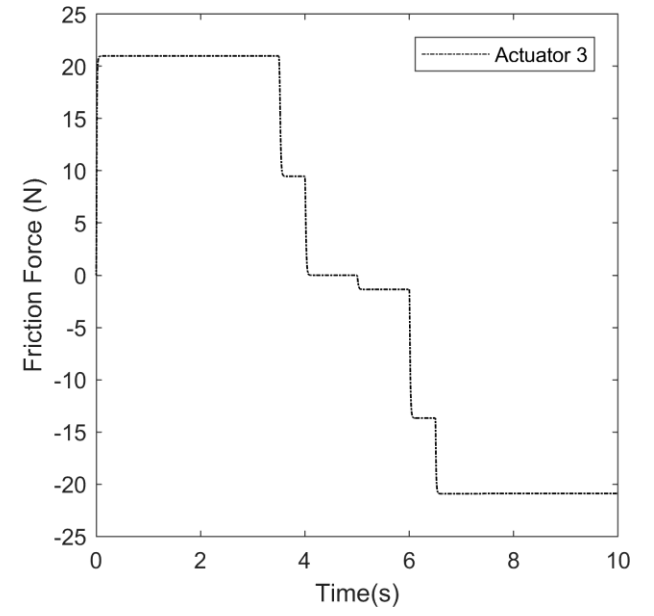
Figure 112 Motion of the end-effector in planar task space



a)

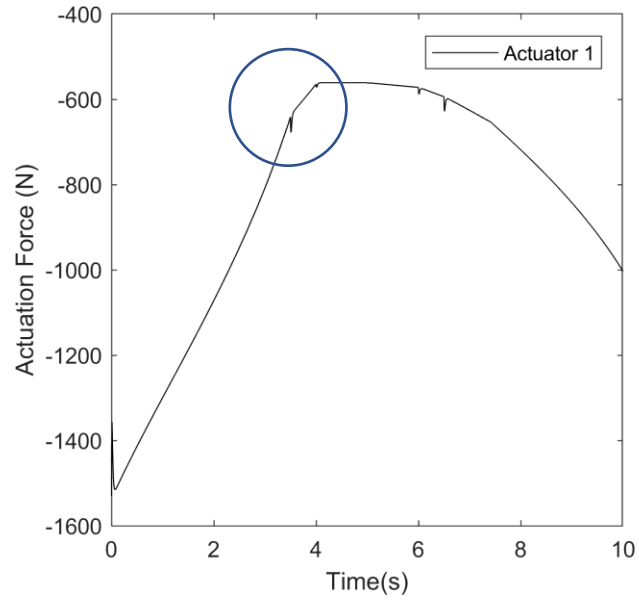


b)

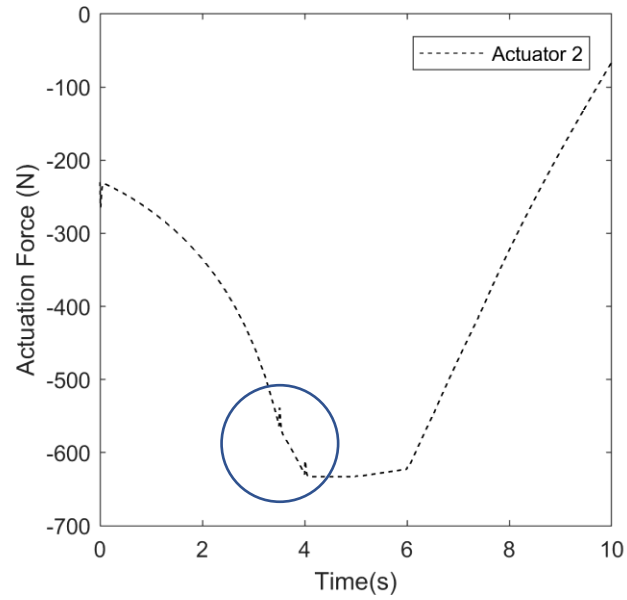


c)

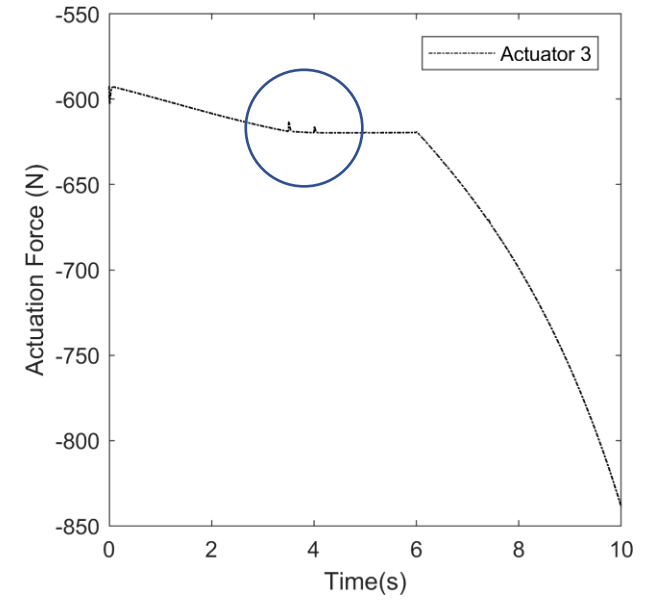
Figure 113 a-c) Friction force at actuator



a)

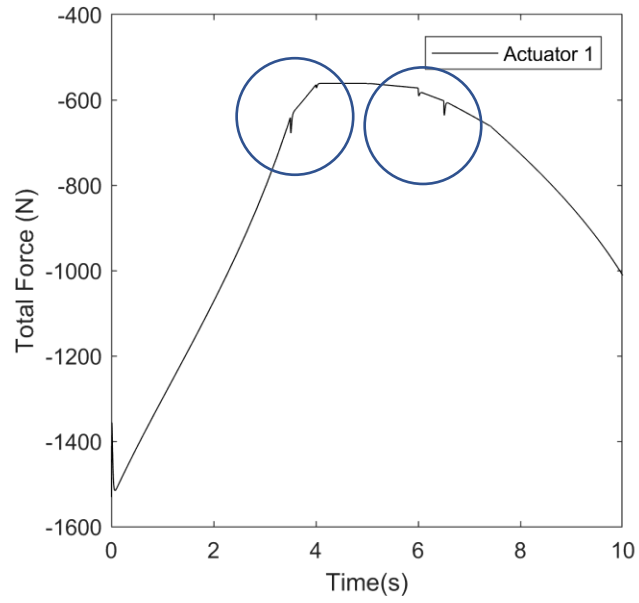


b)

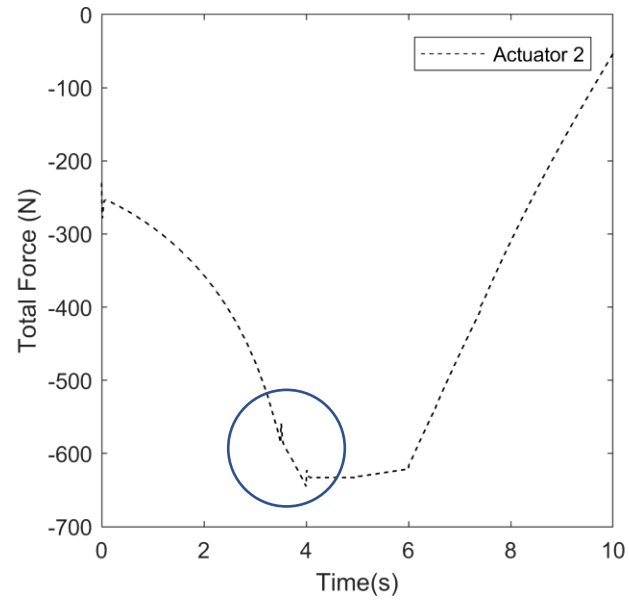


c)

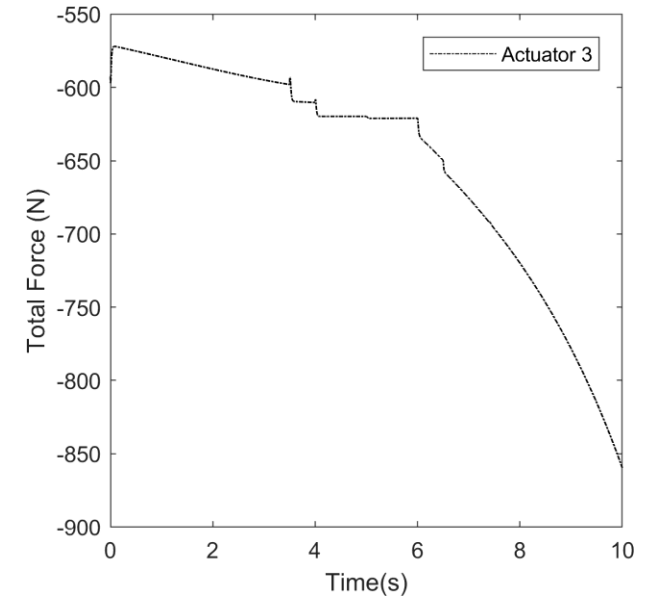
Figure 114 a-c) Actuation force



a)

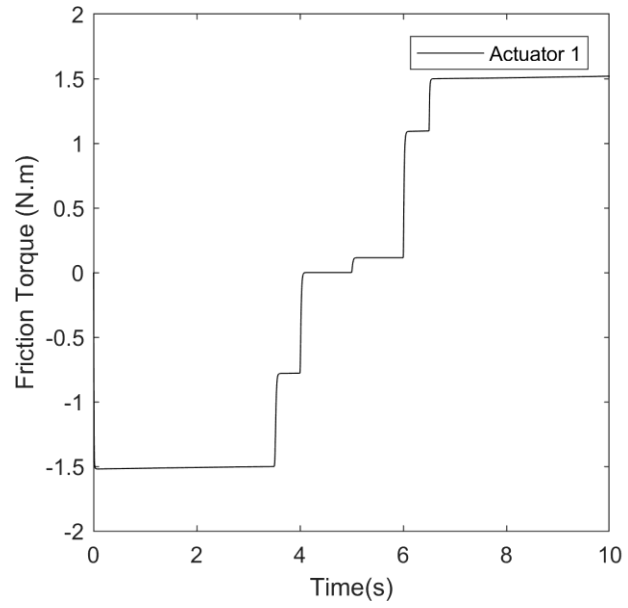


b)

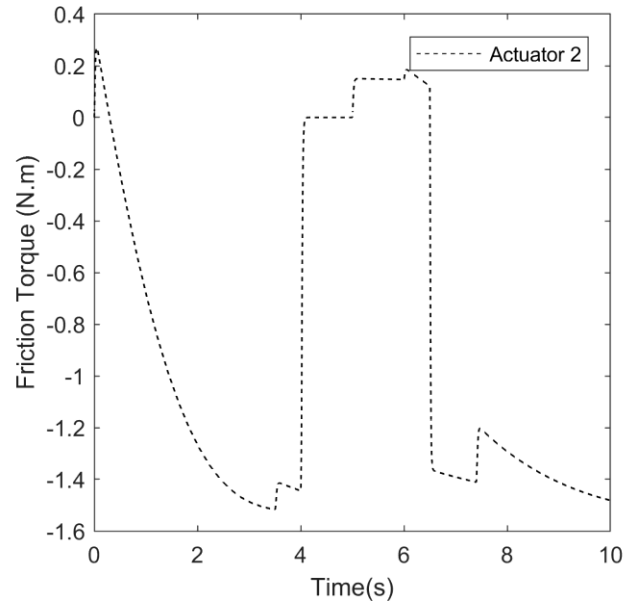


c)

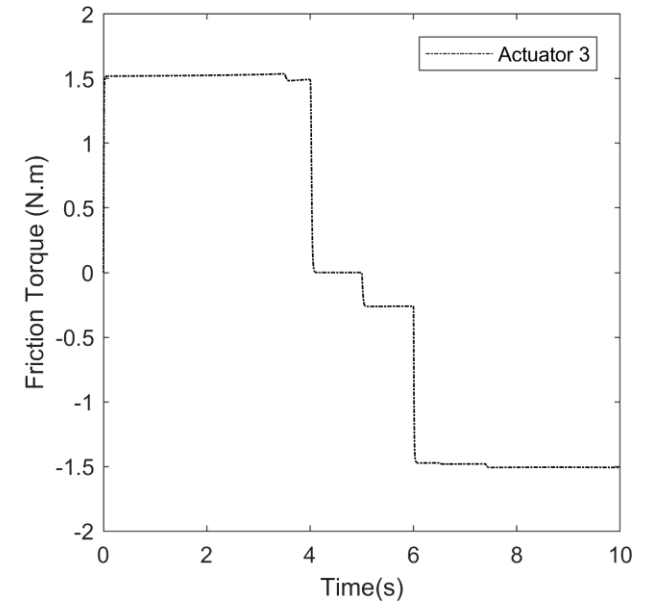
Figure 115 a-c) Total force



a)

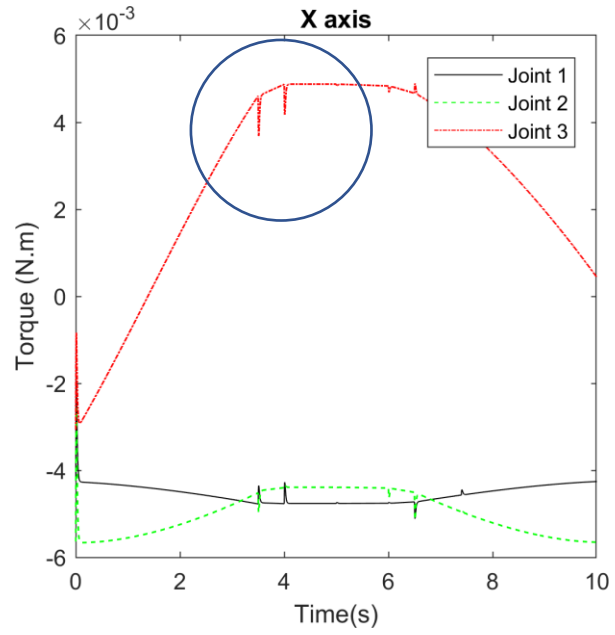


b)

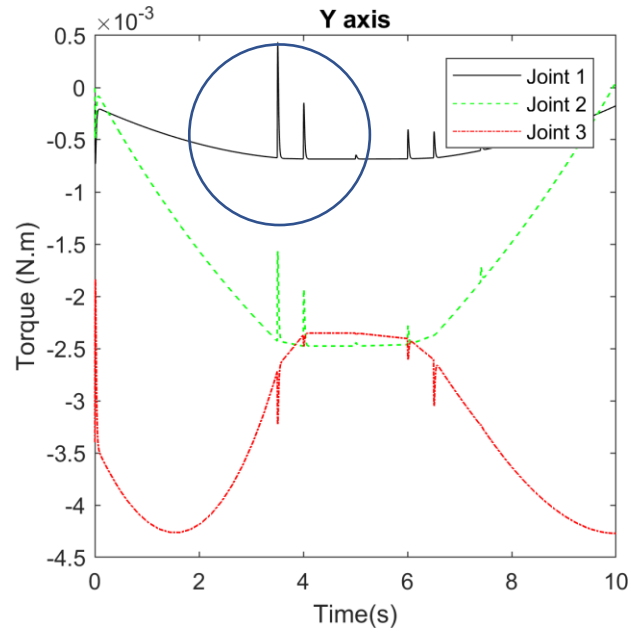


c)

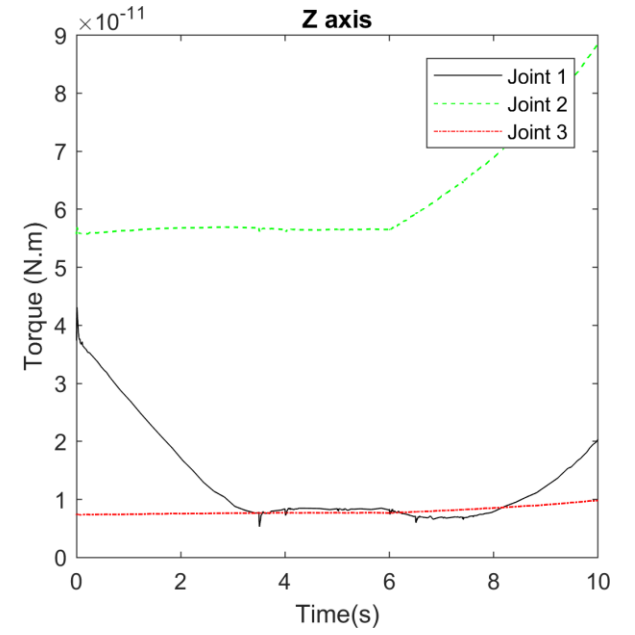
Figure 116 a-c) Friction torque at revolute joint



g)



h)

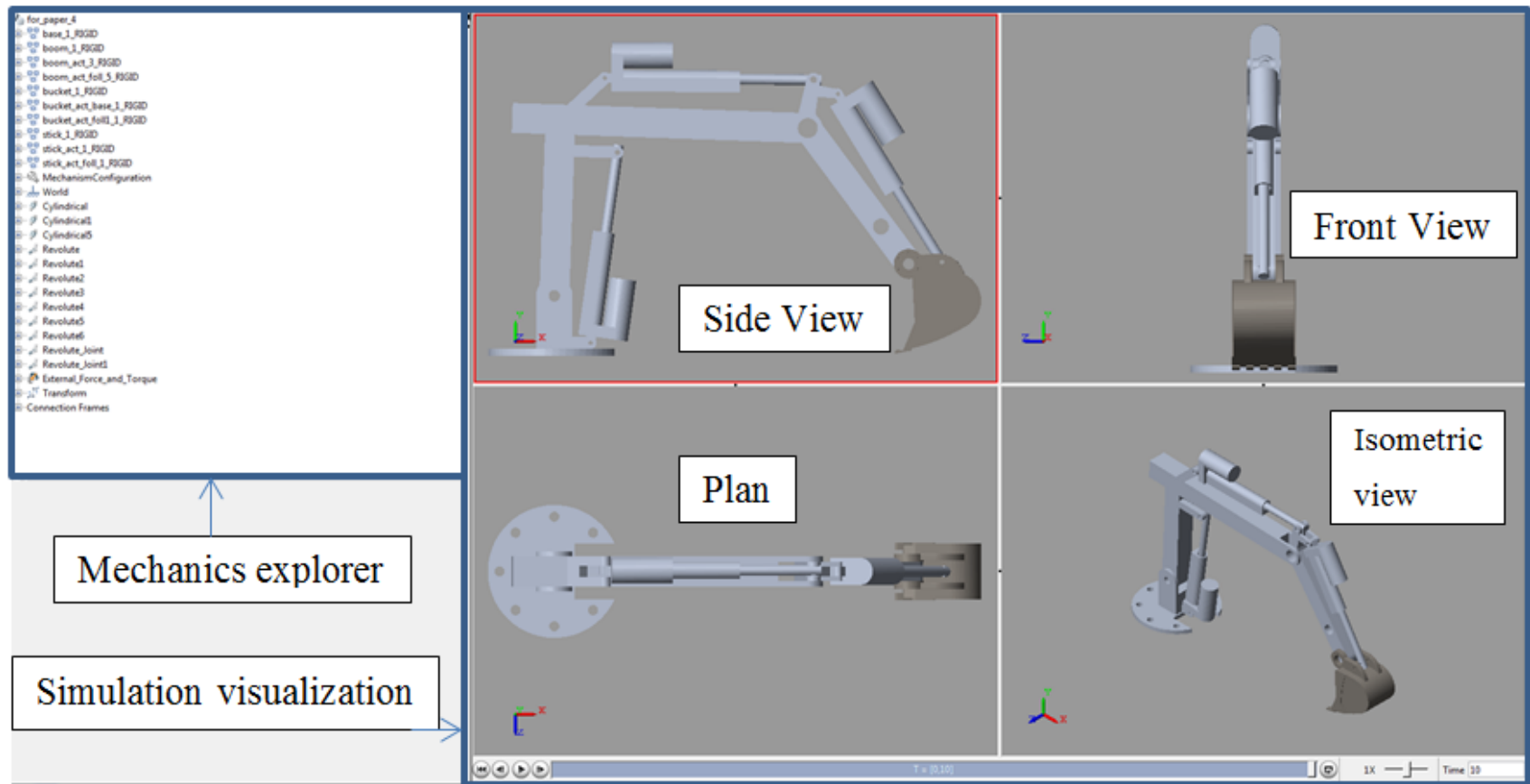


i)

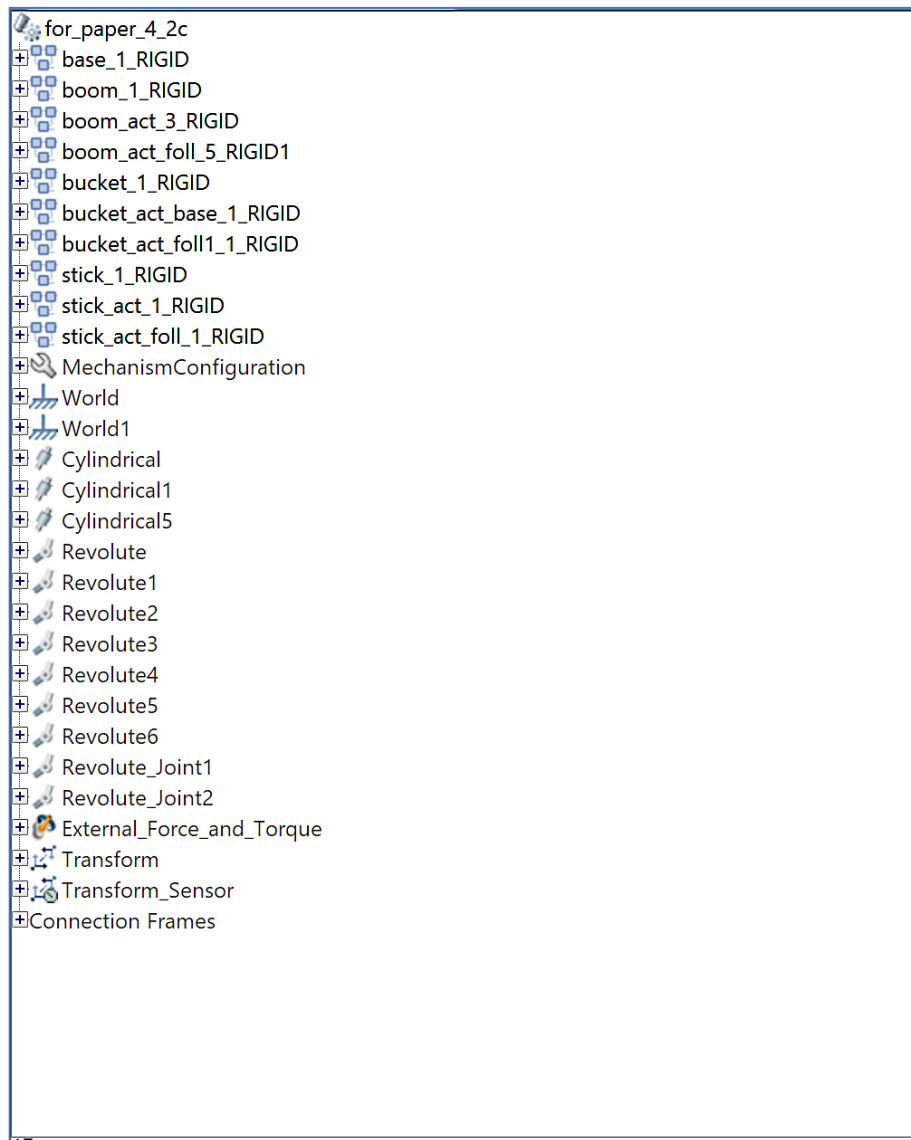
Figure 117 a-c) Torque



The information conveyed through the use of two-dimensional graphical representation of data for understanding manipulator behaviour in three-dimensional space is limited. This is overcome by using the three-dimensional visualisation of the manipulator operating in three-dimensional space using the mechanics explorer window which displays the simulation (Figure 118). This is a major advantage of the MBD environment since it does not require separate generation of visualisation of mechanics simulation. In the figure, the mechanics explorer shows the model tree i.e., names and properties of the links, which in this case were named base, boom, stick and actuators after the main links of the excavator manipulator. The four windows on the right-hand side of the image displays the perspective views of the manipulator mechanism. The reference frames for the different axes, the centres of gravity and coordinate axis assignments for each link as well as joint of the mechanical linkage is displayed in the mechanics explorer window. The use of this technique reduces the reliance on building physical prototypes of the manipulator mechanism resulting in time and cost-savings.



a)



b)

Figure 118 a) Mechanics explorer window showing the dynamic simulation views and b) components of the simulation model

## 6.3 Discussion

The CAD-MBD approach was successfully applied as shown in this chapter and the process is evaluated as part of addressing the first research objective.

### 6.3.1 Evaluation of CAD-MBD simulation analysis

#### 6.3.1.1 Advantages

The following are some of the advantages of CAD-MBD simulation analysis:

- i. Ease of modelling, rapid product development and virtual prototyping: complex shapes and designs can be modelled, incorporating the

material for the link, with comparative ease for improved simulation accuracy. Time taken from design inception to completion is considerably shortened. Design iterations are made easier.

- ii. Evaluation of complex designs: Derivation of numerical or equation model is a complex task. Using CAD-MBD, the process of deriving modelling equations is automated. Control system design parameters can be obtained from the model.
- iii. Ease of assigning link materials: Links can be assigned suitable material and the performances analysed.
- iv. Accurate modelling: Instead of assuming the centre of gravity to be link centric, this approach allows for calculation of centre of gravity based on geometry and material which ensures greater accuracy.
- v. Design validation and verification, analysis of kinematic coordinate frames assignment: Interference checks can be conducted easily. Coordinate frames can be viewed in the visualisation which enables simultaneous verification and validation of the process.
- vi. Elimination of errors in equation modelling: Likelihood of errors in the complex equations are higher, which is eliminated by using this approach.
- vii. Friction model: Joint friction model is incorporated into the simulation.

#### **6.3.1.2 Disadvantages**

Some disadvantages of MBD simulation analysis are as follows:

- i. Modelling equations are not explicitly accessible.
- ii. Only NE method is followed.
- iii. Inclusion of friction modelling slows simulation. Coefficients in the friction model are required to be experimentally determined.
- iv. While importing from CAD to MBD environment, errors may be propagated e.g. some distances which are assumed to have null value may have very minute positive values (of the order of  $10^{-16}$  to  $10^{-17}$ m).
- v. Visual implementation of soil tool model does not seem possible in this simulation environment.

Comparing the advantages and disadvantages of the technique, it becomes evident that using the technique for analysis of prototypes during initial stages of design, and during subsequent design iterations, not only shortens design cycles considerably but also yields accurate, usable results.

#### **6.4 Summary**

In this chapter, the results of simulations of the anthropoid mechanism and closed-loop manipulator were presented using three case studies following the same pattern presented in Chapter 4 namely i) the anthropoid manipulator, ii) the serial open chain manipulator and iii) the closed loop manipulator. Simulation results were successfully validated using the serial open-chain linkage and first kinematic loop of the closed-loop linkage in SimMechanics 1<sup>st</sup> and 2<sup>nd</sup> generation simulation platforms. The simulation results included kinematics, dynamics and friction dynamics which were computed for different sets of input signals. A brief discussion on the advantages and disadvantages of using this approach, in light of successfully carrying out design and simulation, was also presented. The kinematics for the reciprocating tribometer was computed and is presented in Chapter 7.

## Chapter 7 Results and discussion – 2: Tribological analysis of 16MnCr5 and EN19 steels

### 7.1 Introduction

In this chapter, the results of tribological analysis of 16MnCr5 and EN19 steels (discussed in Chapter 5) are presented. This chapter has two subdivisions: Part 1 deals with the experimental determination of the coefficient of friction (COF) for 16MnCr5-EN19 steel alloy pair and part 2 deals with the experimental determination of COF for 16MnCr5 alloy coated with nickel alumina nanocomposite and EN19 pair.

From literature review presented in Chapter 3, the understanding of grease-lubricated contacts is very limited. For this purpose, experiments on oil lubricated contacts were conducted to provide reference values for grease lubricated contacts in the uncoated and coated 16MnCr5 steels against the EN19 counter-face. Also, since literature review revealed that oil lubrication would be infeasible for SAR applications, assessment of tribo-characteristics of grease lubricated contact was the focus of this study. In part -2, experimental determination of COF was conducted for grease lubricated contacts to be compared against the grease lubricated contacts of the uncoated specimens. The schematic is presented in Figure 119.

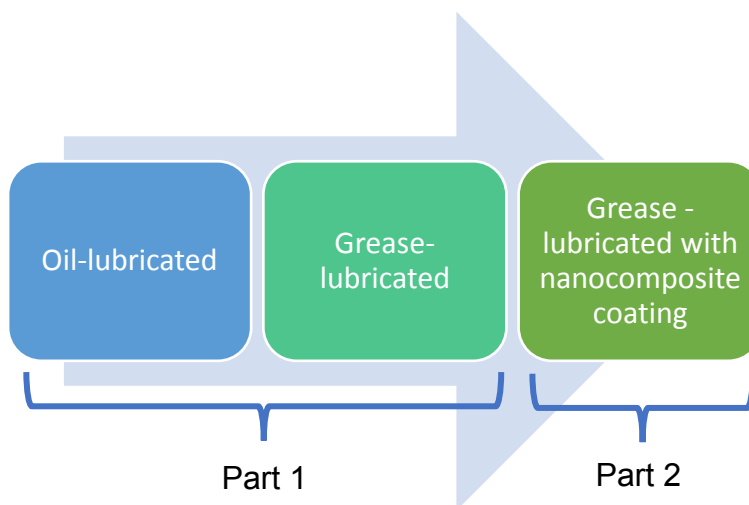
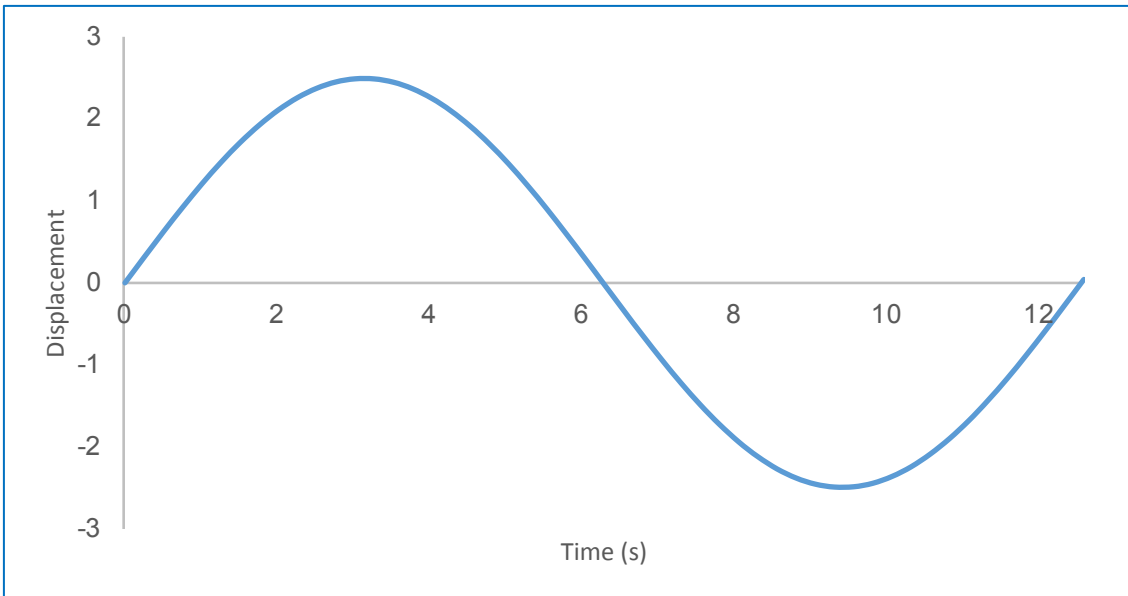


Figure 119 Classification of test results based on lubrication

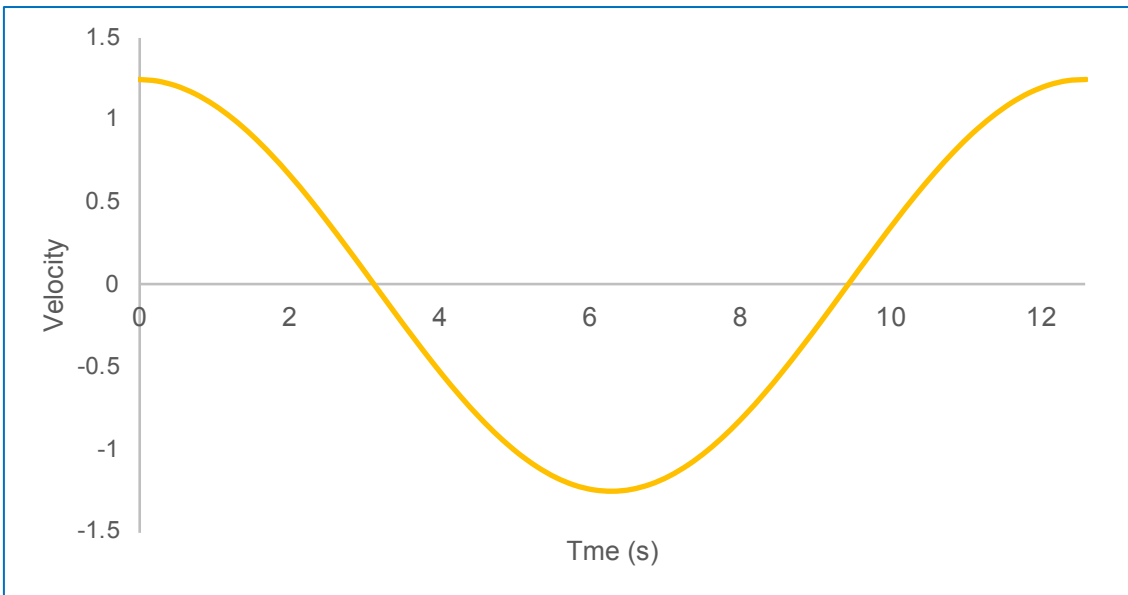
The tribo-performance characteristics of 16MnCr5-EN19 steel alloy pair have not been widely reported in literature and as it was selected as the material pair for experimental investigation of mainly COF, the effect of coating was investigated in this work to evaluate feasibility for application in the SAR environment. Nickel alumina nanocomposite coating deposition of 16MnCr5 using pulse electro deposition (PED) has not been reported and so far, and therefore was analysed and presented in part-2. For reporting results with confidence, standard deviation and standard error was calculated for each set of the experimental results and presented in the respective sections. The equations for calculating these values are presented in Appendix M.

## **7.2 Simulation of tribometer kinematics**

In this research, analysis of the coefficient of friction (COF) generated in the sliding contact of the 16MnCr5-EN19 alloy pair was conducted using the reciprocating tribometer described in section 5.2.1 of Chapter 5. Kinematic equations for the tribometer were developed and presented in section 5.2.2 of Chapter 5. Using these equations, the displacement, velocity and acceleration of the scotch-yoke mechanism used in the tribometer to convert rotatory motion from the electric motor to the reciprocating motion of the slider was computed in Simulink and the results of simulation are presented below. This provides insight into the entrainment velocity of the lubricant entering the contact, which is an important factor influencing the performance of grease lubricant in sliding contacts and consequently the COF generated in the contact. The tribometer kinematics were simulated by setting the value of displacement of the scotch-yoke mechanism to  $(r =) \pm 2.5\text{mm}$  and frequency to  $(F =) 10\text{Hz}$ . The corresponding peak velocity and acceleration were computed as  $\pm 1.25\text{mm/s}$  and  $\pm 0.6242\text{mm/s}^2$  respectively.

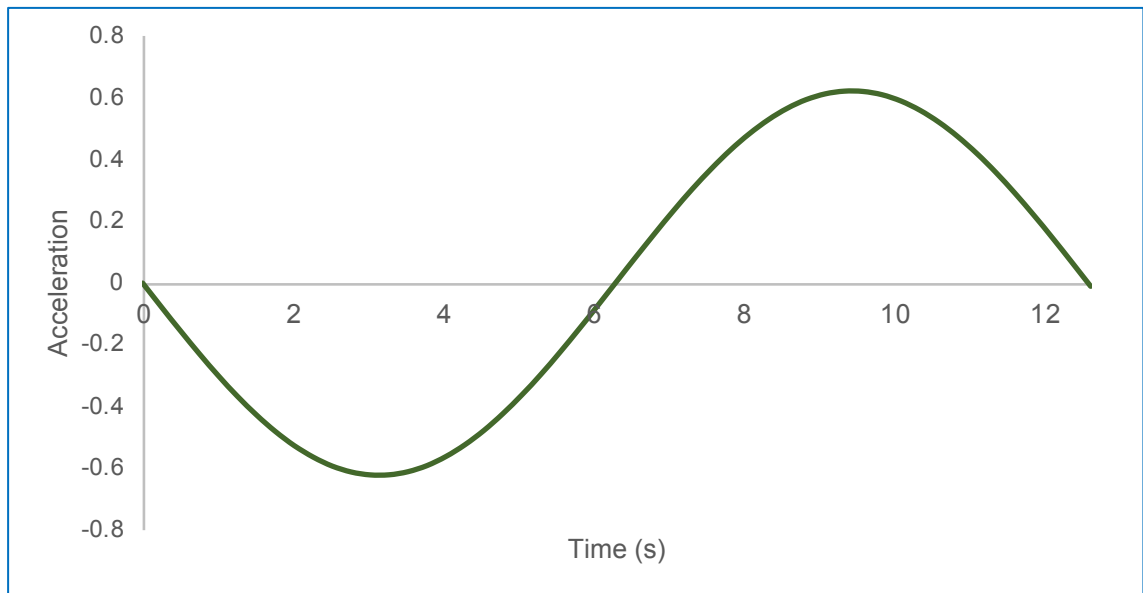


a)



b)





c)

Figure 120 Kinematics of the reciprocating mechanism for  $r = 5\text{mm}$  and frequency  $F = 10\text{Hz}$   
a) displacement (mm) b) velocity (mm/s) and c) acceleration (mm/s<sup>2</sup>)

Firstly, experimental determination of COF for uncoated 16MnCr5 and EN19 steel alloy pair is presented in the following section.

### **Part – 1: Experimental determination of COF for uncoated 16MnCr5 and EN19 steels**

In chapter 4, the combined friction model was incorporated into the simulation of mobile manipulators designed for SAR operations. However, owing to the limitations of the friction model in terms of accurately representing the actual physical joint and difficulties in obtaining accurate parameters for such a model, the experimental determination of COF for the selected joint was conducted using level 3 and level 4 tribo-simulation according to the guidelines presented in literature (Blau 2001), as presented in section 3.1. These tests were conducted on the 16MnCr5-EN19 steel alloy pair which was selected based on its widespread use in the manufacture of commercial equipment parts as presented in section 3.1.1 of the literature review.

The importance of the COF and friction characteristics of the sliding joint contact was presented in section 2.2.3 of the literature review. Currently, the

understanding of grease-lubricated contacts is very limited and also tribo-performance characteristics of 16MnCr5-EN19 steel alloy pair has not been widely reported in literature as discussed previously. Therefore, considering the importance of COF in SAR equipment, the analysis was carried out and the results are presented below. It may be noted that in the graphs presented, the abscissa and ordinate represent the data count and COF respectively.

### **7.3 Sliding cylindrical contacts**

Friction characteristics of the grease-lubricated sliding cylindrical tribo-contacts were measured in the tribo-tests using the TE57 reciprocating tribometer as explained in Chapter 5. Test parameters are recapitulated below:

- i. Load range: 10N to 40N load was used (10,25,40) for conducting these tests and the tests conducted using 40N load was used to compare the COF's across different contact conditions,
- ii. Lubricant: Two types of lubricants were used for conducting the tests, namely 10W40 engine oil and Molybdenum grease,
- iii. Surface condition: Specimen surface conditions varied in terms of roughness and hardness.

COF measurements from tests run using oil lubricant were used to generate reference COF curves for the 16MnCr5-EN19 steel alloy pair. After obtaining reference values, tests were conducted to measure the COF using molybdenum grease-lubricated contact over the same load range. All tests were conducted under fully-flooded conditions to simulate well-lubricated operation conditions.

#### **7.3.1 COF from tribo-analysis**

The following nomenclature is used to identify test specimens:

- 'CO' denotes cylindrical oil-lubricated contacts,
- 'CG' denotes cylindrical grease-lubricated contacts.

##### **7.3.1.1 Oil-lubricated contacts**

The tests were conducted for 40N load and the measured COF data is presented in Figure 121. Oil-lubricated contacts exhibited a steady-state COF.

The average and maximum values of COF recorded ranges from 0.0710 to 0.0807 and from 0.0985 to 0.1032 respectively as shown in Table 14 below. For the COF measurements, standard deviation was calculated as  $s = 0.0049$  and standard error as  $\sigma = 0.0028$ . Oil being a freely flowing lubricant maintains a continuous film in the contact under an entrainment velocity of 1.25mm/s (as presented in section 7.2).

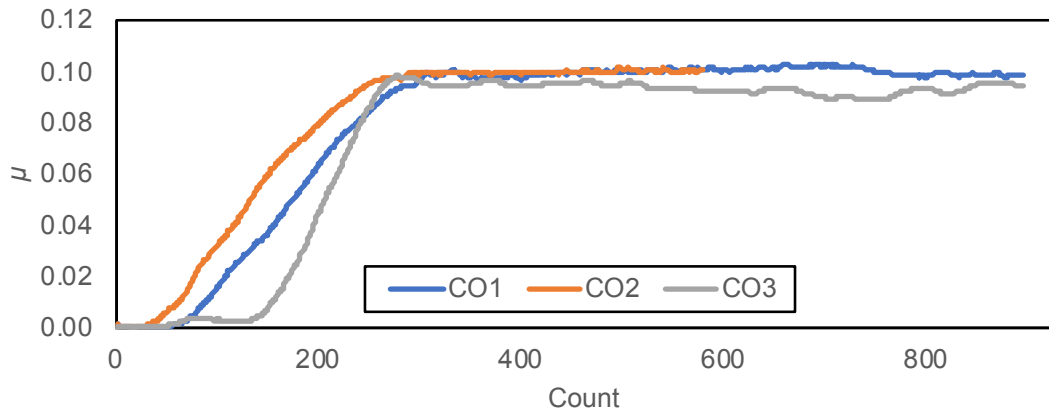


Figure 121 COF for oil-lubricated sliding cylindrical contact

Oil		Average COF	Maximum COF
40N	CO1	0.0807	0.1032
40N	CO2	0.0763	0.1025
40N	CO3	0.0710	0.0985

Table 14 Average and maximum COF for sliding oil-lubricated cylindrical contacts

### 7.3.1.2 Grease-lubricated contacts

Similarly, results from tribo-tests conducted for grease-lubricated contacts are presented in this section. COF characteristics curves for test results are presented below from Figure 122. Different loads in the range of 10N to 40N were used for conducting the tests. COF generated for lighter loads (10N-25N) are presented in Figure 122 a and b and for heavier loads (40N) in Figure 122 c.

The average and maximum COF values are presented in Table 15. For the data presented Table 15 (CG5-CG10) standard deviation was calculated as  $s = 0.0092$  and standard error as  $\sigma = 0.0038$ . Maximum value of maximum COF was recorded in the case of the CG1 i.e. 10N load which could be attributed to intermittent contact arising from failure of lubricating film. The COF values for

CG2-CG4 (Figure 122 a and b) were observed to stabilise to the region of 0.1 during the test, which would indicate boundary lubrication as reported in literature (Armstrong-Hélouvy et al. 1994). CG3 and CG4 were run for relatively short duration as they formed initial tests and exhibited relatively smooth COF characteristics. For higher loads, COF data exhibited spikes especially in the cases of CG5 and CG6, with the CG5 data exhibited sustained spikes owing to intermittent contact between specimens throughout the test.

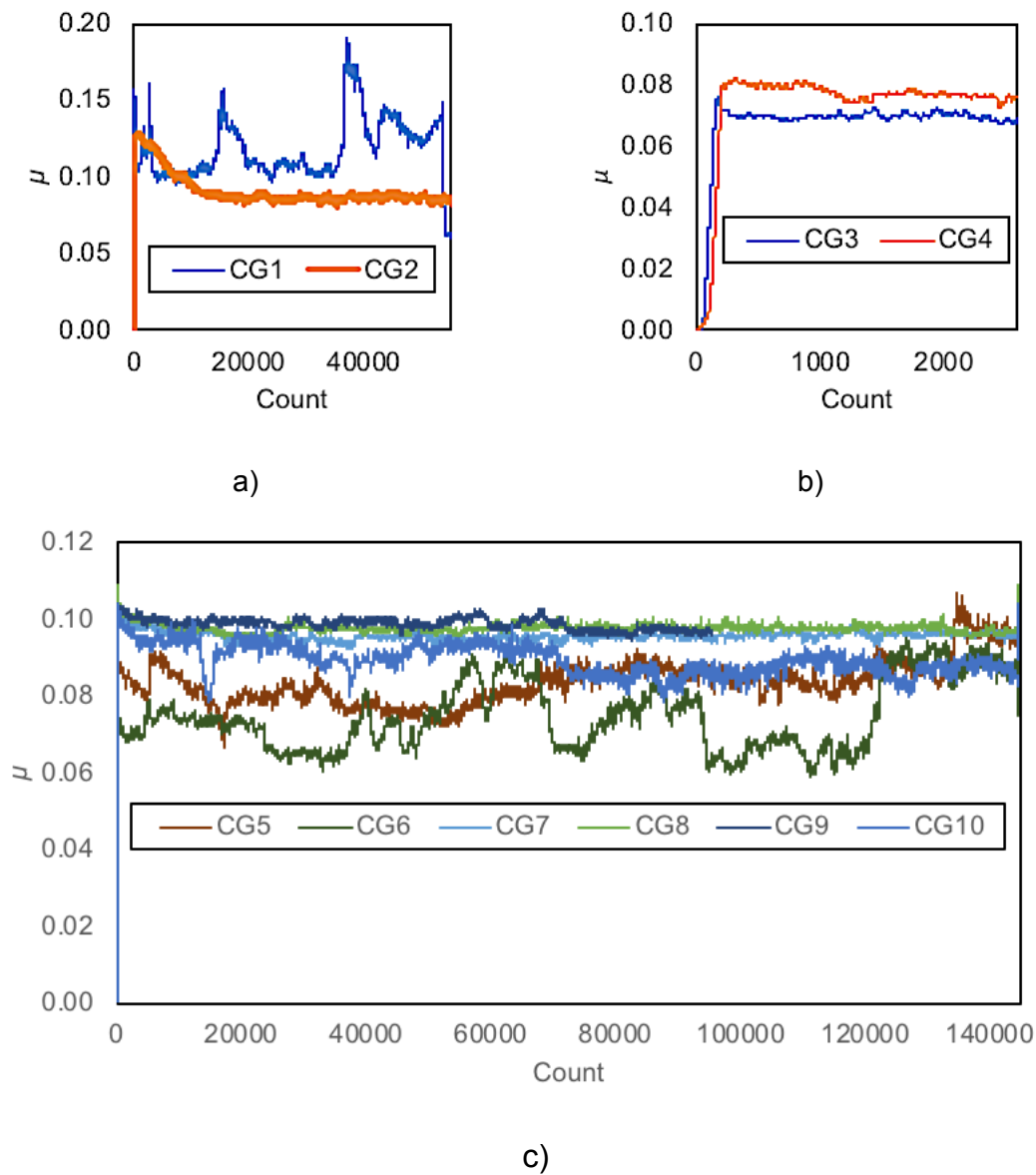


Figure 122 COF for grease-lubricated sliding cylindrical contacts

Grease		Average COF	Maximum COF
10N	CG1	0.1038	0.1904
25N	CG2	0.0896	0.1285
	CG3	0.0648	0.0859

Grease		Average COF	Maximum COF
	CG4	0.0705	0.0825
40N	CG5	0.0836	0.1067
	CG6	0.0748	0.0958
	CG7	0.0957	0.1058
	CG8	0.0977	0.1088
	CG9	0.0978	0.1040
	CG10	0.0893	0.1043

Table 15 Average and maximum COF for sliding grease-lubricated cylindrical contacts

Tests CG1 to CG4 were conducted using soft counter face fixed specimens and CG5 to CG10 were conducted using flame-hardened counter-faces and the recorded values of average COF for CG1 to CG4 ranges from 0.0648 (CG3) to 0.1038 (CG1); average COF for CG5 to CG10 ranges from 0.0748 (CG6) to 0.0978 (CG9).

Even though other parameters such as frequency, temperature and lubrication were time-invariant for the tests, a large variation in COF within tests results for the same type of contact as well between different contact conditions which included geometry of counter-face and lubricants was observed. COF measurement and characteristics for the sliding pin contact is presented in the following section.

## 7.4 Sliding pin contacts

Friction characteristics which were experimentally measured for the sliding pin contacts using similar test parameters as for sliding cylindrical contacts are reported here. Oil lubricant was used to generate reference COF values for the steel alloy pair in the same manner as of the cylindrical sliding specimens. The values of COF for tests conducted using molybdenum grease are presented and compared.

### 7.4.1 COF from tribo-analysis

Test specimen prefixes were designated as follows:

- 'FO' denotes oil-lubricated pin contacts,

- 'FG' denotes grease-lubricated contacts.

### 7.4.1.1 Oil-lubricated contacts

COF data from the tests conducted for oil-lubricated contacts are presented in Figure 123 from which it can be observed that these tests were run for shorter durations since they exhibited relatively stable friction curves.

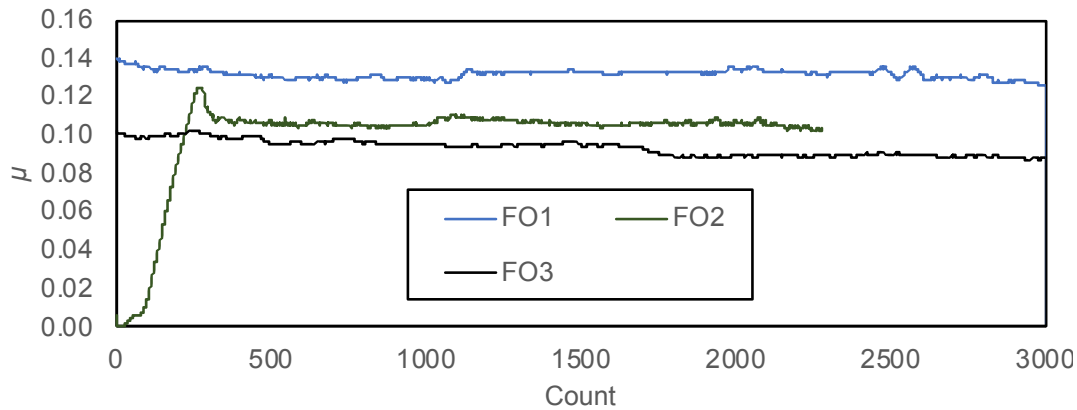


Figure 123 COF for oil-lubricated sliding pin contacts

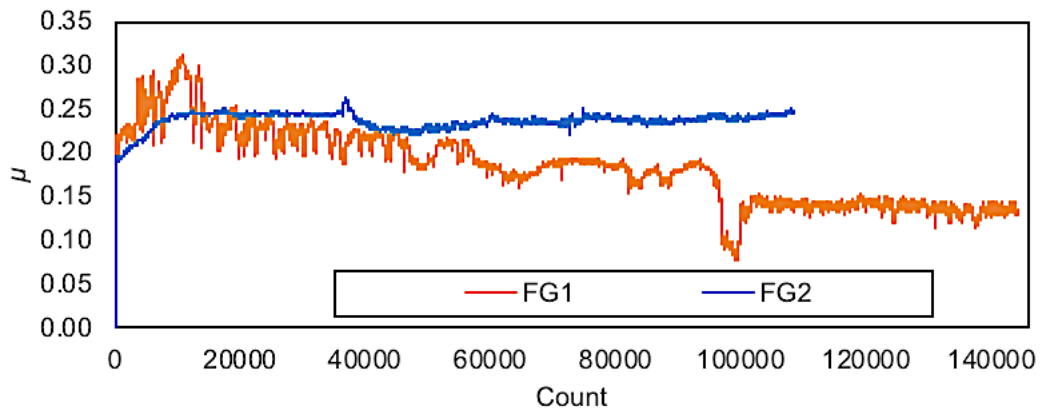
Oil		Average Friction	Maximum Friction
40N	FO1	0.1294	0.1395
	FO2	0.0996	0.1247
	FO3	0.0916	0.1024

Table 16 Average and maximum COF for sliding oil-lubricated pin contacts

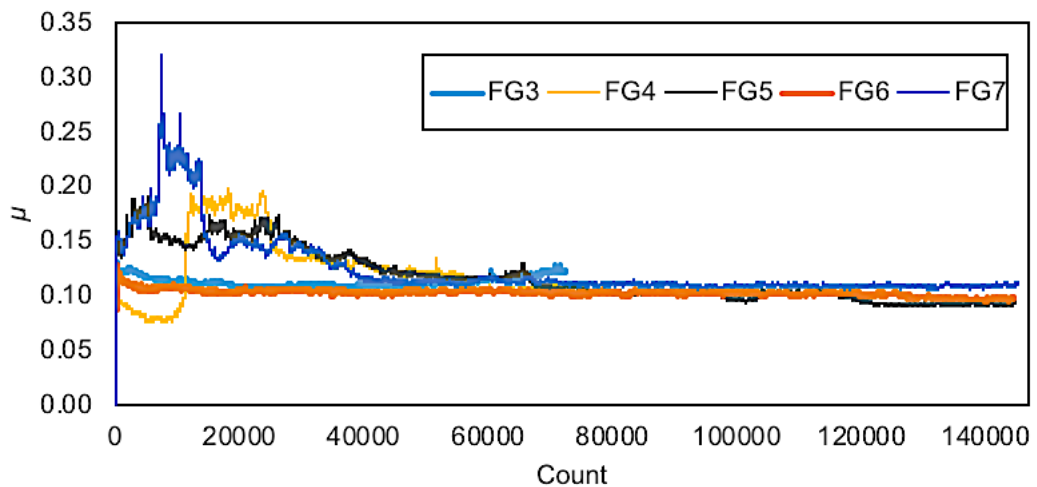
The maximum and average COF recorded for the individual tests are presented in Table 16 and standard deviation was calculated as  $s = 0.0199$  and standard error  $\sigma = 0.0115$  for this data set. The average COF values ranged from 0.0916 for FO3 to 0.1294 for FO1 and maximum COF values ranged from 0.1024 for FO3 to 0.1395 for FO1.

### 7.4.1.2 Grease-lubricated contacts

COF data from the tests conducted for grease-lubricated contacts are presented in Figure 124.



a)



b)

Figure 124 COF for grease-lubricated sliding pin contacts

From Figure 124 a) it can be seen that the COF for 10N load presented against FG1 starts off with high values i.e. greater than 0.2 and falls to the range of 0.15 at the end of the test. FG2 had similar COF values which were sustained throughout the test period while FG3 presented a smooth curve despite the short test duration. From Figure 124 b), it was observed that FG4 to FG5 presented initial spikes in measured COF data which settled down as the test progressed. Compared to these, FG6 and FG7 showed almost identical COF characteristics for the duration of the test although FG7 exhibited a spike in the value at the beginning of the test which occurred due to breakdown in lubrication.

Grease		Average Friction	Maximum Friction
10N	FG1	0.2548	0.3104
	FG2	0.2265	0.2474
40N	FG3	0.1132	0.1313
	FG4	0.1263	0.1975
	FG5	0.1176	0.1913
	FG6	0.1028	0.1292
	FG7	0.1241	0.3198

Table 17 Average and maximum COF for sliding grease-lubricated pin contacts

The average and maximum COF values are presented in Table 17 for which standard deviation was calculated as  $s = 0.0094$  and standard error  $\sigma = 0.0042$ . For these experiments, average COF value varied from 0.1028 for FG6 to 0.2548 for FG1. The maximum friction varied from 0.1292 for FG6 to 0.3198 for FG7.

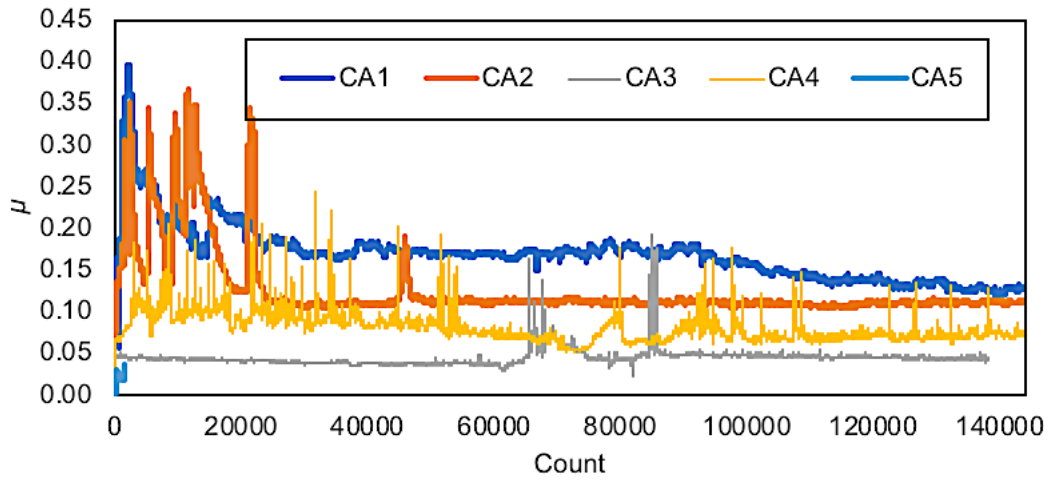
## Part – 2: Experimental determination of COF for coated specimens

This section presents the results of COF for both sliding cylinder and sliding pin contacts in which the 16MnCr5 specimens were coated with thick film of nickel alumina nanocomposite coating.

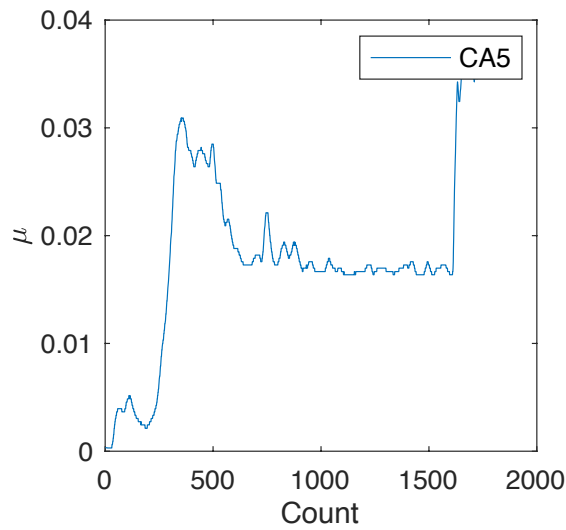
### 7.5 Sliding cylindrical contact with nanocomposite coating

In this section, COF for 16MnCr5 specimens with nickel alumina nanocomposite coating against EN19 cylinder counter-face is presented for grease lubrication. The data for these measured COFs are assigned the prefix 'CA' and the COF for five 16MnCr5 specimens coated with nickel alumina nanocomposite is presented in Figure 125 a. Specimen CA5 which failed is extracted from Figure 125 a and presented separately in Figure 125 b.





a)



b)

Figure 125 COF for grease-lubricated nickel alumina nanocomposite coated sliding cylindrical contacts

From the average and maximum COF values presented in Table 18, it can be seen that the range of average COF values varies from 0.0177 for CA5 to 0.1683 for CA1 and the range of maximum COF varies from 0.0361 for CA5 to 0.3965 for CA1. For this data, standard deviation was calculated as  $s = 0.0607$  and standard error  $\sigma = 0.0272$ .

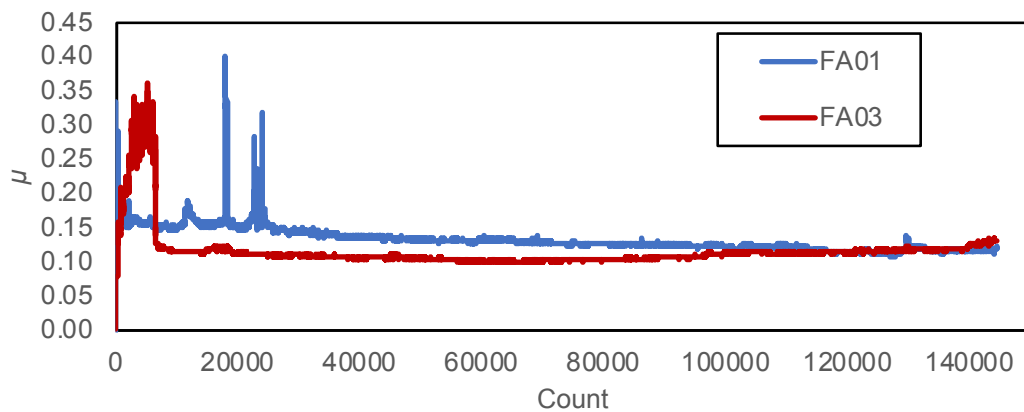
Alumina		Average COF	Maximum COF
40N	CA1	0.1683	0.3965
	CA2	0.1253	0.3656

Alumina		Average COF	Maximum COF
	CA3	0.0443	0.1931
	CA4	0.0796	0.2419
	CA5	0.0177	0.0361

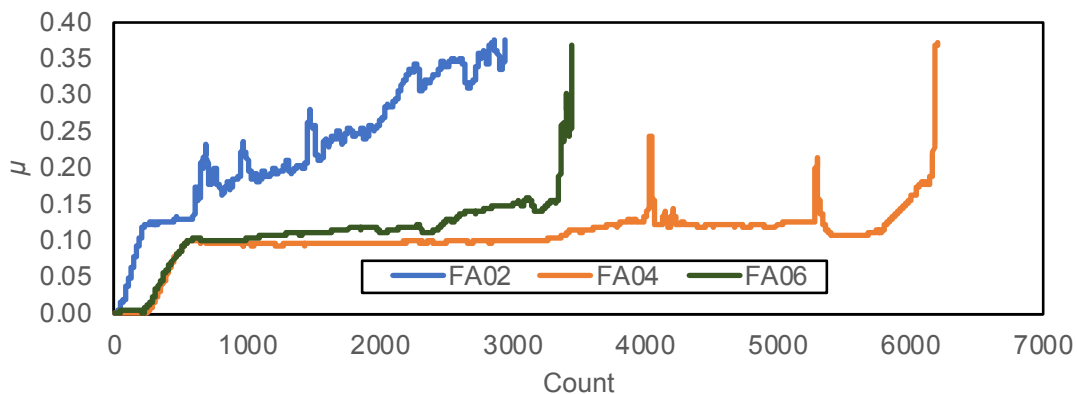
Table 18 Average and maximum COF for grease-lubricated sliding cylindrical contacts with nickel alumina nanocomposite coating

## 7.6 Sliding pin contact with nanocomposite coating

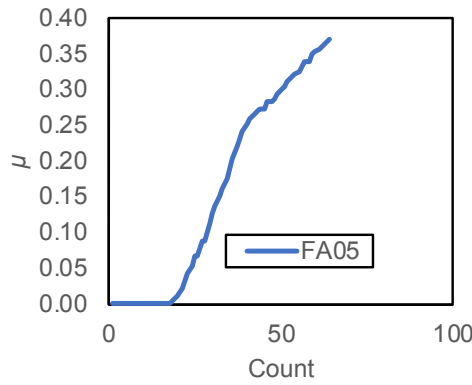
In this section, COF results from grease-lubricated nickel alumina nanocomposite coated test specimens are presented in Figure 126, and corresponding maximum and average COF recorded for the individual specimen pairs are presented in Table 19. For these specimens coated against the EN19 pin counter-face, the COF measurement data are assigned the prefix 'FA'.



a)



b)



c)

Figure 126 COF for grease-lubricated nickel alumina nanocomposite coated sliding pin contacts

Alumina		Average Friction	Maximum Friction
40N	FA01	0.1322	0.4008
	FA02	0.2273	0.3474
	FA03	0.1163	0.3632
	FA04	0.1062	0.3741
	FA05	0.1624	0.3708
	FA06	0.1114	0.3677

Table 19 Average and maximum COF for grease-lubricated sliding pin contacts with nickel alumina nanocomposite coating

The average and maximum COF are presented in Table 19 and for this data  $s = 0.0462$  and standard error  $\sigma = 0.0189$ . For grease-lubricated contacts, average COF values ranged from 0.1062 for FA04 to 0.2273 for FA03, and maximum COF ranged from 0.3474 for FA08 to 0.4008 for FA01. Tests were also conducted for nickel graphene coated sliding pin contacts and the results are presented in Appendix L.

## 7.7 Discussion

The results of experimental measurement of COF under different loads, lubrication and coating were presented for the 16MnCr5-EN19 steel alloy pair. Two contact geometries namely, cylinder on plane and pin on plane were used in order to determine the COF for oil and molybdenum grease lubricants, where oil lubricated contacts were used to generate the reference values. The COF for 16MnCr5 specimens with nickel alumina nanocomposite coating were also determined by tribo-testing.

Results indicated that oil-lubricated contacts (CO1-CO3) offered lowest COF with time-invariant COF characteristics in cylindrical sliding contacts. For the same contact geometry, grease lubricated contacts presented higher and time variant COF characteristics even for extended tests for lowest load setting of 10N. CG1 presents intermittent spikes throughout the test duration which can be attributed to the failure of lubrication between the sliding surfaces. CG2 at 25N exhibits initial increase in COF which subsequently stabilised to COF in the range of over 0.1. In the case of CG3 and CG4, with the same load of 25N, the COF stabilises between 0.06 and 0.08 and the COF is steady. For 40N tests, CG5 and CG6 exhibit considerable fluctuation in COF between 0.06 and 0.11. However, in the case of CG7, this is reduced. CG8 to CG10 exhibit steady COF throughout the duration of test.

For FO1, the COF lies in the range of 0.14 and progressively reduces during the test. For FO2, a sharp increase in the COF values at the beginning is followed by stabilisation of the curve in the region of 0.10 and for FO3, the COF values at the beginning of the test lies near the region of 0.1 and reduces the region of 0.09 towards the end of the test.

For FG1 the COF values appear to lie in the range of 0.20 and 0.25, whereas for FG2 the COF initially rises to 0.30 and drops to the region of 0.10 in the latter half of the test. For FG4, FG5 and FG7, COF values in the first half of the test shows increased values and later settles down to the range of 0.1. Contrastingly, FG3 and FG6 show stable COF characteristics. FG5 to FG7, exhibit COF in the range of 0.10 during the latter duration of the test. Sliding cylinder contact with nanocomposite coatings exhibit wider range of COF characteristics ranging from 0.05 to 0.470 again, and much of the spikes in the COF values were encountered in the former half of the test except in the cases CA3 and CA4 which continue to exhibit spikes in COF. CA2 exhibited time invariant COF characteristics in the range of 0.1 except in the latter half of the test. CA1 exhibits higher COF in the range of 0.2 coming down to range of 0.1 by the end of the test. CA5 specimen, fails from seizure after a short duration. In comparison, literature reveals COF range of ~0.065 to 0.080 for elliptical

contacts under oil lubrication (Bajwa, Khan, Nazir, et al. 2016). The novelty aspect of this research is that COF for these geometries were reported previously for this material pair as understood from literature (Mahidashti et al. 2017).

In the pin contact geometry, more failure from seizure occurred which can be attributed to the higher hardness of coating compared to the 16MnCr5 specimen. From the graphs FA01 and FA03 show initial spikes in COF values in the range of 0.3 to 0.4 after which they exhibit stable friction characteristics. Seizure occurred beyond the threshold value of approximately 0.37 in the case of FA03, FA04, FA05 and FA06.

Therefore, the use of nanocomposite coatings resulted in higher COF compared to oil-lubricated uncoated contacts. The range of values of the COF fall within the boundary lubrication conditions except in cases where abrasive contact occurred which resulted higher COF values ( $\text{COF} > 0.1$ ). Also, no clear pattern emerged between load and COF, although low loads in oil-lubricated contacts presented higher values of COF.

However, oil lubrication cannot be used for equipment operating in the field because of its free-flowing characteristic and flammability among others. Similarly, nanocomposite coatings were found to increase the COF for the selected material pair and even resulted in seizure of contact in certain cases. Contact geometries namely cylinder and pin, lubricants namely oil and grease, and surface conditions namely plain or coated are the main variables considered in the tribo-tests.

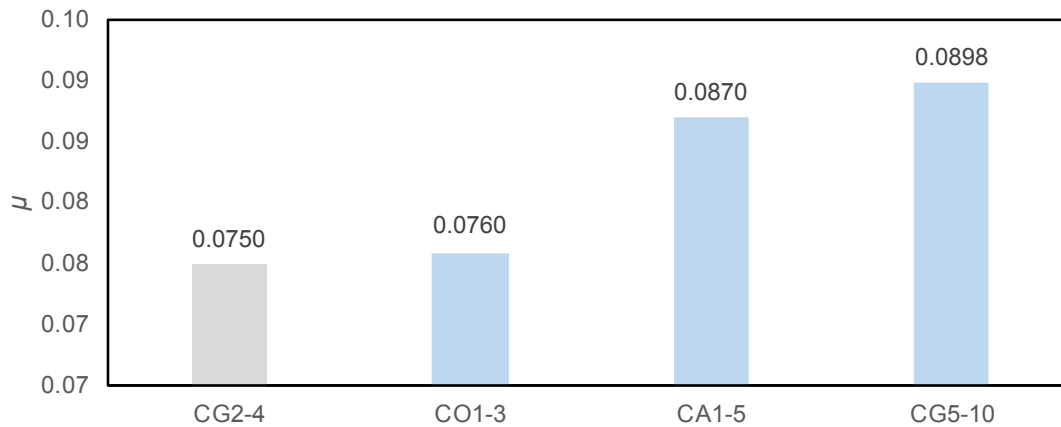


Figure 127 Average COF for coated and uncoated sliding cylindrical contacts

From the above graph for cylindrical sliding contacts (where CG2-4 represents the COF for 25N load, while the rest, for 40N), it can be concluded that:

1. Grease lubricated uncoated samples at medium load (25N) has the lowest COF followed by oil-lubricated contacts at 40N.
2. For parity, across 40N load which is the general operating load discussed in literature, oil showed the lowest COF of 0.0760 (CO1-3). COF of grease lubricated uncoated specimens (CG5-10) averaged at 0.0898, showing an increase of 17.11%. This COF was marginally improved by the nickel alumina nanocomposite coated (and grease-lubricated) specimens with average COF of 0.0870. While not very substantial, the coating shows a 3.11% decrease.

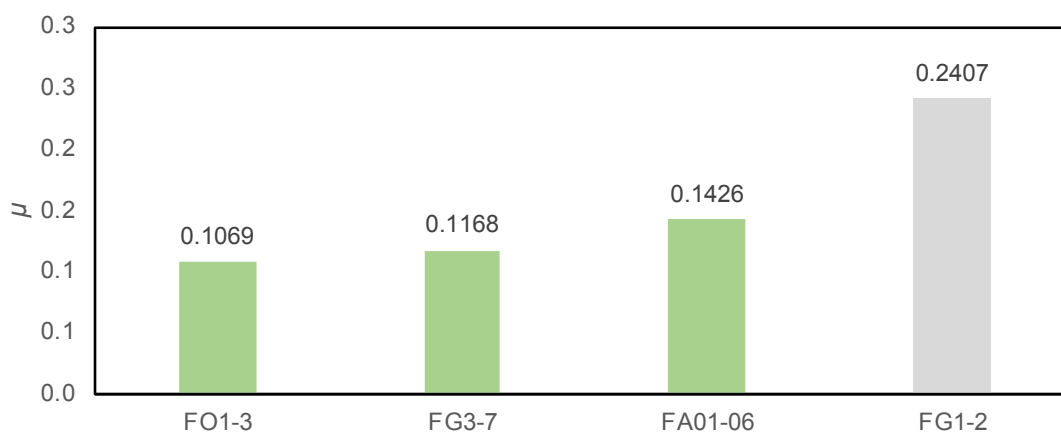


Figure 128 Average COF for coated and uncoated sliding pin contacts

Similarly, from the graph for pin sliding contacts, it can be concluded that:

3. Amongst tests conducted with 40N load, oil lubricated uncoated contacts (FO1-3) showed the least COF of 0.1069, compared to grease lubricated

uncoated sample (FG3-7) at the same load with COF of 0.1168, which is an increase of 9.26%.

4. Unlike the cylindrical sliding contact (where FG1-2 represents the COF for 10N load, while the rest, for 40N) grease lubricated uncoated specimens exhibits a lower average COF compared to nickel alumina nanocomposite coated specimens i.e. 0.1168 against 0.1426, implying that the coating did not help lower COF even marginally and to the contrary, COF for uncoated samples were 22.1% better than coated samples.

Where grease lubrication was successful, the results above are supported by (Lugt 2016) in that that molybdenum grease lubrication lowers COF i.e. in the case of sliding cylindrical contacts, COF for oil and grease lubricated contacts do not show any substantial difference.

Of the two contact geometries, the sliding cylinder contact in general shows better COF characteristics than sliding pin contact given that even the COF of oil lubricated uncoated samples of pin contact is greater than that of the highest value of the average COF of the sliding cylindrical contact as expected.

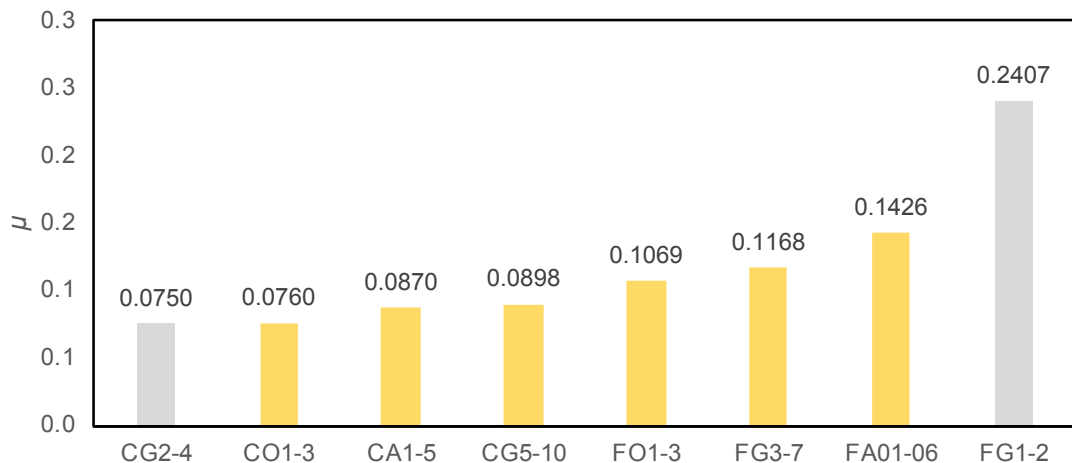


Figure 129 Average COF for coated and uncoated sliding pin and cylindrical contacts

While nickel alumina nanocomposite coating has shown marginal improvement of COF in sliding cylindrical contact, the opposite is seen in sliding pin contact i.e. the nickel alumina nanocomposite coating proves to be detrimental to the improvement of COF. This may be attributed to the contact geometry of the pin

sliding contact since the nanocomposite coating gets removed in the initial abrasive wear that occurs in the contact.

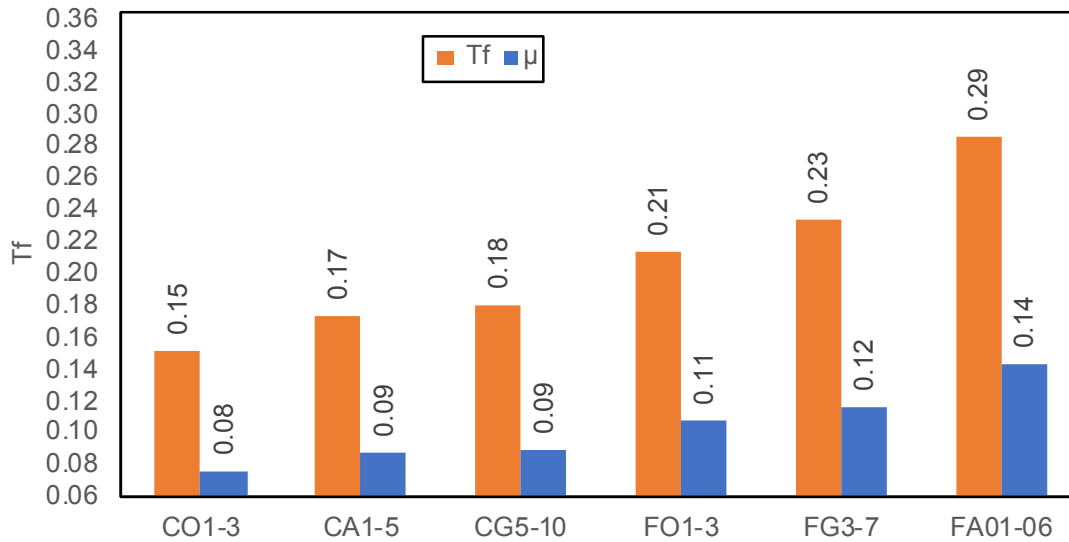


Figure 130 Friction computed using the equation presented in (Colbert et al. 2010)

Since the load and radius of the simple friction contact parameter remain time-invariant, the computed friction torque also remains proportional to the COF. The COF measured using the tribometer was used to compute friction torque and these values are presented along with the corresponding COF in Figure 130. Pin sliding contacts with nickel alumina nanocomposite coating presents the maximum friction torque followed by pin sliding uncoated specimens and oil lubricated pin specimens. Among the sliding cylindrical contact specimens, grease lubricated uncoated specimens present the maximum friction torque, followed by alumina coated specimens and oil lubricated uncoated specimens. Oil lubricated contacts present a good solution to COF reduction; however, because of the fluid nature of this lubricant among others and design constraints involving oil lubricated joints, this type of lubricant cannot be used for SAR environments. Also, the estimated torque presented in Figure 130 is expected to be an underestimation and more accurate estimations can be made through a pertinent numerical model (Colbert et al. 2010). Therefore, grease-lubricated contacts still remain the viable design solution in terms of COF and offer best performance under the given conditions.



In order to accommodate the dimensional change, as well as deviation due to reduced manufacturing tolerance, two novel specimen holders or adapters were designed, fabricated and successfully deployed.

### Part – 3: Analysis of surface characteristics

#### 7.8 Measurement of surface hardness

Results of the Vickers micro-indentation tests conducted using two loads namely 1kgf and 5kgf corresponding to ~10N and ~50N at loading speed of 40µm/s and 5s loading time are presented for uncoated and coated specimens in this section. For coated samples, coating current was also reported to correlate load, coating current and hardness.

Sample	Load (kgf)	HV	Mean	Standard Deviation (s)	Standard Error ( $\sigma$ )
CO1	1	210	210.0	0.0	0.0
		210			
		210			
CG6	5	208	206.5	1.9	1.0
		208			
		204			
		206			
CG9	5	190	195.7	6.0	3.0
		195			
		202			

Table 20 Results of Vickers micro-indentation tests for uncoated 16MnCr5 specimens

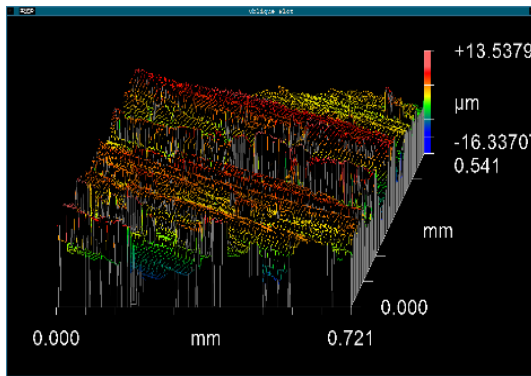
Sample	Coating current (A)	Load (kgf)	HV	Mean	Standard Deviation (s)	Standard Error ( $\sigma$ )
FA01	0.70A	1	330	327.3	13.2	6.6
			339			
			313			
CA1	0.70A	5	303	294.5	6.2	3.1
			296			
			286			
			293			
CA4	0.35A	1	263	251.3	15.3	7.7
			257			
			234			
CA3	0.35A	5	241	220.5	9.6	4.8
			234			
			221			

Table 21 Results of Vickers micro-indentation tests for coated 16MnCr5 specimens

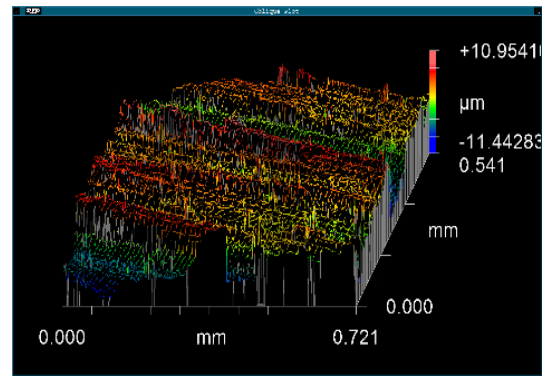
The consolidated results of the micro-indentation tests to measure hardness are presented in Table 20 and Table 21 along with the corresponding standard deviation and standard error parameters for the measurements. The specimens were machined from the same stock bar and coated under identical conditions. Therefore, averaging of the hardness over each selected specimen surface was conducted. Specimens tested under 1kgf load include CO1, CA4, FA01 and the latter specimens are coated with nickel alumina nanocomposite coating. Specimens tested using 5kgf load include CG6, CG9, CA1 and CA3 of which the last two specimens are coated with nickel alumina nanocomposite. CO1 presented 210HV whereas CG6 presented 206.5HV and CG9 presented 195.7HV for the 16MnCr5 specimens without coating. For coated specimens, CA4 and FA01 presented 251.3HV and 327.3HV under 1kgf load and CA1 and CA3 presented 294.5HV and 220.5HV respectively. Hardness of CA4 and CA3 were measured under 1kgf and 5kgf respectively and these specimens were coated using 0.35A current during the PED process and these specimens present lower hardness compared to FA01 and CA1 which were coated using 0.70A and from this it can be concluded that specimens coated under higher current possess increased hardness. For the same coating current, higher micro indentation test load lead to a decrease in measured hardness.

## **7.9 Measurement of surface characteristics**

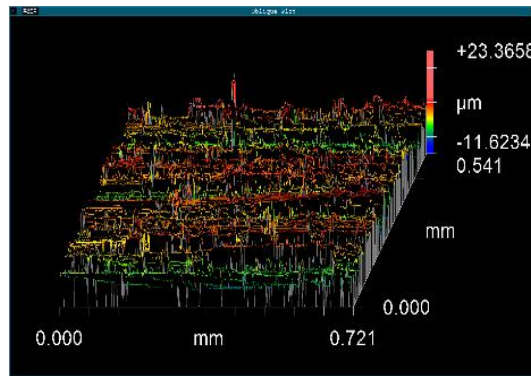
White light interferometry was used to analyse the 16MnCr5 specimen surfaces in their original rough state (when received from the manufacturer) and after polishing. Three specimen surfaces were analysed after the deposition of nickel alumina nanocomposite coating were also analysed using the same technique prior to experimentation in order to obtain reference values for surface roughness. Three-dimensional surface profiles were generated, and these are presented in Figure 131: a-e present profile of rough surfaces, f-j present profile of polished surfaces and k-m present profile of coated surfaces. The size of the measured area in these samples is 0.72mm by 0.54mm.



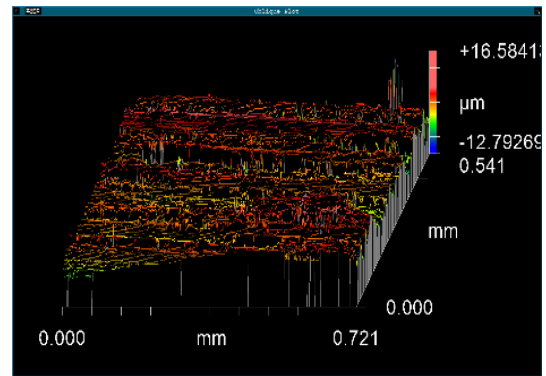
a)



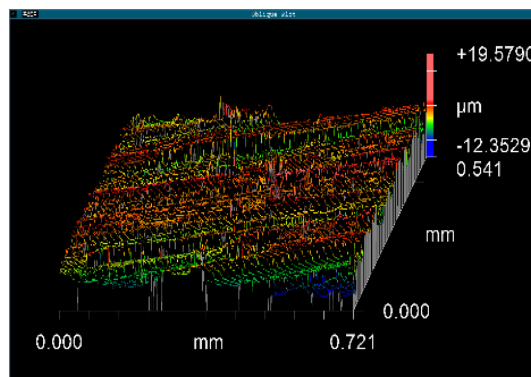
b)



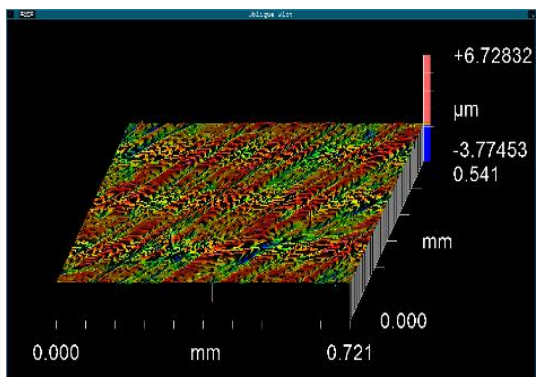
c)



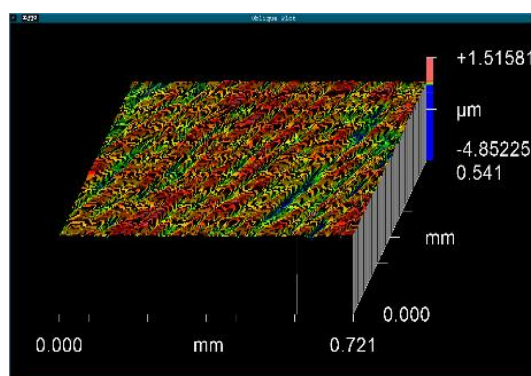
d)



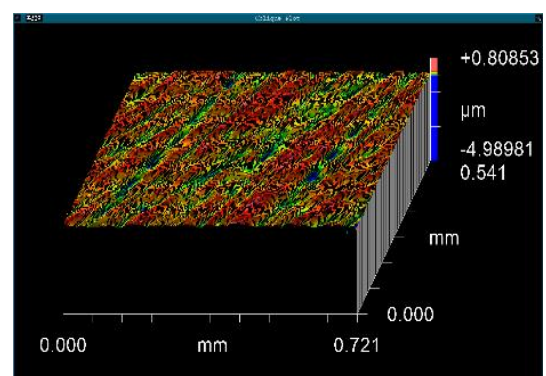
e)



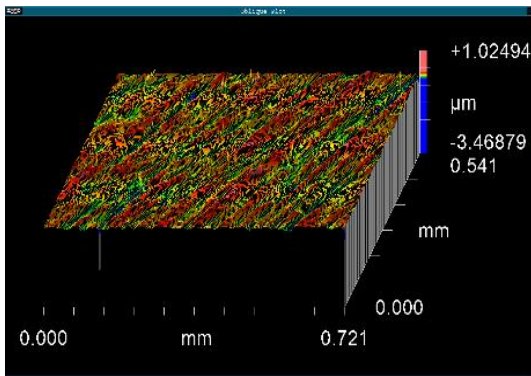
f)



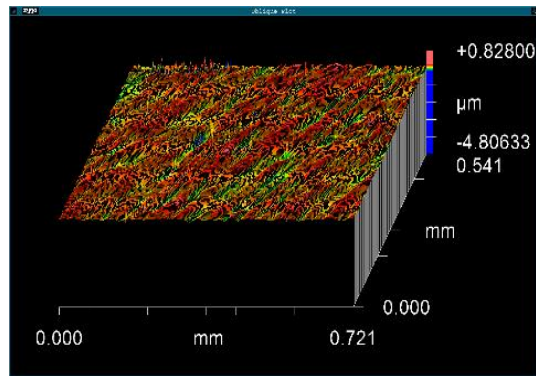
g)



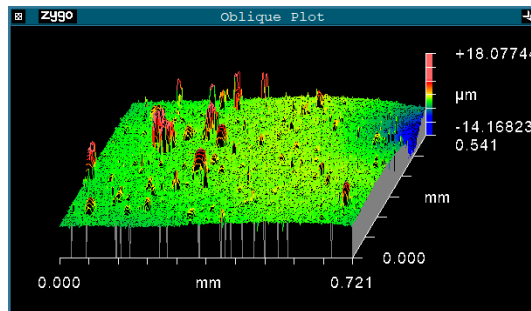
h)



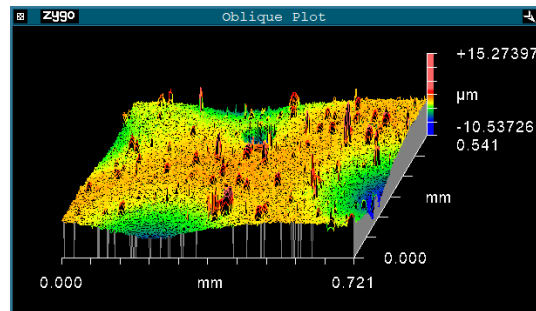
i)



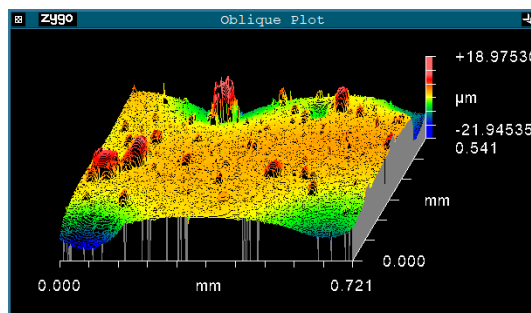
j)



k)



l)



m)

Figure 131 a-e) Profiles for rough surfaces, f-j) profiles for the polished surface and k-m) coated surface profiles

The surface characteristics are consolidated and presented in Table 22 where PV stands for the maximum value, RMS stands for root mean squared and  $R_a$  stands for the roughness average.

Specimen name	Maximum Value ( $\mu\text{m}$ )	RMS ( $\mu\text{m}$ )	$R_a$ ( $\mu\text{m}$ )
a)	29.875	4.001	3.227
b)	22.397	3.814	3.165
c)	34.989	3.587	2.922

Specimen name	Maximum Value ( $\mu\text{m}$ )	RMS ( $\mu\text{m}$ )	$R_a$ ( $\mu\text{m}$ )
d)	29.377	3.087	2.446
e)	31.932	2.524	2.030
f)	10.503	0.068	0.045
g)	6.368	0.066	0.043
h)	5.798	0.072	0.049
i)	4.494	0.061	0.043
j)	5.634	0.093	0.045
k)	32.246	1.446	0.830
l)	25.811	1.389	0.960
m)	36.707	2.947	1.983

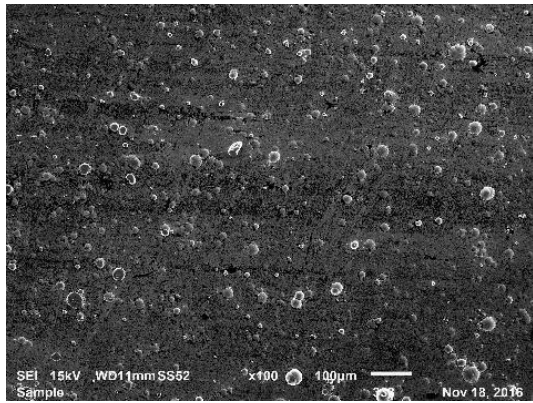
Table 22 Surface profiles parameters corresponding to images from interferometry measurements

From Table 22, the standard deviation and standard errors for  $R_a$  from each data set were computed and the average, standard deviation and standard error presented in Table 23 show the precision of measurements recorded using white-light interferometry. This data is used in the discussion to correlate the COF and surface roughness. Also, as in mentioned in section 5.3, the specimen surface roughness required for depositing nickel alumina nanocomposite is  $0.05\mu\text{m}$  and the values measured in f-j of polished specimens presented in Table 23 support this requirement. Therefore, this ensures that coatings deposited were under identical conditions to literature (Bajwa, Khan, Nazir, et al. 2016).

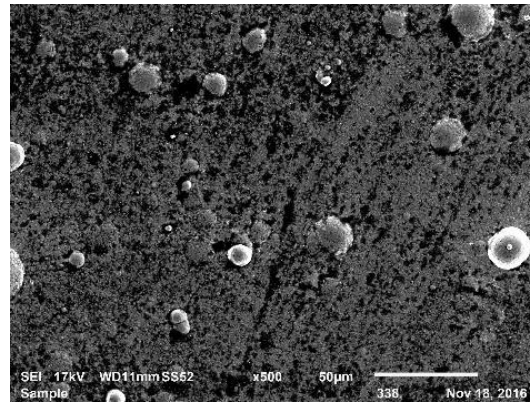
Specimen set	Average	Standard deviation (s)	Standard error ( $\sigma$ )
(a-e) Rough	2.758	0.510	0.228
(f-j) Polished	0.045	0.002	0.001
(k-m) Coated	1.258	0.632	0.365

Table 23 Measurement uncertainties for  $R_a$  from interferometry data

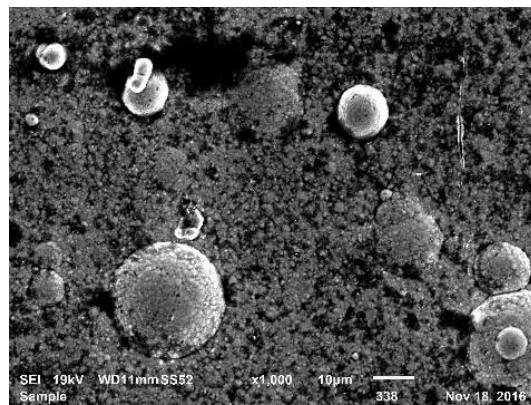
Coated specimen surfaces were also analysed using SEM and the results are presented below. Figure 132 shows surfaces coated with nickel alumina nanocomposite coating using PED with pulse current intensity of 0.35A corresponding to 5A/dm<sup>2</sup> and Figure 133 shows surfaces coated using current intensity of 0.70A corresponding to 10A/dm<sup>2</sup>.



a)

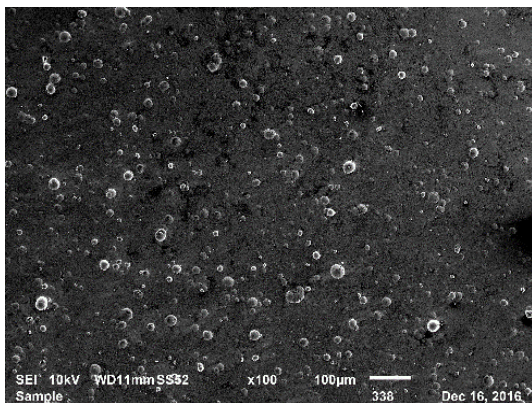


b)

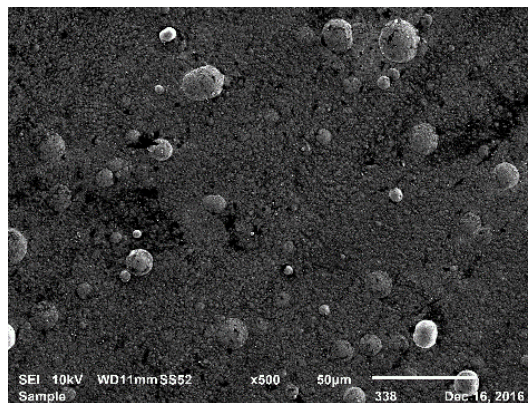


c)

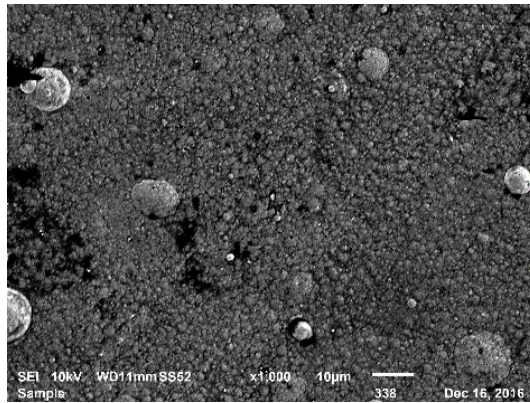
Figure 132 Test specimen surface for nickel alumina nanocomposite coating deposited at 5A/dm<sup>2</sup> at a) x100 b) x500 and c) x1000 magnification factor



a)



b)

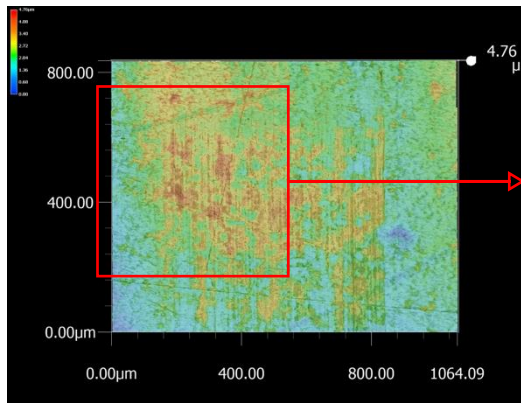


c)

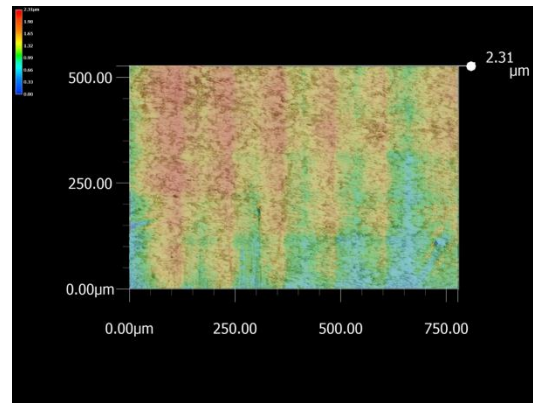
Figure 133 Test specimen surface for nickel alumina nanocomposite coating deposited at 10A/dm<sup>2</sup> at a) x100 b) x500 and c) x1000 magnification

These images can be read together with the data presented in section 7.8; the surface coated at 0.70A produces a more uniform coating leading to greater hardness.

The test specimens were analysed using digital microscopy and the images are presented below.



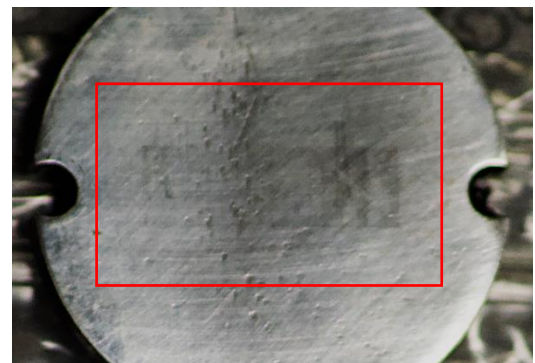
a)



b)



c)



d)

Figure 134 Oil-lubricated specimens a-b) CO1 c) CO2 d) CO3

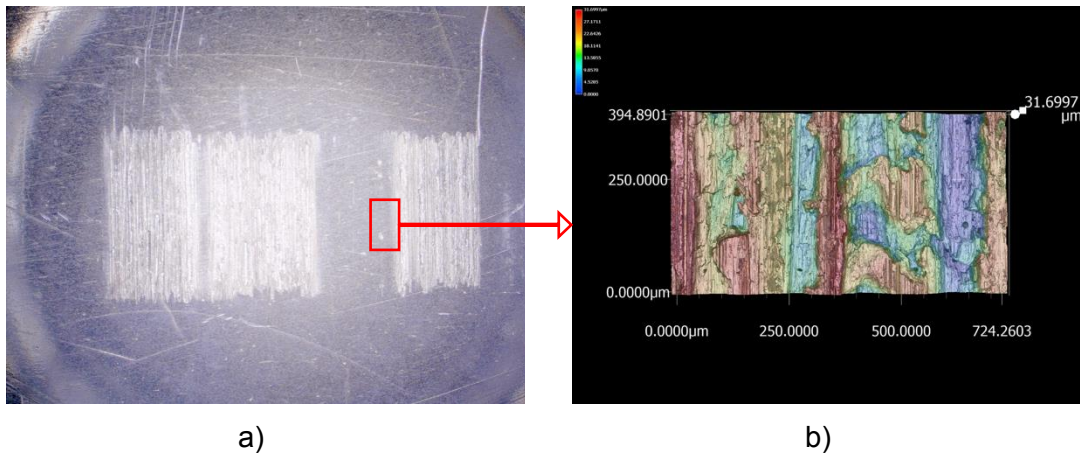


Figure 135 Grease-lubricated uncoated specimen, CG1

Test specimens surface which includes height map for CO1 is show in Figure 134 a and the enlarged wear section is shown in Figure 134 b. Test specimen surfaces for CO2 and CO3 are shown in Figure 134 c and d respectively. From the COF measurements, it could be observed that the values for COF were stable and stable near 0.1 which is supported by the presence of only nominal track on the specimen surfaces. Figure 135 a shows the images for specimen CG1 and Figure 135 a shows the height map for an enlarged portion of the wear track. From this image, it can be observed that abrasive (ploughing) action has occurred with clearly visible grooves which correlate with the high COF observed in the tribometer tests, with average of 0.1038 and maximum value of 0.1904. The ploughing action supports the higher COF which occurs during the initial phase of the test. For CG2-10, steady COF characteristics were recorded which corresponded to only nominal wear tracks and these images are presented in the Appendix J.



Figure 136 Grease-lubricated coated specimen, CA1



Similarly, Figure 136 shows specimen CA1 and from this image it can be observed that abrasive (ploughing) action occurred with clearly visible grooves which correlate with the high COF observed in the tribometer tests, with average of 0.1683 and maximum value of 0.3965. The ploughing action supports the higher COF which occurs during the initial phase of the test.

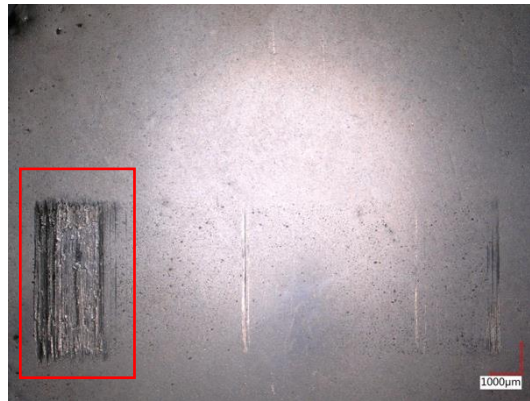


Figure 137 Grease-lubricated coated specimen, CA2

Similarly, Figure 137 specimen CA2 and from this image it can be observed that unbalanced abrasive (ploughing) action has occurred with clearly visible grooves on the left side of the image which correlate with the high COF observed in the tribometer tests, with average value of 0.1253 and maximum value of 0.3656. The modified adapter design prevents wobbling in the specimen in such cases.

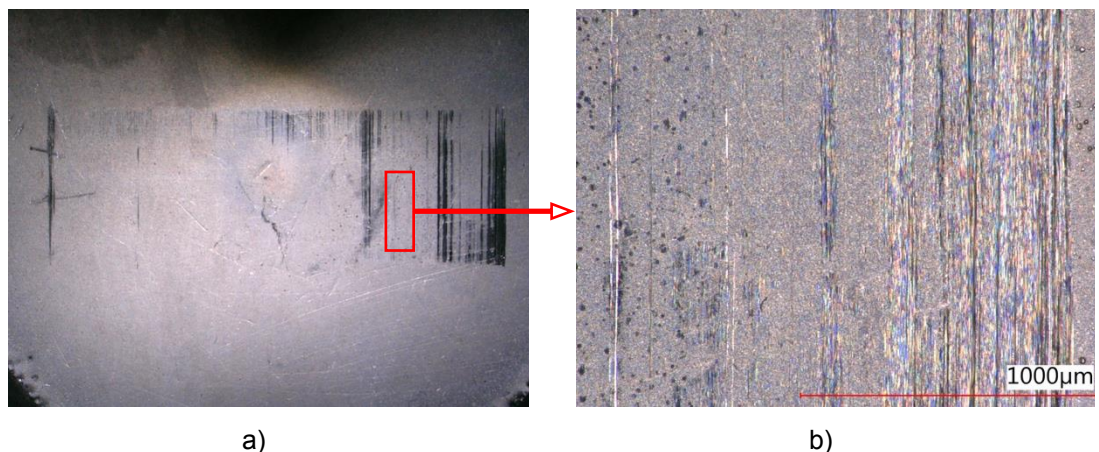
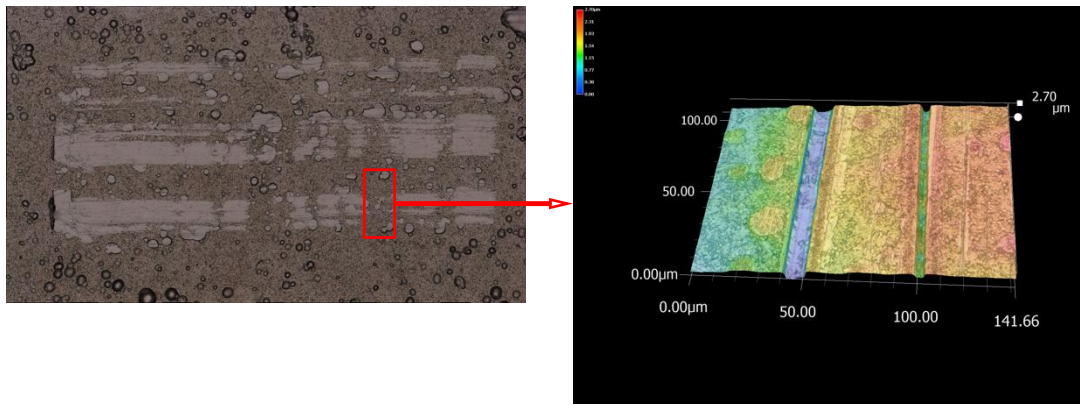
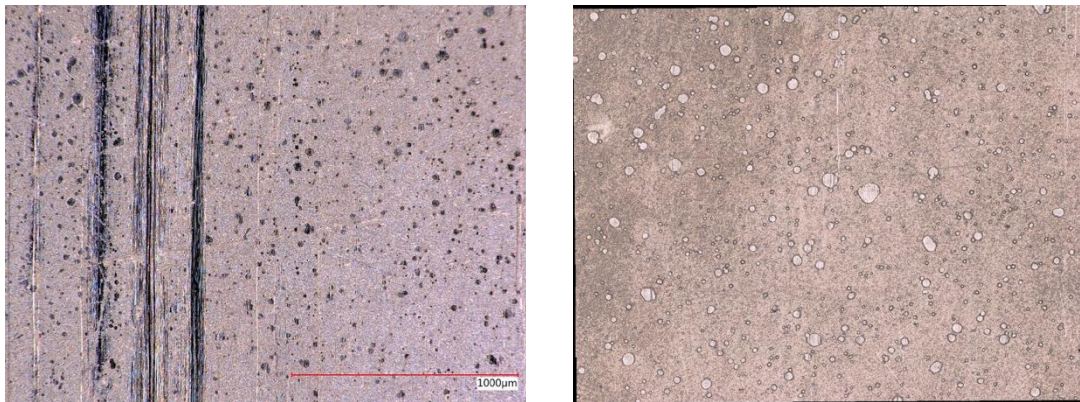


Figure 138 a-b) Grease-lubricated coated specimen, CA3

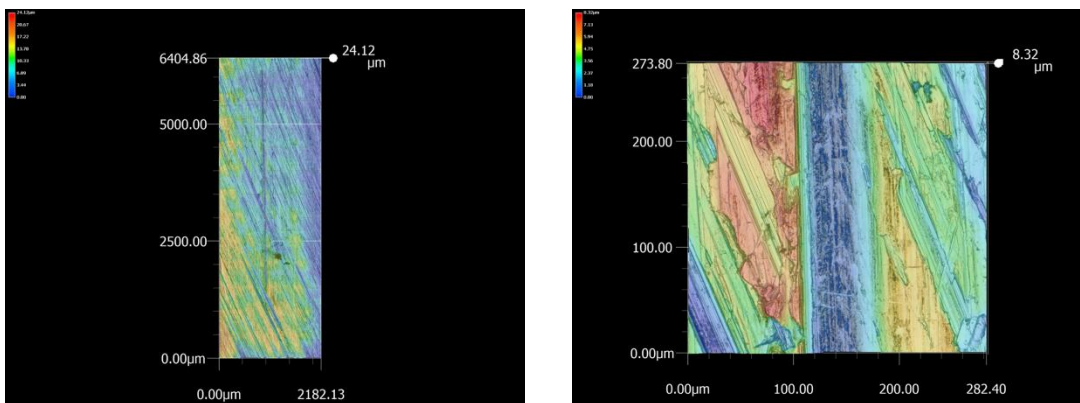


a) b)  
 Figure 139 a-b) Grease-lubricated coated specimen, CA4



a) b)  
 Figure 140 a-b) Grease-lubricated coated specimen, CA5

For specimens CA3 to CA5 presented in Figure 138 to Figure 140, wear tracks and grooves occur but not to the extent of the first two specimens and the corresponding COF values are reported to be steady. Microscopy images for sliding pin contacts are presented below.



a) b)  
 Figure 141 a-b) Oil-lubricated uncoated specimen, FO1

In the case of FO1 presented in Figure 141, it can be seen that grooves were formed in the wear track with only nominal wear occurring outside the groove. Figure 141 b shows the enlarged image of the groove. COF characteristics of FO1 show the initial value of 0.14 which settles at about 0.13 during the test. In the case of FO2, presented in Figure 142, the wear track is visible a section of which is enlarged and presented in Figure 142 b. The initial rise in COF recorded in the case of this specimen can be attributed to the material removal which occurs initially. For specimen FO3 presented in Figure 143 no substantial wear was recorded, and the COF varied in the range of 0.0916 to 0.1024 characteristic of a well-lubricated contact.

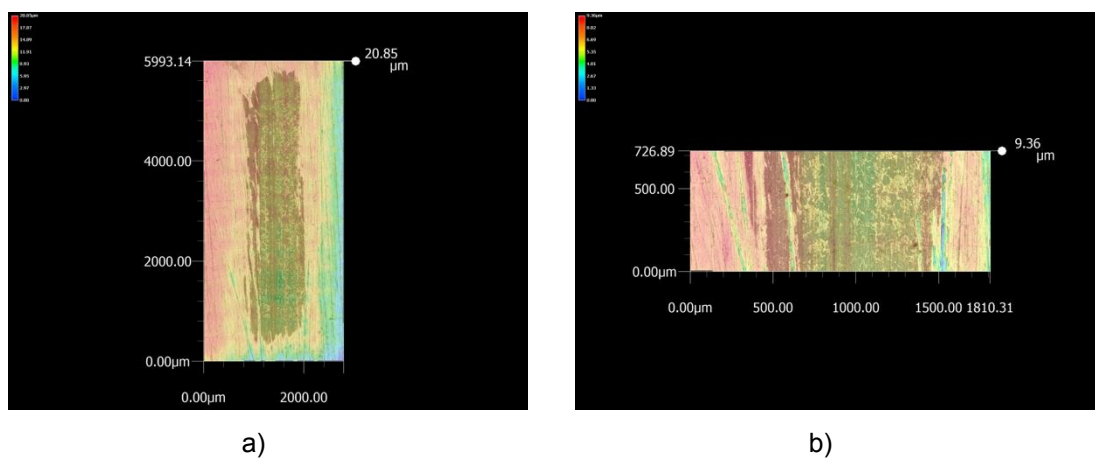


Figure 142 a-b) Oil-lubricated uncoated specimen, FO2

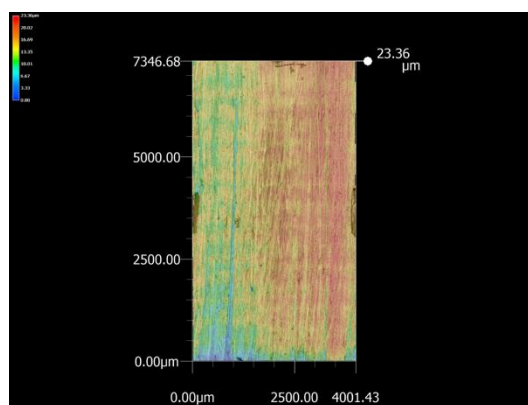


Figure 143 Oil-lubricated uncoated specimen, FO3

FG1 and FG2 were both grease-lubricated uncoated specimens conducted under 10N load (Figure 144 and Figure 145). FG1 (Figure 144) shows relative wear as evidenced by the average COF of 0.2548 and maximum of 0.3104. FG2 (Figure 145) in comparison, after an initial rise and a minor maximum,

settles down as shown by the average COF of 0.2265 and 0.2474. These high COF values correspond to relative amount of wear when contrasted against the specimens tested under the load of 40N – FG3 (Figure 146) and FG6 (Figure 149) exhibit very stable COF curves with average COF of 0.1132 and 0.1028 and maximum COF values of 0.1313 and 0.1292 respectively. These specimens also show very limited wear. In the case of FG4 (Figure 147), FG5 (Figure 148) and FG7 (Figure 150) initial spikes were observed following which the COF values settle to the range exhibited by FG3 and FG6 (Figure 149). The average COFs of FG4, FG5 and FG7 are spaced closely at 0.1263, 0.1176 and 0.1241. However, while the maximum COFs of FG4 and FG5 are 0.1975 and 0.1913, FG7 exhibits a maximum COF value of 0.3198 in the initial phase because of the transverse roughness of the particular sample as can be seen in Figure 150.



Figure 144 Grease-lubricated uncoated specimen, FG1

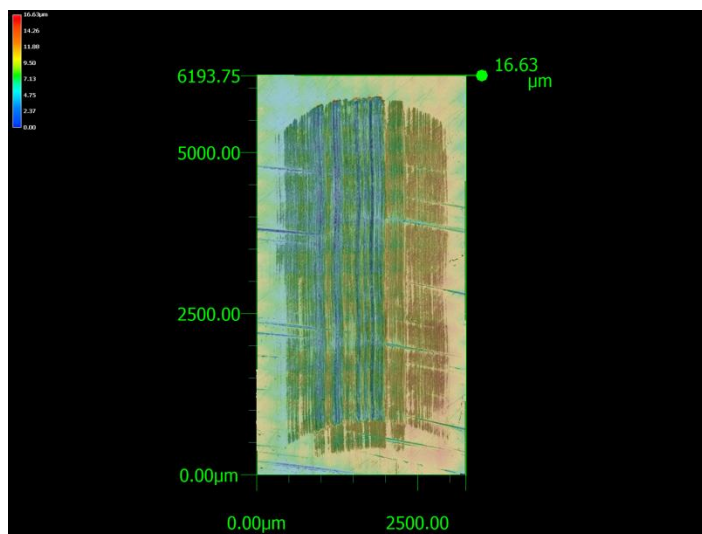


Figure 145 Grease-lubricated uncoated specimen, FG2

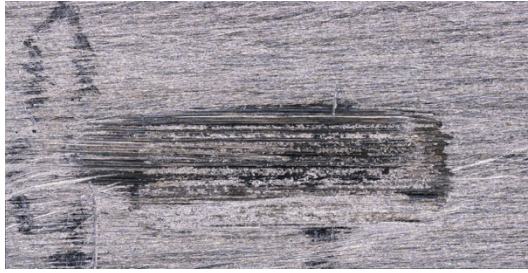


Figure 146 Grease-lubricated uncoated specimen, FG3

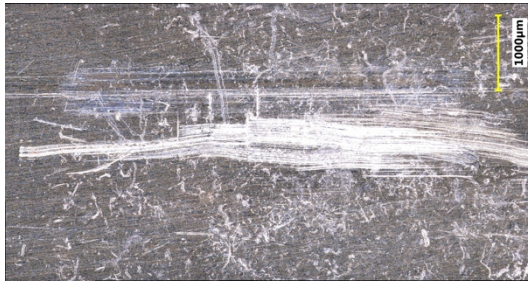


Figure 147 Grease-lubricated uncoated specimen, FG4

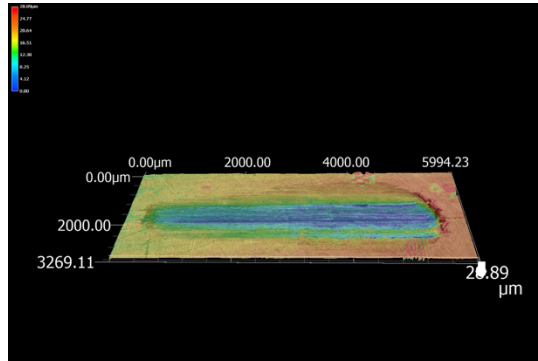
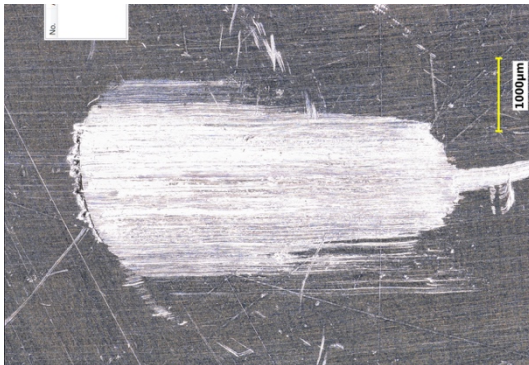


Figure 148 Grease-lubricated uncoated specimen, FG5



Figure 149 Grease-lubricated uncoated specimen, FG6



Figure 150 Grease-lubricated uncoated specimen, FG7

In the case of nickel alumina nanocomposite coated sliding pin contacts FA01 (Figure 151) and FA02 (Figure 152), there is initial material removal or

delamination following which the COF curve stabilises within the region of 0.1322 and 0.1163 respectively. In the cases of FA02 (Figure 152), FA04 (Figure 153) and FA06 (Figure 154), specimen failure due to high friction can be observed. Unlike the previous case material removal led to high COF and seizure. In the singular case of FA05 (Figure 154), the test duration was exceptionally short due to seizure within a short duration and shows a corresponding maximum COF of 0.3708. In the pin sliding contact, the high initial values of COF can be attributed to the direct ploughing action and material removal.

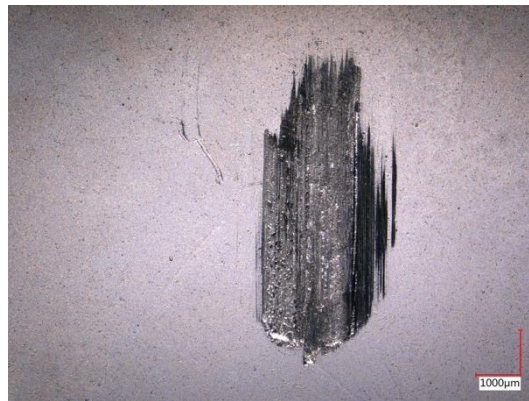


Figure 151 Grease-lubricated coated specimen, FA01

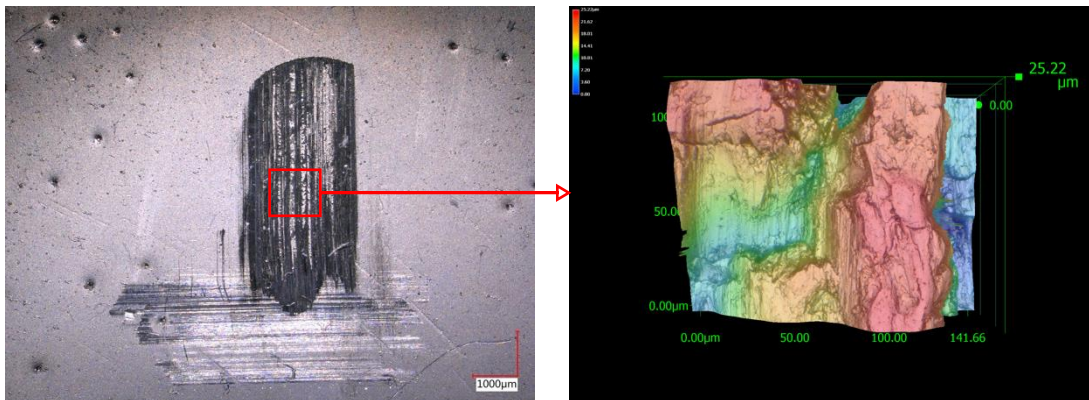
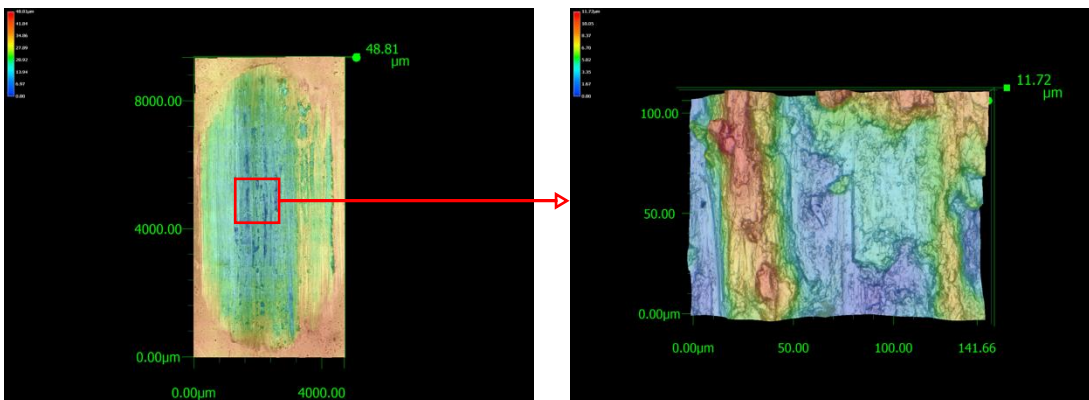
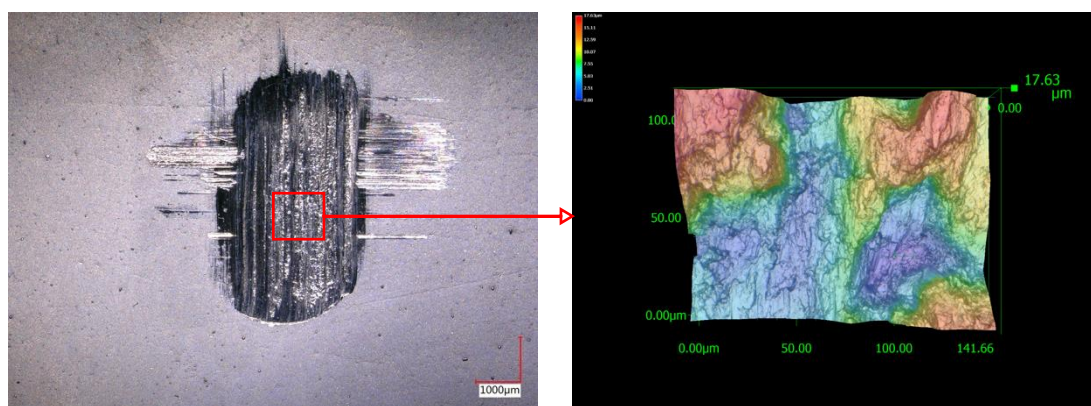


Figure 152 Grease-lubricated coated specimen, FA02, FA03



a) b)  
Figure 153 Grease-lubricated coated specimen, FA04



a)

b)

Figure 154 Grease-lubricated coated specimen, FA05, FA06

## 7.10 Discussion

Regarding hardness measured from the specimens, higher hardness of 375HV has been presented in literature for similar coating deposited on mild steel substrate (Bajwa, Khan, Bakolas, et al. 2016b). Hardness of 330HV has been reported for 35nm alumina (Saha and Khan 2010) and 285 HV has been reported for 45nm alumina (Jung et al. 2009). (Thiemig et al. 2007) reports coating hardness in the range of 250HV for nanocomposite coatings, which is in the region of hardness for coatings developed in this research. This is supported by the SEM images which show more uniform coating in the case of higher coating current of 0.70A. In this context, the use of Plasma Immersion Ion Implantation and Deposition technique provided DLC coatings of the order of 'tens of GPa' for 16MnCr5, which corresponds to over 1000HV (SantAna et al. 2017) and presents a possible alternative to PED for improving COF.

The relationship between hardness and coating can be understood in depth only once the H/E ratio is evaluated and other tests such as scratch test etc are performed on the coating (Leyland and Matthews 2000, Bajwa, Khan, Bakolas, et al. 2016a). However, from the observations, it can be surmised that for the same coating current, if load increases hardness decreases for instance in the case of CA3 and CA5, for the same coating current intensity of 0.35A, CA3 under 5kgf indentation load has a mean hardness of  $220.5 \pm 4.8$  HV while CA4 under 1kgf indentation load shows  $351.3 \pm 7.7$  HV. Comparing the hardness of the specimens revealed that coating at 0.35A increased the hardness over

uncoated specimens by 19.7% and coating at 0.70A increased the hardness over uncoated specimen by 55.9% and between the two coating currents, the higher coating current increased hardness by 30.2% over the lower coating current. From the comparison of COF values and coating hardness, the influence of coating current and therefore hardness on the COF value was indiscernible.

Therefore, contributions from this research include design modifications to the conventional tribometer adapter such as the introduction of the v-notch for holding the test specimen securely. Further design modifications such as the introduction of chamfers and recesses in the design are instrumental in avoiding collision with screw fasteners at the end of the stroke in a single cycle of motion of the test specimen. The resulting adapter designs for the cylinder on two contact geometries are a step forward in the design of tribometer adapters which successfully address the issue of low manufacturing tolerances for specimens.

In this work it can be observed that with the increase in coating current, the hardness also increases. Pulse electrodeposition of nickel alumina nanocomposite coating on the 16MnCr5 specimen surface requires higher current densities in the range of 5-10 A/dm<sup>2</sup> compared to the 1-4 A/dm<sup>2</sup> required for mild steel specimens. However, the relationship between coating current and hardness differs in literature for different substrates. The reasons for this variation however need to be analysed.

## **7.11 Summary**

Results of experimental determination of the COF of uncoated 16MnCr5 and En19 steel alloy pair followed by that of nickel alumina nanocomposite coated 16MnCr5-EN19 steel alloy pair for two contact geometries i.e. sliding cylinder and sliding pin were presented. Oil lubrication was used to generate reference values for that of molybdenum grease lubrication and the main load for which the specimens were tested was 40N. Analysis of surface characteristics consisting of surface hardness measurements and surface characteristics measurements were presented using Vickers hardness test and white-light



interferometry. Additionally, digital microscopy was used to analyse the surfaces of the specimens after tribo-testing.

## **Chapter 8 Conclusions and Future Research**

### **8.1 Background**

The introduction to this thesis posed four research questions which were developed into four corresponding research aims for which research objectives were assigned following detailed literature review. This chapter aims at tying the strands developed across two interconnected research themes whose results are presented in Chapters 6 and 7 against the initial research aims and objectives. Even though SAR is a growing research domain and SAR robots have been researched, it appears from the literature review that the use of mobile manipulators is not widespread, necessitating the use of heavy equipment such as excavators which are unsuitable for SAR. In this context, the need for developing application-specific mobile manipulators was established since conventional numerical modelling is tedious. The incorporation of friction into the simulation and experimental investigation into the friction characteristics of the 16MnCr5-EN19 steel alloy pair and the influence on the COF of 16MnCr5 with nickel alumina nanocomposite coating are presented.

### **8.2 Research outcomes**

The research outcomes for this thesis have been weighed against the research objectives derived at the end of the literature review (sections 2.3 and 3.4). In the first part of the work, virtual prototypes of two specific mobile manipulator designs were designed in CAD and were presented in three case studies. These were also successfully simulated in the MBD simulation environment and therefore represent proof of concept for CAD-MBD approach for design and simulation of mobile manipulators, which are not only application specific but also have a very minimal turnaround time which addresses the time-criticality aspect of SAR. In the same portion of the research, different models of friction were surveyed, and the combined friction model was incorporated into the simulation of mobile manipulator discussed above. This however, presented limitations in the sense that it was not possible to accurately identify coefficients and parameters. Thereafter, adopting the experimental approach outlined in Blau (2001), investigation into the role of friction in manipulator dynamic was

conducted for a selected steel-alloy pair. 16MnCr5-EN19 steel alloy pair was selected because it is widely used commercially [insert reference] (therefore would provide replication of field operating conditions and also because literature on the tribological characteristics of this combination have not been reported.

The coefficient of friction (COF) which is the main tribological component affecting the dynamic performance of an sDOF joint as is selected in this work was experimentally determined using a reciprocating tribometer for two contact geometries (sliding cylinder on plane and sliding pin on plane) for which results have hitherto not been reported. Oil *is used as lubricant* to generate reference values, against which the COF of grease lubricated contacts were compared. For uncoated samples, over the same load, oil lubrication showed lesser COF than grease lubricated contacts although it was subsequently established that oil lubrication would not provide a feasible solution because of its fluid nature.

To address the fourth and final research aim, the 16MnCr5 specimens were coated with nickel alumina nanocomposite coating, using pulse electrodeposition, a combination of processes which again has not been reported before. Experimental determination of COF for coated samples revealed that while the coating marginally improved the COF of sliding cylindrical contacts, due to the difference in contact geometry, no such effect was to be found in sliding pin specimens.

As regards surface characterisation, hardness of a specimen of coated and uncoated surface revealed that coated specimens show better hardness properties than uncoated specimens (as proposed in literature) and the increase of coating current resulted in lower hardness. Furthermore, when coating current remained constant, higher load led to lower hardness. Surface roughness was also measured for rough, polished and coated specimens and digital microscopy and SEM images of the specimens corroborate the findings. The linear relationship presented in Colbert was used to assess the influence of how COF affects joint friction torque, other factors being equal. However, the limitation of this approach is that this a static computation and more detailed

dynamic computation through the use of an appropriate friction model will shed further light into the effect of friction torque on manipulator dynamics.

Since this investigation is the first of its kind in SAR robotics and falls outside of the mainstream commercial manipulators, there is scope for future development of mobile manipulators especially with respect to assessment of joint friction.

### **8.3 Contributions to knowledge**

The contributions to knowledge from this research are:

- i. Application of CAD-MBD approach to SAR mobile manipulators:  
Three case-studies were designed, modelled and simulated, and simulation results were validated. This approach which has been used successfully in other domains (Wood and Kennedy 2003, Grossman and Gmitterko 2008, Udai et al. 2011, Le et al. 2013, Dooner et al. 2015, Mahapatra 2015) is applied to SAR environments. Visualisation of complex mechanisms provides better understand of their operation.
- ii. Incorporation of friction modelling:  
Friction modelling for manipulators in SAR has not been reported in literature. In this work, the combined friction model was incorporated into the dynamic simulation of the two designs using the MBD approach and the simulation results revealed friction characteristics. However, it was revealed that this method poses difficulties due to complexity of friction model and in accurately identifying coefficients and parameters for complex friction models for use in sDOF revolute joints.
- iii. COF characteristics of 16MnCr5-EN19 steel alloy pair:  
Only limited understanding of COF characteristics of 16MnCr5-EN19 steel alloy pair exists in literature and this investigation provides in-depth understanding of COF through experimental determination across two contact geometries, using oil and grease lubricant, which revealed that oil-lubricated contacts exhibited lower COF than grease-lubricated contacts for the same load of 40N. For sliding cylinder contacts, the average COF for oil-lubricated specimens was 15.4% less than the COF of grease-lubricated specimens and it was 8.5% less in the case of sliding pin contacts.
- iv. Pulse electrodeposition of nanocomposite coating:

16MnCr5 was coated successfully with nickel alumina nanocomposite coating using pulse electrodeposition (PED) at coating currents of 0.35A and 0.70A. The novel aspect of this portion of the research is that firstly nickel alumina nanocomposite coating was deposited on the 16MnCr5 specimen, which is the moving specimen in the tribo-test, using PED - a combination of processes which has hitherto not been reported in literature, and the subsequent effect on COF was analysed.

- v. COF characteristics of nanocomposite coated 16MnCr5-EN19 steel alloy pair:  
Analysis of COF characteristics for the same load and grease lubricant revealed that coating improved the COF for sliding cylindrical contacts by 3.1% over uncoated specimens. Coating adversely affected COF for sliding pin contacts with COF increasing by 22.1% over uncoated specimens.
- vi. Microhardness of the specimens:  
Coating improved the microhardness by 19.7% over uncoated specimens for 0.35A and for by 55.9% for 0.70A. higher coating current increased hardness by 30.2% over the lower coating current.

#### **8.4 Practical applications and benefits**

The practical outcomes and applications for this research include:

- i. Reduced turnaround time from design to fabrication of mobile manipulators using CAD-MBD approach,
- ii. Creation of virtual prototypes help rescue agents prepare for SAR operations as envisaged in section 2.2.5,
- iii. Providing a platform for modelling and testing control systems for complex manipulators.

The practical applications of design and modelling are schematically presented in Figure 155.

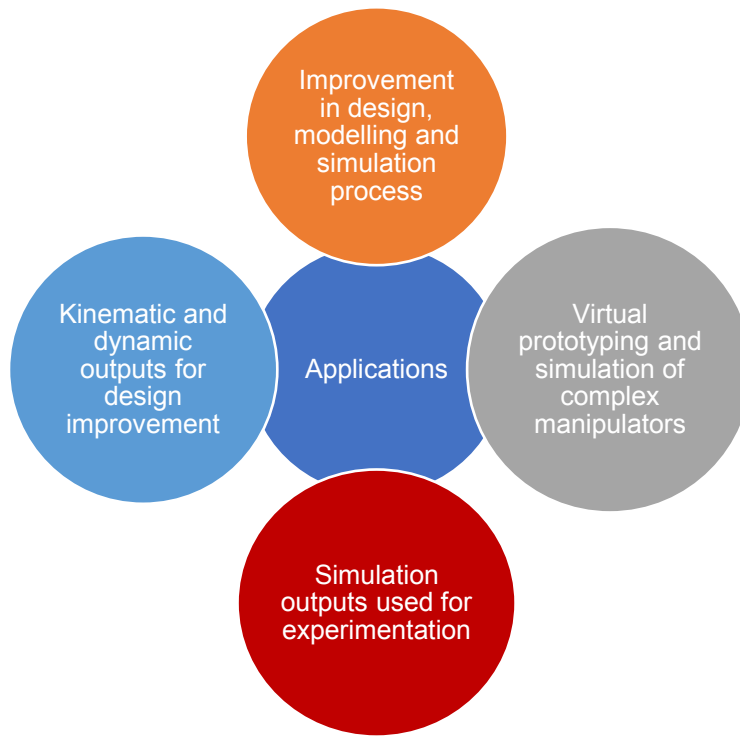


Figure 155 Application of modelling outcomes for practical applications

- iv. Incorporation of friction model improves simulation accuracy of models,
- v. Animated visualisation provides better understanding of mechanism operation (Mahapatra 2011),
- vi. Given that 16MnCr5-EN19 steel alloy pair is widely used in commercial applications such as manipulator joints, the results of this work can be applied to physical prototypes fabricated on the basis of designs presented in this thesis,
- vii. Since modified tribometer adapters were designed and fabricated using Electro discharge machining (EDM) from CAD drawings, the same principle can be applied to the CAD drawings of the manipulator designs, thereby providing a very cost-effective solution.

### 8.5 Limitations and difficulties of this work

Working within the scope and study restrictions presented in section 3.5, the following limitations and difficulties were encountered:

- i. Manipulator design analysis such as Finite Element Analysis (FEA) was not incorporated due to change in research direction and adoption of tribological analysis,

- ii. Only limited loading conditions were incorporated into the simulation since this area has been considered separately in literature due to complexity of soil-tool interaction model (Chacko et al. 2014),
- iii. Combined friction model parameters were not investigated in detail
- iv. Hardened 16MnCr5 specimens were not considered,
- v. Wear analysis was not analysed in this work given that this work proposes a preliminary design analysis of mobile manipulators. Additionally, because of the lower pair kinematic joints were selected, 'which are mechanically attractive since wear is spread over the whole surface and lubricant is trapped in the small clearance space (in nonidealized systems) between the surfaces, resulting in relatively good lubrication' (Waldron et al. 2008),
- vi. Wider load range was not considered for all contact conditions,
- vii. Effect of operating temperature was not considered,
- viii. EN19 counter-face hardening was restricted to flame hardening because of specimen form and size,
- ix. COF measurement for nanocomposite coated specimens under oil-lubrication was not considered since this could not be used for practical applications.

Future research directions envisaged to overcome these limitations are presented in the following section.

## **8.6 Future directions**

Given that this work proposes initial designs for mobile manipulators in SAR using CAD-MBD, and analyses COF for coated and uncoated 16MnCr5 specimens, the following research directions open up new avenues of research to build on this work.

### **Design, modelling and simulation**

- i. Design of links and end-effectors can be improved by incorporating further design analysis using FEA. For non-linear dynamic loads, fatigue analysis can be conducted to predict design life of links,
- ii. Similarly, simulation of complex linkages can be extended to three-dimensional operation while also incorporating time-varying load on end-effector to increase simulation accuracy. For conducting simulations for

the whole robot, the robotic platform or base can be incorporated as can be hybrid actuators for optimising design thereby improving performance and operational safety. Suitable control systems for the manipulator can also be developed using the CAD-MDB approach use in this work.

### **Tribological analysis**

- iii. Given that there are multiple parameters in this experimental section, there exists several combinations of approaches. The effect of different greases on the COF, the influence of particles and corrosives found in SAR can be analysed, the effect of surface texturing including different surface roughness such as dimpling to promote lubricant retention can be analysed and the specimen can be surface activated before coating. Effect of pulse reverse plating and electroless coating and the influence of the additives on coating properties is an area open to study. Nickel base coating layer before nanocomposite deposition and multi-layer coating can be provided and scratch tests, nano-indentation tests, and X-ray diffraction (XRD) analysis can be used to investigate crystal structure and orientation of coating for 16MnCr5 specimens. In this study, as 16MnCr5 was the surface coated, it is also possible to analyse the effect of coating on EN19 steel alloy instead. In this study, only pin sliding contact showed considerable wear and wear analysis of the same is also open to further study.

### **8.7 Final considerations and summary**

In conclusion, the work undertaken in this research is interdisciplinary in nature in that design, modelling and simulation as well as experimental tribological analysis for determination of the COF for coated and uncoated 16MnCr5 with EN19 counter-face have been studied. Friction, the tribological component which affects the dynamic performance of the mobile manipulator links these two domains in this work as a better understanding of friction characteristics and attempts to reduce COF lead to better performance. The scope of this current research has been limited due to the fact that preliminary stage investigations of processes hitherto not reported in literature for SAR application have been studied. Therefore, this final concluding chapter presents not only



the combined conclusions from chapters 6 and 7 but also presents directions for future work, which is expected to build on the framework provided in this thesis.

## References

- AAAI, 2002. *In the Aftermath of September 11: What Roboticians Learned from the Search and Rescue Efforts* [online]. Available from: <http://www.aaai.org/Pressroom/Releases/release-02-0910.php> [Accessed 1 Jan 2014].
- Adams, A. L., Schmidt, T. A., Newgard, C. D., Federiuk, C. S., Christie, M., Scorvo, S., and DeFreest, M., 2007. Search Is a Time-Critical Event: When Search and Rescue Missions May Become Futile. *Wilderness & Environmental Medicine* [online], 18 (2), 95–101. Available from: <http://linkinghub.elsevier.com/retrieve/pii/S1080603207702181>.
- Aleem Maqbool, 2017. 'Hurricane Maria destroyed everything' - BBC News [online]. [bbc.co.uk](http://www.bbc.co.uk/news/av/world-us-canada-41460514/puerto-rico-hurricane-maria-destroyed-everything). Available from: <http://www.bbc.co.uk/news/av/world-us-canada-41460514/puerto-rico-hurricane-maria-destroyed-everything> [Accessed 9 Oct 2017].
- Alphin, M. S., Sankaranarayanan, K., and Sivapirakasam, S. P., 2010. Experimental Evaluation of Whole Body Vibration Exposure from Tracked Excavators with Hydraulic Breaker Attachment in Rock Breaking Operations. *Journal of Low Frequency Noise, Vibration and Active Control* [online], 29 (2), 101–110. Available from: <http://journals.sagepub.com/doi/10.1260/0263-0923.29.2.101>.
- Alqasemi, R., Mahler, S., and Dubey, R., 2007. A Double Claw Robotic End-Effector Design. *In: Recent Advances in Robotics*. 1–6.
- Anand, M., Hadfield, M., Thomas, B., and Cantrill, R., 2017. The depletion of ZDDP additives within marine lubricants and associated cylinder liner wear in RNLI lifeboat engines. *Proceedings of the Institution of Mechanical Engineers, Part L: Journal of Materials: Design and Applications* [online], 231 (1–2), 162–170. Available from: <http://journals.sagepub.com/doi/10.1177/1464420716663235>.
- Anand, M., Hadfield, M., Viesca, J.-L., Thomas, B., González, R., Cantrill, R., and Hernández Battez, A., 2016. Assessing Boundary Film Forming Behavior of Phosphonium Ionic Liquids as Engine Lubricant Additives. *Lubricants* [online], 4 (4), 17. Available from: <http://www.mdpi.com/2075-4442/4/2/17>.

- Andersson, P., Koskinen, J., Varjus, S., Kolehmainen, J., Tervakangas, S., and Buss, W., 2008. Lubrication improvement and friction reduction of DLC-coated sliding surfaces by in-process structuring and post polishing. *Tribotest* [online], 14 (2), 97–112. Available from: <http://doi.wiley.com/10.1002/tt.55>.
- Andrade-Cetto, J. and Koivo, A. J., 1995. Controller for Excavator During Digging Operations. *In: IASTED International Conference on Robotics and Manufacturing*. Cancun, 177–180.
- Anon., 2012. *Local university unveils its 'baby elephant' robot* [online]. China.org.cn. Available from: [http://www.china.org.cn/china/2012-11/08/content\\_27042373.htm](http://www.china.org.cn/china/2012-11/08/content_27042373.htm) [Accessed 20 Mar 2002].
- Anon., 2015. *JCB Announces \$ 500,000 Donation of Kit to Philippines Disaster* [online]. Earthmovers. Available from: <http://www.earthmoversmagazine.co.uk/jcb-announces-500000-donation-of-kit-to-philippines-disaster/>.
- Anthes, G., 2010. Robots gear up for disaster response. *Communications of the ACM*, 53 (4), 15–16.
- Armstrong-Hélouvy, B., Dupont, P., and De Wit, C. C., 1994. A survey of models, analysis tools and compensation methods for the control of machines with friction. *Automatica* [online], 30 (7), 1083–1138. Available from: <http://linkinghub.elsevier.com/retrieve/pii/0005109894902097>.
- Aruna, S. T., William Grips, V. K., and Rajam, K. S., 2009. Ni-based electrodeposited composite coating exhibiting improved microhardness, corrosion and wear resistance properties. *Journal of Alloys and Compounds* [online], 468 (1–2), 546–552. Available from: <http://linkinghub.elsevier.com/retrieve/pii/S0925838808001060>.
- Badarulzaman, N. A., Purwadaria, S., Mohamad, A. A., and Ahmad, Z. A., 2009. The production of nickel–alumina composite coating via electroplating. *Ionics* [online], 15 (5), 603–607. Available from: <http://link.springer.com/10.1007/s11581-008-0307-z>.
- Bahrololoom, M. E. and Sani, R., 2005. The influence of pulse plating parameters on the hardness and wear resistance of nickel–alumina composite coatings. *Surface and Coatings Technology* [online], 192 (2–3), 154–163. Available from:

<http://linkinghub.elsevier.com/retrieve/pii/S0257897204009089> [Accessed 20 Mar 2017].

Bai, Z. F. and Zhao, Y., 2012. Dynamics modeling and quantitative analysis of multibody systems including revolute clearance joint. *Precision Engineering* [online], 36 (4), 554–567. Available from:

<http://linkinghub.elsevier.com/retrieve/pii/S014163591200058X> [Accessed 6 Jan 2017].

Bajwa, R. S., Khan, Z. A., Bakolas, V., and Braun, W., 2016a. Effect of bath ionic strength on adhesion and tribological properties of pure nickel and Ni-based nanocomposite coatings. *Journal of Adhesion Science and Technology* [online], 30 (6), 653–665. Available from:

<http://www.tandfonline.com/doi/full/10.1080/01694243.2015.1117276>.

Bajwa, R. S., Khan, Z. A., Bakolas, V., and Braun, W., 2016b. Water-Lubricated Ni-Based Composite (Ni–Al<sub>2</sub>O<sub>3</sub>, Ni–SiC and Ni–ZrO<sub>2</sub>) Thin Film Coatings for Industrial Applications. *Acta Metallurgica Sinica (English Letters)* [online], 29 (1), 8–16. Available from:

<http://link.springer.com/10.1007/s40195-015-0354-1>.

Bajwa, R. S., Khan, Z. A., Nazir, H., Chacko, V., and Saeed, A., 2016. Wear and Friction Properties of Electrodeposited Ni-Based Coatings Subject to Nano-enhanced Lubricant and Composite Coating. *Acta Metallurgica Sinica (English Letters)* [online], 29 (10), 902–910. Available from:

<http://link.springer.com/10.1007/s40195-016-0470-6>.

Balafoutis, C. A., 1994. A survey of efficient computational methods for manipulator inverse dynamics. *Journal of Intelligent and Robotic Systems* [online], 9 (1), 45–71. Available from: <https://doi.org/10.1007/BF01258313>.

Barone, S., Curcio, A., and Pierucci, F., 2002. Virtual Prototyping simulation for the design of two-wheeled vehicles. In: *DS 30: Proceedings of DESIGN 2002, the 7th International Design Conference, Dubrovnik*.

BBC, 2015. India building collapse kills 13 in Uttar Pradesh. *BBC News India* [online]. Available from: <http://www.bbc.co.uk/news/world-asia-india-31478708>.

Beake, B. D., Ogwu, A. A., and Wagner, T., 2006. Influence of experimental factors and film thickness on the measured critical load in the nanoscratch test. *Materials Science and Engineering: A* [online], 423 (1–2), 70–73.

Available from:

<http://linkinghub.elsevier.com/retrieve/pii/S092150930600089X>.

- Beater, P. and Otter, M., 2003. Multi-domain simulation: Mechanics and hydraulics of an excavator. *Paper presented at the 3rd International Modelica Conference* [online]. Available from: [https://www.modelica.org/events/Conference2003/papers/h36\\_excavator\\_Beater\\_color.pdf](https://www.modelica.org/events/Conference2003/papers/h36_excavator_Beater_color.pdf).
- Benson, C. and Clay, E. J., 2004. *Economic and financial impacts of natural disasters: an assessment of their effects and options for mitigation*. World Bank Publications.
- Bernold, L. E., 1993. Motion and Path Control for Robotic Excavation. *Journal of Aerospace Engineering*, 6 (1), 1–18.
- Bhushan, B., 2013a. *Introduction to tribology*. John Wiley & Sons.
- Bhushan, B., 2013b. Friction and Wear Screening Test Methods. *In: Principles and Applications to Tribology* [online]. The Atrium, Southern Gate, Chichester, West Sussex, PO19 8SQ, UK: John Wiley & Sons, Ltd, 789–803. Available from: <http://doi.wiley.com/10.1002/9781118403020.ch12>.
- Bicchi, A. and Member, S., 2000. Hands for Dexterous Manipulation and Robust Grasping : A Difficult Road Toward Simplicity, 16 (6), 652–662.
- Bilandi, S. T., 1997. Identification of frictional effects and structural dynamics for improved control of hydraulic manipulators. *Department of Electrical Engineering* [online]. The University of British Columbia. Available from: <https://circle.ubc.ca/handle/2429/6805>.
- Billing, R. and Fleischner, R., 2011. Mars science laboratory robotic arm. *In: 14th European Space Mechanisms & Tribology Symposium, Constance, Germany, Sept. 28–30*.
- Bittencourt, A. C., Wernholt, E., Sander-Tavallaey, S., and Brogårdh, T., 2010. An extended friction model to capture load and temperature effects in robot joints. *In: Intelligent Robots and Systems (IROS), 2010 IEEE/RSJ International Conference on*. 6161–6167.
- Blau, P. J., 1997. Fifty years of research on the wear of metals. *Tribology International*, 30 (5), 321–331.
- Blau, P. J., 2001. Simulative friction and wear testing. *Handbook of Modern Tribology*, 1, 511–522.

- Borkar, T. and Harimkar, S. P., 2011. Effect of electrodeposition conditions and reinforcement content on microstructure and tribological properties of nickel composite coatings. *Surface and Coatings Technology* [online], 205 (17–18), 4124–4134. Available from: <http://linkinghub.elsevier.com/retrieve/pii/S0257897211001575> [Accessed 11 Jan 2017].
- Borutzky, W., 2010. Bond Graph Based Physical Systems Modelling. *Bond Graph Methodology: Development and Analysis of Multidisciplinary Dynamic System models* [online], 17–88. Available from: [http://link.springer.com/chapter/10.1007/978-1-84882-882-7\\_2](http://link.springer.com/chapter/10.1007/978-1-84882-882-7_2).
- Bose, K., Wood, R. J. K., and Wheeler, D. W., 2005. High energy solid particle erosion mechanisms of superhard CVD coatings. *Wear* [online], 259 (1–6), 135–144. Available from: <http://linkinghub.elsevier.com/retrieve/pii/S0043164805001353>.
- Burke, J. L., Murphy, R., Coovert, M., and Riddle, D., 2004. Moonlight in Miami: Field Study of Human-Robot Interaction in the Context of an Urban Search and Rescue Disaster Response Training Exercise. *Human-Computer Interaction* [online], 19 (1), 85–116. Available from: <http://www.scopus.com/inward/record.url?eid=2-s2.0-3142777269&partnerID=tZOtx3y1>.
- Camargo, P. H. C., Satyanarayana, K. G., and Wypych, F., 2009. Nanocomposites: synthesis, structure, properties and new application opportunities. *Materials Research* [online], 12 (1), 1–39. Available from: [http://www.scielo.br/scielo.php?script=sci\\_arttext&pid=S1516-14392009000100002&lng=en&tlng=en](http://www.scielo.br/scielo.php?script=sci_arttext&pid=S1516-14392009000100002&lng=en&tlng=en).
- Cann, P. M. E., 2006. Grease degradation in a bearing simulation device. *Tribology International*, 39 (12), 1698–1706.
- Carlson, J. and Murphy, R. R., 2003. Reliability analysis of mobile robots. *2003 IEEE International Conference on Robotics and Automation (Cat. No.03CH37422)* [online], 1, 274–281. Available from: <http://ieeexplore.ieee.org/document/1241608/>.
- Carlson, J. and Murphy, R. R., 2005. How UGVs physically fail in the field. *IEEE Transactions on Robotics*, 21 (3), 423–437.
- Casper, J. L. and Murphy, R. R., 2003. Human–Robot Interactions During the

- Robot-Assisted Urban Search and Rescue Response at the World Trade Center. *IEEE TRANSACTIONS ON SYSTEMS, MAN, AND CYBERNETICS—PART B: CYBERNETICS* [online], 33 (3), 367–385. Available from:  
[http://ieeexplore.ieee.org/xpls/abs\\_all.jsp?arnumber=1200160](http://ieeexplore.ieee.org/xpls/abs_all.jsp?arnumber=1200160).
- Chacko, V., 2014. Model excavator for entertainment at Jifa Agricultural Sightseeing Garden (Qinhuangdao).
- Chacko, V. and Khan, Z. A., 2017. Dynamic Simulation of a Mobile Manipulator with Joint Friction. *Tribology in Industry* [online], 39 (2), 152–167. Available from: <http://eprints.bournemouth.ac.uk/29280/>.
- Chacko, V., Yu, H., Cang, S., and Vladareanu, L., 2014. State of the art in excavators. *Proceedings of the 2014 International Conference on Advanced Mechatronic Systems* [online], 481–488. Available from:  
[http://ieeexplore.ieee.org/xpls/abs\\_all.jsp?arnumber=6911593](http://ieeexplore.ieee.org/xpls/abs_all.jsp?arnumber=6911593).
- Chandrasekar, M. S. and Pushpavanam, M., 2008. Pulse and pulse reverse plating—Conceptual, advantages and applications. *Electrochimica Acta* [online], 53 (8), 3313–3322. Available from:  
<http://linkinghub.elsevier.com/retrieve/pii/S0013468607014065>.
- Chang, K.-H., 2015. *Design Theory and Methods Using CAD/CAE* [online]. Design Theory and Methods Using CAD/CAE. Elsevier. Available from:  
<http://www.sciencedirect.com/science/article/pii/B9780123985125000013>  
 [Accessed 18 Feb 2016].
- Chawla, N. and Shen, Y.-L., 2001. Mechanical Behavior of Particle Reinforced Metal Matrix Composites. *Advanced Engineering Materials* [online], 3 (6), 357–370. Available from: <http://doi.wiley.com/10.1002/1527-2648%28200106%293%3A6%3C357%3A%3AAID-ADEM357%3E3.0.CO%3B2-I>.
- Chen, D. H. and Ushijima, K., 2014. Prediction of the mechanical performance of McKibben artificial muscle actuator. *International Journal of Mechanical Sciences* [online], 78, 183–192. Available from:  
<http://linkinghub.elsevier.com/retrieve/pii/S0020740313003123>.
- Chen, L., Wang, L., Zeng, Z., and Xu, T., 2006. Influence of pulse frequency on the microstructure and wear resistance of electrodeposited Ni-Al<sub>2</sub>O<sub>3</sub> composite coatings. *Surface and Coatings Technology*, 201 (3–4), 599–

605.

- Ching-Ping Chou and Hannaford, B., 1996. Measurement and modeling of McKibben pneumatic artificial muscles. *IEEE Transactions on Robotics and Automation* [online], 12 (1), 90–102. Available from:  
<http://ieeexplore.ieee.org/lpdocs/epic03/wrapper.htm?arnumber=481753>.
- Choi, S. H. and Cheung, H. H., 2008. A versatile virtual prototyping system for rapid product development. *Computers in Industry* [online], 59 (5), 477–488. Available from:  
<http://linkinghub.elsevier.com/retrieve/pii/S0010448503001106>.
- Choi, S. H. H. and Chan, A. M. M., 2004. A virtual prototyping system for rapid product development. *CAD Computer Aided Design*, 36, 401–412.
- Ciubotariu, A., Benea, L., Lakatos–Varsanyi, M., and Dragan, V., 2008. Electrochemical impedance spectroscopy and corrosion behaviour of Al<sub>2</sub>O<sub>3</sub>–Ni nano composite coatings. *Electrochimica Acta* [online], 53 (13), 4557–4563. Available from:  
<http://linkinghub.elsevier.com/retrieve/pii/S0013468608000649>.
- Colbert, R. S., Alvarez, L. A., Hamilton, M. A., Steffens, J. G., Ziegert, J. C., Burris, D. L., and Sawyer, W. G., 2010. Edges, clearances, and wear: Little things that make big differences in bushing friction. *Wear* [online], 268 (1–2), 41–49. Available from:  
<http://linkinghub.elsevier.com/retrieve/pii/S0043164809004475>.
- Cooke, K. O., 2016. Parametric Analysis of Electrodeposited Nano-composite Coatings for Abrasive Wear Resistance. In: *Electrodeposition of Composite Materials* [online]. InTech. Available from:  
<http://www.intechopen.com/books/electrodeposition-of-composite-materials/parametric-analysis-of-electrodeposited-nano-composite-coatings-for-abrasive-wear-resistance>.
- Daumas, B., Xu, W. L., and Bronlund, J., 2005. Jaw mechanism modeling and simulation. *Mechanism and Machine Theory* [online], 40 (7), 821–833. Available from:  
<http://linkinghub.elsevier.com/retrieve/pii/S0094114X05000248>.
- Davis, J. R., 2001. *Surface engineering for corrosion and wear resistance*. ASM international.
- Dede, M. I. C. and Tosunoglu, S., 2006. Virtual Rapid Robot Prototyping. *ASME*



*Early Career Technical Journal*, 5 (1), 1–8.

- Ding, B., Li, Y., and Tang, Y., 2015. Workspace analysis for a 3-DOF compliant parallel mechanism based on SimMechanics. *Proceedings of the 2015 7th IEEE International Conference on Cybernetics and Intelligent Systems, CIS 2015 and Robotics, Automation and Mechatronics, RAM 2015*, 48–53.
- Donald, B. and Spong, M. W., n.d. Forward Kinematics: The Denavit-Hartenberg Convention. *In*: [online]. Available from: <http://www.cs.duke.edu/brd/Teaching/Bio/asmb/current/Papers/chap3-forward-kinematics.pdf>.
- Donnet, C. and Erdemir, A., 2004. Historical developments and new trends in tribological and solid lubricant coatings. *Surface and Coatings Technology*, 180–181, 76–84.
- Dooner, M., Wang, J., and Mouzakitis, A., 2015. Dynamic modelling and experimental validation of an automotive windshield wiper system for hardware in the loop simulation. *Systems Science & Control Engineering* [online], 3 (1), 230–239. Available from: <http://www.tandfonline.com/doi/full/10.1080/21642583.2015.1012309>.
- Egawa, E. ., Kawamura, K. ., Ikuta, M. ., and Eguchi, T. ., 2013. Use of construction machinery in earthquake recovery work. *Hitachi Review* [online], 62 (2), 136–141. Available from: <http://www.scopus.com/inward/record.url?eid=2-s2.0-84876211338&partnerID=40&md5=fd8148f3f5a04c504a3721fe44f5b82d>.
- El-Sherik, A. M., Erb, U., and Page, J., 1997. Microstructural evolution in pulse plated nickel electrodeposits. *Surface and Coatings Technology* [online], 88 (1–3), 70–78. Available from: <http://www.sciencedirect.com/science/article/pii/S0257897296029283>.
- Electrolytics inc., 2016. *Faraday's law* [online]. Available from: <http://www.electrolytics.org/faradaysLaw.html> [Accessed 12 Jun 2016].
- Erdemir, A., 2005. Review of engineered tribological interfaces for improved boundary lubrication. *Tribology International* [online], 38 (3), 249–256. Available from: <http://linkinghub.elsevier.com/retrieve/pii/S0301679X04001641>.
- Erdemir, A., Ramirez, G., Eryilmaz, O. L., Narayanan, B., Liao, Y., Kamath, G., and Sankaranarayanan, S. K. R. S., 2016. Carbon-based tribofilms from

- lubricating oils. *Nature* [online], 536 (7614), 67–71. Available from: <http://www.nature.com/doi/10.1038/nature18948>.
- Falk, M., Brugger, H., and Adler-Kastner, L., 2002. Avalanche Survival Chances. <http://www.avalanche.org> [online]. Available from: <http://www.avalanche.org/moonstone/rescue/avalanche>.
- Farhat, Z. N., Ding, Y., Northwood, D. O., and Alpas, A. T., 1996. Effect of grain size on friction and wear of nanocrystalline aluminum. *Materials Science and Engineering: A* [online], 206 (2), 302–313. Available from: <http://linkinghub.elsevier.com/retrieve/pii/0921509395100164>.
- Featherstone, R. and Orin, D. E., 2008. Dynamics. *Robotics*, 35–65.
- Feng, Q., Li, T., Yue, H., Qi, K., Bai, F., and Jin, J., 2008. Preparation and characterization of nickel nano-Al<sub>2</sub>O<sub>3</sub> composite coatings by sediment co-deposition. *Applied Surface Science* [online], 254 (8), 2262–2268. Available from: <http://linkinghub.elsevier.com/retrieve/pii/S016943320701313X> [Accessed 12 Jan 2017].
- Findik, F., 2014. Latest progress on tribological properties of industrial materials. *Materials and Design* [online], 57, 218–244. Available from: <http://dx.doi.org/10.1016/j.matdes.2013.12.028>.
- Flores, P., 2009. Modeling and simulation of wear in revolute clearance joints in multibody systems. *Mechanism and Machine Theory* [online], 44 (6), 1211–1222. Available from: <http://dx.doi.org/10.1016/j.mechmachtheory.2008.08.003>.
- Flores, P. and Ambrósio, J., 2004. Revolute joints with clearance in multibody systems. *Computers and Structures*, 82 (17–19), 1359–1369.
- Flores, P., Ambrósio, J., Claro, J. C. P., and Lankarani, H. M., 2008. Multibody systems formulation. In: *Lecture notes in applied and computational mechanics* [online]. Available from: [http://link.springer.com/10.1007/978-3-540-74361-3\\_1](http://link.springer.com/10.1007/978-3-540-74361-3_1).
- Flores, P., Ambrósio, J., Claro, J. C. P., Lankarani, H. M., and Koshy, C. S., 2006. A study on dynamics of mechanical systems including joints with clearance and lubrication. *Mechanism and Machine Theory* [online], 41 (3), 247–261. Available from: <http://linkinghub.elsevier.com/retrieve/pii/S0094114X05001618>.

- García-Lecina, E., García-Urrutia, I., Díez, J. A., Morgiel, J., and Indyka, P., 2012. A comparative study of the effect of mechanical and ultrasound agitation on the properties of electrodeposited Ni/Al<sub>2</sub>O<sub>3</sub> nanocomposite coatings. *Surface and Coatings Technology* [online], 206 (11–12), 2998–3005. Available from: <http://dx.doi.org/10.1016/j.surfcoat.2011.12.037>.
- Garland, N. P., 2004. Sustainable Design of Hydrocarbon Refrigerants Applied to The Hermetic Compressor. [online]. Bournemouth University. Available from: [http://eprints.bournemouth.ac.uk/311/1/Nigel\\_Garland.pdf](http://eprints.bournemouth.ac.uk/311/1/Nigel_Garland.pdf).
- van Geffen, V., 2009. *A study of friction models and friction compensation* [online]. Available from: <http://www.mate.tue.nl/mate/pdfs/11194.pdf>.
- Giannotti, D., Patrizi, G., Di Rocco, G., Vestri, A. R., Semproni, C. P., Fiengo, L., Pontone, S., Palazzini, G., and Redler, A., 2013. Play to Become a Surgeon: Impact of Nintendo Wii Training on Laparoscopic Skills. *PLoS ONE* [online], 8 (2), e57372. Available from: <http://dx.plos.org/10.1371/journal.pone.0057372>.
- Gimson Robotics, 2015. GLA200 12V DC Linear Actuator. [online]. Available from: [http://www.gimsonrobotics.co.uk/GLA200\\_12V-linear-actuator.html](http://www.gimsonrobotics.co.uk/GLA200_12V-linear-actuator.html).
- Głowiński, S., Krzyżyński, T., Pecolt, S., and Maciejewski, I., 2015. Design of motion trajectory of an arm exoskeleton. *Archive of Applied Mechanics* [online], 85 (1), 75–87. Available from: <http://link.springer.com/10.1007/s00419-014-0900-8%5Cnfile:///Users/jurgen/Documents/Hybrid/downloads/Springer/Springer Confirmed OA/art%3A10.1007%2Fs00419-014-0900-8.pdf%5Cnpapers2://publication/doi/10.1007/s00419-014-0900-8>.
- Gomes, A., Pereira, I., Fernández, B., and Pereiro, R., 2011. Electrodeposition of metal matrix nanocomposites: improvement of the chemical characterization techniques. *In: Advances in nanocomposites-synthesis, characterization and industrial applications*. InTech.
- Góral, A., Lityńska-Dobrzyńska, L., and Kot, M., 2017. Effect of Surface Roughness and Structure Features on Tribological Properties of Electrodeposited Nanocrystalline Ni and Ni/Al<sub>2</sub>O<sub>3</sub> Coatings. *Journal of Materials Engineering and Performance* [online], 26 (5), 2118–2128. Available from: <http://link.springer.com/10.1007/s11665-017-2662-2>.
- Government Queen's Printer and Controller and Government Maritime

- Coastguard Agency, 2008. Search and Rescue Framework for the United Kingdom of Great Britain and Northern Ireland. [online]. Available from: [https://www.gov.uk/government/uploads/system/uploads/attachment\\_data/file/291770/mca\\_uksar.pdf](https://www.gov.uk/government/uploads/system/uploads/attachment_data/file/291770/mca_uksar.pdf).
- Granda, J. and Montgomery, R., 2003. Automated Modeling And Simulation Using The Bond Graph Method For The Aerospace Industry. *2003 AIAA Modeling and Simulation Technologies Conference*.
- Groover Jr., M. P. and Zimmers Jr., E. W., 1997. *CAD/Cam: Computer-Aided Design and Manufacturing*. 1st ed. Upper Saddle River, NJ, USA: Prentice Hall PTR.
- Grossman, M. and Gmitterko, A., 2008. N-link inverted pendulum , LQR control , some observations. *AT&P journal PLUS1*, 62–65.
- Grzesik, W., Zalisz, Z., Krol, S., and Nieslony, P., 2006. Investigations on friction and wear mechanisms of the PVD-TiAlN coated carbide in dry sliding against steels and cast iron. *Wear* [online], 261 (11–12), 1191–1200. Available from: <http://linkinghub.elsevier.com/retrieve/pii/S0043164806001219>.
- Gurrappa, I. and Binder, L., 2008. Electrodeposition of nanostructured coatings and their characterization—a review. *Science and Technology of Advanced Materials* [online], 9 (4), 43001. Available from: <http://stacks.iop.org/1468-6996/9/i=4/a=043001>.
- Haessig, D. A. and Friedland, B., 1991. On the Modeling and Simulation of Friction. *Journal of Dynamic Systems, Measurement, and Control* [online], 113 (3), 354. Available from: <http://dx.doi.org/10.1115/1.2896418>.
- Hardell, C., 1996. An integrated system for computer aided design and analysis of multibody systems. *Engineering with Computers* [online], 12 (1), 23–33. Available from: <http://link.springer.com/10.1007/BF01200259>.
- Hirayama, A. and Ito, K., 2008. Development of rescue manipulator to search narrow space for victims. *Artificial Life and Robotics* [online], 13 (1), 331–335. Available from: <http://link.springer.com/10.1007/s10015-008-0557-x>.
- Hoan, L. Q., Jeong, C. S., Kim, H. S., Yang, L. H., Yang, S., and Yang, H. L., 2011. Study on modeling and control of excavator. *laarc* [online]. Available from: <http://www.iaarc.org/publications/fulltext/S28-3.pdf>.
- Hollerbach, J. M., Hunter, I. W., and Ballantyne, J., 1991. A comparative

- analysis of actuator technologies for robotics. *The Robotics Review* 2.
- Hroncova, D. and Pastor, M., 2013. Mechanical System and SimMechanics Simulation. *American Journal of Mechanical Engineering*, 1 (7), 251–255.
- Ibrahim, R. A., 1994. Friction-Induced Vibration, Chatter, Squeal, and Chaos—Part II: Dynamics and Modeling. *Applied Mechanics Reviews* [online], 47 (7), 227. Available from: <http://appliedmechanicsreviews.asmedigitalcollection.asme.org/article.aspx?articleid=1395345>.
- Ivaldi, S., Padois, V., and Nori, F., 2014. Tools for dynamics simulation of robots: a survey based on user feedback. *CoRR*, 15.
- Johansson, P., Bengtsson, S., and Dizdar, S., 2002. RCF-testing of selectively densified rollers of P/M materials for gear applications. *Advances in Powder Metallurgy and Particulate Materials*, (5), 5–180.
- Julthongpiput, D., Ahn, H., Sidorenko, A., Kim, D., and Tsukruk, V. V., 2002. Towards self-lubricated nanocoatings, 35, 829–836.
- Jung, A., Natter, H., Hempelmann, R., and Lach, E., 2009. Nanocrystalline alumina dispersed in nanocrystalline nickel: enhanced mechanical properties. *Journal of Materials Science* [online], 44 (11), 2725–2735. Available from: <http://link.springer.com/10.1007/s10853-009-3330-1>.
- Karkee, M., Steward, B. L., Kelkar, A. G., and Kemp, Z. T., 2011. Modeling and real-time simulation architectures for virtual prototyping of off-road vehicles. *Virtual Reality*, 15 (1), 83–96.
- Kato, K., 2014. Tribology in the past and future. *Mechanical Engineering Reviews* [online], 1 (1), DSM0008--DSM0008. Available from: <http://jlc.jst.go.jp/DN/JST.JSTAGE/mer/2014dsm0008?lang=en&from=CrossRef&type=abstract>.
- Kavitha, C., Shankar, S. A., Ashok, B., Ashok, S. D., Ahmed, H., and Kaisan, M. U., 2018. Adaptive suspension strategy for a double wishbone suspension through camber and toe optimization. *Engineering Science and Technology, an International Journal* [online], 21 (1), 149–158. Available from: <http://linkinghub.elsevier.com/retrieve/pii/S2215098617306833>.
- Kelly, G. L. and Finlayson, T. R., 1998. Modification of a pin-on-disk wear machine for rolling contact wear. *Wear* [online], 214 (2), 287–288. Available from: <http://linkinghub.elsevier.com/retrieve/pii/S0043164897001932>

[Accessed 21 Jun 2017].

- Khan, Z. A., Chacko, V., and Nazir, H., 2017. A review of friction models in interacting joints for durability design. *Friction* [online], 5 (1), 1–22. Available from: <http://link.springer.com/10.1007/s40544-017-0143-0>.
- Khurshid, A., Khan, Z. A., Chacko, V., Ghafoor, A., Malik, M. A., and Ayaz, Y., 2016. Modelling and Simulation of a Manipulator with Stable Viscoelastic Grasping Incorporating Friction. *Tribology in Industry* [online], 38 (4), 559–574. Available from: <http://www.tribology.fink.rs/journals/2016/2016-4/13.pdf>.
- Kiapei, M. A. and M. E. S. and H. J. and E. G. and A., 2014. Factor Resistance Comparison of a Long Shaft in 955 and 1055 John Deere Grain Combine . *International Journal of Mechanical, Aerospace, Industrial, Mechatronic and Manufacturing Engineering* [online]. Available from: <http://waset.org/publications/10001342> PU - World Academy of Science, Engineering and Technology NX - International Science Index 96, 2014.
- Kim, W. and Weil, R., 1989. Pulse plating effects in nickel electrodeposition. *Surface and Coatings Technology* [online], 38 (3), 289–298. Available from: <http://www.sciencedirect.com/science/article/pii/0257897289900911>.
- Kim, Y. B., Ha, J., Kang, H., Kim, P. Y., Park, J., and Park, F. C., 2013. Dynamically optimal trajectories for earthmoving excavators. *Automation in Construction* [online], 35, 568–578. Available from: <http://dx.doi.org/10.1016/j.autcon.2013.01.007>.
- Kliesen, K. L. and Mill, J. S., 1994. The economics of natural disasters. *The regional economist*, 332.
- Koike, H., Kanemasu, K., Itakura, K., Saruwatari, K., Rozwadowska, J., Uryu, M., Santos, E. C., and Kida, K., 2013. Wear and Transmission Error between PEEK Bush and 7075 Aluminium Alloy Cam Plate Components in Robot Joints. *Applied Mechanics and Materials* [online], 307, 3–8. Available from: <http://www.scientific.net/AMM.307.3>.
- Koivo, A. J., 1994. Kinematics of Excavators (Backhoes) for Transferring Surface Material. *Journal of Aerospace Engineering* [online], 7 (1), 17–32. Available from: [http://dx.doi.org/10.1061/\(ASCE\)0893-1321\(1994\)7:1\(17\)](http://dx.doi.org/10.1061/(ASCE)0893-1321(1994)7:1(17)).
- Koivo, A. J., Thoma, M., Kocaoglan, E., and Andrade-Cetto, J., 1996. Modeling and Control of Excavator Dynamics during Digging Operation. *Journal of*

- Aerospace Engineering* [online], 9 (1), 10–18. Available from:  
<http://ascelibrary.org/doi/10.1061/%28ASCE%290893-1321%281996%299%3A1%2810%29>.
- Kollia, C., Spyrellis, N., Amblard, J., Froment, M., and Maurin, G., 1990. Nickel plating by pulse electrolysis: textural and microstructural modifications due to adsorption/desorption phenomena. *Journal of Applied Electrochemistry* [online], 20 (6), 1025–1032. Available from:  
<http://dx.doi.org/10.1007/BF01019584>.
- Korayem, M. H. and Shafei, A. M., 2013. Application of recursive Gibbs–Appell formulation in deriving the equations of motion of N-viscoelastic robotic manipulators in 3D space using Timoshenko Beam Theory. *Acta Astronautica* [online], 83, 273–294. Available from:  
<http://www.sciencedirect.com/science/article/pii/S0094576512004043>.
- Kramer, J. A. and Murphy, R. R., 2006. Endurance testing for safety, security and rescue robots. *Performance Metrics for Intelligent Systems* [online]. Available from: [http://www.mind-melt.com/Mind-Melt/Papers\\_files/Jeffrey Kramer - PERMIS 2006.pdf](http://www.mind-melt.com/Mind-Melt/Papers_files/JeffreyKramer - PERMIS 2006.pdf).
- De Laurentis, N., Kadiric, A., Lugt, P., and Cann, P., 2016. The influence of bearing grease composition on friction in rolling/sliding concentrated contacts. *Tribology International* [online], 94, 624–632. Available from:  
<http://dx.doi.org/10.1016/j.triboint.2015.10.012> [Accessed 18 Sep 2017].
- Le, Q. H., Jeong, Y. M., Nguyen, C. T., and Yang, S., 2012. Control of virtual excavating system base on real-time simulation. *Control, Automation and Systems (ICCAS), 2012 12th International Conference on*, 1 (1), 703–707.
- Le, Q. H., Jeong, Y. M. Y. M., Nguyen, C. T. C. T., and Yang, S. Y. Y., 2013. Development of a Virtual Excavator using SimMechanics and SimHydraulic. *Journal of The Korean Society for Fluid Power & Construction Equipments* [online], 10 (1), 29–36. Available from:  
[http://www.koreascience.or.kr/article/ArticleFullRecord.jsp?cn=OGSSB4\\_2013\\_v10n1\\_29](http://www.koreascience.or.kr/article/ArticleFullRecord.jsp?cn=OGSSB4_2013_v10n1_29).
- Leyland, A. and Matthews, A., 2000. On the significance of the H/E ratio in wear control: A nanocomposite coating approach to optimised tribological behaviour. *Wear*, 246 (1–2), 1–11.
- Li, C., Wang, Y., and Pan, Z., 2013. Wear resistance enhancement of

electroless nanocomposite coatings via incorporation of alumina nanoparticles prepared by milling. *Materials & Design* [online], 47, 443–448. Available from: <http://www.sciencedirect.com/science/article/pii/S0261306912008424> [Accessed 29 May 2015].

Liljeström, J. and Isomaa, J.-M., 2013. *Electrification of excavator*.

Lima, P. U., 2012. Search and rescue robots: The civil protection teams of the future. In: *Emerging Security Technologies (EST), 2012 Third International Conference on*. 12–19.

Lingard, H., Cooke, T., and Gharaie, E., 2013. A case study analysis of fatal incidents involving excavators in the Australian construction industry. *Engineering, Construction and Architectural Management* [online], 20 (5), 488–504. Available from: <http://emerald-test.literatumonline.com/doi/abs/10.1108/ECAM-08-2011-0073>.

Lioy, P. J., Weisel, C. P., Millette, J. R., Eisenreich, S., Vallero, D., Offenber, J., Buckley, B., Turpin, B., Zhong, M., Cohen, M. D., Prophete, C., Yang, I., Stiles, R., Chee, G., Johnson, W., Porcja, R., Alimokhtari, S., Hale, R. C., Weschler, C., and Chen, L. C., 2002. Characterization of the Dust/Smoke Aerosol that Settled East of the World Trade Center (WTC) in Lower Manhattan after the Collapse of the WTC 11 September 2001. *Environmental Health Perspectives* [online], 110 (7), 703–14. Available from: <http://www.pubmedcentral.nih.gov/articlerender.fcgi?artid=1240917%7B%7Dtool=pmcentrez%7B%7Drendertype=abstract>.

Lischinsky, P., Canudas de Wit, C., and Morel, G., 1999. Friction compensation for an industrial hydraulic robot. *IEEE Control Systems Magazine* [online], 19 (1), 25–32. Available from: <http://ieeexplore.ieee.org/document/745763/>.

Low, C. T. J., Wills, R. G. A., and Walsh, F. C., 2006. Electrodeposition of composite coatings containing nanoparticles in a metal deposit. *Surface and Coatings Technology*, 201 (1–2), 371–383.

Lu, Y., Wang, P., and Ye, N., 2018. Kinematics/dynamics analysis of novel 3UPUR + SP-type hybrid hand with three flexible fingers. *Nonlinear Dynamics* [online], 91 (2), 1127–1144. Available from: <http://link.springer.com/10.1007/s11071-017-3935-x>.



- Ludema, K. C., 1996. *Friction, Wear, Lubrication - A Textbook in Tribology* [online]. CRC Press. Available from: <http://www.crcnetbase.com/isbn/9781439821893>.
- Lugt, P. M., 2016. Modern advancements in lubricating grease technology. *Tribology International* [online], 97 (February), 467–477. Available from: <http://dx.doi.org/10.1016/j.triboint.2016.01.045> [Accessed 18 Sep 2017].
- Machado, M., Moreira, P., Flores, P., and Lankarani, H. M., 2012. Compliant contact force models in multibody dynamics: Evolution of the Hertz contact theory. *Mechanism and Machine Theory* [online], 53, 99–121. Available from: <http://dx.doi.org/10.1016/j.mechmachtheory.2012.02.010>.
- Mahapatra, A., 2015. Motion Control Strategies based on PD Control for a Four Degree-of-Freedom Serial Robotic Manipulator to Mimic Human Index Finger Articulations. *International Journal of Computer Applications*, 109 (13), 35–42.
- Mahapatra, S., 2011. Enhancing Simulation Studies with 3D Animation. *AIAA Modeling and Simulation Technologies Conference* [online]. Available from: <http://dx.doi.org/10.2514/6.2011-6244>.
- Mahapatra, S., 2013. Introduction to Simulink 3D Animation. [online]. Available from: <http://youtu.be/rZWdqODYVhQ>.
- Mahidashti, Z., Aliofkhaezai, M., and Lotfi, N., 2017. Review of Nickel-Based Electrodeposited Tribo-Coatings. *Transactions of the Indian Institute of Metals* [online], 1–39. Available from: <http://link.springer.com/10.1007/s12666-017-1175-x>.
- Maier, O., Györfi, B., Wrede, J., and Kasper, R., 2018. Design and validation of a multi-body model of a front suspension bicycle and a passive rider for braking dynamics investigations. *Multibody System Dynamics* [online], 42 (1), 19–45. Available from: <http://link.springer.com/10.1007/s11044-017-9576-5>.
- Majidi, H., Aliofkhaezai, M., Karimzadeh, A., and Rouhaghdam, A. S., 2016. Corrosion and wear behaviour of multilayer pulse electrodeposited Ni–Al<sub>2</sub>O<sub>3</sub> nanocomposite coatings assisted with ultrasound. *Bulletin of Materials Science* [online], 39 (7), 1691–1699. Available from: <http://link.springer.com/10.1007/s12034-016-1307-7>.
- Marconi, L., Melchiorri, C., Beetz, M., Pangercic, D., Siegwart, R., Leutenegger,

- S., Carloni, R., Stramigioli, S., Bruyninckx, H., Doherty, P., Kleiner, A., Lippiello, V., Finzi, A., Siciliano, B., Sala, A., and Tomatis, N., 2012. The SHERPA project: Smart collaboration between humans and ground-aerial robots for improving rescuing activities in alpine environments. *In: 2012 IEEE International Symposium on Safety, Security, and Rescue Robotics (SSRR)* [online]. IEEE, 1–4. Available from: <http://ieeexplore.ieee.org/document/6523905/>.
- Mare, J.-C., 2012. Friction modelling and simulation at system level: a practical view for the designer. *Proceedings of the Institution of Mechanical Engineers, Part I: Journal of Systems and Control Engineering* [online], 226 (6), 728–741. Available from: <http://journals.sagepub.com/doi/10.1177/0959651812441749>.
- Marques, F., Flores, P., and Lankarani, H. M., 2015. On the Frictional Contacts in Multibody System Dynamics. *ECCOMAS Thematic Conference on Multibody Dynamics*, 565–576.
- Marques, F., Flores, P., and Lankarani, H. M., 2016. *Study of Friction Force Model Parameters in Multibody Dynamics* [online]. The 4th Joint International Conference on Multibody System Dynamics. Available from: <https://repositorium.sdum.uminho.pt/bitstream/1822/42173/1/p178.pdf>.
- Mathis, A., Fregene, K., and Satterfield, B., 2009. Creating High Quality Interactive Simulations Using MATLAB® and USARSim. *Proceedings of the IROS Workshop: Robots, Games and Research: Success Stories in USARSim*, 55–59.
- Merlet, J.-P. and Gosselin, C., 2008. Parallel Mechanisms and robots. *In: Springer Handbook of Robotics*. 269–285.
- Merriam-Webster, n.d. Disaster. *Encyclopaedia Britannica* [online]. Available from: <http://www.merriam-webster.com/dictionary/disaster>.
- Mikhlin, N. M. and Lyapin, K. S., 1970. Hardness dependence of the coefficient of friction. *Soviet Physics Journal* [online], 13 (3), 317–321. Available from: <http://link.springer.com/10.1007/BF00818317>.
- Minami, I., Yamazaki, A., Nanao, H., and Mori, S., 2007. A Cylinder and Assembled Four-Block Type Tribo-Test: Novel Method to Study Tribo-Chemistry of Lubricant and Material. *Tribology Online* [online], 2 (1), 40–43. Available from: <http://joi.jlc.jst.go.jp/JST.JSTAGE/trol/2.40?from=CrossRef>.

- Mirzamohammadi, S., Khorsand, H., and Aliofkhaezai, M., 2017. Effect of different organic solvents on electrodeposition and wear behavior of Ni-alumina nanocomposite coatings. *Surface and Coatings Technology* [online]. Available from: <http://linkinghub.elsevier.com/retrieve/pii/S0257897217300257>.
- Mohan, C. B., Divakar, C., Venkatesh, K., Gopalakrishna, K., Mahesh Lohith, K. S., and Naveen, T. N., 2009. Design and development of an advanced linear reciprocating tribometer. *Wear* [online], 267 (5–8), 1111–1116. Available from: <http://linkinghub.elsevier.com/retrieve/pii/S0043164809002233> [Accessed 21 Jun 2017].
- Mosleh, M., Saka, N., and Suh, N. P., 2002. A mechanism of high friction in dry sliding bearings. *Wear* [online], 252 (1–2), 1–8. Available from: <http://linkinghub.elsevier.com/retrieve/pii/S004316480100583X>.
- Mukras, S., Kim, N. H., Mauntler, N. A., Schmitz, T. L., and Sawyer, W. G., 2010. Analysis of planar multibody systems with revolute joint wear. *Wear*, 268 (5–6), 643–652.
- Murphy, R., Kravitz, J., Stover, S., and Shoureshi, R., 2009. Mobile robots in mine rescue and recovery. *IEEE Robotics & Automation Magazine* [online], 16 (2), 91–103. Available from: <http://ieeexplore.ieee.org/document/5069840/>.
- Murphy, R. R., 2004a. Trial by fire [rescue robots]. *Robotics & Automation Magazine, IEEE*, 11 (3), 50,61.
- Murphy, R. R., 2004b. Human–Robot Interaction in Rescue Robotics. *IEEE Transactions on Systems, Man and Cybernetics, Part C (Applications and Reviews)* [online], 34 (2), 138–153. Available from: <http://ieeexplore.ieee.org/document/1291662/>.
- Murphy, R. R., 2004c. Trial by fire. *IEEE Robotics and Automation Magazine* [online], 11 (3), 50,61. Available from: <http://ieeexplore.ieee.org/stamp/stamp.jsp?tp=&arnumber=1337826&isnumber=29512>.
- Murphy, R. R., 2014. *Disaster Robotics*. MIT Press.
- Murphy, R. R., Tadokoro, S., Nardi, D., Jacoff, A., Fiorini, P., Choset, H., and Erkmen, A. M., 2008. Search and rescue robotics. In: *Springer Handbook*

- of Robotics* [online]. 1151–1173. Available from:  
<http://www.ece.wpi.edu/~rjduck/MQP>.
- Musil, J., 2000. Hard and superhard nanocomposite coatings. *Surface and Coatings Technology* [online], 125 (1–3), 322–330. Available from:  
<http://linkinghub.elsevier.com/retrieve/pii/S0257897299005861>.
- Musil, J., 2012. Hard nanocomposite coatings: Thermal stability, oxidation resistance and toughness. *Surface and Coatings Technology* [online], 207, 50–65. Available from:  
<http://linkinghub.elsevier.com/retrieve/pii/S0257897212004793>.
- NC State University, 2015. *Representing Significant Digits* [online]. Available from: <https://labwrite.ncsu.edu/res/gh/gh-sigdig.html>.
- Ni, T., Zhang, H., Yu, C., Zhao, D., and Liu, S., 2013. Design of highly realistic virtual environment for excavator simulator. *Computers & Electrical Engineering* [online], 39 (7), 2112–2123. Available from:  
[10.1016/j.compeleceng.2013.06.010](http://dx.doi.org/10.1016/j.compeleceng.2013.06.010).
- Noy, I., 2012. The enduring economic aftermath of natural catastrophes. *Vox*, <http://www.voxeu.org/article/economic-consequences-natural-catastrophes>.
- Oh, K. W., Kim, D., Kim, N. H., and Hong, D., 2011. The Virtual Environment For Force-Feedback Experiment Of Excavator Using A Novel Designed Haptic Device. *In: Proceedings of the 28th ISARC* [online]. Seoul, Korea, 51–56. Available from: <http://www.iaarc.org/publications/fulltext/S02-2.pdf>.
- Olsson, H., Åström, K. J., Canudas de Wit, C., Gäfvert, M., and Lischinsky, P., 1998. Friction Models and Friction Compensation. *European Journal of Control* [online]. Available from:  
<http://www.sciencedirect.com/science/article/pii/S094735809870113X?via%3Dihub>.
- Osero, N. M., 1986. An overview of pulse plating. *Plat. Surf. Finish.*, 73 (3), 20–22.
- Panas, A., Comouth, A., Saathoff, H., Leisner, T., Al-Rawi, M., Simon, M., Seemann, G., D??ssel, O., M??lhopt, S., Paur, H. R., Fritsch-Decker, S., Weiss, C., and Diabat??, S., 2014. Characterization of the Dust / Smoke Aerosol that Settled East of the World Trade Center ( WTC ) in Lower Manhattan after the Collapse of the WTC 11 September 2001. *Beilstein*

- Journal of Nanotechnology*, 5 (1), 1590–1602.
- Papadopoulos, E., Mu, B., and Frenette, R., 2003. On modeling, identification, and control of a heavy-duty electrohydraulic harvester manipulator. *IEEE/ASME Transactions on Mechatronics*, 8 (2), 178–187.
- Patel, B. P. and Prajapati, J. M., 2013. Kinematics of Mini Hydraulic Backhoe Excavator – Part: I. *Int. J. Mech. Eng & Rob. Res. 2013* [online], 2 (1), 166–182. Available from: <http://www.inderscience.com/link.php?id=57301>.
- Patel, B. P. and Prajapati, J. M., 2014. Dynamics of Mini Hydraulic Backhoe Excavator: A Lagrange-Euler (LE) Approach. *International Journal of Mechanical, Aerospace, Industrial, Mechatronic and Manufacturing Engineering Vol:8, No:1* [online], 8 (1), 202–211. Available from: <http://www.waset.org/publications/9997585>.
- Peiper, D. L., 1968. *The kinematics of manipulators under computer control*.
- Peipmann, R., Thomas, J., and Bund, A., 2007. Electrocodeposition of nickel–alumina nanocomposite films under the influence of static magnetic fields. *Electrochimica Acta* [online], 52 (19), 5808–5814. Available from: <http://linkinghub.elsevier.com/retrieve/pii/S0013468607003489>.
- Piedboeuf, J. C., 1993. Kane’s equations or Jourdain’s principle? *Proceedings of the 36th Midwest Symposium on Circuits and Systems*, 2 (7), 1471–1474.
- Popić, S. and Miloradović, B., 2015. Light weight robot arms-an overview. *INFOTEH-JAHORINA*, 14.
- Popinchalk, S., 2008. *What is a Composite Signal?* [online]. Mathworks Blogs - Guy and Seth on Simulink. Available from: <https://blogs.mathworks.com/simulink/2008/03/27/what-is-a-composite-signal/>.
- Qing-hua, H. E., Da-qing, Z., Peng, H. A. O., and Hai-tao, Z., 2006. Modelling and control of hydraulic excavator’s arm. *J. Cent. South Univ. Technol.*, 13 (4), 422–427.
- Quan, Z., Quan, L., and Zhang, J., 2014. Review of energy efficient direct pump controlled cylinder electro-hydraulic technology. *Renewable and Sustainable Energy Reviews* [online], 35, 336–346. Available from: <http://dx.doi.org/10.1016/j.rser.2014.04.036>.
- Raghavendra, C. R., Basavarajappa, S., and Sogalad, I., 2016.

Electrodeposition of Ni-Al<sub>2</sub>O<sub>3</sub> nano composite coating and evaluation of wear characteristics. *IOP Conference Series: Materials Science and Engineering* [online], 149, 012110. Available from: <http://stacks.iop.org/1757-899X/149/i=1/a=012110?key=crossref.12131487848477a84e828ec8ec984ba0>.

Raibert, M., Blankespoor, K., Nelson, G., and Playter, R., 2008. BigDog, the Rough-Terrain Quadruped Robot. *IFAC Proceedings Volumes* [online], 41 (2), 10822–10825. Available from: <http://linkinghub.elsevier.com/retrieve/pii/S1474667016407020>.

Rashid, M. Z. A., Aras, M., Radzak, A. A., Kassim, A. M., and Jamali, A., 2012. Development of Hexapod Robot with Manoeuvrable Wheel. *International Journal of Advanced Science and Technology*, 49.

Rashidi, A. M. and Amadeh, A., 2009. The effect of saccharin addition and bath temperature on the grain size of nanocrystalline nickel coatings. *Surface and Coatings Technology* [online], 204 (3), 353–358. Available from: <http://dx.doi.org/10.1016/j.surfcoat.2009.07.036>.

Rouleau, G., 2012. *Applying Motion to SimMechanics Models* [online]. Mathworks Blogs - Guy and Seth on Simulink. Available from: <http://blogs.mathworks.com/seth/2012/02/01/applying-motion-to-simmechanics-models/> [Accessed 12 May 2015].

Rouleau, G., 2015. *Why you should never break a continuous algebraic loop with a Memory block* [online]. Simulink & Model-Based Design: Guy on Simulink. Available from: <https://blogs.mathworks.com/simulink/2015/07/18/why-you-should-never-break-an-algebraic-loop-with-with-a-memory-block/> [Accessed 2 Jan 2018].

Roy, R., Roy, R. A., and Roy, D. M., 1986. Alternative perspectives on quasi-crystallinity: non-uniformity and nanocomposites. *Materials Letters*, 4 (8–9), 323–328.

Ruff, R., Stephens, C., and Mahapatra, S., 2012. Applying Model-Based Design to Large-Scale Systems Development: Modeling, Simulation, Test, & Deployment of a Multirotor Vehicle. *AIAA Modeling and Simulation ...* [online], 1–17. Available from: <http://arc.aiaa.org/doi/pdf/10.2514/6.2012-4939>.

- Saha, R. K. and Khan, T. I., 2010. Effect of applied current on the electrodeposited Ni–Al<sub>2</sub>O<sub>3</sub> composite coatings. *Surface and Coatings Technology* [online], 205 (3), 890–895. Available from: <http://linkinghub.elsevier.com/retrieve/pii/S0257897210006845> [Accessed 12 Jan 2017].
- Sahoo, P. and Das, S. K., 2011. Tribology of electroless nickel coatings - A review. *Materials and Design* [online], 32 (4), 1760–1775. Available from: <http://dx.doi.org/10.1016/j.matdes.2010.11.013>.
- Šalinić, S., Bošković, G., and Nikolić, M., 2014. Dynamic modelling of hydraulic excavator motion using Kane's equations. *Automation in Construction*, 44, 56–62.
- SantAna, P. L., Dos Santos, L. V., Silva, T. F., Dos Santos, R. J., Bortoleto, J. R. R., Da Cruz, N. C., Rangel, E. C., and Durrant, S. F., 2017. Study of a-C:H thin films grown by PIII in different times for Mechanical and Tribological applications. *Revista Brasileira de Aplicações de Vácuo* [online], 36 (2), 52. Available from: <http://www.sbvacu.org.br/rbav/index.php/rbav/article/view/1065>.
- Sarata, S., Sato, K., and Yuta, S., 1995. Motion Control System for Autonomous Wheel Loader Operation. In: *In Proceedings, International Symposium on Mine Mechanization and Automation*. Colorado.
- Sargent, R. G., 2005. Verification and validation of simulation models. In: *Proceedings of the 2005 Winter Simulation Conference*. 130–143.
- Sawyer, W. G., Diaz, K. I., Hamilton, M. A., and Micklos, B., 2003. Evaluation of a Model for the Evolution of Wear in a Scotch-Yoke Mechanism. *Journal of Tribology* [online], 125 (3), 678. Available from: <http://tribology.asmedigitalcollection.asme.org/article.aspx?articleid=1466947>.
- Schiehlen, W., 1997. Multibody System Dynamics: Roots and Perspectives. *Multibody System Dynamics* [online], 1 (2), 149–188. Available from: <http://link.springer.com/article/10.1023/A:1009745432698%5Cnhttp://link.springer.com/article/10.1023/A:1009745432698>.
- Schlotter, M., 2003. Multibody System Simulation with SimMechanics. *Analysis*, (May), 1–23.
- Schneider, M. J. and Chatterjee, M. S., 2013. Introduction to surface hardening

of steels. *ASM Handbook, Volume 4A, Heat treating* [online], 4, 259–267.

Available from:

<http://scholar.google.com/scholar?hl=en%7B&%7DbtnG=Search%7B&%7Dq=intitle:Introduction+to+Surface+Hardening+of+Steels%7B#%7D0>.

Sebastian, K. S. and Bhaskar, V. R., 1995. A new design for the pin and V-blocks tribometer. *Tribology International* [online], 28 (4), 219–223.

Available from:

<http://linkinghub.elsevier.com/retrieve/pii/0301679X9400005B> [Accessed 21 Jun 2017].

Seymour, N. E., Gallagher, A. G., Roman, S. A., O'Brien, M. K., Bansal, V. K., Andersen, D. K., and Satava, R. M., 2002. Virtual Reality Training Improves Operating Room Performance: Results of a Randomized, Double-Blinded Study. *Ann Surg* [online], 236 (4), 458–464. Available from:

<http://www.ncbi.nlm.nih.gov/pmc/articles/PMC1422600/pdf/20021000s00008p458.pdf>.

Shafiei, M. and Alpas, A. T., 2008. Effect of sliding speed on friction and wear behaviour of nanocrystalline nickel tested in an argon atmosphere. *Wear* [online], 265 (3–4), 429–438. Available from:

<http://www.sciencedirect.com/science/article/pii/S004316480700751X> [Accessed 28 May 2017].

Shen, W., Jiang, J., Su, X., and Reza Karimi, H., 2015. Control strategy analysis of the hydraulic hybrid excavator. *J. Franklin Inst.* [online], 352 (2), 541–561. Available from:

<http://www.sciencedirect.com/science/article/pii/S0016003214001082%5Cn>  
<http://dx.doi.org/10.1016/j.jfranklin.2014.04.007>.

Siciliano, B. and Khatib, O., 2008. *Springer Handbook of Robotics* [online]. 1st ed. Springer-Verlag Berlin Heidelberg. Available from:

<http://www.springer.com/gb/book/9783540239574>.

Singh, H., Ramirez, G., Eryilmaz, O. L., Greco, A., Doll, G., and Erdemir, A., 2016. Fatigue resistant carbon coatings for rolling/sliding contacts.

*Tribology International* [online], 98, 172–178. Available from:

<http://dx.doi.org/10.1016/j.triboint.2016.02.008>.

Singh, S., 1995a. Synthesis of Tactical Plans for Robotic Excavation. *The Robotics Institute* [online]. Carnegie Mellon University, Pittsburgh, PA



15213. Available from:

[http://www.researchgate.net/publication/2306381%7B\\_%7DSynthesis%7B\\_%7Dof%7B\\_%7DTactical%7B\\_%7DPlans%7B\\_%7Dfor%7B\\_%7DRobotic%7B\\_%7DExcavation/file/72e7e52adb782e95d3.pdf](http://www.researchgate.net/publication/2306381%7B_%7DSynthesis%7B_%7Dof%7B_%7DTactical%7B_%7DPlans%7B_%7Dfor%7B_%7DRobotic%7B_%7DExcavation/file/72e7e52adb782e95d3.pdf).

Singh, S., 1995b. Learning to predict resistive forces during robotic excavation.

*Proceedings of 1995 IEEE International Conference on Robotics and Automation* [online], 2, 2102–2107. Available from:

<http://ieeexplore.ieee.org/document/526025/>.

Sinha, R., Paredis, C. J. J., Liang, V.-C., and Khosla, P. K., 2001. Modeling and Simulation Methods for Design of Engineering Systems. *Journal of Computing and Information Science in Engineering* [online], 1 (1), 84.

Available from:

<http://computingengineering.asmedigitalcollection.asme.org/article.aspx?articleid=1399186>.

Song, H., Rong, X., and Li, Y., 2013. A Co-simulation Approach based on ADAMS-SIMULINK for Development of Manipulator Position Controller. *In: Proceeding of the 32nd Chinese Control Conference* [online]. 8648–8652.

Available from:

[http://ieeexplore.ieee.org/xpls/abs%7B\\_%7Dall.jsp?arnumber=6640974](http://ieeexplore.ieee.org/xpls/abs%7B_%7Dall.jsp?arnumber=6640974).

Sparkfun, 2015. HS-805BB+. [online]. Available from:

<https://www.sparkfun.com/products/11881>.

Stachowiak, G. and Batchelor, A. W., 2013. *Engineering tribology*. Butterworth-Heinemann.

Statheropoulos, M., Agapiou, a., Pallis, G. C., Mikedi, K., Karma, S.,

Vamvakari, J., Dandoulaki, M., Andritsos, F., and Thomas, C. L. P., 2014.

Factors that affect rescue time in urban search and rescue (USAR) operations. *Natural Hazards* [online], 75 (1), 57–69. Available from:

<http://link.springer.com/10.1007/s11069-014-1304-3>.

Steel, W. Y., 2017. *EN 19 steel* [online]. Available from:

<https://www.westyorkssteel.com/alloy-steel/engineering-steel/en19t/>.

Stepanova, E. R., von der Heyde, M., Kitson, A., Schiphorst, T., and Riecke, B.

E., 2017. Gathering and Applying Guidelines for Mobile Robot Design for Urban Search and Rescue Application. *In: International Conference on Human-Computer Interaction*. 562–581.

- Stolarski, T. A., 1990. Elements of contact mechanics. *In: Tribology in Machine Design* [online]. Elsevier, 64–96. Available from:  
<http://linkinghub.elsevier.com/retrieve/pii/B9780434918263500067>.
- Stone, H. W. and Edmonds, G., 1992. HAZBOT: a hazardous materials emergency response mobile robot. *Proceedings 1992 IEEE International Conference on Robotics and Automation*, 67–73.
- Stoneking, E., 2007. Newton-Euler Dynamic Equations of Motion for a Multi-Body Spacecraft. *In: AIAA Guidance, Navigation and Control Conference and Exhibit* [online]. Reston, Virginia: American Institute of Aeronautics and Astronautics, 1–13. Available from: Stoneking 2007 - Newton-Euler Dynamic Equations of Motion.pdf.
- Szewczyk, R., Zieliński, C., and Kaliczyńska, M., eds., 2015. *Progress in Automation, Robotics and Measuring Techniques* [online]. Cham: Springer International Publishing. Available from:  
<http://link.springer.com/10.1007/978-3-319-15796-2>.
- Tadić, B., Ivković, B., and Todorović, P., 2002. Theoretical Basis of Pin and Block Carrier Design at Tribometer Tpd-2000. *Tribology in Industry* [online], 24 (3&4), 39–41. Available from:  
<http://www.tribology.fink.rs/journals/2002/3-4/3.pdf>.
- Tadokoro, S., Verhoeven, R., Hiller, M., and Takamori, T., 1999. A portable parallel manipulator for search and rescue at large-scale urban earthquakes and an identification algorithm for the installation in unstructured environments. *Proceedings 1999 IEEE/RSJ International Conference on Intelligent Robots and Systems. Human and Environment Friendly Robots with High Intelligence and Emotional Quotients (Cat. No.99CH36289)*, 2, 1222–1227.
- Tafazoli, S., Lawrence, P. D., and Salcudean, S. E., 1999. Identification of inertial and friction parameters for excavator arms. *IEEE Transactions on Robotics and Automation* [online], 15 (5), 966–971. Available from:  
<http://ieeexplore.ieee.org/lpdocs/epic03/wrapper.htm?arnumber=795801>.
- Tafazoli, S., Lawrence, P. D., Salcudean, S. E., Chan, D., Bachmann, S., and De Silva, C. W., 1996. Parameter estimation and actuator friction analysis for a mini excavator. *In: Proceedings of IEEE International Conference on Robotics and Automation* [online]. IEEE, 329–334. Available from:

- [http://ieeexplore.ieee.org/xpls/abs\\_all.jsp?arnumber=503798](http://ieeexplore.ieee.org/xpls/abs_all.jsp?arnumber=503798).
- Tafazoli, S., Salcudean, S. E., Hashtrudi-Zaad, K., and Lawrence, P. D., 2002. Impedance control of a teleoperated excavator. *IEEE Transactions on Control Systems Technology*, 10 (3), 355–367.
- Tan, C. L. and Vonderembse, M. A., 2006. Mediating effects of computer-aided design usage: From concurrent engineering to product development performance. *Journal of Operations Management* [online], 24 (5), 494–510. Available from:  
<http://linkinghub.elsevier.com/retrieve/pii/S0272696305001518>.
- Texas A&M University, 2008. *Dr. Robin Murphy* [online]. Available from:  
<http://faculty.cse.tamu.edu/murphy/>.
- The Mathworks Inc. UK, 2015a. *Translational Friction* [online]. Mathworks Documentation. Available from:  
<http://uk.mathworks.com/help/physmod/simscape/ref/translationalfriction.html> [Accessed 3 Jul 2015].
- The Mathworks Inc. UK, 2015b. *Rotational Friction* [online]. Mathworks Documentation. Available from:  
[http://uk.mathworks.com/help/physmod/simscape/ref/rotationalfriction.html?s\\_tid=gn\\_loc\\_drop](http://uk.mathworks.com/help/physmod/simscape/ref/rotationalfriction.html?s_tid=gn_loc_drop) [Accessed 2 Jul 2015].
- Thiemig, D. and Bund, A., 2009. Influence of ethanol on the electrocodeposition of Ni/Al<sub>2</sub>O<sub>3</sub> nanocomposite films. *Applied Surface Science* [online], 255 (7), 4164–4170. Available from:  
<http://linkinghub.elsevier.com/retrieve/pii/S0169433208022745>.
- Thiemig, D., Bund, A., and Talbot, J. B., 2009. Influence of hydrodynamics and pulse plating parameters on the electrocodeposition of nickel–alumina nanocomposite films. *Electrochimica Acta* [online], 54 (9), 2491–2498. Available from:  
<http://www.sciencedirect.com/science/article/pii/S0013468608004921> [Accessed 29 May 2017].
- Thiemig, D., Lange, R., and Bund, A., 2007. Influence of pulse plating parameters on the electrocodeposition of matrix metal nanocomposites. *Electrochimica Acta* [online], 52 (25), 7362–7371. Available from:  
<http://www.sciencedirect.com/science/article/pii/S0013468607007852> [Accessed 29 May 2017].

- Thomas, B., Hadfield, M., and Austen, S., 2009. Experimental wear modelling of lifeboat slipway launches. *Tribology International* [online], 42 (11–12), 1706–1714. Available from: <http://dx.doi.org/10.1016/j.triboint.2009.04.043>.
- Tiwari, R., Knowles, J., and Danko, G., 2013. Bucket trajectory classification of mining excavators. *Automation in Construction* [online], 31, 128–139. Available from: <http://linkinghub.elsevier.com/retrieve/pii/S0926580512002014>.
- Tondu, B., 2012. Modelling of the McKibben artificial muscle: A review. *Journal of Intelligent Material Systems and Structures*, 23 (3), 225–253.
- Towarek, Z., 2003. Dynamics of a single-bucket excavator on a deformable soil foundation during the digging of ground. *International Journal of Mechanical Sciences* [online], 45 (6–7), 1053–1076. Available from: <http://linkinghub.elsevier.com/retrieve/pii/S0020740303001644>.
- Udai, A. D., Rajeevlochana, C. G., and Saha, S. K., 2011. Dynamic Simulation of a KUKA KR5 Industrial Robot using MATLAB SimMechanics. *15th National Conference on Machines and Mechanisms* [online], 96, 1–8. Available from: [http://web.iitd.ernet.in/~mez108088/files/udai\\_nacomm\\_2011.pdf](http://web.iitd.ernet.in/~mez108088/files/udai_nacomm_2011.pdf).
- Uicker, J. J., Pennock, G. R., Shigley, J. E., and McCarthy, J. M., 2003. Theory of Machines and Mechanisms. *Journal of Mechanical Design*.
- University of Twente, 2016. *Tribometers* [online]. Available from: <http://www.tribonet.org/tribometers/>.
- Vähä, P. ., Skibniewski, M. J., and Koivo, A. J., 1991. Excavator dynamics and effect of soil on digging. *Proceedings of the 8th ISARC, Stuttgart, Germany*, 297–306.
- Vähä, P. K. and Skibniewski, M. J., 1993. Dynamic Model of Excavator. *J. Aerosp. Eng.* [online], 6 (2), 148–158. Available from: [http://ascelibrary.org/doi/abs/10.1061/\(ASCE\)0893-1321\(1993\)6:2\(148\)](http://ascelibrary.org/doi/abs/10.1061/(ASCE)0893-1321(1993)6:2(148)).
- Vanderborght, B., Albu-Schäffer, A., Bicchi, A., Burdet, E., Caldwell, D. G., Carloni, R., Catalano, M. G., Eiberger, O., Friedl, W., Ganesh, G., Garabini, M., Grebenstein, M., Grioli, G., Haddadin, S., Hoppner, H., Jafari, A., Laffranchi, M., Lefeber, D., Petit, F. P., Stramigioli, S., Tsagarakis, N. G., Van Damme, M., Van Ham, R., Visser, L. C., and Wolf, S., 2013. Variable impedance actuators: A review. *Robotics and Autonomous Systems*

- [online], 61 (12), 1601–1614. Available from:  
<http://dx.doi.org/10.1016/j.robot.2013.06.009>.
- Vaughan, N., Dubey, V. N., Wee, M. Y. K., and Isaacs, R., 2013. A review of epidural simulators: Where are we today? *Medical Engineering and Physics* [online], 35 (9), 1235–1250. Available from:  
<http://dx.doi.org/10.1016/j.medengphy.2013.03.003>.
- Vergnano, A., Berselli, G., and Pellicciari, M., 2017. Parametric virtual concepts in the early design of mechanical systems: a case study application. *International Journal on Interactive Design and Manufacturing (IJIDeM)* [online], 11 (2), 331–340. Available from: <https://doi.org/10.1007/s12008-015-0295-y>.
- Virgala, I., Gmitterko, A., Surovec, R., Vacková, M., and Prada, E., 2012. Manipulator end-effector position control, 48, 684–692.
- Volle, C. E. E., 2014. Simscape Modeling Verification in the Simulink Development Environment.
- Voyles, R. and Choset, H., 2008. Editorial: Search and rescue robots. *Journal of Field Robotics* [online], 25 (1–2), 1–2. Available from:  
<http://onlinelibrary.wiley.com/doi/10.1002/rob.20231/abstract>.
- Waldron, K., Schmiedeler, J., Waldron, K., Schmiedeler, J., and Schmiedeler, J., 2008. Kinematics. *Springer Handbook of Robotics*, 9–33.
- Walker, P., 1991. International search and rescue teams: A League discussion paper. *In: Field Studies Paper*. League of Red Cross and Red Crescent Societies.
- Wang, B., Jin, Y., Yan, T., and Cheng, M., 2013. Mechanism Simulation and Optimal Design of Five-Link Bionic Joint Driven by Two Antagonistic Pneumatic Muscles. *Advances in Mechanical Engineering* [online], 2013 (c), 1–11. Available from:  
<http://www.hindawi.com/journals/ame/2013/824085/>.
- Wang, G. G., 2002. Definition and Review of Virtual Prototyping. *Journal of Computing and Information Science in Engineering* [online], 2 (3), 232. Available from:  
<http://link.aip.org/link/JCISB6/v2/i3/p232/s1%7B&%7DAgg=doi>.
- Wang, H., Wang, Q., Hu, B., and Feng, Q., 2013. The novel hybrid energy storing unit design for hybrid excavator by the effective integration of

- ultracapacitor and battery. *2013 IEEE/ASME International Conference on Advanced Intelligent Mechatronics* [online], 1585–1590. Available from:  
<http://ieeexplore.ieee.org/lpdocs/epic03/wrapper.htm?arnumber=6584322>.
- West Yorkshire Steel, 2017. *16MnCr5 Steel* [online]. Available from:  
<https://www.westyorkssteel.com/alloy-steel/case-hardening-steel/16mncr5/>.
- Wisnivesky, J. P., Teitelbaum, S. L., Todd, A. C., Boffetta, P., Crane, M., Crowley, L., De La Hoz, R. E., Dellenbaugh, C., Harrison, D., Herbert, R., Kim, H., Jeon, Y., Kaplan, J., Katz, C., Levin, S., Luft, B., Markowitz, S., Moline, J. M., Ozbay, F., Pietrzak, R. H., Shapiro, M., Sharma, V., Skloot, G., Southwick, S., Stevenson, L. a., Udasin, I., Wallenstein, S., and Landrigan, P. J., 2011. Persistence of multiple illnesses in World Trade Center rescue and recovery workers: A cohort study. *The Lancet* [online], 378 (9794), 888–897. Available from:  
<http://linkinghub.elsevier.com/retrieve/pii/S014067361161180X>.
- Wood, G. D. and Kennedy, D. C., 2003. Simulating mechanical systems in Simulink with SimMechanics. *The Mathworks Report* [online], 1–25. Available from:  
[http://www.mathworks.com/tagteam/12634\\_SimMechanics.pdf](http://www.mathworks.com/tagteam/12634_SimMechanics.pdf).
- Wu, B., Xu, B., Zhang, B., and Lü, Y., 2007. Preparation and properties of Ni/nano-Al<sub>2</sub>O<sub>3</sub> composite coatings by automatic brush plating. *Surface and Coatings Technology* [online], 201 (16–17), 6933–6939. Available from:  
<http://linkinghub.elsevier.com/retrieve/pii/S0257897206014848>.
- Wu, C.-C., 2013. Static and dynamic analyses of mountain bikes and their riders. [online]. University of Glasgow. Available from:  
[theses.gla.ac.uk/4159/1/2013Wuphd.pdf](http://theses.gla.ac.uk/4159/1/2013Wuphd.pdf).
- Xuetao, Y., Yu, W., Dongbai, S., and Hongying, Y., 2008. Influence of pulse parameters on the microstructure and microhardness of nickel electrodeposits. *Surface and Coatings Technology* [online], 202 (9), 1895–1903. Available from:  
<http://linkinghub.elsevier.com/retrieve/pii/S0257897207008961> [Accessed 10 Dec 2016].
- Yoo, S., Park, C.-G., Lim, B., Kyo Il Lee, and Park, F. C., 2010. Bandwidth Maximizing Design for Hydraulically Actuated Excavators. *Journal of Vibration and Control* [online], 16 (14), 2109–2130. Available from:

<http://journals.sagepub.com/doi/10.1177/1077546309348855>.

Z. Ahmed, 2014. India landslide: Hopes fade for survivors as toll rises to 66.

*BBC News India* [online]. Available from: <http://www.bbc.co.uk/news/world-asia-india-28598775>.

Zhang, J., Meng, Y., Tian, Y., and Zhang, X., 2015. Effect of concentration and addition of ions on the adsorption of sodium dodecyl sulfate on stainless steel surface in aqueous solutions. *Colloids and Surfaces A: Physicochemical and Engineering Aspects* [online], 484, 408–415.

Available from: <http://dx.doi.org/10.1016/j.colsurfa.2015.06.057>.

BLANK



## Appendix A: Excavator manipulator parameters

### APPENDIX II - List of Symbols

Lengths of links

$$\begin{aligned} a_1 &= 0.05 \text{ m} \\ a_2 &= 5.16 \text{ m} \\ a_3 &= 2.59 \text{ m} \\ a_4 &= 1.33 \text{ m} \end{aligned}$$

Mass centers

$$\begin{aligned} l_{1g} &= 0.61 \text{ m} & l_{3g} &= 0.64 \text{ m} \\ l_{1gz} &= 0.21 \text{ m} & l_{4g} &= 0.65 \text{ m} \\ l_{2g} &= 2.71 \text{ m} & & \end{aligned}$$

$$\begin{aligned} \theta_5 &= \text{angle between lines AP and AC (0.2566 rad)} \\ \theta_6 &= \text{angle between lines CD and CQ (0.3316 rad)} \\ \theta_7 &= \text{angle between lines DR and DN (0.3944 rad)} \\ \theta_8 &= \text{angle between lines AB and AC (0.4957 rad)} \\ \theta_9 &= \pi - \theta_{91} - \theta_{92} \\ \theta_{91} &= \text{angle between lines CD and CF (2.71049 rad)} \\ \theta_{92} &= \text{angle between lines CA and CI (0.47822 rad)} \\ \theta_{10} &= \pi - \theta_{101} - \theta_{102} \\ \theta_{101} &= \text{angle between lines DN and DG (2.19737)} \\ \theta_{102} &= \text{angle between lines CL and CD (0.15359)} \\ \theta_{11} &= \text{angle between lines JL and LD (0.13265)} \end{aligned}$$

Masses of links

$$\begin{aligned} m_1 &= 6420 \text{ kg} & m_3 &= 735 \text{ kg} \\ m_2 &= 1566 \text{ kg} & m_4 &= 432 \text{ kg} \end{aligned}$$

Inertial moments

$$\begin{aligned} I_{z1} &= 11748.6 \text{ kg m}^2 & I_{z3} &= 727.7 \text{ kg m}^2 \\ I_{z2} &= 14250.6 \text{ kg m}^2 & I_{z4} &= 224.6 \text{ kg m}^2 \end{aligned}$$

Length between points I and J is denoted as  $l_{ij}$ , i.e.:

$$\begin{aligned} l_{ab} &= 2.31 \text{ m} & l_{jl} &= 1.93 \text{ m} & l_{he} &= 0.42 \text{ m} & l_{gl} &= 0.40 \text{ m} \\ l_{ah} &= 0.56 \text{ m} & l_{kl} &= 0.50 \text{ m} & l_{cf} &= 0.77 \text{ m} & l_{gm} &= 0.40 \text{ m} \\ l_{ci} &= 2.80 \text{ m} & l_{km} &= 0.50 \text{ m} & l_{3cy} &= 1.37 \text{ m} & l_{4cy} &= 0.63 \text{ m} \end{aligned}$$

$l_{3cy}$  and  $l_{4cy}$  are the tangential distances from points I and J to lines AC and CD, respectively.

$$g = -9.87 \text{ m/s}^2$$

Figure 156 Physical parameters of the excavator manipulator (Vähä et al. 1991)

## Appendix B: Design of anthropoid and complex manipulator

### Anthropoid manipulator

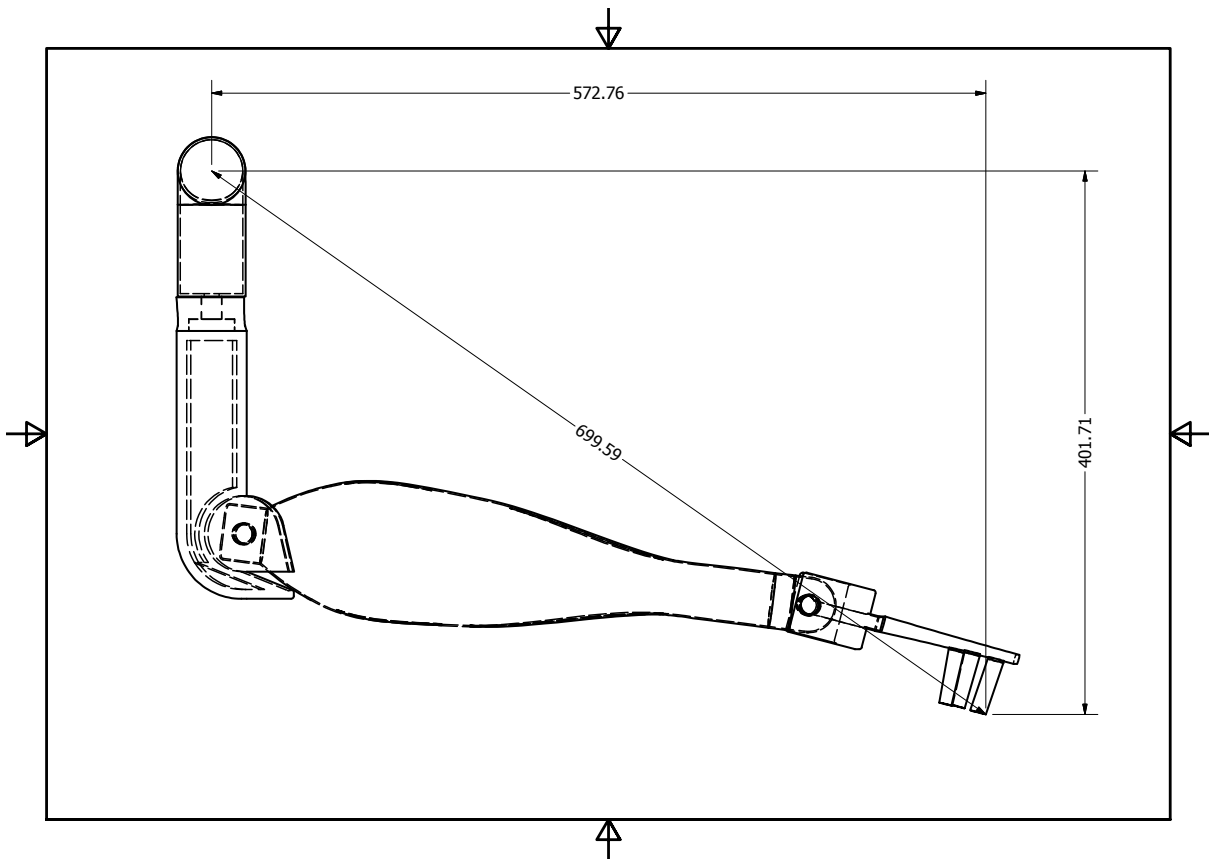


Figure 157 Two-dimensional sketch of the anthropoid manipulator created in CAD

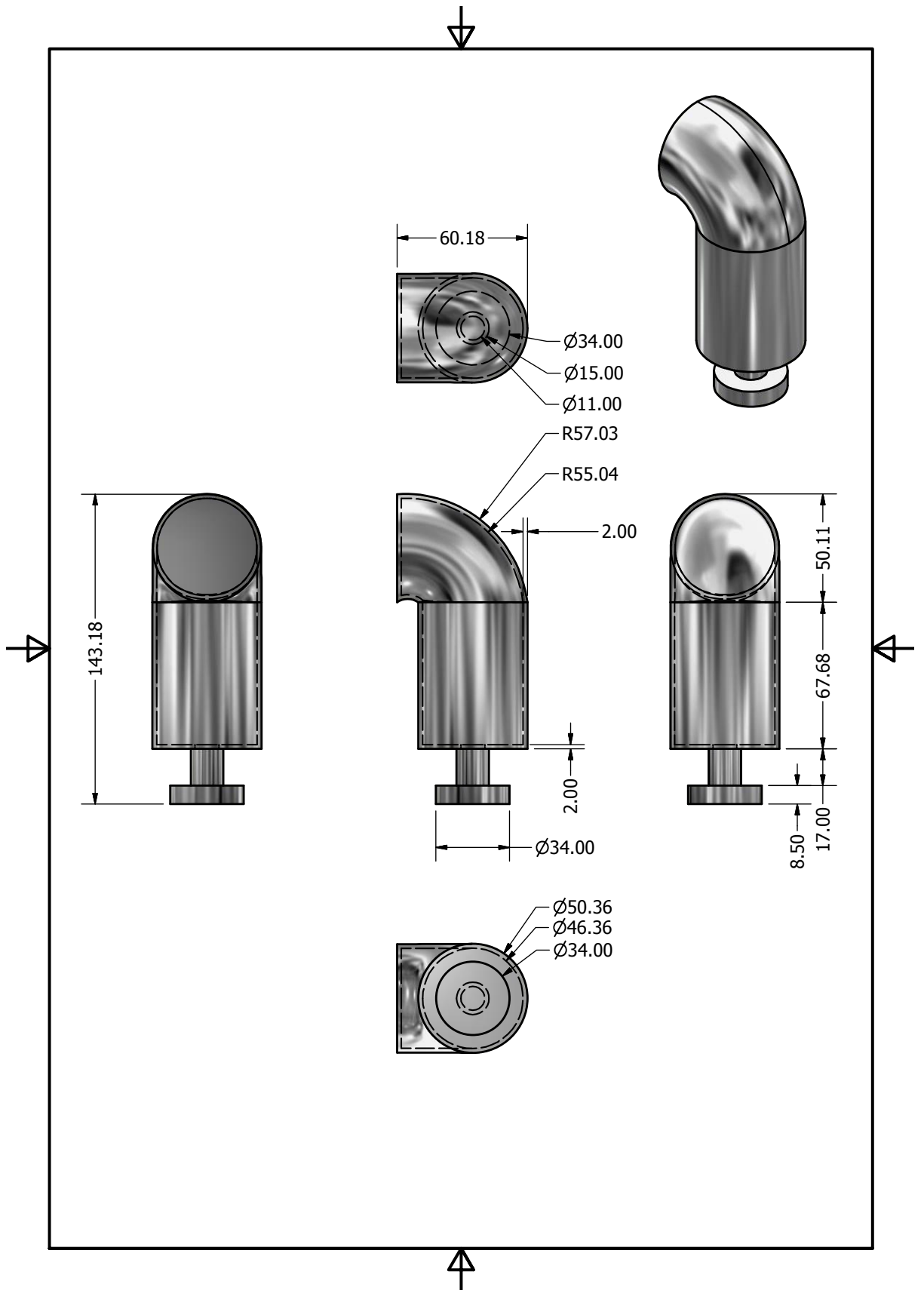


Figure 158 Upper arm of the anthropoid manipulator

## Physical Properties for the upper arm

### General Properties:

Material: {Aluminum 6061}

Density: 2.700 g/cm<sup>3</sup>

Mass: 0.140 kg (Relative Error = 0.727158%)

Area: 44763.375 mm<sup>2</sup> (Relative Error = 0.228969%)

Volume: 52022.857 mm<sup>3</sup> (Relative Error = 0.727158%)

### Center of Gravity:

X: -4.424 mm (Relative Error = 0.727158%)

Y: 57.521 mm (Relative Error = 0.727158%)

Z: -0.000 mm (Relative Error = 0.727158%)

### Mass Moments of Inertia with respect to Center of Gravity (Calculated using negative integral)

I<sub>xx</sub> 298.311 kg mm<sup>2</sup> (Relative Error = 0.727158%)

I<sub>yx</sub> I<sub>yy</sub> 34.468 kg mm<sup>2</sup> (Relative Error = 0.727158%) 71.559 kg mm<sup>2</sup>  
(Relative Error = 0.727158%)

I<sub>zx</sub> I<sub>zy</sub> I<sub>zz</sub> -0.002 kg mm<sup>2</sup> (Relative Error = 0.727158%) 0.002 kg mm<sup>2</sup>  
(Relative Error = 0.727158%) 307.153 kg mm<sup>2</sup> (Relative Error = 0.727158%)

### Mass Moments of Inertia with respect to Global (Calculated using negative integral)

I<sub>xx</sub> 763.050 kg mm<sup>2</sup> (Relative Error = 0.727158%)

I<sub>yx</sub> I<sub>yy</sub> 70.211 kg mm<sup>2</sup> (Relative Error = 0.727158%) 74.308 kg mm<sup>2</sup>  
(Relative Error = 0.727158%)

I<sub>zx</sub> I<sub>zy</sub> I<sub>zz</sub> -0.002 kg mm<sup>2</sup> (Relative Error = 0.727158%) 0.005 kg mm<sup>2</sup>  
(Relative Error = 0.727158%) 774.641 kg mm<sup>2</sup> (Relative Error = 0.727158%)

### Principal Moments of Inertia with respect to Center of Gravity

I<sub>1</sub>: 303.435 kg mm<sup>2</sup> (Relative Error = 0.727158%)

I<sub>2</sub>: 66.436 kg mm<sup>2</sup> (Relative Error = 0.727158%)

I<sub>3</sub>: 307.153 kg mm<sup>2</sup> (Relative Error = 0.727158%)

### Rotation from Global to Principal

R<sub>x</sub>: -0.00 deg (Relative Error = 0.727158%)

R<sub>y</sub>: 0.03 deg (Relative Error = 0.727158%)

R<sub>z</sub>: -8.45 deg (Relative Error = 0.727158%)

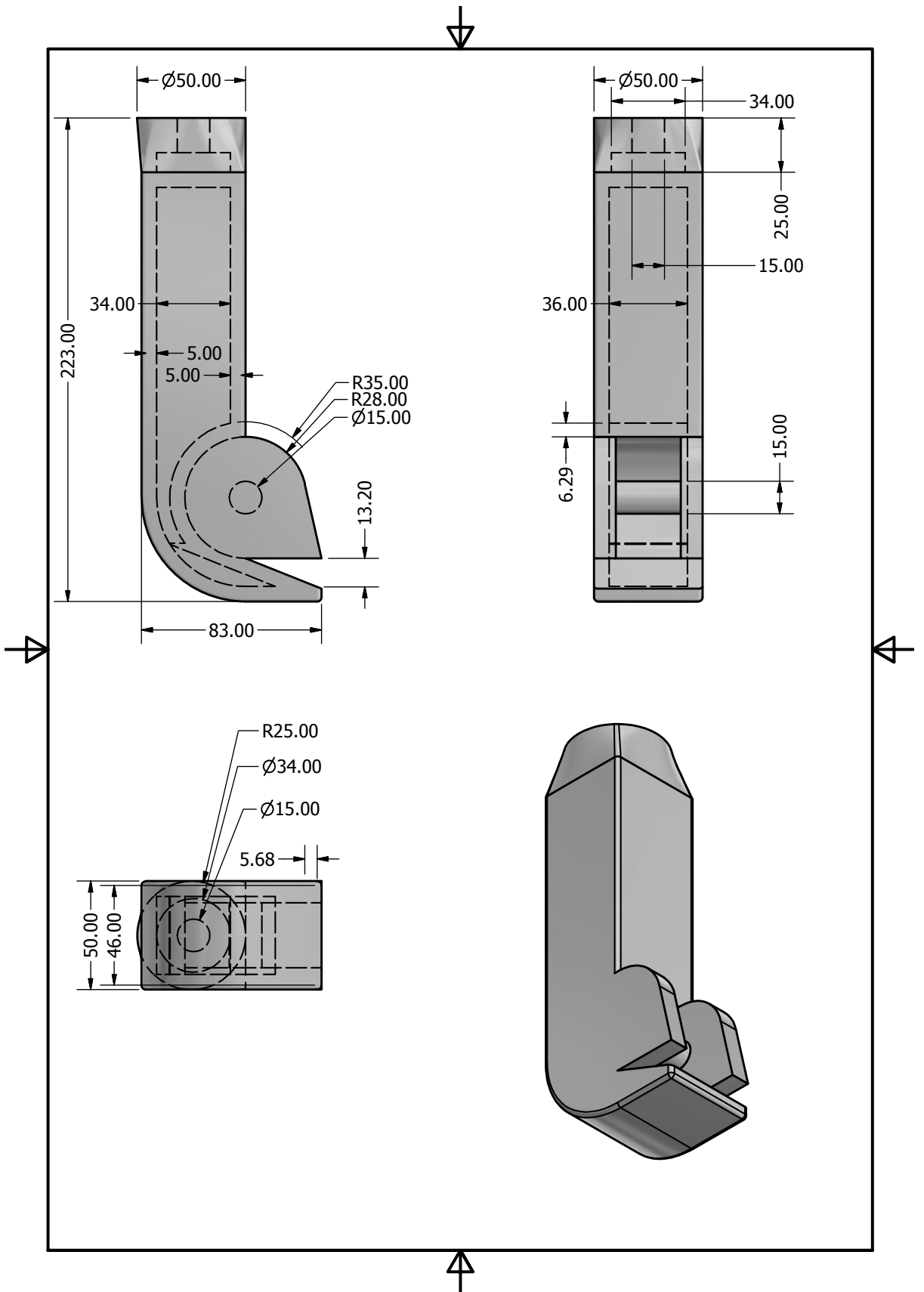


Figure 159 Lower arm of the anthropoid manipulator

## Physical Properties for the lower arm

### General Properties:

Material: {Aluminum 6061}

Density: 2.700 g/cm<sup>3</sup>

Mass: 0.947 kg (Relative Error = 0.002125%)

Area: 90215.548 mm<sup>2</sup> (Relative Error = 0.000216%)

Volume: 350901.478 mm<sup>3</sup> (Relative Error = 0.002125%)

### Center of Gravity:

X: -18.038 mm (Relative Error = 0.002125%)

Y: 55.377 mm (Relative Error = 0.002125%)

Z: 0.001 mm (Relative Error = 0.002125%)

### Mass Moments of Inertia with respect to Center of Gravity (Calculated using negative integral)

I<sub>xx</sub> 4793.113 kg mm<sup>2</sup> (Relative Error = 0.002125%)

I<sub>xy</sub> I<sub>yy</sub> 449.672 kg mm<sup>2</sup> (Relative Error = 0.002125%) 649.487 kg mm<sup>2</sup> (Relative Error = 0.002125%)

I<sub>xz</sub> I<sub>zy</sub> I<sub>zz</sub> 0.020 kg mm<sup>2</sup> (Relative Error = 0.002125%) -0.077 kg mm<sup>2</sup> (Relative Error = 0.002125%) 4904.049 kg mm<sup>2</sup> (Relative Error = 0.002125%)

### Mass Moments of Inertia with respect to Global (Calculated using negative integral)

I<sub>xx</sub> 7698.474 kg mm<sup>2</sup> (Relative Error = 0.002125%)

I<sub>xy</sub> I<sub>yy</sub> 1396.031 kg mm<sup>2</sup> (Relative Error = 0.002125%) 957.743 kg mm<sup>2</sup> (Relative Error = 0.002125%)

I<sub>xz</sub> I<sub>zy</sub> I<sub>zz</sub> 0.033 kg mm<sup>2</sup> (Relative Error = 0.002125%) -0.117 kg mm<sup>2</sup> (Relative Error = 0.002125%) 8117.666 kg mm<sup>2</sup> (Relative Error = 0.002125%)

### Principal Moments of Inertia with respect to Center of Gravity

I<sub>1</sub>: 4841.350 kg mm<sup>2</sup> (Relative Error = 0.002125%)

I<sub>2</sub>: 601.249 kg mm<sup>2</sup> (Relative Error = 0.002125%)

I<sub>3</sub>: 4904.049 kg mm<sup>2</sup> (Relative Error = 0.002125%)

### Rotation from Global to Principal

R<sub>x</sub>: 0.00 deg (Relative Error = 0.002125%)

R<sub>y</sub>: -0.01 deg (Relative Error = 0.002125%)

R<sub>z</sub>: -6.12 deg (Relative Error = 0.002125%)

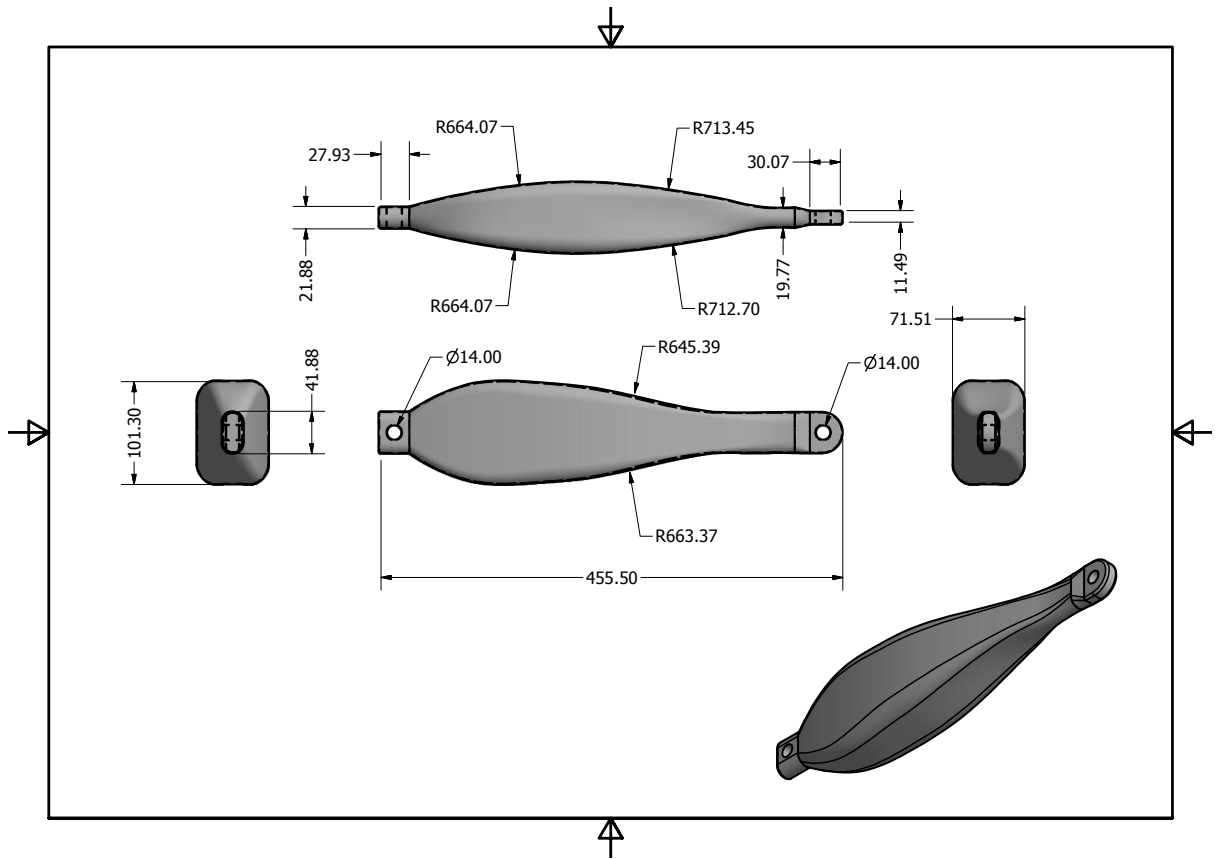


Figure 160 Forearm of the anthropoid manipulator

### Physical Properties for the forearm

#### General Properties:

Material: {Aluminum 6061-AHC}

Density: 2.700 g/cm<sup>3</sup>

Mass: 0.257 kg (Relative Error = 0.049310%)

Area: 190150.963 mm<sup>2</sup> (Relative Error = 0.000747%)

Volume: 95079.783 mm<sup>3</sup> (Relative Error = 0.049310%)

#### Center of Gravity:

X: 21.260 mm (Relative Error = 0.049310%)

Y: 0.003 mm (Relative Error = 0.049310%)

Z: 0.001 mm (Relative Error = 0.049310%)

#### Mass Moments of Inertia with respect to Center of Gravity (Calculated using negative integral)

I<sub>xx</sub> 344.413 kg mm<sup>2</sup> (Relative Error = 0.049310%)

I<sub>yy</sub> -0.119 kg mm<sup>2</sup> (Relative Error = 0.049310%) I<sub>zz</sub> 3383.315 kg mm<sup>2</sup> (Relative Error = 0.049310%)

I<sub>zx</sub> I<sub>zy</sub> I<sub>zz</sub> -0.039 kg mm<sup>2</sup> (Relative Error = 0.049310%) 0.009 kg mm<sup>2</sup>  
(Relative Error = 0.049310%) 3471.759 kg mm<sup>2</sup> (Relative Error = 0.049310%)  
Mass Moments of Inertia with respect to Global (Calculated using negative  
integral)

I<sub>xx</sub> 344.413 kg mm<sup>2</sup> (Relative Error = 0.049310%)

I<sub>yx</sub> I<sub>yy</sub> -0.135 kg mm<sup>2</sup> (Relative Error = 0.049310%) 3499.351 kg  
mm<sup>2</sup> (Relative Error = 0.049310%)

I<sub>zx</sub> I<sub>zy</sub> I<sub>zz</sub> -0.046 kg mm<sup>2</sup> (Relative Error = 0.049310%) 0.009 kg mm<sup>2</sup>  
(Relative Error = 0.049310%) 3587.795 kg mm<sup>2</sup> (Relative Error = 0.049310%)  
Principal Moments of Inertia with respect to Center of Gravity

I<sub>1</sub>: 344.413 kg mm<sup>2</sup> (Relative Error = 0.049310%)

I<sub>2</sub>: 3383.315 kg mm<sup>2</sup> (Relative Error = 0.049310%)

I<sub>3</sub>: 3471.759 kg mm<sup>2</sup> (Relative Error = 0.049310%)

Rotation from Global to Principal

R<sub>x</sub>: 0.01 deg (Relative Error = 0.049310%)

R<sub>y</sub>: 0.00 deg (Relative Error = 0.049310%)

R<sub>z</sub>: -0.00 deg (Relative Error = 0.049310%)



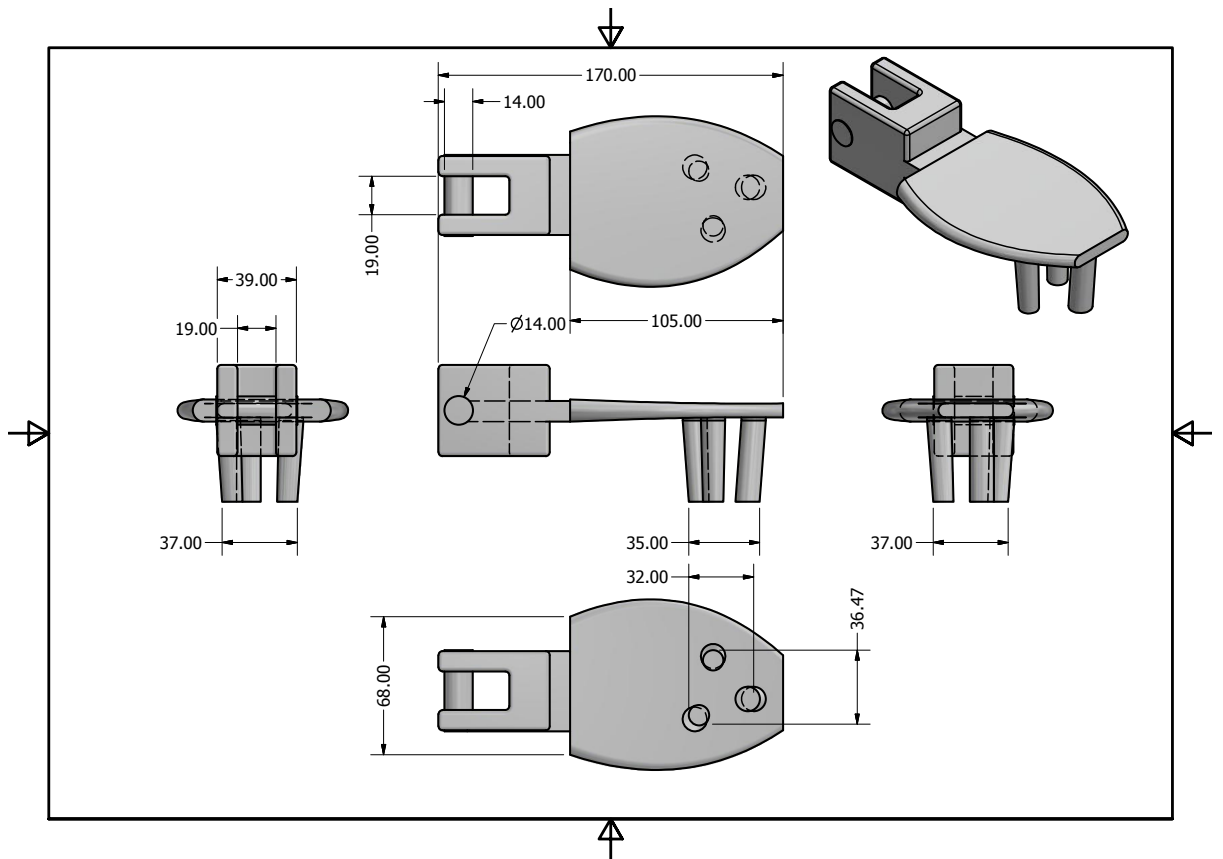


Figure 161 Hand of the anthropoid manipulator

### Physical Properties for the hand

#### General Properties:

Material: {Aluminum 6061}

Density: 2.700 g/cm<sup>3</sup>

Mass: 0.395 kg (Relative Error = 0.018800%)

Area: 36294.294 mm<sup>2</sup> (Relative Error = 0.001084%)

Volume: 146355.948 mm<sup>3</sup> (Relative Error = 0.018800%)

#### Center of Gravity:

X: 46.345 mm (Relative Error = 0.018800%)

Y: -2.039 mm (Relative Error = 0.018800%)

Z: 0.897 mm (Relative Error = 0.018800%)

#### Mass Moments of Inertia with respect to Center of Gravity (Calculated using negative integral)

I<sub>xx</sub> 165.841 kg mm<sup>2</sup> (Relative Error = 0.018800%)

I<sub>yy</sub> 52.945 kg mm<sup>2</sup> (Relative Error = 0.018800%) 1004.678 kg mm<sup>2</sup> (Relative Error = 0.018800%)

$I_{xz}$   $I_{zy}$   $I_{zz}$  -9.925 kg mm<sup>2</sup> (Relative Error = 0.018800%) -1.208 kg mm<sup>2</sup> (Relative Error = 0.018800%) 944.560 kg mm<sup>2</sup> (Relative Error = 0.018800%)

Mass Moments of Inertia with respect to Global (Calculated using negative integral)

$I_{xx}$  167.801 kg mm<sup>2</sup> (Relative Error = 0.018800%)

$I_{yx}$   $I_{yy}$  90.281 kg mm<sup>2</sup> (Relative Error = 0.018800%) 1853.746 kg mm<sup>2</sup> (Relative Error = 0.018800%)

$I_{zx}$   $I_{zy}$   $I_{zz}$  -26.348 kg mm<sup>2</sup> (Relative Error = 0.018800%) -0.486 kg mm<sup>2</sup> (Relative Error = 0.018800%) 1794.953 kg mm<sup>2</sup> (Relative Error = 0.018800%)

Principal Moments of Inertia with respect to Center of Gravity

$I_1$ : 162.389 kg mm<sup>2</sup> (Relative Error = 0.018800%)

$I_2$ : 1008.059 kg mm<sup>2</sup> (Relative Error = 0.018800%)

$I_3$ : 944.631 kg mm<sup>2</sup> (Relative Error = 0.018800%)

Rotation from Global to Principal

$R_x$ : 1.69 deg (Relative Error = 0.018800%)

$R_y$ : 0.61 deg (Relative Error = 0.018800%)

$R_z$ : 3.62 deg (Relative Error = 0.018800%)

## Complex closed-loop manipulator

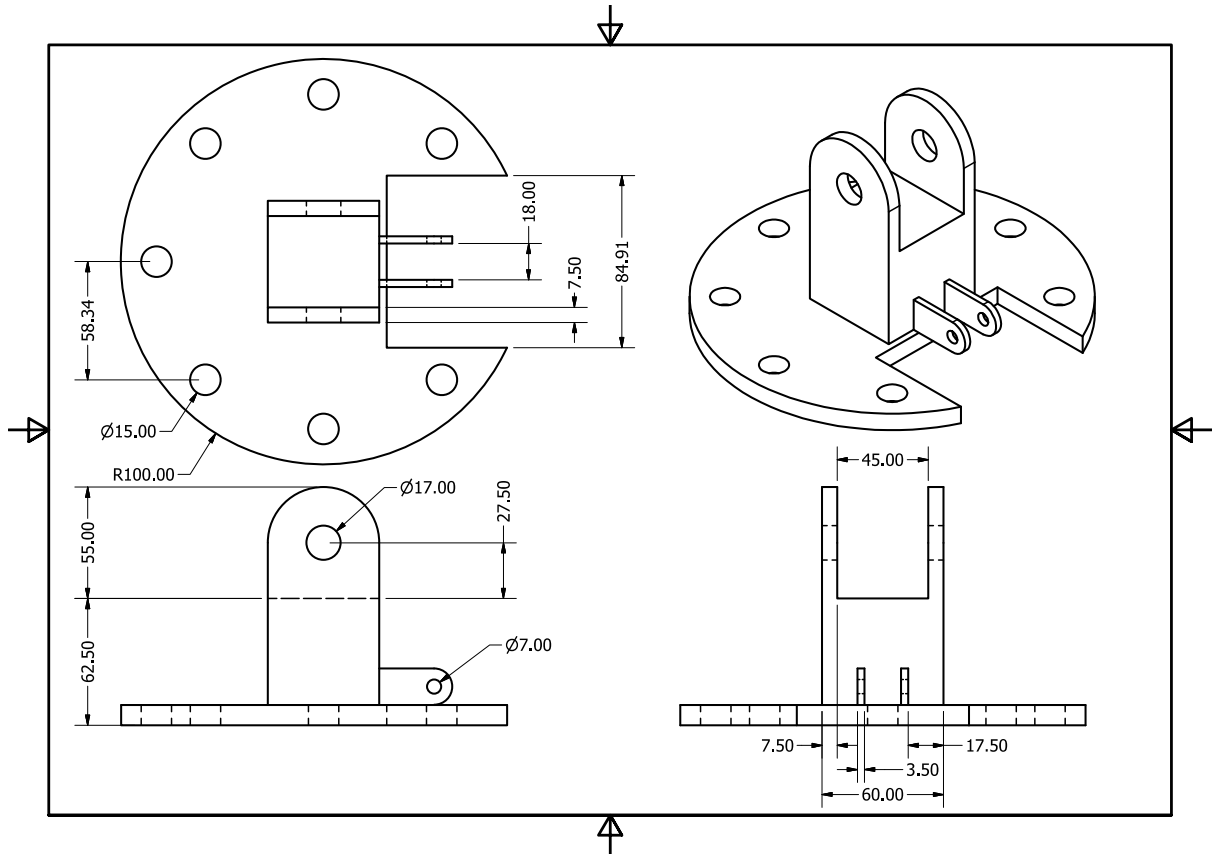


Figure 162 Base of the complex closed-loop manipulator

### Physical Properties for the base

#### General Properties:

Material: {SolidWorks Materials|7075-O (SS)}

Density: 2.810 g/cm<sup>3</sup>

Mass: 1.293 kg (Relative Error = 0.008603%)

Area: 86842.388 mm<sup>2</sup> (Relative Error = 0.000000%)

Volume: 460280.400 mm<sup>3</sup> (Relative Error = 0.008603%)

#### Center of Gravity:

X: -7.077 mm (Relative Error = 0.008603%)

Y: -66.489 mm (Relative Error = 0.008603%)

Z: -0.000 mm (Relative Error = 0.008603%)

#### Mass Moments of Inertia with respect to Center of Gravity (Calculated using negative integral)

I<sub>xx</sub> 3081.519 kg mm<sup>2</sup> (Relative Error = 0.008603%)

I<sub>yx</sub> I<sub>yy</sub> -176.387 kg mm<sup>2</sup> (Relative Error = 0.008603%) 3709.829 kg mm<sup>2</sup> (Relative Error = 0.008603%)

I<sub>zx</sub> I<sub>zy</sub> I<sub>zz</sub> 0.000 kg mm<sup>2</sup> (Relative Error = 0.008603%) -0.000 kg mm<sup>2</sup>  
(Relative Error = 0.008603%) 2390.894 kg mm<sup>2</sup> (Relative Error = 0.008603%)  
Mass Moments of Inertia with respect to Global (Calculated using negative  
integral)

I<sub>xx</sub> 8799.393 kg mm<sup>2</sup> (Relative Error = 0.008603%)

I<sub>yx</sub> I<sub>yy</sub> -784.989 kg mm<sup>2</sup> (Relative Error = 0.008603%) 3774.608 kg  
mm<sup>2</sup> (Relative Error = 0.008603%)

I<sub>zx</sub> I<sub>zy</sub> I<sub>zz</sub> 0.000 kg mm<sup>2</sup> (Relative Error = 0.008603%) -0.000 kg mm<sup>2</sup>  
(Relative Error = 0.008603%) 8173.547 kg mm<sup>2</sup> (Relative Error = 0.008603%)

Principal Moments of Inertia with respect to Center of Gravity

I<sub>1</sub>: 3035.389 kg mm<sup>2</sup> (Relative Error = 0.008603%)

I<sub>2</sub>: 3755.960 kg mm<sup>2</sup> (Relative Error = 0.008603%)

I<sub>3</sub>: 2390.894 kg mm<sup>2</sup> (Relative Error = 0.008603%)

Rotation from Global to Principal

R<sub>x</sub>: 0.00 deg (Relative Error = 0.008603%)

R<sub>y</sub>: 0.00 deg (Relative Error = 0.008603%)

R<sub>z</sub>: -14.66 deg (Relative Error = 0.008603%)

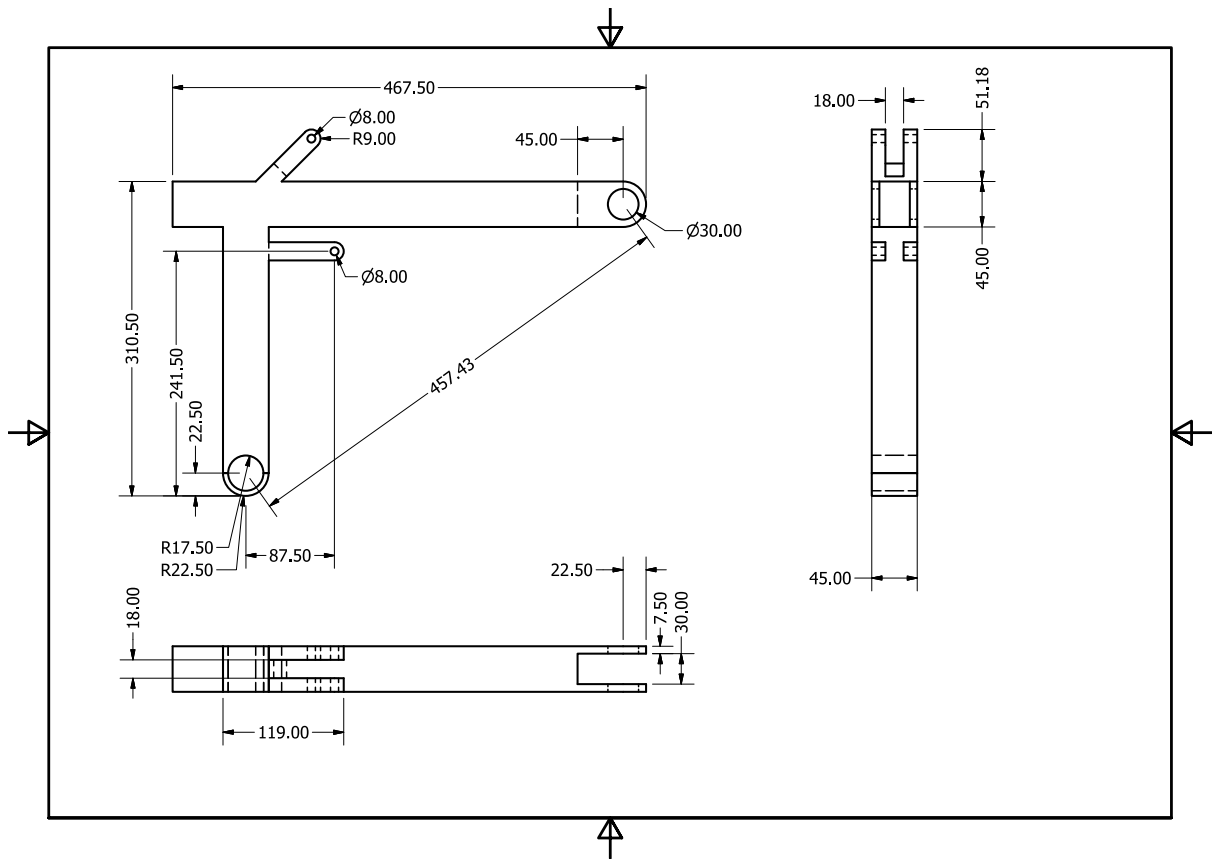


Figure 163 Boom of the complex closed-loop manipulator

## Physical Properties for the boom

### General Properties:

Material: {SolidWorks Materials|7075-O (SS)}

Density: 2.810 g/cm<sup>3</sup>

Mass: 3.923 kg (Relative Error = 0.003803%)

Area: 0.156 m<sup>2</sup> (Relative Error = 0.000000%)

Volume: 0.001 m<sup>3</sup> (Relative Error = 0.003803%)

### Center of Gravity:

X: 0.084 m (Relative Error = 0.003803%)

Y: 0.216 m (Relative Error = 0.003803%)

Z: 0.000 m (Relative Error = 0.003803%)

### Mass Moments of Inertia with respect to Center of Gravity (Calculated using negative integral)

I<sub>xx</sub> 0.026 kg m<sup>2</sup> (Relative Error = 0.003803%)

I<sub>yy</sub> -0.016 kg m<sup>2</sup> (Relative Error = 0.003803%) 0.052 kg m<sup>2</sup>

(Relative Error = 0.003803%)

$I_{zx} \ I_{zy} \ I_{zz} \ -0.000 \ \text{kg m}^2 \ (\text{Relative Error} = 0.003803\%) \ 0.000 \ \text{kg m}^2$   
(Relative Error = 0.003803%)  $0.077 \ \text{kg m}^2 \ (\text{Relative Error} = 0.003803\%)$   
Mass Moments of Inertia with respect to Global (Calculated using negative  
integral)

$I_{xx} \ 0.209 \ \text{kg m}^2 \ (\text{Relative Error} = 0.003803\%)$

$I_{yx} \ I_{yy} \ -0.088 \ \text{kg m}^2 \ (\text{Relative Error} = 0.003803\%) \ 0.080 \ \text{kg m}^2$   
(Relative Error = 0.003803%)

$I_{zx} \ I_{zy} \ I_{zz} \ -0.000 \ \text{kg m}^2 \ (\text{Relative Error} = 0.003803\%) \ 0.000 \ \text{kg m}^2$   
(Relative Error = 0.003803%)  $0.288 \ \text{kg m}^2 \ (\text{Relative Error} = 0.003803\%)$

Principal Moments of Inertia with respect to Center of Gravity

$I_1: \ 0.018 \ \text{kg m}^2 \ (\text{Relative Error} = 0.003803\%)$

$I_2: \ 0.060 \ \text{kg m}^2 \ (\text{Relative Error} = 0.003803\%)$

$I_3: \ 0.077 \ \text{kg m}^2 \ (\text{Relative Error} = 0.003803\%)$

Rotation from Global to Principal

$R_x: \ 0.00 \ \text{deg} \ (\text{Relative Error} = 0.003803\%)$

$R_y: \ 0.00 \ \text{deg} \ (\text{Relative Error} = 0.003803\%)$

$R_z: \ -25.96 \ \text{deg} \ (\text{Relative Error} = 0.003803\%)$

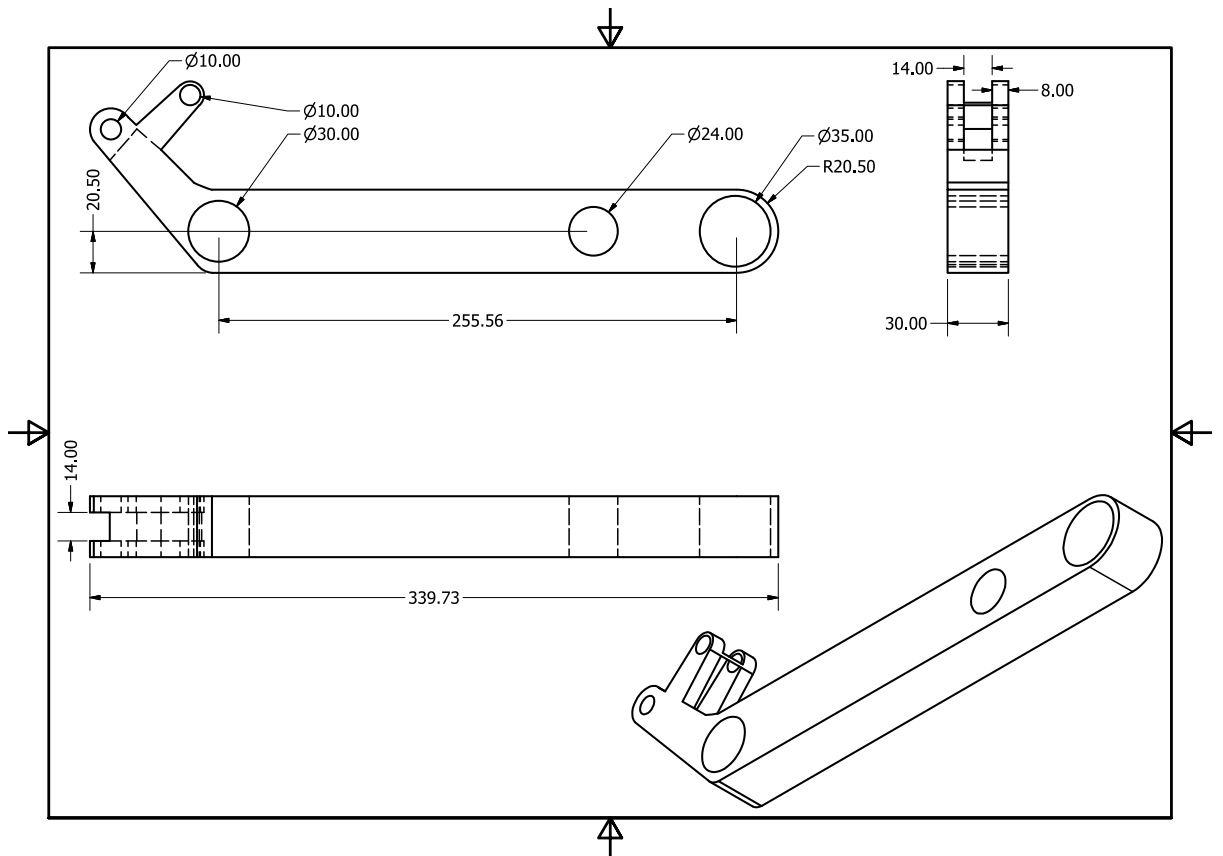


Figure 164 Stick of the complex closed-loop manipulator

### Physical Properties for the stick

#### General Properties:

Material: {SolidWorks Materials|7075-O (SS)}

Density: 2.810 g/cm<sup>3</sup>

Mass: 0.938 kg (Relative Error = 0.014853%)

Area: 57225.775 mm<sup>2</sup> (Relative Error = 0.000000%)

Volume: 333870.769 mm<sup>3</sup> (Relative Error = 0.014853%)

#### Center of Gravity:

X: 101.689 mm (Relative Error = 0.014853%)

Y: 4.399 mm (Relative Error = 0.014853%)

Z: 0.000 mm (Relative Error = 0.014853%)

#### Mass Moments of Inertia with respect to Center of Gravity (Calculated using negative integral)

I<sub>xx</sub> 347.589 kg mm<sup>2</sup> (Relative Error = 0.014853%)

I<sub>yy</sub> 559.356 kg mm<sup>2</sup> (Relative Error = 0.014853%) 7060.579 kg mm<sup>2</sup> (Relative Error = 0.014853%)

I<sub>zx</sub> I<sub>zy</sub> I<sub>zz</sub> -0.000 kg mm<sup>2</sup> (Relative Error = 0.014853%) -0.000 kg mm<sup>2</sup> (Relative Error = 0.014853%) 7263.967 kg mm<sup>2</sup> (Relative Error = 0.014853%)

Mass Moments of Inertia with respect to Global (Calculated using negative integral)

I<sub>xx</sub> 365.744 kg mm<sup>2</sup> (Relative Error = 0.014853%)

I<sub>yx</sub> I<sub>yy</sub> 139.672 kg mm<sup>2</sup> (Relative Error = 0.014853%) 16762.028 kg mm<sup>2</sup> (Relative Error = 0.014853%)

I<sub>zx</sub> I<sub>zy</sub> I<sub>zz</sub> -0.000 kg mm<sup>2</sup> (Relative Error = 0.014853%) -0.000 kg mm<sup>2</sup> (Relative Error = 0.014853%) 16983.572 kg mm<sup>2</sup> (Relative Error = 0.014853%)

Principal Moments of Inertia with respect to Center of Gravity

I<sub>1</sub>: 301.300 kg mm<sup>2</sup> (Relative Error = 0.014853%)

I<sub>2</sub>: 7106.868 kg mm<sup>2</sup> (Relative Error = 0.014853%)

I<sub>3</sub>: 7263.967 kg mm<sup>2</sup> (Relative Error = 0.014853%)

Rotation from Global to Principal

R<sub>x</sub>: 0.00 deg (Relative Error = 0.014853%)

R<sub>y</sub>: 0.00 deg (Relative Error = 0.014853%)

R<sub>z</sub>: 4.73 deg (Relative Error = 0.014853%)



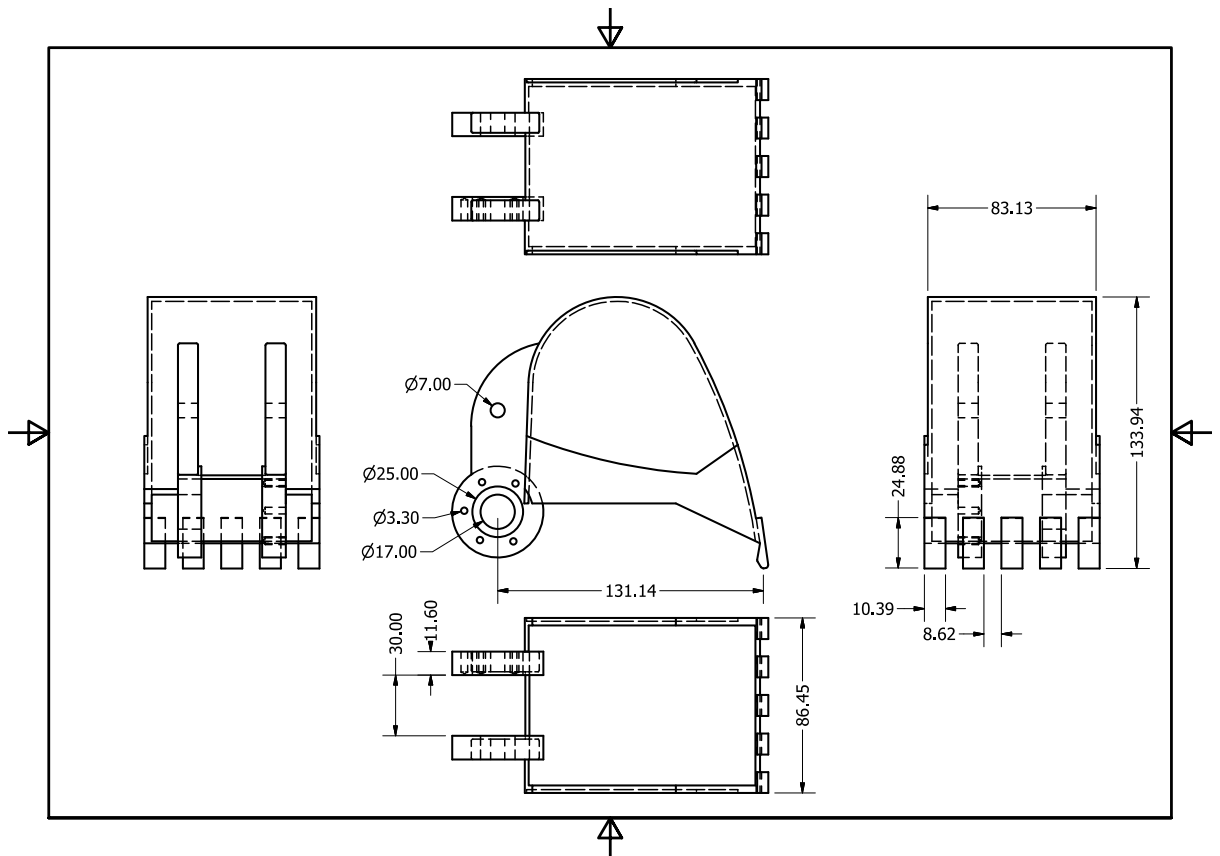


Figure 165 Bucket of the complex closed-loop manipulator

### Physical properties for the bucket

#### General Properties:

Material: {SolidWorks Materials|AISI Type A2 Tool Steel}

Density: 7.860 g/cm<sup>3</sup>

Mass: 1.190 kg (Relative Error = 0.012450%)

Area: 0.099 m<sup>2</sup> (Relative Error = 0.000292%)

Volume: 0.000 m<sup>3</sup> (Relative Error = 0.012450%)

#### Center of Gravity:

X: 0.045 m (Relative Error = 0.012450%)

Y: 0.038 m (Relative Error = 0.012450%)

Z: -0.000 m (Relative Error = 0.012450%)

#### Mass Moments of Inertia with respect to Center of Gravity (Calculated using negative integral)

I<sub>xx</sub> 0.002 kg m<sup>2</sup> (Relative Error = 0.012450%)

I<sub>yx</sub> I<sub>yy</sub> -0.000 kg m<sup>2</sup> (Relative Error = 0.012450%) 0.004 kg m<sup>2</sup>

(Relative Error = 0.012450%)

$I_{zx} \ I_{zy} \ I_{zz} \ -0.000 \text{ kg m}^2 \text{ (Relative Error = 0.012450\%)} \ -0.000 \text{ kg m}^2$   
 $\text{(Relative Error = 0.012450\%)} \ 0.004 \text{ kg m}^2 \text{ (Relative Error = 0.012450\%)}$   
Mass Moments of Inertia with respect to Global (Calculated using negative  
integral)

$I_{xx} \ 0.004 \text{ kg m}^2 \text{ (Relative Error = 0.012450\%)}$

$I_{yx} \ I_{yy} \ -0.002 \text{ kg m}^2 \text{ (Relative Error = 0.012450\%)} \ 0.006 \text{ kg m}^2$   
 $\text{(Relative Error = 0.012450\%)}$

$I_{zx} \ I_{zy} \ I_{zz} \ -0.000 \text{ kg m}^2 \text{ (Relative Error = 0.012450\%)} \ 0.000 \text{ kg m}^2$   
 $\text{(Relative Error = 0.012450\%)} \ 0.008 \text{ kg m}^2 \text{ (Relative Error = 0.012450\%)}$

Principal Moments of Inertia with respect to Center of Gravity

$I_1: \ 0.002 \text{ kg m}^2 \text{ (Relative Error = 0.012450\%)}$

$I_2: \ 0.004 \text{ kg m}^2 \text{ (Relative Error = 0.012450\%)}$

$I_3: \ 0.004 \text{ kg m}^2 \text{ (Relative Error = 0.012450\%)}$

Rotation from Global to Principal

$R_x: \ -3.00 \text{ deg (Relative Error = 0.012450\%)}$

$R_y: \ 0.87 \text{ deg (Relative Error = 0.012450\%)}$

$R_z: \ -4.43 \text{ deg (Relative Error = 0.012450\%)}$

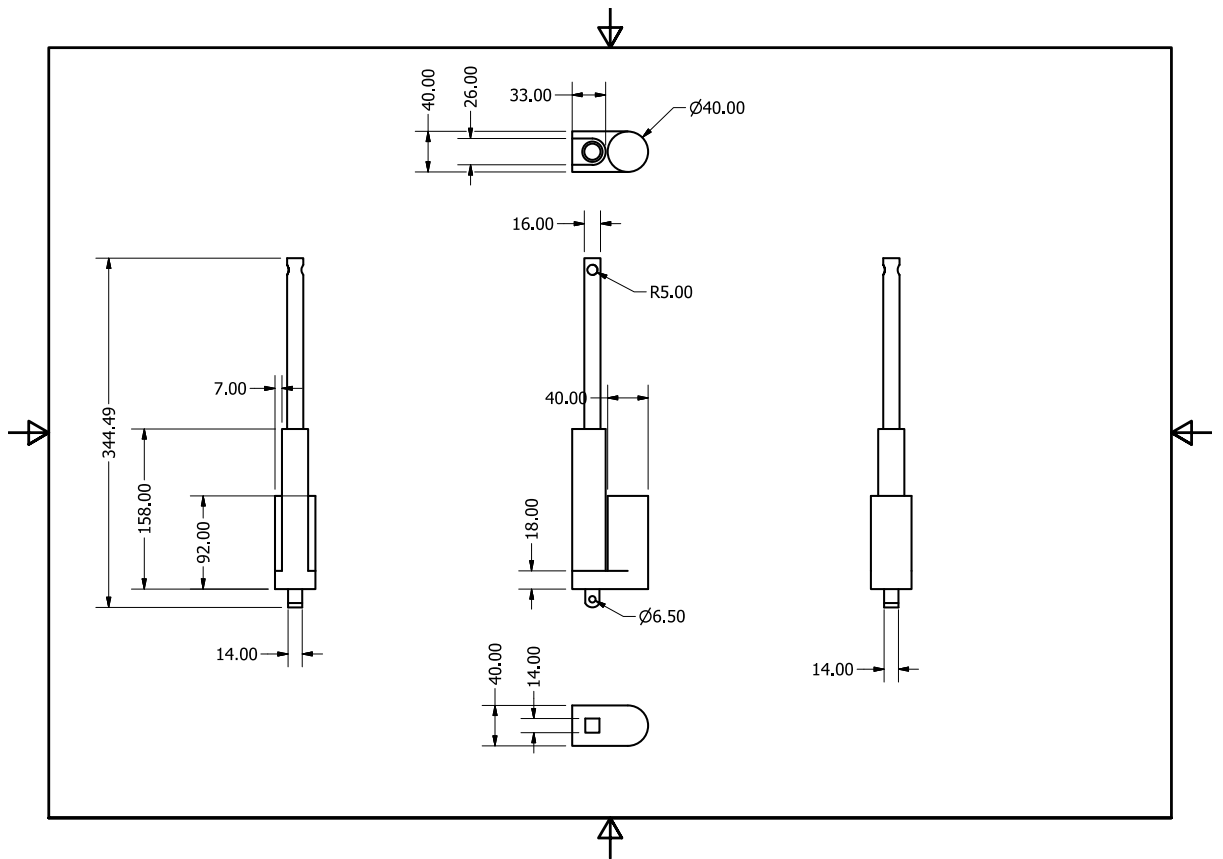


Figure 166 Boom actuator of the complex closed-loop manipulator

### Physical Properties for the boom actuator

#### General Properties:

Material: {Stainless steel}

Density: 2.810 g/cm<sup>3</sup>

Mass: 0.696 kg (Relative Error = 0.142202%)

Area: 53394.267 mm<sup>2</sup> (Relative Error = 0.147913%)

Volume: 247711.422 mm<sup>3</sup> (Relative Error = 0.142202%)

#### Center of Gravity:

X: 14.212 mm (Relative Error = 0.142202%)

Y: 88.878 mm (Relative Error = 0.142202%)

Z: -0.000 mm (Relative Error = 0.142202%)

#### Mass Moments of Inertia with respect to Center of Gravity (Calculated using negative integral)

Ixx 4021.951 kg mm<sup>2</sup> (Relative Error = 0.142202%)

Iyy 386.677 kg mm<sup>2</sup> (Relative Error = 0.142202%) 389.958 kg mm<sup>2</sup> (Relative Error = 0.142202%)

I<sub>zx</sub> I<sub>zy</sub> I<sub>zz</sub> 0.000 kg mm<sup>2</sup> (Relative Error = 0.142202%) 0.000 kg mm<sup>2</sup>  
(Relative Error = 0.142202%) 4294.541 kg mm<sup>2</sup> (Relative Error = 0.142202%)  
Mass Moments of Inertia with respect to Global (Calculated using negative  
integral)

I<sub>xx</sub> 9520.401 kg mm<sup>2</sup> (Relative Error = 0.142202%)

I<sub>xy</sub> I<sub>yy</sub> -492.580 kg mm<sup>2</sup> (Relative Error = 0.142202%) 530.560 kg  
mm<sup>2</sup> (Relative Error = 0.142202%)

I<sub>zx</sub> I<sub>zy</sub> I<sub>zz</sub> 0.000 kg mm<sup>2</sup> (Relative Error = 0.142202%) 0.000 kg mm<sup>2</sup>  
(Relative Error = 0.142202%) 9933.593 kg mm<sup>2</sup> (Relative Error = 0.142202%)

Principal Moments of Inertia with respect to Center of Gravity

I<sub>1</sub>: 4062.662 kg mm<sup>2</sup> (Relative Error = 0.142202%)

I<sub>2</sub>: 349.247 kg mm<sup>2</sup> (Relative Error = 0.142202%)

I<sub>3</sub>: 4294.541 kg mm<sup>2</sup> (Relative Error = 0.142202%)

Rotation from Global to Principal

R<sub>x</sub>: 0.00 deg (Relative Error = 0.142202%)

R<sub>y</sub>: -0.00 deg (Relative Error = 0.142202%)

R<sub>z</sub>: -6.01 deg (Relative Error = 0.142202%)

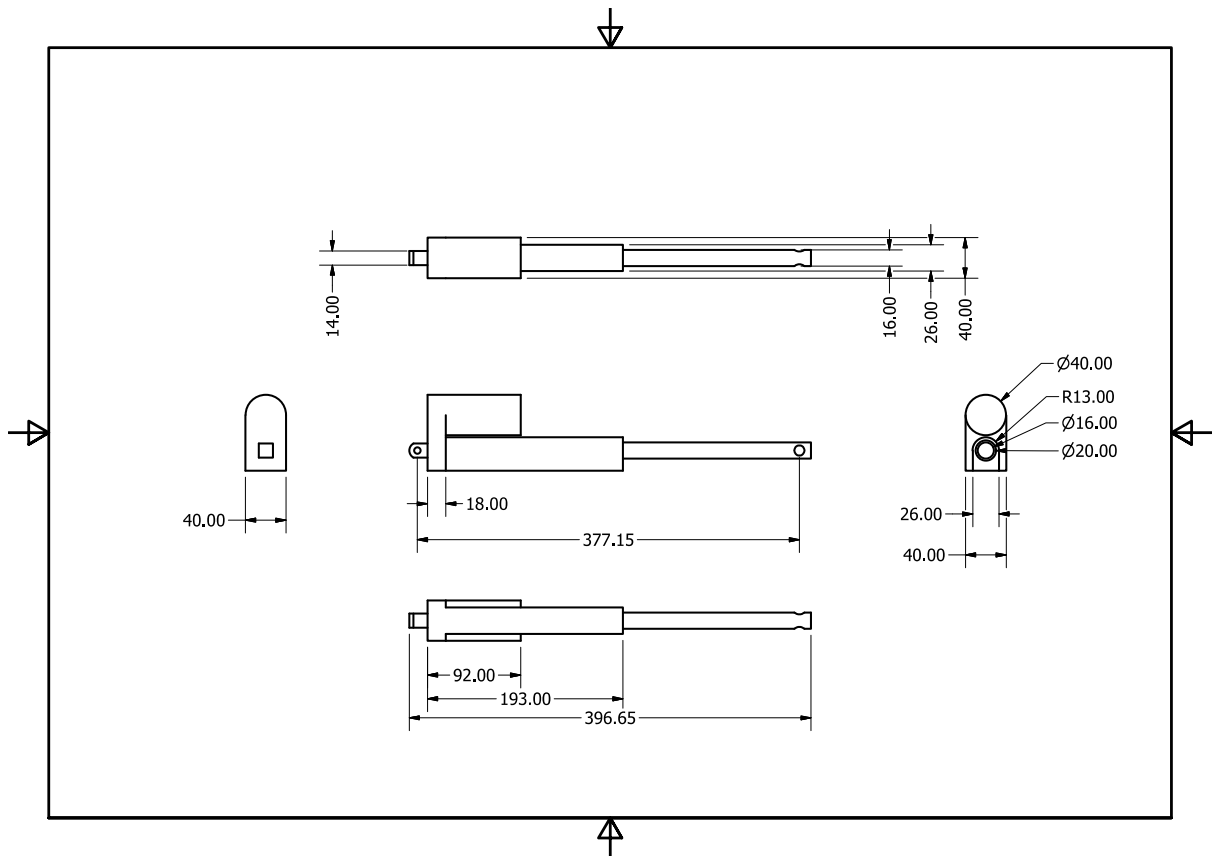


Figure 167 Stick actuator of the complex closed-loop manipulator

### Physical Properties for stick actuator

#### General Properties:

Material: {Stainless steel}

Density: 2.810 g/cm<sup>3</sup>

Mass: 0.754 kg (Relative Error = 0.153615%)

Area: 60338.116 mm<sup>2</sup> (Relative Error = 0.130891%)

Volume: 268228.346 mm<sup>3</sup> (Relative Error = 0.153615%)

#### Center of Gravity:

X: 103.271 mm (Relative Error = 0.153615%)

Y: 12.638 mm (Relative Error = 0.153615%)

Z: 0.000 mm (Relative Error = 0.153615%)

#### Mass Moments of Inertia with respect to Center of Gravity (Calculated using negative integral)

I<sub>xx</sub> 420.901 kg mm<sup>2</sup> (Relative Error = 0.153615%)

I<sub>yy</sub> 559.283 kg mm<sup>2</sup> (Relative Error = 0.153615%) I<sub>zz</sub> 6300.251 kg mm<sup>2</sup> (Relative Error = 0.153615%)

I<sub>zx</sub> I<sub>zy</sub> I<sub>zz</sub> 0.000 kg mm<sup>2</sup> (Relative Error = 0.153615%) -0.000 kg mm<sup>2</sup>  
(Relative Error = 0.153615%) 6596.999 kg mm<sup>2</sup> (Relative Error = 0.153615%)  
Mass Moments of Inertia with respect to Global (Calculated using negative  
integral)

I<sub>xx</sub> 541.282 kg mm<sup>2</sup> (Relative Error = 0.153615%)

I<sub>yx</sub> I<sub>yy</sub> -424.425 kg mm<sup>2</sup> (Relative Error = 0.153615%) 14338.684 kg  
mm<sup>2</sup> (Relative Error = 0.153615%)

I<sub>zx</sub> I<sub>zy</sub> I<sub>zz</sub> -0.000 kg mm<sup>2</sup> (Relative Error = 0.153615%) -0.000 kg  
mm<sup>2</sup> (Relative Error = 0.153615%) 14755.813 kg mm<sup>2</sup> (Relative Error =  
0.153615%)

Principal Moments of Inertia with respect to Center of Gravity

I<sub>1</sub>: 368.171 kg mm<sup>2</sup> (Relative Error = 0.153615%)

I<sub>2</sub>: 6352.981 kg mm<sup>2</sup> (Relative Error = 0.153615%)

I<sub>3</sub>: 6596.999 kg mm<sup>2</sup> (Relative Error = 0.153615%)

Rotation from Global to Principal

R<sub>x</sub>: 0.00 deg (Relative Error = 0.153615%)

R<sub>y</sub>: 0.00 deg (Relative Error = 0.153615%)

R<sub>z</sub>: 5.39 deg (Relative Error = 0.153615%)

## Appendix C: MATLAB code for revolute friction joint

```
function x = fcn(w)
%#codegen

brkwy_trq = 25;    % N*m ;           % Breakaway friction torque
Col_trq = 20;     % ' N*m' ;         % Coulomb friction torque
visc_coef = 0.001; % N*m*s/rad' ;   % Viscous friction coefficient
trans_coef = 10;  % s/rad' ;        % Transition approximation coefficient
vel_thr = 1e-4;   % rad/s' ;        % Linear region velocity threshold
%brkwy_trq_th = 24.995; % N*m ;     % Breakaway torque at threshold velocity

% Computing breakaway torque at threshold velocity
brkwy_trq_th = visc_coef * vel_thr + Col_trq + (brkwy_trq - Col_trq) * ...
    exp(-trans_coef * vel_thr);

if (abs(w) <= vel_thr)
    % Linear region
    t = brkwy_trq_th * w / vel_thr;
elseif w > 0
    t = visc_coef * w + Col_trq + ...
        (brkwy_trq - Col_trq) * exp(-trans_coef * w);
else
    t = visc_coef * w - Col_trq - ...
        (brkwy_trq - Col_trq) * exp(-trans_coef * abs(w));
end

x=t;
```

Figure 168 MATLAB code for torque generated in sDOF revolute joint using CFM

## **Appendix D: Kinematics of manipulator**

*[The kinematics of the mobile manipulator is an area of study that immediately precedes investigation into dynamics presented in section 2.2.2. This aspect is presented here in order to do ensure adherence scope of the thesis with the revised title as well as to adhere to the prescribed word limit. This section presents defines the two types of sDOF joints and their forward kinematic relation besides presenting the reason why wear falls beyond the scope of this study.]*

‘Kinematics pertains to the motion of bodies in a robotic mechanism with no regard to the forces or torques that cause the motion’ (Waldron et al. 2008).

Kinematic equations of the manipulator are developed by using the geometric relationship between links, the first and second time derivatives of spatial parameters which are their velocity and acceleration. The relationship between links is developed by using coordinate frames and the assignment is governed by the Denavit-Hartenberg convention (Donald and Spong n.d., Głowiński et al. 2015). The kinematics of a manipulator with three revolute joints (Figure 169) has been presented in (Koivo 1994). Forward Kinematics (FK) usually refers to calculations of end effector position for a given set of input parameters. Inverse Kinematics (IK) refers to the computation of link parameters given the end effector positions. The computation of inverse kinematics (IK) is complex for higher number of links ( $n > 2$ ) because multiple solutions exist for the same tool centre point location point on the extremity of the manipulator.



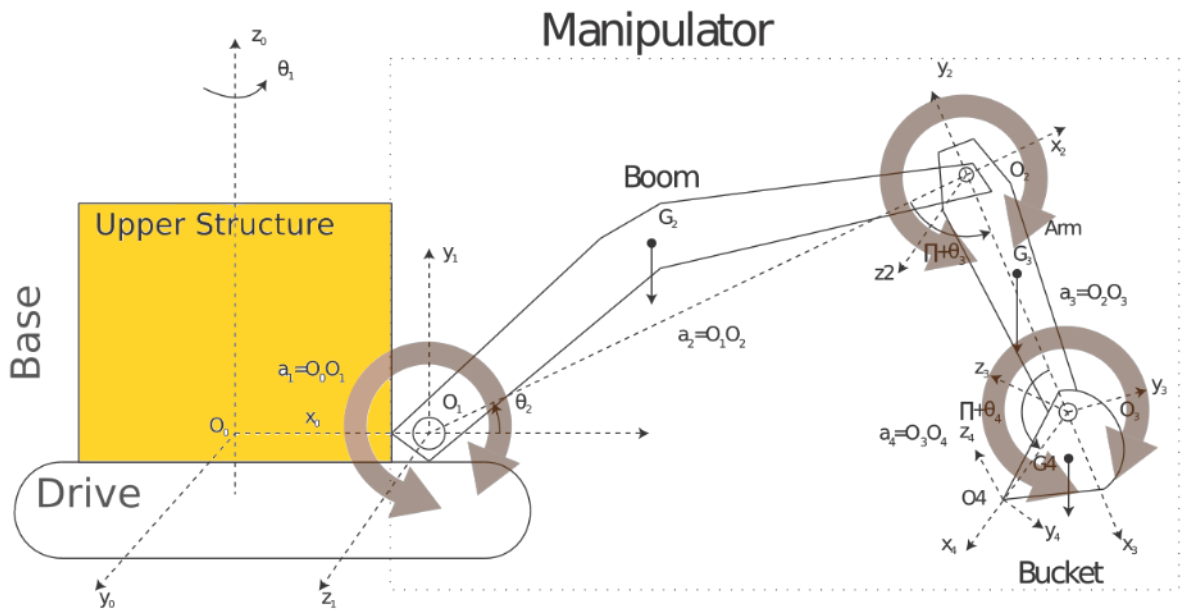


Figure 169 Generic robot manipulator as a serial open-chain linkage with the link coordinate and base coordinate system (Chacko et al. 2014, Chacko and Khan 2017)

Kinematic joints may be classified as a higher or lower pair based on the nature of contact. A lower order pair is constrained to having at most 2 degrees of freedom at most e.g. a pin and bushing with transition fit can be treated as a lower order kinematic pair having one degree of freedom which lies along its axis of revolution (Stolarski 1990).

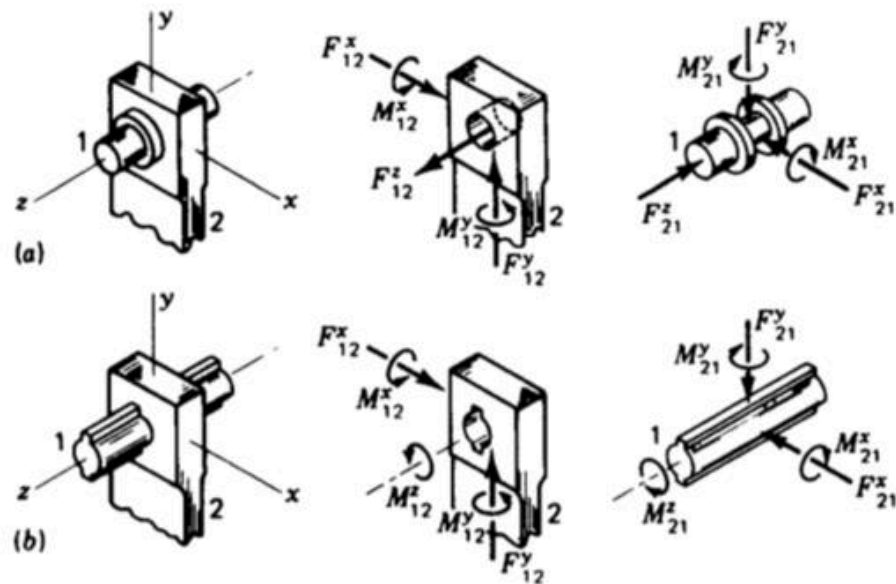


Figure 170 a) revolute joint b) prismatic joint (Uicker et al. 2003)

It was assumed that the links of the manipulator are interconnected through revolute (Figure 170 a) and prismatic (Figure 170 b) joints, both lower pair joints

‘which are mechanically attractive since wear is spread over the whole surface and lubricant is trapped in the small clearance space (in nonidealized systems) between the surfaces, resulting in relatively good lubrication (Waldron et al. 2008)’.

The general kinematic transformation for expressing a point on link  $i$  in the  $i-1^{th}$  coordinate system can be expressed as (Koivo 1994):

$${}^i p = A_{i-1}^i {}^{i+1} p \quad (26)$$

where  $A_{i-1}^i$  is given by:

$$A_{i-1}^i = \begin{bmatrix} \cos \theta_i & -\cos \alpha_i \sin \theta_i & \sin \alpha_i \sin \theta_i & a_i \cos \theta_i \\ \sin \theta_i & \cos \alpha_i \cos \theta_i & -\sin \alpha_i \sin \theta_i & a_i \sin \theta_i \\ 0 & \sin \alpha_i & \cos \alpha_i & d_i \\ 0 & 0 & 0 & 1 \end{bmatrix} \quad (27)$$

Once geometric relations are defined, their derivatives yield velocity and acceleration for the points concerned on the link. However, equipment operating in hazardous environments can undergo substantial wear that affects the joint fit i.e. a transition fit may be transformed into a clearance fit under continued operation. This affects the joint kinematics (Flores and Ambrósio 2004, Flores et al. 2008) by introducing an additional degree of freedom. The numerical study of joints with clearance is a separate and ongoing research theme for several investigations and is not considered within the scope of this work.

## Appendix E: Simulink diagram for tribometer kinematics

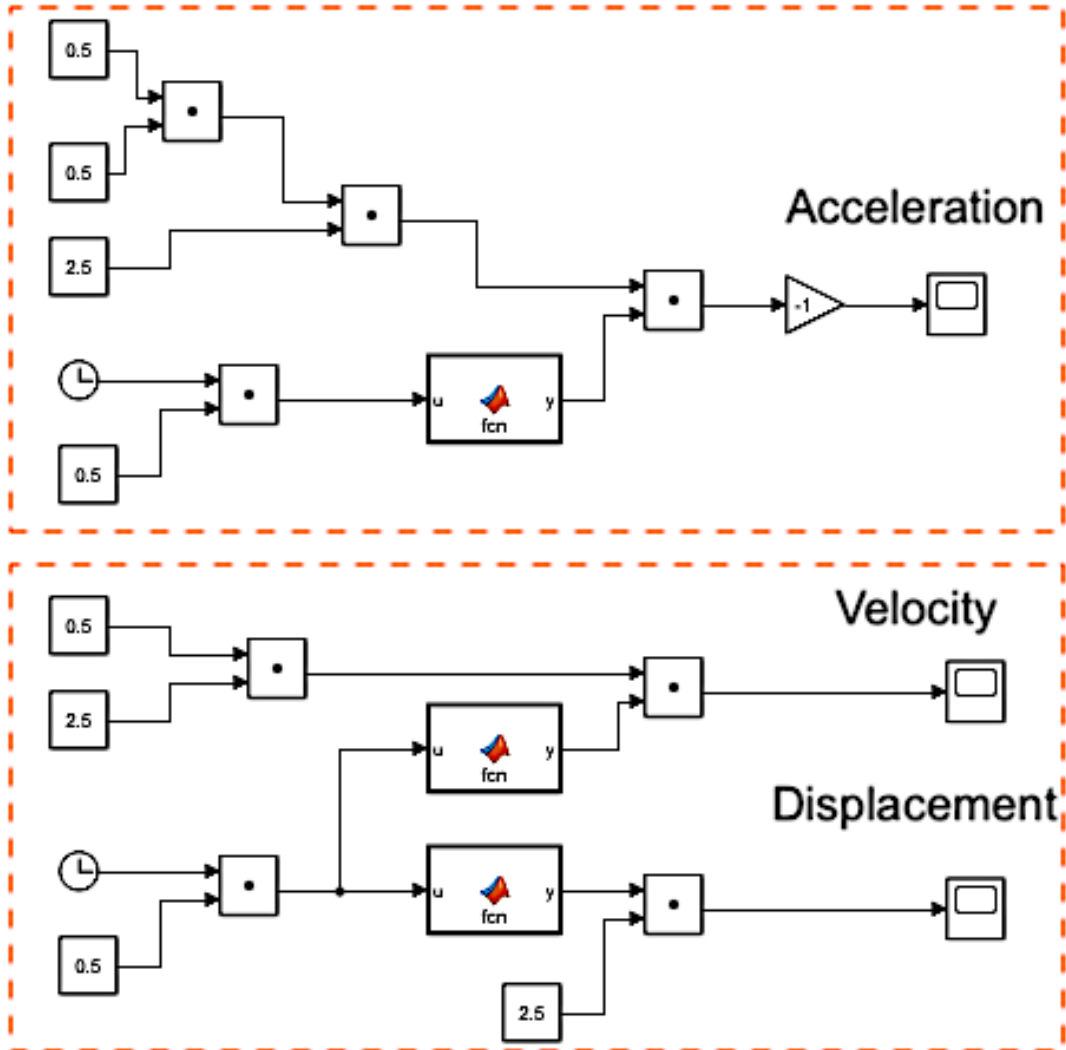


Figure 171 Block diagram representation of tribometer kinematics in Simulink environment

The above block diagram represents equations 21 to 23 presented in section 5.2.2.

# Appendix F: Lubricant properties

We use cookies to help personalise your web experience and improve our websites. To find out more about what cookies are, how we use them and how to delete them, see our [Cookie Statement](#).

By continuing to use this site, you are consenting to the use of cookies.

[Dismiss](#)



## car engine oils



### Mobil Super™ 2000 X1 10W-40

Mobil Super 2000 X1 10W-40 is a semi-synthetic motor oil that provides long engine life and protection against sludge & wear.

#### Tech Details

Mobil Super 2000 X1 10W-40	Value
Viscosity, ASTM D 445	
cSt @ 40° C	97
cSt @ 100° C	14.4
Sulfated Ash, wt%, ASTM D 874	0.91
Phosphorous	0.144
Flash Point, °C, ASTM D 92	230
Density @15°C kg/l, ASTM D 4052	0.87
Pour Point, °C, ASTM D 97	-30

Figure 172 Specifications of the 10W40 oil lubricant



Product Information:  
**K48 Moly Grease**

**Description:**

K48 is a premium quality multi-purpose grease for use in all anti-friction and plain bearings subjected to high load conditions. The incorporation of Molybdenum Disulphide imparts a high degree of wear protection against load, shock loading and dusty environments. Used extensively for applications throughout industry and the automotive sector.

**Features:**

- Excellent extreme pressure and anti-wear performance.
- High degree of corrosion protection.
- Excellent shock loading Protection.

**Applications:**

K48 is specially formulated for use in industrial equipment, cars, vans, trucks and construction plant such as bulldozers, scrapers, loading shovels and dump trucks where it will give superior performance, in all industrial plain and rolling element bearings. It is particularly recommended for constant velocity joints and fifth wheel lubrication. It is particularly effective where movements are small or intermittent and where fretting corrosion is a problem.

As with all greases used for the first time, check compatibility with the grease applied previously and if necessary purge prior to application. Likewise, as a general rule, take care not to over-lubricate and apply the quantity of grease recommended by the manufacturer.

**Performance Level:**

DIN 51502 KPF2N-20  
 ISO 6743-9 L-XBDHB2

**Physical Characteristics:**

Appearance	Grey/Black
NLGI Consistency	2
Thickener	Lithium
Molybdenum Disulphide Content	1%
Base Oil	Solvent refined mineral oil
Base Oil Viscosity @ 40 °C (cSt)	180
Worked Penetration	265 to 295
Dropping Point (°C)	185
Oil Separation (%)	5
Copper Corrosion	Pass
Resistance to Corrosion EMCOR	0:0
Water Washout @ 39 °C (%)	3
Four Ball Weld Load (Kgs)	315
Timken OK load (lbs)	50
Operating Temperature Range (°C)	-20 to +140

Part No.s: KMO180, KMO400, KMO050, KMO075, KMO500, KMO003

(TDS K48 – 231015 Issue 5)



[www.morrislubricants.co.uk](http://www.morrislubricants.co.uk)

Figure 173 Specifications of the molybdenum grease lubricant

## **Appendix G: Models governing pulse electro deposition (PED)**

Two main theoretical models governing pulse electro deposition (PED) of MMCs are the Guglielmi model and Celis model (Jung et al. 2009). The Guglielmi model explains the effect of particle concentration on incorporation rate as a function of current density (Bahrololoom and Sani 2005). However, it does not account for the effect of hydrodynamics, particle size, and ageing effects (Gomes et al. 2011). The two main steps in particle deposition according to this model are:

- i. a loose physical absorption step, and
- ii. a simultaneous strong absorption with electrochemical discharge and embedding.

The Celis model addresses the shortcomings of the Guglielmi model and has been successfully applied to the Cu-Al<sub>2</sub>O<sub>3</sub> and Au-Al<sub>2</sub>O<sub>3</sub> systems (Gomes et al. 2011). This 5-step model explains the mechanism of hydrodynamic flow during pulse-off time in PED. The five steps of this model are (Gomes et al. 2011):

- i. formation of an ionic cloud around the particles,
- ii. transport of the particles by convection to the hydrodynamic boundary layer
- iii. transport of the particles by diffusion to the cathode
- iv. free ions and electro-active ions adsorbed on the particles are adsorbed at the cathode, and
- v. electrochemical reduction of the absorbed ions at the cathode with the embedding of the particles into the growing metallic matrix.

A third model called the Fransaer model applies to particles having sub-micron dimensions has also been reported (Gomes et al. 2011). Other models in literature include the Vereecken model and Lee-Talbot model. These models have been validated for specific coating conditions and material pairs only. The process is shown in Figure 174 and the 4-step process of particle incorporation into a metal matrix composite has been described in (Gomes et al. 2011) as follows:

- i. formation of surface charge on particles in suspension,

- ii. particle mass transfer from the bulk of the suspension to the electrode surface,
- iii. particle-electrode interaction, and
- iv. particle incorporation and irreversible entrapment simultaneously into growing metal layer.

According to (Low et al. 2006), the alternative explanation has been that particle co-deposition in an MMC occurs through four stages. These stages have been identified as:

- i. electrophoresis,
- ii. convective diffusion,
- iii. mechanical entrapment and
- iv. adsorption.

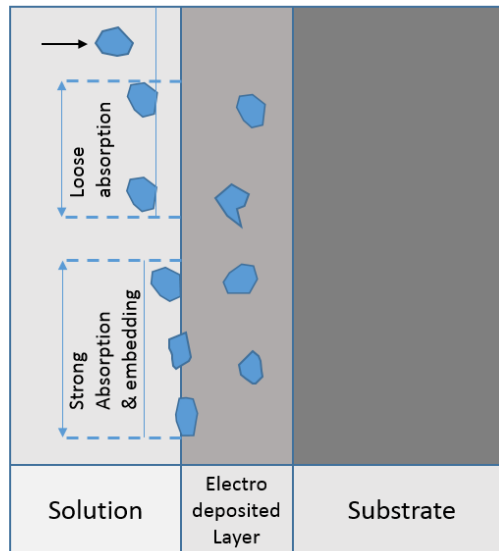


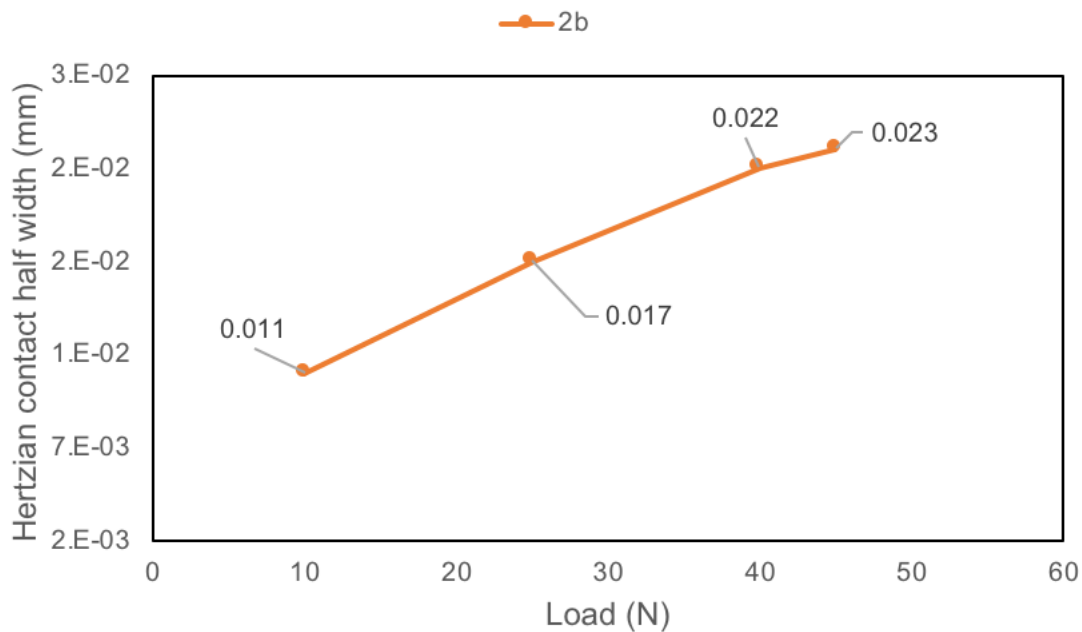
Figure 174 The process of nanocomposite surface coating development based on (Jung et al. 2009)

## Appendix H: Hertzian contact parameters

The following were used for computation of Hertzian contact: Elastic moduli,  $E_1 = E_2 = 200$  GPa, Poisson's ratio,  $\nu_1 = \nu_2 = 0.30$ , and specimen dimensions,  $d_1 = 8$  mm,  $d_2 = \infty$ ,  $l = 16$  mm (section 5.2.5.1) and load  $F = 10, 25, 40, 45$  N. The consolidated Hertzian contact characteristics are tabulated in Table 24 and graphically presented in Figure 175.

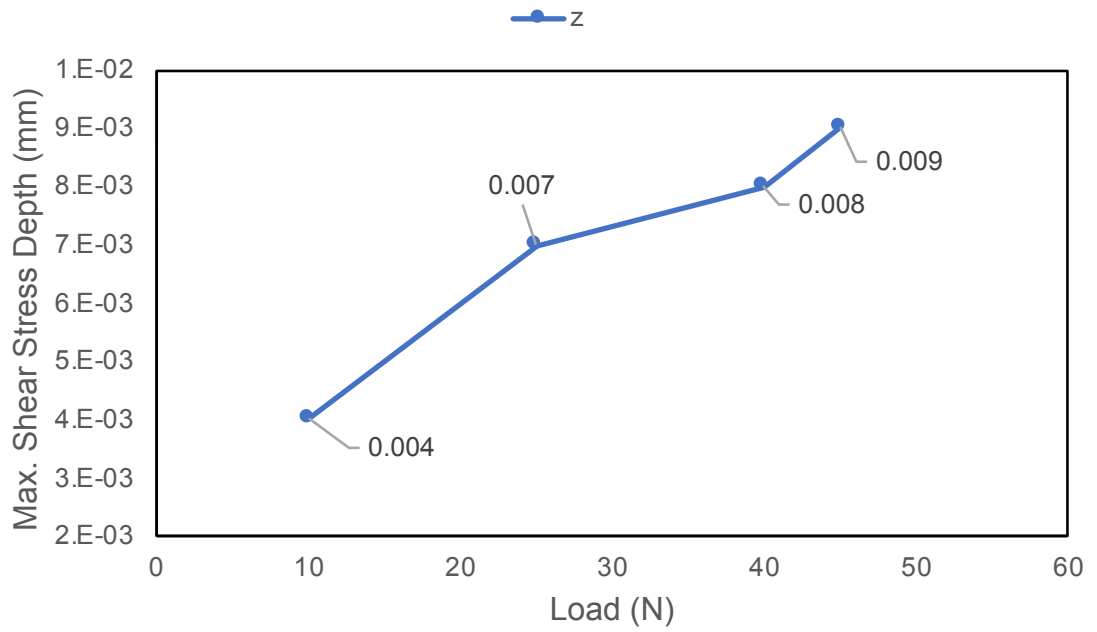
Load (N)	10	25	40	45
$P_{\max}$ (MPa)	73.9	116.9	147.9	156.8
$T_{\max}$ (MPa)	22.2	35.1	44.4	47.1
$z$ (mm)	0.004	0.007	0.008	0.009
$2b$ (mm)	0.011	0.017	0.022	0.023

Table 24 Parameters for computing Hertzian contact characteristics

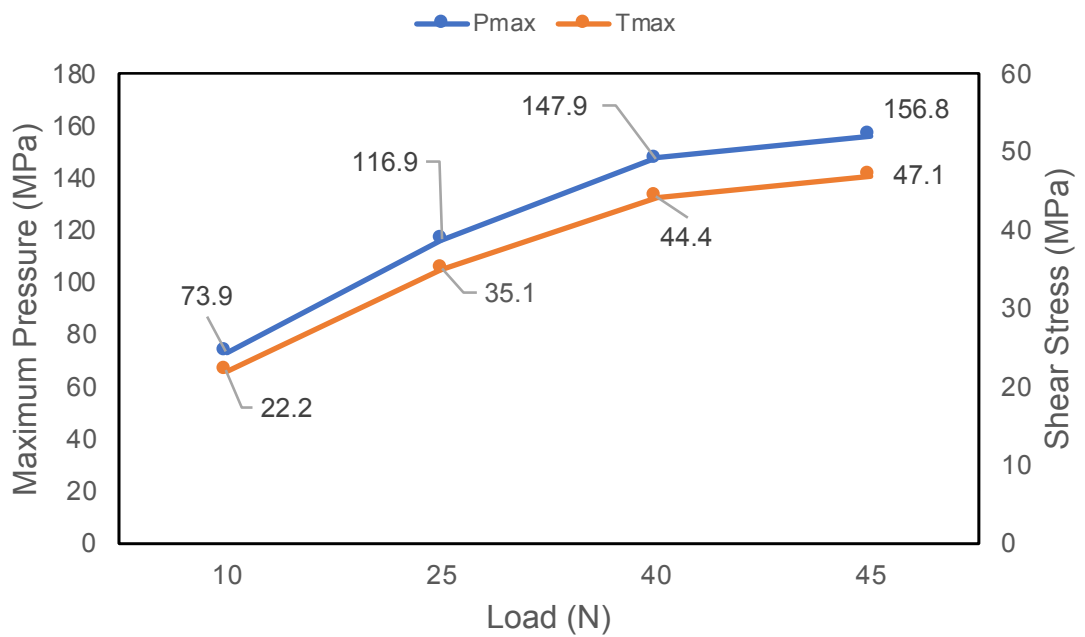


a)





b)



c)

Figure 175 a) Hertzian contact pressure b) shear stress depth and c) maximum pressure and shear stress

### Appendix I: Calculation of pulse current parameters and coating thickness

		Sample dimensions			Surface area (dm <sup>2</sup> )	Pulse current parameters							Coating Duration	Coating Thickness	
Calculation #	Sides	Length (dm)	Breadth (dm)	Height (dm)	Plating area (dm <sup>2</sup> )	Peak current (A)	Current density (A/dm <sup>2</sup> )	Current density (mA/cm <sup>2</sup> )	T <sub>on</sub> (ms)	T <sub>off</sub> (ms)	Duty cycle (%)	Average current (A)	Test Duration (s)	Test Duration (min)	Thickness (μm)
1	1	0.33	0.10	0	0.033	0.10	3.0	30.30	20	80	20	0.02	3600.00	60.00	37.28
2	1	0.33	0.10	0	0.033	0.10	3.0	30.30	30	70	30	0.03	3600.00	60.00	37.28
3	1	0.33	0.10	0	0.033	0.20	6.1	60.61	20	80	20	0.04	3600.00	60.00	74.56
4	1	0.33	0.10	0	0.033	0.30	9.1	90.91	20	80	20	0.06	3600.00	60.00	111.84
5	1	0.33	0.10	0	0.033	0.30	9.1	90.91	30	70	30	0.09	3600.00	60.00	111.84
6	1	0.33	0.10	0	0.033	0.40	12.1	121.21	20	80	20	0.08	3600.00	60.00	149.12

Figure 176 Calculation of pulse current parameters and coating thickness

**Appendix J: Additional images**

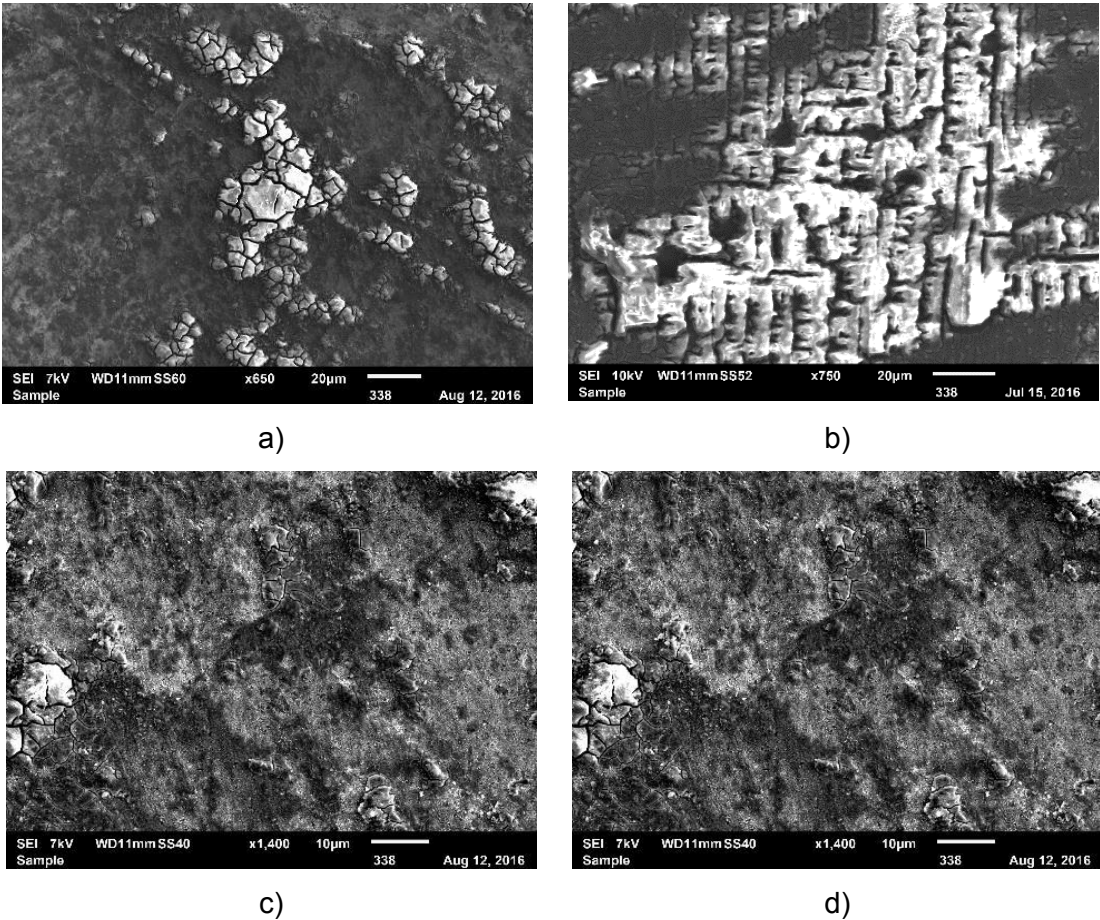


Figure 177 a-d) Specimens coated with 2A exhibit inferior deposition characteristics for lower current intensities



Figure 178 a-b) Specimens coated with 2.0A current b) 0.05A current exhibit inferior characteristics



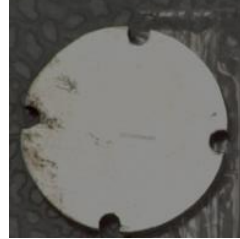
a)



b)



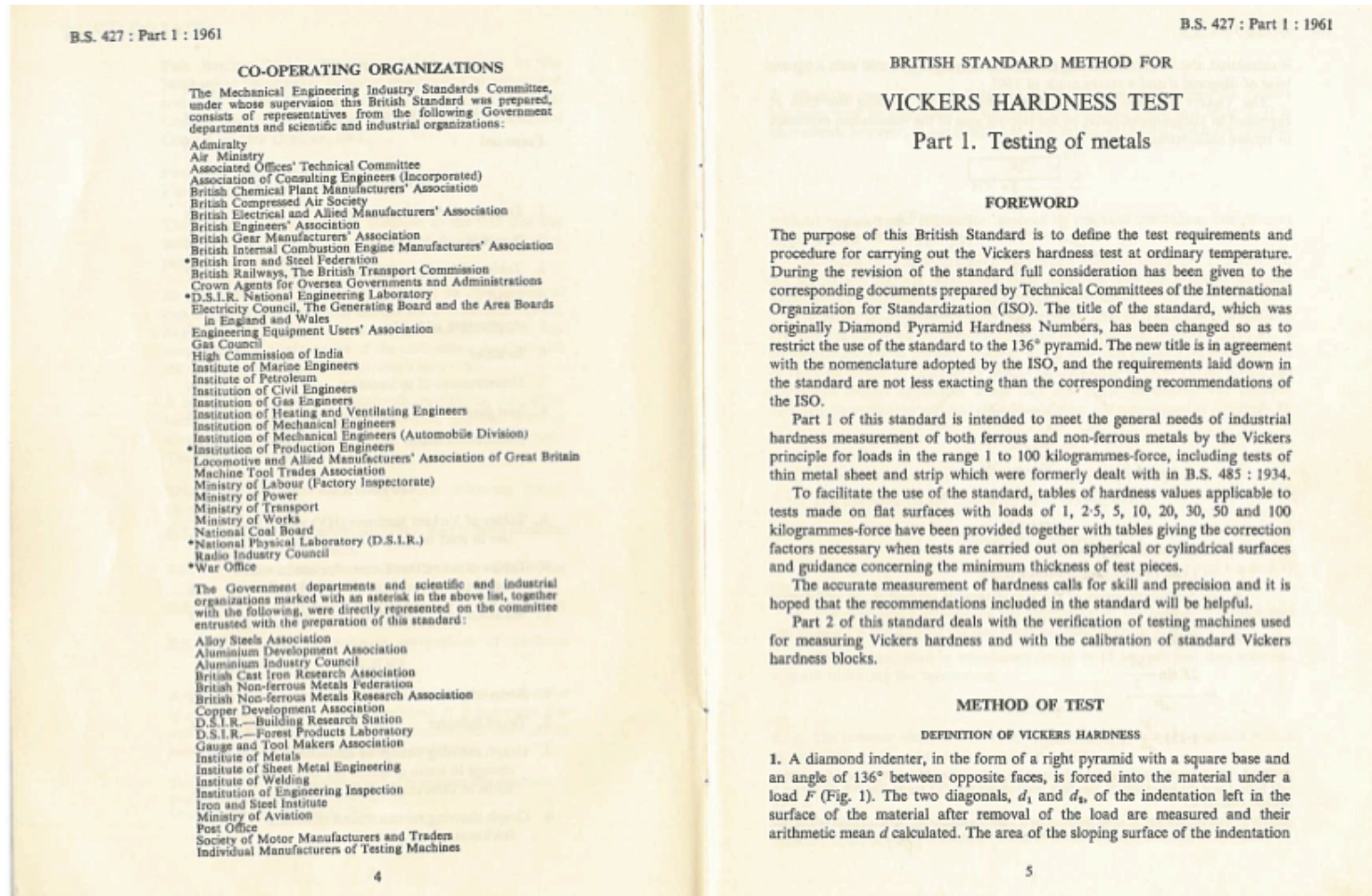
c)



d)

Figure 179 Grease-lubricated uncoated specimens CG4-7

## Appendix K: Buehler Vickers hardness micro-indentation manual



a)  
37

is calculated, the indentation being considered as a right pyramid with a square base of diagonal  $d$  and a vertex angle of  $136^\circ$ .

The Vickers hardness is the quotient obtained by dividing the load  $F$ , expressed in kilogrammes-force, by the sloping area of the indentation expressed in square millimetres.

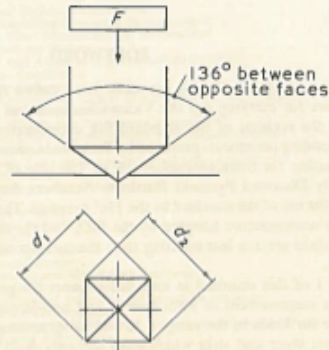


Fig. 1 Form of Indentation

SYMBOLS

2. The symbols used are as follows:

- $F$  = Load in kilogrammes-force (kgf).
  - $d$  = Arithmetic mean of the two diagonals,  $d_1$  and  $d_2$ , in millimetres (mm).
  - HV = Vickers hardness
- $$HV = \frac{2F \sin \frac{136^\circ}{2}}{d^2}$$
- $$= 1.854 \frac{F}{d^2} \text{ approximately.}$$

NOTE 1. The kilogramme-force is that force which, acting alone on a mass of one kilogramme, will impart to it the international standard acceleration  $980.665 \text{ cm/s}^2$  (see B.S. 350, Part 1, Section One (2) a.)

NOTE 2. The symbol HV is supplemented by a number indicating the load used in the test. Thus, HV 30 indicates that the Vickers hardness was measured with a load of 30 kgf.

TABLES OF HARDNESS VALUES

3. When the mean diagonal of the indentation has been determined the Vickers hardness may be computed by means of the formula given in Clause 2. It is convenient, however, to use tables and such tables, calculated from the formula

$$HV = \frac{2F \sin \frac{136^\circ}{2}}{d^2}$$

without regard to the limitations imposed by practical conditions, are given in Appendix A.

The tables have been prepared for certain selected loads, i.e. 1, 2.5, 5, 10, 20, 30, 50 and 100 kgf, and when these loads are used the required hardness values may be obtained by direct reference to the tables.

The tables in Appendix A apply to hardness tests in which the indentations are made in flat surfaces. When the surface is of spherical or cylindrical form a correction should be applied, the magnitude of which depends on the diagonal of the indentation in relation to the curvature of the surface. Tables giving the correction factors applicable when tests are made on convex and concave surfaces, for both spherical and cylindrical forms, are reproduced as Appendix B.

LOAD

- 4. a. The selected load shall lie within the range 1 to 100 kgf.
- b. The tolerance on the load shall be  $\pm 0.5$  per cent.

APPLICATION OF LOAD

- 5. a. The load shall be applied along the axis of the indenter and normal to the surface of the test piece.
- b. The mechanism controlling the application of the load shall ensure that the indenter is forced into the test piece without shock or vibration.
- c. The full load shall be maintained for 10 to 15 seconds and then removed without distorting the indentation.

INDENTER

- 6. a. The indenter shall be a diamond in the form of a right pyramid with a square base rigidly mounted in a suitable holder.
- b. The angle between opposite faces of the diamond pyramid shall be  $136 \pm 0.3^\circ$ .
- c. Each face of the diamond pyramid shall be inclined to the axis of the indenter at an angle of  $68 \pm 0.3^\circ$ .

b)

*d.* All four faces of the diamond pyramid shall meet in a point. This requirement is satisfied if the line of junction between opposite faces (Fig. 2) is less than 0.002 mm.

*e.* Each of the four angles in a section normal to the axis of the indenter shall be  $90 \pm 0.2^\circ$ .

*f.* The diamond pyramid shall be well polished and free from cracks or other surface defects (see Clause 9 *c*).

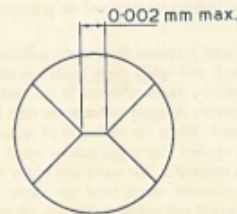


Fig. 2. Tip of Indenter

#### MEASUREMENT OF INDENTATION

7. *a.* The measuring microscope or other measuring device used for measuring the diagonals of the indentation shall be graduated to read directly to 0.001 mm or less.

*b.* The microscope shall permit the intervals of a calibrated stage micrometer to be measured to the following accuracy:

Intervals up to and including 0.2 mm:  $\pm 0.001$  mm.

Intervals exceeding 0.2 mm:  $\pm 0.5$  per cent.

#### TEST PIECE

8. *a.* The surface finish of the test piece shall be such as to permit accurate measurement of the diagonals of the indentation.

NOTE. Precautions should be taken to ensure that the surface tested is representative and that its hardness is not affected by any unsuitable machining, grinding or polishing process applied to it.

*b.* The thickness of the test piece or of the layer under test shall be at least 1.5 times the diagonal of the indentation (see Clause 9 *e* and Appendix C).

*c.* The test piece shall be rigidly supported so that the surface to be indented is at right angles to the axis of the indenter.

*d.* The distance between the centre of any indentation and any edge of the test piece or edge of any other indentation shall be not less than 2.5 times the diagonal of the indentation.

#### RECOMMENDATIONS

9. *a.* The testing machine should not be sited in gritty or dusty conditions nor in a position subject to vibration or excessive temperature changes.

*b.* The testing machine should be frequently checked by means of standardized blocks (see B.S. 427 : Part 2\*).

*c.* Periodic examination of the indenter for surface defects is strongly recommended. These are clearly reproduced in the indentations and can be detected by carefully scrutinizing an indentation whilst viewing it through the measuring microscope.

*d.* Where the Vickers hardness test is carried out to ascertain the surface hardness of surface-hardened metals, it is recommended that several indentations should be made with decreasing loads until substantially the same hardness value is given by two successive loads.

*e.* When testing metal in thin sheet or strip form, special care is required if erroneous hardness values are to be avoided. If the requirement as to thickness laid down in Clause 8 *b* is satisfied, it is unlikely that hardness measurements on either ferrous or non-ferrous metals will be faulty provided the under surface of the test piece is smooth and in intimate contact with the supporting anvil. If, in particular circumstances, it becomes necessary to accept a ratio of thickness to diagonal of less than 1.5, the hardness value may depend on the load and on the size and hardness of the anvil, and a special investigation may be needed to establish what influence these factors exert on the true hardness as obtained from thicker test pieces.

*f.* To achieve maximum accuracy, the load should be reasonably large having regard to the composition, treatment and dimensions of the test piece.

Although a maximum load of 30 kgf is generally recommended, heavier loads, e.g. 100 kgf, may be desirable to yield average hardness values when testing metals having a coarse structure, but it should be borne in mind that the use of high loads on hard metals tends to reduce the life of the diamond indenter.

*g.* As there is no general procedure for accurately converting Vickers hardness into other scales of hardness, it is recommended that such conversions should be avoided except for special cases where a reliable basis for the conversion has been established beforehand by direct test on the material concerned.

NOTE. Approximate comparisons of hardness scales are given in B.S. 860, 'Table of approximate comparison of hardness scales'.

\* B.S. 427, 'Vickers hardness test', Part 2, 'Verification of the testing machine'.

c)

APPENDIX A

TABLES OF VICKERS HARDNESS VALUES (HV) FOR USE IN TESTS MADE ON FLAT SURFACES

The following tables, for loads of 1, 2.5, 5, 10, 20, 30, 50 and 100 kgf have been calculated from the formula

$$HV = \frac{2F \sin \frac{136^\circ}{2}}{d^2}$$

without regard to the limitations imposed by practical conditions.

In industrial tests carried out in accordance with this standard, using testing machines in good order, the principal limitation will arise in the measurement of the diagonals of the indentation, and it is unlikely that the accuracy of determination of the mean diagonal will be better than  $\pm 0.001$  mm. The corresponding accuracy in the resulting hardness value may be obtained from the graphs reproduced at the end of the tables (Fig. 3) which show the change of hardness value equivalent to a change of 0.001 mm in the length of the mean diagonal for various loads at different levels of hardness.

Load = 1 kgf

TABLE I

Diagonal of indentation mm	0.000	0.001	0.002	0.003	0.004	0.005	0.006	0.007	0.008	0.009
0.03	2060	1930	1811	1703	1604	1514	1431	1355	1284	1219
0.04	1159	1103	1051	1003	958	916	876	839	806	772
0.05	742	713	686	660	636	613	591	571	551	533
0.06	515	498	482	467	453	439	426	413	401	389
0.07	378	368	358	348	339	330	321	313	306	297
0.08	290	283	276	269	263	257	251	245	239	234
0.09	229	224	219	214	210	205	201	197	193	189
0.10	185	182	178	175	171	168	165	162	159	156
0.11	153	151	148	145	143	140	138	135	133	131
0.12	129	127	125	123	121	119	117	115	113	111
0.13	110	108	106	105	103	102	100	98.8	97.4	96.0
0.14	94.6	93.3	92.0	90.7	89.4	88.2	87.0	85.8	84.7	83.5
0.15	82.4	81.3	80.3	79.2	78.2	77.2	76.2	75.2	74.3	73.4
0.16	72.4	71.5	70.7	69.8	68.9	68.1	67.3	66.5	65.7	64.9
0.17	64.2	63.4	62.7	62.0	61.2	60.6	59.9	59.2	58.5	57.9
0.18	57.2	56.6	56.0	55.4	54.8	54.2	53.6	53.0	52.5	51.9
0.19	51.4	50.8	50.3	49.8	49.3	48.8	48.3	47.8	47.3	46.8
0.20	46.4	45.9	45.4	45.0	44.6	44.1	43.7	43.3	42.9	42.5
0.21	42.0	41.7	41.3	40.9	40.5	40.1	39.7	39.4	39.0	38.7
0.22	38.3	38.0	37.6	37.3	37.0	36.6	36.3	36.0	35.7	35.4
0.23	35.1	34.8	34.5	34.2	33.9	33.6	33.3	33.0	32.7	32.5
0.24	32.2	31.9	31.7	31.4	31.1	30.9	30.6	30.4	30.2	29.9
0.25	29.7	29.4	29.2	29.0	28.7	28.5	28.3	28.1	27.9	27.6
0.26	27.4	27.2	27.0	26.8	26.6	26.4	26.2	26.0	25.8	25.6
0.27	25.4	25.2	25.1	24.9	24.7	24.5	24.3	24.2	24.0	23.8
0.28	23.7	23.5	23.3	23.2	23.0	22.8	22.7	22.5	22.4	22.2
0.29	22.0	21.9	21.7	21.6	21.5	21.3	21.2	21.0	20.9	20.7
0.30	20.6	20.5	20.3	20.2	20.1	19.9	19.8	19.7	19.6	19.4
0.31	19.3	19.2	19.0	18.9	18.8	18.7	18.6	18.5	18.3	18.2
0.32	18.1	18.0	17.9	17.8	17.7	17.6	17.4	17.3	17.2	17.1
0.33	17.0	16.9	16.8	16.7	16.6	16.5	16.4	16.3	16.2	16.1
0.34	16.04	15.96	15.88	15.76	15.67	15.58	15.49	15.40	15.31	15.22
0.35	15.14	15.06	14.97	14.88	14.80	14.71	14.63	14.55	14.47	14.39
0.36	14.31	14.23	14.15	14.07	14.00	13.92	13.84	13.77	13.69	13.62
0.37	13.55	13.47	13.40	13.33	13.26	13.19	13.12	13.05	12.98	12.91
0.38	12.84	12.77	12.71	12.64	12.58	12.51	12.45	12.38	12.32	12.25
0.39	12.19	12.13	12.07	12.01	11.95	11.89	11.83	11.77	11.71	11.65
0.40	11.59	11.53	11.47	11.42	11.36	11.31	11.25	11.19	11.14	11.09
0.41	11.03	10.98	10.92	10.87	10.82	10.77	10.72	10.66	10.61	10.56

d)

Figure 180 Manual for Vickers micro-hardness indenter



## Appendix L: Nickel graphene nanocomposite coatings

Similarly, results from specimens with graphene nanocomposite test specimens were presented in Figure 181 and Figure 182 corresponding to the peak and average values of measured coefficient of friction obtained from the friction curves for oil-lubricated contacts were recorded in Figure 182. For grease-lubricated contacts, average COF ranged from 0.0926 for FG01 to 0.3786 for FG03, and peak COF ranged from 0.1195 for FG01 to 0.7488 for FG03.

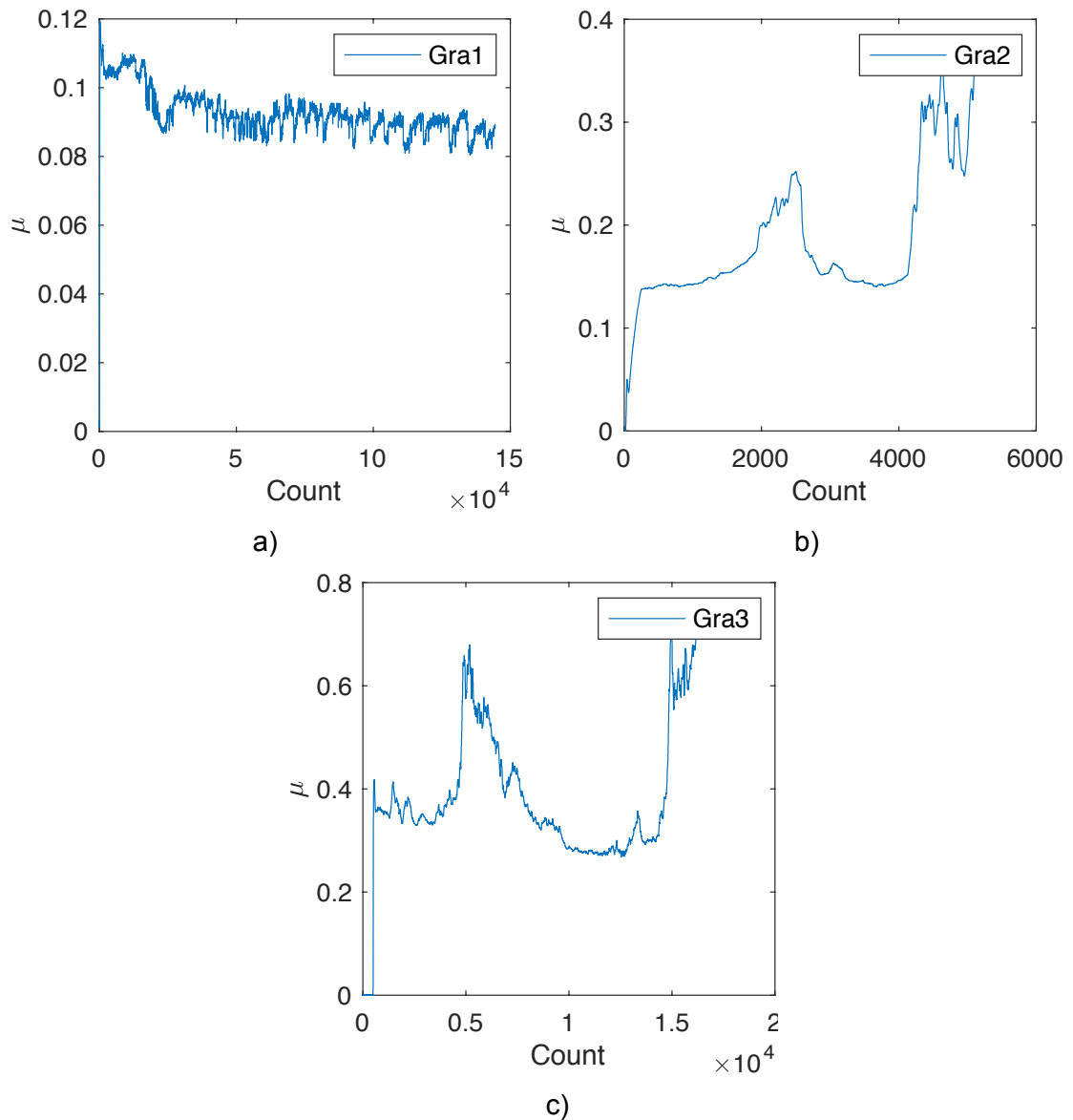


Figure 181 a-c) COF for grease-lubricated sliding pin contacts with nickel graphene coating

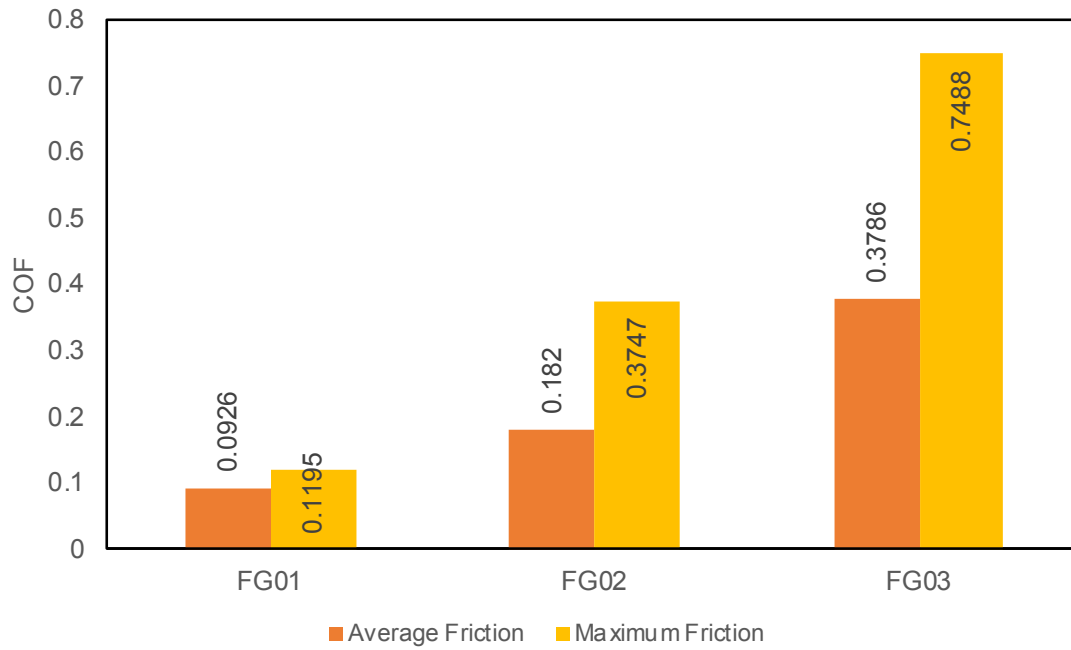


Figure 182 Peak and average COF for nickel graphene coated sliding pin contact

Graphene		Average Friction	Maximum Friction
40N	FG01	0.0926	0.1195
	FG02	0.1820	0.3747
	FG03	0.3786	0.7488

Table 25 Average and maximum COF for grease-lubricated pin contact with nickel graphene coating

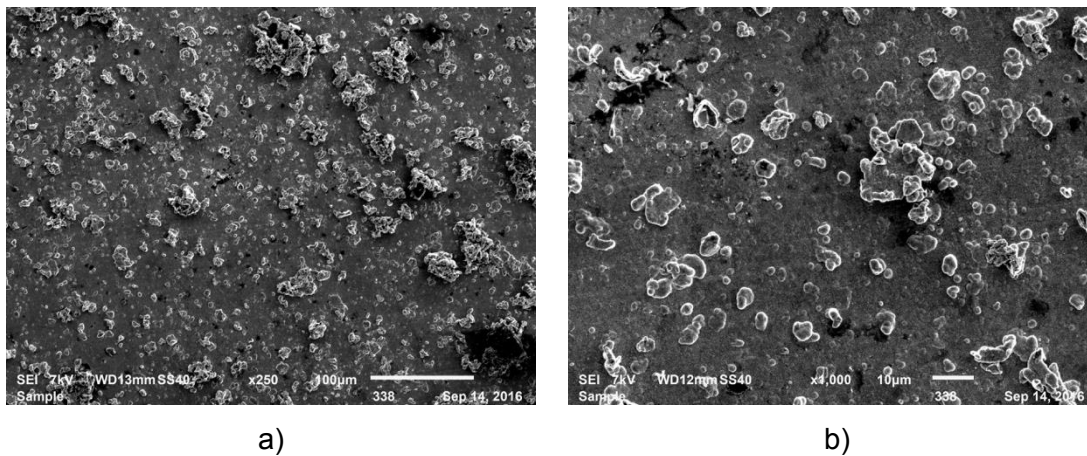


Figure 183 SEM images for nickel graphene nanocomposite coating

## Appendix M: Uncertainty measurements

The equations for standard deviation and standard error are presented below:

$$s = \sqrt{\frac{\sum_i^n (x_i - \bar{x})^2}{n-1}} \quad (28)$$

$$\sigma = \frac{s}{\sqrt{n}} \quad (29)$$

where  $\{x_1, x_2, x_3 \dots x_n\}$  are the observed values of the sample items,  $\bar{x}$  is the mean value of these observations and  $n$  is the number of observations in this sample.

These equations were used to compute the respective parameters for the experimental observations. Standard deviation represents the scatter of the observed values and standard error represents the margin of error in these observations (NC State University 2015).

# Appendix N: Publications

Proceedings of the 2014 International Conference on  
Advanced Mechatronic Systems, Kumamoto, Japan, August 10-12, 2014

## State of the Art in Excavators

Vivek Chacko<sup>1</sup>, Hongnian Yu<sup>2</sup>, Shuang Cang<sup>3</sup>, and Luige Vladareanu<sup>4</sup>

<sup>1,2</sup>Faculty of Science and Technology, Bournemouth University, Poole, United Kingdom

<sup>3</sup>School of Tourism, Bournemouth University, Poole, United Kingdom

<sup>4</sup>Institute of Solid Mechanics, Romanian Academy, C-tin Mille 15, Bucharest 1, ROMANIA

**Abstract**—Survey of literature has revealed research on excavators in trajectory analysis, modeling, control, soil-tool interaction, energy efficiency, and simulators. Kinematics of excavators has largely remained unchanged over time. Dynamic models of 3 degree of freedom (DOF) manipulator have been applied in literature. Soil-tool interaction models are becoming computationally less demanding and more accurate, for predicting interaction forces of end effector or bucket. Control of excavators through adaptive/robust control and high level behavioral control may fully automate such systems. Simulators provide platforms for testing and operator training and require dynamically accurate models. Even though much research has occurred in different areas of excavators, still fully automated excavators are rare. This paper investigates the state of art in excavators and reports the recent progress. The aim of this paper is to identify gaps in existing technology and the demands on excavators with the idea of suggesting future trends in research and as a reference for new research.

**Keywords**—kinematics, dynamics, control, soil-tool model, simulator

### I. INTRODUCTION

Excavators are used for excavating in the construction industry owing to their versatility and convenience [1, 2]. These machines are classified based on digging capacity, bucket volume, and transport configuration. Even a small improvement in machine performance would improve overall productivity [3-5]. Excavators are also used in mining, agriculture, waste management, forestry, tunneling, level digging, flat surface finishing work, pipe laying and military applications which require high workload efficiency, low maintenance cost, and levels of safety level [2, 6]. Recent urban disasters have highlighted the requirement for specialized excavators to lead rescue operations which are hazardous for human/canine rescue teams owing to unstable debris, as well as the presence of hazardous chemicals that may be present [9-11].

This paper surveys the research on excavators from the aspects of control, soil-tool modeling, trajectory analysis, energy efficiency, and search and rescue (SAR). Reviews focusing on control [12], and robots in SAR [9] have been reported in surveyed literature. In addition, a market survey of excavators has been conducted, which reveals current trends in the industry. A holistic review considering academic, industry and SAR demands is presented. This review paper intends to cover these key parameters towards complete automation of excavators and propose future trends in research.

### II. DEMANDS TOWARDS AUTOMATION

#### A. Construction Industry

Construction industry constantly demands for higher productivity, decreased operating costs (fuel, wear and tear),

reduced risk to human beings, and improved equipment uptime with the increasing demand in built property [1, 2]. Civil engineering tasks are often dangerous and distressing [3] though they are carried out in controlled environments[4]. Automation of excavators is expected to reduce accidents[3], improve efficiency[5, 6] and enhance the ability to operate in hazardous environments[7]. Automation enables human operators to focus on high-level tasks such as designating the areas of dig to relieve fatigue and operator error. The excavation task is subjective i.e. it varies with operator, equipment, and environment [8]. Therefore, it would be desirable to identify optimal operating parameters for excavators and integrate it into a planned construction environment [9]. Simulators can be used for training novice operators, validation and analysis of control systems and sensors, resulting in a reduction of overall equipment costs and training costs [4, 10].

Excavator systems which are efficient – considering energy and execution time, follow planned activity schedule, have increased safety features are required for the future. Simulators capable of providing visually and dynamically realistic training would augment excavator technology.

#### B. Academic demand and requirements

Academic demands have been classified into controllers, soil-tool models, sensors, actuators and simulations.

- a. Automatic control: Kinematic modeling has remained unchanged since 1994[11]. Human operators' trajectories differ from dynamic controllers'. Dynamics have been modeled in 3 methods as explained in the pertinent section. Manipulator dynamics have been reported only for 3 degrees of freedom (DOF) owing to the complexity of the problem. Adaptive and robust control has been found to be promising and superior to PD or PID for handling large nonlinear time varying forces typical of excavation systems. Advanced controllers such as haptic devices [12] and brain-machine interface [13-15] along with human-machine shared control[16-18] offer promising operation improvements.
- b. Soil tool interaction modeling is highly nonlinear and dynamic. Recent models have overcome long computational times to arrive at sufficiently accurate models for digging interaction [19]. Test environments in laboratory and real life excavation sites vary greatly[20]. The digging task is not repeatable owing to a highly dynamic environment; therefore predictive methods for estimating forces fail[21]. The capability of digging different soil types is imperative to excavators. Recently developed tools such as robust adaptive control [22], along with more accurate soil-tool interaction models [19,

# Multi-body simulation methods for rigid manipulators

Vivek Chacko, Hongnian Yu

**Abstract**— This paper examines CAD- multi body dynamics approach of modeling and simulation for rigid manipulators. CAD is used for designing mechanical links that can be assembled into linkages and mechanisms. The technique of using CAD designs in multi-body simulation environments has been studied. A summary of procedures is included. Further, the design prototype has been actuated using two input devices popular in the gaming industry, and an overview is presented below.

## I. INTRODUCTION

This research is based on material removal after search and rescue (SAR) lifesaving operation scenario. For this purpose, the excavator manipulator mechanism was chosen since they are ubiquitous in SAR sites. In recent years, there have been advances in multibody simulation software. In design methodology, CAD-multi-body dynamic (MBD) simulation in the initial design phase reduces design cycle time. Commercial engineering simulation software have been adapting to changing user requirements by being more user friendly and intuitive. Simulation using combination of CAD-dynamic simulation packages also enables the engineer to access the specific capabilities of different software packages.

Using the appropriate combination of design and analysis packages reduces design cycle times, and permits the analysis of complex mechanical systems. In addition, the design engineer and control engineer can work concurrently thus making the overall design process more efficient. The concept of a simulation environment e.g. game engines, can be advantageous for low cost robot simulation and training[1].

In this paper, the Newton-Euler approach using MBD has been presented. This method helps overcome errors in equations, with accurate and instant calculation of body parameters such as mass and moments of inertia. Joint motion parameters can be easily applied and the respective motion or force parameters can be easily read by using sensors.

Kinematics and dynamics have been considered in both cases. The method can be applied across serial and parallel mechanisms, with the latter offering more robust performance. The different concepts, approaches and procedures have been examined in this paper.

## II. MODELING OF THE SYSTEM

### A. Kinematic modeling

The 3-link excavator kinematic mechanism has been modeled in the 90's [2] following the Denavit-Hartenberg convention of axis assignment, which has 4 degrees of

freedom (DoF). The kinematic formulation for the RRR (3DoF) mechanism is considered, since the cab does not slew during digging.

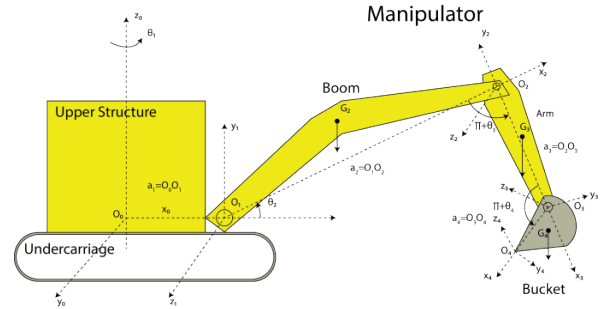


Figure 1 Coordinate assignment and nomenclature of excavator

### B. Dynamic modeling

There are 2 approaches to modeling a dynamic system, the classic approach of numerical modeling, and the concept of physical modeling. The advantages and disadvantages of both systems have to be considered while designing the multi-body simulation. Rigid links are assumed.

In traditional numerical modeling, the dynamic model is derived from first principles. Three approaches can be found in literature:

1. Newton - Euler method (force-torque)[3]
2. Euler - Lagrange method (energy)[4]
3. Kane's equation (virtual work)[5]

For 3-link excavator mechanism, having 3R planar configuration the three methods has been presented in literature. Method 1 is seen to be most computationally efficient and is used widely. This is also the method followed in the multi-body dynamic simulation package. The third method allows for the elimination of pseudo-forces forces in the joints.

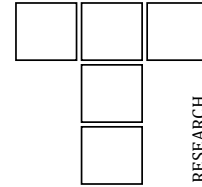
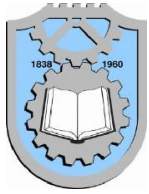
According to the energy approach, the dynamics equation can be given as[6]:

$$D_a(\theta)\ddot{\theta} + C_a(\theta, \dot{\theta})\dot{\theta} + G_a(\theta) + B_a(\dot{\theta}) = \Gamma\tau_a - F_L$$

where  $\theta = [\theta_1 \ \theta_2 \ \theta_3 \ \theta_4]^T$  is the vector of joint angles  $D_a(\theta)$  is a 4x4 matrix which represents inertia,  $C_a(\theta, \dot{\theta})$  represents Coriolis and centripetal effects,  $G_a(\theta)$  represents gravity forces,  $B_a(\dot{\theta})$  represents frictional forces,  $\Gamma$  is the input matrix corresponding to joint torques  $\tau_a = [\tau_1 \ \tau_2 \ \tau_3 \ \tau_4]^T$ ,  $F_L$  represents soil-tool or machine-environment interaction forces during digging operation. The first angle,  $\theta_1$  represents the rotation of the manipulator about the base of the excavator; the manipulator operation is assumed planar during digging

V. Chacko is with the Dept. of Computing, Faculty of Science and Technology, Bournemouth University, Poole, United Kingdom (e-mail: vchacko@bournemouth.ac.uk).

Prof H. Yu is with the Faculty of Science and Technology, Bournemouth University, Poole, United Kingdom (e-mail: yuh@bournemouth.ac.uk).



## Modelling and Simulation of a Manipulator with Stable Viscoelastic Grasping Incorporating Friction

A. Khurshid<sup>a</sup>, Z. Khan<sup>b</sup>, V. Chacko<sup>b</sup>, A. Ghafoor<sup>c</sup>, M.A. Malik<sup>d</sup>, Y. Ayaz<sup>c</sup>

<sup>a</sup>Department of Mechatronics Engineering, Air University, Sector E-9, Islamabad 44000, Pakistan,

<sup>b</sup>NanoCorr, Energy and Modelling (NCEM), Faculty of Science & Technology, Bournemouth University, Dorset BH12 5BB United Kingdom,

<sup>c</sup>School of Mechanical and Manufacturing Engineering, National University of Sciences and Technology Sector H-12, Islamabad 44000, Pakistan,

<sup>d</sup>Department of Mechanical Engineering, Air University, Sector E-9, Islamabad 44000, Pakistan.

### Keywords:

Anthropomorphic arm  
Computer aided design  
Multi-body mechanics simulation  
Dynamics  
Joint friction  
Bond graph model  
Viscoelasticity

### ABSTRACT

Design, dynamics and control of a humanoid robotic hand based on anthropological dimensions, with joint friction, is modelled, simulated and analysed in this paper by using computer aided design and multibody dynamic simulation. Combined joint friction model is incorporated in the joints. Experimental values of coefficient of friction of grease lubricated sliding contacts representative of manipulator joints are presented. Human fingers deform to the shape of the grasped object (enveloping grasp) at the area of interaction. A mass-spring-damper model of the grasp is developed. The interaction of the viscoelastic gripper of the arm with objects is analysed by using Bond Graph modelling method. Simulations were conducted for several material parameters. These results of the simulation are then used to develop a prototype of the proposed gripper. Bond graph model is experimentally validated by using the prototype. The gripper is used to successfully transport soft and fragile objects. This paper provides information on optimisation of friction and its inclusion in both dynamic modelling and simulation to enhance mechanical efficiency.

### Corresponding author:

Zulfiqar Khan  
NanoCorr, Energy and Modelling,  
(NCEM),  
Faculty of Science & Technology,  
Bournemouth University,  
Dorset BH12 5BB,  
United Kingdom.  
E-mail: zkhan@bournemouth.ac.uk

© 2016 Published by Faculty of Engineering

### 1. INTRODUCTION

Robotic manipulators are usually used for tasks which have been historically performed by human beings by using their hands e.g. in a factory production line. The use of robotic arms is beneficial in several ways as it helps to accomplish repetitive tasks which can cause fatigue in human beings, use of robotic

manipulators in hazardous environments reduces risk to human beings (in a paint shop on a factory floor) and exposure to airborne hazardous particles can be avoided. The aim of this research is to develop a humanoid hand with joint friction model and viscoelastic end effectors to provide solutions for performing automated mechanical tasks at maximum performance.

# Wear and Friction Properties of Electrodeposited Ni-Based Coatings Subject to Nano-enhanced Lubricant and Composite Coating

Rizwan Bajwa<sup>1</sup> · Zulfiqar Khan<sup>1</sup> · H. Nazir<sup>1</sup> · Vivek Chacko<sup>1</sup> · Adil Saeed<sup>1</sup>

Received: 10 April 2016 / Revised: 13 June 2016  
© The Chinese Society for Metals and Springer-Verlag Berlin Heidelberg 2016

**Abstract** This paper presents research findings on the tribological performance of electrodeposited coatings subject to nano-lubricants with the addition of nano-Al<sub>2</sub>O<sub>3</sub> and graphene and Ni/nano-Al<sub>2</sub>O<sub>3</sub> composite coatings. Electrodeposited coatings were produced by using a pulse electrodeposition method. Tribological experiments were conducted by using a linear reciprocating ball on flat sliding tribometer. Experimental results confirmed that the wear and friction resistance properties were significantly enhanced by doping of nano-effects in the lubricating oil and composite coating. The addition of Al<sub>2</sub>O<sub>3</sub> nanoparticles in the lubricating oil showed the best tribological properties, followed by Ni–Al<sub>2</sub>O<sub>3</sub> composite coatings and nano-oil with graphene. The surface morphology and microstructure of electrodeposited coatings were examined by scanning electron microscopy, energy-dispersive spectroscopy and X-ray diffraction. The wear mechanisms of these coatings subjected to tribological testing were investigated by post-test surface analyses. This research provides a novel approach to design durable nano-coatings for tribological applications in various industries such as automotive, aerospace, locomotive and renewable energy technologies.

**KEY WORDS:** Tribology; Nanoparticles; Graphene; Nano-additives; Nano-coatings

## 1 Introduction

This paper enables researchers to fully understand the advantages of two distinct approaches of nano-additives within lubricants and nano-coatings, to solve complex tribological issues in terms of design for durability and reliability. Optimisation of surfaces in contact and in relative motion is needed to enhance their tribological performance. This research is focus on enhancing the tribological performance of contact surfaces through nano-composite coatings and nano-additives in lubrication. Almost one-


third of the energy losses in mechanically interacting systems or components are attributed to friction or wear behaviour. For a long time, oil lubricants or greases have been used to reduce these frictional forces and wear asperities between two interacting surfaces. In recent years, nanoparticles have been widely studied in various applications due to their unique wear, friction and corrosion resistant properties. Nanoparticles are used both as an additive in the lubricant oil and as a metal matrix nano-composite (MMC) materials. The term nano-additive is commonly used for nanoparticles when they are used as an additive to conventional lubricants. Many studies have reported an effective role of nano-additives in lubricants in terms of the improvement of anti-friction and anti-wear properties of materials [1–3]. These nano-additives are made up of nano-sized metals [4], metal-oxides [5] and diamond nanoparticles [6]. The optimum fraction of nano-additives in lubricants is an important factor. Several studies have been conducted to investigate the optimised

Available online at <http://link.springer.com/journal/40195>.

✉ Rizwan Bajwa  
rbajwa@bournemouth.ac.uk

<sup>1</sup> NanoCorr, Energy and Modelling Research Group,  
Bournemouth University, Poole, UK

Published online: 05 August 2016

 Springer

# A review of friction models in interacting joints for durability design

Zulfiqar A. KHAN\*, Vivek CHACKO, Hammad NAZIR

*NanoCorr; Energy & Modelling (NCEM) Research, Department of Design & Engineering, Bournemouth University, Bournemouth, United Kingdom*

*Received: 31 July 2016 / Revised: 26 October 2016 / Accepted: 16 December 2016*

© The author(s) 2017. This article is published with open access at Springerlink.com

**Abstract:** This paper presents a comprehensive review of friction modelling to provide an understanding of design for durability within interacting systems. Friction is a complex phenomenon and occurs at the interface of two components in relative motion. Over the last several decades, the effects of friction and its modelling techniques have been of significant interests in terms of industrial applications. There is however a need to develop a unified mathematical model for friction to inform design for durability within the context of varying operational conditions. Classical dynamic mechanisms model for the design of control systems has not incorporated friction phenomena due to non-linearity behaviour. Therefore, the tribological performance concurrently with the joint dynamics of a manipulator joint applied in hazardous environments needs to be fully analysed. Previously the dynamics and impact models used in mechanical joints with clearance have also been examined. The inclusion of reliability and durability during the design phase is very important for manipulators which are deployed in harsh environmental and operational conditions. The revolute joint is susceptible to failures such as in heavy manipulators these revolute joints can be represented by lubricated conformal sliding surfaces. The presence of pollutants such as debris and corrosive constituents has the potential to alter the contacting surfaces, would in turn affect the performance of revolute joints, and puts both reliability and durability of the systems at greater risks of failure. Key literature is identified and a review on the latest developments of the science of friction modelling is presented here. This review is based on a large volume of knowledge. Gaps in the relevant field have been identified to capitalise on for future developments. Therefore, this review will bring significant benefits to researchers, academics and industry professionals.

**Keywords:** friction; dynamics; joint clearance; numerical models; impact; durability

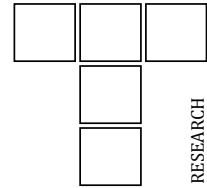
## 1 Introduction

Friction is a ubiquitous phenomenon which occurs at the interface of two surfaces in physical contact and in relative motion. It may be at times beneficial and/or detrimental in other scenarios. The phenomenon of friction is complex because it has time dependent non-linear characteristics and it is influenced by multiple factors. Friction phenomenon applies to scales ranging from nanometre level interactions to micron level interfaces to large geological interactions [1, 2]. Friction is directly linked to the durability and

reliability of interacting systems and if it is not fully optimised then it leads to significant efficiency losses. According to the Jost report of 1966, "a sizeable portion of the GDP of a nation is spent in alleviating friction and its effects namely wear". Although tribology is a relatively new area, it is formed from a confluence of theory and empiricism, continued experimental analyses, mechanics, surface engineering, chemical interactions and more recently computational methodology. Since the phenomenon has both widespread and deep-rooted influence, this review paper seeks to gain an insight into the history of the development of friction and

\* Corresponding author: Zulfiqar A. KHAN, E-mail: zkhan@bournemouth.ac.uk





## Dynamic Simulation of a Mobile Manipulator with Joint Friction

V. Chacko<sup>a</sup>, Z.A. Khan<sup>a</sup>

<sup>a</sup>NanoCorr, Energy & Modelling (NCEM) Research Group, Department of Design and Engineering, Faculty of Science & Technology, Bournemouth University, United Kingdom BH12 5BB.

### Keywords:

Virtual prototyping  
Manipulator  
Degree of freedom  
Dynamics  
Friction

### ABSTRACT

Mission criticality in disaster search and rescue robotics highlights the requirement of specialized equipment. Specialized manipulators that can be mounted on existing mobile platforms can improve rescue process. However specialized manipulators capable of lifting heavy loads are not yet available. Moreover, effect of joint friction in these manipulators requires further analysis. To address these issues, concepts of model based design and concurrent engineering are applied to develop a virtual prototype of the manipulator mechanism. Closed loop manipulator mechanism actuated by prismatic actuators is proposed herein. The mechanics model of the manipulator is presented here as a set of equations and as multibody models. Mechanistic simulation of the virtual prototype has been conducted and the results are presented. Combined friction model that comprises Coulomb, viscous and Stribeck friction is used to compute frictional forces and torques generated at each one degree of freedom translational and rotational joints. Multidisciplinary approach employed in this work improves product design cycle time for complex mechanisms. Kinematic and dynamic parameters are presented in this paper. Friction forces and torques from simulation are also presented in addition to the visual representation of the virtual prototype.

### Corresponding author:

Zulfiqar A Khan  
NanoCorr, Energy & Modelling  
(NCEM) Research Group,  
Department of Design and  
Engineering,  
Faculty of Science & Technology,  
Bournemouth University, United  
Kingdom BH12 5BB  
E-mail: zkhan@bournemouth.ac.uk

© 2017 Published by Faculty of Engineering

### 1. INTRODUCTION

Search and rescue operation (SAR) is time critical - only a small window of opportunity exists to search out and rescue the disaster victims who are trapped [1]. Currently only a few rescue teams have access to specialized rescue robots that are durable and resilient to hazardous environments available in such disaster sites e.g. [2,3]. Durability of the robot is

important because rescue sites contain abrasives, corrosive fluids and vapour-borne particulates. Robotic platforms have been proposed for carrying load e.g. [4] but manipulators that can assist rescuers to lift heavy rubble are yet to be seen. A scalable manipulator design is proposed in this work, which can be deployed with existing mobile robotic platforms.

### Surface Engineering III

---

**Session Chair:** Z. Khan, Faculty of Science & Technology, Bournemouth University, Bournemouth, United Kingdom

**Session Vice Chair:** A. Saeed, GCET, Muscat, Oman

8 - 8:30 am

Tribological Characteristics of En-19 And 16mncr5 Steel under Varying Roughness and Lubrication

Vivek Chacko, Zulfiqar Khan, Bournemouth University, Poole, Dorset, United Kingdom

The interacting combination of EN-19 and 16MnCr5 steel is widely used in heavy industrial applications. EN-19 steel is ductile, shock and wear resistant. 16MnCr5 steel is a case hardening, forgeable steel. However, the analysis of the friction and wear characteristics for this material combination has not been reported before. This paper presents both experimental and analytical results of tribological performance of EN-19 and 16MnCr5. The experiment is conducted on a reciprocating tribometer. The coefficient of friction for grease lubricated contact is recorded within the range of 0.15-0.25. Later Nickel-Alumina nano composite coating was applied onto 16MnCr5 steel. Interfacial surface roughness profiles of nano coated 16MnCr5 and EN-19 samples are presented in conjunction with a detailed study of wear failure modes and the wear volume at varying test conditions. Comparative results of tribological performance of nano coated versus non coated 16MnCr5 are also presented.

# Modelling and Adaptive Control of an Excavator

Researcher (PhD) : Vivek Chacko (vchacko@bournemouth.ac.uk)  
Supervisors: Prof. Hongnian Yu, Dr. Shuang Cang

## 1. Introduction

In the wake of recent natural and man-made disasters, rescue robots have gained focus of the international scientific community. It is desired to introduce robotic rescue teams in order to minimize loss of life, as well as safeguard rescuers.

Autonomous robots are especially desirable since in the disaster affected zone owing to stress and fatigue in human rescuers, as well as due to difficulty in communication.

Autonomous robotic excavators can spearhead rescue operations and act as forerunners for other specialized rescue robots which would enhance effectiveness of disaster rescue operations.

## 2. Aim

The aim of this research is to model, and design adaptive control of an excavator to be used in rescue operations in disaster zones

## 3. Motivation

Recent natural and man-made **urban disasters** e.g. Fukushima incident and WTC collapse, have highlighted the need for **specialized rescue robots** to assist human rescue teams.

Quick response and identification of trapped human beings is essential for **saving human lives**.

Disaster sites can be **hazardous** for human beings owing to instability of debris, limited perception, chemical and biological hazards.<sup>[1]</sup>

While manually operated **excavators** are ubiquitous, autonomous excavators are difficult to model owing to their **complex dynamics**, and their **complex environment interaction models**.<sup>[3]</sup> Moreover, excavator systems with autonomous digging capability for rescue operations are **yet to be implemented**.

Design of an adaptive control of excavator system capable of performing automatic excavation in **different types of terrain** would be the first step towards achieving a remote controlled and/or autonomous excavator suitable for diverse applications ranging from rescue operations to construction industry.

## 4. Current Work/Methodology

1. Literature survey of technical papers on excavator dynamic modelling and adaptive control, and on soil-tool interaction models
2. Modelling excavator systems (Kinematic and Dynamic models)
3. Design suitable adaptive control system

## 5. Challenges

1. Incorporating an accurate environment interaction (soil-tool) model <sup>[3]</sup>
2. Designing the Adaptive Control System for the above model



Fig.1. Typical mini-excavator

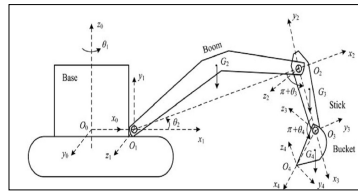


Fig.2. Schematic of an excavator<sup>[2]</sup>

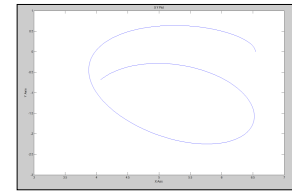


Fig.3. From dynamic model: path of excavator bucket end at constant load

## 6. Research Progress

1. Survey of relevant literature including technical and knowledge improvement journals/articles seeking inspiration from nature *"Nature provides us with some of the best designs which can inspire engineering design towards higher efficiency and better durability."*
2. Development of forward and inverse kinematic models for mini-excavator
3. Development of Dynamic model for excavator systems
4. Results from model developed in suitable software environment (Fig.3)

## 7. Future Research Plan

1. Incorporate accurate and efficient soil-tool interaction model into current dynamic model
2. Design adaptive control for above model
3. Implement the new model and validate results

## References

- [1] Y. Liu and G. Nejat, "Robotic Urban Search and Rescue: A Survey from the Control Perspective," Journal of Intelligent & Robotic Systems, vol. 72, 2013.
- [2] Y. Liu, M. Hasan, and H. Yu, "Modelling and remote control of an excavator." Int. Journal of Automation and Computing, Vol. 7, Issue 3, pp 349-358, 2010.
- [3] S. Singh, "Learning to predict resistive forces during robotic excavation," vol. 2. IEEE, pp. 2102-2107, 1995.

# Simulations in the design of a 3-link manipulator prototype

## Introduction

Simulation is the imitation of the operation of a real-world process or system over time (Banks et al). Computer aided design (CAD) software is used by engineers to construct virtual prototypes.

These enable faster product development and reduces overall cost, and represent physical objects in a virtual space with increased accuracy. Virtual prototypes can be used for kinematic/motion analysis.

Advanced analysis – Dynamics, deflection, requires specialized software for simulation.

Our research interest is dynamics and control of 3 link mechanisms, serial and parallel actuated.

In existing literature, rudimentary approximations in numerical model, especially on physical parameters of links, unchanged over decades. To overcome this, CAD-Multi-body dynamics package method of simulation is used.

## CAD Design

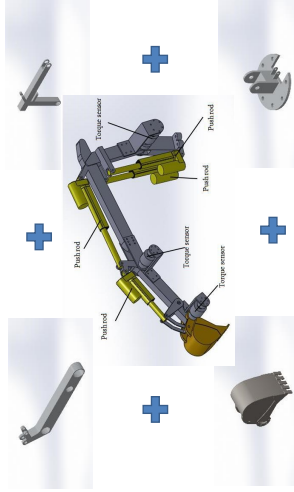


Fig 1 CAD assembly of prototype for parallel actuated mechanism

Table 1 Link properties of main mechanism links

Part Part Name	Design	Material	Density(g/m <sup>3</sup> )	Mass(kg)	Centre of mass (m)
1	Base			1.29	(-0.01,-0.07,0)
2	Boom	Al 7075-T6	2810	3.52	(0.08,0.22,0)
3	Slick			0.94	(0.1,0.0)
4	Bucket	A2 Tool steel	7850	1.19	(0.05,0.04,0)

## Multi-body Dynamics

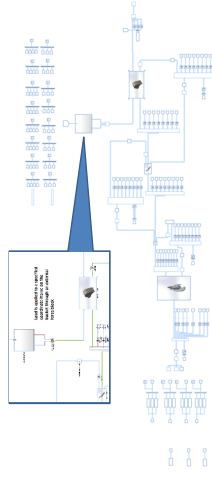


Fig 2 SimMechanics 2G simulation model for parallel mechanism. Inset shows the low load is applied on the end effector

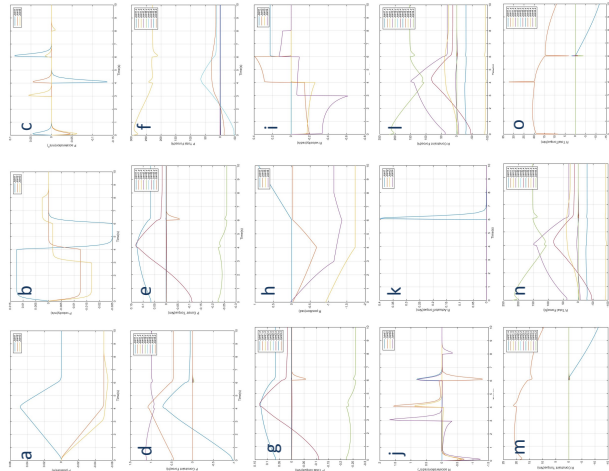


Fig 3 Multi-body dynamics simulation for 4 degrees of freedom system a-g: Performance parameters for the parallel actuators, h-o: Performance parameters for revolute joints

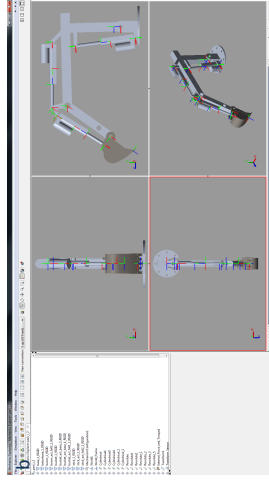
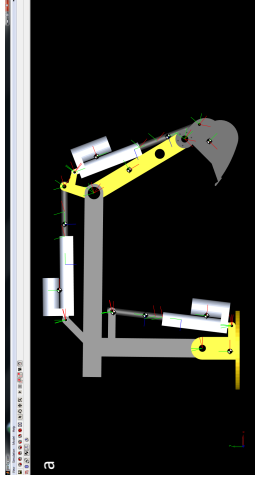


Fig 4 a. Visualization from SimMechanics 3G b. visualization from SimMechanics 2G

## Conclusion

Advanced simulations across multiple platforms and methods have been conducted. Tested under load conditions, and different performance parameters have been recorded and analysed.

## Future Work

Input signal design  
Advanced Controller design for automated actuation  
Hardware in loop simulation  
Physical prototype and control

## References

Banks, J., Carson, J. S., and Nelson, B. L., 2000. *DM Nicol, Discrete-Event System Simulation*. Prentice Hall Englewood Cliffs, NJ, USA.

The authors wish to acknowledge the funding from Erasmus Mundus program under EU cLINK project and the IRSES program under the RABOT project (FP7-PEOPLE-2012-IRSES-318902).

# MODELLING, CONTROL AND SIMULATION OF EXCAVATOR MANIPULATOR

## Aim

The aim of this research is to develop a user-friendly, next generation excavator having behaviour-based control, resulting in an advanced simulator package for Search and Rescue/Construction Industry.

## Objective

1. Reduce risk
2. Improve skills
3. Novel technique

## Challenges

1. Replicating human behaviour
2. Modelling
3. Safe Operation
4. Simulation techniques

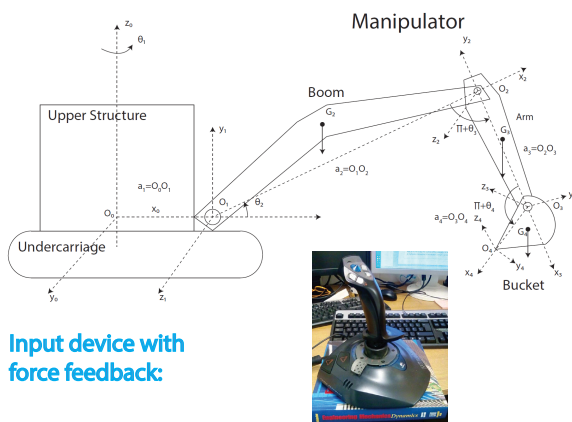
## Task Plan

1. Dynamic Model
  - a. Compare existing dynamic models
  - b. Derive dynamic model from first principles using Euler-Lagrange Method
  - c. Improve upon dynamic model
2. Control Techniques
  - a. Add external controller device
  - b. Behaviour based control  
-combination of PID,CTC,RC/AC/ILC
  - c. Identify rules for behaviour switching
3. Simulation
  - a. Compare existing simulators
  - b. Select appropriate simulator
  - c. Combine physics model with simulator
4. Testing
  - a. Performance testing
  - b. Sensor input for data modelling

Generalized dynamics equation:

$$D_a(\theta)\ddot{\theta} + C_a(\theta, \dot{\theta})\dot{\theta} + G_a(\theta) + B_a(\dot{\theta}) = \Gamma\tau_a - F_L$$

Schematic of excavator nomenclature:

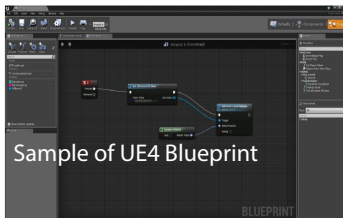


Input device with force feedback:

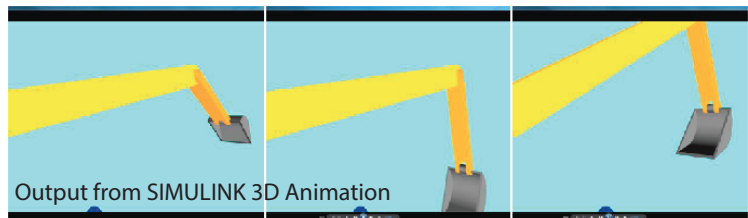
## Tools

MATLAB/Simulink  
Autodesk Inventor  
Unreal Engine 4  
Visual Studio

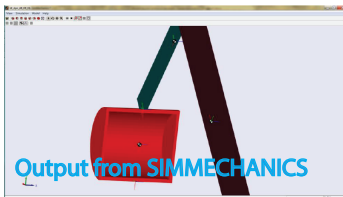
## Results



Sample of UE4 Blueprint



Output from SIMULINK 3D Animation



Output from SIMMECHANICS

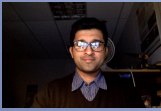
## Publications

Chacko, V.; Hongnian Yu; Shuang Cang; Vladareanu, L., "State of the art in excavators," Advanced Mechatronic Systems (ICAMechS), 2014 International Conference on , vol., no., pp.481,488, 10-12 Aug. 2014

## Acknowledgements

Thanks to Dr. Glyn Hadley, Neil Vaughn and Navid Aslani for their support





# Complex Interacting Systems working in Harsh Operating Condition



Vivek Chacko ([vchacko@bournemouth.ac.uk](mailto:vchacko@bournemouth.ac.uk))

Dr. Zulfiqar Khan, Dr. Mehran Koohgilani

NanoCorr, Energy & Modelling Research Theme, Department of Design & Engineering, SciTech, Bournemouth University

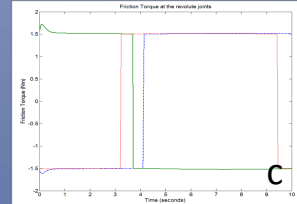
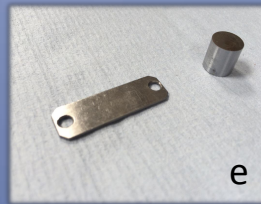
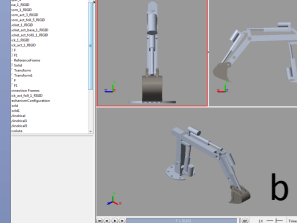
## Introduction

The effect of pollutants harsh environments on load bearing interactive surfaces of manipulators deployed in harsh environments need to be investigated develop a durable and reliable design.

First, the dynamics of the mobile manipulator has been designed in CAD (SolidWorks), and analysed using the cutting edge multi body dynamics simulation (SimMechanics 2<sup>nd</sup> generation).

Friction model has been applied to the revolute and prismatic joints and their outputs have been recorded.

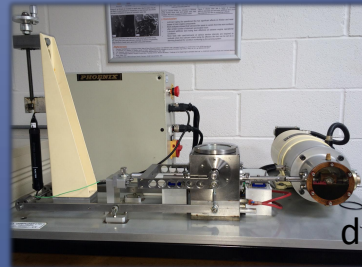
Experiments are being conducted for the evaluation of the contact performance characteristics under the effect of harsh environments in contacts.



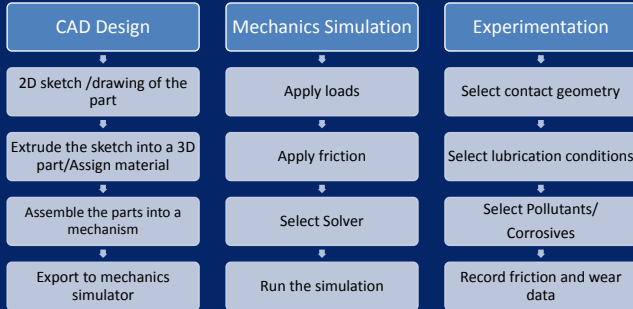
## Research Questions

- How to improve modelling and simulation of the manipulator arm dynamics seen in literature?
- How are friction and wear at the contact influenced by the harsh environment?
- Is there a unified model linking the dynamics and the tribological performance of the contact for the given operating condition?

Figure:  
 a. High quality virtual prototype  
 b. Manipulator mechanics simulation  
 c. Friction torque exerted at revolute joints  
 d. TE57/77 Tribometer  
 e. Fixed and moving samples for use in the tribometer



## Methodology



## Results

- New dynamic simulation method has been validated
- The effect of friction on the manipulator dynamics has been analysed.
- Friction and wear values recorded from experiment

## Future Work

- Continuation of experimental analysis
- Consolidation of empirical data for different contact conditions
- Mathematical model of friction and wear based on the experimental data

### Acknowledgements

- The author is grateful to Bournemouth University for the research funding
- Special thanks to Dr. Nigel Garland, Dr. Adil Saeed, Rizwan Bajwa and Abu Saifullah



## Glossary

$\alpha$	Bearing contact angle, exponential coefficient for revolute friction model or generalised angular acceleration
$\alpha_i$	Offset/twist angle of link $l_i$
${}^{i+1}\vec{\alpha}_{0i}$	Angular acceleration of $i^{\text{th}}$ coordinate in the $i + 1^{\text{th}}$ coordinate system
${}^{i+1}\vec{\alpha}'_{0G_i}$	Angular acceleration of the centre of gravity $i^{\text{th}}$ coordinate in the $i + 1^{\text{th}}$ coordinate system
$\gamma$	Duty cycle of pulse coating current
$\varepsilon_i$	Angle between link $l_i$ and x axis
$\theta$	Angle of contact in the bearing, position vector
$\dot{\theta}$	Angular velocity vector
$\ddot{\theta}$	Angular acceleration vector
$\theta_i$	Joint angle between links $i$ and $i + 1$
$\dot{\theta}_{i+1}$	Angular velocity of link $i + 1$
$\ddot{\theta}_{i+1}$	Angular acceleration of link $i + 1$
$\dot{\psi}_m, \dot{\psi}_s$	State parameter (angular velocity) for friction torque equation
$\mu$	Coefficient of friction or COF
$\mu\text{m}$	micron
$\rho$	Density
$\tau$	Actuation torque, differential coefficient
$\tau_{brk}$	Breakaway friction torque
$\tau_C$	Coulomb friction torque
$\tau_f$	Friction Torque
$\tau_L$	External torque applied on end-effector
$\tau_s$	Stribeck friction torque
$\tau_v$	Viscous friction torque
$\varkappa$	State parameter for generalised friction equation
$\omega$	Angular velocity generalised, scotch-yoke mechanism
$\dot{\omega}$	Generalised angular velocity derivative
$\omega_{thr}$	Threshold velocity
${}^{i+1}\vec{\omega}_{0i}$	Angular velocity of $i^{\text{th}}$ coordinate in the $i+1^{\text{th}}$ coordinate system



$a$	Generalised acceleration
$a_i$	Length of link
A	Ampere, atomic weight of the metal in grams per mole
${}^i a_{0G_i}$	Acceleration of the centre of gravity of link
$A_{i-1}^i$	Coordinate frame transformation matrix
Al	Aluminium
ASTM	American Society for Testing and Materials
$B(\dot{\theta})$	Frictional Torque matrix
BS	British standards
°C	Degree Celsius
C	Carbon
$C(\theta, \dot{\theta})$	Coriolis/Centripetal force matrix
CA	Prefix denoting cylindrical grease-lubricated contact specimens
with	nickel alumina nanocoating
CAD	Computer Aided Designing
CAE	Computer Aided Engineering
CFM	Combined friction model
CG	Prefix denoting cylindrical grease-lubricated contact specimens
CO	Prefix denoting cylindrical oil-lubricated contact specimens
COF	Coefficient of friction
$\cos \theta_i$	Cosine of the angle $\theta_i$
cm	centimetre
Cr	Chromium
.csv	Comma separated value
$c_v$	Velocity coefficient
CVD	Chemical vapour deposition
$D(\theta)$	Inertia matrix
DAE	Differential algebraic equation
DC	Direct current

$D_f$	Distance from the lowest point of the upper shaft to the top of the fixed specimen
$d_i$	Scaling factor in kinematic transformation equation, Distance between two adjacent links
$D_t$	Total inner distance between the upper shaft and the lower shaft
DIN	Deutsches Institut für Normung
DLC	Diamond like carbon
dm	decimetre
ED	Electrodeposition
EDM	Electro discharge machining
EL	Euler Lagrange method
EN	European norms
EOM	Equations of motion
$f$	frequency of the pulse current, viscous friction coefficient
F	Prefix for grease lubricated contacts
$F$	Generalised force exerted on the body, Faraday's constant in coulombs per equivalent charge
FA	Prefix denoting grease-lubricated pin sliding contact specimens with alumina nanocoating
$F_{brk}$	Breakaway friction force
$F_C$	Coulomb friction force
FEA	Finite element analysis
FG	Prefix denoting grease-lubricated pin contacts
FG0	Prefix denoting grease-lubricated pin sliding contact specimens with nickel graphene nanocoating
$f_i$	Degrees of freedom
$F_f$	Total friction force
FO	Prefix denoting oil-lubricated pin contacts
${}^i F_0^i$	Force acting on the centre of the link expressed in coordinate frame $i$
$F_n$	Normal force acting on the joint
$G(\theta)$	Gravity force matrix
g/l	grams per litre
GFM	Generalised friction model

GUI	Graphical user interface
H	Hydrogen
HDR	High dynamic range
$H_p$	Distance to the top of the pin holder
HV	Vickers hardness
Hz	Hertz
$I$	Generalised moment of inertia
$I_{av}, I_{ave}$	Average current
$i_{an}$	Anodic peak current density
${}^i I_{0i}$	Moment of inertia of link $i$ in its native coordinate frame
$i_p, I_p$	Cathodic peak current density
IJE	Impinging jet electrode
$I_L$	Limiting current density
ISO	International standards organisation
$j$	Number of joints
K	Kelvin
${}^{i+1} \vec{k}_{zi}$	Unit vector along z axis of the revolute joint
kg	kilogram
kgf	kilogram force
kV	kilo volt
$l_i$	Length of link $i$
$L_f$	Length/radius of the fixed specimen
$m$	Generalised mass of the body
$M$	Generalised momentum, mobility of linkages
M,mol	Mole
mA	milli Ampere
.mat	MATLAB data file
MBD	Multibody dynamics
$m_i$	Mass of the $i^{\text{th}}$ link
${}^i \vec{M}_0^i$	Torque acting on the centre of the link expressed in coordinate frame $i$
mDOF	Multiple degrees of freedom
MMC	Metal matrix composite

Mn	Manganese
MPa	Mega pascal
ms <sup>-1</sup>	metres per second
ms <sup>-2</sup>	metres per square second
n	Number of links
$n$	Valence in equivalents per mole
N	Number of links of an open chain manipulator, count, Newton
Na	Sodium
NE	Newton Euler method
NLGI	National Lubricating Grease Institute
nm	nano metre
Nm	Newton metre - unit of torque
O	Oxygen
ODE	Ordinary differential equation
P	Phosphorous
PAM	Pneumatic air muscle
${}^i p, p^i$	Generalised position in the $i^{\text{th}}$ coordinate system
$p_{ix}$	Position of a point on the link projected on to the $x$ axis of the coordinate reference frame
${}^{i+1} \vec{p}_{0(i+1)}$	Position in the $i + i^{\text{th}}$ coordinate system
$\vec{p}_{0G_i}$	Position of the centre of gravity of the $i^{\text{th}}$ link
PED	Pulse electrodeposition
PEEK	Polyether ether ketone
pH	potenz hydrogen
PIIID	Plasma Immersion Ion Implantation and Deposition
PL	Particle loading
$P_{max}$	Maximum pressure inside the contact
PP	Pulse plating
PPE	Parallel plate electrode
PRP	Pulse reverse plating
PS	Physical signal
PVC	Polyvinyl chloride
PVD	Physical vapour deposition
$[q, \dot{q}, \ddot{q}]$	Generalised position, velocity and acceleration coordinates

$R$	Radius of bearing/bushing, radius of the scotch-yoke pin
RA	Research aim
$R_a$	Roughness average
rad	radian
RAM	Random-access memory
RMS	Root mean squared
RO	Research objective
RP	Rapid prototyping
rpm	Revolutions per minute
RQ	Research question
$R_s$	Radius of contact
$s$	Differential coefficient
$S$	Area of coating
S	Sulphur
SAR	Search and Rescue
sDOF	Single (one) degree of freedom
SEM	Scanning electron microscope
Si	Silicon
.slx	Simulink file
.stl	Stereolithography
$r_t$	x-coordinate of end effector
$t$	Time
$T$	Torque required to overcome friction, thickness of coating
$T_c$	Thickness of the cup.
$T_e$	External resultant torque
$T_f$	Friction torque
.tif	Transferable image format
$t_{on}, T_{on}$	Cathodic pulse length
$t_{off}, T_{off}$	Pulse pause
$t_{rev}, T_{rev}$	Anodic pulse length
$T_m$	Thickness of the moving flat test specimen
$T_{pl}$	Plate specimen thickness
$T_s$	Thickness of shim
U	Urban Search and Rescue

UK	United Kingdom
$v$	Velocity/Relative velocity
$\dot{v}$	Generalised differential of velocity or acceleration
V	Vanadium
${}^{i+1}\vec{v}_{0i}$	Translational velocity of the $i^{\text{th}}$ coordinate in the $i + 1^{\text{th}}$ coordinate system
${}^{i+1}\vec{v}_{0G_i}$	Translational velocity of the centre of gravity of $i^{\text{th}}$ coordinate in the $i + 1^{\text{th}}$ coordinate system
VDU	Visual display unit
VE	Virtual environments
VP	Virtual prototypes
$v_{thr}$	Threshold velocity/Relative velocity
$v_R, v_C$	Absolute velocities across terminals
$W$	Load acting on the bearing
W	Tungsten (Wolfram)
WTC	World Trade Centre
$x$	Magnitude of Simulink signal
$x, \dot{x}, \ddot{x}$	Linear displacement, velocity and acceleration of the scotch-yoke mechanism
XRD	X-ray diffraction
$z_t$	y-coordinate of end-effector